

**CHARACTERISATION OF CROSS-LINKING AND MOISTURE
INGRESS DETECTION IN AN EPOXY/AMINE RESIN USING
FIBRE-OPTIC SENSORS**

by

RAMANI SALMALEE MAHENDRAN

A thesis submitted to
The University of Birmingham
for the degree of

DOCTOR OF PHILOSOPHY

School of Metallurgy and Materials
College of Engineering and Physical
Science
The University of Birmingham
November 2010

UNIVERSITY OF
BIRMINGHAM

University of Birmingham Research Archive

e-theses repository

This unpublished thesis/dissertation is copyright of the author and/or third parties. The intellectual property rights of the author or third parties in respect of this work are as defined by The Copyright Designs and Patents Act 1988 or as modified by any successor legislation.

Any use made of information contained in this thesis/dissertation must be in accordance with that legislation and must be properly acknowledged. Further distribution or reproduction in any format is prohibited without the permission of the copyright holder.

ABSTRACT

Thermosetting resins are being used increasingly as matrix materials in advanced fibre-reinforced composites. It is well known that the processing conditions used to manufacture the composite can have a major influence on its mechanical integrity in service. In addition, the processing parameters can also affect the ingress of moisture in thermosetting resin and composites. The feasibility of using optical fibre-based sensor systems for monitoring cross-linking reaction has been demonstrated previously. However, little work has been reported on the deployment of a single sensor to study the cross-linking kinetics and the diffusion of moisture.

In the current work, four low-cost sensor designs were evaluated for *in situ* monitoring of the cross-linking reactions of an epoxy/amine resin system. One of these sensor designs was selected and used to investigate in detail the cross-linking kinetics. Excellent correlation was observed between the cross-linking data obtained from the sensors and conventional transmission spectroscopy. Semi-empirical models were used successfully to describe the cross-linking behaviour of the epoxy/amine resin system that was used in this study.

Subsequent to monitoring the cross-linking reactions, the fibre-optic sensors were used to study the diffusion of moisture in the cross-linked resin system. Conventional gravimetric measurements were also carried out to enable the correlation with the data obtained from the fibre optic sensors. It was demonstrated that the fibre-optic sensors were capable of giving information on the “localised” diffusion of moisture in the neat-resin plaques. Three previously published models were investigated and localised diffusion of moisture in the neat-resin showed non-Fickian behaviour.

ACKNOWLEDGEMENTS

I am deeply grateful to my research supervisors Dr S N Kukureka and Prof G F Fernando, without whose enthusiasm, kindness, knowledge, support and continuous guidance, none of this work would have been possible.

I also grateful and special appreciation must be due to Dr R Badcock without whose constructive criticism and valuable guidance, completing this work would not be possible.

Appreciation must also go to the following members of the academic staff of the University of Moratuwa, Sri Lanka for their knowledge, encouragement and guidance: Dr N Munasignhe (former head of department, Materials Engineering), Dr Y Gunapala (former senior lecturer, Materials Engineering) and Dr O Gunapala (senior lecturer, Chemical Engineering). I would be remiss if I did not acknowledge the influence on my early career by Mr K Dherasekara (Director – Operations), Mr S Wijesinghe (Chief Operations Officer) and Mr L Peiris (Director – Administration) of Agro Marine Group, Sri Lanka, who shaped my professional career and were role models of my past and for the future.

I also like to acknowledge senior and former members of the Sensors and Composites Group, Dr R Chen, Dr L Wang, Dr V R Machavaram and Dr S D Pandita for all the support, bringing new ideas and for sharing research experience and expertise in their respective fields during my research. I would also like to thank Mr F Biddlestone for his technical assistance, guidance and input on various aspects of experimental methods, instrumentation and data analysis. I would also like to acknowledge Mr C Barrow and Mr P Turner of Bruker UK Limited for their

continual assistance and support on hardware and software issues related to Fourier transform infrared spectroscopy. Appreciation must also be due to my colleagues in the Sensors and Composites Group for their help and support during my study. Special thanks are due to Mr AKR Nair and Mr M Shafiq Irfan for their valuable help on completing my thesis.

I would also like to thank the current and former staff members of the school of Metallurgy and Materials for their valuable assistance throughout my research: Mrs. A Cabezas, Mrs. J Corbett, Mr D Boole, Mr J Lane, Mr P Stanley, Mr M T Cunningham, and Ms. A Rogers.

Finally, the largest debt is due to my husband who made many sacrifices in his career in order to help me to realise my goal of completing my PhD and for his dedication in helping me in every way possible during my study. I would like to express my deepest gratitude and love for my mum, dad, my brother and my daughter for their never-ending love, guidance and encouragement. I could not have completed this work without their support.

CONTENTS

CHAPTER 1. INTRODUCTION

1.1 MOTIVATION.....	1
1.2 AIMS AND OBJECTIVES.....	4
1.3 OUTLINE OF THE THESIS.....	4

CHAPTER 2. CROSS-LINKING AND HYGROTHERMAL AGEING OF THERMOSETTING RESINS

2.1 INTRODUCTION.....	6
2.2 CHEMISTRY OF EPOXY/AMINE RESIN SYSTEMS.....	7
2.2.1 Reaction mechanism during cross-linking.....	10
2.2.2 Cross-linking kinetics.....	18
2.3 MONITORING OF CROSS-LINKING IN EPOXY/AMINE RESIN SYSTEMS.....	27
2.3.1 Conventional analytical techniques.....	27
2.3.1.1 Fourier transform infrared spectroscopy.....	29
2.3.1.2 Differential scanning calorimetry.....	40
2.3.2 <i>In situ</i> fibre-optic based techniques.....	43
2.3.2.1 Absorption-based fibre-optic techniques.....	44
2.3.2.2 Intensity-based fibre-optic techniques.....	52
2.3.2.3 Other fibre-optic techniques.....	53
2.4 HYGROTHERMAL AGEING IN EPOXY/AMINE RESIN SYSTEMS.....	55
2.4.1 Nature of water in epoxy resins due to moisture absorption.....	55
2.4.2 Fundamental laws of diffusion in polymers.....	57
2.4.2.1 Fickian diffusion.....	57

2.4.2.2 Non – Fickian diffusion.....	59
2.4.3 Parameters affecting diffusion kinetics of water.....	66
2.4.3.1 Influence of temperature.....	66
2.4.3.2 Influence of processing conditions.....	66
2.4.3.3 Influence of hygrothermal history.....	67
2.4.3.4 Influence of mixing ration of epoxy/amine formulations.....	68
2.4.3.5 Influence of microstructure.....	69
2.5 MONITORING OF HYGROTHERMAL AGEING IN EPOXY/AMINE RESIN SYSTEMS.....	69
2.5.1 Conventional analytical techniques.....	69
2.5.1.1 Differential scanning calorimetry.....	70
2.5.1.2 Thermo gravimetric analysis.....	72
2.5.1.3 Dynamic mechanical thermal analysis.....	72
2.5.1.4 Fourier transform infrared spectroscopy.....	74
2.5.2 <i>In situ</i> Fibre-optic based techniques.....	77
2.5.2.1 Absorption-based fibre-optic techniques.....	79
2.5.2.2 Other fibre-optic techniques.....	80
2.6 CONCLUSIONS.....	81

CHAPTER 3. EXPERIMENTAL METHODS

3.1 INTRODUCTION.....	82
3.2 MATERIALS.....	83
3.2.1 Resins.....	83
3.2.2 Fibres.....	84
3.3 SENSOR INTERROGATION.....	84
3.4 FIBRE-OPTIC SENSOR FABRICATION.....	84
3.4.1 Single-fibre transmission sensor.....	85
3.4.1.1 Basic sensing concept.....	85
3.4.1.2 Epoxy substrate sensor design.....	86
3.4.1.3 Capillary support sensor design	90
3.4.1.4 Abraded capillary sensor design	92

3.4.2	Single-ended reflectance sensor.....	94
3.4.2.1	Basic sensing concept.....	94
3.4.2.2	Capillary reflector sensor design	96
3.5	PREPARATION OF FIBRE CONNECTORS.....	98
3.6	DETERMINATION OF OPTIMUM GAP AT THE SENSING REGION.....	100
3.6.1	Single-fibre transmission sensor.....	100
3.6.2	Single-ended reflection sensor.....	101
3.7	CHARACTERISATION OF CROSS-LINKING KINETICS OF THE EPOXY/AMINE RESIN SYSTEM.....	103
3.7.1	Temperature monitoring.....	103
3.7.2	<i>In-situ</i> monitoring of cross-linking reactions.....	104
3.7.2.1	Fibre-optic transmission spectroscopy.....	104
3.7.2.2	Fibre-optic reflectance spectroscopy.....	106
3.8	CHARACTERISATION OF DIFFUSION KINETICS OF WATER IN THE EPOXY/AMINE RESIN SYSTEM.....	107
3.8.1	Conventional analytical techniques.....	107
3.8.1.1	Sample fabrication for conventional diffusion analysis.....	108
3.8.1.2	Environmental conditioning of the cast resin for diffusion experiments.....	109
3.8.1.3	Diffusion experiments.....	109
3.8.1.4	Gravimetric analysis.....	110
3.8.1.5	Thermo-mechanical analysis.....	110
3.8.1.6	Dynamic scanning calorimetry.....	111
3.8.1.7	Thermo-gravimetric analysis.....	112
3.8.1.8	Fourier transform infrared spectroscopy.....	112
3.8.2	Fibre-optic transmission spectroscopy.....	112
3.8.2.1	Sensor interrogation for monitoring moisture ingress.....	120
3.9	PROOF-OF-CONCEPT OF MULTI-FUNCTIONAL SENSOR.....	121
3.9.1	Sensor design.....	121
3.9.2	Sensor fabrication.....	123
3.9.3	Sensor interrogation and monitoring of cross-linking reaction.....	124
3.9.4	Characterization of EFPI and FBG Sensors.....	126

3.10 CONCLUSIONS.....	128
-----------------------	-----

CHAPTER 4. FIBRE-OPTIC NEAR-INFRARED SPECTROSCOPY AND OPTIMISATION OF SENSOR DESIGNS

4.1 INTRODUCTION.....	130
4.2 RAY-OPTIC CONSIDERATIONS FOR FIBRE-OPTIC SPECTROSCOPY.....	131
4.2.1 Fibre-optic transmission spectroscopy.....	131
4.2.2 Fibre-optic reflectance spectroscopy.....	134
4.3 FIBRE-OPTIC SENSOR DESIGNS.....	137
4.3.1 Fibre-optic transmission spectroscopy.....	137
4.3.1.1 Epoxy substrate sensor design.....	138
4.3.1.2 Capillary support sensor design.....	139
4.3.1.3 Abraded capillary sensor design	141
4.4 OPTIMUM CAVITY LENGTH FOR FIBRE-OPTIC SPECTROSCOPY.....	145
4.4.1 Fibre-optic transmission spectroscopy.....	145
4.4.2 Fibre-optic reflectance spectroscopy.....	148
4.5 CONCLUSIONS.....	153

CHAPTER 5. MONITORING CROSS-LINKING USING FIBRE-OPTIC SPECTROSCOPY

5.1 INTRODUCTION.....	155
5.2 PEAK ASSIGNMENTS FOR THE EPOXY/AMINE RESIN SYSTEM.....	156
5.2.1 Analysis of absorption bands during cross-linking.....	160
5.3 QUANTITATIVE ANALYSIS OF CHANGE IN FUNCTIONAL GROUPS DURING CROSS-LINKING.....	169
5.3.1 Deconvolution of epoxy absorption band.....	170
5.3.2 Quantitative analysis of functional groups using fibre-optic transmission spectroscopy.....	184
5.3.2.1 Epoxy group analysis.....	184

5.3.2.2	Primary amine group analysis.....	186
5.3.2.3	Secondary amine group analysis.....	187
5.3.2.4	Tertiary amine group analysis.....	191
5.3.2.5	Hydroxyl group analysis.....	192
5.3.2.6	Summary of functional group analysis.....	194
5.3.3	Quantitative analysis of functional groups using fibre-optic reflectance spectroscopy.....	199
5.4	EMPIRICAL MODELLING OF CROSS-LINKING KINETICS USING FIBRE-OPTIC SPECTROSCOPY.....	205
5.4.1	Fibre-optic transmission spectroscopy.....	205
5.4.2	Fibre-optic reflectance spectroscopy.....	211
5.4.3	Comparison of cross-linking kinetics obtained using fibre-optic spectroscopy.....	214
5.4.4	Relationship of degree of cross-linking and refractive index.....	216
5.4.4.1	Ray optics of fibre-optic transmission spectroscopy.....	216
5.4.4.2	Ray optics of fibre-optic reflectance spectroscopy.....	220
5.4.4.3	Comparison of ray optics of different fibre-optic techniques.....	223
5.5	CONCLUSIONS.....	226

CHAPTER 6. PROOF-OF-CONCEPT OF MULTI-FUNCTIONAL SENSOR DESIGN

6.1	INTRODUCTION.....	228
6.2	TEMPERATURE AND STRAIN SENSITIVITY OF THE SENSOR DESIGN.....	229
6.2.1	Temperature sensitivity of Fabry-Perot interference sensor and fibre Bragg grating sensor.....	229
6.2.2	Strain sensitivity of Fabry-Perot interference sensor and fibre Bragg grating sensor.....	236
6.3	MONITORING OF CROSS-LINKING REACTIONS.....	239
6.3.1	Quantitative monitoring of cross-linking reactions.....	239
6.3.2	Qualitative monitoring of cross-linking reactions.....	241

6.3.3 Simultaneous strain and temperature monitoring.....	243
6.4 CONCLUSIONS	246

CHAPTER 7. MOISTURE INGRESS MONITORING USING CONVENTIONAL TECHNIQUES

7.1 INTRODUCTION.....	248
7.2 GRAVIMETRIC METHOD.....	249
7.2.1 Kinetics of water absorption.....	249
7.2.2 Determination of the through-thickness concentration profile of the absorbed moisture.....	256
7.3 EFFECT OF HYGROTHERMAL CONDITIONING ON THE PROPERTIES OF THE EPOXY/AMINE RESIN SYSTEM.....	262
7.3.1 Thermo gravimetric analysis.....	264
7.3.2 Differential scanning calorimetry.....	266
7.3.3 Dynamic mechanical thermal analysis.....	272
7.3.4 Fourier transform near-infrared spectroscopy.....	282
7.4 CONCLUSIONS.....	285

CHAPTER 8. MONITORING OF MOISTURE INGRESS USING FIBRE- OPTIC TRANSMISSION SPECTROSCOPY

8.1 INTRODUCTION.....	287
8.2 QUANTITATIVE ANALYSIS OF CHANGES IN FUNCTIONAL GROUPS DURING HYGROTHERMAL CONDITIONING.....	288
8.2.1 Specimen configuration – I.....	288
8.2.2 Specimen configurations –II and –III.....	304
8.2.2.1 Absorption kinetics: specimen configuration – II.....	307
8.2.2.2 Absorption kinetics: specimen configuration – III.....	314
8.3 CONCLUSIONS.....	320

CHAPTER 9. GENERAL CONCLUSIONS AND FUTURE RECOMMENDATIONS

8.1 INTRODUCTION.....	321
8.2 CONCLUSIONS.....	321
8.3 FUTURE RECOMMENDATIONS.....	326
REFERENCES.....	330
APPENDIX – I	376
APPENDIX – II.....	379
APPENDIX – III.....	383
APPENDIX – IV.....	386

Chapter 1

Introduction

1.1 Motivation

Epoxy resins are widely used as a matrix material in fibre-reinforced composites (FRC) [1,2,3,4,5]. Generally, liquid and semi-solid epoxy resin systems are cross-linked using heat, light or e-beam to form a rigid irreversible network polymer. This transition involves the formation of a three-dimensional chemical network within the resin system. The ultimate physical and mechanical performance of a cross-linked resin and its applications in service environments are strongly dependent on the kinetics of cross-linking reactions.

Reaction kinetics is the study of the reaction rate and the factors that affect this rate. The reaction speed or the rate of reaction is the change of concentration of a reacting constituent in a given time. Cross-linking kinetics is important in the process optimisation of FRC with thermosetting resins as the matrix. In commercial high-performance FRC, the processing of matrix resins takes place at elevated temperatures (80 – 180 °C). The exothermic heat released during the cross-linking reactions can cause an increase in temperature in the interior of thick resin sections [6]. The presence of temperature gradients within the resin greatly

affects the uniformity of the reaction kinetics and extent of conversion of the reactants across the thickness of the resin [7,8]. Under extreme processing conditions, this may lead to permanent mechanical failure due to excessive resin shrinkage and/or the development of residual stresses when the resin cooled down to ambient temperature. Hence, a good understanding of the relationship between processing conditions and the reaction kinetics of the resin is one of the critical requirements for overall process optimisation. Numerous studies have been carried out to predict the reaction kinetics of thermosetting resins using various mathematical models.

For many years, significant attention has been focused on monitoring of cross-linking reactions using conventional off-line techniques. With reference to various on-line techniques developed for monitoring of cross-linking reactions, fibre-optic sensors attracted wide acceptance in engineering applications where robustness and cost of the sensing techniques are paramount. In comparison with other *in situ* sensing techniques, the relatively small size of fibre-optic sensors is suitable for embedded sensing applications within high-performance FRC structures.

In addition to process-related issues associated with epoxy-based systems, their behaviour under deleterious environmental conditions is also one of the major concerns [9,10]. Mechanical properties of thermosetting resin systems are strongly influenced by various weathering conditions. In many engineering applications, structural polymers are exposed to varying weathering conditions such as high temperature, lightning and electric discharge, ozone, moisture and contact with organic liquids such as fuels, lubricants and de-icing fluids. Amongst these harsh media, water is the most commonly encountered and epoxies show considerable affinity to absorbed moisture due to the polar nature of the cross-linked

structure. Research in the diffusion of moisture in polymers is continues to be of interest [11,12,13] and numerous efforts have been paid to predict absorption behaviour related to various types of epoxy resins and FRC using analytical methods [14,15,16,17,18]. Reduction in physical, thermal and mechanical properties, especially at elevated temperatures due to the absorbed moisture in epoxy resins has been reported.

In order to predict and enhance the lifetime of these glassy polymers in service environments, it is necessary to have an understanding of the internal chemical changes that take place in polymers due to absorbed moisture. The effect of processing conditions, residual stresses and resin shrinkage on the diffusion kinetics of water also needs to be understood. The majority of research in this current respect has been focussed on the influence of hygrothermal ageing on bulk properties of the cross-linked resin.

In situ sensing techniques can be used as an alternative solution for in-depth investigation of localised moisture diffusion phenomena in thermosetting polymers. Fibre-optic sensing techniques are ideally suited for remote monitoring of moisture diffusion [19,20]. However, the inherent characteristics of fibre-optic sensors for monitoring of moisture ingress in composites have not been explored fully. A limited amount of research has reported using embedded fibre-optic sensors for *in situ* monitoring of moisture diffusion in thermosetting resins [21,22,23]. However, the demonstrated sensing techniques have their own limitations that need to be addressed.

1.2 Aims and objectives

The overall aim of this research was to design and develop low-cost fibre-optic sensors for *in situ* monitoring of cross-linking reactions and monitoring of moisture diffusion in an epoxy resin system. The specific aims of the research were as follows:

- (i) To design and demonstrate the feasibility of using fibre-optic chemical sensors for performing *in situ* near-infrared spectroscopy;
- (ii) To monitor the cross-linking reactions of an epoxy resin system via fibre-optic near-infrared spectroscopy and to compare the reaction kinetics of the resin system obtained using different sensing concepts;
- (iii) To investigate the effect of hygrothermal ageing on the thermal, chemical and viscoelastic properties of the epoxy resin system using conventional analytical techniques;
- (iv) To monitor and predict the moisture transport phenomena in the epoxy resin using fibre-optic near-infrared spectroscopy.

1.3 Outline of the thesis

This thesis consists of nine chapters. The first part of Chapter Two provides a review of monitoring and modelling of cross-linking kinetics using conventional and fibre-optic based sensing techniques. The second part provides a literature survey on predicting diffusion of water in thermosetting resin systems.

Chapter Three presents a detailed description of the material and experimental procedures used in this study. Two main streams of experiments were carried out: (i) monitoring of cross-linking reactions of LY3505/XB3403 epoxy/amine resin system and (ii) monitoring of diffusion of moisture in the cross-linked resin system using conventional and fibre-optic techniques.

In Chapter Four, the feasibility of using different sensor designs for embedded applications is assessed and a discussion on the theory of optics involved in the sensing concepts is provided. Chapter Five presents the results of monitoring of cross-linking reactions of the epoxy/amine resin system via fibre-optic near-infrared spectroscopy. In particular, the chapter contains a detailed description of peak assignments of the resin system, and spectral analysis for predicting reaction kinetics as a function of cross-linking time and temperature. Both phenomenological and mechanistic approaches for explaining the reaction kinetics are discussed. Chapter Six describes proof-of-concept of a new multi-functional sensor design for *in situ* monitoring of the cross-linking reactions.

Chapter Seven considers the diffusion kinetics of water in the epoxy/amine resin system using traditional analytical techniques. The influence of absorbed moisture on the physical, thermal, chemical and viscoelastic properties of the bulk resin is also characterised. *In situ* monitoring of diffusion of moisture using fibre-optic near-infrared spectroscopy is demonstrated in Chapter Eight. Anomalies associated with localised diffusion behaviour of water in the resin system are discussed in detail. Finally, in Chapter Nine, overall conclusions of the research and recommendations for further work are presented.

Chapter 2

Cross-linking and hygrothermal ageing of thermosetting resins

2.1 Introduction

The first part of this chapter contains a literature survey on reaction mechanism of epoxy/amine resin systems, cross-linking kinetics and various techniques used for monitoring of cross-linking reactions. The second part reviews diffusion kinetics of water in epoxy/amine resin systems and conventional and *in situ* techniques used for monitoring hygrothermal ageing in the resin systems.

2.2 Chemistry of epoxy/amine resin systems

Epoxy resins are widely used as adhesives, coatings, encapsulants and more importantly as matrix materials for high performance FRC [24,25,26,27,28,29]. “Epoxy” is a term describing an oxygen atom bound to two linked carbon atoms. The term is commonly applied to a three-membered ring called an oxirane (see Figure 2.1). Examples of common epoxy resins used in engineering applications are shown in Figure 2.1.

Epoxies require cross-linking agents and/or catalysts to promote cross-linking [26]. Addition of a hardener or a cross-linking agent containing hydrogen atoms opens the three-membered ring with formation of a hydroxyl group. Application characteristics and ultimate physical, thermal and chemical properties of the resulting cross-linked network can be tailored by the selection of appropriate cross-linking agents. These properties include pot life, impregnation and wettability of the resin system. Commonly used cross-linking agents in commercial epoxy formulations are aliphatic and aromatic amines, anhydrides and polyamides [30]. The current review is focused on amine-based cross-linking agents.

Generally, amines can be categorised into two main classes: aliphatic and aromatic amines according to the types of hydrocarbon backbones involved and chemical structures of commonly used amines are shown in Figure 2.2. Numerous variations of aliphatic polyamines that contain a linear chemical chain between the amine groups have been synthesised and reported in the literature. Among them, widely used aliphatic amines are ethylenediamine (EDA), diethylenetriamine (DETA) and triethylenetriamine (TETA). Epoxies that polymerise with aliphatic amines exhibit highly cross-linked layers with good

thermal and chemical resistance. However, they are rather brittle and possess poor flexibility and impact resistance. Also they show high affinity to moisture and humidity, which make them unsuitable for use under damp conditions.

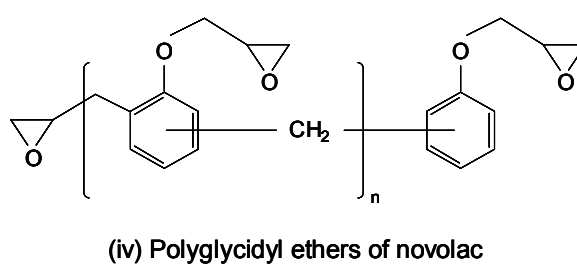
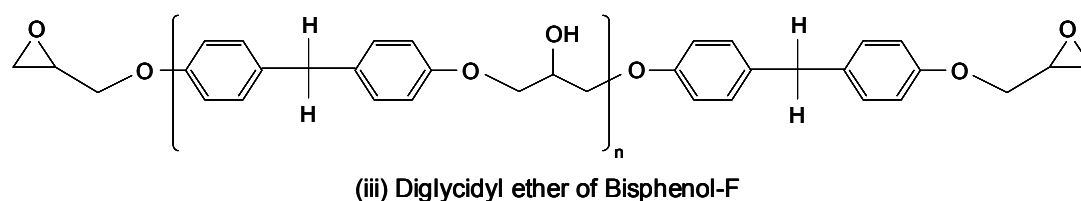
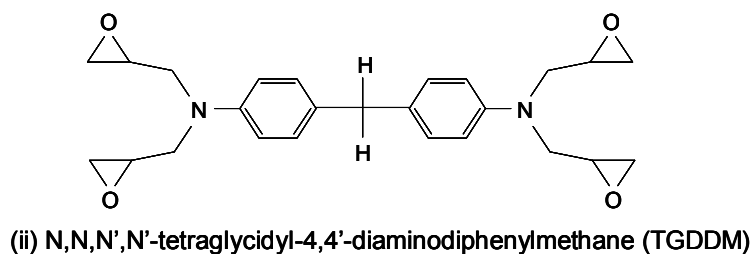
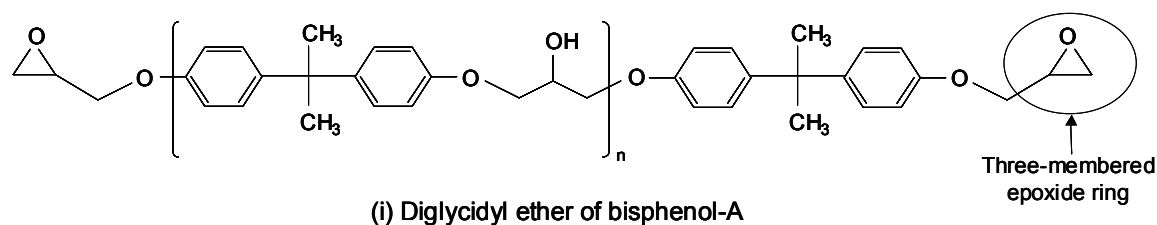


Figure 2.1 Main commercial epoxy resins, which are identified by monomer structure.

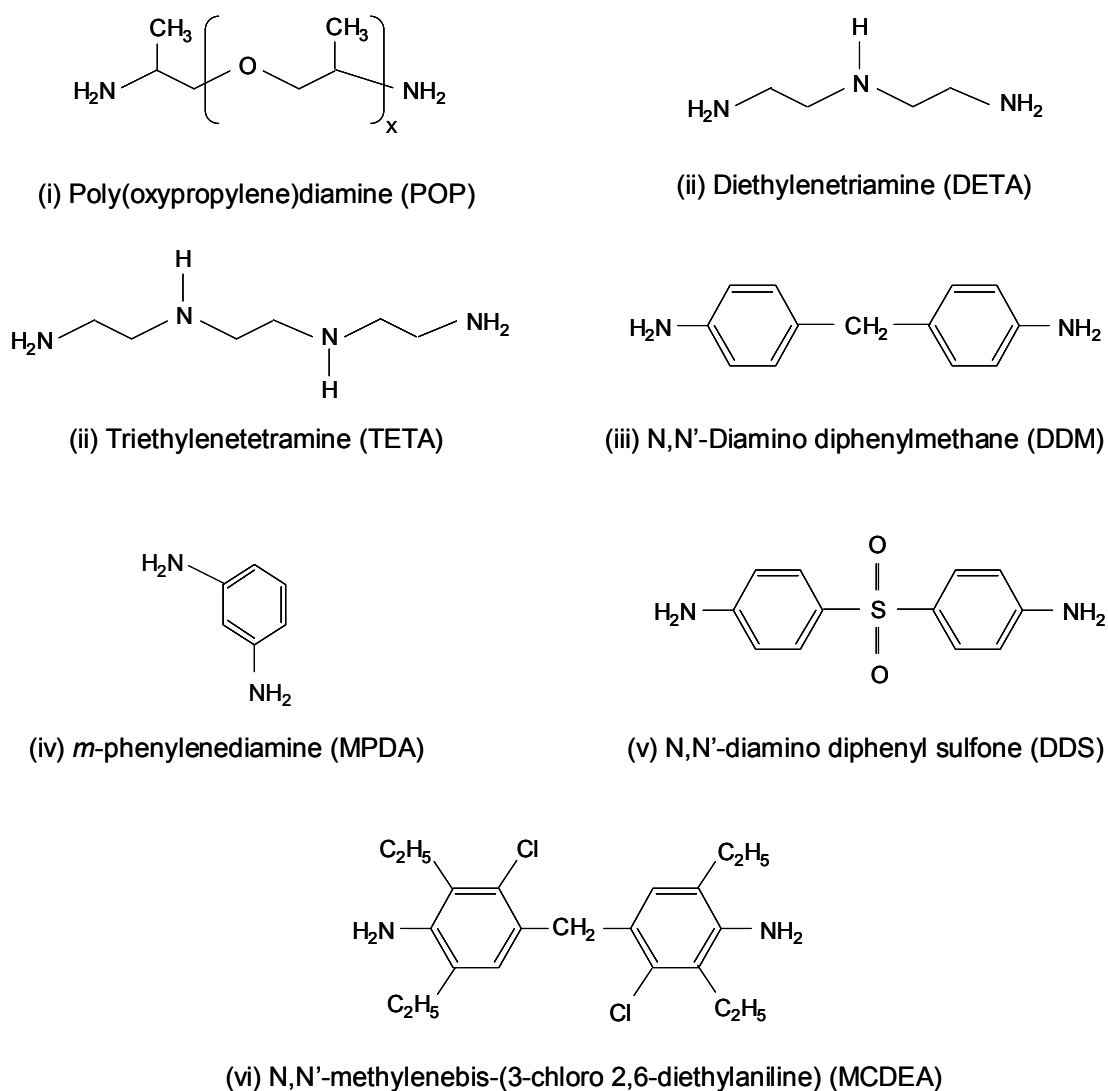


Figure 2.2 Main commercial amine-based cross-linking agents [30].

In the aromatic amines, the amine group is separated from the main backbone by rigid benzene rings. Most common aromatic amines are diamino diphenyl sulphone (DDS), diaminodiphenyl methane (DDM) and metaphenylenediamine (MPDA). The cross-linked epoxies with aromatic amines have high impact resistance as well as high thermal and chemical resistance compared to that possessed by epoxies cross-linked with aliphatic amines [31,32]. The aromatic ring unit with the newly-created hydroxyl as a result of cross-linking, improves the thermal and corrosion properties of the epoxy [33,34]. Furthermore, FRC

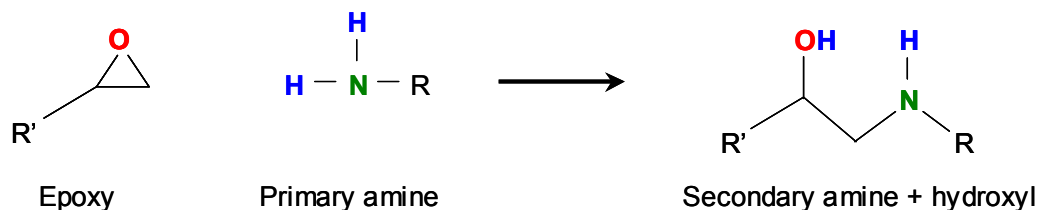
containing epoxies cross-linked with aromatic amines possess better mechanical properties compared with aliphatic amines [35,36].

Amine compounds are again sub-divided into primary, secondary, and tertiary amines, in which one, two, and three molecule(s) of ammonia (NH_3) have been substituted for hydrogen, respectively. The active hydrogen atoms attached to primary and secondary amines react with the oxirane (epoxy group) ring unit on the ends of the epoxy molecule. The reaction creates an OH (hydroxyl) pendant group. Tertiary amines are generally used as catalysts, commonly known as accelerators for cross-linking reactions.

2.2.1 Reaction mechanisms during cross-linking

The reaction mechanism involving cyclic compounds such as epoxides is identified as ring-opening polymerisation [37]. In the current research, attention is focussed only on the reaction mechanism and kinetics of cross-linking reactions of epoxy/amine systems. A review of cross-linking mechanism and reaction kinetics of epoxy/amine systems was reported by Rozenberg [38]. In cross-linking of an epoxy resin with an amine hardener, the epoxy group can react either with primary or secondary amine. Figure 2.3 shows the reaction mechanism for a primary amine with an epoxy group yielding a β -hydroxyl secondary amine, which in turn is able to react with another epoxy to give a chemical network cross-linked by three bonds around the nitrogen atom (tertiary amine). As the reaction proceeds, further branching reactions lead to the formation of a three-dimensional network molecule.

(i) Primary amine – epoxy addition



(ii) Secondary amine – epoxy addition

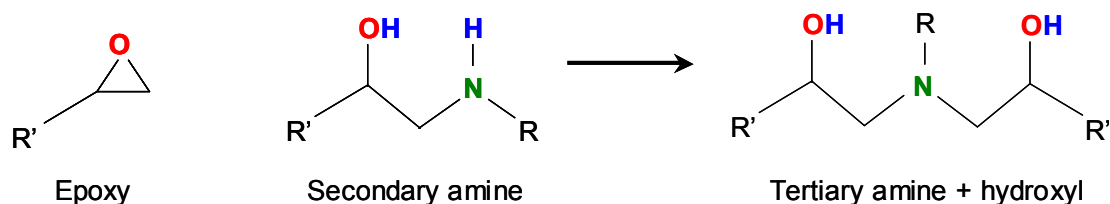


Figure 2.3 Reaction mechanism of epoxy-amine ring-opening polymerisation [39].

Generally, the above reactions take place under two conditions: catalytic and autocatalytic [40]. Absorbed moisture in constituent materials, residual hydroxyl groups present in epoxy resins and solvents catalyse the epoxy/amine reaction in its early stage and known as catalytic reaction. In addition, the hydroxyl groups generated by epoxy/amine reactions also act as active catalysts. Rozenberg [38] explained the activation of carbon atoms of the epoxy ring for nucleophilic attack by hydroxyl-containing molecules as shown in Figure 2.4, which was identified as a “termolecular transition state”. These secondary hydroxyl groups catalyse the reaction through the formation of a termolecular complex, which facilitates the nucleophilic attack of the amino groups. Therefore, as the reaction progresses the cross-linking reaction shows an accelerating rate, which is known as an autocatalytic reaction [41,42,43].

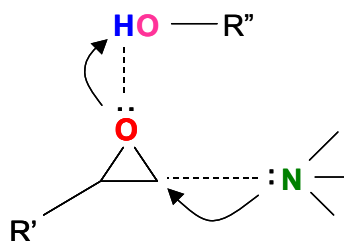


Figure 2.4 Termolecular transition state of the Epoxy-amine addition in the presence of hydroxyl-containing groups [44].

The above mentioned reaction mechanisms for epoxy amine systems are the general scheme of consecutive and competitive reactions, which take place during cross-linking. However, the exact reaction mechanism is dependent on the chemistry of the constituent materials and the reaction temperature [45,46,47]. Attention has been focused on investigating the effect of chemical structure on the relative reactivity of cross-linking agents, the reaction mechanism and the reaction kinetics of epoxy/amine resin systems [44,48]. Girard-Reydet *et al.* [44] studied the effect of chemical structure of different aromatic amines on the reactivity of the amine groups and proposed that electron-withdrawing groups such as *sulphones* ($-\text{SO}_2-$) and electronegative groups such as chloride ions attached to a phenyl ring affect the reactivity as illustrated in Figure 2.5. Their findings were based on DSC and high-pressure liquid chromatography (HPLC) techniques. Based on dynamic DSC analyses of DGEBA with aromatic amines, Gupta and Warma [48] observed reduced nucleophilicity with amines containing carbonyl groups ($-\text{CO}-$). Mijovic and Wijaya [49] found relatively lower reactivity of amines with a nitro group ($-\text{NO}_2$), which has a stronger electron-withdrawing effect compared with that of amines containing *sulphone* groups. The authors investigated the nucleophilicity of different aromatic amines with PGE using quantitative functional group analyses based on HPLC. Furthermore, they observed an improved reactivity of aromatic

amines containing methoxy groups ($-\text{OCH}_3$), which have a strong electron-donating nature. The amine with a methoxy group that used for their investigation was *p*-anisidine, an aniline with the methoxy group in the para position.

In alternative research, Soni *et al.* [34] investigated the effect of aliphatic and aromatic amines on the cross-linking kinetics of epoxy/amine resin systems using DSC analysis. By considering the characteristics of the DSC isotherms obtained, they concluded that the aliphatic amines are more reactive than the aromatic amines. They explained the low reactivity of aromatic amines based on the electron-withdrawing groups available in their chemical structure. In addition, the reported values of pre-exponential factor (A) for different amines also give an indication of steric hindrance of aromatic amines compared with that of aliphatic amines. A is a term which includes factors such as the frequency of collisions of constituent molecules and their orientation and the value depends on the complexity of the reacting molecules [50,51].

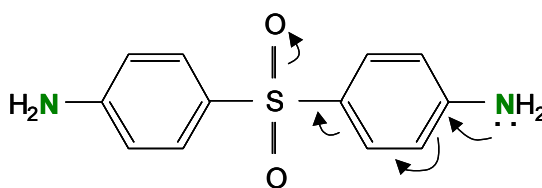


Figure 2.5 The electron-withdrawing effect of *sulphone* group in DDS [44].

Generally, empirical kinetic models consider the primary amine – epoxy (PA-E) reaction and the secondary amine – epoxy (SA-E) reaction as a single step and interpret as a combined reaction using a single activation energy and rate of reaction. However, the relative reactivities of the primary and secondary amino groups towards the epoxide ring-opening

reaction are not clear and conflicting results have been published [38,39,52]. Cole and co-workers [39,52] predicted the reaction scheme of cross-linking of epoxy/amine resin systems assuming the reactivity of PA-E reaction is the same as that of SA-E reaction. The model was validated for isothermal data obtained via differential scanning calorimetry (DSC). Different formulations of neat TGDDM/DGEBA/DDS system were studied. A method of integration by partial fractions was used to solve the kinetic equations and the evolution of cross-linking reaction was described in terms of the degree of overall epoxy conversion and the extent of epoxy-amine reaction at a given time.

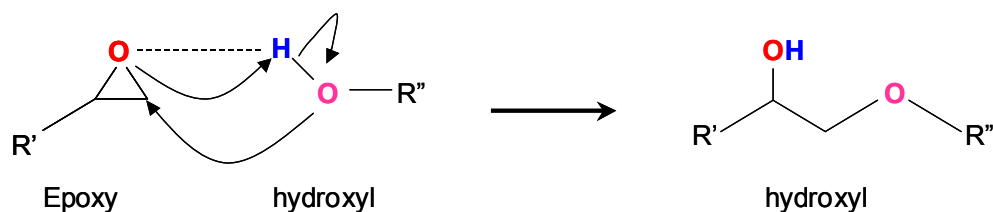
In contrast, Chiao [46] reported that for cross-linking of commercial TGDDM/DDS epoxy systems, the reactivity of the PA-E reaction is an order of magnitude higher than that of the SA-E reaction. The conclusions were based on quantitative results obtained based on Fourier transform infrared (FTIR) spectroscopic data and isothermal DSC data. Furthermore, the author highlighted that the relative reactivities predicted based on FTIR spectroscopy gives more meaningful evidence of real chemical change taking place during the cross-linking reaction compared with that obtained based on empirical assumptions. Considering cross-linking of a tri-functional epoxy with different aromatic amines, Girard-Reydet *et al.* [44] came to a similar conclusion. Although the nucleophilicity of different amines were different, reactivity ratios and reaction rates of SA-E reaction and PA-E reaction showed similar values.

In spite of the relative reactivity of primary and secondary amines, solvents used in the resin formulations were also found to have a considerable influence on the reaction rate of epoxy/amine addition [40,53,54]. Shechter *et al.* [54] observed a distinct influence of the chemical structure and the concentration of solvents in an epoxy/amine resin system on the reaction rates of amine-epoxy addition. They studied the reaction of phenyl glycidyl (PGE)

ether with diethylamine and observed that benzene or acetone decelerates the reaction while isopropanol, nitromethane and water accelerate the epoxy-amine addition. The authors proposed that the effect is dependent on the polarity or the ability of a given solvent to donate or accept a proton and the same catalytic effect takes place as explained in Figure 2.4 by making a termolecular intermediate state of epoxy and amine molecules with the solvents. Hong and Wu [55] analysed cross-linking behaviour of the epoxy/dicyandiamide/solvent system. They investigated the effect of solvents by means of isothermal DSC and Fourier transform infrared (FTIR) spectroscopy. The DSC analyses revealed that the presence of solvent results in decreases in the cross-linking exotherm, the initial cross-linking rate, the glass transition temperature, the reaction rate and the reaction order of the epoxy resin. The FTIR spectroscopy analyses confirmed that the composition of the cross-linked resin was affected by the solvent, the cross-linking temperature and the specimen configuration.

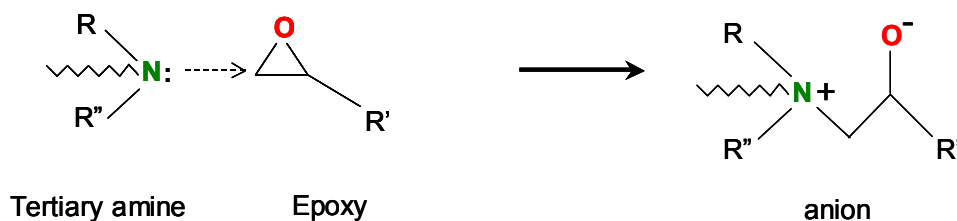
The lack of general agreement of relative reactivities of PA-E and SA-E reactions can be attributed to the effects of the chemistry of the constituent materials including impurities, catalysts and solvents available in the resin system. On the other hand, the discrepancy may also be due to the different experimental techniques used and use of different mathematical models used for calculating the kinetic parameters [38]. Mijovic *et al.* [56] summarised and highlighted the variation in reactivity ratio as a function of resin chemistry, reaction medium used and analytical technique employed. Rozenberg [38], Smith [40] and Mijovic *et al.* [56] reviewed published results for reactivity ratios of a wide range of epoxy/amine formulations and stated that defining a general relationship for reactivities of the primary and secondary amino groups in amine based cross-linking agents is difficult since even a minor amount of impurities available in the reactants makes a considerable difference on the reaction rates.

(i) Hydroxyl – epoxy addition (etherification)



(ii) Homopolymerization

Stage-I



Stage-II

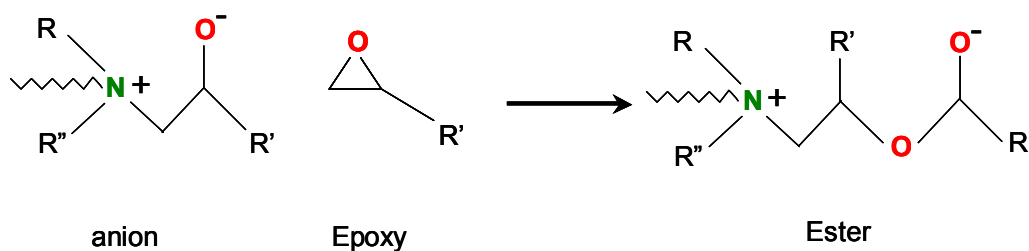


Figure 2.6 Reaction mechanism of etherification and homopolymerisation of epoxy resin [39,47].

In spite of the main ring-opening reaction between epoxy and amine, slow side reactions such as homopolymerisation of epoxides and epoxy-hydroxyl reaction (etherification) take place at elevated temperatures as shown in Figure 2.6(i) [57]. Progression of the epoxy-amine cross-linking also activates the homopolymerisation of epoxy resin by tertiary amine that is produced during the epoxy/amine reaction. Tertiary amines are the general class of anionic catalysts commercially used for cross-linking of epoxy resins. The tertiary amine is an organic base containing an atom with an unpaired electron in its outer orbital [58]. The tertiary amine approaches one of the carbon atoms of the epoxide group as shown in Figure 2.6(ii) and, in the presence of a hydroxyl group, bonds to the oxygen atom of the epoxy [59].

The anion generated from this reaction is capable of opening a second epoxy ring and thus continuing the cross-linking reaction. Nevertheless, Rozenberg [38] suggested that the homopolymerization that catalysed by tertiary amines (Figure 2.6(ii)) may not be possible when aromatic amines are used as cross-linking agents. This could be attributed to the steric hindrance and electron-withdrawing groups attached to the main chain and to phenyl rings [34,44].

The contribution of the etherification reaction towards the overall epoxy conversion depends on the resin chemistry, resin formulation and reaction temperature. Based on FTIR spectroscopic data published by Morgan and Mones [60], Chao [46] reported that in TGDDM/DDS resin systems the etherification reaction becomes significant at cross-linking temperatures above 150 °C. This appears to be in satisfactory agreement with the temperature dependence of vitrification published by other researchers [31,47]. Jiawu *et al.* [31] observed a decrease in vitrification time at reaction temperatures above 158 °C and below the glass transition temperature of fully cross-linked resin (T_g^∞). Their work was based on torsional braid analysis (TBA) (see Section 2.3.1) and DSC of a TGDDM/DDS resin system at a range of isothermal cross-linking temperatures. The vitrification time was defined based on loss tangent curves obtained from TBA analyses. Xu and Schulp [47] observed a considerable increase in the reaction rate corresponding to vitrification above 160 °C for a TGDDM/methylaniline resin system. The analysis was based on FTIR spectroscopy and the concentration of ether groups formed during etherification was determined using the concentrations of epoxide and secondary amine groups obtained from FTIR spectral data. In addition to the temperature dependence, the authors observed that the etherification reaction is more apparent in formulations with excess epoxy compared with that observed in formulations with correct stoichiometry. However, in both cases the observed reaction rates

of etherification was much slower than that of amine-epoxy addition reaction within the range of reaction temperatures studied.

2.2.2 Cross-linking kinetics

The extent of reaction or degree of conversion of reactants at any stage of the cross-linking reaction can be expressed by the percentage of total reactant concentration that has been consumed. In addition, the rates of reaction are determined by the chemical kinetics of the specific reactions involved [61].

Considerable attention has been paid of investigating the cross-linking kinetics of epoxy resin systems, and a number of different kinetic models have been proposed in the literature. Generally, researchers have studied the connection of the chemical reactions with the other independent variables, such as time and temperature. Cross-linking kinetic models can be classified into two categories: phenomenological models and mechanistic models. Mechanistic models are made from the balance of chemical species taking part in the chemical reaction [62]. These models are used to represent the actual chemical reactions occurring in the cross-linking process of epoxy resins [63] and are able to account for the variation in a resin formulation. On the other hand, phenomenological models are based on an empirical relation between reaction kinetics and are only applicable to a specific class of thermosets [64]. However, a detailed knowledge of the chemical formulae of epoxy resins is necessary to set up a mechanistic model. Therefore, efforts have been directed towards establishing phenomenological models for epoxy resins using thermal analysis techniques or spectroscopic measurements. These equations can be very simple, although they do not supply direct mechanistic information.

For thermosetting polymers, cross-linking mechanism can be divided into two general categories: n^{th} order and autocatalytic. Many empirical forms have been suggested for rate equations and they show a dependence on the resin system used [62,65].

The general kinetic equation for the case of n^{th} -order kinetics is given by [66]:

$$\frac{d\alpha}{dt} = k(1 - \alpha)^n \quad \text{Equation 2.1}$$

where α is the the fractional conversion of epoxy groups with respect to the concentration of epoxy groups present in the system at the start of the reaction, k is the reaction rate constant, n is the reaction order and t is the reaction time. At the start of the reaction α is assumed to be equal to zero. There are two characteristics for an n^{th} order type cross-linking mechanism: the relationship between $\ln(d\alpha/dt)$ and $\ln(1-\alpha)$ should be linear and the maximum cross-linking rate ($d\alpha/dt$) should be reached at $\alpha = 0$.

Fuller *et al.* [66] observed that the cross-linking behaviour can be modelled with a second-order kinetic model. They found good correlation between experimental results and the conversion calculated based on Equation 2.1 where the reaction is not diffusion-controlled. They also observed that the thermal properties of the resin were cure-path independent, that is, irrespective of the cross-linking conditions, for a given conversion, the resin had a constant glass transition temperature.

Acitelli *et al.* [67] predicted the cross-linking kinetics of a DGEBA/m-phenylene diamine resin system using the same model. In another investigation, the authors applied the n^{th} order

model successfully for DSC data obtained for the cross-linking of DGEBA/dicyandiamide (dicy) systems [68]. The applicability of the kinetic model was explained in terms of molecular weight of the DGEBA resin, particle size of dicyandiamide and effect of surfactants on the reaction order and the activation energy for cross-linking.

However, an n^{th} -order equation cannot realistically describe the progress of the entire reaction because the material undergoes different transitions (gelation and vitrification) during cross-linking [69,70]. The gel point is the point in the polymerisation reaction at which a polymer network just begins to form as a result of cross-linking. If the cross-linking temperature (T_c) is above the glass transition temperature (T_g) of the resin system, the reaction continues beyond the gel point to complete the network formation. However, the rate of reaction become slower as the kinetics become diffusion-controlled due to the reactants in the unreacted mixture having to diffuse through the rubbery gel to react with functional groups attached to the network. The cross-linking reaction will cease as the T_g of the network increases to such an extent that the system vitrifies [38]. Vitrification is known as glass formation due to T_g increasing from below T_c to above T_c as a result of the cross-linking reaction, and is defined as the point where $T_g = T_c$ [61,62,66].

Tai and Chou [71] reported that a simple n^{th} order reaction kinetic equation does not fit the experimental data effectively. Instead, a kinetic equation for the autocatalytic type was proposed. An expression for an autocatalytic reaction is given by [72]:

$$\frac{d\alpha}{dt} = k\alpha^m(1-\alpha)^n \quad \text{Equation 2.2}$$

where n and m are reaction orders and k is the rate constant.

The rate constant can be expressed by Arrhenius function. The empirical relationship between the rate of a reaction, temperature and the activation energy of the reaction is called Arrhenius equation. The Arrhenius equation is based on collision theory, which states that in a chemical system the molecules must collide with both the correct orientation and with sufficient kinetic energy for converting reactants into products. In simple form, the relationship between temperature and rate constant for a reaction has the following equation [50]:

$$k = Ae^{-E_a/RT} \quad \text{Equation 2.3}$$

where A is a pre-exponential factor which accounts factors such as the frequency of collisions and their orientation, E_a is the activation energy for the reaction, R is the universal gas constant in $\text{J mol}^{-1} \text{K}^{-1}$, and T is the temperature in Kelvin.

By taking into account the autocatalytic reaction, where initial reaction rate of a reaction is not zero, the generalized autocatalytic equation proposed by Sourour and Kamal [70] is given below:

$$\frac{d\alpha}{dt} = (k_1 + k_2\alpha^m)(1-\alpha)^n \quad \text{Equation 2.4}$$

$$k_1 = A_1 \exp\left(-\frac{E_1}{RT}\right) \quad \text{Equation 2.5}$$

$$k_2 = A_2 \exp\left(-\frac{E_2}{RT}\right) \quad \text{Equation 2.6}$$

where α is the conversion, T the temperature, R universal gas constant and m , n , A_1 , A_2 , E_1 , E_2 are constants, k_1 and k_2 are rate constants which have an Arrhenius form and are dependent on temperature; m and n are reaction orders and dependent on the resin system. The reaction order, n , and rate constant, k_1 are related to the consumption of epoxy functional groups due to both general epoxy-amine addition and homopolymerisation reactions as shown in Figure 2.3 and Figure 2.6. The constant, m and k_2 are related to the concentration of hydroxyl groups that are being generated as the cross-linking reaction proceeds [73,74].

The applicability of the empirical model for different resin systems has been widely explored and the dependency of the kinetic parameters on resin chemistry and processing conditions have been investigated. Table 2.1 gives a summary of kinetic models that have been used to analyse the cross-linking kinetics of relevant epoxy-based resin systems.

Table 2.1 Summary of kinetic models used for epoxy/amine resin systems.

Resin system	Kinetic model	Kinetic parameters
DGEBA/poly(oxypropylene) diamine (POP) [42]	$\frac{d\alpha}{dt} = (k_1 + k_2\alpha^m)(1-\alpha)^n$	$m+n=2$ $E_1 = 67.2 \text{ kJ mol}^{-1}$ $E_2 = 22.5 \text{ kJ mol}^{-1}$

DGEBA/POP [75]	$\frac{d\alpha}{dt} = k(\alpha + B)(1 - \alpha)(r - \alpha)$ <p>where kB – initial rate of reaction r – initial ratio of amine to epoxide</p>	$E_1 = 65.1 \text{ kJ mol}^{-1}$, $E_2 = 31.3 \text{ kJ mol}^{-1}$ $\ln A_1 = 14.39$, $\ln A_2 = 4.54$
DGEBA/MDA (4,4'-methylene diamine)/MN (malononitrile) [76]	$\frac{d\alpha}{dt} = (k_1 + k_2\alpha^m)(1 - \alpha)^n$	$m + n = 2$ $E = 37.58 \text{ kJ mol}^{-1}$ $A = 2.37 \text{ min}^{-1}$
DGEBA/DDS [73]	$\frac{d\alpha}{dt} = k(1 - \alpha)^n$	$E = 46.4 \text{ kJ mol}^{-1}$
DGEBA/ m-phenylene diamine (m-PDA) [67]	$\frac{d\alpha}{dt} = k(1 - \alpha)^n$	$n = 0.47 - 2.3$ $E = 51.5 \text{ kJ mol}^{-1}$
DGEBA/DDM [73]	$\frac{d\alpha}{dt} = k\alpha^m(1 - \alpha)^n$	$m + n = 3$ $E = 47.2 \text{ kJ mol}^{-1}$
Structural fibreglass/epoxy prepreg [77]	$\frac{d\alpha}{dt} = (k_1 + k_2\alpha^m)(1 - \alpha)^n$	$m = 0.593$, $n = 1.269$ $E1/R = 1687.886$, $E2/R = 561.192$
DGEBA/m-PDA [78]	$\frac{d\alpha}{dt} = (k_1 + k_2\alpha^m)(1 - \alpha)^n$	$m + n = 2$ $E = 4.56 \times 10^7 \text{ J/kgmol}$
DGEBA/m-PDA [79]	$\frac{d\alpha}{dt} = K(B + \alpha^m)(1 - \alpha)^n$	$m = 1$, $n = 2$ $E = 50.5 \text{ kJ mol}^{-1}$
TGDDM/DDS [80]	$\frac{d\alpha}{dt} = (k_1 + k_2\alpha^m)(\alpha_{\max} - \alpha)^n$	$m + n = 2$ $E = 80.4 \text{ kJ mol}^{-1}$
DGEBA/1,6-diaminohexane [81]	$\frac{d\alpha}{dt} = (k_1 + k_2\alpha^m)(\alpha_{\max} - \alpha)^n$	$m = 1.060$, $n = 0.898$ $E_1 = 70.0 \text{ kJ mol}^{-1}$, $E_2 = 27.0 \text{ kJ mol}^{-1}$ $A_1 = 3.72 \times 10^9 \text{ min}^{-1}$, $A_2 = 898 \text{ min}^{-1}$
DGEBA/1,6-diaminohexane [82]	$\frac{d\alpha}{dt} = (k_1 + k_2\alpha^m)(1 - \alpha)^n$	$m = 0.853$, $n = 1.390$ $E_1 = 40.75 \text{ kJ mol}^{-1}$, $E_2 = 65.43 \text{ kJmol}^{-1}$ $\ln A_1 = 9.51$, $\ln A_2 = 22.0$

However, there are partially conflicting relations observed in recent years for the reaction orders, m and n obtained for different epoxy resin systems using general autocatalytic models [42,73,78,83]. Costa *et al.* [73] investigated a DGEBA/4,4'-diamine-diphenylmethane (DDM) epoxy system based on isothermal DSC analysis. They proposed an autocatalytic

reaction mechanism for the resin system and observed that the rate constant and the reaction order, n increase proportionally as a function of temperature. On the other hand the reaction order, m decreased as the temperature increases satisfying the overall reaction order, $n + m = 3$. They suggested that these observations are due to the fact that as the reaction temperature increases, higher numbers of molecules acquires enough energy for successful collision by increasing n . Hence the reaction rate and rate constant increase accordingly. Also the authors hypothesised that as the reaction temperature increases, the thermal catalysis prevails the autocatalytic effect of m .

Macan *et al.* [42] investigated the cross-linking kinetics of a DGEBA/poly(oxypropylene) diamine (POP) resin system. In their study, isothermal DSC data was analysed using the Sourour and Kamal model assuming $m + n = 2$. Based on the kinetic parameters obtained, m and n found to be insensitive to temperature while the rate constants follow Arrhenius temperature dependence. Larranaga *et al.* [83] observed the same insensitivity of reaction orders to cross-linking temperature. They investigated the cross-linking kinetics of a DGEBA-DDM epoxy-amine system and reported that the reaction orders did not seem to vary very much with the cross-linking temperature. However, it is necessary to emphasis that the kinetic models discussed in the above studies are based on empirical relations and may not be able to interpret the exact reaction scheme for cross-linking of thermosetting resin systems. Therefore, in-depth investigation of the influence of resin chemistry and the reaction conditions on the reaction mechanism is crucial for developing general trends of reaction orders as a function of reaction temperature.

There have been several efforts to improve the correlation between kinetic models and experimental data [70]. Some of the modified models are discussed. Sourour and Kamal [70]

investigated a DGEBA/*m*-phenylene diamine (*m*-PDA) resin system using isothermal DSC analysis. Epoxy conversion was assumed based on two simultaneous reactions: initially the reaction is initialised and catalysed by hydrogen-bonded electron-donating HX molecules present in the system and secondly the reaction autocatalysed by the hydroxyl groups generated during the reaction. Then the total rate of epoxy conversion was expressed as below:

$$\frac{d\alpha}{dt} = k_1 C (1 - \alpha)(B - \alpha) + K_2 \alpha (1 - \alpha)(B - \alpha) \quad \text{Equation 2.7}$$

where C is the concentration of the HX molecules, B is the initial ratio of diamine equivalents to epoxide equivalents and k_1 and K_2 are rate constants. The model showed good correlation at lower epoxy conversions while a deviation was observed at higher epoxy conversions. The authors suggested that the observed trend was due to the dependence of the rate constants on the degree of conversion, which was not considered in the model.

Zhao *et al.* [84] also reported a discrepancy between the autocatalytic model and the experimental data at a later stage of cross-linking with a DGEBA/3-methyl-1,2,3,6-tetrahydrophthalic anhydride (MeTHPA) system. As the reaction progresses, the model tends to deviate due to the onset of gelation and vitrification. The authors proposed that the deviation of the general autocatalytic model from the experimental data is due to the reduction in reaction rate as a result of diffusion-controlled reaction rather than the effect of kinetic factors. The investigators interpreted this trend based on free-volume theory. They used a modified autocatalytic model by introducing a diffusion factor, $d(\alpha)$, as shown below:

$$\frac{d\alpha}{dt} = (k_1 + k_2 \alpha^m)(1 - \alpha)^n d(\alpha) \quad \text{Equation 2.8}$$

$$d(\alpha) = \frac{1}{1 + \exp[C(\alpha - \alpha_c)]} \quad \text{Equation 2.9}$$

where C is the diffusion coefficient and α_c is the critical conversion depending on the curing temperatures. They found good correlation between the modified kinetic model and the experimental data for the resin system suggesting diffusion-controlled effects at a later stage of the cross-linking reaction.

In addition, the ultimate degree of conversion of thermosetting resins is dependent on the cross-linking temperature. However, the Sourour and Kamal model does not consider incomplete cross-linking reaction due to vitrification. It always gives the results that conversion continues to unity or complete reaction when the prediction is performed. Several studies have been discussed using the ultimate degree of conversion (α_{max}) achieved at a given T_c to reflect the effect of vitrification in the kinetic models [80,81,85]. Kenny and Trivisano [86] proposed a modified extended Kamal model and Equation 2.4 can be rewritten as:

$$\frac{d\alpha}{dt} = (k_1 + k_2\alpha^m)(\alpha_{max} - \alpha)^n \quad \text{Equation 2.10}$$

Musto *et al.* [80] investigated the reaction kinetics of a TGDDM/DDS epoxy resin system using the general Sourour and Kamal model and Equation 2.10 and found good agreement between the modified model and the experimental data. Their investigation was based on FTIR spectroscopy in the near-infrared (NIR) and the mid-infrared (MIR) regions.

2.3 Monitoring of cross-linking reaction in epoxy/amine resin systems

The cross-linking of thermosetting matrix resins plays a key role in polymer-matrix composite manufacturing. For many years, great attention has been paid to understanding the potential impact of processing of thermosetting resin systems on the performance of related engineering materials against mechanical and environmental conditions [87,88,89,90,91,92,93]. The shrinkage associated with the cross-linking of thermosetting resins contributes to a reduction in performance of the finished composite product [94,95,96]. Furthermore, storage conditions of thermosetting resins, cross-linking agents, prepreg materials as well as of the reinforcing materials before processing, greatly affect the cross-linking kinetics [97,98,99,100]. Therefore, it is commonly accepted that the optimisation of processing parameters leads not only to optimise the mechanical performance of composites but also reduces cycle time, energy requirements and hence reduces manufacturing and maintenance costs [94,101,102].

2.3.1 Conventional analytical techniques

In general, numerous studies have been performed to monitor the cross-linking kinetics and predict the effect of chemical, thermal and rheological changes associated with processing of composites [103,104,105,106]. The most commonly used analytical techniques include FTIR spectroscopy, DSC, Fourier transform Raman spectroscopy, fluorescence spectroscopy, high-pressure liquid chromatography [49,107], gel permeation chromatography [63], nuclear

magnetic resonance (NMR), torsional braid analysis (TBA) [84,108] and chemical titration of the functional groups [107]. In torsional braid analysis, a glass braid consisting of woven glass fibre yarns is impregnated with the unreacted resin to be analysed. The technique is a complementary method to the DMTA technique and has been used to study polymer systems that are liquids at the beginning of the reaction [109,110,111]. The impregnated braid is used under a sinusoidal torsional mode of mechanical excitation to monitor the change in viscoelastic properties of the resin due to cross-linking as a function of temperature or time. The change in complex modulus as a function of cross-linking time can be used to determine the gelation and vitrification of the resin system at the specified reaction temperature. The dimensions of the supporting braid, number of glass yarns and the type of the weave are dependent on the viscoelastic properties of the resin system. The stiffness of the braid under torsion should not dominate the change in relatively weak stiffness of the resin during the reaction [109]. Compared to cross-linking monitoring techniques such as DSC and FTIR, dynamic mechanical thermal analysis (DMTA) has the unique advantage of being able to track the gelation and vitrification during cross-linking [112,113]. Rheological and dielectric measurements have also been deployed to study the reaction kinetics of thermosets [114,115,116,117,118,119].

This review is focussed only on the techniques those related to the current research project. Fibre-optic sensing techniques that are demonstrated in this research were mainly based on FTIR spectroscopy. Therefore, applications of FTIR spectroscopy for monitoring of cross-linking will be discussed in detail. However, a brief review of using DSC for monitoring cross-linking of epoxy resins will be given since the technique has been widely deployed for characterisation of the cross-linking kinetics of thermosetting resins.

2.3.1.1 Fourier transform infrared spectroscopy

Infrared spectroscopy is one of the main analytical techniques used in chemical analysis. The technique has many advantages over other analytical techniques such as being able to give quantitative comparison of functional groups in materials [120,121]. Various modes of interaction between IR radiation and specimens are used; namely transmission, specular reflection, diffuse reflectance, attenuated total reflection, emission and photo acoustics [122]. The advantages and disadvantages of using different modes of interaction of radiation with the specimen, especially the choice of appropriate mode, instrumentation, sampling techniques and spectral analysis have been discussed extensively [123,124,125,126]. Li *et al.* [125] demonstrated using a non-contact diffuse reflectance attachment for quality control of manufacturing prepreg cloth by the solution impregnation method. The technique was used for determining the resin content, volatile content of ethanol and extent of pre-cure during prepreg manufacturing. Calibration and validation of the measurement technique were carried out using a principal regression components algorithm and reasonable agreement was observed between predicted results and the online measurements. Occhiello *et al.* [127] reviewed a range of spectroscopy techniques, which were used to characterise interfaces in polymer composites.

In the recent past, demand for the technique was further broadened with hyphenated-FTIR instruments with thermal characterisation techniques [103,128,129,130]. Hyphenated techniques combined with FTIR spectroscopy reveal useful information compared with individual analytical methods due to several inherent advantages of combined systems: (i) the test specimen is same for both experiments; (ii) thermal and chemical properties of the specimen are subjected to the same test environment and (iii) direct cross-correlation of the thermal and chemical changes is possible due to the above-mentioned features. De Bakker *et*

al. [103] demonstrated using a hyphenated system in which a DSC attachment was used to achieve thermal and chemical properties of a TGDDM/DDS resin system during cross-linking. Simultaneous monitoring of the cross-linking reaction was carried out on a resin sample in a glass DSC pan and an empty glass pan was used as a reference for DSC experiments. FTIR spectra were recorded under emission mode and good spectral sensitivity was achieved with approximately 20 mg of resin, which creates a resin layer of 1 mm path-length. The influence of instrumental baseline on the isothermal results showed marked effect on the heat flow measurements. However, the deviation between experimental DSC values and predicted results was used to define a correct baseline for isothermal DSC experiments and good reproducibility of the experimental results was obtained. Reasonable agreement was observed between cross-linking kinetics obtained using DSC and FTIR spectroscopy.

The infrared spectrum of a material contains absorption bands that appear at the natural frequencies due to the vibration of atomic bonds in molecules. The atoms in the molecules oscillate at specific frequencies unique for the bond strength and the masses of the atoms bonded together [131]. The same atomic bond may have different oscillation modes at different frequencies. Therefore at that particular frequency, the atoms absorb infrared radiation and jump from the lowest quantum level to a higher excited quantum level. Depending on the mode of atomic vibrations, characteristic absorbance bands appear in the infrared spectrum showing the absorbance of IR radiation at the specified frequencies.

Peak assignments of epoxy/amine resin systems

Characteristic absorption bands of epoxy/amine resin systems in mid- and near-IR ranges have been assigned. Since the fibre-optic sensor designs developed in the current study were based on near-IR spectroscopy, attention of the review was only focussed on identification of

epoxy/amine based resin systems in the near-IR range. A summary of peak assignments for epoxy resins and amine-based cross-linking agents in the near-IR range is given in Table 2.2 and Table 2.3.

Table 2.2 Summary of peak assignments for epoxy resins in the near-IR range

[47,80,82,103,131,132,133,134,135,136,137,138,139,140].

Chemical group	Peak assignment (nm)
Epoxy ring combination 2 nd overtone (epoxy ring stretching and C-H bending vibration)	2205
Terminal epoxy group 1 st overtone (-CH stretching vibration)	1650
Terminal epoxy group 2 nd overtone (C-H stretching vibration)	1131-1160
Hydroxyl combination (stretching and bending vibrations)	2042
Hydroxyl 1 st overtone (O-H stretching vibration)	1428
Hydroxyl 2 nd overtone (O-H stretching vibration)	981
Hydroxyl combination (-OH vibration modes)	2090
Hydroxyl combination (-OH absorption/interactions)	2325
Hydroxyl due to moisture (- OH stretching vibration)	1908
Aromatic 1 st overtone (C-H stretching vibration)	1670-1698
Aromatic ring combination (-CH stretching vibration)	2138, 2165
Aliphatic 1 st overtone (C-H stretching vibration)	1732, 1773
Aliphatic 3 rd overtone (-CH asymmetric bending vibration)	1720
-CH overtones of -CH ₂ , -CH ₃	1700-1770
Methyl symmetric bending “umbrella” vibration	2410-4260
Aromatic conjugated combination (C=C stretching vibration)	2136

Table 2.3 Summary of peak assignments for amine-based cross-linking agents in the near-IR range

[47,80,82,103,131,132,133,134,135,136,137,138,139,140,141].

Chemical group	Peak assignment (nm)
Primary amine combination band (N-H symmetric stretching and deformation vibrations)	2024
Primary amine combination (-NH ₂ asymmetric stretching and bending vibration)	1973
Aromatic amines – primary amine combination (N-H symmetric stretching and C-N stretching vibrations)	2194
Combination band of secondary amine and overtones of symmetric and asymmetric stretching vibrations of primary amine	1495-1535
Primary amine 1 st overtone (N-H symmetric stretching vibration)	1521
Primary amine 1 st overtone (N-H asymmetric stretching vibration)	1454
Primary amine 2 nd overtone (N-H asymmetric stretching vibration)	1020
Secondary amine 1 st overtone (N-H stretching vibration)	1538

Functional group analysis of epoxy/amine resin systems during cross-linking

In addition, for qualitative identification of chemicals, FTIR spectroscopy is a useful tool for determining relative concentrations of functional groups. The basis for quantitative analysis of functional groups using the infrared absorbance spectrum is each functional group has its characteristic frequency. The Beer–Lambert law relates absorbance to concentration of specified functional groups or chemical species [120]. For a single compound in a homogeneous medium, the absorbance at a frequency is proportional to the fractional change in concentration of the compound and can be expressed as below [120]:

$$1 - A_{\lambda} = \exp(-\epsilon lc) \quad \text{Equation 2.11}$$

For low thickness and low concentrations, the equation 2.11 can be reduced to:

$$A_{\lambda} = \varepsilon_{\lambda}lc \quad \text{Equation 2.12}$$

where A_{λ} is peak area of absorption band at the wave length, λ , ε_{λ} is molar absorptivity at wavelength, λ , l is the thickness of the sample and c is the fractional concentration. The molar absorptivity is a function of the functional group as well as the wavelength at which the characteristic absorbance band appears. The Beer–Lambert law can be extended for a mixture of compounds at a specified wavelength. In general, for a mixture of n number of different functional groups, the total absorbance, $A_{\lambda,T}$ of the mixture at a given wavelength can be written as [128]:

$$A_{\lambda,T} = \varepsilon_1lc_1 + \varepsilon_2lc_2 + \dots + \varepsilon_nlc_n \quad \text{Equation 2.13}$$

where $\varepsilon_1, \varepsilon_2, \dots, \varepsilon_n$ and c_1, c_2, \dots, c_n are molar absorptivity values and concentrations of different functional groups, respectively.

FTIR spectroscopy has been extensively employed not only for quantitative analysis but also for quantitative analysis of monitoring of cross-linking reaction of epoxy/amine resin systems [55,60,142,143,144,145]. In monitoring of cross-linking reaction of an epoxy/amine system, the degree of conversion of a specific functional group as a function of reaction time can be determined using the change in concentration of the functional group in the mixture. It was shown that the peak area related to an absorption band is linearly proportional to the concentration of the corresponding functional group in the mixture (see Equation 2.12) [146,148]. Therefore using infrared spectroscopy, the degree of conversion of epoxide groups with respect to a non-reacting chemical group (in most epoxy systems, aromatic C-H group) can be determined using the equation below:

$$\alpha = 1 - \frac{(A_{EP,t} \times A_{CH,0})}{(A_{EP,0} \times A_{CH,t})} \quad \text{Equation 2.14}$$

where α is degree of conversion, $A_{EP,0}$ and $A_{EP,t}$ are peak area related to $t = 0$ and $t = t$ respectively and $A_{CH,0}$ and $A_{CH,t}$ are peak area related to $t = 0$ and $t = t$ respectively.

Attention has been also paid to determining the change in concentration of other chemical groups during cross-linking for predicting reaction kinetics and overall thermal and physical properties of cross-linked resin systems. Among chemical reactions taking place during cross-linking, reaction kinetics of primary amine, secondary amine, tertiary amine, hydroxyl groups and ether links are of major importance. Different spectral manipulation methods have been developed to investigate the contribution of different functional groups to combination absorption bands [103,129,147,148,149,150]. Lohman and Norteman [141] developed a method for determining primary and secondary amine concentrations using characteristic absorption bands appear at 2023 nm and 1538 nm. Their method involved using a series of concentration solutions of desired primary and secondary amines using chloroform as a solvent and analysing near-IR absorbance spectra of each solution. Calibration curves obtained for primary amines using the absorption band at 2023 nm were used to determine secondary amine absorption by subtracting primary amine contribution. Furthermore, molar absorptivities of the absorption bands also determined. The Beer-Lambert law was validated for low concentrations of tetradecylamine in CHCl_3 . Crosby [149] also reported using a similar chemical analysis to determine the contribution of primary and secondary amine concentrations for the combination band at 1538 nm. In his work, different solutions of dibutylamine and 1,6-hexanediamine in chloroform were used and near-IR spectra were obtained for each primary amine/chloroform and primary amine/secondary

amine/chloroform solution. Concentration of the secondary amine was determined by subtracting the absorbance of primary amine from the absorbance of the combination band. Alternatively, the author used Fourier self-deconvolution to determine the individual concentrations of primary and secondary amines.

However, discrepancies were observed when applying predetermined molar absorptivities at absorbance frequencies of primary and secondary amine using the above methods for monitoring of cross-linking of epoxy/amine resin systems. Considerable influence of the solvent used for making different concentration solutions of amines on the peak shift and the peak intensity of the characteristic peaks was reported. Difficulties of using the molar absorptivities obtained using the former method for cross-linking monitoring of epoxy/amine resin systems were discussed. A negative absorption due to secondary amine groups was observed in the early stage of cross-linking reaction of a TGDDM/DDS resin system [149]. Lohman and Norteman [141] hypothesised that the influence of type of solvent on the peak intensity of the individual peaks contributing to the amine combination band at 1538 nm was mainly due to the concentration or the purity of the solvent. In addition, the authors proposed that the effect of solvent on the peak separation and peak broadening is due to amine-solvent interactions. Therefore, the method showed less accuracy in determining the change in concentration of primary and secondary amines during cross-linking. On the other hand, although Fourier self-deconvolution splits the combination band into two separate absorption peaks, the deconvoluted secondary amine peak still showed the combined effect of secondary and primary amine [149]. To overcome these discrepancies, a mechanistic approach has been deployed in which weight balance equations were used to determine the concentrations of unknown chemical groups in the resin system using known concentrations [46,53,80,132,148,151,152].

Chiao [46] proposed a weight balance equation based on well-resolved epoxy and primary amine absorption bands related to a TGDDM/DDS resin system and the equation is given below:

$$[SA]_0 = 2([PA]_0 - [PA]_t) - ([EP]_0 - [EP]_t) \quad \text{Equation 2.15}$$

where $[EP]$, $[PA]$ and $[SA]$ are molar concentration of epoxy groups, primary amine and secondary amine, respectively. Subscripts 0 and t represent the start of reaction and a particular time t , respectively. St John and George [151] proposed a method based on the Beer-Lambert law for a mixture of chemicals and applied it to determine the change in secondary amine concentration based on the combination band from 1507 – 1572 nm. In general, for a mixture of n number of different functional groups, the total absorbance at wavelength λ is given in Equation 2.13 [153]. For the combination band of primary and secondary amine groups, Equation 2.13 can be rewritten as [80,148,151,152]:

$$\Delta A = E_1[PA]_t + E_2[SA]_t \quad \text{Equation 2.16}$$

where ΔA is the area of the peak from 1507 – 1572 nm, and E_1 and E_2 are constants for the primary amine groups and secondary amine groups, respectively.

For cross-linking of an epoxy/amine system, two main epoxy/amine reactions have been identified (see Section 2.1.1) and the mass balance equation can be written as [151]:

$$[PA]_0 = [PA]_t + [SA]_t + [TA]_t \quad \text{Equation 2.17}$$

where $[TA]$ is the concentration of tertiary amine groups. It was assumed that during early stage of cross-linking, there is no reaction between the secondary amine and epoxy groups. Then Equation 2.17 can be simplified as below:

$$[PA]_0 = [PA]_t + [SA]_t \quad \text{Equation 2.18}$$

Xu *et al.* [53] discussed possible reaction mechanisms to satisfy the weight balance equations proposed by both Chiao [46] and St John and George [151] and reported that Equation 2.15 is only valid if etherification reactions are negligible. A method for defining the time period in which Equation 2.18 is valid was proposed by Crosby [149]. The study involved employing various techniques for determining secondary amine concentration using the combination band from 1507 – 1572 nm. The findings have shown that a plot of primary amine concentration based on the absorption peak at 2026 nm against epoxy concentration can be used to find out the time period within which Equation 2.18 explains the state of the reaction. The author concluded that the method proposed by St John and George [148,151,152] gives a more accurate approximation compared with the alternative techniques assessed.

Monitoring of cross-linking of epoxy/amine resin systems

The mid-infrared (MIR) range, which extends from about 2500 to 25000 nm, consists of fundamental absorptions of chemical groups such as C-H, N-H and O-H. However, the MIR spectra of epoxy/amine systems are very complex, with the epoxy peak at 915 cm^{-1} , which is difficult to follow as described by several authors [103,135,140]. Mijovic and Andjelic [154] employed remote MIR spectroscopy to study the cure of a multifunctional epoxy/amine formulation composed of diglycidyl ether of bisphenol-F (DGEBF) and 4,4'-methylene dianiline. They utilized a pair of gold-coated, hollow nickel tubes with NaCl windows bonded on to each ends of the tubes for guiding IR beam across the resin sample, which contained in a

disposable reaction vessel. The incoming IR beam travels along the receiving gold-coated nickel tube by internal reflection, travels through the mixed resin sample and then guides along the second reflective wave-guide towards the detector. Intensities of characteristic absorption bands of epoxy/amine resin systems were monitored and used to evaluate the degree of conversion. Good agreement was obtained between NIR data [155] and MIR data up to about 60% conversion, after which point the MIR data quickly level off without exceeding 75% conversion. The authors proposed that the discrepancy is due to the interference of peaks appeared at 11049 nm and 10928 nm; however, they were unable to develop a method to determine the actual conversion using MIR data.

Investigations on the use of remote near-infrared (NIR) spectroscopy to study reactive polymeric systems have appeared in recent years [132]. The NIR wavelength region extends from about 700 to 2500 nm and consists of overtones and combination bands that appear from fundamental absorption bands found in the MIR region. In the NIR region, the frequency range has one major advantage in that it can be transmitted through glass, which is a common material used for containing chemical samples and also used for *in situ* spectroscopic monitoring using silica multimode optical fibres [135,154]. The NIR spectral range mainly contains overtones and combinations of stretching and bending vibrations of N–H, C–H, and O–H groups and therefore NIR spectroscopy is a useful technique in mapping cross-linking reactions in epoxy/amine resin systems [103].

As the epoxy peak at 2208 nm and the primary amine peak at 2024 nm appear in the region between 1960 – 2500 nm, satisfactory quantitative information has been obtained for epoxy/aliphatic amine resins. Mijovic *et al.* [136] investigated the use of NIR spectroscopy for *in situ* monitoring of cross-linking reaction of commercial epoxy/amine resin systems and

detailed band assignments for the epoxy/amine systems were presented. Xu and Schlup [47] used an *in situ* NIR spectroscopic method to study the relative rates of reaction of etherification and non-catalytic reactions of a TGDDM/methylaniline system. They reported that even with excess epoxy in the epoxy/amine mixture, the non-catalytic amine reaction is several times faster than the autocatalytic etherification reaction. Rigail-Cedeño and Sung [132] used fluorescence, mid-IR and near-IR spectroscopic techniques to study the degree of conversion of different formulations of DGEBA and low molecular-weight aliphatic diamines. The cross-linking agents that used for the study were polyoxyethylenediamine (POE) and POP. Good correlation was observed between the degree of conversion achieved based on NIR spectroscopy with that achieved based on MIR spectroscopy. The change in concentration of primary, secondary and tertiary bands based on absorption of primary amine and epoxide bands were also plotted as a function of cross-linking time. DGEBA/POE showed faster rate of amine conversion compared with that of DGEBA/POP resin system. However, no attempt was made to correlate this information with kinetic models.

Min *et al.* [156] studied the influence of cross-linking reactions of DGEBA/DDS on the development of glass transition temperature, T_g . The degree of conversion as a function of time was monitored using NIR spectroscopy. Assuming T_g is linearly proportional to the degree of conversion, a relationship was established between the extent of reaction based on NIR spectroscopy and the T_g of the system. The T_g of a cross-linked polymer was expressed as a function of the T_g of unreacted resin mixture (T_{g0}), the limiting T_g of cross-linked resin ($T_{g\infty}$), the degree of conversions of linear polymerisation reaction (α_L) and the cross-linking reactions (α_C):

$$T_g = T_{g0} + \alpha_L [(T_{g\infty})_L - T_{g0}] + \alpha_C [T_{g\infty} - (T_{g\infty})_L] \quad \text{Equation 2.19}$$

where $(T_{g\infty})_L$ is the limiting T_g of linear polymer of infinite molecular weight. In their study, epoxy-primary amine reaction was considered as linear polymerisation with the epoxy-secondary amine reaction contributing for branching and cross-linking. The change in concentration of epoxy, primary amine and secondary amine groups was achieved using NIR spectroscopy. Good correlation was observed between the predicted T_g during cross-linking and that measured via DSC.

2.3.1.2 Differential scanning calorimetry

One of the widely accepted means of determining resin cross-linking kinetics is through the application of DSC [74,76,157,158,159]. In DSC analysis, the released heat during the reaction is measured and quantified to determine the degree of chemical reaction or conversion. A detailed review has been done on kinetic analysis for a number of epoxy systems based on DSC [160].

Analysis of reaction kinetics under DSC is mainly divided into two categories; one is isothermal scanning and the other is dynamic scanning [157]. There are advantages and disadvantages of each different approach [157,161]. Many workers have investigated quantitative and qualitative comparisons between an isothermal scan and dynamic scan of epoxy resins. In an isothermal scan, both rate of cure and conversion change at a constant temperature as the reaction proceeds can be monitored. The curve-fitting to determine reaction kinetics is performed by correlating conversion and rate of reaction measured at an isothermal temperature and it can be done successively for another isothermal temperature. Then, the effect of temperature can be found from the parameters determined at the former

stage. Therefore, most empirical rate equations are suitable for quantifying isothermal DSC data. The isothermal approach is equally valid for standard (n^{th} order) and autocatalysed resins. However, isothermal experiments clearly showed possible errors in both the initial and final stages of reaction [161,162]. Fava [162] observed reliable repeatability of isothermal results at low reaction temperatures. However, at higher isothermal temperatures a shift of the conversion curve along the time axis was noticed due to unavoidable temperature lags in the early stage of reaction. In addition, at higher reaction temperatures a lower H_T was observed due to the interference of the heat absorbed during sample equilibrating at the isothermal temperature and the exothermic cross-linking reaction. Therefore at higher reaction temperatures, the total heat of reaction that can be calculated using the thermogram is not accurate because there can be a significant progress of the chemical reaction before reaching the temperature of the isothermal scan. In other words, initial isothermal data are not sufficiently accurate. To overcome this problem, Brnardic *et al.* [75] proposed a method in which the value of the heat flow was extrapolated to time = 0. Their investigation was based on a DGEBA/POP resin system. In an alternative study, the sample cell was preheated to a desired reaction temperature before insert the resin sample to overcome the temperature lag in the early stage of reaction [163]; however, the authors concluded that the lower conversions achieved with increasing reaction temperature may be due to the increasing error in determining the initial reaction.

In contrast, direct manipulation of dynamic temperature scans is identified as a time-efficient method for studying reaction kinetics. Especially, the dynamic scanning mode can be used to achieve more accurate results for fast cross-linking resins if a suitable model is given. For kinetic analysis, the measured heat flow at time, t was assumed to be proportional to the rate of conversion at the specified time [85,164,165]. As the compound reaches a high degree of

conversion at higher temperatures, the diffusion of the unreacted groups involves the movement of the highly cross-linked network and the reaction cannot achieve a complete conversion within a short period of time [71]. Therefore, lower H_T in dynamic DSC scan was reported compared with that obtained in isothermal scan at reaction temperatures above T_g of the resin system. Kim *et al.* [85] revealed that the total heat of reaction (H_T) under dynamic scans is sensitive to heating rate and decreases with increasing scan rate and suggested this trend is due to the use of a linear baseline. In their work, the baseline was approximated by a straight line connecting the assumed starting point and ending point of the chemical reaction. Nevertheless, they were unable to predict the effect of heating rate on H_T using baseline correction. Lu *et al.* [165] demonstrated using a modified Avrami equation for predicting cross-linking kinetics of a DGEBA/4,4'-methylene dianiline (MDA) using DSC dynamic scanning mode. The modified model was capable of explaining the whole cross-linking process; however, the dynamic data revealed two reaction mechanisms depending on the reaction temperature. The activation energy obtained for the lower reaction temperatures agreed well with the isothermal data and the authors hypothesised that this could be due to similar reaction mechanism under isothermal conditions and the primary stage of dynamic conditions during which the reaction is kinetic-controlled. Zvetkov [79] investigated a DGEBA/*m*-PDA resin system using dynamic DSC scans. The author proposed a four-stage kinetic analysis in which following were considered: (i) effect of heating rate; (ii) peak temperature of the dynamic DSC thermograms; (iii) integral and differential curve fitting for single DSC curves and (iv) comparison of predicted model and the experimental data. The approach showed good correlation at lower heating rates and he hypothesised that the deviation of the model at higher heating rates may occur due to side reactions taking place at higher degree of conversion.

It is known that both isothermal and dynamic scan modes may be applied independently, but a combination consisting of the use of the isothermal method to determine the reaction degree and the dynamic method to evaluate the maximum enthalpy involved in the process can be more useful [166,167,168].

2.3.2 *In situ* fibre-optic based techniques

It is important to note that most of the analytical investigations mentioned in Section 2.3.1 were carried out in laboratory environment. This can underestimate the real effect of processing conditions in industrial manufacturing techniques such as autoclave processing, filament winding, pultrusion and resin transfer moulding [169]. Among *in situ* cross-linking monitoring methods, electrical-based sensing techniques attracted considerable demand over the last decade as reliable process monitoring solutions in composites [170]. Dielectrometry [171,172,173,174] and electrical resistivity [115,175,176] are known to be well-established sensing technique used in the composites process monitoring.

None of these direct methods may be used to measure the extent of reaction at specific locations within a large structure during fabrication. Also cross-correlation of dielectric data with other measurement methods such as spectroscopy and thermal analysis (DSC) seems to be difficult as the dielectric properties depend on frequency. Therefore further data processing is required to reduce the dielectric data to cross-linking kinetics that are free from frequency effects. However, attempts have been made to quantify cure kinetics using dielectric parameters those can provide absolute values of viscosity, reaction rate and degree of conversion [115,177,178]. Experimental studies are also reported on Hall Effect sensing [179] and electromagnetic wave monitoring [180], which are capable of measuring localised

reaction kinetics. These methods give a qualitative interpretation of cross-linking, which involves complex measurement systems and require frequent calibration [181].

Increased attention has been paid to using fibre-optic sensing techniques for monitoring of cross-linking reaction of thermosets, due to their outstanding sensing capabilities compared with that of other electrical-based sensing techniques [170,182,183]. They are capable of monitoring chemical reactions continuously even in harsh environments in which most of the electrical-based sensors fail to exhibit their sensing performance. Smart composite applications with embedded fibre-optic sensors within the structure for process monitoring have been proposed and investigated [181,170,184,185].

One of the advantages of choosing optical fibre-based sensors is that the dimensions of sensors are small compared with the electrical-based sensing techniques [186]. For example, in the case of biomedical sensing, sensors must be small and can utilise only a fairly restricted set of biocompatible materials [187,188]. On the other hand, low cost, multi-sensing capabilities [189,190] and long life with minimum maintenance are important requirements for process and/or health monitoring of smart composite structures.

2.3.2.1 Absorption-based fibre-optic techniques

Among the wide range of fibre-optic techniques developed for remote sensing, absorption-based sensors have attracted considerable interest due to their low-cost, robustness, ease of use and low requirements for sample preparation [191,192]. Examples of these types of fibre sensors include those based on absorption and fluorescence [193]. Two general groups of spectral-based optical sensors are available, those that directly probe a spectro-chemical

property of the sample [21] and those that indicate or infer the presence/absence of a chemical species of interest [194].

Fibre-optic Fourier transform infrared spectroscopy

George *et al.* [147] and Rogers *et al.* [195] studied the effect of microwave and thermal processing on cross-linking kinetics of TGDDM/DDS epoxy resin systems using a fibre-optic sensor design in transmission mode. In addition, the effect of cell geometry on the cross-linking kinetics of microwave processing was investigated using rectangular and cylindrical cell in comparison with the thermal processing. Fluorine-doped silica-clad silica fibre was used for sensing and two cleaved fibres were aligned facing each other using a micro-capillary as shown in Figure 2.7. The cavity was filled with resin and near-IR spectra were recorded on-line during cross-linking.

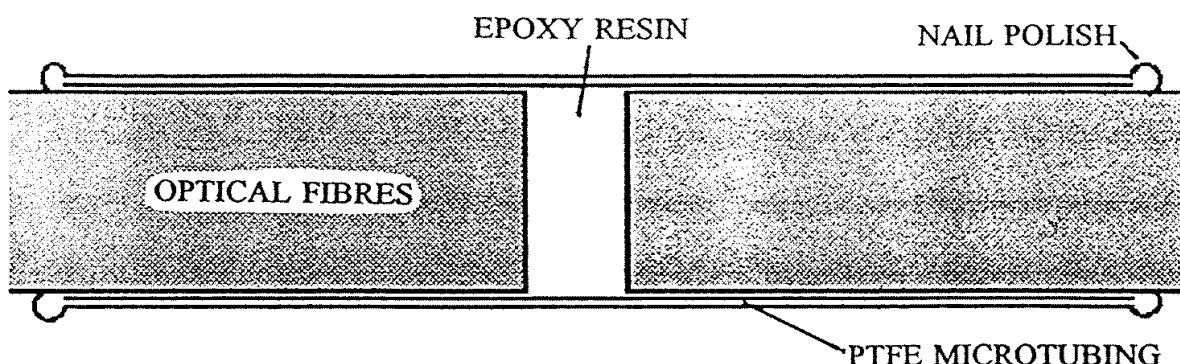


Figure 2.7 Schematic diagram of the NIR transmission cell used for process monitoring [147,195].

The change in peak area of absorption bands due to primary amine and epoxy groups was analysed and an anomalous trend of rate of chemical conversion was observed with microwave processing compared with that observed with thermal processing. The observed behaviour was explained in terms of thermal gradient in two different cell geometries used for microwave processing. Mijović *et al.* [136] proposed a similar fibre-optic transmission cell

design for *in situ* process monitoring in which transmitting and receiving fibres are aligned in a capillary. Reaction kinetics of selected epoxy/amine resin systems were investigated using remote near-infrared transmission spectroscopy and reproducible spectral quality was achieved with the sensor design. A slower initial rate of reaction was observed in a DGEBA/DDM resin system compared with that of a DGEBA/DDM resin system and the authors hypothesised that the trend was due to the presence of $[-C-(CH_3)_2]$ group in the former epoxy resin system.

Powell and co-workers [196] reported fibre-optic transmission spectroscopy for monitoring reaction kinetics of a DGEBA/1,6-diaminohexane resin system. A transmission cell was constructed by holding two cleaved silica optical fibres on a pre-cured epoxy alignment V-groove as shown in Figure 2.8.

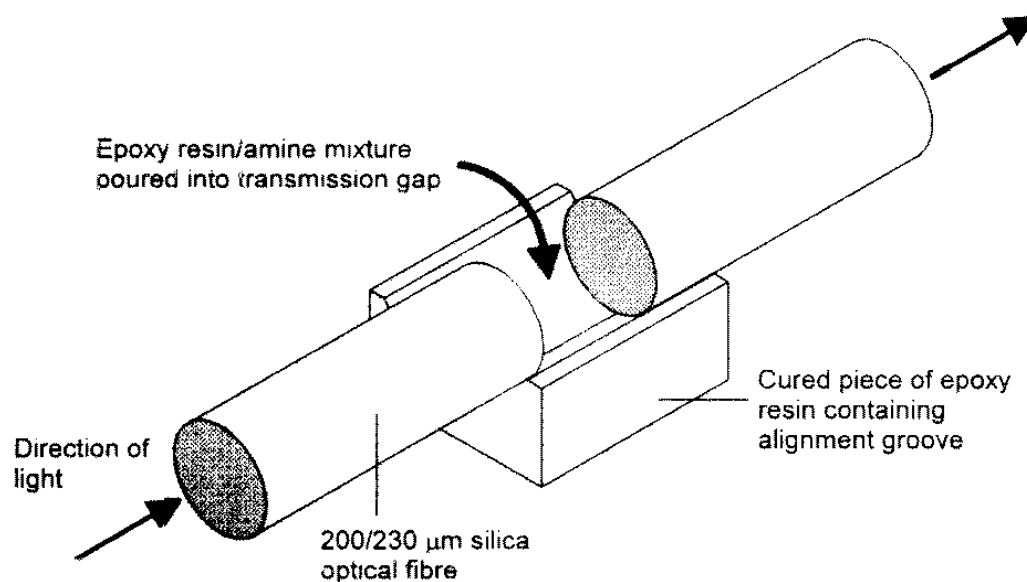


Figure 2.8 Schematic diagram of transmission spectroscopic sensor [196].

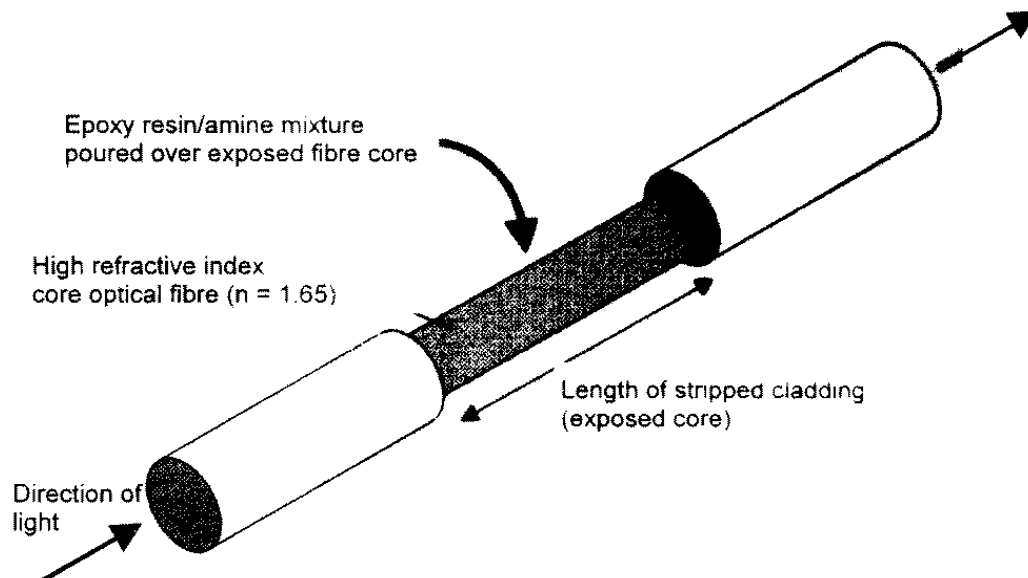


Figure 2.9 Schematic diagram of optical fibre evanescent absorption sensor/stripped cladding refractive index sensor [196].

The authors also carried out a comparative investigation on monitoring of cross-linking reaction based on both evanescent wave absorption spectroscopy and intensity modulation of evanescent excitation using high-refractive index optical fibre. A schematic illustration of the stripped section of an optical fibre for evanescent sensing is shown in Figure 2.9. Good spectral quality was observed with the single-fibre transmission spectroscopy. Several other on-line and off-line sensor design configurations for cross-linking monitoring based on transmission spectroscopy have been successfully demonstrated [81,82].

Calvert *et al.* [21] reported on another sensing configuration in which a single embedded fibre was used for obtaining near-infrared spectroscopy. A cleaved silica-clad silica fibre was embedded in a free-formed epoxy substrate facing perpendicular to a flat edge of the substrate as shown in Figure 2.10.

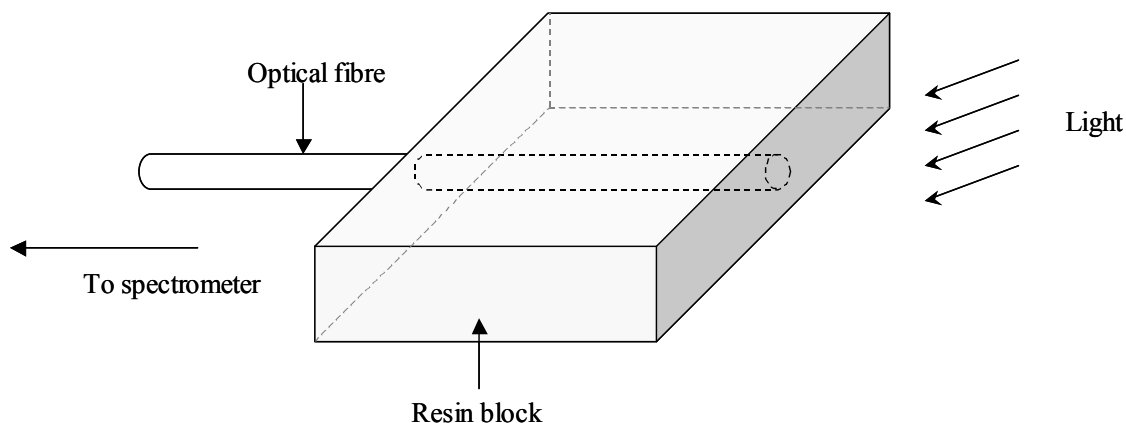


Figure 2.10 Schematic diagram of an optical fibre embedded in a resin block. [21].

The gap between the substrate edge and the fibre end face was approximately 2 mm. The substrate edge was illuminated while the free end of the fibre was connected to a near-infrared spectrometer for spectral acquisition. Infrared radiation coupled in to the fibre through the thin layer of resin was used for spectroscopic measurements. However, the feasibility of using this sensor design for on-line process monitoring is restricted due to the following limitations: (i) strict requirements of sensor location, (ii) the surface of the substrate edge needs to be smooth in order to reduce radiation loss due to scattering and diffuse reflections and (iii) external illumination is required which may not be possible with most industrial processing techniques.

Liu and Fernando [197] proposed and investigated a method for measuring homogeneity of mixed multi-component thermoset resin system using absorbance spectroscopy under transmission mode. A two-wavelength optical fibre-based sensor system was successfully demonstrated for on-line monitoring of amine concentration in commercial epoxy/amine-based resin systems. Furthermore, the feasibility of using fibre-optic spectroscopic sensor designs in reflection mode for *in situ* cross-linking monitoring was demonstrated. The

majority of research work in the literature has been focussed on designing non-contact reflection spectroscopy [129,130,138,198].

Fibre-optic evanescent wave spectroscopy

Fibre-optic evanescent wave spectroscopy has been extensively used as absorption-based sensing technique where absorption characteristics of excited evanescent wave at the fibre/analyte medium are monitored [137,199,200,201,202]. The sensing technique has also been successfully demonstrated using industrial reinforcing glass fibres for cross-linking monitoring of composites [203,204,205] and issues related to using reinforcing fibres as a sensor have been discussed in detail [206]. Hence this technique possesses major advantage of eliminating dimensional mismatch among reinforcing fibres and conventional optical fibres.

Fibre-optic fluorescence spectroscopy

Fluorescence spectroscopy involves analysing fluorescence from a sample, which contains fluorescence-emitting compounds. It involves using a beam of light, usually ultraviolet light, that excites the electrons in molecules of certain compounds and causes them to emit light of a lower energy, typically, but not necessarily, visible light. In fluorescence spectroscopy, a molecule of the fluorescence-emitting compound absorbs a photon and jumps from its ground electronic state to an excited electronic state. The molecule drops down to the ground electronic level again emitting a photon due to collisions with other molecules. Depending on the vibrational energy level in the ground state, the photon may have different energies and thus frequencies. Therefore, fluorescence spectroscopy involves analysing the emitted light at different frequencies and relative intensities.

Use of fibre-optic fluorescence spectroscopy for monitoring the cross-linking reactions of thermosetting resins was based on the shift of fluorescence peak due to the change in resin viscosity during cross-linking. *In situ* fibre-optic fluorescence spectroscopy was deployed for the investigation of cross-linking process of epoxy resins [207,208,209,210,211]. In more detailed studies, evanescent wave fluorescence spectroscopy was applied for process control of resin transfer moulding (RTM) [212,213]. The evanescent fluorescent sensor design is based on the monitoring of the fluorescence wavelength shift that can be monitored upon evanescent excitation at the fibre/analyte surface.

Fibre-optic Raman spectroscopy

When electromagnetic radiation interacts with a vibrating molecule in matter and the scattered photon is lower in energy by an amount equal to a vibrational transition, Raman scattering occurs. Raman spectroscopy has become a very popular *in situ* process monitoring technique in composites due to recent advancements in associated instrumentation [214]. Cooney *et al.* [215] discussed the effect of optical properties of optical fibres on Raman probe designs and probe performance. Different fibre-optic Raman probe designs were evaluated in terms of probe geometry for laser transmission and collection of backscattered light. They concluded that the degree of sensitivity and relative sample location can be optimised by varying probe design parameters such as fibre radius, number of fibres, fibre separation, numerical aperture and presence or absence of focussing lenses. Fibre-optic Raman spectroscopic techniques also had a significant advancement in assessing reaction kinetics in composite processing [216,217,218]. Aust and co-workers [219] used fibre-optic Raman spectroscopy for *in situ* cross-linking monitoring of a DGEBA/POP epoxy resin system. They were capable of resolving polymer cracking at the fibre/resin interface with their sensor

configuration in which the distal end of an optical fibre was inserted into a Teflon[®] tube that has been filled with an epoxy resin system to be examined.

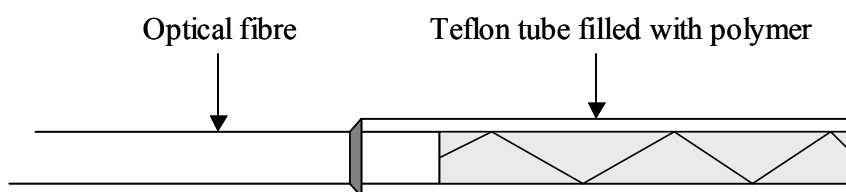


Figure 2.11 Schematic diagram of the fibre-optic Raman probe tip. [219].

Lyon *et al.* [217] employed a pair of 250 μm quartz, step-index fibres for acquiring *in situ* fibre-optic Raman spectroscopy of a PEG/diethylamine (DEA) resin system during cross-linking. The fibre-optic probe consists of two polished optical fibres bonded side-by-side into a SMA connector for immersing into the epoxy/amine resin system. A GaAlAs diode laser was used with a bandpass filter and a microscope for illuminating the resin sample at the probe tip and the second fibre in the probe was used to collect the scattered light. A holographic filter and collimating lenses were used to focus the scattered light to a charge-coupled device (CCD) detector. Spectral calibration of Raman spectra was carried out in the MIR region using different concentrations of DGEBA dissolved in DGEBA-DEA adduct. Cross-linking kinetics of the epoxy/amine resin system at room temperature was investigated using the change in ratio of Raman scattered intensity of the characteristic peak at 1245 cm^{-1} due to epoxide groups. Good agreement was observed between the data obtained using fibre-optic Raman spectroscopy and FTIR spectroscopy.

2.3.2.2 Intensity-based fibre-optic techniques

Zimmermann *et al.* [220] and Lam and Afromowitz [221,222] reported a fibre-optic sensing technique where modulation of transmitted light intensity through a sensing fibre was used as a measure of the extent of cross-linking. The sensing fibre was fabricated using the same resin system that was used as matrix in the composite prepreg to avoid the possible negative influence of embedded fibre-optic sensors on the structural integrity of the composite. It was observed that the transmitted light intensity is a function of the refractive index of the resin. Conventional multimode fibres were used to guide light to and from the epoxy-sensing element. In addition, the sensing concept was also demonstrated under two modes of operation; reflection and higher-order launch modes and feasibility of operating the sensor under each mode was discussed [181]. Lam and Afromowitz [223] derived a model for optical transmission characteristics of the sensor design. Moreover, the model can be used successfully to describe reaction kinetics of the cross-linking process based on the sensor response. The same sensing principle was applied for composite process monitoring based on intensity modulation of transmitted light through de-cladded optical fibre [224]. In an alternative approach, the sensing concept was demonstrated for monitoring of cross-linking reaction in hot-press, model autoclave and also in a large industrial autoclave [225] and for flow control and cross-linking monitoring of resin transfer moulding [226].

A simple fibre optic technique for cross-linking monitoring of epoxies based on the principle of Fresnel reflections has been studied. When light travels from one medium to another medium which has a different refractive index from that of the first, it undergoes both reflection and refraction at the interface. The fraction of the incident light reflected back to the incident medium at the interface is known as the Fresnel reflection [227]. The sensor configuration consists of cleaved fibre inserted in to the composite structure where the

reflected light intensity is measured as a function of cross-linking [82,149,228,229,230]. The sensing principle is based on the refractive index mismatch between resin and the fibre core at the resin/fibre interface and the sensor configuration has inherent advantages such as simple and inexpensive design and less induced effects within the composite structure due to the sensor dimensions. The same phenomenon of Fresnel reflection is used in a different fibre-optic design, which can be used not only for process monitoring but also for structural health monitoring [231]. In this sensor design, a conventional extrinsic Fabry-Perot interferometer (EFPI) was used with a modified reflector fibre to monitor degree of conversion based on reflectometry. In the modified sensor design, the free end of the reflector fibre was cleaved. The fibre illumination source and the Fabry-Perot cavity length were chosen such that reflected light intensity at the cleaved reflector fibre was used for process monitoring while the EFPI sensor can be used for strain measurements after processing.

Surface plasmon resonance has also been exploited in various forms to study surface and bulk chemical reactions. Fibre-optic sensors based on this phenomenon demonstrate high sensitivity to refractive index changes and allow cross-linking reactions to be monitored directly, without the need for a reagent [232].

2.3.2.3 Other fibre-optic techniques

Recently, a considerable research effort has been focused on using fibre Bragg grating (FBG) sensors for chemical sensing [233,234]. These sensors have a number of distinct advantages over other sensing schemes; one of the most important of which is that the sensed information is encoded directly into wavelength, which is an absolute parameter [235,236]. Therefore the

output does not depend directly on the total light levels, losses in the connecting fibres and couplers, or recalibration or re-initialisation of the system.

Because a FBG is compact and simple in fabrication, it has become an important component for optical sensing devices in measuring process monitoring in composites [237,238,239,240,169]. Long-period gratings (LPG) have been used for flow monitoring and cross-linking monitoring in resin transfer moulding (RTM) [241]. Buggy *et al.* [237] presented a methodology to obtain a change in refractive index of resin during processing using LPG and tapered fibre Bragg gratings (TFBG). Furthermore, FBG sensors also can be used for monitoring real-time strain development in composites during processing [242].

In addition to multiplexed FBG sensor arrays, fibre-optic sensors based on optical time domain refractometry (OTDR) are also used for process monitoring where multiplexing of sensors is required [243].

2.4 Hygrothermal ageing in epoxy/amine resin systems

2.4.1 Nature of water in epoxy resins due to moisture absorption

The importance of understanding the absorption mechanisms and the nature of water in epoxy resins has been widely emphasised and investigated. Water is said to be present in two forms in cross-linked thermosetting resins [15,244]: bound and unbound water. Water molecules occupying the free volume present in polymers are referred as unbound/free water. On the other hand, water molecules that are chemically attached to hydrophilic functional groups in polymers such as hydroxyl and amine groups are considered as bound water [245].

A systematic approach was reported by Soles *et al.* [246] to quantify the contributions of free volume and polar interactions on equilibrium moisture content in various epoxy amine systems using positron annihilation lifetime spectroscopy (PALS). They summarised that the existence of free and bound water is interactive and competitive and the dominating factor strongly depends on the network topology of the epoxy/amine system and the cross-linking density. However, the same authors [247] reported that the absorption kinetics of water in the resin systems studied is independent of the free volume present in the resin. Furthermore, they postulated that the free volume present in the polymer only takes part in the initial stage of diffusion in the dry polymer and the polar interactions govern the absorption kinetics in epoxy/amine resin systems. They also have given a graphical interpretation to explain the above contradictory conclusions and suggested that in epoxy/amine systems, nanopores associated with cross-linked junctions assist water molecules to be transported in to the membrane but the association/disassociation of hydrogen bonding between polar sites in the

epoxy and water molecules regulates the diffusion kinetics [248]. In other research, Li *et al.* [249] observed a similar absorption mechanism and stated that the equilibrium moisture content of a polyetherimide (PEI) modified DGEBA/DDS epoxy system is insensitive to the free volume.

Zhou and Lucas [250] suggested that there are two main types of absorbed water in epoxies while Apicella and co-workers [251] proposed that there may be three types of absorbed water in epoxy resins: (i) formation of a solution of polymer and solute, (ii) adsorption to hydrophilic groups via hydrogen bonding, and (iii) absorption into the “holes” of the glassy structure. In the former work, the authors investigated the sorption characteristics of DGEBA/meta-phenylene diamine (*mPDA*) and TGDDM/DDS systems based on nuclear magnetic resonance (NMR). They suggested that the absorbed water can adhere to the epoxy main chain via single hydrogen bonds (*Type-I*), which possesses low activation energy or multiple interconnecting hydrogen bonding (*Type-II*) at higher conditioning temperatures and longer exposure time. They postulated that the *Type-I* water breaks the original van der Waals forces presented in the polymer network dominating plasticisation while the *Type-II* bond complexes dominate secondary cross-linking between polymer chains. Apicella *et al.* [251] studied DGEBA/TETA and TGDDM/DDS systems based on gravimetry and DSC analysis and discussed possible absorption mechanisms in both resin systems.

2.4.2 Fundamental laws of diffusion in polymers

2.4.2.1 Fickian diffusion

Peppas and Meadows [252] and Frisch [253] reviewed theories involved in water diffusion in glassy polymers. They discussed two main approaches that have been employed for describing transport phenomenon of low-molecular weight substances in polymers. One approach is based on the principles of irreversible thermodynamics that employs phenomenological coefficients to correlate the diffusion gradient across the membrane [254]. The most popular approach is based on the generalised Fickian diffusion equations derived for steady-state diffusion of binary systems [255,256,257,258]. The moisture absorption behaviour of polymeric materials has been treated as a steady-state or diffusion-controlled process as described by Fick's first law [259,260]:

$$j = -D \frac{\partial c}{\partial x} \quad \text{Equation 2.20}$$

where j is flux in the x direction, which is along the thickness of a specimen and the only direction in which mass transfer is taking place, D is diffusivity/diffusion coefficient and c is the concentration of diffusing species.

The conservation of species equation in one dimension is given by:

$$\frac{\partial c}{\partial t} = -\frac{\partial}{\partial x} j \quad \text{Equation 2.21}$$

where t is time.

Combining Equation 2.20 and 2.21, the one-dimensional diffusion in a specimen of thickness L and with constant diffusivity is expressed as:

$$\frac{\partial c}{\partial t} = \frac{\partial}{\partial x} \left(D \frac{\partial c}{\partial x} \right) \quad \text{Equation 2.22}$$

Assuming the temperature and the diffusion constant are constant inside the material, based on Fick's second law Equation 2.22 can be written as:

$$\frac{\partial c}{\partial t} = D \frac{\partial^2 c}{\partial x^2} \quad \text{Equation 2.23}$$

Applying appropriate boundary conditions for a specimen exposed to water on both sides and for constant D , the solution to Equation 2.23 leads to the following expression [260]:

$$\frac{M_t}{M_\infty} = 1 - \frac{8}{\pi} \sum_{m=0}^{\infty} \frac{1}{2m+1} \exp \left[-\frac{D(2m+1)^2 \pi^2 t}{L^2} \right] \quad \text{Equation 2.24}$$

where M_t is absorbed moisture at time, t and M_∞ is the equilibrium moisture content.

For $\frac{Dt}{L^2} > 0.05$, Equation 2.24 can be approximated to

$$\frac{M_t}{M_\infty} = \frac{4}{\pi^{1/2}} \left(\frac{Dt}{L^2} \right)^{1/2} \quad \text{Equation 2.25}$$

Shen and Springer and co-workers [255,261] demonstrated the absorption kinetics of unidirectional and quasi-isotropic Fiberite T-300/1034 and woven Fiberite T-300/976

composites based on a Fickian model. Effects of different hygrothermal conditions were investigated and good correlation was observed with the model and experimental results [262].

2.4.2.2 Non-Fickian diffusion

It has been found that in practical situations, the accuracy and validity of considering the diffusion coefficient as a constant is dependent on the chemical composition of the polymer and the hygrothermal exposure conditions [252,263,264]. Deviations from Fickian diffusion towards anomalous transport behaviour have been observed for many polymers [246,247,249,265]. Some of the basic assumptions made for deriving Fickian diffusion models about mass transfer break down in glassy polymers. Glassy polymers are not at equilibrium, but they relax slowly towards it. Due to this viscoelastic relaxation of polymers, the Boltzmann scaling in absorption is no longer satisfied [266]. In these cases the diffusion coefficient becomes dependent not only on the temperature, but also on the exposure time and the concentration [267,268]. Furthermore, moisture uptake does not reach saturation, but increases slowly with time. Therefore the prediction of diffusion phenomenon in complex systems including multi-components systems such as composites is not possible with simple kinetic models. In case of composites, the absorption kinetics of water depends on the diffusivities of fibres and matrices, fibre volume fraction, void content, residual stresses and the geometry of the reinforcing fibres [269,270,271].

Carter and Kibler [272] suggested a dual-mode sorption model to explain the anomalous diffusion behaviour of water in epoxy resins. Their model is based on the existence and interactions of mobile and bound water molecules within a material and derived expressions for explaining diffusion behaviour of water are summarised below. The model assumes the

mobile water molecules diffuse with a concentration-independent diffusion coefficient, D_γ and become bound with a probability per unit time γ and the bound molecules become mobile, with a probability per unit time β . Also at time t , the number of mobile molecules per unit volume of the material is n and the number of bound molecules per unit volume is N . A value κ was defined as the parameter that determines the rate of saturation of absorbed moisture in the material based on one-dimensional Fickian diffusion theory and is given below:

$$\kappa = \frac{\pi^2 D_\gamma}{(2\delta)^2} \quad \text{Equation 2.26}$$

where 2δ is the thickness of the specimen. Furthermore, assuming the diffusion of mobile molecules obeys the simple diffusion theory, for the one-dimensional case, the molecular number densities at position z along the thickness and time t satisfy the coupled pair of equations:

$$D_\gamma \frac{\partial^2 n}{\partial z^2} = \frac{\partial n}{\partial t} + \frac{\partial N}{\partial t} \quad \text{Equation 2.27}$$

$$\frac{\partial N}{\partial t} = \gamma n - \beta N \quad \text{Equation 2.28}$$

Solutions for Equation 2.27 and 2.28 can be obtained by considering boundary conditions for an initially dry specimen exposed to a constant hygrothermal conditions on both sides. At $t = 0$, the appropriate boundary and initial conditions are:

$$n(z, 0) = 0 \text{ and } N(z, 0) = 0 \text{ for } |z| < \delta$$

and

$$n(\delta, t) = n_\infty \text{ and } n(-\delta, t) = n_\infty \text{ for all } t.$$

Using the above boundary conditions, expressions for the spatial distribution of the bound molecules $N(z, t)$ and the mobile molecules $n(z, t)$ can be expressed as:

$$N(z, t) = \frac{\gamma}{\beta} n_\infty \left\{ 1 - \frac{4}{\pi} \sum_{l=0}^{\infty(\text{odd})} \frac{(-1)^{(l-1)/2}}{l(r_l^+ - r_l^-)} \left[r_l^+ \exp(-r_l^- t) - r_l^- \exp(-r_l^+ t) \right] \cos \frac{\pi l z}{2\delta} \right\} \quad \text{Equation 2.29}$$

$$n(z, t) = \frac{\gamma}{\beta} n_\infty \left\{ 1 - \frac{4}{\pi} \sum_{l=1}^{\infty(\text{odd})} \frac{(-1)^{(l-1)/2}}{l(r_l^+ - r_l^-)} \left[r_l^+ \exp(-r_l^- t) - r_l^- \exp(-r_l^+ t) \right] \cos \frac{\pi l z}{2\delta} \right\} \\ + n_\infty \frac{4}{\pi \beta} \sum_{l=1}^{\infty(\text{odd})} \frac{(-1)^{(l-1)/2}}{l(r_l^+ - r_l^-)} (r_l^+ r_l^-) \left[\exp(-r_l^- t) - r_l^- \exp(-r_l^+ t) \right] \cos \frac{\pi l z}{2\delta} \quad \text{Equation 2.30}$$

where

$$r_l^\pm = \frac{1}{2} \left[(\kappa l^2 + \gamma + \beta) \pm \sqrt{(\kappa l^2 + \gamma + \beta)^2 - 4\kappa\beta l^2} \right]$$

Integration of the above results along the specimen thickness gives the moisture uptake (M_t) in an initially dry one-dimensional specimen after exposure time t , is given by:

$$M_t = M_\infty \left\{ \begin{aligned} &1 - \frac{8}{\pi} \sum_{l=1}^{\infty (odd)} \left[\frac{r_l^+ \exp(-r_l^- t) - r_l^- \exp(-r_l^+ t)}{l^2 (r_l^+ - r_l^-)} \right] \\ &+ \frac{8}{\pi} \left(\frac{\kappa \beta}{\gamma + \beta} \right) \sum_{l=1}^{\infty (odd)} \left[\frac{r_l^+ \exp(-r_l^- t) - r_l^- \exp(-r_l^+ t)}{r_l^+ - r_l^-} \right] \end{aligned} \right\} \quad \text{Equation 2.31}$$

The above equation can be simplified when 2γ and 2β are both smaller compared with κ , as follows:

$$M_t ; M_\infty \left\{ \begin{aligned} &\frac{\beta}{\gamma + \beta} e^{-\gamma t} \left[1 - \frac{8}{\pi} \sum_{l=1}^{\infty (odd)} \frac{e^{-\kappa l^2 t}}{l^2} \right] \\ &+ \frac{\beta}{\gamma + \beta} (e^{-\beta t} - e^{-\gamma t}) + (1 - e^{-\beta t}) \end{aligned} \right\} ; \quad 2\gamma, 2\beta \ll \kappa \quad \text{Equation 2.32}$$

When $\gamma = 0$, Equation 2.31 reduces to one-dimensional Fickian diffusion. For short exposure times where κt is approximately less than 0.7, Equation 2.31 can be approximated as follows:

$$M_t ; \frac{4}{\pi^{2/3}} \left(\frac{\beta}{\gamma + \beta} M_\infty \right) \sqrt{\kappa t} ; \quad 2\gamma, 2\beta \ll \kappa, t \leq 0.7/\kappa \quad \text{Equation 2.33}$$

Also, for longer exposure times when κt is large compared with unity, Equation 2.31 can be approximated as follows:

$$M_t = M_\infty \left[1 - \frac{\gamma}{\gamma + \beta} e^{-\beta t} \right] \quad 2\gamma, 2\beta \ll \kappa, t \gg 1/\kappa \quad \text{Equation 2.34}$$

Furthermore, the moisture uptake seems to be consistent with a quasi-equilibrium moisture content which appears at times, $\kappa t = 5$ and is given by:

$$M_t = M_\infty \left(\frac{\beta}{\gamma + \beta} \right); \quad t = 5/\kappa \quad \text{Equation 2.35}$$

Popineau *et al.* [273] observed the same absorption phenomenon in an ambient-temperature, flexible epoxy adhesive confirming the validity of the Carter and Kibler model [272] that explains the dual-mode/Langmuir-type absorption. They employed deuterium NMR analysis to study the mobility of water absorbed. They have postulated the water transport in the epoxy system in four steps assuming two types of absorbed water, “free/mobile” and “bound/clustered” water:

“(i) at the beginning of absorption, molecular water with strong interactions diffuses into the polymer. These are ‘solo’ molecules and thus quite free or mobile; (ii) after a given absorption time (depending on the temperature), the interaction sites for molecular water become saturated: absorption reaches a quasi-equilibrium; (iii) water absorption recommences, but water molecules can only stay in micro voids, and form clusters. These are large, inertial and thus, to all intents and purposes, bound and (iv) water absorption reaches a real equilibrium when all the micro voids are filled”.

They highlighted that the terms, mobile and bound used were referred to the kinetics of the types of water and not directly to interactions of water with the polymer molecules. Reasonable correlation was observed between NMR results and the Carter and Kibler model.

Marsh *et al.* [274] observed multi-stage diffusion behaviour of water in neat epoxy and glass-epoxy composites. Epoxy resin system used was a blend of a brominated bisphenol A and Cresol Novolac, with dicyanamide as the cross-linking agent. They investigated the applicability of the Carter-Kibler model and the relationship of the conditioning temperature and the kinetic parameters, γ and β . Furthermore, they proposed a method of modelling multi-stage diffusion characteristics of water considering time-dependent diffusion coefficient. The diffusion coefficient was obtained using a simplified one-dimensional Fickian diffusion model proposed by Shen and Springer [255] and given below:

$$M_t = M_i + \left\{ (M_\infty - M_i) \left[1 - \exp(-7.3) \left(\frac{Dt}{L^2} \right) \right] \right\}^{3/4} \quad \text{Equation 2.36}$$

where M_i is initial moisture content. Equation 2.36 can be rearranged as follows:

$$D = \left(\frac{L^2}{t} \right) \left\{ \left(-\frac{1}{7.3} \right) \ln \left(\frac{M_\infty - M_t}{M_\infty - M_i} \right) \right\}^{4/3} \quad \text{Equation 2.37}$$

Different stages of sorption isotherms were analysed in terms of the diffusion coefficients corresponding to each stage. They observed a decrease in diffusion coefficient as a function of immersion time due to the endothermic nature of the sorption process within the epoxy system.

Roy *et al.* [268] proposed and validated a new methodology based on finite element analysis (FEA) for characterising non-Fickian diffusion in an epoxy adhesive. The model was based on history-dependent diffusion related to viscoelastic relaxation of polymers. They modified

the one-dimensional Fickian diffusion model considering time-varying diffusivity of water. Assuming that the diffusivity can be expressed in the form of a Prony Series:

$$D(t) = D_0 + \sum_{r=1}^R D_r \left(1 - e^{-t/\tau_r}\right) \quad \text{Equation 2.38}$$

where $D(t)$ is time-varying diffusivity, D_0 , D_r are unknown temperature-dependent Prony coefficients, τ_r are the corresponding retardation times and R is the number of terms in the Prony series.

Substituting Equation 2.38 in Equation 2.24 results in an expression for fraction of moisture uptake as a function of time:

$$\frac{M_t - M_i}{M_\infty - M_i} = 1 - \frac{8}{\pi^2} \sum_{m=0}^{\infty} \frac{1}{(2m+1)^2} \exp \left\{ \frac{-(2m+1)^2 \pi^2}{h^2} \times \left[D_0 + \sum_{r=0}^R D_r \left[t + \tau_r \left(e^{-t/\tau_r} - 1 \right) \right] \right] \right\} \quad \text{Equation 2.39}$$

where M_i is the initial moisture content. Good agreement between the predicted model and test data was observed at all temperatures that were considered. However, it was stated that defining a universal model to describe all types of moisture sorption phenomena may not be practical as the diffusion and absorption mechanism is complex and specific to molecular interactions between the water and polymer network of interest [272,274].

2.4.3 Parameters affecting the diffusion kinetics of water

2.4.3.1 Influence of temperature

Temperature has a most profound influence on the absorption kinetics. The temperature dependence of the diffusion coefficient assumed to be followed the Arrhenius relation and is given as follows [275]:

$$D = D_0 \exp\left(-\frac{Q_d}{RT}\right) \quad \text{Equation 2.40}$$

where D_0 is a temperature-independent pre-exponential factor, Q_d is the activation energy for diffusion, R is the universal gas constant and T is the temperature in °K.

Apicella *et al.* [267] studied the effect of immersion temperature on the diffusion constant in a DGEBA/TETA resin system. The diffusion behaviour of the resin system was studied at 23, 45 and 75°C and Arrhenius temperature dependence of the diffusion coefficient was observed at the immersion temperatures studied. Based on an analysis of absorption data of over seventy resin formulations, Wright [12] summarised that the diffusion coefficient is very much dependent upon the temperature of exposure.

2.4.3.2 Influence of processing conditions

It is a well-established fact that the extent of cross-linking and network relaxation has considerable influence on the effects of absorbed water in epoxy resin systems [276,277,278]. The presence of water has been found to have an influence on the reaction mechanisms and therefore on the cross-linking kinetics of epoxy/amine systems and visa versa. Wu *et al.* [279] observed that the absorbed moisture alters the reaction rate and degree of cross-linking

of two epoxy/amine resin systems. Cross-linking kinetics of the resin systems was characterised using isothermal DSC analysis and the effect of absorbed moisture was investigated with 2, 4 and 6 % water of total weight of resin/hardener mixture. Epoxy resin without water showed typical autocatalytic behaviour and when the water was added, the initial reaction rate increased and the reaction mechanism showed n^{th} order reaction behaviour. Chen *et al.* [280] studied the effect of absorbed moisture on the reaction kinetics of a DGEBA/POP resin system using near-IR FTIR spectroscopy. The effect of the absorbed moisture on the reaction kinetics of the resin system was studied varying the ratio of the weight of water to the hardener, $w = 0$ to 0.1 . Increase in reaction rate was observed with increase in moisture up to $w = 0.06$.

2.4.3.3 Influence of hygrothermal history

Published work on water absorption in epoxy resins showed that both the absorption kinetics and the equilibrium moisture content could be strongly influenced by the history of hygrothermal conditions that the sample has undergone in service [281,282]. A DGEBA/TETA epoxy system that was conditioned in water at $60\text{ }^{\circ}\text{C}$ and cooled back down to $20\text{ }^{\circ}\text{C}$ has shown higher equilibrium moisture content than that conditioned at $20\text{ }^{\circ}\text{C}$ [251]. Similar history-dependent apparent equilibria have been reported in the literature [267] and this has been attributed to hygrothermally-induced microcavitation or irreversible physical damage at higher conditioning temperatures [283]. It was also reported that the extent of irreversible damage is a function of both temperature and exposure time.

Xiao and Shanahan [284] investigated hygrothermal ageing of a DGEBA/DDA epoxy resin system using gravimetry. Epoxy systems that show dual-mode sorption behaviour have shown single-stage sorption in the subsequent conditioning after drying above their glass

transition temperature. Residual moisture within the aged and subsequently dried specimens at lower drying temperatures was observed when the specimens were dried after the resin reached to first transition stage. Lin and Chen [285] studied the effect of cyclic hygrothermal ageing on properties of a DGEBA/DDA resin system based on molecular dynamic (MD) simulation. Considering MD simulation results of absorption and desorption process in epoxy resins, the residual moisture present in the aged epoxy specimens was attributed to the requirement of higher activation energy for removing bound water from the molecular structure.

2.4.3.4 Influence of mixing ratio of epoxy/amine formulations

The mixing ratio of epoxy/amine formulations has been found to have an influence on the absorption behaviour of the cross-linked resin system. Wu *et al.* [279] studied the effect of mixing ratio on the diffusion kinetics of water in a DGEBA/TETA resin system using density measurements, dynamic mechanical analysis (DMA) and FTIR spectroscopy. An increase in the mixing ratio of cross-linking agent showed an increase in the equilibrium moisture content. They postulated that the difference in cross-linked epoxy network and the concentration of polar groups with change in epoxy/amine mixing ratio affects the diffusion kinetics of water.

Papanicolaou *et al.* [286] investigated the effect of mixing ratio of a DGEBA/DETA system as a function of the mixing ratio of resin/hardener formulation using gravimetry. They observed an increase in diffusivity and equilibrium moisture content as the amine content decreases. The authors hypothesised that in non-stoichiometric epoxy formulations, there is either an excess of unreacted epoxy or excess of unreacted amine. This means that in the sample there are regions of high cross-linking density and regions with less density. These

two phases of the material may show quite different properties. Thus, the rate of diffusion into the lower density phase is much higher than that of the higher density phase.

2.4.3.5 Influence of microstructure

The absorption kinetics and equilibrium moisture content of epoxy systems are governed not only by the hygrothermal environmental conditions but also by the chemical structure of the resin and the cross-linking agent [246,247,287]. A study conducted by VanLandingham *et al.* [288] confirmed that the rate of interaction of epoxy resin with water molecules is markedly dependent on the polarity of the epoxy molecules. Furthermore, the microstructure of epoxy resin systems has been found to have an influence on the free volume and also on the size of voids present in the polymer [289]. Epoxy resins modified with halogen-containing groups have shown reduced absorption [290] compared with that reported for unmodified systems [291]. However, an in-depth investigation is required on the effect of halogen-containing groups on the cross-linking reaction kinetics and on the optimum cross-linking density with typical stoichiometric ratios.

2.5 Monitoring of hygrothermal ageing in epoxy/amine resin systems

2.5.1 Conventional analytical techniques

An essential part of predicting the influence of absorbed moisture on the basic engineering properties of polymers is acquiring their physical, chemical, thermal, viscoelastic and mechanical properties as a function of exposure to humidity and temperature. Without these

fundamental data, lifetime predictions of engineering polymers may not be realistic and cost-effective. Vesely [13] reviewed various analytical techniques that are used for characterising the absorption kinetics of polymers. Among these techniques, conventional gravimetry, DSC, DMTA, FTIR spectroscopy, thermogravimetric analysis (TGA), scanning electron microscopy (SEM) [278,292,293,294,295], Raman spectroscopy, fluorescence spectroscopy are widely used.

In the current study, conventional gravimetry analysis was used as the basic method for determining absorption kinetics of an epoxy/amine system and also used to cross correlate with results obtained using other analytical and fibre-optic sensing techniques. Furthermore, the thermal and viscoelastic properties of the resin system under accelerated ageing conditions were characterised based on DSC, TGA, DMTA and FTIR spectroscopy. The DSC, TGA and DMTA techniques were used to investigate the types of water in the epoxy system and type of molecular interactions during the sorption process. Conventional FTIR spectroscopy was used mainly to analyse possible chemical changes occur during hygrothermal ageing such as post-curing, presence of unreacted monomers, types of water in the epoxy network and also to relate the conventional data with the data obtained using fibre-optic near-infrared transmission spectroscopy. Therefore the review focussed on using the above-mentioned conventional analytical techniques for assessing effect of hygrothermal ageing of epoxy resin systems.

2.5.1.1 Differential scanning calorimetry

Differential scanning calorimetry (DSC) is a technique that provides changes in thermal characteristics of materials associated with both physical and chemical processes. Experimental techniques and the advantages and disadvantages of using DSC for cross-linking monitoring of epoxy resin systems have been discussed previously (see Section

2.3.1.2). The technique is also used widely for characterising the effect of absorbed water in epoxy resin systems on their thermal properties [296,297,298,299]. A DSC thermogram of an aged polymer is a useful means of interpreting change in T_g due to the plasticization of the polymer network, possible post-curing taking place during hygrothermal ageing, physical aging due to prolong exposure to conditioning temperatures [296].

Zhou and Lucas [297] investigated the influence of hygrothermal conditioning on the T_g of a series of epoxy amine resin systems using TMA and DSC analyses. Their study revealed the following results: (i) the change in T_g does not depend only on the equilibrium moisture content, (ii) T_g depends on the hygrothermal history of the polymer, (iii) at longer immersion times and higher exposure temperature result higher T_g . Decrease in T_g was observed followed by an increase in T_g at longer immersion times for all the resin systems studied. Lowest T_g was observed when the specimen first reached saturation. The trend was explained in terms of different types of water/polymer interactions observed based on NMR analyses [250]. A mathematical model was also used to predict the change in T_g as a function of immersion time and temperature:

$$T_{g_{wet}} = \frac{\alpha_e V_e T_{ge} + \alpha_w (1 - V_e) T_{gw}}{\alpha_e V_e + \alpha_w (1 - V_e)} \quad \text{Equation 2.41}$$

$$\text{where } V_e = \frac{1}{1 + 0.01 M_m \left(\frac{\rho_e}{\rho_w} \right)} \quad \text{Equation 2.42}$$

$T_{g_{wet}}$ is of water saturated epoxy, T_{ge} is of dry epoxy, T_{gw} is of water, α_e is epoxy volumetric expansion coefficient, α_w is water expansion coefficient, M_m is equilibrium water content, ρ_e , ρ_w is the density of water. However, a deviation was observed between the experimental

results and the predicted T_g using Equation 2.41. The authors concluded that the model is not capable of explaining the change in T_g of resin systems containing strong polar sites such as hydroxyl groups.

2.5.1.2 Thermo gravimetric analysis

Thermo gravimetric analysis (TGA) of polymers provides important information on their thermal stability and thermal degradation behaviour as a function of time or temperature [267,300,301]. A TGA trace of a material shows the weight changes arising from both physical processes such as evaporation or chemical processes such as decomposition or oxidation. Moisture ingress into a polymer matrix leads to a range of effects including plasticization through interaction of the water molecules with polar groups in the matrix, creation of micro crazes through environmental stress cracking, leaching of unreacted monomer and in certain cases degradation of the resin [302,303]. TGA analysis is a useful tool for analysing possible reversible and irreversible changes take place during hygrothermal ageing. The analysis can be optimised by choosing an inert atmosphere to study the absolute reactions taking place within the polymer sample or by choosing an oxidising atmosphere that stimulate the effect of real environment on the reactions involved [244].

2.5.1.3 Dynamic mechanical thermal analysis

Dynamic mechanical thermal analysis (DMTA) is a technique that used to characterise polymers in terms of their visco-elastic response either as a function of a linear heating rate, function of frequency or as a function of time at a constant temperature.

Most polymers are viscoelastic and their mechanical properties show a marked time- and temperature-dependence. Viscoelastic materials respond to an applied displacement or force

by exhibiting either elastic or viscous behaviour, or a combination of both. The elastic and viscous stresses are related to material properties through the modulus, which is the ratio of stress to strain. The ratio of the elastic stress to strain is the storage (or elastic) modulus E' and the ratio of the viscous stress to strain is the loss (or viscous) Modulus E'' . E' represents the elastic or fully recoverable energy during deformation while E'' represents the viscous or net energy dissipated. The tangent of δ is the ratio of loss modulus to storage modulus, which combines the viscous and elastic components into a single term. In dynamic mechanical analysis, T_g can either be defined as the temperature where the maximum loss tangent or the maximum loss modulus is observed, or as the inflexion point at which a significant drop of the storage modulus occurs [304,305]. However, the respective peaks or points usually occur at different temperatures, which results in a broad transition region for polymeric resins [306,307,308].

DMTA is widely used to investigate the absorption behaviour of water in polymers. The technique has found to be very useful for understanding the mechanical behaviour of epoxy resin systems under hygrothermal ageing conditions [271,294,309]. The unique advantage of using this technique is that the possibility of converting rheological data generated in minutes or hours into information on long-term material performance based on time-temperature superposition, time-strain superposition, or time-concentration superposition using the Boltzmann superposition principle [310,311].

Among common features encountered with the storage modulus, loss modulus and loss tangent traces of aged epoxy resins, peak splitting of the loss tangent has been highlighted. The splitting of the loss tangent peak has been attributed to different chemical [244,301] and physical [15,278,302,312,313,314] phenomena depending on the chemical nature of the

material analysed. It was argued that the heterogeneous (nodular) structure of epoxy/amine based resins not necessarily imply the presence of a multi-phase molecular structure [315]. However deviations from the general amorphous nature have been discussed. Chateauminois *et al.* [316] and Xian and Karbhari [14] have postulated that the peak splitting under dynamic temperature scan is attributed to the dry skin and wet core of the specimen.

2.5.1.4 Fourier transform infrared spectroscopy

In terms of characterising the diffusion behaviour of water in polymers, FTIR spectroscopy provides a strong link between the mechanical and thermal behaviour of the aged material with the chemical modifications occurring at the molecular level [317,318]. In addition, this technique is capable of distinguishing multi-component diffusion. A detailed introduction to the technique and also to the quantitative analysis of chemical groups was given previously (see Section 2.3.1.1). The FTIR technique has been extensively used to postulate the types of chemical interaction between the water and epoxy systems [319,320,321] and also to investigate the leaching taking place in epoxy resin systems under hot-wet conditions [312].

The majority of the moisture ingress characterisation of epoxy systems has been carried out under attenuated total reflection (ATR) mode [322]. Attention has been paid to deriving general expressions for evaluating spectroscopic data based on ATR evanescent field spectroscopy [320,323]. Philippe *et al.* [17] investigated an *in situ* ATR-FTIR technique for determining the absorption kinetics of a series of epoxy-based paints and the hygrothermal conditioning was carried out at room temperature. The absorption band in the range of 3000 – 3700 cm^{-1} was used to achieve the extent of moisture uptake as a function of immersion time. The one dimensional Fickian diffusion model (see Equation 2.24) was modified to take

account of the evanescent electric field with the diffusion profile and the modified equation is given below:

$$\frac{A_t - A_0}{A_\infty - A_0} = 1 - \frac{8\gamma}{\pi \left[1 - \exp\left(\frac{2L}{\gamma}\right) \right]} \sum_{n=0}^{\infty} \left[\frac{\exp\left[\left(D\pi^2 t / 2L^2\right)\pi\right] + (-1)^n \left(\frac{2}{\gamma}\right)}{\left[\left((2n+1)/2L\right)\pi\right]^2 + \left(\frac{4}{\gamma^2}\right)} \right] \times \exp\left[-\left(\frac{2n+1}{2L}\pi\right)^2 Dt\right]$$

Equation 2.43

where A_0 is absorbance of a dried polymer specimen, A_t is the absorbance at time t , A_∞ is the absorbance at saturation, L is thickness of the specimen and D is the diffusion coefficient.

$$\gamma = \frac{2n_2\pi \left[\sin^2 \phi - \left(\frac{n_1}{n_2}\right) \right]^{1/2}}{\lambda}$$

Equation 2.44

where n_1 and n_2 are refractive indices of the polymer specimen and the ATR crystal, respectively and ϕ is the angle of incident of the infrared radiation.

Spectral data were successfully used to predict the absorption behaviour of water in the resin systems and observed dual-mode diffusion behaviour. This anomalous diffusion behaviour was attributed to

“two different water hydrogen bonding distributions. One resulted from rapidly sorbed, strongly hydrogen-bonded water at polymer ‘active’ sites. The second distribution was connected with the (slower) sorption into microvoids in the cured polymer network”.

Cotugno and co-workers [324,325] discussed disadvantages associated with determining absorption kinetics using ATR- FTIR and proposed a novel *in situ* spectroscopic technique under transmission mode in MIR region.

The technique has been successfully used to develop absorption and desorption isotherms in a TGDDM/DDS resin system. Conditioning experiments were carried out at different water vapour activities (0.08 – 0.8) and at 24 °C. The spectral analysis was carried out in the frequency range of 3800 – 2800 cm^{-1} . Spectral subtraction and curve-fitting techniques were used to deconvolute the absorption bands due to different water/polymer interactions (see Figure 2.13) and the resultant spectra with the original absorption band are shown in Figure 2.12.

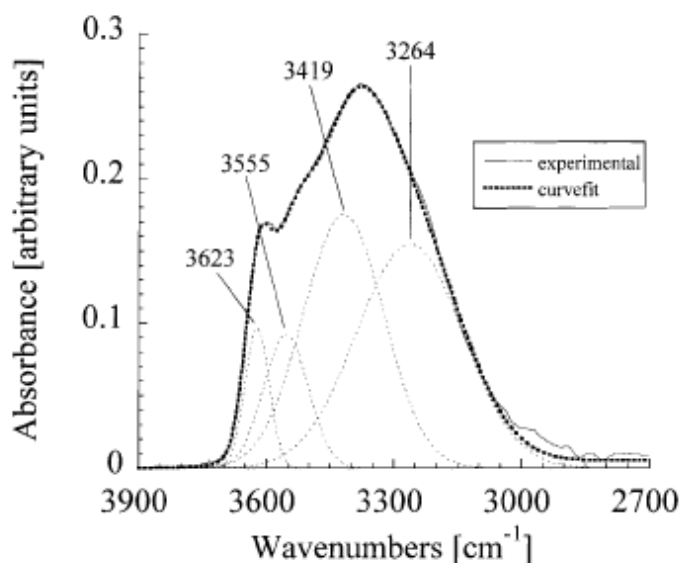


Figure 2.12 Four resolved peaks, simulated profile and the experimental line shape [324].

The peak at 3623 cm^{-1} was identified as the asymmetric O-H stretching vibration of un-associated water (S_0). The peak at 3555 cm^{-1} was said to be due to S_1 or with weakly interacting S_2 molecules. The peaks at 3419 and 3264 cm^{-1} were attributed S_2 molecules

having stronger hydrogen bonded interactions with proton acceptors (PA). However, the authors were unable to evaluate the peak change quantitatively as a function of immersion time.

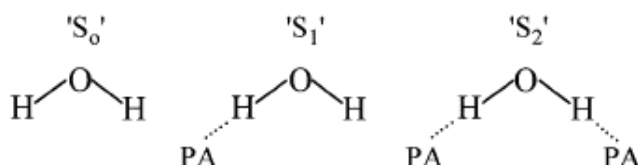


Figure 2.13 Different hydrogen-bonding schemes [324].

Musto *et al.* [326] reported using FT-NIR spectroscopy in transmission mode for water absorption monitoring in a TGDDM/DDS resin system. The authors assumed that moisture absorption in the cross-linked resin system is proportional to moisture desorption and spectroscopic measurements were carried out on a saturated epoxy specimen during desorption at 22 °C in a N₂ atmosphere. Quantitative analysis of moisture desorption in the resin system was carried out using the absorption band appeared at 5209 cm⁻¹ due to combination of O-H stretching and bending vibrations. Good correlation was observed between gravimetric data obtained during moisture absorption and spectral data obtained during desorption process.

2.5.2 *In situ* fibre-optic based techniques

As humidity and moisture are very common in our environment, measurements and/or control of relative humidity and moisture levels are important for a wide range of industrial applications. Among different types of humidity and moisture sensors, the majority is based on electrical properties such as impedance (or resistance) and capacitance of humidity-

sensitive materials such as electrolytes, polymers and porous ceramics [327]. However it was highlighted above that the electrical-based humidity and moisture sensors cannot be used for *in situ* monitoring due to their poor response to environmental and EM interference [20]. For example, the sensitivity of capacitance-based moisture sensors showed decay upon exposure to high temperatures and storage [19].

Apart from remote sensing capabilities, optical fibre based humidity and moisture sensors have attracted increasing interest in recent years due to their inherent characteristics such as immunity to lightening and electric discharge, low sensitivity to deleterious media such as water, fuel, seawater and solvents. These features make them a powerful tool for environmental and industrial process monitoring.

A number of authors have reported on the use of optical fibre-based sensor designs for sensing humidity. A wide range of fibre-optic sensor systems have been used for monitoring moisture and humidity and these can be classified into qualitative and quantitative techniques. The qualitative techniques include intensity-based sensor designs [328,329,330,331,332,333,334]. Quantitative analysis of the absorption kinetics is obtained using sensor designs based on UV-visible [335,336,337,338,339,340], infrared and evanescent wave [341,342,343,344,345,346,347] spectroscopy. A novel humidity sensor design based on the extrinsic Fabry-Perot interferometry (EFPI) has been demonstrated [348]. *In situ* monitoring of relative humidity based on the shift in the resonance wavelength of long period gratings (LPG) has also been demonstrated [349,350,351]. Furthermore, chemical sensing capability of fibre Bragg gratings (FBG) has been exploited for humidity and moisture detection in range of applications [352]. Yeo *et al.* [353,354] observed linear and

reversible Bragg wavelength shift due to swelling strain induced on the polyimide-coated FBG sensor due to absorbed moisture.

However, only a limited number of publications have reported the use of optical-fibre sensors to study the diffusion of water in thermosetting resins [355,356,357,358]. Generally, optical fibre-based sensor designs for detecting moisture ingress are based on polymer-coatings on a de-clad portion of the waveguide via evanescent wave spectroscopy.

2.5.2.1 Absorption-based fibre-optic techniques

Sensors based on infrared absorption spectroscopy exhibit distinct features over the other techniques due to their capability of detection and quantification of related chemical variations within the material due to absorbed moisture. Fernando *et al.* [81] demonstrated a simple sensor design for process monitoring and water ingress monitoring. The sensing concept was based on near-infrared transmission spectroscopy and was capable of monitoring water diffusion in a cross-linked epoxy/amine resin system. Calvert *et al.* [21] also proposed and investigated a simple single-fibre spectroscopic sensor for water ingress monitoring in epoxy resins. However, restrictions associated with using the sensor design for remote sensing in real structural applications need to be addressed.

Real-time moisture absorption monitoring in polymeric materials based on fibre-optic evanescent wave spectroscopy (FEWS) has been proposed and investigated [22,359]. The authors demonstrated using uncladded AgClBr fibres for acquiring infrared spectroscopy during ageing. The fibres were coated with a thin layer of polymer to be assessed. Good spectral sensitivity was observed and absorption kinetics was derived for water transport in the polymeric layers. Typically, chemical FBG sensors reported so far have been based on

the use of a swelling sensing material that can either be coated directly on the optical fibre or arranged in a way in which the volume expansion of the material can have direct effect on the FBG. Karakekas *et al.* [23] demonstrated the feasibility of using FBG sensors for monitoring moisture ingress in epoxy resins. The axial strain built up in epoxy due to absorbed moisture was used to predict the diffusion kinetics. Good correlation was observed with sensor response and the weight uptake measurements. However, debonding of the sensing fibre and the epoxy matrix was observed after prolonged exposure to water.

2.5.2.2 Other fibre-optic techniques

In contrast, Texier and Pamukcu [360] developed a fibre optic sensor for humidity monitoring in subsurface environments. The sensor is based on Brillouin scattering and optical time domain reflectometry (OTDR) and demands low optical power loss in distributed sensing arrays over “optical interaction/loss” based fibre optic sensors. However, the optical signals arising from the OTDR are highly complex due to interfering effects from external parameters such as localised fibre straining and temperature changes. Lyons *et al.* [361] overcome this disadvantage by using an artificial neural network signal processing techniques which allow the sensor to be addressed using an optical time domain reflectometer (OTDR) and the resulting signals to be characterised using pattern recognition. The optical fibre sensor is capable of detecting the presence of water at any axial position along the fibre length. The sensor is based on detection of water in the evanescent wave of a 200 m polymer clad silica fibre which had its cladding removed in the sensing regions.

2.6 Conclusions

In order to achieve optimum processing quality of epoxy/amine resin systems, it is necessary to have an in-depth understanding of chemical structure of the constituent materials, the reaction mechanism involved and the rate of reactions during cross-linking. Various mathematical models have been proposed and investigated for determining cross-linking kinetics of epoxy resin systems. Conventional and *in situ* fibre-optic techniques used for monitoring of cross-linking reaction were reviewed with an emphasis on spectroscopy-based techniques.

The second part of the review was focused on the effect of hygrothermal conditioning on the properties of epoxy/amine resin systems. Proposed transport phenomena of water in epoxy resin systems were discussed and various models used for describing diffusion kinetics of water in polymers were reviewed and summarised. Although traditional analytical techniques have been widely used for characterising moisture absorption in epoxy/amine resin systems, less attention paid on developing *in situ* fibre-optic techniques for moisture ingress monitoring in the resin systems.

Chapter 3

Experimental Methods

3.1 Introduction

This chapter gives details of the materials and experimental procedures used under three main sections:

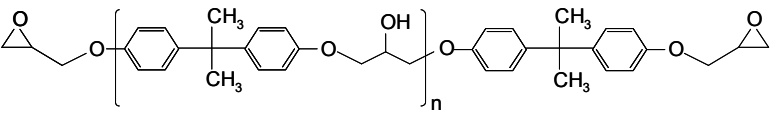
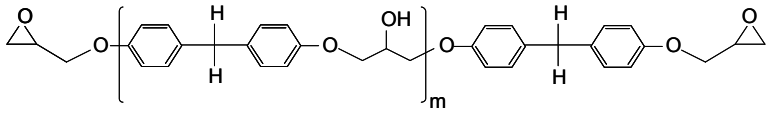
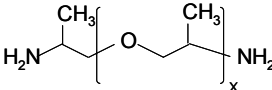
- Sensor fabrication and characterisation;
- Monitoring of cross-linking reaction in an epoxy/amine resin system; and
- Monitoring of hygrothermal conditioning of a cross-linked epoxy/amine system.

3.2 Materials

3.2.1 Resins

The research was carried out on two-part epoxy/amine resin system, LY3505[®] epoxy resin and XB3403[®] aliphatic amine-based hardener as a cross-linking agent, which was supplied by Huntsman Advanced Materials, UK. Chemical information for the two components is shown in Table 3.1. The resin and the cross-linking agent were mixed thoroughly in the ratio of 100:35 respectively by weight followed by degassing in a vacuum chamber at 18.5 inches of mercury (62648 Pa) pressure for 15 minutes.

Table 3.1 Chemical structure of the epoxy system.

Component	Chemical structure
<u>LY3505</u> Diglycidyl ether of bisphenol A (DGEBA)	
Diglycidyl ether of bisphenol F (DGEBF)	
<u>XB3403</u> polyoxypropylene diamine (POP)	

The flexible moulds used for fabricating sensor fixtures and test specimens were made using Silastic M RTV two-part silicone rubber (Dow Corning Co.). UV 304-T UV-curable resin was used for fabricating sensor fixtures and also for securing sensing fibres on to sensor fixtures.

3.2.2 Fibres

Two types of optical fibres were used in this study for constructing fibre-optic sensors: (i) multi-mode step-index silica core ($105\pm 3\text{ }\mu\text{m}$) and fluorine-doped silica cladding ($125\pm 4\text{ }\mu\text{m}$) optical fibres (Aomolin Ltd, China) and (ii) single-mode ($9/125\pm 1\text{ }\mu\text{m}$) Germanium-Boron (Ge-B) co-doped optical fibre (PS1250/1500, Fibercore Ltd., UK). Quartz capillaries having inner and outer diameters of $128\pm 13\text{ }\mu\text{m}$ and $300\pm 30\text{ }\mu\text{m}$, respectively (VitroCom, USA) were used for fabricating the sensor designs investigated in this study.

3.3 Sensor interrogation

A Bruker MATRIX™-F duplex 6-channel fibre-coupled FT-NIR spectrometer (Bruker Optics, UK) was used for interrogating the sensors. The FTIR spectrometer was operated in the range of 1000 – 2500 nm at a resolution of 0.025 nm and 64 scans. The 6-channel fibre-coupled FTIR spectrometer used in these experiments was equipped with a near-infrared (IR) tungsten light source, a near-IR beam splitter (T401) and an InGaAs detector.

3.4 Fibre-optic sensor fabrication

Several fibre-optic chemical sensors were designed for *in situ* monitoring of cross-linking reaction and/or moisture ingress in epoxy resin system based on spectral analysis of specified chemical species. Broadband light was transmitted through the optical fibres and the light that was transmitted through the resin was analysed using FTIR spectroscopy. Sensors were

constructed using multi-mode (105/125 μm) step-index silica core and fluorine-doped silica cladding optical fibres (Aomolin Ltd, China).

3.4.1 Single-fibre transmission sensor – sensor designs

3.4.1.1 Basic sensing concept

The basic sensing principle for this sensor is shown schematically in Figure 3.1. The input fibre transmits the broadband infrared light from the spectrometer to the sensing region. Here the sensor element consists of a cleaved optical fibre that is aligned and secured in position with a defined gap. The gap allows the analyte solution to flow in to the cavity through which the light from the input fibre passes and proceeds to the second fibre, which transmits the light to the detector. A FTIR spectrometer is used for interrogation.

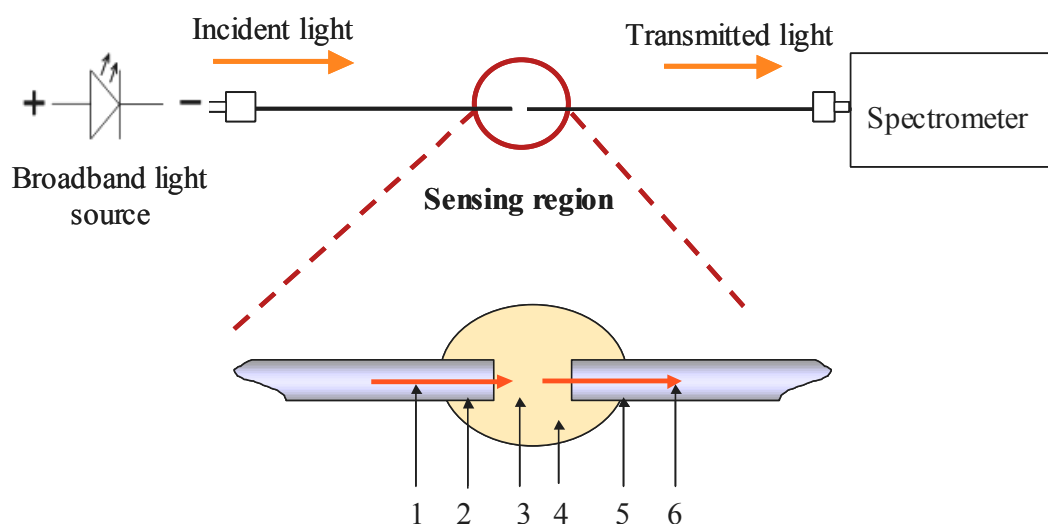


Figure 3.1 Schematic illustration of the sensor concept with enlarged sensing region: [1]: incident light, [2]: first cleaved fibre, [3]: gap between cleaved fibre ends, [4]: analyte solution, [5]: second cleaved fibre and [6]: transmitted light.

In order to convert this sensing concept to a real sensor configuration, it was necessary to develop a method to align the two fibres. A feasibility study was carried out with three different sensor fixtures to assess these fixtures for sensor fabrication methodology and the development of these devices for monitoring of the cross-linking reactions. Subsequently, one of these sensor fixtures was chosen for an in-depth behaviour characterisation study for monitoring the cross-linking reaction and moisture ingress behaviour. Consideration was also given to issues related to robustness during fabrication, ease of handling and cost-effectiveness.

3.4.1.2 Epoxy substrate sensor design

In this sensor fixture, a capillary, which holds the fibre sensor, was embedded in a thin layer of neat epoxy resin. Thin cross-linked neat-epoxy substrates with embedded quartz capillaries having inner and outer diameters of 128 μm and 300 μm , respectively (VitroCom, USA) were used to hold and position optical fibres precisely to create the transmission sensor. A flexible mould was fabricated using Silastic M RTV two-part silicone rubber (Dow Corning Co.) to make strips of epoxy substrates with embedded capillaries. A schematic diagram of the mould is shown in Figure 3.2(a). A single capillary with stripped fibre in it was embedded in thin cross-linked neat epoxy as shown Figure 3.2(b). A sacrificial fibre inside the capillary was used to keep the capillary bore clear during the fabrication process. A V-shaped groove at the centre of the short-side of the mould cavities was used (as shown in Figure 3.2(a)) to hold the capillaries in place until the resin cross-links.

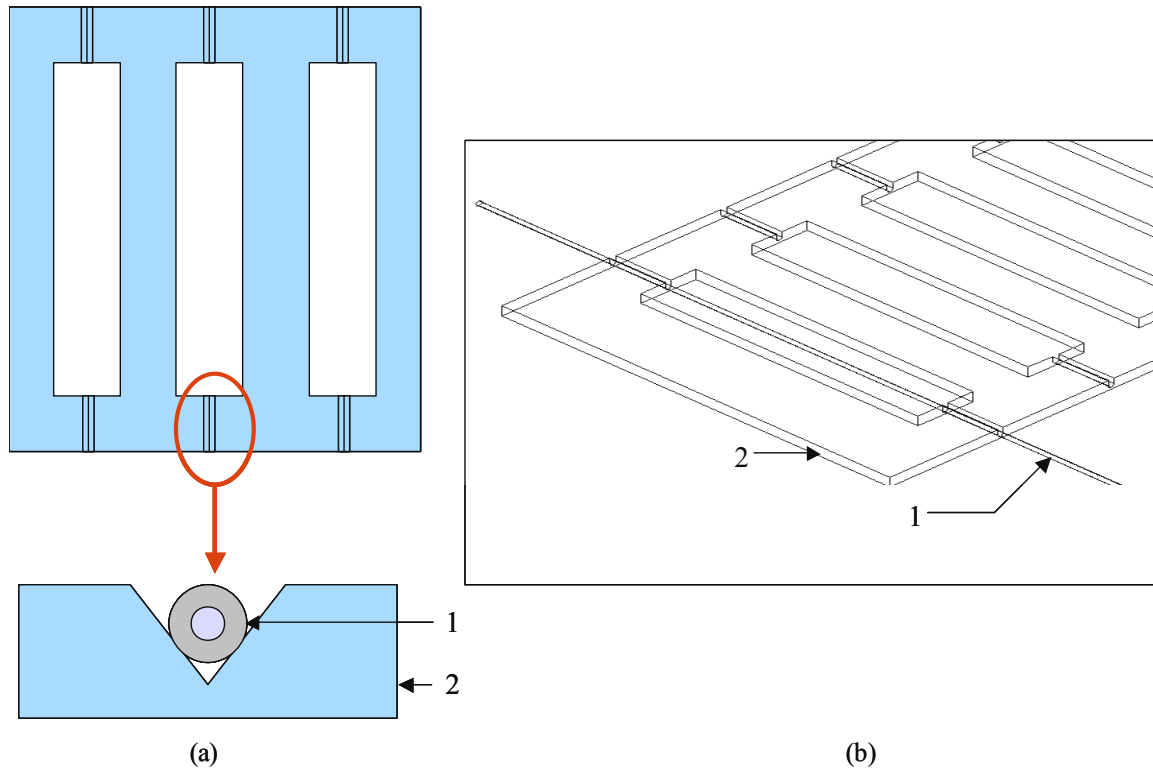


Figure 3.2 Schematic views of the custom-made silicone mould for making strips of sensor substrates:

- (a) silicone mould with an expanded end-view of the v-groove region for holding quartz capillaries; (b) 3-dimensional view of the mould with an array of mould cavities and a capillary at the middle of a cavity; [1]: precision-bore capillary with a sacrificial fibre and [2]: silicone mould.

These substrates were made out of the same resin system. The dimensions of the mould cavities were 40 mm in length, 5 mm in width and the depth was 0.5 mm.

With reference to Figure 3.3, a single strip of the cross-linked resin was used to make several sensor substrates by cutting them to the required length. In this study the substrates were cut into lengths of 16 mm using a 0.5 mm thick and 22 mm in diameter diamond-tipped blade (RS Components, UK) followed by polishing the edges with 800 grit and 1200 grit SiC grinding papers using water as a lubricant. The sequence of steps for converting a cured epoxy strip, with an embedded capillary, to a sensor is shown in Figure 3.3(a-c). The

previously mentioned diamond-tipped blade was used to introduce a groove perpendicular to the length of the capillary. A vertical translation stage was used to move the cross-linked resin fixture towards the fixed diamond-tipped blade so that groove depth could be controlled.

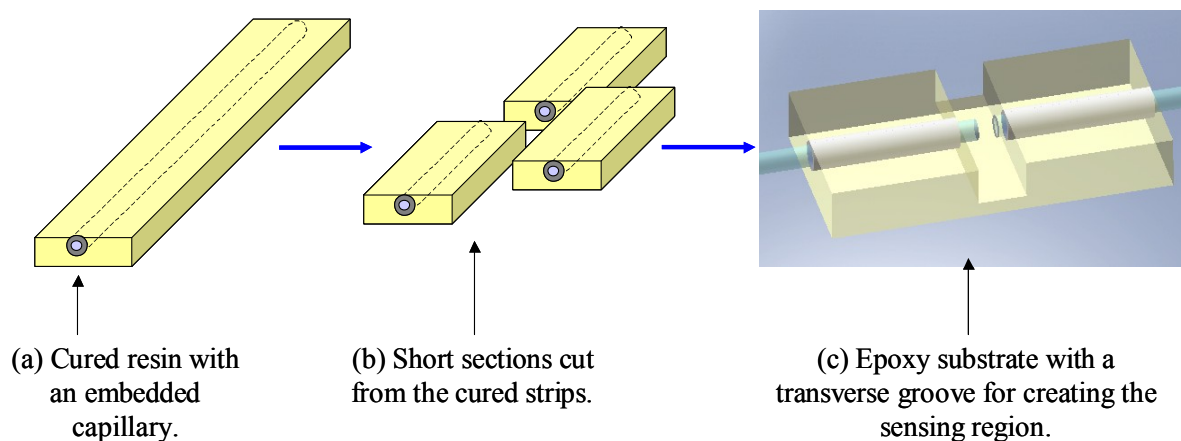


Figure 3.3 Fabrication steps of the sensor substrate.

The purpose of having a groove across the substrate was two-fold: the first was to expose the sensing fibres to the analyte medium, in the current case, an epoxy/amine resin mixture. The second reason was to create a “cell” to enable the resin system to flow into the gap in between cleaved fibre ends to enable transmission spectroscopy through the resin.

The fibre that was originally inserted into the capillary was removed and the bore of the capillary was cleaned using 125 μm diameter tungsten wire. An optical image of the actual sensor substrate is shown in Figure 3.4(a) together with the cross-sectional view across the capillary in Figure 3.4(b).

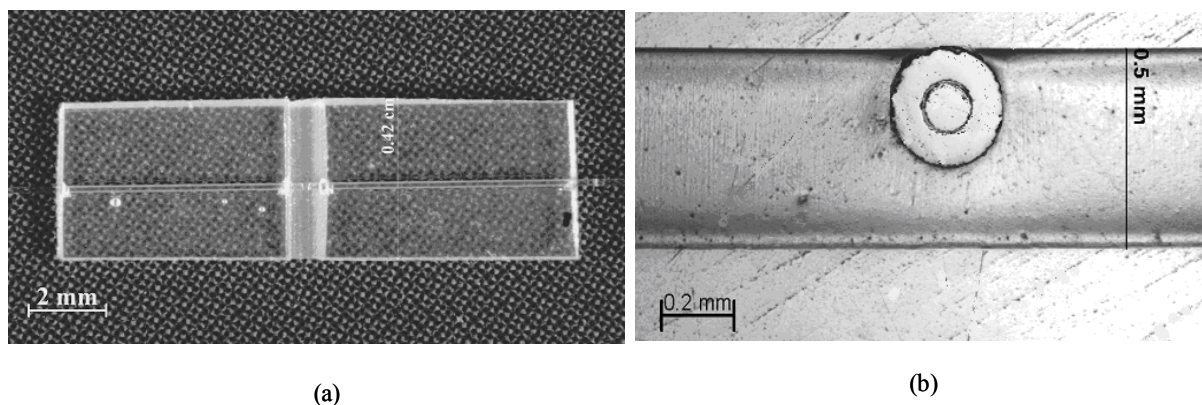


Figure 3.4 Optical images of the sensor substrate: (a) an epoxy substrate, (b) a cross-sectional view of the sensor substrate across the embedded capillary for holding the sensing fibres; A sacrificial fibre inside the capillary represents the location of the sensing fibres.

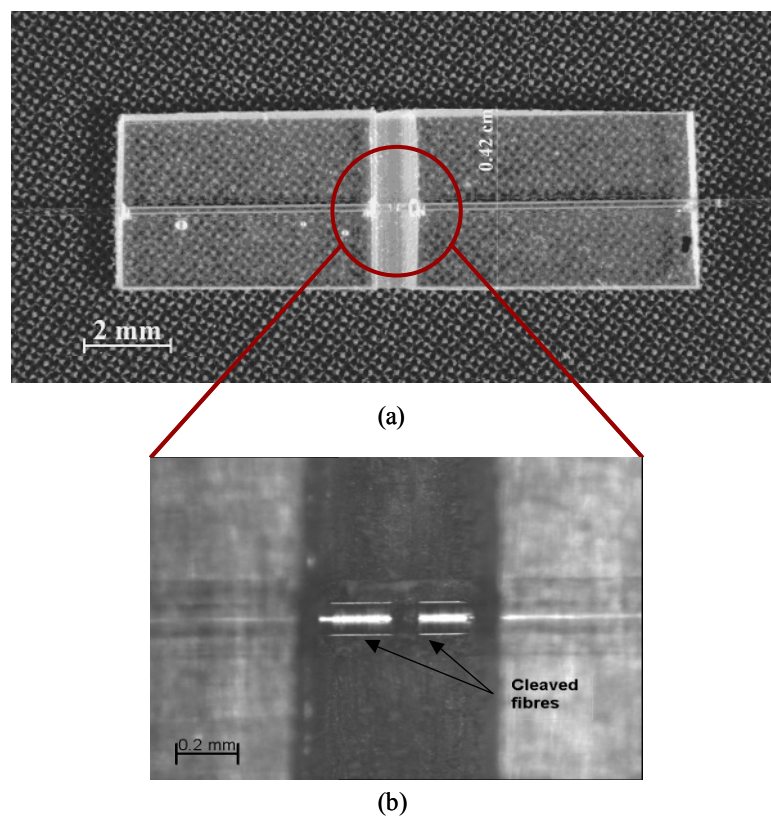


Figure 3.5 (a) Optical image of a transmission sensor fabricated using an epoxy substrate; (b) Enlarged view of the sensing region.

The fixture for conducting transmission infrared spectroscopy was constructed by securing two ends of a cleaved multi-mode step-index silica optical fibre in the resin capillary

assembly. The stripped and cleaved fibres were inserted into the capillaries using a precision translation stage. The sensing region was created at the groove across the substrate by leaving a pre-determined gap in between the cleaved fibre ends as shown in Figure 3.5(b). The cleaved optical fibres were secured in position using a UV 304-T UV-curable resin. This resin was cured using a UV light source (UV75, Thorlabs Inc. UK).

3.4.1.3 Capillary support sensor design

The second fixture was constructed using only the quartz capillaries mentioned in Section 3.1.1.2. The sequence of the fixture fabrication is shown in Figure 3.6. Here, a stripped optical fibre: [C] was inserted into the precision bore of a “supporting” capillary: [A] of length 10 mm. Another supporting capillary: [A’] of the same length was inserted on to the optical fibre and this assembly was bonded onto a third short “substrate” capillary: [B] using UV-curable epoxy with a defined gap between the capillary end-faces. The third capillary supports the first two capillaries that hold the sensing fibres and also maintains the alignment of the sensing fibres. A stripped fibre was used to keep the two supporting capillaries aligned whilst fixing them on to the third substrate capillary. This fibre was removed before making the transmission sensor and stripped and cleaved sensing fibres were inserted along two aligned capillaries. The pre-determined gap between the cleaved fibre ends was obtained by fixing the fibres on to far ends of the supporting capillaries.

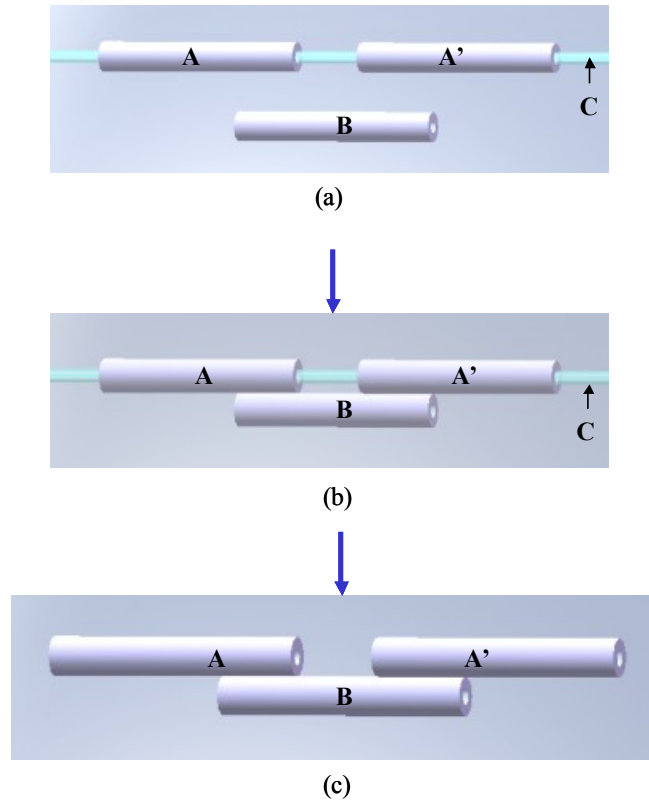


Figure 3.6 Main steps of fabrication of the sensor fixture: (a) aligning two supporting capillaries using a sacrificial optical fibre; (b) bonding the aligned supporting capillaries on to a substrate capillary and (c) resultant sensor fixture; [A and A']: supporting capillaries, [B]: substrate capillary and [C]: sacrificial optical fibre.

A schematic illustration of the capillary support is shown in Figure 3.7(a) along with an optical image of the sensing region of the design in Figure 3.7(b).

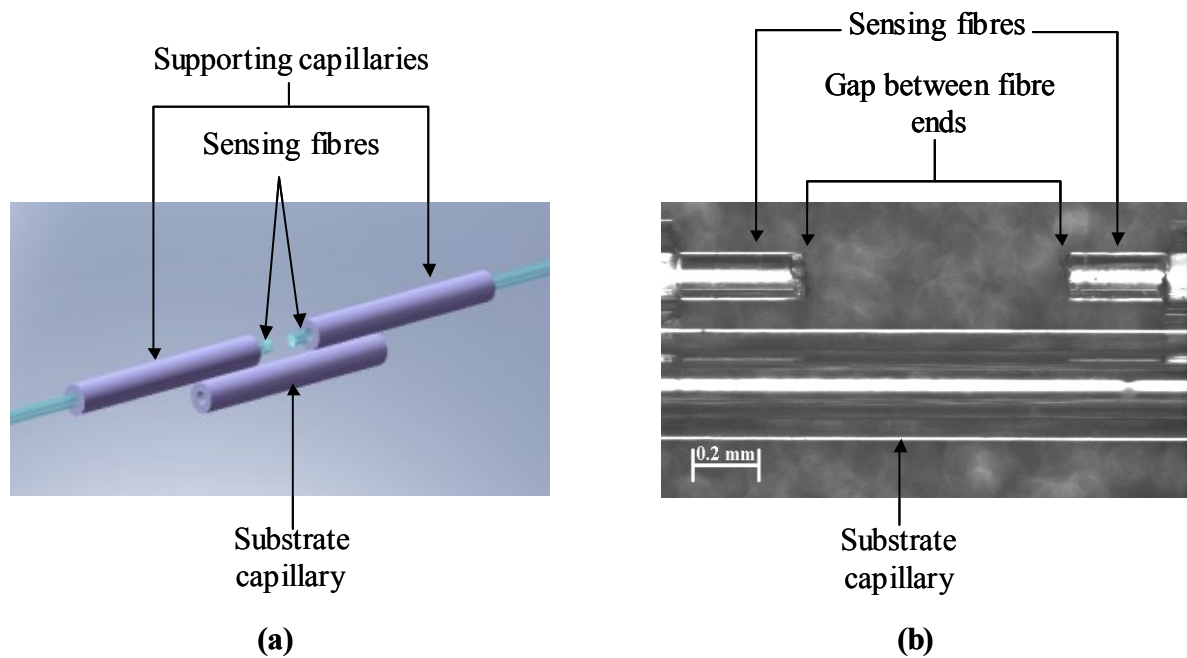


Figure 3.7 (a) Schematic illustration of the sensor design and (b) a micrograph of the sensing region of a transmission sensor that was fabricated with the capillary support.

3.4.1.4 Abraded capillary sensor design

The third sensor design consists of a precision-bore capillary tube that was ground along its length to create a U-groove. The ground section of the capillary creates a U-groove on which the stripped and cleaved fibre ends can be aligned. The approximate length of the ground capillary is 15 mm. Hence in this case a single capillary was used as a fixture for the transmission sensor.

The procedure for grinding and polishing the capillary involved mounting it on to a V-groove of 0.375 mm depth and inclusive angle of 45° using low-melt mounting wax (Contamac Ltd, UK) as shown in Figure 3.8(a). A sacrificial optical fibre was inserted into the precision bore during the grinding operation to provide support for the capillary. This also helped to prevent debris entering the cavity hole of the capillary while mounting and polishing. The capillary

was ground and polished using 2400 grit silicon carbide (SiC) grinding paper using water as a lubricant followed by polishing using 3 μm diamond paste on MD NapTM polishing cloth (Struers Ltd., UK). The ground capillaries were cleaned with isopropanol in an ultrasonic bath for one minute to remove any trapped debris. A schematic view of the sensor substrate is shown in Figure 3.8(b).

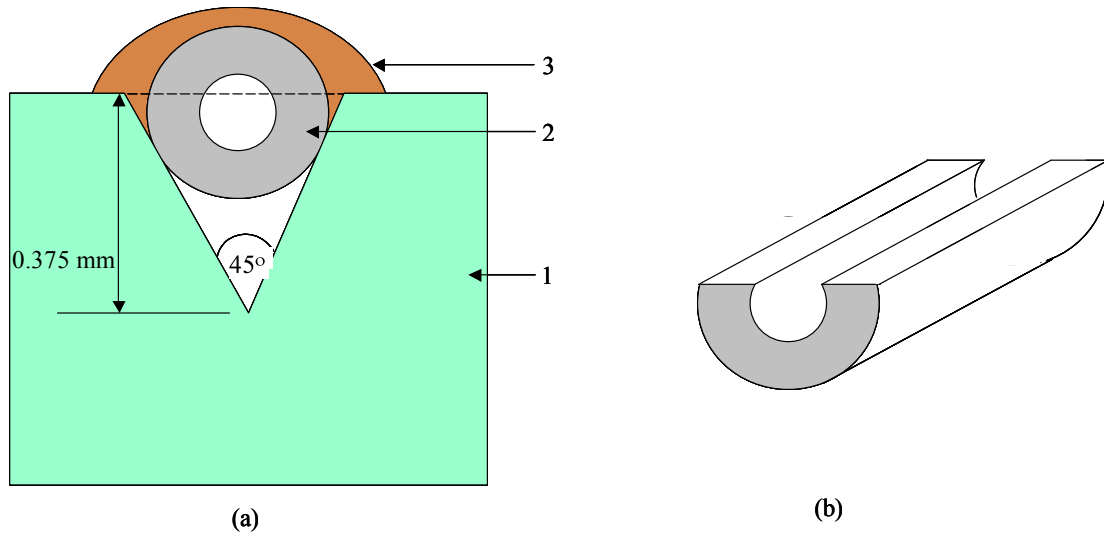


Figure 3.8 (a) schematic illustration of a capillary mounted on to the V-groove: [1]: V-groove mount, [2]: a quartz capillary and [3]: low-melting wax and (b) 3-dimensional view of ground and polished U-section of an abraded capillary fixture.

The sensor was constructed by positioning and securing the cleaved ends of an optical fibre in the ground capillary using the UV-curable adhesive mentioned previously. A schematic illustration of the sensor design and an optical image of the sensing region are shown in Figure 3.9(a and b), respectively.

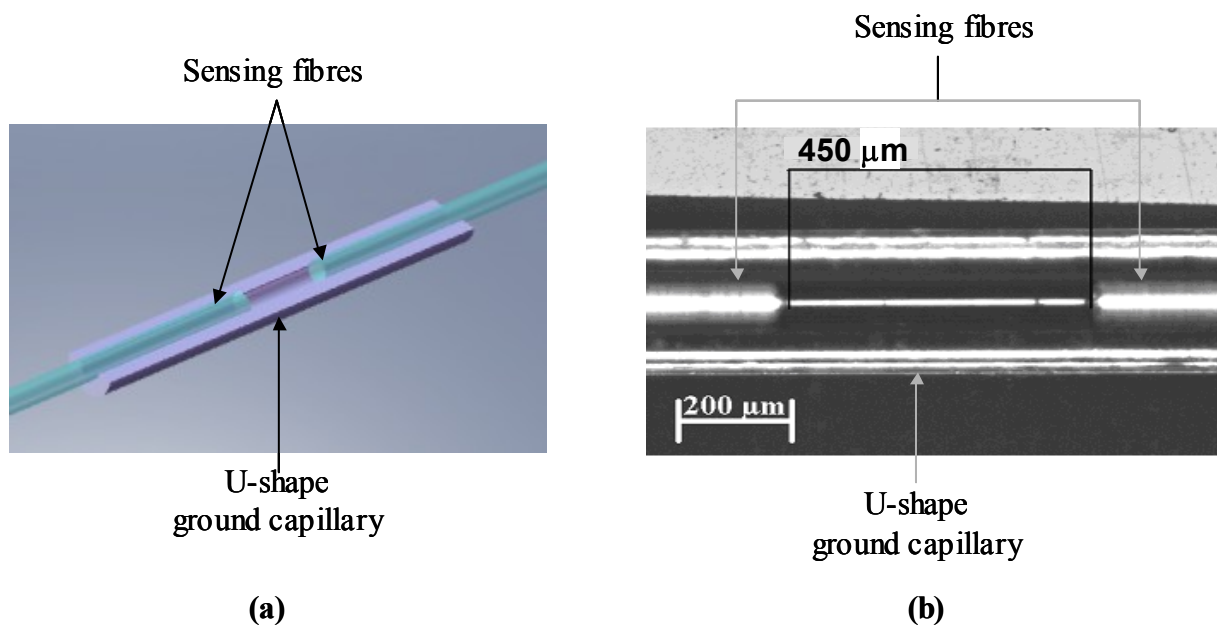


Figure 3.9 (a) Schematic illustrations of the sensor design fabricated with an abraded capillary and (b) a micrograph of the sensing region.

3.4.2 Single-ended reflectance sensor – sensor designs

3.4.2.1 Basic sensing concept

In this design, fibre-optic near-infrared reflectance spectroscopy was carried out using a multi-mode fibre. Here, a cleaved fibre was simply mounted perpendicular to a reflective surface having approximately 500 μm separation in between the cleaved fibre face and the reflective surface as shown in Figure 3.10. One fibre of one side of the 2 x 2 coupler carries light from the broadband light source to the coupler. Then the coupler splits and transmits the light to two fibres on the other side. The light leaves the fibre at the fibre/analyte interface, travels through the analyte, reflects back at the reflector surface and enters in to the sensing

fibre again. The reflected light transmits back to the detector of the FTIR spectrometer via the coupler.

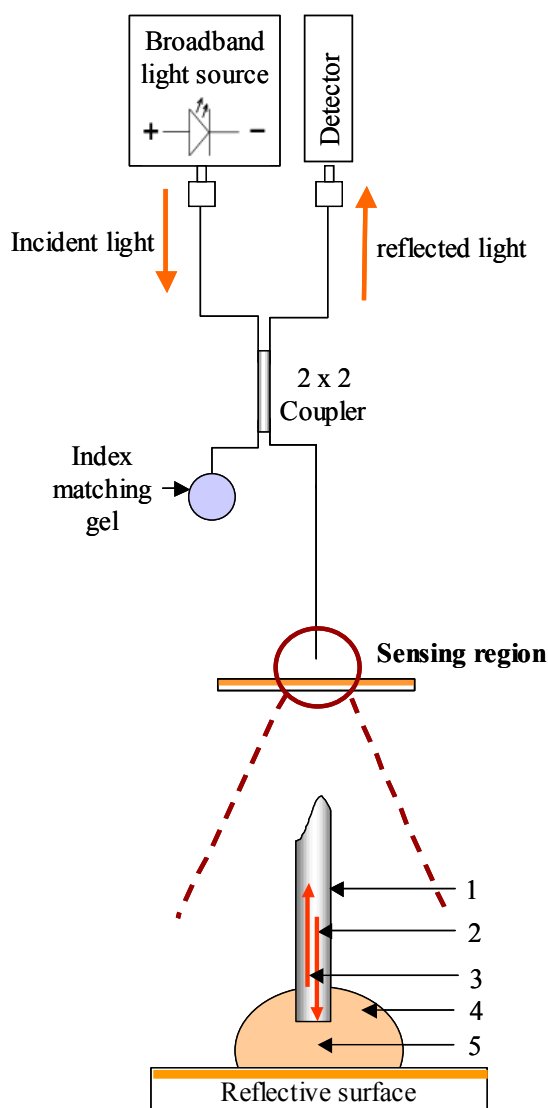


Figure 3.10 Schematic diagram of the sensor concept for the single-fibre reflectance sensor: [1]: stripped and cleaved fibre end, [2]: incident light, [3]: reflected light, [4]: analyte solution and [5]: gap between cleaved fibre end and the reflector.

Near-infrared reflectance spectroscopy can be obtained either with one fibre or with both fibres. If one fibre for sensing (as shown in Figure 3.10), the second fibre should be left in

refractive index-matching gel to minimize spectral noise due to interference of reflected light from both fibres.

3.4.2.2 Capillary reflector sensor design

In this sensor design a polished and gold sputter-coated end face of a short quartz capillary section was used as a reflector for the sensing fibre. The one end-face of the capillary used for the sensor design was polished as oppose to cleaving to obtain a flat and smooth surface finish. Inner and outer diameters of the quartz capillary were $128\pm13\text{ }\mu\text{m}$ and $300\pm30\text{ }\mu\text{m}$, respectively. Thereby the overall thickness of the sensor was reduced down to $300\text{ }\mu\text{m}$ and the length of the sensor depends on the length of the capillary section, which has to be polished, and gold sputter-coated for use as a reflector. Due to practical difficulties of mounting capillaries for polishing, in the current research, the capillary length for sensor fabrication was chosen as $10.0\pm0.5\text{ mm}$.

The quartz precision-bore capillary was potted in a 1 mm bore SMA fibre connectors using a high viscosity adhesive (2-component Araldite® rapid, Bostik Ltd., UK) as shown in Figure 3.11 (a). A sacrificial optical fibre was inserted into the bore of the capillary tube prior to potting to offer mechanical stability and to reduce contaminant ingress into the capillary during polishing. The connectors were polished using a Senko APC8000 high-volume fibre-optic connector polisher. The polished capillary was then de-mounted from the connector by burning off the adhesive in a furnace at 400°C for 4 hours. This capillary was then cleaned with isopropanol in an ultrasonic bath. The polished end of the capillary was sputter-coated with gold using an Emscope SC500A gold coater (Emscope Laboratories Ltd., UK). Sputter coating at 27.5 mV and 1 kV for 4 minutes in vacuum ($p = 8 \times 10^{-2}\text{ mbar}$) yields a gold layer of approximately 12-15 nm in thickness. The coated end-faces of these polished capillaries

were found to produce spectra with a good signal-to-noise ratio at path lengths that were optimised for tracking the progress of cross-linking reaction. During this operation, the bore of the capillary was protected using a sacrificial optical fibre (see Figure 3.11(b)). A schematic illustration of a polished and gold-sputter coated reflector capillary is shown in Figure 3.11 (c).

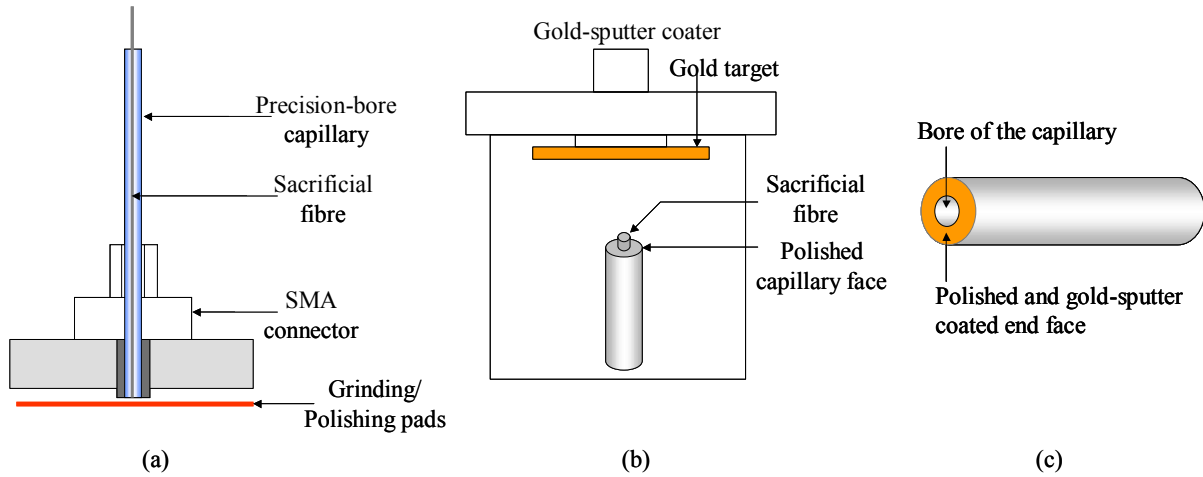


Figure 3.11 Fabrication steps of the reflector capillary: (a) a mounted capillary for polishing, (b) gold-sputter coating of the polished capillary and (c) capillary reflector with polished and gold-coated end face.

The sensor design is illustrated in Figure 3.12. A sacrificial fibre: [B] was inserted and bonded: [D] into the precision bore of the capillary: [A] using UV-curable resin for supporting and holding the sensing fibres in place. Sensing fibres: [E] were fixed onto the supporting fibre using UV-curable resin: [F]. Care was taken to avoid contaminating the cleaved sensing fibre ends during bonding. The gap: [G] between the reflector surface and the cleaved fibre ends were adjusted using a precision translation stage prior fixing on to the supporting fibre. In this sensor design, the reflector and sensing fibres were attached to each other before embedding and sensing. Hence unlike the initial design, the sensor can be used for through-thickness sensing.

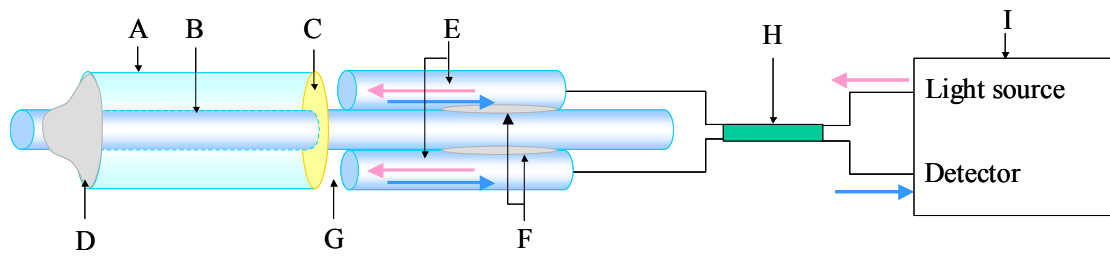


Figure 3.12 Schematic illustration of the single-ended reflectance sensor: [A] capillary with a reflective coating, [B] supporting fibre, [C] polished and sputter gold-coated face, [D] bonding between capillary reflector and supporting fibre, [E] multi-mode sensing fibres, [F] bonding between sensing fibres and supporting fibre, [G] cavity between cleaved fibre tip and the reflector, [H] 2 x 2 multi-mode coupler and [I] FTIR spectrometer.

3.5 Preparation of fibre connectors

Connection between fibre optic sensors and the spectrometer was achieved using sub-miniature A-type (SMA) connectors. Commercially available fibre optic SMA connectors (Amphenol fiber Optic Products) were used to connect multi-mode silica fibres to the spectrometer. Connectors with a 125 μm diameter bore were used with the fibres with a diameter 125 μm . The parts of the connector were assembled with fibres as shown in Figure 3.13. The stripped fibre was potted in to the connector bore using a fast-curable two-part fibre optic connector epoxy (ThorLabs, UK).

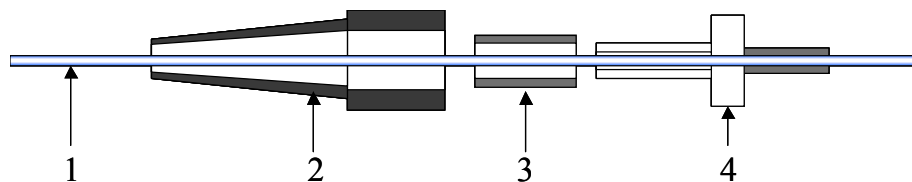


Figure 3.13 Schematic diagram of the fibre connector assembly: [1]: optical fibre, [2]: rubber protective cover, [3]: metal protective sleeve and [4]: SMA connector.

After the fibre was fixed into the connector, the end was ground and polished to achieve optimum light coupling with the spectrometer. An APC 8000 bulk-connector polisher (SENKO Advanced Components Ltd) was used with metal plate for grinding and polishing using 3 μm and 0.5 μm polishing papers, respectively. Preliminary work was carried out to establish the optimum grinding and polishing procedure to obtain a good surface finish of the connector ends.

A special disc holder, which can accommodate up to twelve SMA connectors, was used for grinding and polishing (Figure 3.14). Figure 3.15 shows a micrograph of a polished end of a multi-mode step-index silica fibre.

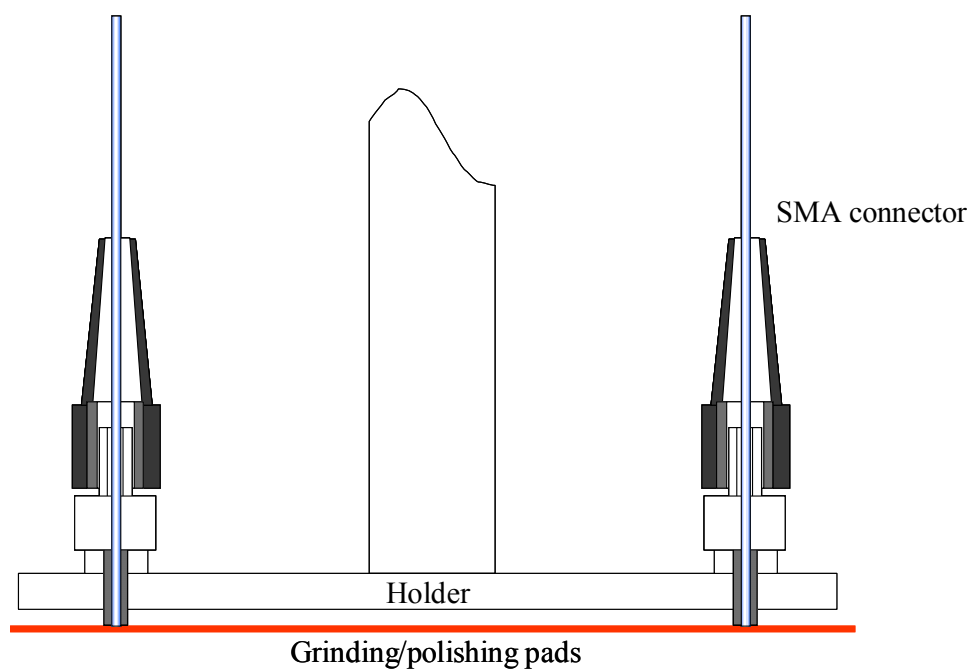


Figure 3.14 Schematic diagram of grinding/polishing set-up for fibre optic connectors.

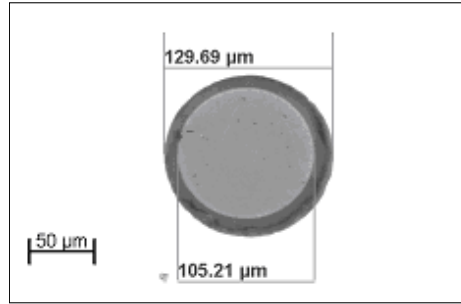


Figure 3.15 Micrograph of a polished end of the silica fibre, which potted into a SMA connector.

3.6 Determination of the optimum gap at the sensing region

3.6.1 Single-fibre transmission sensor

The capillary support sensor design mentioned above was used to determine the optimum cavity length for the fibre-optic near-infrared transmission spectroscopy. For this experiment, one of the sensing fibres inserted into one arm of the capillary support was attached on to a precision translation stage to change the gap between sensing fibre ends (Figure 3.16).

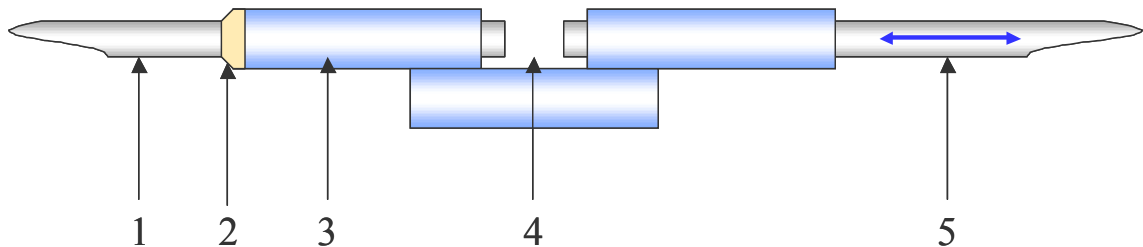


Figure 3.16 Sensor set-up for gap calibration: [1]: fixed sensing fibre, [2]: UV adhesive, [3]: capillary substrate, [4]: variable gap between sensing fibres and [5] movable sensing fibre that was attached to a translation stage.

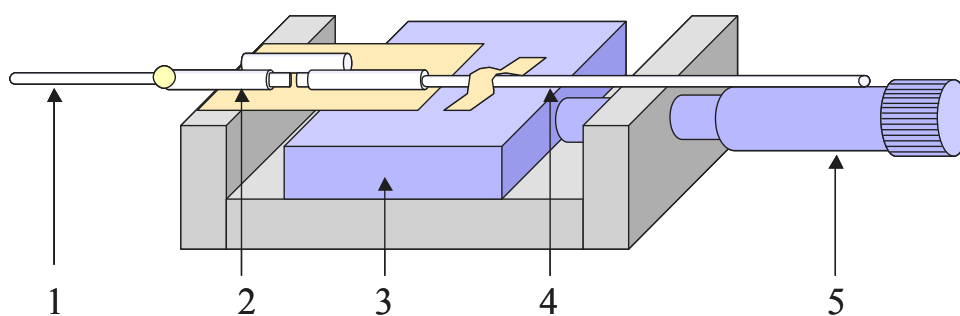


Figure 3.17 Experiment set-up for calibration of cavity length: [1]: fixed sensing fibre, [2]: capillary substrate, [3]: translation stage, [4]: movable sensing fibre that attached to a translation stage and [5] micrometer.

The experimental set-up is illustrated in Figure 3.17. A piece of thin PTFE[®] sheet was positioned under the sensing region to enable the resin to be introduced to the cavity. LY3505[®] epoxy resin was used as the analyte. Spectra of resin with different gaps between the cleaved fibre ends, were recorded and investigated to determine the optimum gap for subsequent cross-linking monitoring and moisture ingress experiments. The gap was changed from 100 to 1500 μm in 100 μm steps. The experiment was repeated three times to obtain the average absorbance corresponding to different gaps between the sensing fibre ends.

3.6.2 Single-ended reflectance sensor

The optimisation of the gap for the single-ended reflectance sensor was done using the capillary reflector design mentioned in Section 3.4.2.2. Investigations were also carried out using the single and both lead-out fibres of the 2 x 2 coupler for sensing purposes. As mentioned in Section 3.4.2.2, it is possible to obtain trans-reflectance spectroscopy either via a single or both lead-out fibres of the 2 x 2 couple. Hence experiments were performed to

find out best sensor configuration for sensing in terms of signal-to-noise ratio and spectral resolution. In this experiment two single-ended reflectance sensors were used as shown in Figure 3.18. In set-up A, one lead-out fibre was used for sensing while the other fibre was immersed in refractive index matching gel (ThorLabs Inc., UK). In set-up B both fibres were used for sensing. Spectral analysis on LY3505[®] resin system using both configurations with different gaps between the cleaved fibre ends and the reflectors was carried out.

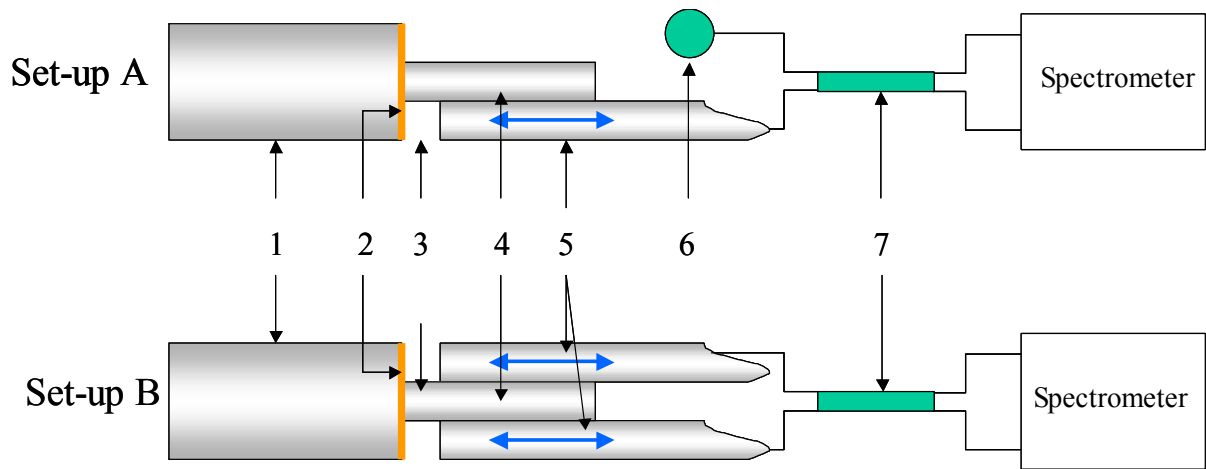


Figure 3.18 Schematic illustration of two sensor configurations: [1]: quartz capillary, [2]: polished and gold-sputter coated end face, [3]: gap between sensors and reflectors, [4]: supporting fibre; [5]: sensing fibres those attached to translation stage, [6]: refractive index-matching gel and [7]: 2 x 2 coupler.

A similar experimental set-up (explained in Section 3.6.1) was used in which the sensing fibres of the sensor were fixed on to a horizontal translation stage to facilitate movement of cleaved fibre end relative to the reflective capillary face. The sensing cavity length was changed from 100 μm up to 1500 μm in 100 μm steps.

3.7 Characterisation of cross-linking kinetics of the epoxy/amine resin system

Cross-linking kinetics of the LY3505/XB3403 resin system was characterised using single-fibre transmission sensor and single-ended reflectance sensor. The resin system was cross-linked at four different temperatures according to the manufacturer's recommended processing schedules as summarised in Table 3.2.

Table 3.2 Recommended processing schedules for the LY3505/XB3403 resin system.

Isothermal processing temperature (°C)	Processing time (hours)
40	20
50	18
60	8
70	7

3.7.1 Temperature monitoring

The exothermic reactions taking place during cross-linking in thermosetting resin systems lead to the generation of higher temperatures within the resin sample especially during the initial part of the cross-linking process. Therefore monitoring the effective temperature within the resin is vital for understanding and predicting actual cross-linking kinetics of the resin system.

For all cross-linking monitoring experiments, an independent temperature monitoring system was used in order to track the temperature in the resin during the experiment. A K-type thermocouple was used to monitor actual resin temperature over the cross-linking period. A custom-written LabView data acquisition program with a SCXI-1100 data conditioning unit (National Instruments, UK) was used for recording and acquiring the temperature profile.

3.7.2 *In situ* monitoring of the cross-linking reactions

3.7.2.1 *Fibre-optic transmission spectroscopy*

For all the process monitoring experiments, the gap between the cleaved fibre ends was set to 500 μm . Detailed cross-linking kinetic modelling was performed on the data obtained using the capillary support sensor fixture assembly (Section 3.2.1.3). This sensor configuration was used for monitoring the cross-linking reactions in the resin system at four isothermal temperatures mentioned above.

A thermo-regulated cell holder (Ocean Optics, UK) was used to control the temperature of the resin during cross-linking and a schematic diagram of the cell holder is shown in Figure 3.19. The temperature controller of the cell holder is capable of controlling the temperature within $\pm 0.01^\circ\text{C}$. A 1 mm path-length demountable glass cuvette (Starna Scientific Ltd., UK) was used to contain the mixed resin system. The transmission sensor was fixed on to the inner wall of the demountable cell as shown in Figure 3.20, using UV 304-T UV-curable epoxy resin.

The resin and cross-linking agent were weighed, mixed and de-gassed as mentioned in Section 3.3.2. The background spectrum was taken in air at room-temperature before introducing the resin system into the demountable cuvette cell. The resin mixture was injected into the cuvette using a disposable syringe. The sample was then heated from room temperature up to the cross-linking temperature; spectra were recorded from the time when the resin system was introduced into the cuvette where the cross-linking was deemed to be completed. Unless otherwise stated, the above-mentioned procedure for spectral acquisition and heating was followed for all the cross-linking experiments.

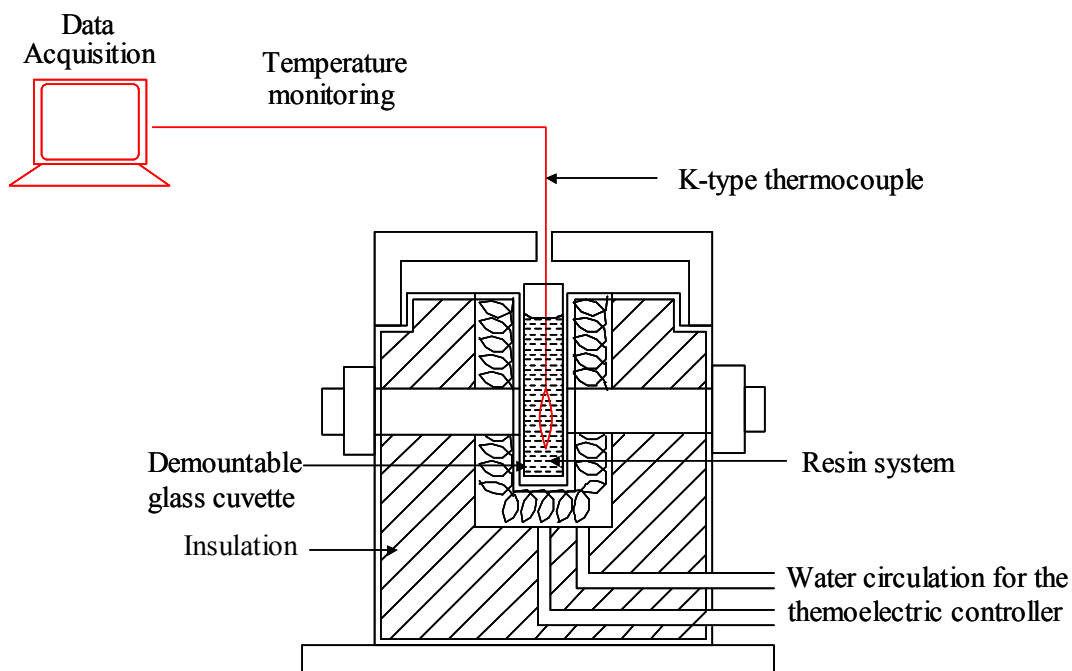


Figure 3.19 Schematic illustration of the thermo-regulated cell holder used for monitoring the cross-linking of the epoxy/amine resin system.

Care was taken to maintain the highest radius of curvature of the fibre at the U-bend as multi-mode fibres show high light attenuation at bends. A schematic illustration of the experimental set-up and sensor interrogation is shown in Figure 3.20. The time between two

consecutive absorbance spectra during cure was decided according to the approximate conversion rate of epoxy groups at different isothermal cure temperatures.

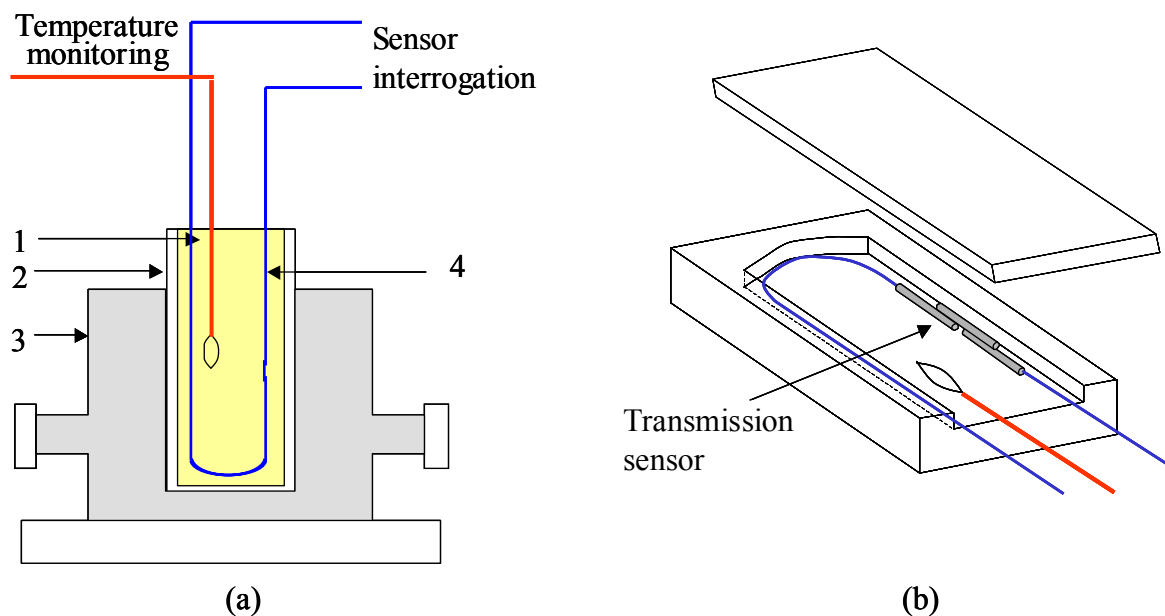


Figure 3.20 Schematic illustration of the experimental set-up: (a) thermo-regulated cell holder and the sensor interrogation: [1]: uncross-linked resin, [2]: demountable cuvette cell, [3]: thermo-regulated cell holder and [4]: transmission sensor; and (b) enlarged description of the sensor location inside the demountable glass cuvette.

3.7.2.2 Fibre-optic reflectance spectroscopy

Monitoring of cross-linking reaction and cross-linking kinetic modelling was performed using a reflectance sensor fabricated with a capillary reflector sensor design (Section 3.2.2.2). Both lead-out fibres from the coupler were used for sensing and the gap between both cleaved fibre ends and the reflective capillary end face was set to 500 μm . The gap was adjusted with an aid of precision translation stage. Cross-linking kinetics at all four processing temperatures was investigated and compared with results obtained via fibre-optic transmission

spectroscopy. A schematic illustration of the sensor interrogation is shown in Figure 3.21 along with the sensor location inside the demountable cuvette cell.

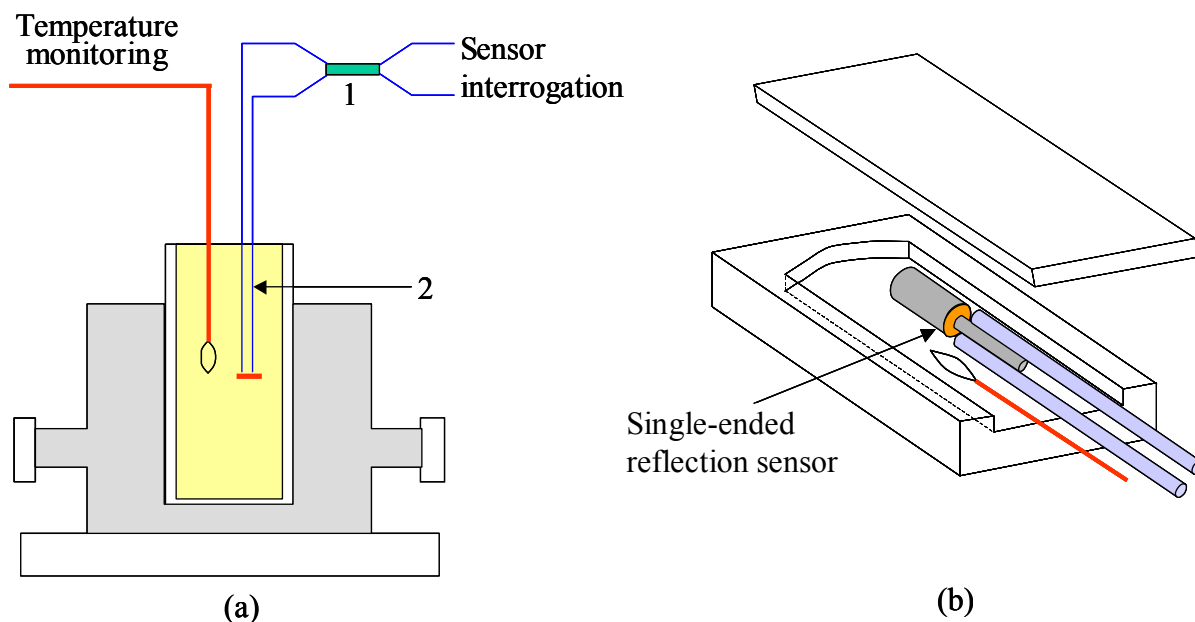


Figure 3.21 Schematic illustration of the experimental set-up; (a) sensor configuration inside the thermo-regulated holder and interrogation: [1] 2 x 2 coupler and [2] single-ended reflectance sensor and (b) enlarged view of the demountable cell with the single-ended reflectance sensor.

3.8 Characterisation of diffusion kinetics of water in the epoxy/amine resin system

3.8.1 Conventional analytical techniques

Moisture absorption characterisation of the cross-linked LY3505/XB3403 epoxy/amine system was carried out at 30, 50 and 70 °C and 100% relative humidity (RH). Neat epoxy

samples for the diffusion experiments were fabricated by cross-linking the resin system at 60 °C for 8 hours.

3.8.1.1 Sample fabrication for conventional diffusion studies

Neat-epoxy specimens for diffusion experiments were fabricated by casting the resin mixture in between glass mould plates as shown in Figure 3.22. Toughened-float glass plates were used to obtain a good surface finish on the specimens. The glass plates were coated with Frekote NC-700 (Aerovac, UK) release agent to enable easy removal of the cross-linked epoxy plaques from the glass plates. Aluminium plates with 2 mm thickness were used as spacer.

Epoxy and amine were mixed as described in Section 3.2.1. The aluminium spacer was placed on one of the glass plate and the inside edge was lined with vacuum sealant tape as shown in Figure 3.22. The second glass plate was sprayed with the release agent and was placed over this assembly. The sandwich structure was clamped together with G-clamps. The degassed resin mixture was poured on to the glass mould assembly. The epoxy plaques were cross-linked in a Memmert laboratory oven with thermal controller with ± 0.1 °C accuracy. The cast resin plaques were cut to the required dimensions, for the diffusion experiments. The dimensions of the specimens were in accordance to BS ISO standards. A hand-held diamond-tipped cutting wheel was used to cut the cast resin plaques. The edges of the specimens were ground using 1200 grit and 2400 grit SiC papers with water acting as a lubricant.

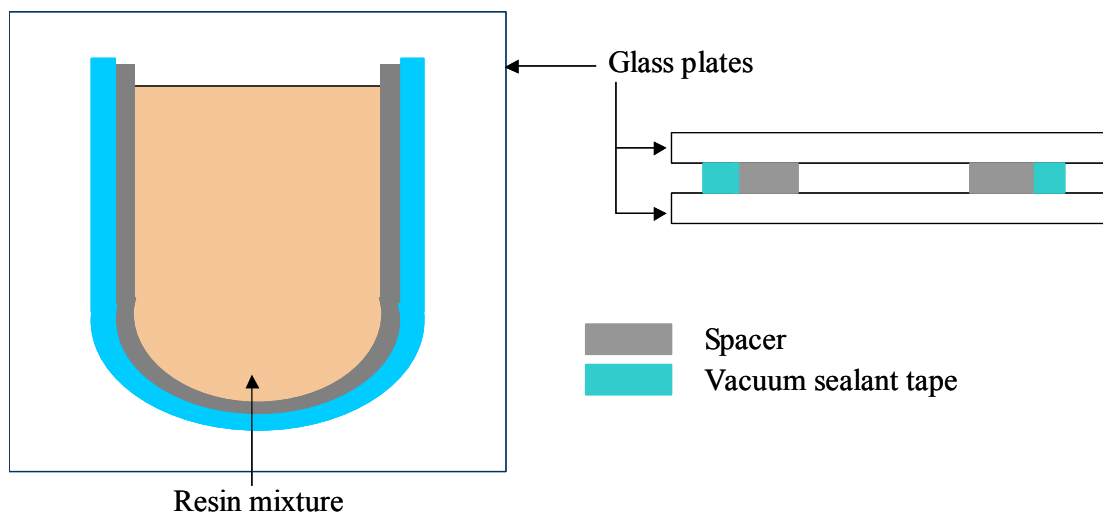


Figure 3.22 Schematic diagram of mould plates used for casting resin plaques.

3.8.1.2 *Environmental conditioning of the cast resin for diffusion experiments*

The cross-linked epoxy specimens were dried until reach to constant mass before starting moisture ingress experiments. The drying was carried out in an environmental chamber maintained at 50 °C. The drying temperature was chosen to be 10 °C below the isothermal cross-linking temperature that was used to cross-link the original specimens. Dry silica gel–Grade II (Sigma-Aldrich) was used to minimise the interaction of atmospheric moisture with the resin during the drying period. The specimens were taken out from the chamber at pre-determined time intervals for weight measurement. Before recording the mass of the test specimens, the samples were left in a desiccator for 2 minutes to enable the samples to equilibrate to room temperature. The mass of the specimens was recorded using an Ohaus electronic analytical balance.

3.8.1.3 *Diffusion experiments*

Before starting the diffusion experiments, the mass and the thickness of each specimen were recorded. The diffusion experiments were carried out in distilled water using individual

water-baths. The diffusion experiments were carried out at 30, 50 and 70 °C. Individual test specimens were used for each set temperature. The water baths were equipped with thermo-controllers that enabled the temperature to be controlled with in $\pm 0.1^\circ\text{C}$. Custom-made PTFE racks were used to hold samples in the water-baths.

3.8.1.4 Gravimetric analysis

Gravimetric measurements of the samples were carried out at pre-determined time intervals. The samples were removed from the water bath, blotted with lint-free tissue and kept in a dessiccator for two minutes before measurements. Their masses were recorded individually using an Ohaus weighing balance. The samples were returned to the water baths as soon as after the weighing operation; the samples were returned to the water-bath approximately in five minutes.

The possibility of desorption of absorbed moisture with in the test specimens during the weighing operation was also investigated. A specimen from each of the conditioning temperatures was measured continuously for 15 minutes. These measurements were recorded using an Ohaus analytical balance via LabView software.

3.8.1.5 Thermo-mechanical analysis

Dynamic mechanical thermal analysis (DMTA) of the cross-linked epoxy resin system was performed using a dynamic mechanical analyser (Metzsch DMA 242, Metzsch Scientific, UK). The dimensions of the test specimen for the DMTA experiments were 10 mm x 50 mm x 2 mm thickness. The sample was loaded sinusoidally using a dual-cantilever beam set-up where 32 mm dynamic displacement amplitude was imposed on the test specimen. The tests were carried out in the dynamic temperature mode from 20 °C to 140 °C at a heating rate of 1

°C/min. The storage modulus (E'), loss modulus (E'') and loss tangent ($\tan \delta$) were measured at test frequencies corresponding to 1, 10 and 30 Hz. The DMTA experiments were carried out on samples that were un-conditioned and pre-conditioned in the water bath at 30°, 50° and 70°C for specified immersion times.

3.8.1.6 Dynamic scanning calorimetry

A Perkin Elmer DSC7 (Perkin Elmer, UK) was used to measure the glass transition temperature of the neat epoxy resin specimens as a function of immersion time in the water bath. Since the analysis requires approximately 15 mg of the material for testing, a corner piece of an aged DMTA specimen was cut out from a free-end as shown in Figure 3.23.

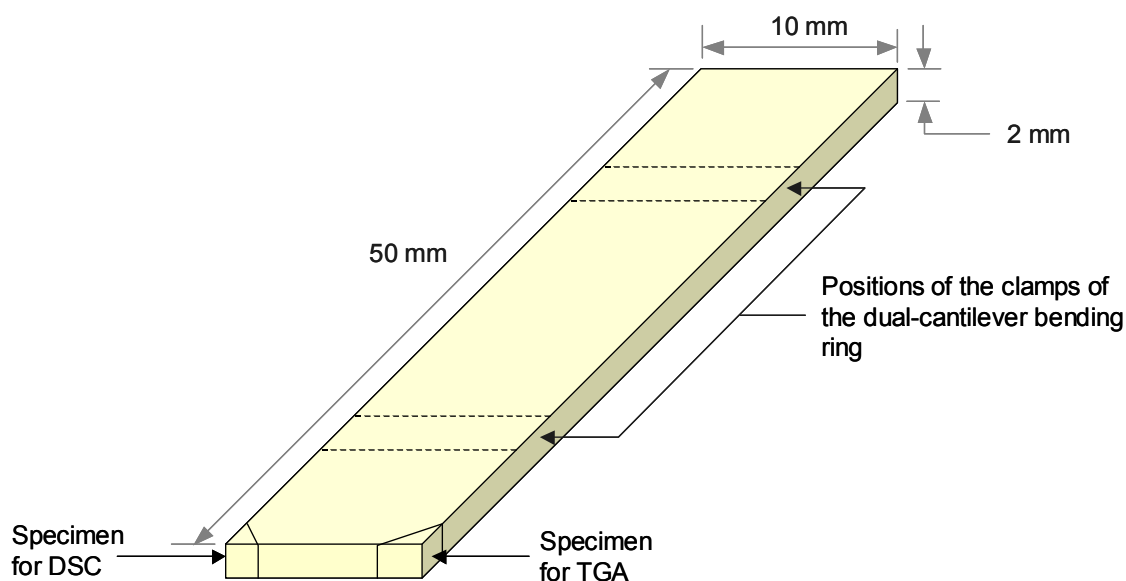


Figure 3.23 A schematic illustration of a DMTA specimen, that were used for a series of experiments involving TGA, DSC, DMTA and FTIR spectroscopy.

The DSC was operated in the dynamic mode using a heating rate of 10 °C/min, from 30 °C to 140 °C in a dry-nitrogen atmosphere. Three consecutive scans were carried out without

removing the sample from the DSC. In order to establish the repeatability of the T_g measurements, three individual test specimens were used per immersion time.

3.8.1.7 Thermo gravimetric analysis

Moisture desorption after hygrothermal ageing was investigated by thermogravimetric analysis (TGA) using a thermal analyser (Metzsch STA 449C, Metzsch Scientific, UK) with a thermo controller (Metzsch TASC 414/3 A, Metzsch Scientific, UK). Similar to the methodology explained in Section 3.6.1.6, approximately 15 mg of the un-conditioned and pre-conditioned specimens were tested under dynamic temperature mode using a heating rate of 5 °C/min, from 30 °C to 180 °C in an air atmosphere.

3.8.1.8 Fourier transform infrared spectroscopy

Conventional FTIR spectroscopy was performed on un-conditioned and pre-conditioned DMTA specimens using the Bruker MATRIX™-F duplex FT-NIR spectrometer and the temperature-regulated cell holder. Spectra were acquired using commercial fibre optic light guides (Ocean Optics, UK) connected to the thermo-regulated cell holder. Spectra were obtained in the wavelength range of 1000 – 2500 nm at a resolution of 0.025 nm and 64 scans using the internal near-infrared light source on the spectrometer and an InGaAs detector.

3.8.2 Fibre-optic transmission spectroscopy

In situ monitoring of moisture ingress was carried out using the capillary support sensor design (Section 3.2.1.3). The rationale for using the fibre-optic transmission sensor inside cross-linked epoxy specimens were; (i) to compare the absorption kinetics obtained using the

fibre optic sensors with that obtained via conventional gravimetry; and (ii) to predict the through-thickness diffusion front inside the specimen at the conditioning temperature.

The diffusion experiments involving the embedded single-fibre transmission sensors were carried out at 50 °C in water baths with the thermo-regulators as mentioned in Section 3.6.1.3. The resin specimens that were used for the diffusion studies with the embedded sensors were previously cross-linked at 60 °C for 8 hours. The dimensions of the specimens were similar to those used for conventional gravimetry experiment (50 mm x 50 mm x 2 mm thickness). The cross-linking of the test specimens was carried out in a Memmert laboratory oven that was custom-modified to accommodate the lead in/lead out optical fibres for online monitoring. Spectra were also recorded during cross-linking to investigate effect of using this conventional oven on the cross-linking kinetics.

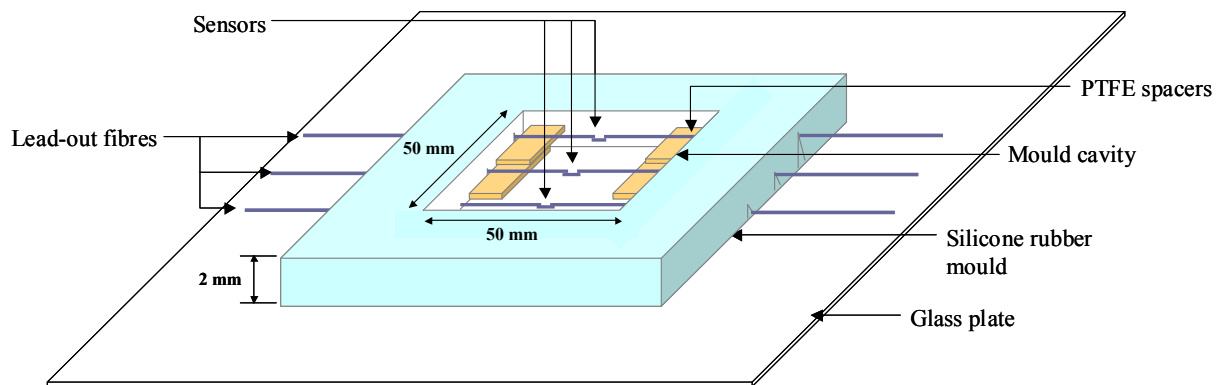


Figure 3.24 Schematic illustration of the silicone mould to fabricate epoxy specimens for *in situ* monitoring of moisture ingress.

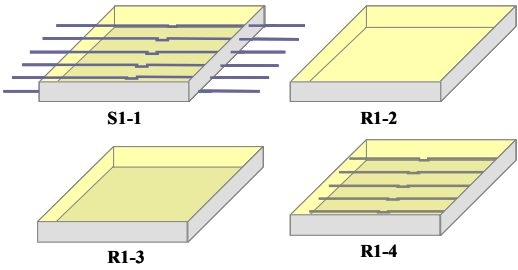
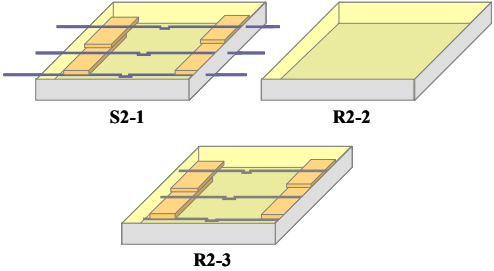
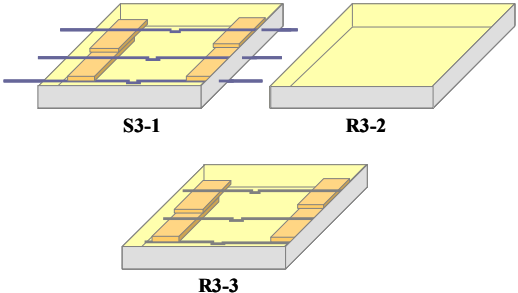
Custom-made silicone rubber moulds were used on toughened-float glass mould plates for fabricating epoxy specimens with embedded optical sensors as shown in Figure 3.24. Reference specimens were also fabricated for gravimetric measurements with and without

embedded sensors. These reference specimens were subjected to the same hygrothermal conditions as those with the embedded sensors for cross-comparison with the conventional gravimetric results. The cross-linked specimens were dried to constant mass at 50°C followed by immersion in distilled water at 50 °C.

For hygrothermal conditioning at 50 °C, three different specimen configurations were considered and summarised in Table 3.3. With reference to specimen numbering, the first letter refers to the type of the specimen; ‘S’ for specimens with embedded sensors and ‘R’ for reference specimens that used for gravimetric measurements. The second digit refers to the specimen configuration and the third digit followed by dash refers to the number of each specimen with in the specified specimen configuration.

A schematic illustration of the first specimen configuration used in this study is shown in Figure 3.25. Here the sensors were secured in place using spacers positioned outside the mould during cross-linking process. Six sensors were embedded and PTFE adhesive spacers were used to locate the sensors at different heights with reference to the thickness of the epoxy specimen. All but one of the surfaces were coated with a silicone sealant. Hence water can only enter from one side of the specimen. As shown in Figure 3.26, sensor-1 was located on the surface of the specimen that was exposed to water. Sensors -2 to -6 were equally-spaced across the thickness of the specimen from the exposed surface and the approximate separation between the two sensors was 0.22 mm.

Table 3.3 Summary of different specimen configurations used for moisture diffusion experiments.

Specimen identification	Description	Schematic illustration of the specimens
Specimen configuration – I	Six embedded sensors were equally spaced across the thickness of a neat epoxy specimen and only one side of the specimen was exposed to water.	 <p>S1-1 R1-2 R1-3 R1-4</p>
Specimen configuration – II	Three sensors were embedded across the thickness of an epoxy specimen and only one side of the specimen was exposed to water.	 <p>S2-1 R2-2 R2-3</p>
Specimen configuration – III	Three sensors were embedded across the thickness of the specimen and both sides of the specimen were exposed to water.	 <p>S3-1 R3-2 R3-3</p>

Specimen configuration – I

Schematic illustrations of the specimens that were used for the hygrothermal conditioning experiments are shown in Figure 3.27 (a-d). The set includes:

- S1-1:** *In situ* monitoring of moisture ingress – An epoxy specimen with six sensors embedded at different heights and only one side is exposed to water;
- R1-2:** Reference specimen – A neat-epoxy specimen where two sides were exposed to water;

- c) **R1-3**: Reference specimen– A neat-epoxy specimen were only one side was exposed to water; and
- d) **R1-4**: Reference specimen – An epoxy specimen with six (dummy) sensors and only one side was exposed to water.

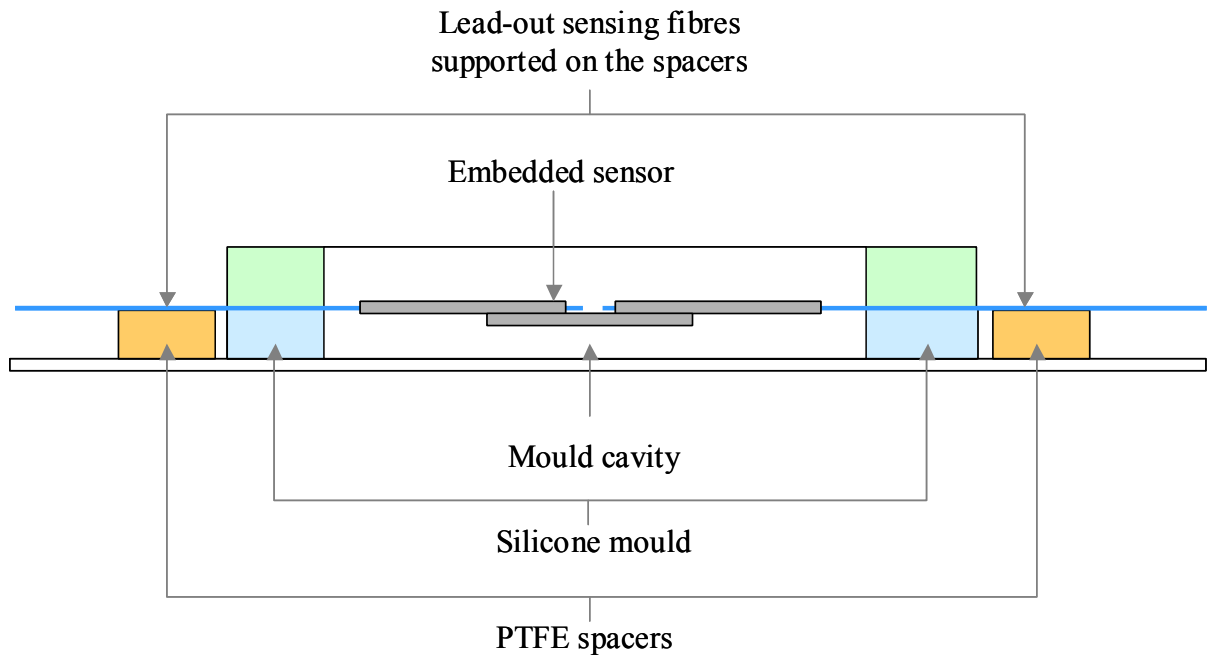


Figure 3.25 Schematic illustration of the mould set-up with a sensor secured outside the mould cavity.

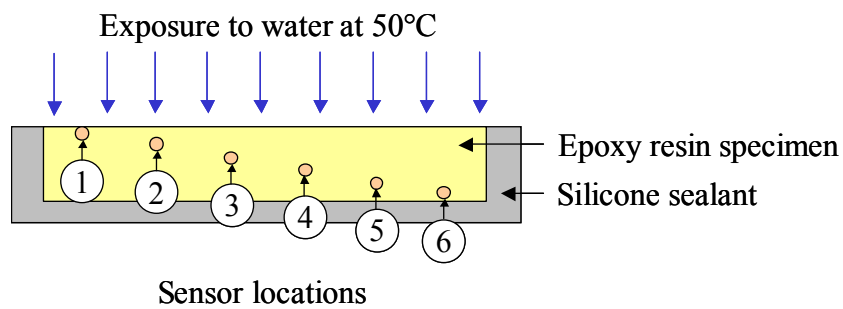


Figure 3.26 Schematic illustration of the relative locations of the embedded sensors across the thickness of the epoxy specimen.

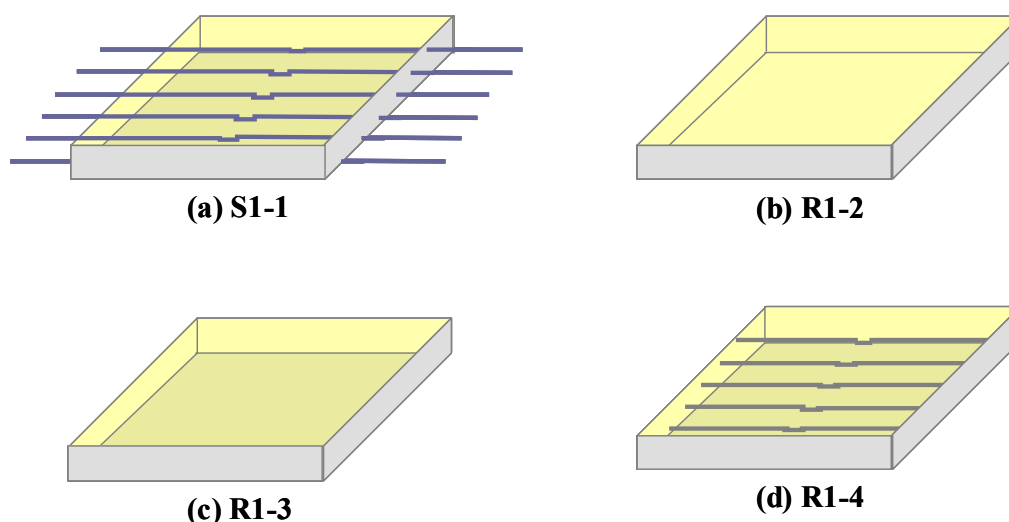


Figure 3.27 Schematic illustration of the set of specimens used for hygrothermal conditioning at 50°C;

Hatched sides of the specimens represent the surfaces with silicone sealant to eliminate the ingress of moisture through those sides.

Specimen S1-1 was used for real-time monitoring of moisture ingress using fibre-optic near-infrared transmission spectroscopy. Specimen R1-2 was used to correlate with the previously mentioned gravimetric measurements, and to investigate the repeatability when using specimens fabricated at different periods. Specimen R1-3 was used to study the effect of thickness on the absorption kinetics by exposing only one surface of the specimen. The specimen coded R1-4 was used to investigate the effect of the embedded sensors on the sorption kinetics of the epoxy/amine resin system in terms of weight-gain.

However in specimen configuration – I, it was not possible to guarantee the location of the sensors across the thickness due to movement during cross-linking. This will be discussed in more detail in Chapter 8. In order to overcome this possibility, with reference to specimen configurations – II and – III, sensors were located and secured at desired depths inside the mould using the PTFE spacers as shown in Figure 3.28. In the specimen configurations

discussed here, only three sensors were embedded. In the specimen configuration – II, only one side of the specimens was exposed to water at 50 °C while both sides of the specimens were exposed to water in the configuration – III.

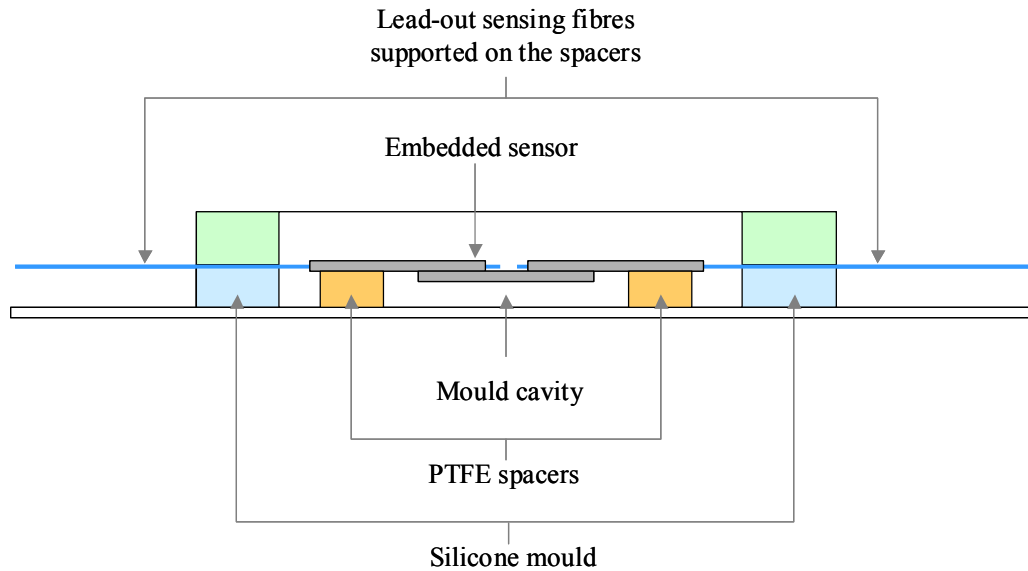


Figure 3.28 Schematic illustration of the mould set-up with a sensor secured inside the mould cavity.

As mentioned previously, a set of specimens were fabricated for *in situ* moisture ingress monitoring as well as for conducting independent gravimetric analysis. Schematic representation of the specimen configurations – II and – III are shown in Figure 3.29, and the sets include:

Specimen configuration – II

- a) **S2-1:** *In situ* moisture ingress monitoring – An epoxy specimen with three embedded sensors and only one side exposed to water;
- b) **R2-2:** Reference specimen – A neat-epoxy specimen where only one side was exposed to water; and
- c) **R2-3:** Reference specimen – A neat-epoxy specimen with three dummy embedded sensors; here only one side was exposed to water.

Specimen configuration – III

- a) **S3-1**: *In situ* moisture ingress monitoring – An epoxy specimen with three sensors embedded at different depths; here both sides were exposed to water,
- b) **R3-2**: Reference specimen – A neat-epoxy specimen where both sides were exposed to water; and
- c) **R3-3**: Reference specimen – A neat-epoxy specimen with three dummy embedded sensors where both sides were exposed to water.

Figure 3.30 shows a schematic illustration of the relative locations of the sensors that were embedded at specified depth in the cast neat-epoxy resin. These specimens were used for *in situ* monitoring of moisture ingress.

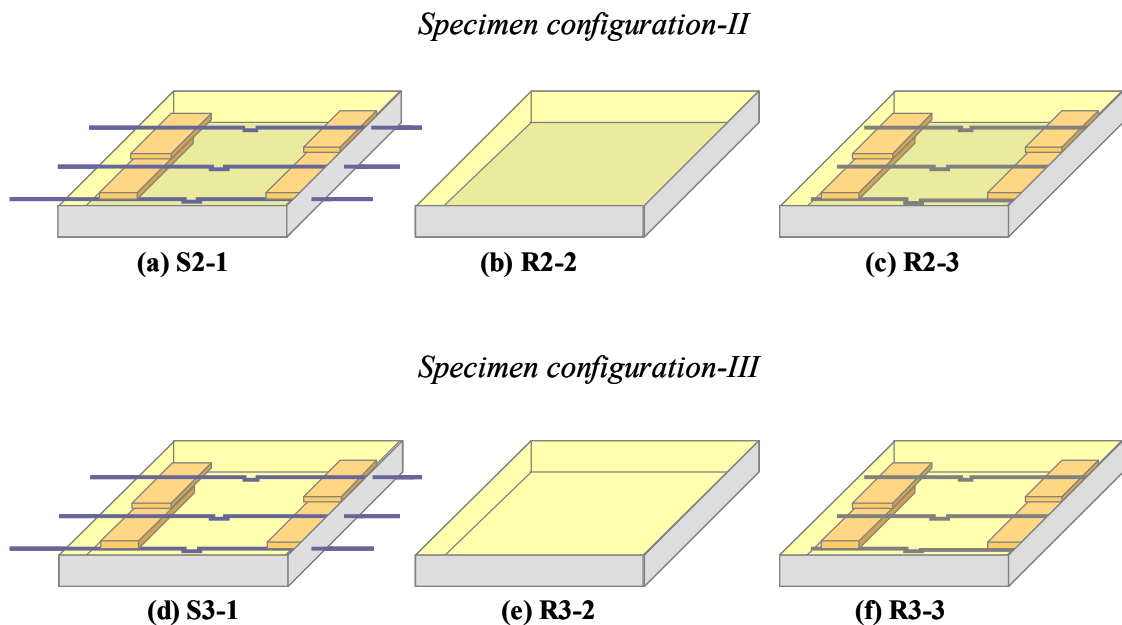


Figure 3.29 Schematic illustration of the set of specimens used for moisture ingress experiments at 50 °C; hatched faces represent the surfaces, that were sealed with silicone sealant to eliminate moisture ingress through during hygrothermal conditioning.

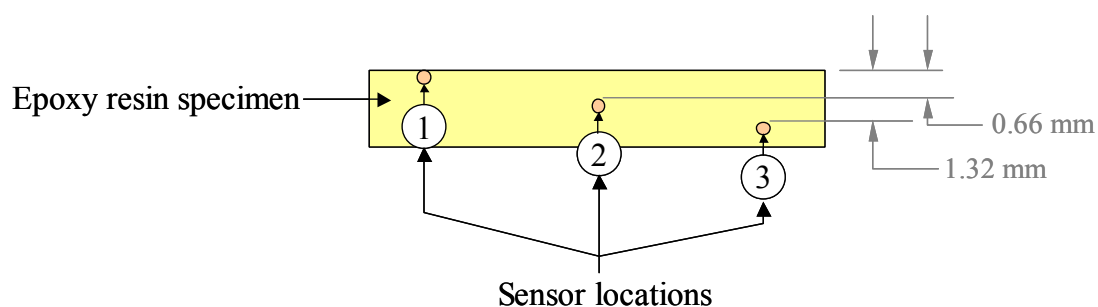


Figure 3.30 Schematic illustration of the relative locations of the embedded sensors that were located at specified depths in the cast neat-epoxy specimen of the epoxy specimens.

3.8.2.1 *Sensor interrogation for monitoring moisture ingress*

The Bruker MATRIX™-F FT-NIR spectrometer is capable of recording spectra via a maximum of six channels. Frequent scanning through specified channels is possible via a process control script using the OPUS 5.0 spectral acquisition software. A photograph of a mould cavity with multiple sensors that was ready for specimen fabrication is shown in Figure 3.31(a) together with a schematic illustration of a cross-linked specimen with embedded sensors and interrogation set-up for moisture ingress monitoring (Figure 3.31(b)). Sensing fibres were connected to the spectrometer via SMA connectors.

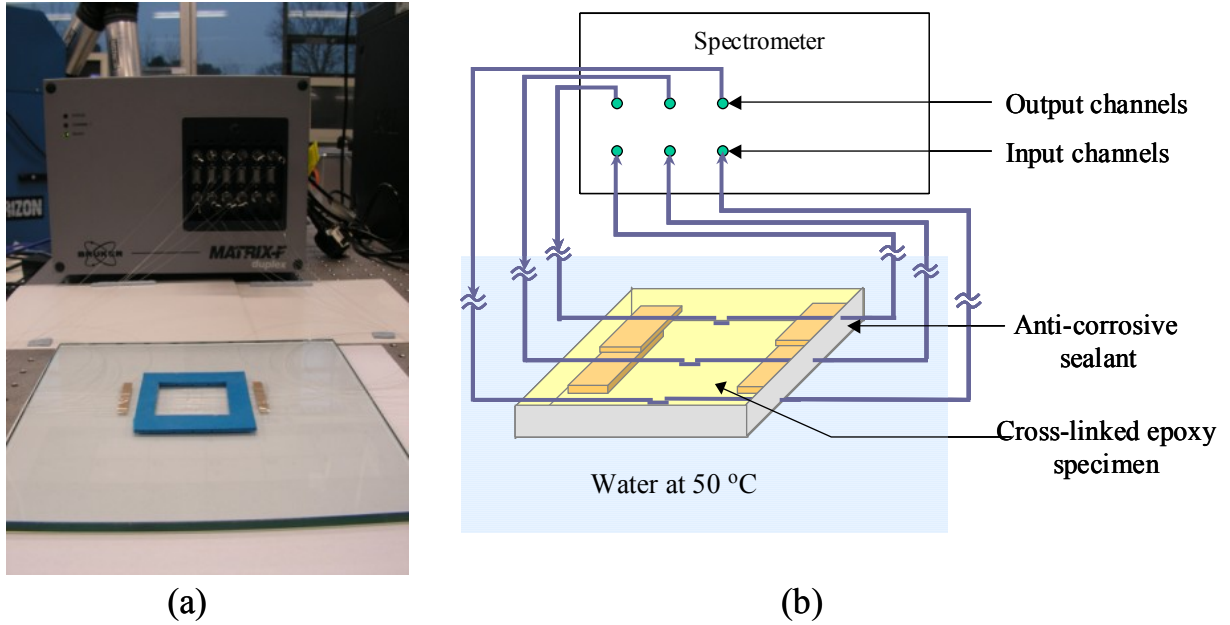


Figure 3.31 (a) photograph of the complete interrogation set-up and (b) Schematic illustration of the sensor interrogation via the Bruker MatrixTM-F FT-NIR spectrometer.

3.9 Proof-of-concept of multi-functional sensor

3.9.1 Sensor design

A schematic illustration of the conventional extrinsic Fabry-Perot interferometry (EFPI) - based multifunctional sensor design is presented in Figure 3.32. The sensor consists of a cleaved optical fibre [B and B'] that is secured within a precision-bore capillary tube [A]. The cleaved fibre is secured to the capillary tube via two fusion joints [D and D']. The air-gap between the cleaved fibres constitutes a Fabry-Perot (FP) cavity. The gauge length is defined as the distance between the fusion joints.

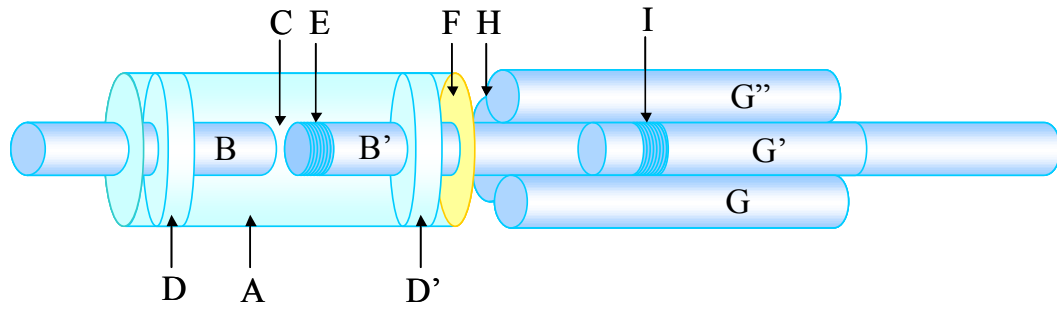


Figure 3.32 Schematic illustration of the multi-functional sensor design.

In this new design, the precision-bore quartz capillary tube was used to house the cleaved optical fibre but in addition, the end-faces of the capillary are used as a reflective surface. The elements that transform the primary EFPI sensor into the “multi-functional sensor” are: (i) the fibre Bragg grating (FBG): [E] that is inscribed in the end-region of the primary optical fibre [B’], (ii) the fibre reflective coating on the end-face of the capillary: [F] and (iii) the secondary optical fibres: [G, G’ and G’'] that are located around the primary optical fibre: [B’]. The secondary fibres are arranged and secured in position to create secondary cavities: [H].

The secondary fibres [G and G’'] illustrated in Figure 3.32 are multi-mode optical fibres. The cavity between the cleaved end-faces and the reflective coating serves as a “cell” for conducting trans-reflectance near-infrared spectroscopy of the resin (see Section 3.4.2.2). Sensing fibres [B’] and [G’] both are single mode-fibres. However, the Bragg gratings that are inscribed on the secondary fibre [G’] can be used to monitor the combined effects of strain and temperature. In contrast, the FBG sensor [E] on the primary optical fibre is in a strain-free condition and thus responds only to temperature. The EFPI sensor can be used to determine the axial strain along the capillary due to process-induced stresses develop during cross-linking of the epoxy resin. Any changes in the cavity length [C] will enable the strain to

be calculated. With regard to qualitative process monitoring, cleaved lead-out fibres from a 2 x 2 coupler can be attached as secondary fibres. These fibres can be attached on to the primary fibre at a suitable distance away from the reflective coating of the capillary end-face to serve as Fresnel reflection-based refractive index sensors.

3.9.2 Sensor fabrication

The conventional EFPI sensor consists of cleaved optical fibres that are secured within a precision-bore capillary tube. The cleaved fibres are secured to the capillary tube via two fusion joints. The gap between the cleaved fibres constitutes a FP cavity. The gauge length is defined as the distance between the fusion joints. Before making the EFPI sensor, the reflective end-face of the capillary was prepared as explained in Section 3.4.2.2.

Germania-Boron (Ge-B) co-doped single-mode fibre (PS1250/1500, Fibercore Ltd., UK) was used for fabricating the primary FP cavity. FBG sensor was inscribed in the Ge-B co-doped primary optical fibre using the phase-mask technique and an excimer laser (Braggstar, Coherent, UK) operating at 248 nm. The FBG sensor was produced using pulse energy of 10 mJ and 1500 pulses. The fibre with the FBG sensor was cleaved ensuring that the grating was located in close proximity to the cleaved-end (see Figure 3.32). The cleaved fibre was secured to the capillary via a fusion joint. With reference to Figure 3.32, secondary fibres were attached around the “primary” optical fibre using a UV curable resin (UV 304-T). This resin was cured using a UV light source (UV75, Thorlabs Inc. UK). The approximate length of 10.0±0.5 mm PTFE sleeve (Adtech Polymer Engineering, UK) was used for locating the secondary fibres around the primary optical fibre before bonding. Internal and outer diameters of the PTFE sleeve are 0.40±0.05 mm and 0.84±0.05 mm, respectively.

3.9.3 Sensor interrogation and monitoring of the cross-linking reaction

A schematic illustration of the experimental set-up that was used for monitoring the cross-linking reaction is shown in Figure 3.33(a). With reference to Figure 3.33(a), the Bruker MATRIX[™]-F FT-NIR spectrometer was used for sensor interrogation. Conventional transmission FTIR spectroscopy and the experiments involving the multi-functional sensors were carried out simultaneously. The conventional transmission FTIR spectroscopy was carried out using a 1 mm path-length de-mountable cuvette: [D]. A commercially-available near-infrared transmitting fibre optic probe: [A] was connected to one of the light output channels of the spectrometer and the other end was attached to a temperature-controlled cuvette holder: [B] via collimating optics: [C]. The transmitted light from [C] and through the de-mountable cuvette cell: [D] and the mixed resin: [E], was collect via collimating optics: [C'] and returned to the corresponding input detector port on the spectrometer. Due care was taken to ensure that the sensor did not obstruct the light-path of the conventional transmission experiment via the collimated optics.

The multi-functional sensor was secured to an internal side-wall of the de-mountable cuvette mentioned above using a UV curable resin (UV 304-T). As discussed previously, the secondary cavities were formed in between the secondary multi-mode fibres (105/125 mm) and the gold-coated end-face of the capillary. The secondary cavity for monitoring the cross-linking reactions and the Fresnel-based (refractive index) sensors, [G] and [I], respectively, were connected to the spectrometer via individual custom-made multi-mode 2 x 2 couplers: [K]. Spectra were obtained using a resolution of 0.025 nm and 64 scans via the chemical

sensor and the cavity length between the reflective end-face and the cleaved fibres was 250 μm . With respect to the FTIR-based interrogation of Fresnel reflection fibre sensor, the amplitude of the interferogram signal corresponding to the reflection from the two lead-out fibres immersed in the medium was monitored. The spare output arm of the coupler: [J] was immersed in index-matching gel. In Figure 3.33, [L] represents the spare channels on the spectrometer that can be used to interrogate additional secondary sensor such as evanescent wave-based sensor or additional FBG sensors for combined temperature and strain measurements. [M] represents a K-type thermocouple for independent monitoring of actual temperature with in the mixed resin during cross-linking.

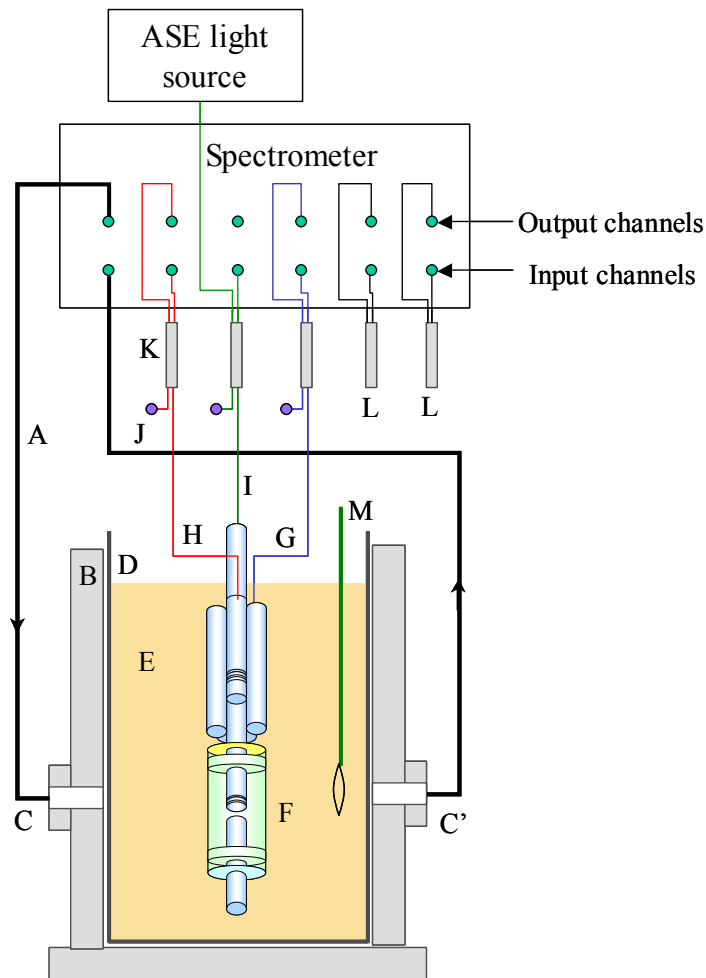


Figure 3.33 Schematic illustration of the experimental set-up and combined EFPI/FBG sensor interrogation using an external light source.

With reference to the combined strain/temperature (EFPI/FBG) sensor: [H], this device can be illuminated by an external light source or the internal light source of the FTIR spectrometer. In the proof-of-concept experiments, the sensor was illuminated by an external light source and also by the internal light source. Difficulties associated with sensor interrogation using the internal light source of the spectrometer will be discussed (Section 6.3.3).

The resin system used for monitoring the cross-linking reaction was LY3505 epoxy resin and XB3403 amine-based cross-linking agent. The mixed resin was injected into the cell at 30 °C and processed at 60 °C for 8 hours. The system was then cooled naturally to 30 °C.

3.9.4 Characterisation of EFPI and FBG Sensors

Two EFPI and five fibre Bragg grating (FBG) sensors (Figure 3.34) was employed to verify the consistency of the response of the EFPI and FBG sensor for temperature and resin shrinkage during cross-linking. Two EFPI sensors and five FBG sensors were attached on to a de-mountable cell and interrogated simultaneously. The EFPI were fabricated in the following manner. Two single-mode fibres were cleaved and secured inside a precision-bore capillary via two fusion joints. The ends of the capillaries with the optical fibres were sealed using a high-temperature resistant epoxy adhesive. This was done to prevent resin seeping into the EFPI cavity during processing and also to reinforce the fusion joints of the sensors [362]. Gauge length of the sensors was measured using an optical microscope.

Three out of five gratings have been sealed into precision-bore fused-silica capillaries, to isolate them from mechanical loads transmitted to the fibre when they are embedded in the epoxy resin. One end of the capillary was sealed completely using fusion arc and the other

side was fused on to the FBG fibre. The fibre-capillary splice was also reinforced with high-temperature resistant epoxy adhesive. These gratings (FBG-T) operate in a strain-free condition and behave as optical fibre thermometers, allowing the measurement of actual temperature. One of these sealed gratings (FBG-T3) was attached outside the cell, while other two gratings (FBG-T1 and FBG-T2) embedded within the epoxy resin. Two remaining unsealed gratings (FBG-S1 and FBG-S2) were embedded in the resin to monitor the combined effect of temperature and strain with in the resin. All the EFPI and FBG sensors were attached to the inner wall of the de-mountable cell as shown in Figure 3.34; however, sensing regions of the sensors were not bonded onto the cell wall. A K-type thermocouple was placed nearby the FBG-T3 optical sensor, outside the 1mm path-length cuvette and used as an independent reference.

Two sensor-interrogation systems were used to cross correlate the sensitivity of the systems against each other and a schematic illustration of the experimental set-up is shown in Figure 3.34. Two EFPI sensors (EFPI-1 and EFPI-2), one embedded FBG (FBG-S1) and one sealed FBG (FBG-T1) that attached inside the de-mountable cell were interrogated using a broadband light source (Lumen Photonics, LPB-1550-D) and an optical spectrum analyser (OSA) (Anritsu MS9710B) via an optical channel selector (Anritsu MN9674A). The sensors were recorded with 0.07 nm resolution. Out of remaining three FBG sensors, one embedded FBG (FBG-S2) and one sealed FBG (FBG-T2) that attached inside the cell and one sealed FBG (FBG-T3) that attached outside the cell, were monitored via a FBG interrogation system (FiberPro IS7000).

The sensor characterisation was carried out in a temperature-controlled cuvette holder (Ocean Optics) with $\pm 0.02^{\circ}\text{C}$ accuracy. Temperature sensitivity of the EFPI and FBG sensors (in air)

was investigated by monitoring the FP cavity length and Bragg peak shift, respectively at fixed temperatures with in the range of 30 – 80 °C. The same sensor set-up was used for measurement of resin shrinkage during cross-linking of an epoxy/amine resin system. Cross-linking of the resin was carried out at 60 °C for 8 hours. The experiment set-up was maintained at 30 °C before starting the experiment, injected the resin into the cell, heated the system up to 60 °C followed by cross-linking the resin isothermally for 8 hours. The system was then naturally cooled back down to 30 °C.

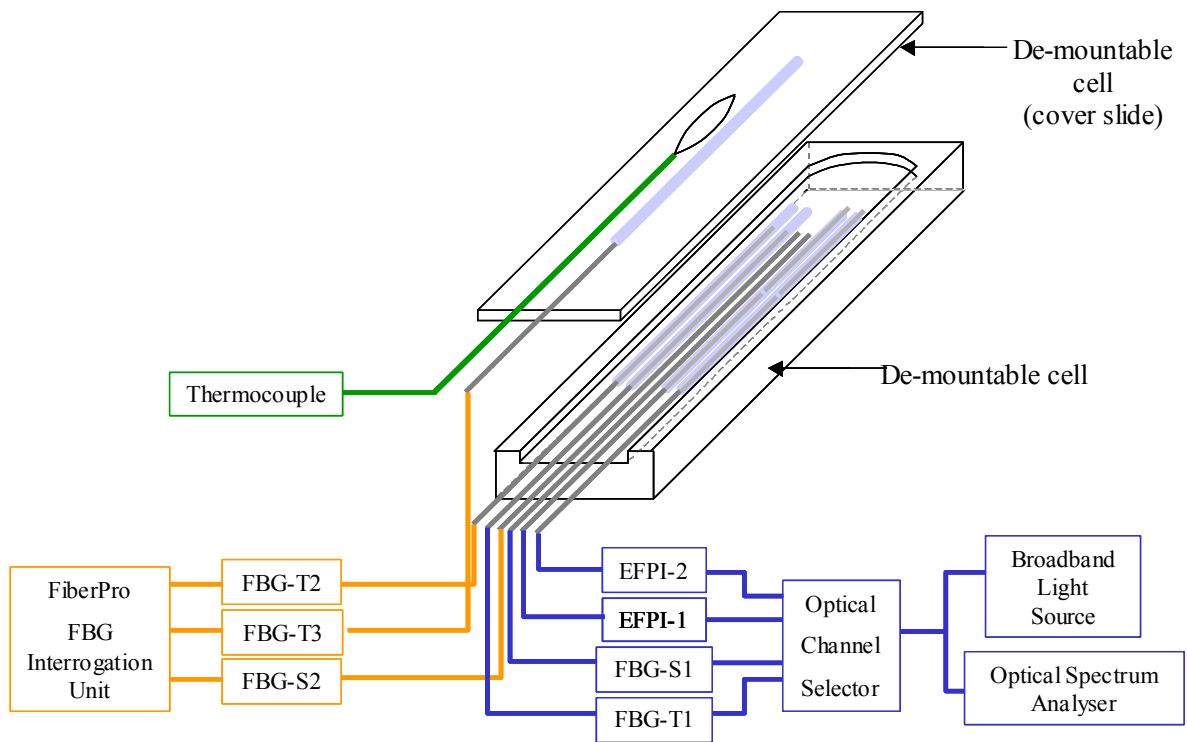


Figure 3.34 Schematic illustration of the experimental set-up and sensor interrogation.

3.10 Conclusions

Two fibre-optic sensing techniques were demonstrated for *in situ* monitoring of cross-linking reaction and moisture ingress in the LY3505/XB3403 epoxy resin system: near-infrared transmission spectroscopy and near-infrared reflection spectroscopy.

In situ monitoring of cross-linking reaction in the epoxy resin system was conducted using the fibre-optic near-infrared spectroscopy under transmission and reflection mode. Cross-linking kinetics of the resin system was evaluated at four isothermal reaction temperatures, 40, 50, 60 and 70 °C.

Influence of hygrothermal conditioning of the cross-linked epoxy resin system was studied using conventional techniques and fibre-optic transmission spectroscopy. Experimental procedures and specimen fabrication techniques associated with the conventional characterisation techniques as well as fibre-optic transmission spectroscopy were discussed. Absorption kinetics of water in the resin system was characterised using conventional techniques at three immersion temperature 30, 50 and 70 °C and 100 % RH. Fibre-optic near-infrared transmission spectroscopy was employed for *in situ* monitoring of moisture ingress at 50 °C and 100 % RH.

In addition, proof-of-concept experiments carried out to demonstrate the feasibility of using a new multi-functional sensor design were explained. The experiments include characterisation of the sensing elements for temperature and strain monitoring as well as using the sensor design for on-line monitoring of multiple parameters during cross-linking of the epoxy resin system.

Chapter 4

Fibre-optic near-infrared spectroscopy and optimisation of sensor designs

4.1 Introduction

Fibre-optic sensors were designed for monitoring the cross-linking reactions and diffusion of moisture in an epoxy/amine resin system using near-infrared spectroscopy. The following issues will be discussed in this chapter:

- The basis for conventional infrared spectroscopy for quantitative analysis using fibre-optic infrared spectroscopy.
- Effectiveness of different sensor designs in terms of reproducibility, dimensions and ease of handling.

- Investigation of the selection of appropriate path-length for constructing fibre-optic sensors.

4.2 Ray-optic considerations for fibre-optic spectroscopy

4.2.1 Fibre-optic transmission spectroscopy

Fabrication of the single-fibre transmission sensor involves holding two cleaved multi-mode fibres aligned and facing each other with a gap in between as shown in Figure 3.1. The cavity between the cleaved fibres serves as a cell to contain an analyte solution. In the current study, the analyte solution was either uncured epoxy/amine resin system in the case of monitoring of cross-linking reaction or cross-linked epoxy/amine resin system in case of moisture-ingress monitoring.

The input fibre that transmits the infrared (IR) light to the sensing region and the output fibre that carries the transmitted light through the resin to the FTIR spectrometer are connected to the light source and the detector, respectively. As shown in Figure 3.1, incident light intensity at the cleaved fibre surface is denoted as I_o and the intensity of the light at the receiving fibre end is denoted as I . The background/reference measurement of this sensor arrangement was recorded with air in between the cleaved fibre faces. The ratio of the sample spectrum of the epoxy resin system to the background spectrum is used to generate the absorbance spectrum of the resin according to the relationship given below:

$$A = -\log_{10} \left(\frac{I}{I_0} \right) \quad \text{Equation 4.1}$$

According to the Beer-Lambert law, the absorbance, A can also be defined as shown in Equation 2.12. The same theory is said to be valid for using fibre-optics for IR transmission spectroscopy [363]. However, for conventional transmission FTIR spectroscopy, absorbance was derived for a parallel beam transmitted through an analyte. Then with air as an analyte, at any wavelength, absorbance, $A \rightarrow 0$ as $I/I_0 \rightarrow 1$. The theory is also valid for commercial infrared fibre-optic spectroscopy, where high-precision beam aligning and beam collimating techniques are used [191,364,365]. But in the case of fibre-optic transmission spectroscopy discussed in this study, the ray-optics of IR radiation at the sensing cavity are different from that mentioned above and can be drawn schematically as shown in Figure 4.1. IR radiation diverges at the fibre/analyte interface due to the difference in refractive indices of the fibre core and the analyte in the sensing cavity. According to the ray optic theory of fibre transmission and considering bound rays, the half-angle of cone of acceptance (θ_0) at the fibre interface can be expressed using Snell's law of refraction, [227,366]:

$$n_{core} \sin \theta_1 = n_0 \sin \theta_0 \quad \text{Equation 4.2}$$

$$\theta_0 = \sin^{-1} \left(\frac{NA}{n_0} \right) \quad \text{Equation 4.3}$$

where n_{core} and n_0 are refractive indices of the fibre core and the analyte, respectively. θ is the angle between the bound rays and an imaginary line drawn perpendicular to the cleaved fibre end and subscripts 1 and 0 represent the incident and transmission media, respectively. NA is the numerical aperture of the step-index multimode fibre (see Appendix – I).

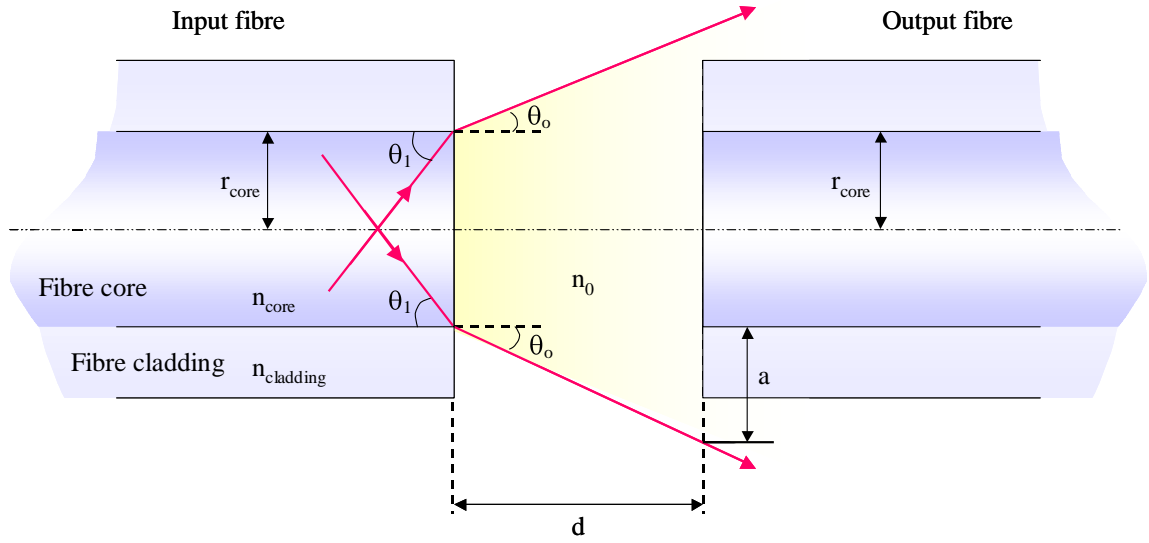


Figure 4.1 Schematic illustration of ray-optic approach for transmission of IR radiation at the fibre-optic sensing cavity.

Then the power of IR radiation that enters into the output fibre, $P_3(\lambda)$ can be represented as a fraction of the power that is leaving the input fibre interface, $P_0(\lambda)$ as below (see Appendix – I) [367]:

$$P_3(\lambda) = \frac{1}{10^A} \left[1 - \left(\frac{n_0 - n_{core}}{n_0 + n_{core}} \right)^2 \right] \left(\frac{r_{core}}{r_{core} + d \tan \theta_o} \right) P_0(\lambda) \quad \text{Equation 4.4}$$

According to the Equation 4.4, the power of IR radiation that couples in to the output fibre is a function of refractive index of the analyte, absorbance at a wavelength, λ and the distance between fibre ends. This can be written as below:

$$P_3(\lambda) = f \ n_0, A, d \ P_0(\lambda) \quad \text{Equation 4.5}$$

Therefore for monitoring of cross-linking reaction of an epoxy/amine resin system, $P_3(\lambda)$ changes throughout the cross-linking reaction as the refractive index of the resin system increases. The change in $P_3(\lambda)$ during cross-linking of the epoxy resin system used in this study will be discussed in more detail in Section 5.4.4.1.

4.2.2 Fibre-optic reflectance spectroscopy

Near-infrared reflectance spectroscopy using multimode fibres involves transmitting light to the sensing region and reflected light from the analyte to the detector using a single fibre. The sensor was constructed using capillary reflector design (see Section 3.4.2.2).

In infrared spectroscopy, the mode of operation used in the fibre-optic design is generally called as trans-reflection spectroscopy. When IR radiation is directed on to an analyte as shown in Figure 4.2, reflected radiation from the analyte consists of “specular” reflections/trans-reflections where the angle of reflection is equal to that of incident and “diffuse” reflections; those reflected in all other directions [368]. For an optically clear, thin layer of analyte placed on a mirror-like surface, the major portion of the radiation transmits in to the medium and reflects back at the reflective surface. Therefore the fibre-optic reflectance sensor explained in this study, can be classified as trans-reflectance spectroscopy (TRS) [122,191,368].

The reflecting face of the capillary reflector was coated with a thin layer of gold, approximately 12 – 15 nm in thickness using a sputter coater (see Figure 4.2). In trans-reflection spectroscopy, the infrared spectrum is generated by calculating the ratio of the single-channel spectrum of an analyte to that of the reference. A bright, optically flat surface

is required to obtain the reference spectrum. Materials that can be used as a reference substrates for different regions in IR spectrum were discussed by Griffiths [369] and recommended that a gold substrate is most suitable for taking a reference spectrum compared with sintered ceramic discs and PTFE[®] discs commonly used in the near-IR range.

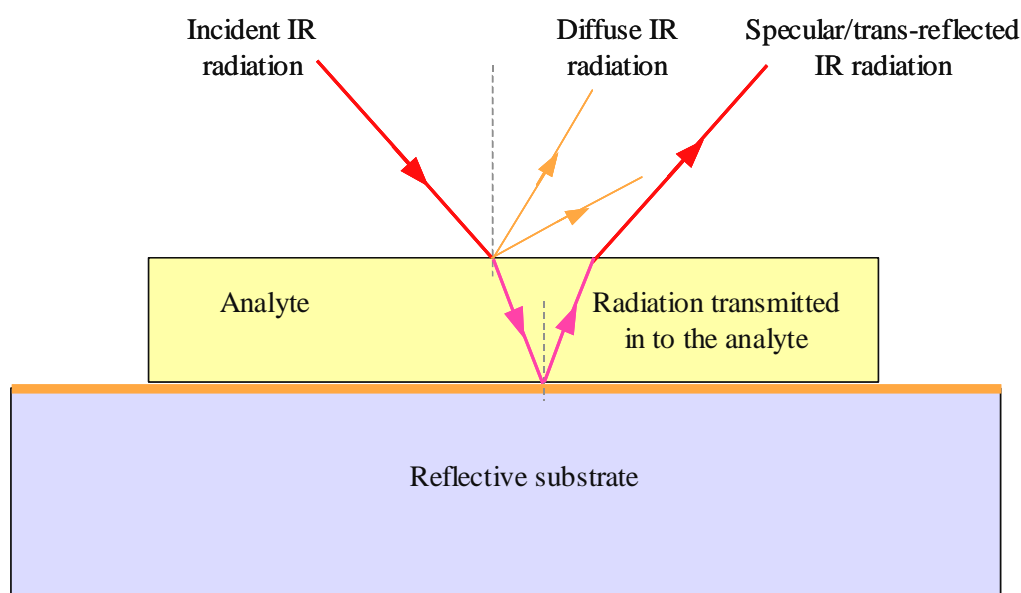


Figure 4.2 Schematic diagram of trans-reflectance (specular) and diffuse reflection; the incident beam is drawn at an arbitrary incident angle.

The fraction of trans-reflection depends on the angle of incidence, refractive index of the analyte, surface roughness of the substrate and absorption characteristics of the analyte. For a thin layer of clear analyte and IR radiation that enters into the sample with an incident angle between $0 - 88^\circ$, the radiation passes through the thin layer, reflects back at the reflective substrate and exits from the analyte after passing through the film for second time. Then the exit radiation from the analyte film is considered as trans-reflectance (specular) radiation and if the analyte layer is thin enough so that the radiation is not totally absorbed by the film, spectral data is equivalent to that obtained using transmission spectroscopy [368,195]. It can be shown that the half-angle of cone of acceptance, θ_o emerging at the cleaved step-index

multimode fibre (considering air as the medium in the sensing cavity) is 12.709° (Equation 4.2). The diameters of the core and the cladding were $105 \pm 3 \mu\text{m}$ and $125 \pm 4 \mu\text{m}$, respectively. Numerical aperture and the refractive index of the core of step-index multi-mode fibre are 0.22 and 1.46, respectively. Schematic illustration of ray optic path of IR beam at the sensing region is shown in Figure 4.3. Therefore according to the law of reflection, the maximum angle of reflection at the reflective substrate is equal to θ_o and the sensing concept of the fibre-optic reflectance spectroscopy is analogous to that of fibre-optic transmission spectroscopy. However, the path-length for reflection spectroscopy will be twice as that for transmission spectroscopy with the same cavity length, d (see Figure 4.3).

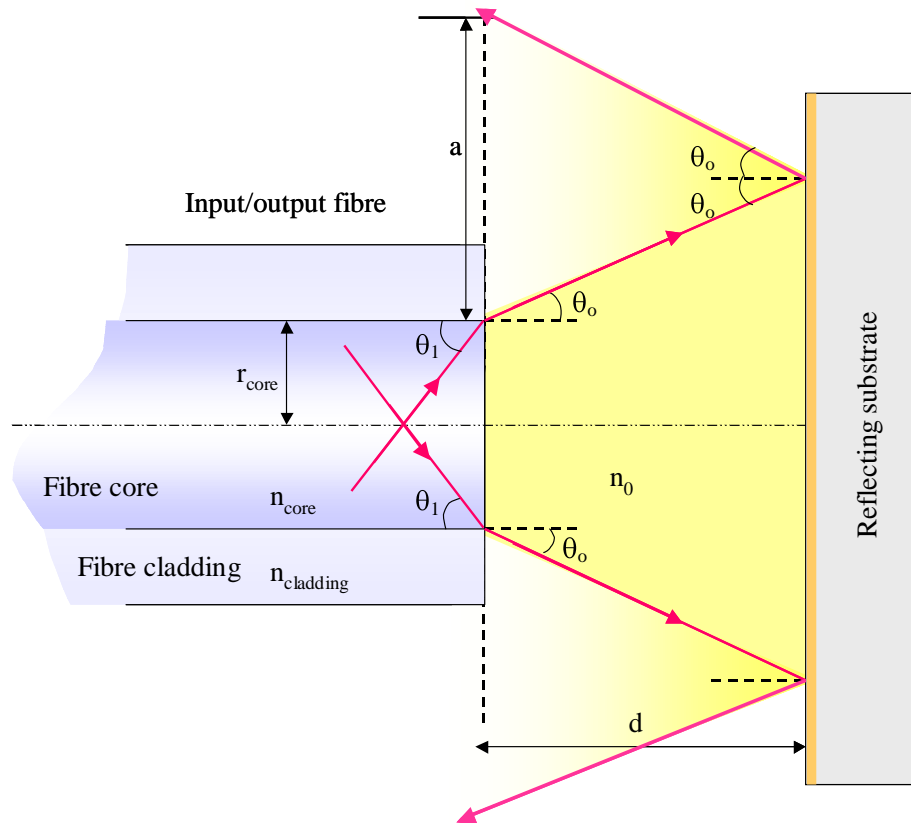


Figure 4.3 Schematic illustration of ray-optic approach for trans-reflectance reflection of IR radiation at the fibre-optic sensing cavity.

Considering the ray optic approach that was used for the fibre-optic transmission spectroscopy, the power of IR radiation that is coupled back to the fibre, $P_5(\lambda)$ in fibre-optic reflectance spectroscopy can be expressed as below (see Appendix – II):

$$P_5(\lambda) = 10^{\left(\frac{A_{refl}}{10} - 2A\right)} \left[1 - \left(\frac{n_0 - n_{core}}{n_0 + n_{core}} \right)^2 \right] \left(\frac{r_{core}}{r_{core} + 2d \tan \theta_0} \right) P_0(\lambda) \quad \text{Equation 4.6}$$

$$P_5(\lambda) = f(n_0, A, d) P_0(\lambda) \quad \text{Equation 4.7}$$

Assuming constant reflectivity at the reflector, $f(n_0, A, d)$ can be expressed as the fraction $P_0(\lambda)$ and is a function of refractive index of the analyte, absorbance at λ and distance between the cleaved fibre and the reflective surface. The change in fraction of power coupled back to the detector in fibre-optic reflectance spectroscopy during cross-linking and a comparison of the efficiency of light coupling under transmission and reflection modes will be discussed in Section 5.4.4.2.

4.3 Fibre-optic sensor designs

4.3.1 Fibre-optic transmission spectroscopy

Fibre-optic transmission spectroscopy was performed using 105/125 μm step-index multimode silica optical fibre. Three different types of sensor fixtures were designed for

constructing the single-fibre transmission sensor and the feasibility of using each sensor design was investigated [357,370].

4.3.1.1 Epoxy substrate sensor design

In this sensor design, precision-bore quartz capillary, which holds the sensing fibres, was embedded in a thin layer of neat-epoxy resin (see Figure 4.4). The approximate dimensions of these rectangular sections were 15 mm (length), 4.2 mm (width) and 0.5 mm (thickness). A groove was cut across the rectangular section using a diamond-tipped cutting wheel to create the sensing region. A similar sensor design was proposed and investigated by Powell *et al.* [196] in which sensing fibres were axially aligned on a cross-linked epoxy v-groove.

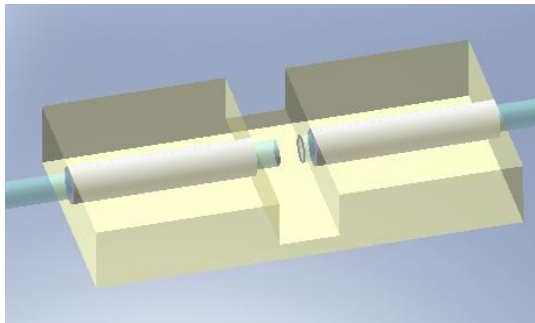


Figure 4.4 Schematic illustration of the epoxy substrate sensor design.

In the epoxy substrate sensor design, it is necessary to embed the capillary in a material, which is compatible with the structure in which the sensor will be embedded. This is to minimise the influence of the embedded sensor on the physical and mechanical performance of the structure. Generally, embedding a foreign object within a composite structure has a major influence on issues related to mechanical and physical integrity of the structure. Therefore ideally, the best option is to use the same resin as the base structure to fabricate the sensor fixture. In the case of epoxy resin matrices, it is necessary to use the same processing

schedule, which is used for composite manufacturing, for the sensor fabrication. Otherwise different processing conditions increase the possibility of building up stresses at the resin/fixture interface.

The dimensions of the sensor fixture also may have an influence on the properties of the base structure. In continuous fibre-reinforced composites, this has a considerable impact on the relative orientation of the reinforcement. Also it may create resin-rich areas due to induced waviness between the prepreg layers. The effects due to the dimensions can be minimised by miniaturising the sensor design. The thickness and the width of the cross-linked resin layer around the capillary were larger compared to the dimensions of the other sensor designs, which will be discussed in Sections 4.3.1.2 and 4.3.1.3. In terms of sensor fabrication, care is required during making the groove across the capillary in order to maintain rigidity of the substrate. Also it was observed that maintaining the dimensional consistency of the sensor fixture is difficult. Therefore, making a good quality sensor considerably depends on the experience of the operator.

4.3.1.2 Capillary support sensor design

The approximate dimensions of the capillary support fixture were 22 mm (length), 0.6 mm (width) and 0.3 mm (thickness). In terms of width and thickness of the sensor fixture, this sensor design is smaller than that of the epoxy substrate sensor design (see Figure 4.5). The length of the fixture can be minimised by using shorter capillaries for supporting capillaries and also for the substrate capillary. However, in order to feed the sensing fibres through the capillaries, care must be taken to keep the bore of the supporting capillaries free from adhesive. Therefore in the current study, the overall length of the sensor design was kept around 20 – 25 mm.

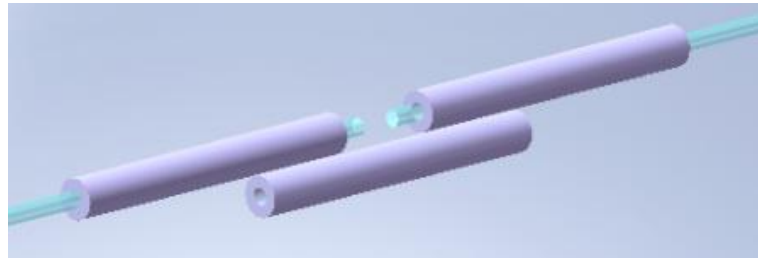


Figure 4.5 Schematic illustration of the capillary support sensor design.

In fibre-reinforced composites, defects within the structure due to the embedded sensors could be reduced using this sensor design. The influence could be further minimised by choosing the correct sensor angle with respect to the direction of the reinforcing fibres. For example, sensors can be embedded along the axis of the reinforcing fibres to reduce fibre waviness and resin-rich regions [220,364]. The problems associated with embedded optical fibres on the mechanical properties of advanced fibre-reinforced composites have been reviewed in references [371,372,372]. From a sensing point-of-view, the sensor design is more stable and rigid compared with the epoxy substrate sensor design. The substrate capillary was fixed on to the supporting capillaries while the sacrificial fibre was kept across the both supporting capillaries. In addition, the substrate capillary is more rigid and stable than the resin layer in the epoxy substrate sensor design and hence required level of fibre alignment can be achieved.

Sensor fabrication is more robust and time-efficient compared to the epoxy substrate sensor design. The quality of this sensor fixture does not depend on skill and experience and also reasonable dimensional consistency can be achieved. The only disadvantage of this design is the brittleness of the fixture design compared with the epoxy substrate sensor design. Nevertheless, the brittleness of the fixture had less influence on handling during sensor fabrication as well as during embedding.

4.3.1.3 Abraded capillary sensor design

The third sensor design (abraded capillary) was constructed by partially abrading a quartz capillary along its length. An attempt was made to minimise the fixture dimensions by using only a single precision-bore capillary as a support to hold the sensing fibres (see Figure 4.6).

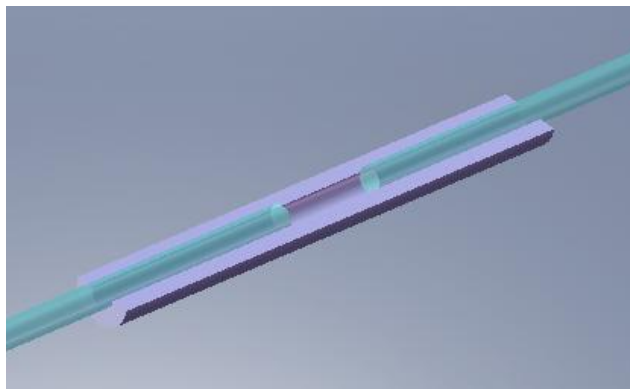


Figure 4.6 Schematic illustration of the abraded capillary sensor design.

George *et al.* [147] demonstrated using a single-fibre sensing concept for fibre-optic near-infrared spectroscopy in transmission mode. In that sensor design, plastic-clad silica optical fibres were aligned with a gap in between the cleaved fibre faces using a glass micro-capillary. Two different diameters of the sensing fibres were used: 600 μm and 1000 μm . However they were unable to observe absorption bands down to 2500 nm due to cut-off wavelength range of the optical fibres. Therefore the authors were unable to use the absorption band due to epoxy ring vibration at 2207 nm for quantitative analysis. Rogers *et al.* [195] deployed the same sensor design for monitoring of cross-linking reaction of a TGDDM/DDS resin system. In this study, fluorine-doped silica-clad silica fibre was used for sensing and two cleaved fibres were aligned facing each other using PTFE micro-bore tubing. The cavity length between two fibre faces was 2 mm. Mijović *et al.* [136] reported a similar transmission cell design for *in situ* monitoring of cross-linking reaction using near-infrared

transmission spectroscopy. The sensor design consists of two 600/630 μm fused silica multimode fibres aligned in a short section of capillary. Good spectral quality was obtained with 2-3 mm cavity length. However, in all investigations mentioned above, the method of inserting the resin system into the sensing cavity, which was created inside the capillary has not been discussed clearly. Fernando *et al.* [81] proposed a sensor design for chemical sensing where two multimode fibres were aligned in a metal capillary. A slot was introduced to the metal capillary to inject resin into the sensing cavity. The reaction mechanism of an epoxy resin system was successfully modelled based on fibre-optic spectroscopy. Only disadvantage associated with their sensor design is that the metal aligning capillary may cause materials mismatch within the composite structure [185].

Although the structural integrity of the composite structure can be less influenced by using the abraded capillary sensor design, there are several disadvantages associated with the sensor fabrication and handling. Due to the brittleness of quartz and very low thickness of the ground section, the sensor fixture was more fragile than the other sensor designs discussed. The approximate thickness of the capillary after grinding was approximately 170 μm . Also difficulties were experienced during feeding the sensing fibres through the abraded bore due to the very-low strength of the capillary after abrading.

Fixture fabrication also is more complicated compared with the fabrication of the other two sensor designs. A metal holder with a precision v-groove was used to grind the capillary along its axis. Non-uniform grinding along the axis (see Figure 4.7) was observed which lead to insufficient depth of the U-shape capillary section for holding the sensing fibres. In Figure 4.7, the dotted grey line shows the expected level of the capillary face after grinding and the dark continuous line shows the angled-flat face due to non-uniform grinding. This may be

attributed to non-uniform pressure applied on the metal support during grinding. This also causes a reduction in the strength of the sensor fixture.

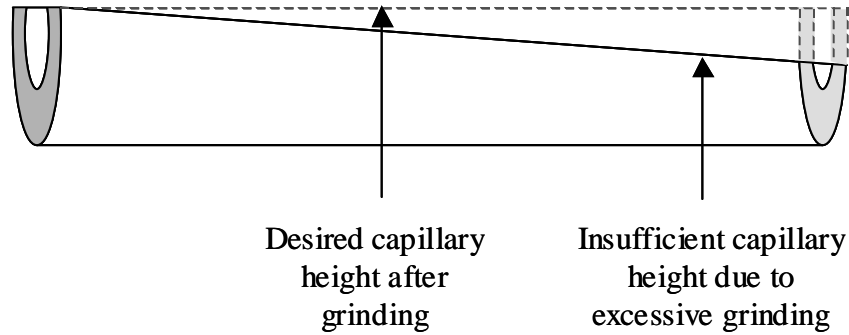


Figure 4.7 Schematic illustrations of an abraded capillary with non-uniform grinding along its axis.

In addition, fracture across the capillary was observed during grinding as well as during cleaning after grinding. Therefore wastage associated with the sensor fabrication process is high compared with the epoxy substrate and capillary support sensor designs.

Several approaches can be used to address above-mentioned issues related to the sensor design and a few suggestions are given below. Fabrication and handling difficulties can be minimised by using a capillary with thicker wall. Also the quartz capillary can be replaced with a rigid polymeric capillary, which is less brittle compared with quartz. However, a polymeric capillary as a substitute may affect the sensor alignment due to bending and warping at elevated temperatures. On the other hand, precision equipment can be used to minimise the issues related to fabrication. However, such alternative measures increase the cost of sensor fabrication.

The advantages and disadvantages associated with each sensor design has been summarised in. With reference to Table 4.1, the selection criteria for identifying the “best” sensor design for the subsequent experiments was based on the following:

- (i) Fixture fabrication – robustness, reproducibility, dimensional consistency;
- (ii) Sensor fabrication – ease of handling, degree of alignment of sensing fibres, stability of the fibre alignment; and
- (iii) Impact on the embedding structure – dimensions of the sensor design, compatibility with the base composite structure.

Table 4.1 Advantages and disadvantages of sensor designs constructed in this study.

Sensor design	Comments
Epoxy substrate	<p><u>Advantages:</u></p> <ul style="list-style-type: none"> • Ease of sensor fabrication. • Low cost. • Can be mass-produced. <p><u>Disadvantages:</u></p> <ul style="list-style-type: none"> • Relatively large dimensions of the sensor fixture. This may cause resin rich regions and waviness between the prepreg layers. • Degree of fibre alignment of the sensor is highly dependent on the thickness of the resin layer at the sensing region. • Dimensional consistency of sensor fixture is low. • Quality of the sensor fixture is considerably dependent on the experience of the operator.
Capillary support	<p><u>Advantages:</u></p> <ul style="list-style-type: none"> • Sensor fabrication is straightforward. • Sensor fixture is more stable and rigid compared with the epoxy substrate sensor design. • Good reproducibility of the quality of the sensor in terms of fibre alignment. • Reasonable dimensional accuracy can be achieved. • Less dependency of the quality of the sensor on operator skills. <p><u>Disadvantages:</u></p> <ul style="list-style-type: none"> • Sensor fixture is brittle when compared with the epoxy substrate. • The relative dimensions are smaller than the design based on the epoxy substrate. But the overall thickness is 300 μm.
Abraded capillary	<p><u>Advantages:</u></p> <ul style="list-style-type: none"> • Sensor design is smaller in size compared with the above-mentioned designs and hence less influence on the relative orientation of the reinforcing fibres. <p><u>Disadvantages:</u></p> <ul style="list-style-type: none"> • Fabrication of the fixture is more complicated and required a custom-made rig to abrade and polish the capillary.

	<ul style="list-style-type: none"> • Dimensions of the fixture are highly dependent on operator skills. • Sensor fixture is more fragile than other sensors. • Wastage associated with the sensor fabrication process is high compared with other sensor designs.
--	--

The issues associated with the fabrication of the fixture and the sensor were concluded. Although the relative dimensions of the sensors are important during embedding in composites, their size did not pose any problem when deployed for studies involving thermosetting resins.

Accordingly, it was decided to use capillary support sensor design for fabricating the single-fibre transmission sensor for monitoring the cross-linking reactions and diffusion of moisture in the epoxy/amine resin system.

4.4 Optimum cavity length for fibre-optic spectroscopy

4.4.1 Fibre-optic transmission spectroscopy

The capillary support sensor design was used to determine the optimum cavity length for fibre-optic transmission spectroscopy. For this experiment, one of the sensing fibres was inserted into one supporting capillary of the sensor fixture and was attached on to a precision translation stage to change the gap between cleaved sensing fibres (see Section 3.6.1). Absorbance spectra obtained with different cavity lengths are shown in Figure 4.8. Well-resolved combination band, due to second overtone of the epoxy ring stretching and C-H bending vibration peak at 2207 nm, was used to investigate the spectral quality as a function of cavity length (detailed peak assignments of LY3505/XB3403 resin system is given in

Table 5.1). According to Figure 4.8, the epoxy peak height increases as the cavity length increases. This is in accordance with Equation 2.12. However, the objective of determining appropriate path length for the sensor is not only to maximise the absorption but also to optimise the intensity of the light coupling into the receiving fibre and hence to obtain good signal-to-noise ratio.

According to Figure 4.9, it can be clearly seen that the peak area increases linearly as the cavity length increases.

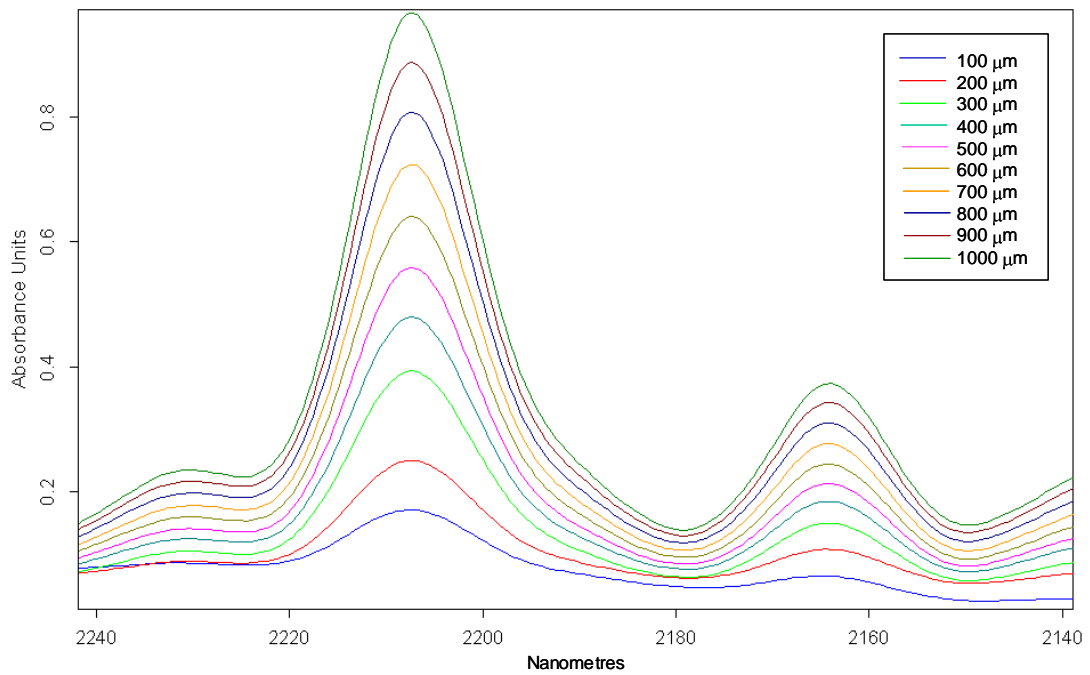


Figure 4.8 Near-infrared spectra of LY3505 bisphenol-A epoxy resin as a function of sensing cavity length. Absorption peak at 2207 nm is due to the absorption band of epoxy.

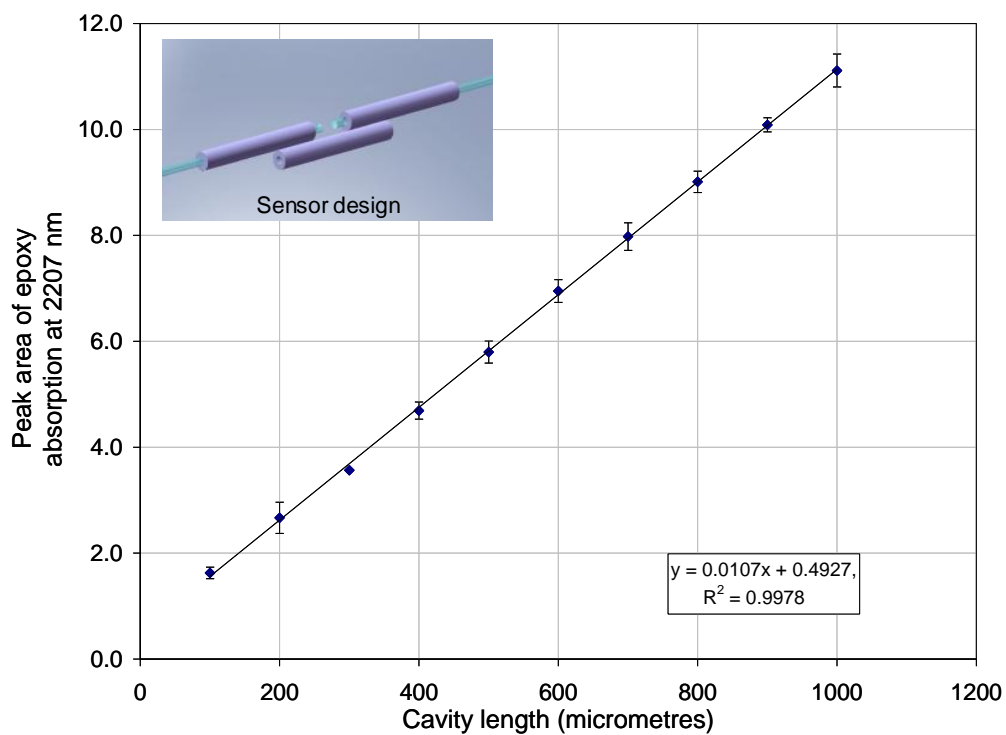


Figure 4.9 Relationship between the epoxy peak area and the cavity length.

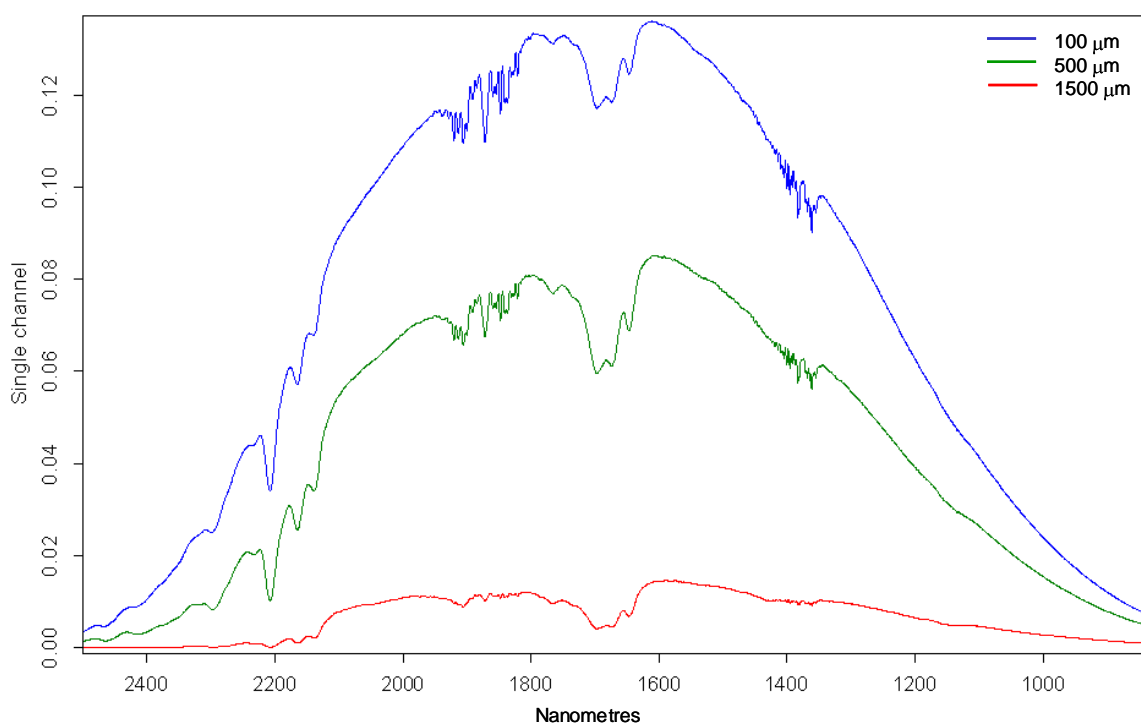


Figure 4.10 Comparison of single-channel spectra obtained for cavity lengths of 100, 500 and 1500 μm using fibre-optic transmission spectroscopy.

It can be shown that with constant refractive index, n_o of an analyte in the sensing cavity, as the cavity length, d increases, “ $d \tan \theta_o$ ” increases and therefore the fraction of power of IR beam couple into the output fibre decreases (see Appendix – I). The increase in power loss of IR beam with increasing cavity length also can be evident from single-channel sample spectra obtained with different cavity lengths as shown in Figure 4.10. As shown in Figure 4.10, a sample signal acquired with a 1500 μm cavity length is very weak compared with that recorded for 100 μm cavity length [365]. Therefore according to Equation 4.1, it can be shown that for $I = I_0$ and $I/I_0 = 1$, absorbance > 1 . However as shown Figure 4.8, peak resolution with 100 μm cavity is very low as the thickness of the analyte within the cavity is not enough to show strong absorption bands. On the other hand, infrared detectors have a threshold light intensity below which the detector is not capable of producing acceptable level of signal-to-noise ratio. Therefore to obtain a reasonable signal without losing spectral resolution, the cavity length for fibre-optic near-infrared transmission spectroscopy was kept approximately as 500 μm .

4.4.2 Fibre-optic reflectance spectroscopy

Two sensor configurations were investigated to optimise the sensor design as shown in Figure 3.17: in set-up A, one fibre was used for sensing whilst the other fibre end was immersed in a refractive index-matching gel to minimise reflections at the fibre end. In set-up B, both lead-out fibres on the sensing side of the coupler were used for sensing. The LY3505[®] epoxy resin was used as an analyte medium. Spectra of resin with different cavity lengths between the cleaved fibre ends were recorded and investigated to determine optimum gap for monitoring

of cross-linking reaction. The gap was changed from 100 to 1500 μm in 100 μm steps. The experiment was repeated three times to obtain an average absorbance.

Capillary reflector sensor design – Set-up A

Figure 4.11 shows absorbance spectra obtained using Set-up A with different cavity lengths. A combination band due to the second overtone of the epoxy ring stretching and C-H bending vibration peak at 2209 nm was used to investigate the spectral quality as a function of cavity length. According to Figure 4.11, the signal-to-noise ratio increases and peak height reduces as the cavity length increases beyond 700 μm .

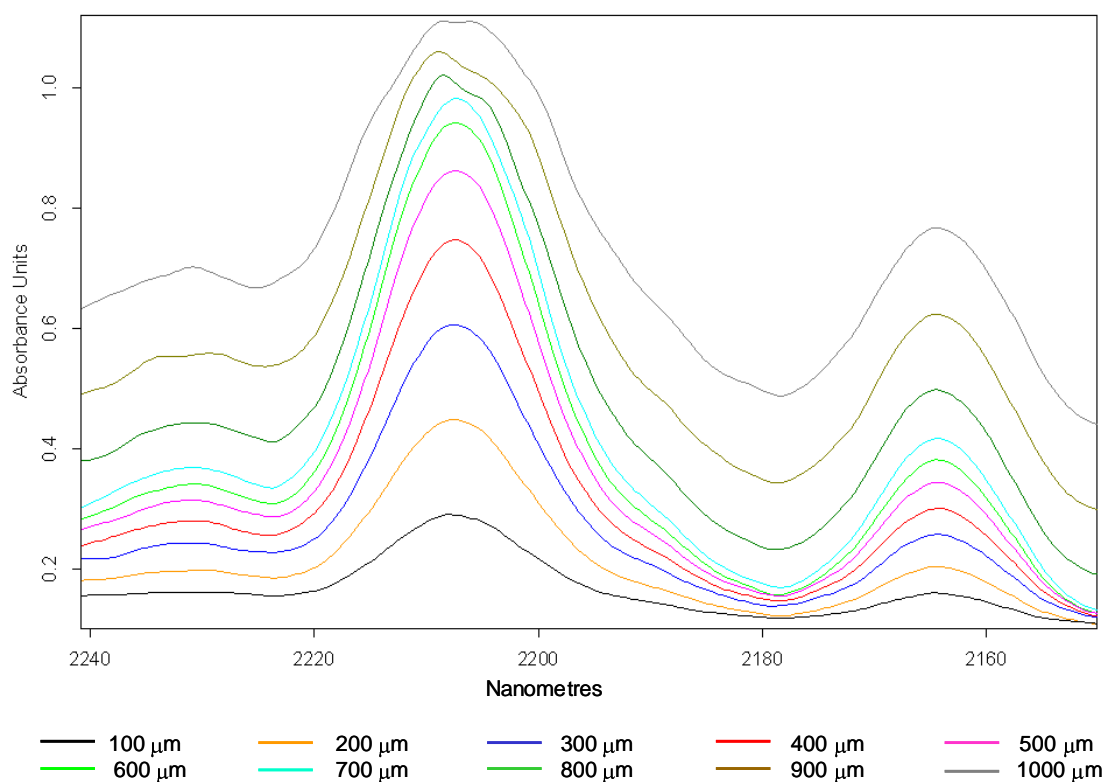


Figure 4.11 Near-infrared spectra of LY3505 bisphenol-A epoxy resin as a function of cavity length obtained using the capillary reflector Set-up A; absorption peak at 2209 nm is due to combination band of epoxy; spectra obtained with cavity lengths greater than 700 μm were expanded along the y-axis to improve the clarity of individual spectra.

Capillary reflector sensor design – Set-up B

Absorbance spectra obtained using Set-up B with different cavity lengths are shown in Figure 4.12. The same combination band due to the epoxy peak at 2209 nm that was used for analysing the spectral data obtained via Set-up B was used to quantify the effect of the cavity length on spectral quality. According to Figure 4.12, the spectral resolution and peak intensity reduce as the cavity length increases beyond 800 μm .

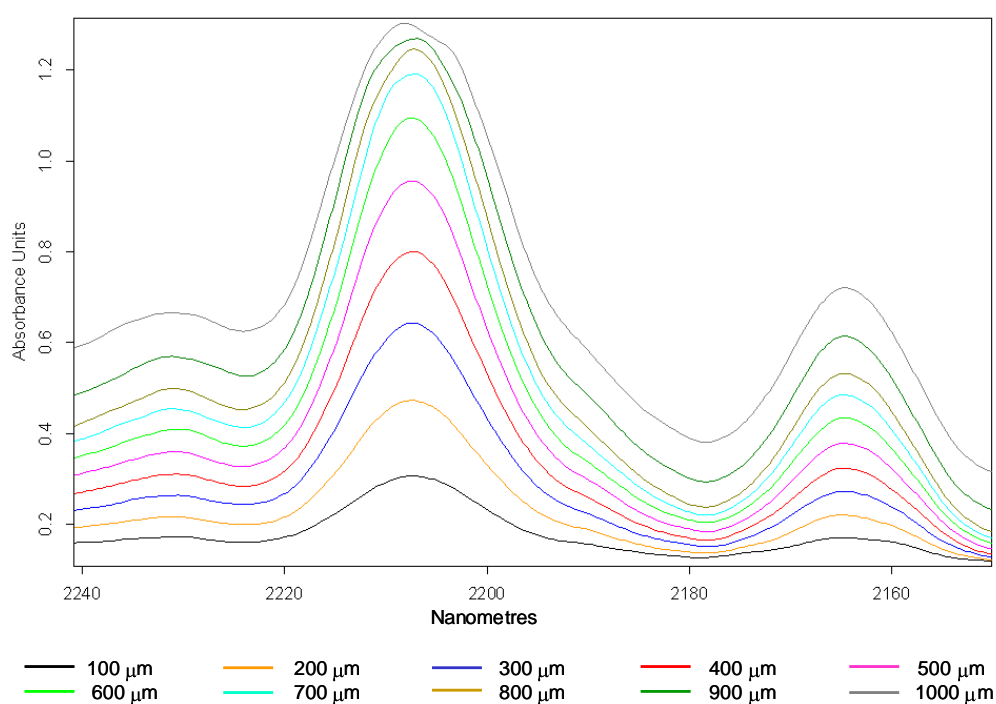


Figure 4.12 Near-infrared spectra of LY3505 bisphenol-A epoxy resin as a function of cavity length obtained using the capillary reflector Set-up B; Absorption peak at 2209 nm is due to combination band of epoxy; spectra obtained with cavity lengths greater than 800 μm were expanded along the y-axis to improve the clarity of individual spectra.

Comparison of capillary reflector – Set-up A and Set-up B

Spectra obtained from both set-ups show an increase in peak height for a cavity length of 700 μm . However, it can be seen from Figure 4.12 and Figure 4.11 that for the 100 – 700 μm cavity length range, the peak intensity of spectra acquired via Set-up B is higher compared to that recorded using Set-up A. Figure 4.13 shows the relationship of epoxy peak area and sensing cavity length. The spectral responses acquired using capillary reflector; Set-up A and B are cross-plotted as a function of cavity length. As the cavity length increases, the difference in peak area obtained with two design configurations increases. Set-up B gives slightly higher peak area compared with the peak area recorded using Set-up A for the same cavity length. According to Figure 4.13, a linear relationship between epoxy peak area and cavity length can be seen up to around 500 μm cavity length irrespective of the sensing configuration.

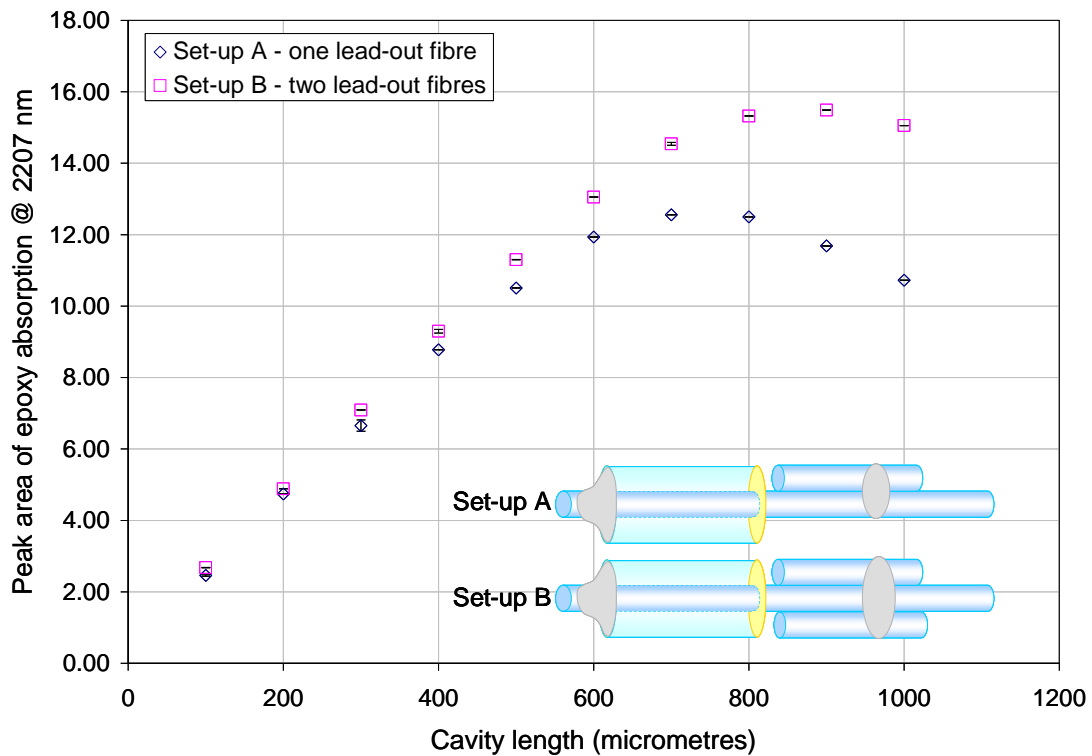


Figure 4.13 Relationship between the epoxy peak area and the cavity length.

However, beyond 600 μm cavity length, the peak area as well as spectral resolution of Set-up A decreases gradually where as Set-up B started losing signal strength beyond 800 μm . The spectral characteristics associated with the sensor Set-up A mentioned above can be attributed to the insufficient IR signal that is transmitted back to the detector with a single sensing fibre, compared with the IR signal coupled back to the detector with two sensing fibres. Furthermore, in Set-up A, one of the lead-out fibres on the sensing side of the 2 x 2 coupler was immersed in refractive index matching gel to reduce Fresnel reflections at the fibre interface. However the refractive index matching gel may not be effective enough to stop reflections in step-index multimode fibres those having broad near-infrared transmission range. Therefore in Set-up A, the reflected signal from the sensing fibre may have an influence of interference of Fresnel reflections from the other fibre end, which could affect the spectral resolution. On the other hand, in Set-up B, the sensing region was illuminated with both lead-out fibres and the reflected IR radiation coupled back to the detector is greater.

Taking the above-mentioned issues in to consideration, the capillary reflector Set-up B was chosen for remote monitoring of cross-linking reaction via fibre-optic reflectance spectroscopy. As stated above, spectral resolution remains linear with respect to cavity length only up to 500 μm . The decrease in reflected IR signal with increase in cavity length can be clearly seen from the sample signal obtained for different cavity lengths as shown in Figure 4.14. Although decrease in cavity length increases the signal intensity of the reflected light, intensities of absorption peaks observed with 100 μm cavity length are not strong enough compared with that obtained with 500 μm as explained in Section 4.4.1. Therefore the

approximate sensing cavity length between the gold-coated capillary face and the sensing fibres was kept as 500 μm for *on-line* monitoring of the cross-linking reaction.

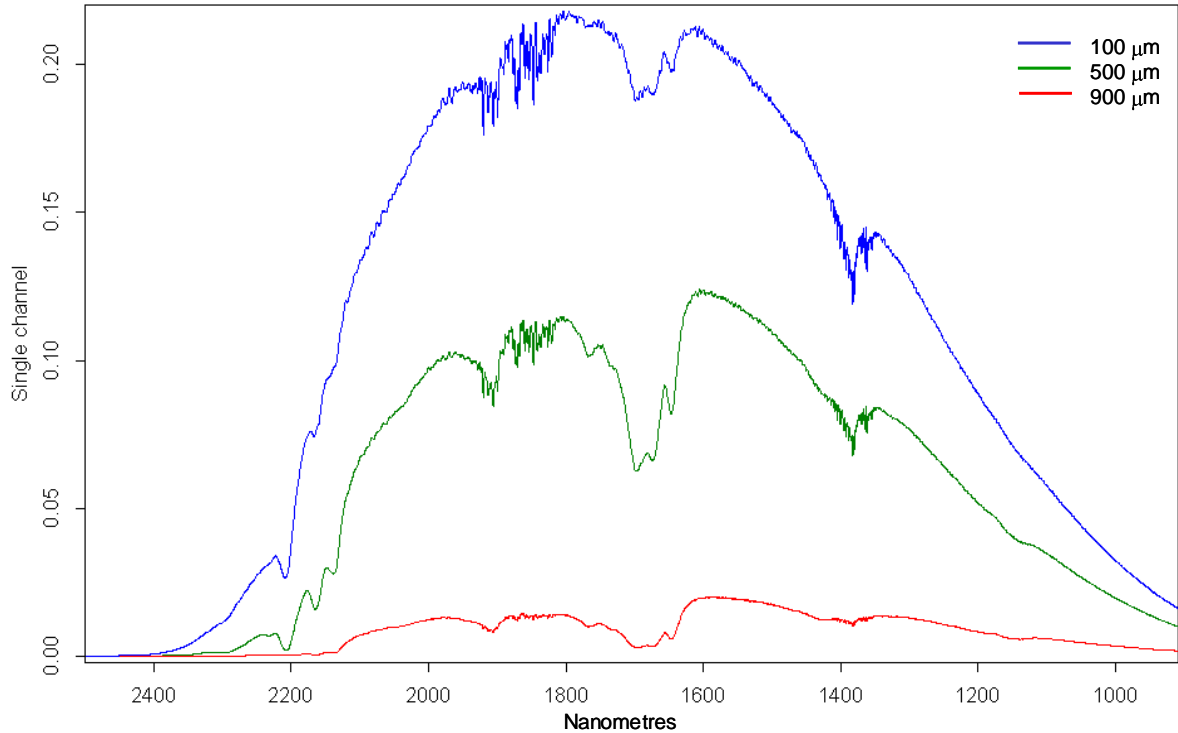


Figure 4.14 Comparison of single-channel spectra obtained for cavity lengths of 100, 500 and 900 μm using fibre-optic reflectance spectroscopy.

4.5 Conclusions

Applicability of the Beer-Lambert law was demonstrated for quantitative analysis of spectral data obtained using fibre-optic near-infrared spectroscopy. A model was developed to explain the light transmission characteristics at the sensing regions of the fibre-optic sensors using a ray-optics approach.

Different sensor designs were developed which can be used to acquire remote fibre-optic near-infrared spectroscopy. The sensor designs were evaluated in terms of reproducibility,

dimensions and ease of handling and difficulties associated with sensor fabrication techniques were discussed. The capillary support and the capillary reflector sensor designs were chosen for *in situ* monitoring of cross-linking reaction in the LY3505/XB3403 epoxy resin system.

Peak area of the absorption band at 2207 nm obtained with different path-lengths was used to determine the appropriate cavity length to obtain good spectral quality using the sensor designs investigated.

Chapter 5

Monitoring cross-linking using fibre-optic spectroscopy

5.1 Introduction

The chapter discusses in detail the use of fibre-optic near-infrared spectroscopy for *in situ* monitoring of the cross-linking reactions in the LY3505/XB3403 epoxy/amine resin system.

The discussion is focused on the following:

- Identification of absorption bands related to the LY3505/XB3403 epoxy/amine resin system.
- Investigation of appropriate spectral analysis techniques for quantitative chemical analysis.

- Determination of the change in concentration of specific functional groups in the resin system as a function of cross-linking.
- Cross-linking monitoring using different fibre-optic sensor designs.
- Application of a semi-empirical kinetic model for describing the cross-linking process.

5.2 Peak assignments for the epoxy/amine resin system

The epoxy/amine resin system that was investigated in this study contains LY3505 epoxy resin and XB3403 amine-based cross-linking agent (Huntsman Advanced Materials). LY3505 resin is a mixture of diglycidyl ether of bisphenol-A (DGEBA) and diglycidyl ether of bisphenol-F (DGEBF) and XB3403 is polyoxypropylenediamine (POP), which is an aliphatic diamine.

Typical near-IR absorption spectra of the mixed resin system that were acquired before and after cross-linking at 70°C are shown in Figure 5.1. Figure 5.2 and Figure 5.3 show expanded spectral regions, 1850 – 2500 nm (Figure 5.1a) and 1000 – 1850 nm (Figure 5.1b), respectively for detailed band assignments.

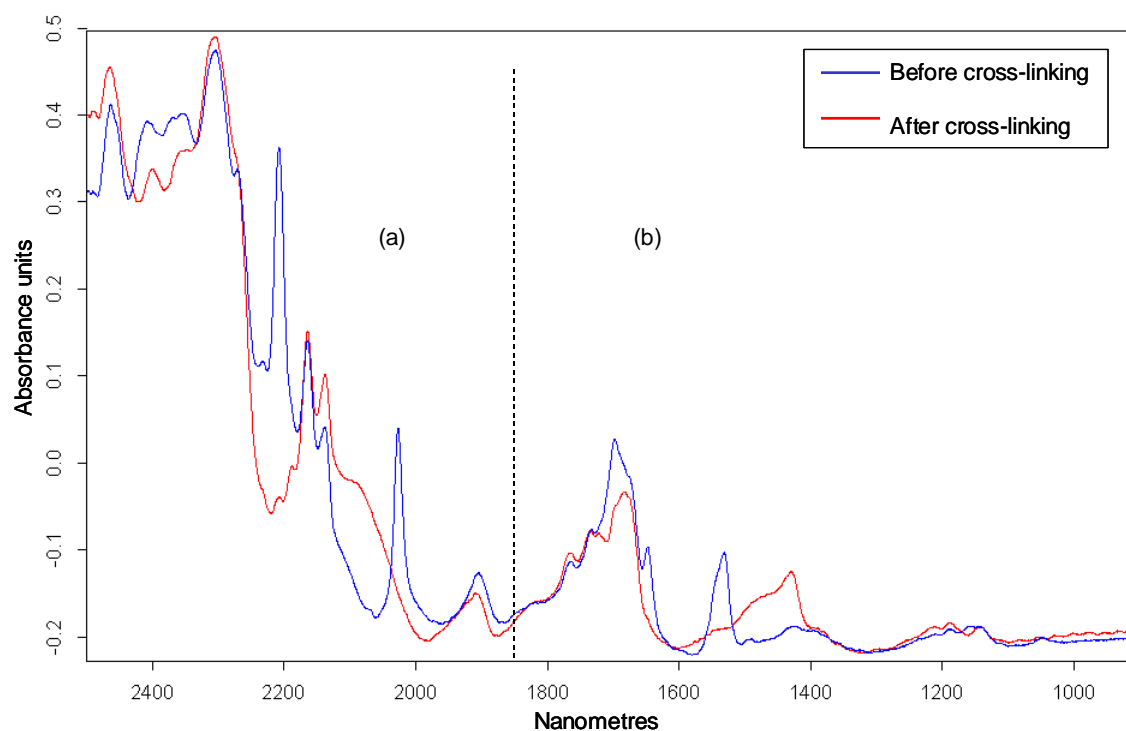


Figure 5.1 Typical Near-IR absorption spectra of the LY3505/XB3403 resin system before and after cross-linking at 70 °C for 7 hours.

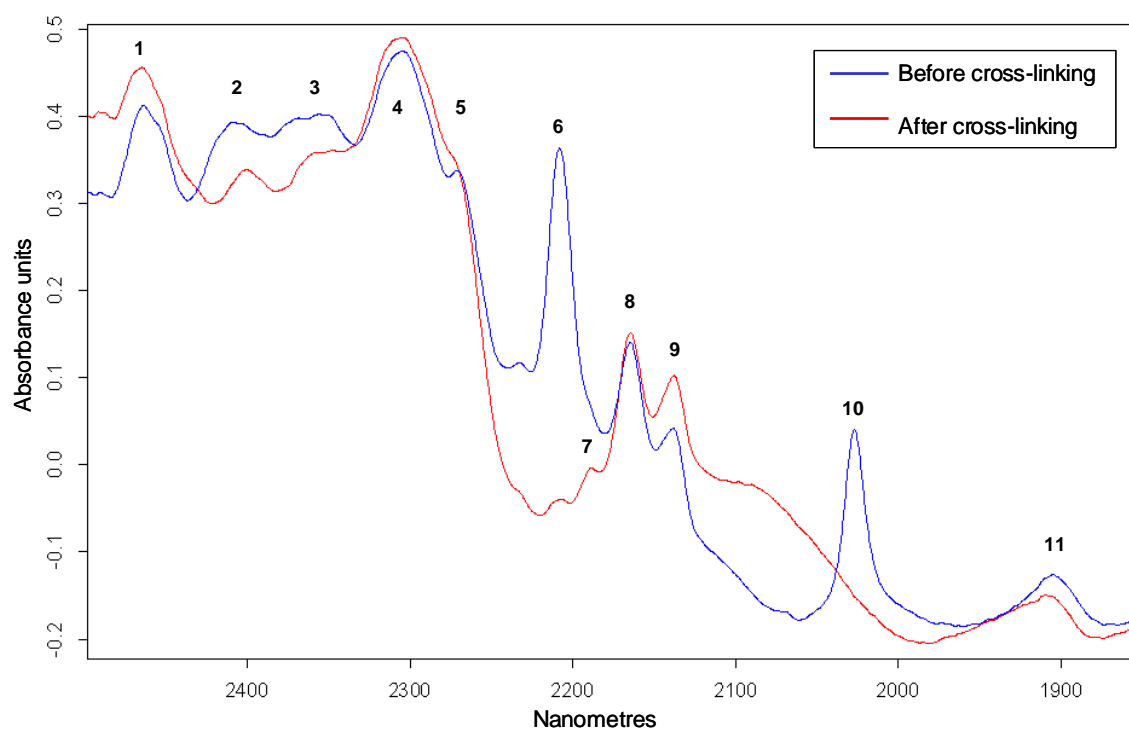


Figure 5.2 Expanded spectral range (1850-2500 nm) of the LY3505/XB3403 resin system before and after cross-linking at 70 °C for 7 hours.

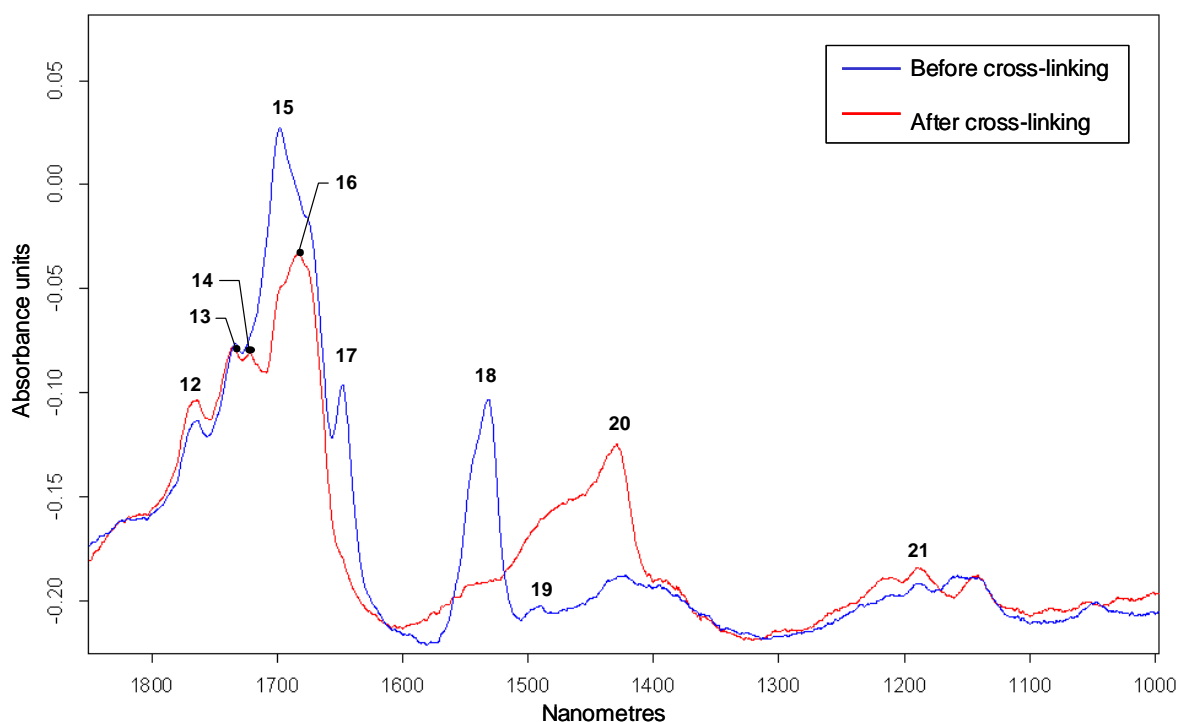


Figure 5.3 Expanded spectral range (1000 - 1850 nm) of the LY3505/XB3403 resin system before and after cross-linking at 70 °C for 7 hours.

Table 5.1 Band assignments for near-infrared spectrum of LY3505/XB3403 resin system (see Figure 5.2 and Figure 5.3) [140,136,133,138,103,131,132,147,82,47,80,135,139,137,374].

Peak identification Code	Wavelength (nm)	Peak assignment
Refer to Figure 5.2		
1	2464	Aromatic ring fundamental (-CH stretching vibration)
2	2400	Methyl fundamental (C-H symmetric bending “umbrella” vibration)
3	2358	Unknown peak
4	2304	-OH absorption/interactions of -OH with reactive groups in the resin system
5	2270	Methyl overtone (C-H symmetric bending mode)
6	2207	Epoxy combination (C-H stretching and epoxy ring breathing modes)

7	2190	Aromatic ring combination (C-H stretching fundamental of aromatic ring at 3276 nm and aromatic C=C conjugated stretching overtone at 6653 nm)
8	2164	Aromatic ring combination (C-H stretching)
9	2137	Aromatic ring combination (C-H stretching fundamental at 6154 nm)
10	2026	Primary amine combination (N-H stretching and bending modes)
11	1905	-OH due to moisture (O-H asymmetric stretching and bending modes)
Refer to Figure 5.3		
12	1764	Aliphatic, terminal R-CH ₃ overtone (stretching mode)
13	1734	Methyl 1 st overtone (C-H stretching mode)
14	1723	Methyl 3 rd overtone (C-H asymmetric bending mode)
15	1698	Combination band of epoxy and primary amine overtones
16	1683	Aliphatic terminal -CH ₃ , branched -CH ₂ and -CH (stretching modes)
17	1648	Terminal epoxy 1 st overtone (C-H stretching vibration)
18	1532	Primary and secondary amine combination (overtone of N-H stretching modes)
19	1492	Primary amine 1 st overtone (N-H asymmetric stretching mode)
20	1430	Alcoholic OH 1 st overtone (O-H symmetric stretching mode)
21	1160	Terminal epoxy 2 nd overtone (C-H stretching mode)

The absorption peaks observed for the epoxy resin and the aliphatic diamine were similar to those reported by previous researchers [103,133,136,138,140] and are summarised in Table 5.1. The wavelength range, 2200 - 2222 nm ($4500-4545\text{ cm}^{-1}$) includes combinations of C-H stretching vibrations. An absorption band due to an overtone of methyl asymmetric bending mode has been reported to be located around 2270 nm [131]. A detailed discussion of the peak assignments in this region will be presented in Section 5.2.1. With reference to Figure 5.3, the peak at 1160 nm can be assigned to the second overtone of C-H stretching of the

terminal epoxy group [132]. The first overtone of the same vibration mode appears at 2207 nm [131].

5.2.1 Analysis of absorption bands during cross-linking

Monitoring of cross-linking reaction in the LY3505/XB3403 resin system was carried out using fibre-optic sensing techniques. The cross-linking kinetics of the resin system was obtained based on both fibre-optic transmission spectroscopy [356,357,370,375] and fibre-optic reflectance spectroscopy [376].

Monitoring of the cross-linking reactions in the epoxy/amine resin system was carried out at 40, 50, 60 and 70 °C. A typical series of spectra acquired using fibre-optic transmission spectroscopy at 70 °C was used for the analysis of spectral evolution during cross-linking. However, the same spectral features were observed via fibre-optic reflectance spectroscopy. A series of typical near-IR spectra within the range of 1400-2250 nm is shown in Figure 5.4. Peak evolution of the main characteristic absorption bands of the resin system during cross-linking can be seen clearly: (i) decrease in epoxy absorptions at 1648 and 2207nm; (ii) decrease in primary and secondary amine absorptions at 1532 and 2026 nm; (iii) non-reacting aromatic ring absorptions at 2137 and 2164 nm and (iv) increase in hydroxyl absorption at 1430 nm. The spectra shown in Figure 5.4 were expanded in Figure 5.5, Figure 5.6, Figure 5.7 and Figure 5.8 will be discussed in sequence.

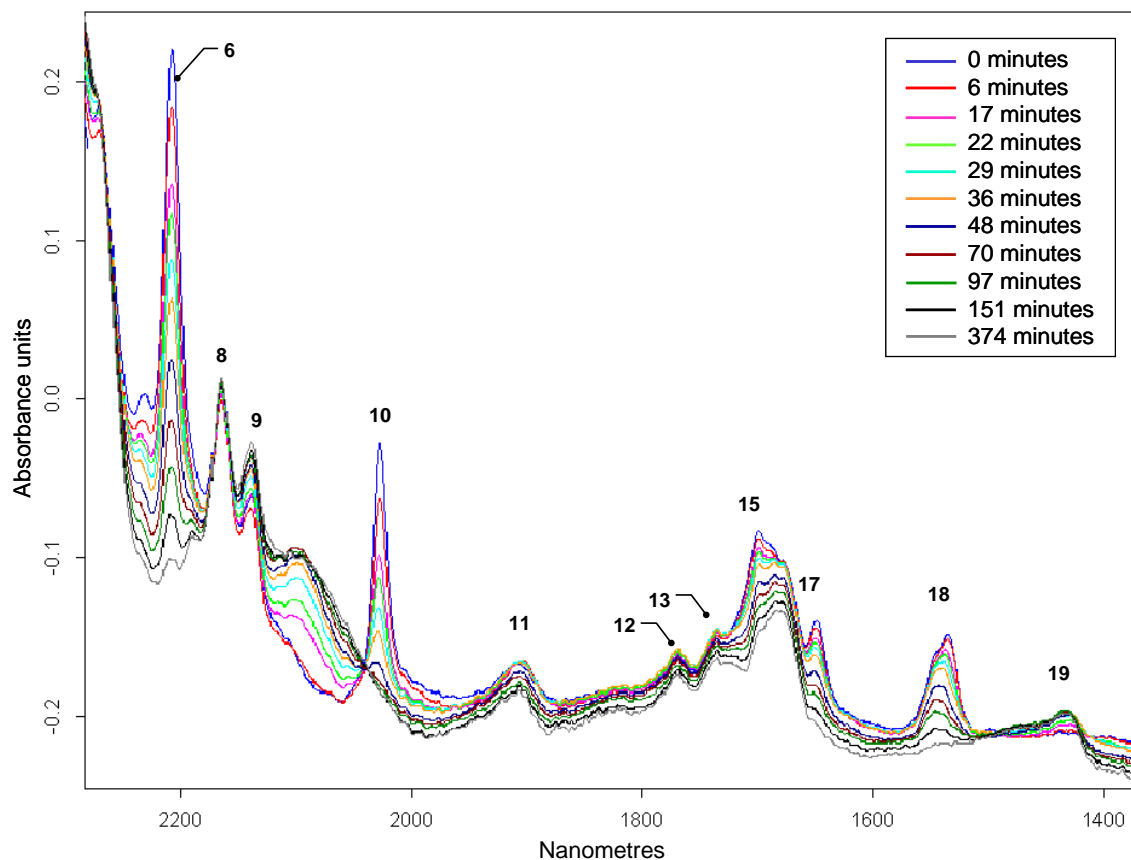


Figure 5.4 Near-IR contour spectra of LY3505/XB3403 resin system during cross-linking at 70 °C.

In Figure 5.5, the following absorption bands were observed:

- i. Absorption band at 2207 nm (Peak no. 6): Combination band due to C-H stretching and epoxy ring vibration is appeared within the range of 2180 – 2226 nm and [47,103,136,140]. This peak has been identified as a well-resolved peak in the near-IR range and has been used extensively for quantitative analysis of epoxy resin systems [132,136].

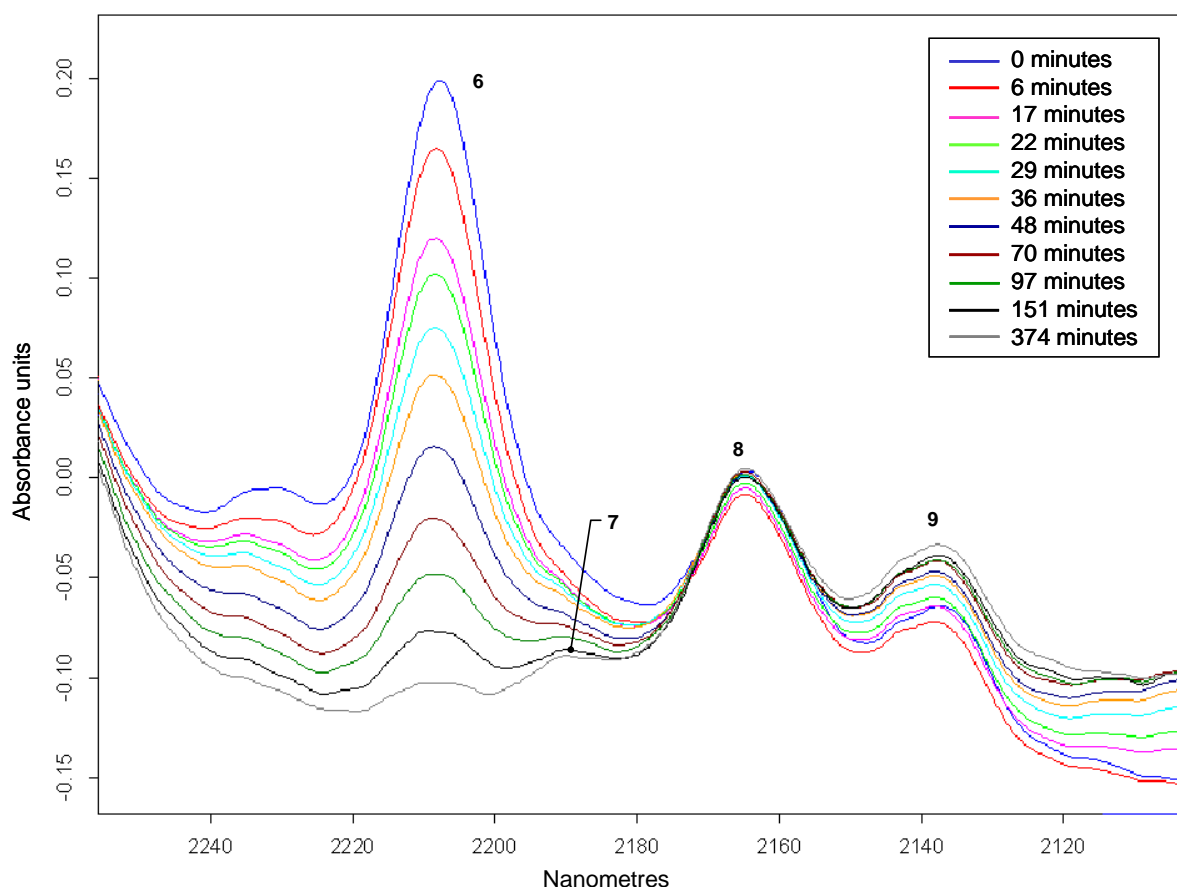


Figure 5.5 Near-IR contour spectra of LY3505/XB3403 resin system during cross-linking at 70 °C.

- ii. Absorption band at 2190 nm (Peak no. 7): It can be seen that, as the epoxy peak is consumed during cross-linking, a minor peak at 2190 nm attains more prominence as the cross-linking reaction progresses. For resin systems with aromatic amines such as DDS and DDM, an absorption band at 2194 nm (4557 cm^{-1}) has been observed due to the N-H vibration of the primary amine [103,135]. This is clearly not the case for the aliphatic amine that was used in the current study. A peak at similar wavelength was also observed with aliphatic amines but the peak assignment was not reported [131,136]. The current study, an attempt was made to identify the unknown peaks. This peak could be due to a combination band related to the aromatic C-H stretching vibration near 3278 nm and an aromatic ring stretching vibration band near 6650 nm.

Maxwell and Pethrick [134] investigated a DGEBA/TETA resin system using mid-infrared FTIR spectroscopy and reported a stretching vibration of the aromatic C=C conjugated bond at 6653 nm (1503 cm^{-1}) and a C-H stretching vibration of aromatic ring at 3276 nm (3053 cm^{-1}). For a *N,N*-diglycidyl-4-glycidyloxyaniline (DGOA) based resin system, the band assignment near 6605 nm (1514 cm^{-1}) was assigned as a stretching vibration of the aromatic ring [145]. However, the epoxy/amine resin system that was reported in the former study is more related to the LY3505/XB3403 resin system and therefore the peak appeared at 2190 nm could be due to a combination band of C-H stretching vibration of aromatic ring and aromatic C=C conjugated stretching vibration.

- iii. Absorption bands at 2164 nm (Peak no. 8) and 2137 nm (Peak no. 9): Aromatic C-H stretching combination bands also appear at 2164 nm and 2137 nm and it can be clearly seen that the peak area does not change during cross-linking.

In Figure 5.6, the following absorption bands were observed:

- iv. Absorption band at 2026 nm (Peak no. 10): This absorption band, centred at 2026 nm, is characteristic of the primary amine combination band due to N-H stretching and bending vibrations. The band was used for quantitative analysis of aliphatic amine-based resin systems [82,132].
- v. Absorption band at 1905 nm (Peak no. 11): The absorption band at 1905 nm has been assigned to O-H asymmetric stretching and bending vibrations of hydroxyl groups. It was reported that this band is not due to the alcoholic hydroxyl that is generated

during the epoxy/amine cross-linking but is a characteristic band for the hydroxyl groups due to absorbed moisture [136].

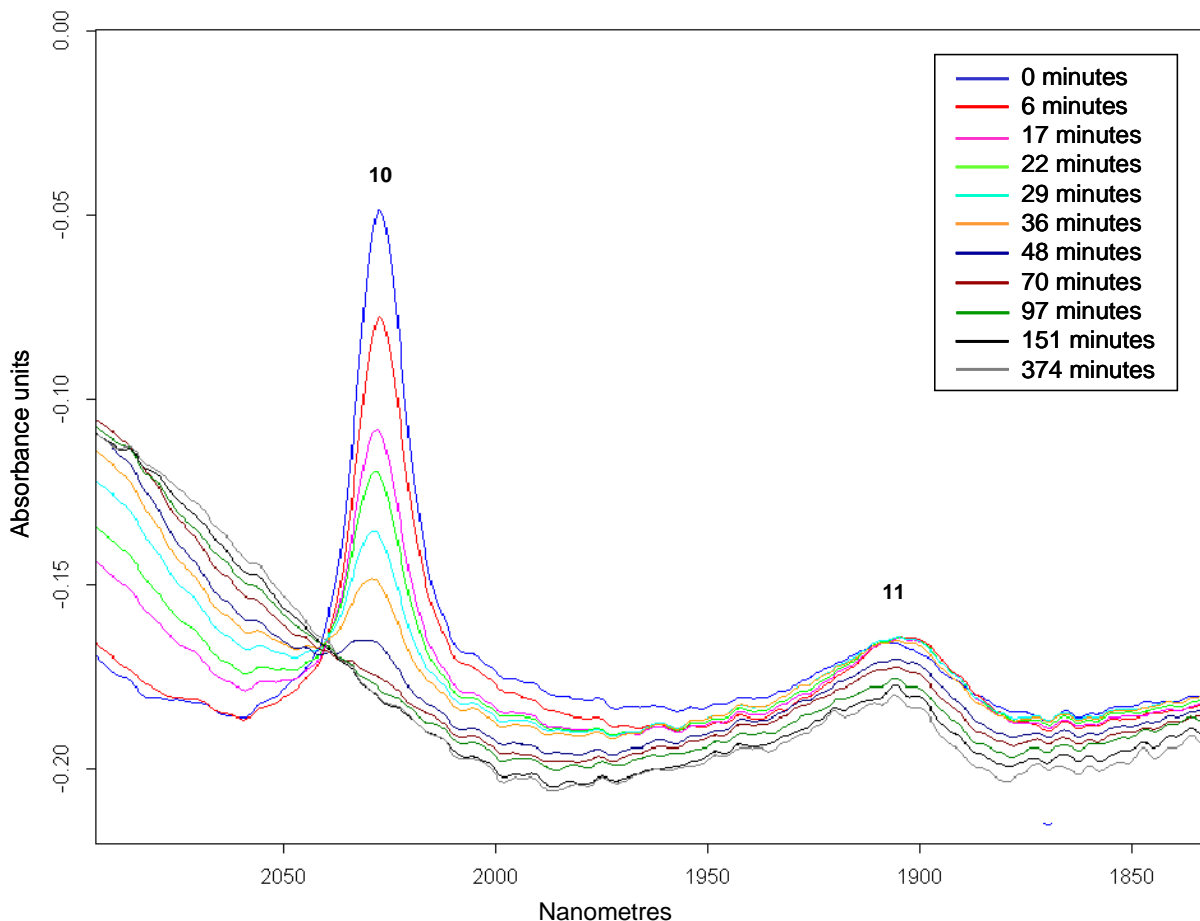


Figure 5.6 Near-IR contour spectra of the LY3505/XB3403 resin system during cross-linking at 70 °C.

In Figure 5.7, the following absorption bands were observed:

- vi. Absorption bands at 1764 nm (Peak no. 12) and 1734 nm (Peak no. 13): These peaks can be attributed to aliphatic, terminal R-CH₃ overtones and the methyl 1st overtone of the C-H stretching mode, respectively. These peak areas were found to remain constant throughout the cross-linking reaction. The third overtone of the C-H asymmetric bending vibration was suggested near 1720 nm (5814 cm⁻¹) [131].

- vii. Absorption bands at 1698 nm (Peak no. 15) and 1683 nm (Peak no. 16): With reference to the Figure 5.7, two overlapped peaks can be seen at 1698 nm and 1683 nm and the former peak decreases with respect to the second peak during cross-linking. Mijović *et al.* [136] observed similar overlapped peaks for a PEG/aniline resin system and they assigned these as an overtone of the epoxy ring at 1698 nm and an overtone of the primary amine stretching vibration at 1683 nm. However, in the current study no major changes in the peak at 1683 nm was observed during the cross-linking reaction. The peak was also assigned as stretching vibrations of aliphatic terminal -CH_3 , branched -CH_2 and branched -CH [131]. Therefore given the uncertainty over the peak assignment for the absorbance peak at 1689 nm & 1683 nm, no firm conclusion can be drawn on the origin of these overtones.
- viii. Absorption band at 1648 nm (Peak no. 17): The peak at 1648 nm is said to be associated with the first overtone of C-H stretching vibration of the terminal epoxy, and it decreases over the course of the cross-linking reaction. The original band appears approximately around 1623 nm (6158 cm^{-1}) and shifts towards the lower frequency due to the strained epoxy ring structure and the oxygen atom [131]. The peak overlapped with the other peaks and spectral manipulation is required in order to use it for quantitative analysis. Nevertheless, this peak has been used widely for determining the degree of conversion of epoxy/amine resin systems [80,147,148,152].

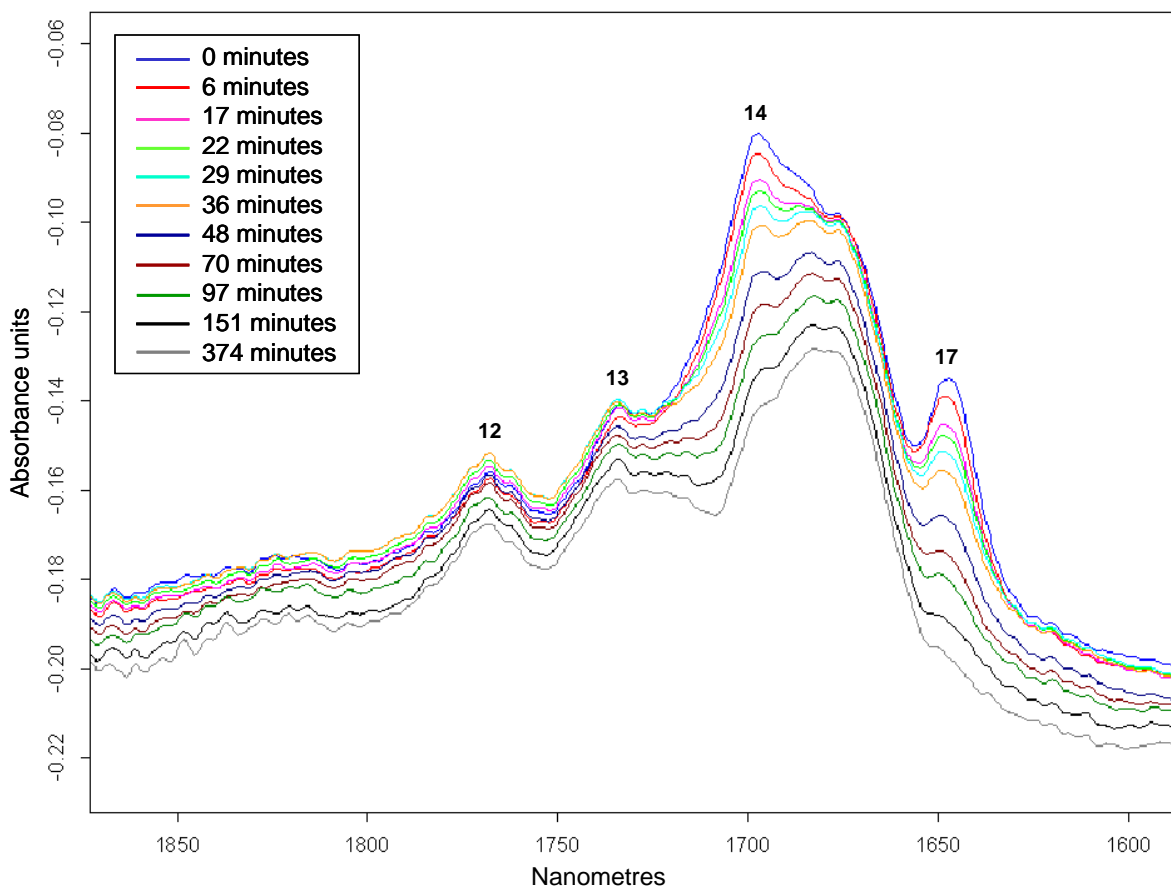


Figure 5.7 Near-IR contour spectra of LY3505/XB3403 resin system during cross-linking at 70 °C.

In Figure 5.8, the following absorption bands were observed:

- ix. Absorption band at 1532 nm (Peak no. 18): The overlapped peak in the range of 1507 – 1572 nm is related to primary and secondary amine functional groups. Therefore, the change in this peak during cross-linking is more complex. As can be seen from Figure 5.8, at the start of the cross-linking reaction, the primary amine peak appears around 1532 nm and then decreases during cross-linking. At the same time, the prominence of the peak at 1545 nm increases due to the generation of the secondary amine groups. This peak then disappears towards end of the cross-linking reaction. This can be attributed to the secondary amine consumption at the later stage of cross-linking. It is also evident from Figure 5.8 that the “clarity” of these peaks gets

significantly poorer at the later stages of the cross-linking reaction. Further research should consider techniques for addressing this issue.

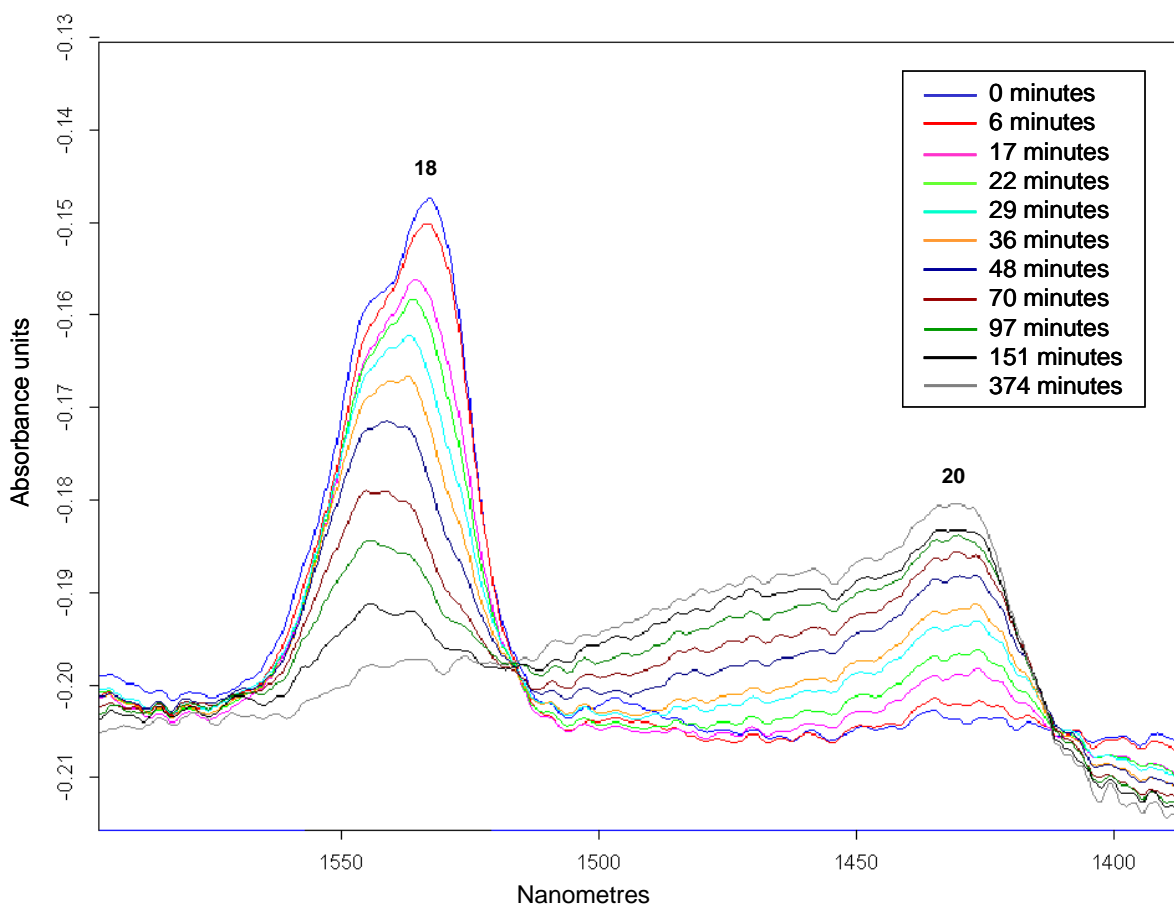


Figure 5.8 Near-IR contour spectra of LY3505/XB3403 resin system during cross-linking at 70 °C.

Absorption band at 1430 nm (Peak no. 20): The weak band that appeared around 1430 nm at the beginning of the cross-linking reaction is due to an O-H stretching vibration of the alcoholic hydroxyl groups. This peak increases as the epoxy is consumed during the reaction. Peak broadening and an upward shift with respect to the peak position before cross-linking can be seen. This feature has been related to complex and extended intramolecular and intermolecular hydrogen bonding among OH--OH groups and nucleophilic interactions between hydroxyl and nitrogen atoms, OH--N [38,47,80,103,136,147,377]. The peak was

identified as less usable for quantitative analysis due to the influence of above-mentioned spectral features.

Two discrepancies were noted in the current study. In previous works, the absorption peaks at 2400 nm and 2358 nm have been assigned as unknown peaks (see Figure 5.2) [131,136]. Nevertheless, Mijović *et al.* [136] observed a decrease in these peaks during cross-linking of PEG/*N*-methyl aniline. Workman and Weyer quoted that the peak at 2400 nm may be due to the symmetric methyl bending “umbrella” vibration in the wavelength range of 2410-2460 nm [131]. It has also been reported that there is an increase in the absorption band at 2304 nm due to the O-H groups and interactions of the O-H groups with the reactive groups in the resin mixture [133,136]. Again, with the LY3505/XB3403 resin system, no change was observed within the wavelength range during the cross-linking reaction.

The expanded views of the spectra show a repetitive fringe pattern imposed on the spectra. The fringe pattern is more apparent in the non-absorbing wavelength domain (see Figure 5.6, Figure 5.7 and Figure 5.8) and is due to a design artefact related to the fibre-optic sensors. These interference fringes can be attributed to Fabry-Pérot interference via the multiple-beam reflections at the cleaved fibre interfaces. Multiple-beam reflection of the IR radiation is possible at the sensing cavity before coupling into the receiving fibre. An attempt was made to determine the path length related to the observed interference fringe pattern. The free spectral range (FSR) and the average path length related to the interference fringe pattern were calculated to be 4 nm and $513 \pm 9 \mu\text{m}$, respectively. FSR is the wavelength separation between adjacent maxima of the interference fringe pattern. In case of fibre-optic transmission sensor design, a separation of 500 μm between the cleaved multi-mode fibres

was set using a translation stage. This shows that the manually set-gap between the cleaved fibres agrees well with the interferometrically measured gap.

5.3 Quantitative analysis of change in functional groups during cross-linking

Quantitative analysis of the functional groups of interest was carried out based on the changes in peak areas of specified absorption bands. According to the Beer-Lambert law, for low path-length and low concentrations, the peak area is linearly proportional to the concentration of the related functional group. A baseline was constructed by joining two points either side of an absorption band. The baseline was adjusted manually in order to account for any peak shifts during the cross-linking process. In order to eliminate effects related to the change in path-length during cross-linking, the peak area of a non-reacting functional group was used to normalise the peak area of the reactive functional group. The peak at 2164 nm is due to an aromatic C-H stretching vibration and since it does not take part in the cross-linking reaction. This can be seen from Figure 5.9, where the change in epoxy peak area at 2207 nm and that of the aromatic CH peak at 2164 nm is plotted as a function of time for the cross-linking of the epoxy/amine resin system at 70 °C. Therefore this peak at 2164 nm was selected as an internal reference for normalising the peak area of other functional groups [357,370,375,378]. The following absorption bands were analysed for interpreting the cross-linking kinetics of the LY3505/XB3403 resin system:

- (i) Epoxy peak (2180 - 2226 nm);
- (ii) Primary amine peak (1964 - 2060 nm); and

(iii) Combination band of primary and secondary amine peak (1507 – 1572 nm)

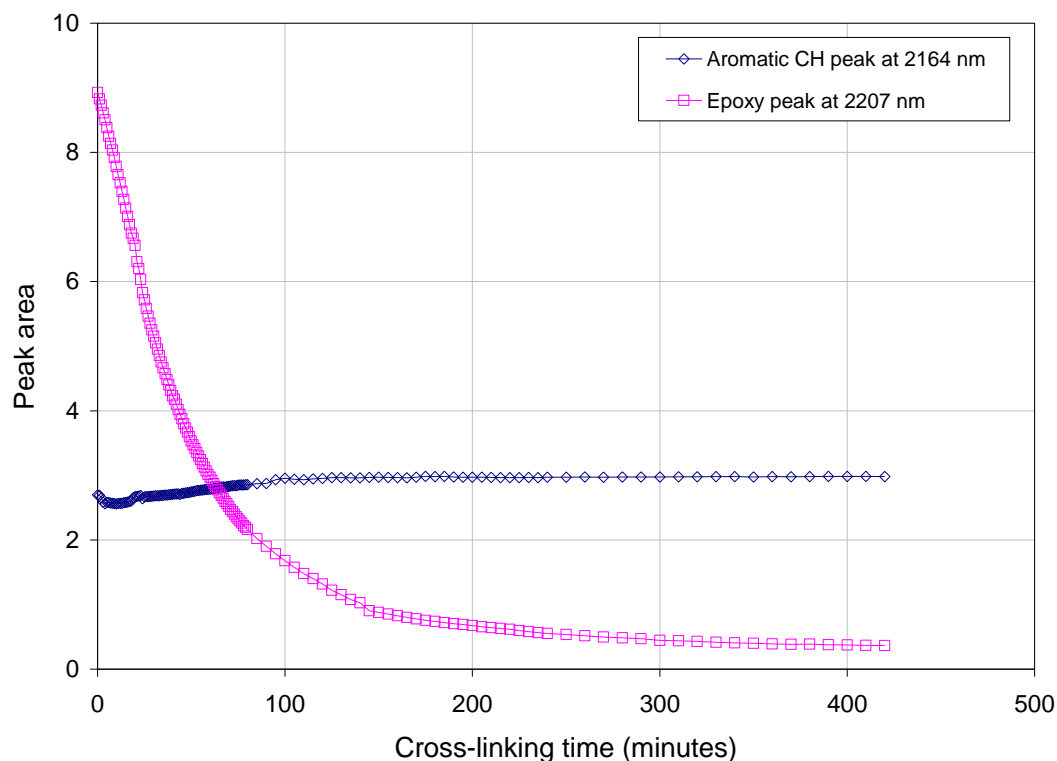


Figure 5.9 Change in peak area of epoxy peak (2207 nm) and aromatic C-H peak (2164 nm) for the LY3505/XB3403 resin system during cross-linking at 70 °C.

5.3.1 Deconvolution of the epoxy absorption band

It was mentioned before that the epoxy absorption peak is overlapped with a weak combination band at 2190 nm, which is related to aromatic ring vibrations (see Section 5.2.1). Previous researchers have used data processing techniques to investigate and isolate the epoxy peak [131,136,149]. In the current study, three different approaches were deployed to investigate the most suitable method to account for “hidden” absorption band at 2190 nm, and to determine the change in concentration of the epoxy groups during cross-linking. A series of spectra was obtained for the LY3505/XB3403 resin system that was cross-linked at 50 °C for 15 hours. The spectra were recorded using capillary support sensor design.

Method-I: determination of epoxy peak area using the total (overlapped) peak area

Figure 5.10 shows a typical set of original near-IR spectra obtained during cross-linking at 50 °C. A baseline was constructed such that the peak area covered the epoxy and the hidden peaks throughout the reaction. Figure 5.11 highlights the calculated peak area before and after cross-linking. Shaded areas in Figure 5.11 represent the peak area based on the baseline as defined. The calculated peak area represents the contributions from both the epoxy peak and hidden peak.

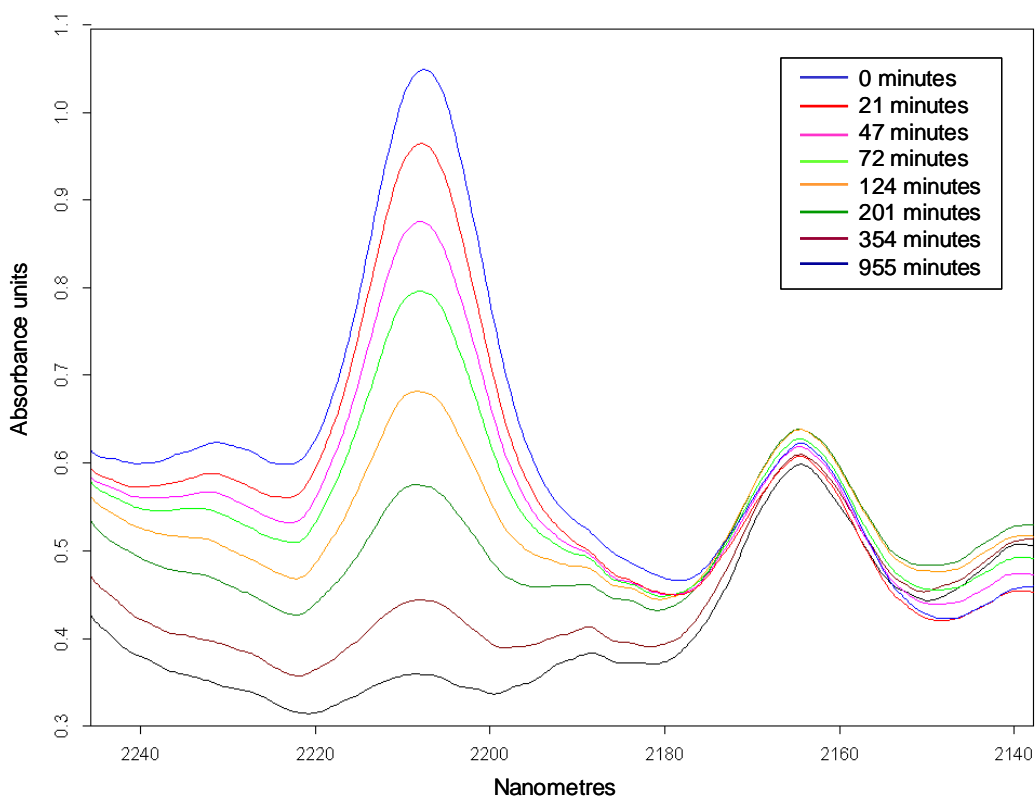


Figure 5.10 Original near-IR contour spectra of the LY3505/XB3403 resin system during cross-linking at 50 °C.

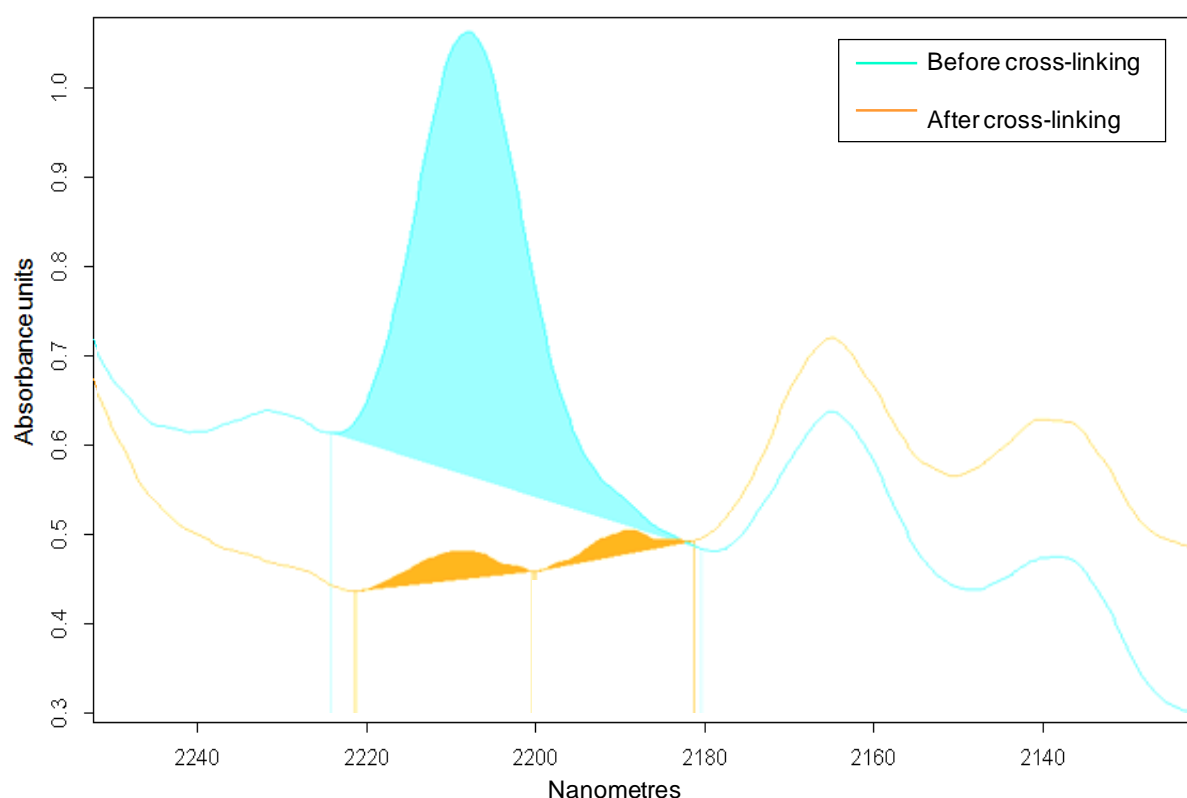


Figure 5.11 Original near-IR spectra of the LY3505/XB3403 resin system before and after cross-linking at 50 °C. The peak areas were calculated according to the *Method-I* are highlighted.

Method-II: determination of epoxy peak area by eliminating hidden peak

The baseline of the epoxy peak was adjusted in order to eliminate the interference of the hidden peak. In this method, defining the baseline at the beginning of the cross-linking reaction was difficult as the contribution from the epoxy peak is higher compared with that of the hidden peak. Therefore it was difficult to define the boundaries of the baseline during early stage of cross-linking. Nevertheless, a shoulder, which appeared due to the overlapping of the hidden peak was taken as one boundary for the baseline. However, the accuracy of this method cannot be guaranteed because determination of the baseline with high accuracy was difficult. Therefore the errors involved in calculating the epoxy peak area based on Method-II can be higher compared with that of Method-I. The shaded areas in Figure 5.12 show the

calculated epoxy peak area corresponding to the spectra obtained before and after cross-linking based on Method-II.

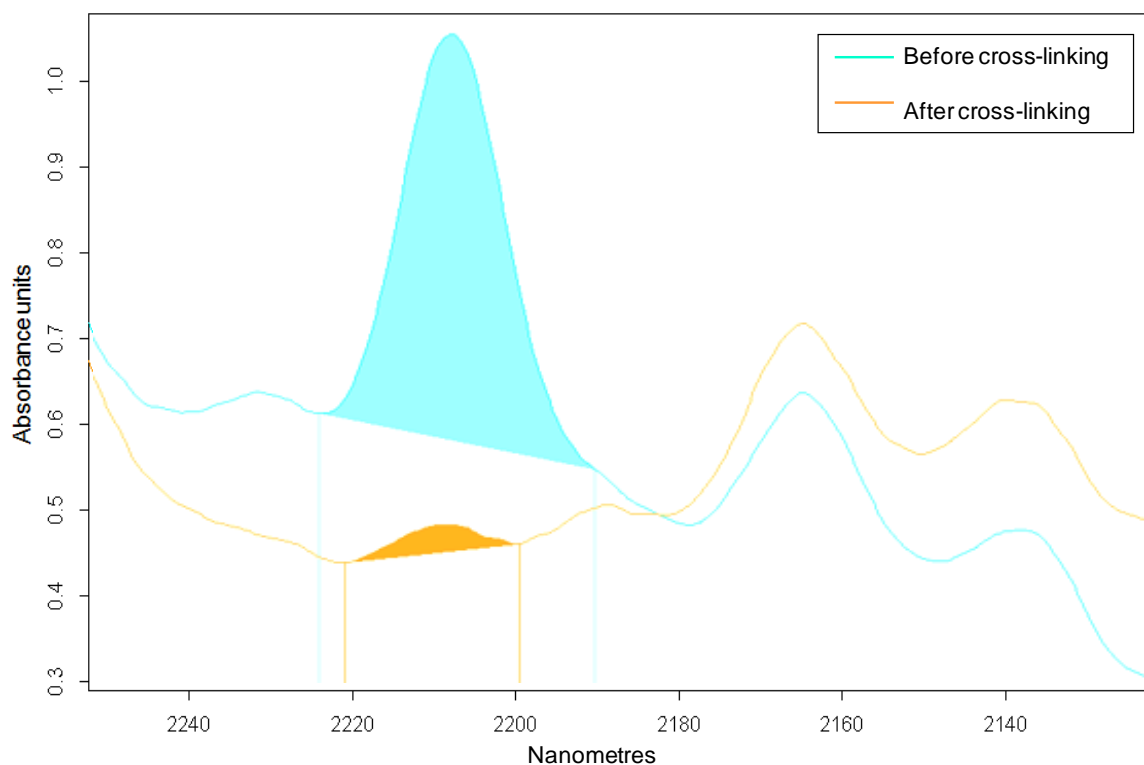


Figure 5.12 Original near-IR spectra of the LY3505/XB3403 resin system before and after cross-linking at 50 °C. The calculated peak areas according to *Method-II* are highlighted.

Method-III: Fourier self-deconvolution – determination of epoxy peak area by subtracting the hidden peak area

In this method, A Fourier self-deconvolution was used to resolve the hidden peak from the overlapped epoxy peak. The method gives an insight into the evolution of the hidden peak during the cross-linking reaction. Deconvolution is the process of enhancing spectral bandwidth in order to resolve overlapping bands. It is necessary to note that instrumental resolution is not increased by spectral deconvolution. Instead, Fourier self-deconvolution involves multiplication of the original interferogram by using a smoothing function and also using a function consists of Gaussian, Lorentzian or Gaussian-Lorentzian band shape [120].

In other words, the technique mathematically enhances the peak resolution. However peak shapes and peak areas are altered during the spectral manipulation using Fourier self-deconvolution.

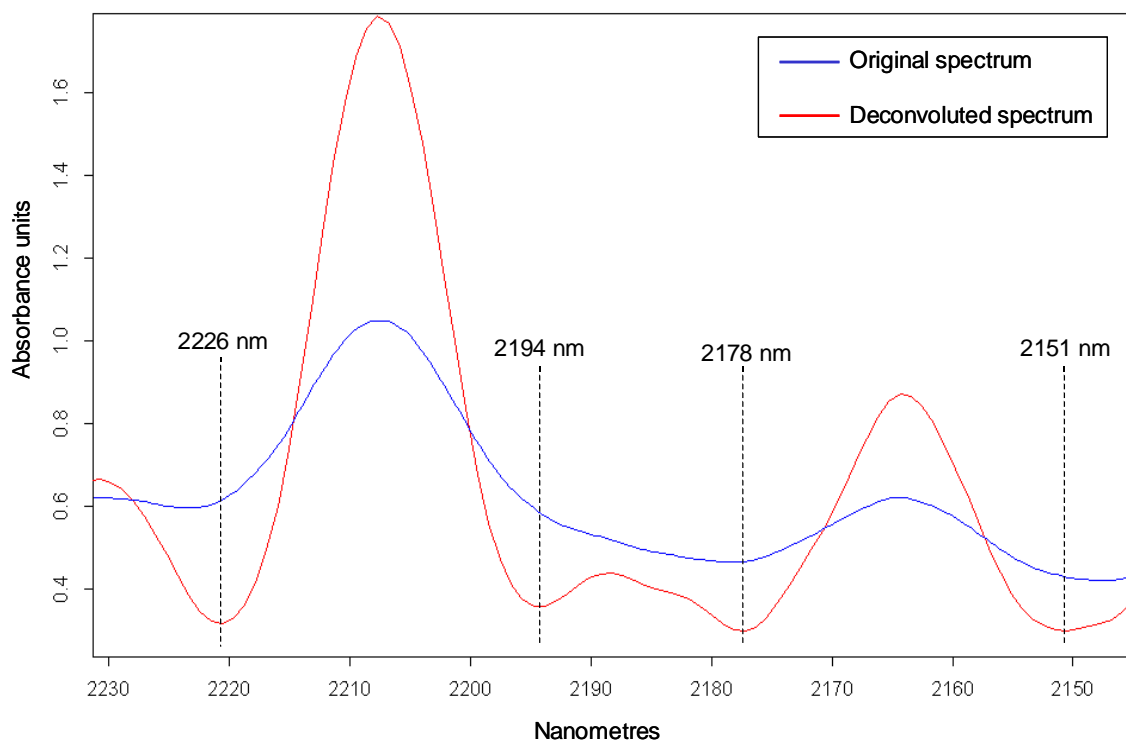


Figure 5.13 An original near-IR spectrum and corresponding deconvoluted spectrum of the LY3505/XB3403 resin system before cross-linking. Baseline wavelengths of the deconvoluted peaks are highlighted; (i) epoxy peak 2194 – 2226 nm; (ii) hidden peak 2178 – 2194 nm and (iii) aromatic reference peak 2151 – 2178 nm.

Bruker OPUS 6.5 software (Bruker Optics, UK) was used for Fourier self-deconvolution of the original spectra. The software allowed three variables to be specified: a function of the line shapes, the noise reduction factor (NRF), and the deconvolution factor (DF). For the current analysis, a Lorentzian line shape function was used. NRF is a function of resolution enhancement and bandwidth of the peak to be deconvoluted. Therefore NRF was taken as 0.5 for spectral deconvolution to retain and enhance the weak and narrow absorption bands.

Figure 5.13 compares the spectral line shape of an original spectrum of the LY3505/XB3403 resin system before cross-linking with a deconvoluted spectrum of the original interferogram. It can be seen that after deconvolution, the baseline of the hidden peak can be clearly defined more clearly.

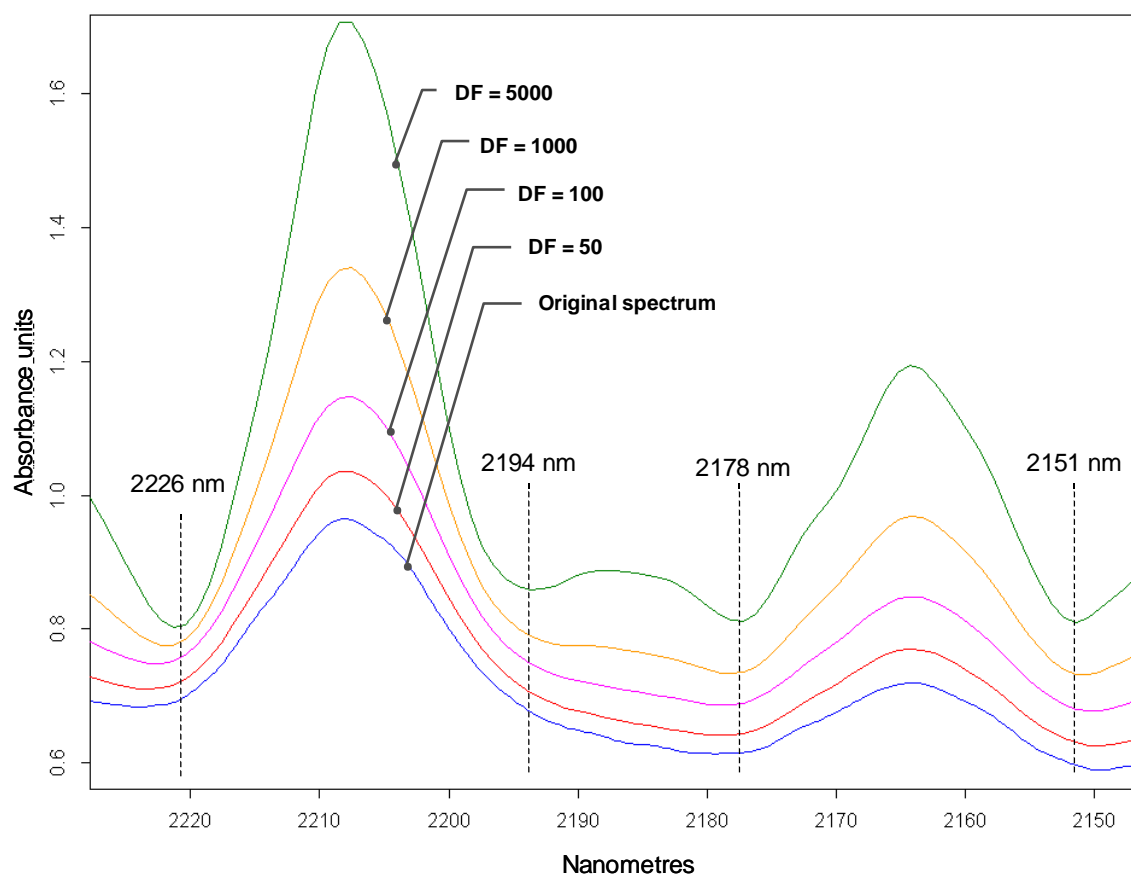


Figure 5.14 An original near-IR spectrum and deconvoluted spectra of the LY3505/XB3403 resin system before cross-linking. Baseline wavelengths of the deconvoluted peaks are highlighted.

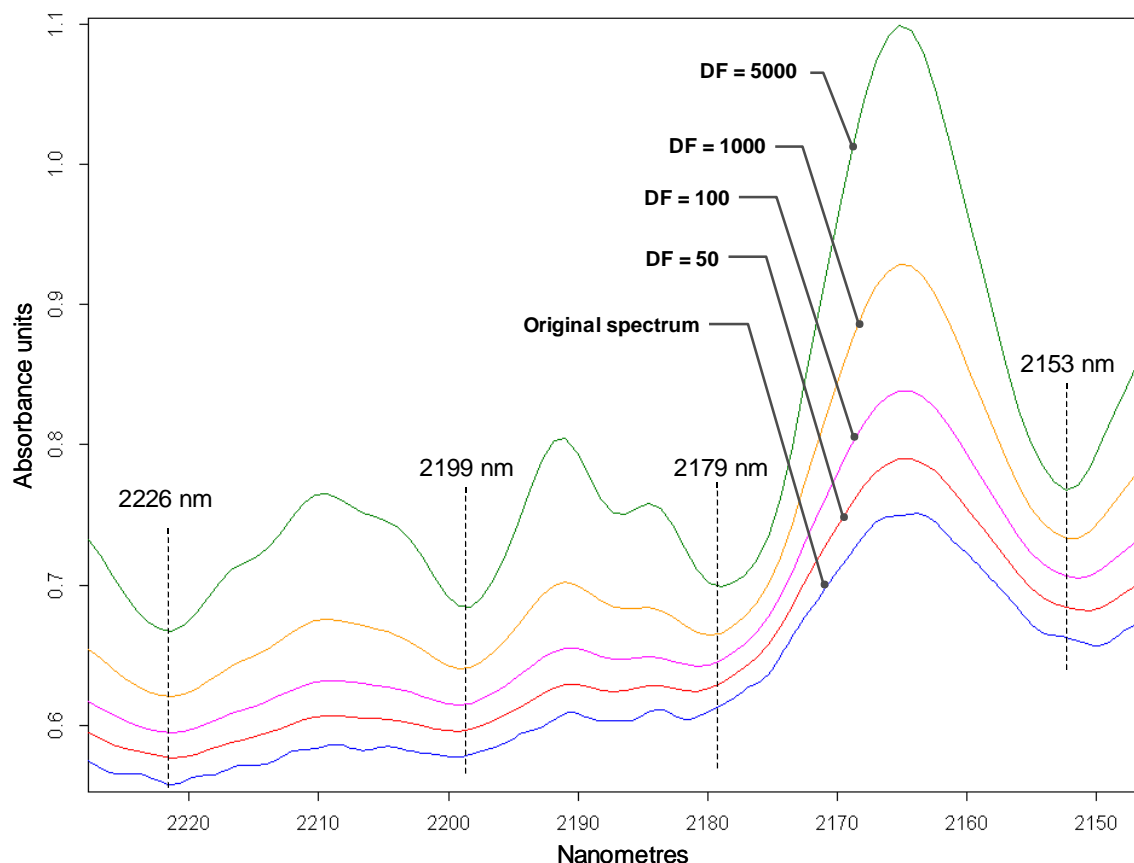


Figure 5.15 An original near-IR spectrum and deconvoluted spectra of the LY3505/XB3403 resin system after cross-linking at 50 °C; the relative position of the baseline wavelengths selected for the deconvoluted peaks are highlighted.

DF is a function of bandwidth and the relationship varies according to the line-shape. DF determines the extent of deconvolution. If DF is too low, the spectral enhancement is low. When DF is too high, artefacts due to the line shape function reduce the resolution of the peak. The distortion of absorption bands is higher with a higher DF, especially when the overlapped original bands are very weak compared with other peaks in the region. This can be clearly seen from Figure 5.14 and Figure 5.15. As shown in Figure 5.14, before cross-linking, the hidden band is less apparent. Therefore, a higher DF was needed to enhance the peak resolution. As the cross-linking reaction approaches completion, the epoxy peak area decreases and the hidden peak becomes more apparent. In this case, choosing a higher DF

distorts the peak shape as shown in Figure 5.15. Therefore a trial-and-error method was used to select the most appropriate DF to analyse the spectra. Figure 5.16 shows a series of deconvoluted spectra for the LY3503/XB3403 resin system during cross-linking at 50 °C for 15 hours. The Lorentzian line shape was used with NRF of 0.5. In order to get adequate peak resolution, the spectral deconvolution was carried out in three consecutive steps. Firstly the raw absorption spectrum was deconvoluted using a DF of 50 and the resulting spectrum was subsequently subjected to a deconvolution at a DF of 100. The result of the second deconvolution was deconvoluted again using a DF of 1000.

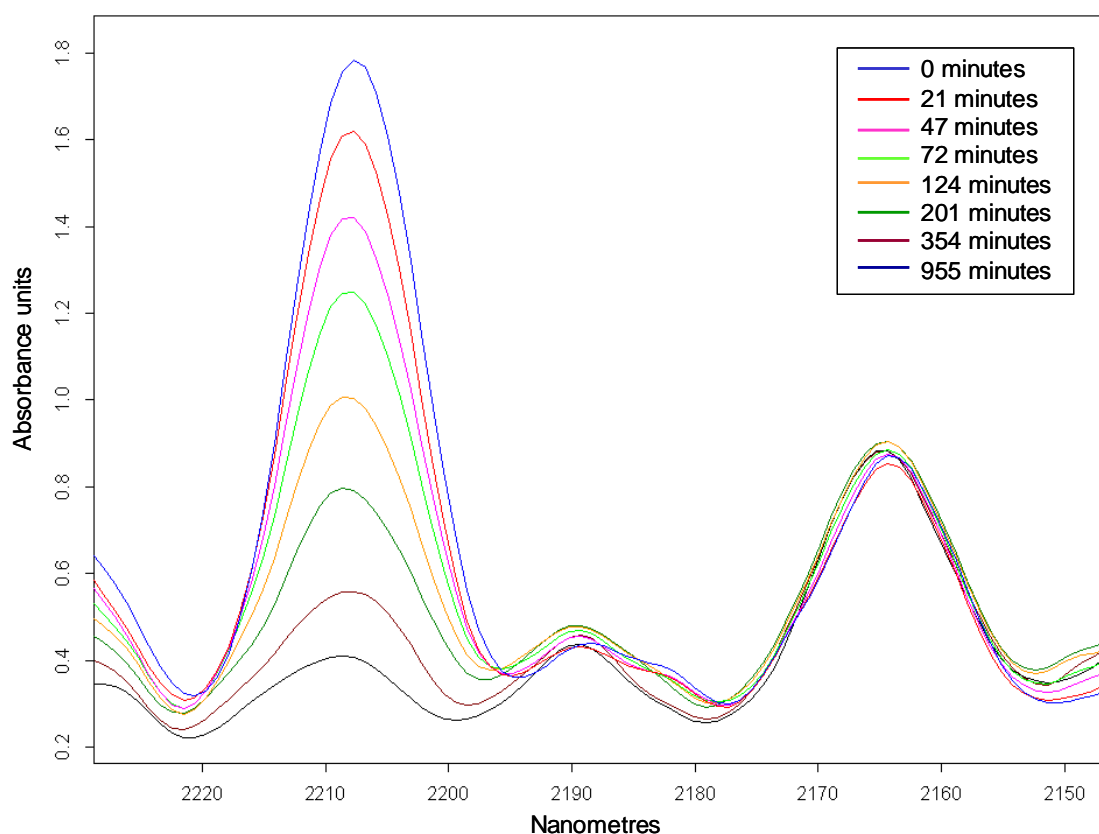


Figure 5.16 Deconvoluted near-IR contour spectra of the LY3505/XB3403 resin system during cross-linking at 50 °C; DF was used up to 1000.

Figure 5.17 shows the change in the peak area of the deconvoluted absorption bands during cross-linking. With reference to Figure 5.17, no remarkable change in the hidden peak area was observed when compared with the change in epoxy peak area.

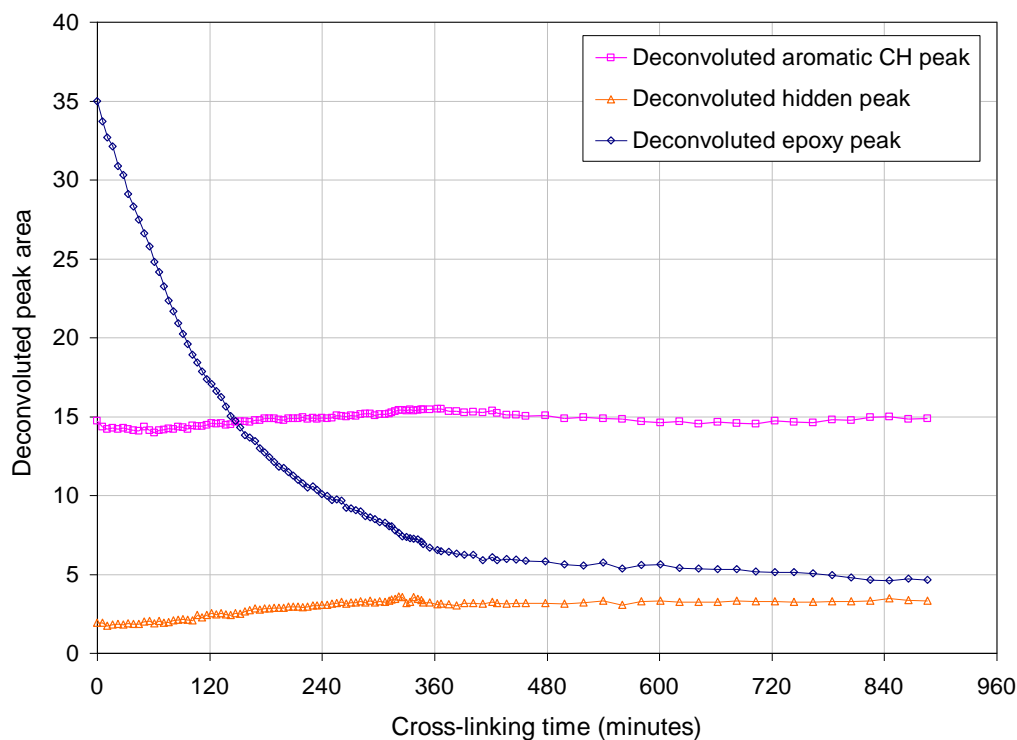


Figure 5.17 Change in deconvoluted peak area of epoxy peak (2207 nm), hidden peak (2190 nm) and aromatic C-H peak (2164 nm) of the LY3505/XB3403 resin system during cross-linking at 50 °C.

However, spectral deconvolution was found to be inconvenient for quantitative spectral analysis as data processing required different DFs to achieve optimum spectral enhancement. Therefore the aim of using this technique was to determine the trend in the evolution of the hidden peak during cross-linking.

As shown previously in Figure 5.10, the hidden band starts to appear after about 200 minutes during cross-linking at 50 °C. Therefore as soon as the hidden peak appeared as a separate band, the area under this band was recorded separately. In order to determine only the epoxy

peak contribution, the hidden peak area was subtracted from the total peak area of the whole set of spectra.

Comparison of spectral analysis techniques

In this case, the isothermal cure at 50 °C was repeated three times and the average and standard deviation of instantaneous epoxy peak area was obtained by employing each method. In these methods, the error involved in determining the epoxy peak area was mainly due to the accuracy of defining the boundaries of the baseline of the epoxy peak. This was due to the fact that during the initial stage of reaction the apparent epoxy peak is an overlapped absorption band that represents the ‘true’ epoxy peak and a weak hidden peak. During cross-linking, the hidden peak area remained fairly constant over the entire period of reaction and was found to have an average of 0.455 ± 0.008 . The overlapped epoxy peak area, which includes that of the hidden peak, evolves as the cure progresses and decreases with the reaction time. In other words, the depletion of epoxy towards the end of the reaction manifests as if the relative contribution of the hidden peak is higher at the end of the reaction (~40 %) in comparison to that at the start of the reaction (~2 %). Nevertheless, the contribution of the hidden peak area is constant through out the reaction.

Figure 5.18 shows the change in original peak area related to the epoxy groups during cross-linking of the LY3505/XB3403 resin system at 50°C based on Method-I and -II. The change in peak area related to the aromatic C-H absorption band and the hidden absorption band were also cross-plotted as a function of cross-linking time.

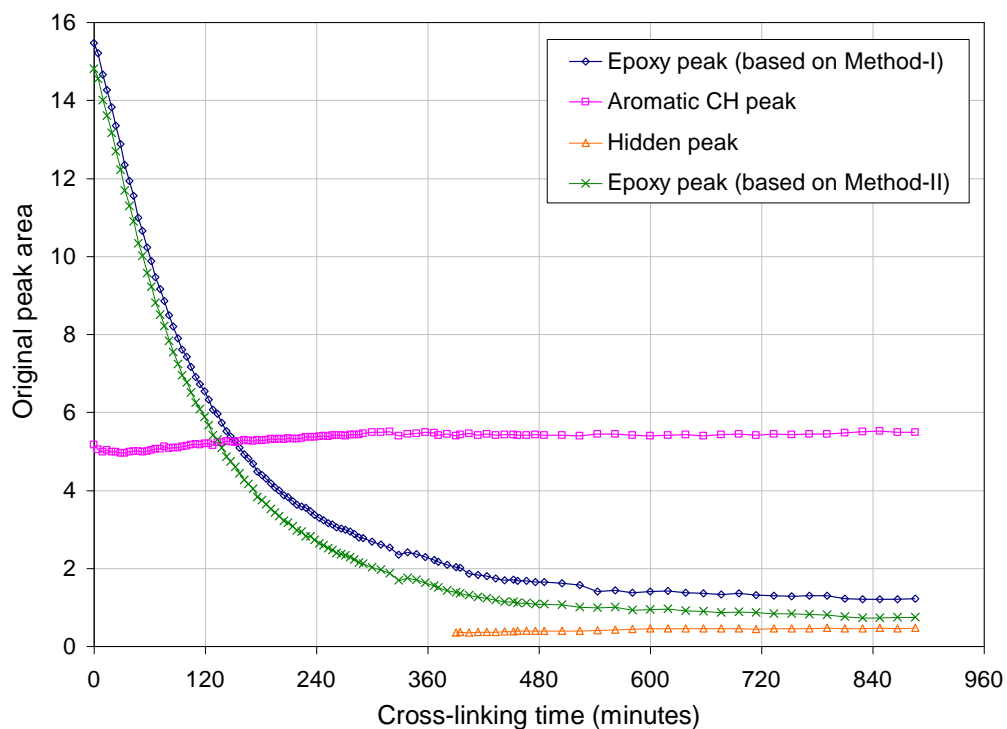


Figure 5.18 Change in original peak area of epoxy peak (2207 nm), hidden peak (2190 nm) and aromatic C-H peak (2164 nm) of the LY3505/XB3403 resin system during cross-linking at 50 °C.

It can be seen that the epoxy peak area calculated using Method-I shows higher residual epoxy groups throughout the cross-linking reaction compared with that calculated based on Method-II. The reason for the difference is that, in Method-I the total overlapped peak area was considered that accounts area of both epoxy and hidden peaks. But based on Method-II, at the later stage of reaction, the baseline of the resolved epoxy peak can be clearly defined and hence the epoxy peak area can be calculated more accurately.

Furthermore, it was observed based on Method-III that the hidden peak behaved similarly to that of the aromatic C-H peak (reference peak), which appeared around 2164 nm. Therefore it can be concluded that the peak assignment made for the hidden peak is more appropriate and the peak appearing around 2190 nm could be a combination band of C-H stretching vibration

of aromatic ring (3276 nm) and aromatic C=C conjugated stretching vibration (6653 nm). Good correlation was found between the spectral evolution of original and deconvoluted peak areas related to the aromatic C-H peak and the hidden peak (see Figure 5.17 and Figure 5.18). Therefore it was assumed that the contribution of the hidden peak towards the overlapped peak area approximately remains constant compared with that of the epoxy peak during cross-linking. The mean peak area of the hidden band was calculated considering the linear region with respect to cross-linking time. The epoxy peak area was then determined by subtracting the mean peak area of the hidden band from the total overlapped peak area.

Figure 5.19 compares the change in normalised epoxy peak area based on three different techniques as a function of cross-linking time. The epoxy peak area was normalised to the area of the aromatic C-H reference peak. As mentioned above, again the area based on Method-I shows a higher peak area compared with Method-II and -III. During the early stages of cross-linking, the area based on Method-II shows lower values compared with that obtained using Method-III while the areas based on both techniques overlapped during later stages of the reaction. This can be attributed to the over-estimation of the baseline of the absorption peak in Method-II. Based on these observations, Method-III was identified as the most suitable technique for determining the change in epoxy peak area of the LY3505/XB3403 resin system during cross-linking.

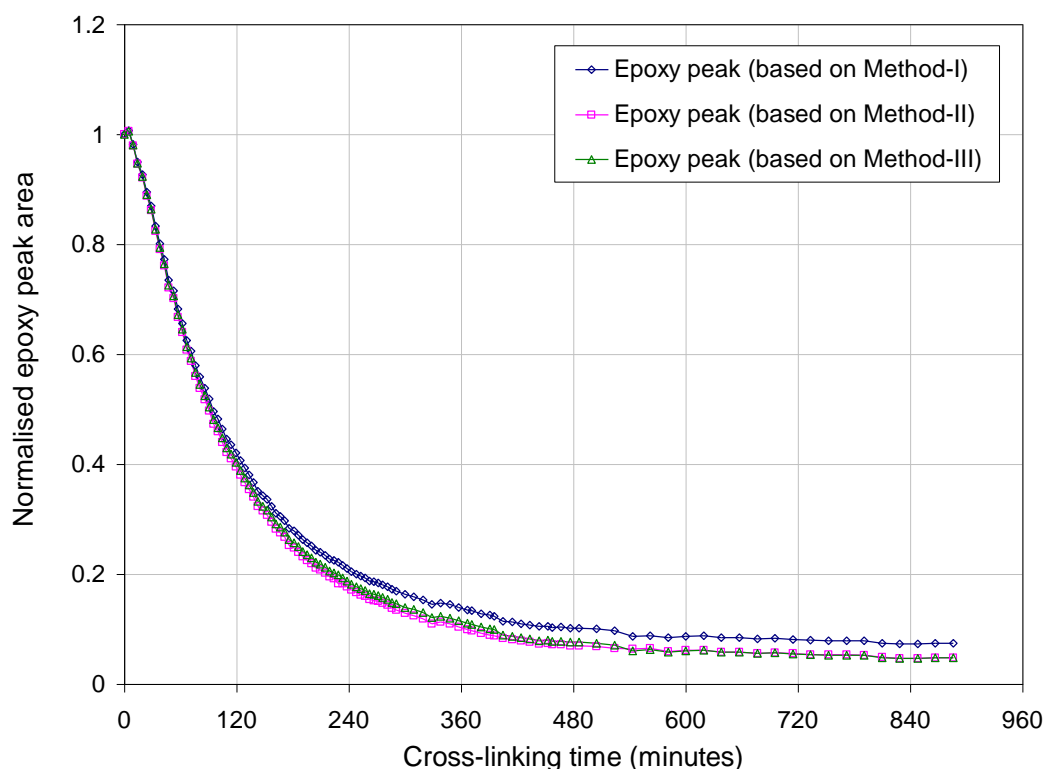


Figure 5.19 Change in the normalised epoxy peak area of the LY3505/XB3403 resin system during cross-linking at 50 °C. Peak area based on three spectral analysis methods is compared.

With reference to Figure 5.20, the standard deviation of the instantaneous peak area with in the first 300 minutes of cure was found to be the largest in the case of Method-II, whilst the Method-III yielded smallest deviation of instantaneous peak area through out the reaction. The average peak areas obtained at the end of the reaction using the Methods -II and -III were found to be equal. The measurement of peak areas using the Methods -II and -III is more accurate in comparison to the Method-I because they account for the hidden peak area. As the epoxy and the hidden peaks are distinctly visible at the end of the cross-linking reaction, the average values of the corresponding epoxy peak area measured using the Methods -II and -III represent the true nature of the completion of the reaction. The smallest standard deviation observed with the method-III was thought to be the correct method to be employed. The

advantages and disadvantages associated with using each method for determining the epoxy peak area are summarised in Table 5.2.

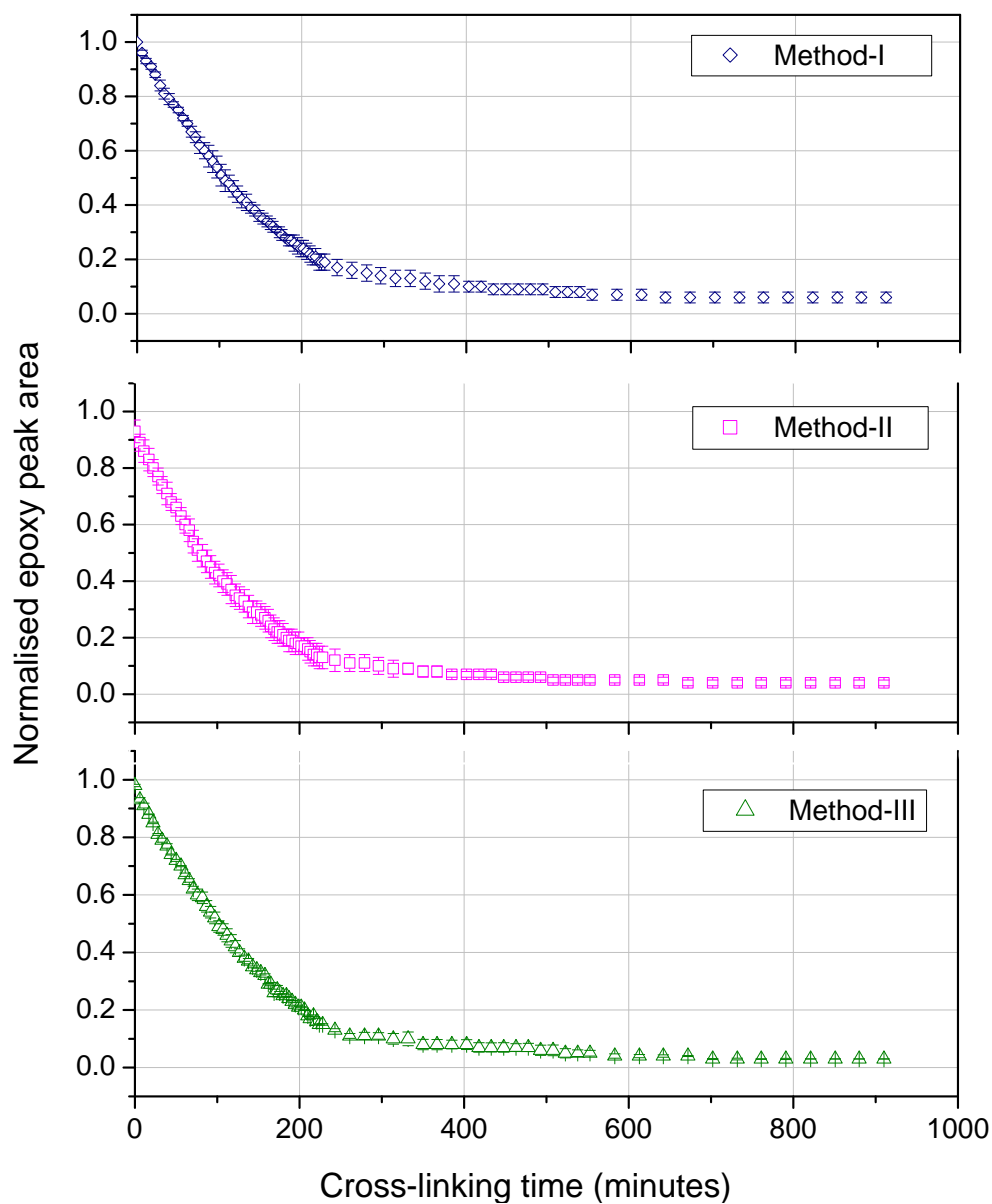


Figure 5.20 Standard deviation of peak area based on each method discussed above as a function of reaction time.

Table 5.2 Advantages and disadvantages of different methods.

Method used	Comments
Method-I	<p><i>Advantages:</i></p> <ul style="list-style-type: none"> • Lower error involved in defining boundaries of the baseline for the epoxy peak. • Reasonable reproducibility of calculating the peak area. <p><i>Disadvantages:</i></p> <ul style="list-style-type: none"> • The peak area includes the area of hidden peak and hence shows a higher amount of residual epoxy compared with the actual residual epoxy content present in the system towards the end of the reaction.
Method-II	<p><i>Advantages:</i></p> <ul style="list-style-type: none"> • The peak area is closer to the expected area of the epoxy peak. <p><i>Disadvantages:</i></p> <ul style="list-style-type: none"> • Higher error involved in defining baseline of the epoxy peak during early stages of cross-linking.
Method-III	<p><i>Advantages:</i></p> <ul style="list-style-type: none"> • Good reproducibility of calculating the peak area throughout the reaction. • Calculated peak area is closer to the expected area of the epoxy peak.

5.3.2 Quantitative analysis of functional groups using fibre-optic transmission spectroscopy

5.3.2.1 Epoxy group analysis

The change in epoxy concentration during cross-linking was calculated based on the combination band due to the epoxy ring at 2207 nm using the equation below:

$$EP_t = EP_0 \left(\frac{\left(\frac{A_{EP}}{A_{CH}} \right)_t}{\left(\frac{A_{EP}}{A_{CH}} \right)_0} \right) \quad \text{Equation 5.1}$$

where $[EP]$ is the concentration of epoxy, A_{EP} is the epoxy peak area and A_{CH} is the peak area of aromatic reference band. Subscripts 0 and t represent the start of reaction and time t , respectively. The epoxy peak area was calculated by subtracting the mean peak area of the hidden peak using methods-III as described in Section 5.3.1. The mean concentration of the epoxy groups, in a stoichiometric mixture of the LY3505/XB3403 resin system before cross-linking, was calculated to be $2.0301 \pm 0.0043 \text{ mol kg}^{-1}$. Figure 5.21 shows the change in epoxy concentration at 70°C as a function of cross-linking time. The peak areas calculated for three repeat experiments are shown and good repeatability of the results can be seen.

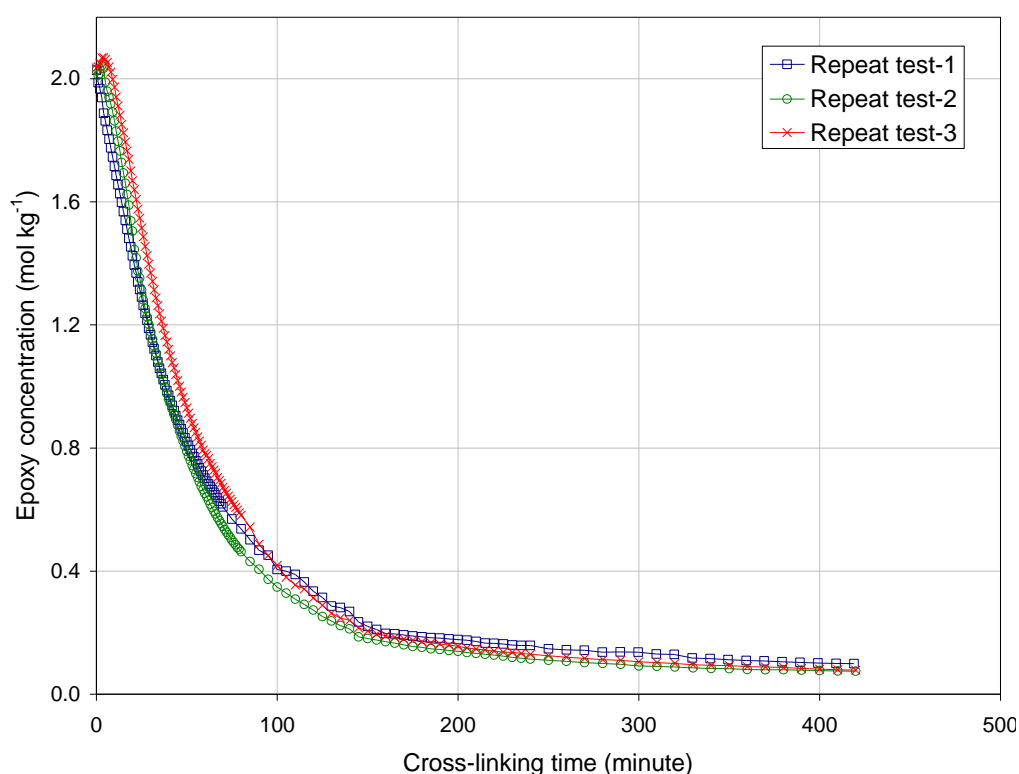


Figure 5.21 Change in the epoxy concentration in the LY3505/XB3403 resin system during cross-linking at 70°C .

5.3.2.2 Primary amine group analysis

The change in the concentration of primary amine was calculated using Equation 5.1 but by replacing the peak area of epoxy with that of the primary amine absorbance band at 2026 nm.

Equation 5.1 was modified as:

$$PA_t = PA_0 \left(\frac{\left(\frac{A_{PA}}{A_{CH}} \right)_t}{\left(\frac{A_{PA}}{A_{CH}} \right)_0} \right) \quad \text{Equation 5.2}$$

where $[PA]$ is the concentration of primary amine, A_{PA} is the primary amine peak area and A_{CH} is the peak area of reference C-H absorption band at 2164 nm. Subscripts 0 and t represent the start of reaction and time t , respectively.

The concentration of primary amine groups in the epoxy/amine resin mixture before cross-linking was found to be $1.1349 \pm 0.0068 \text{ mol kg}^{-1}$. Figure 5.22 shows the change in primary amine concentration at 70°C with respect to cross-linking time. Results obtained from three identical fibre-optic transmission sensors show good repeatability. It can be seen that the primary amine groups were completely consumed within approximately the first 100 minutes of the cross-linking reaction at 70°C. It is assumed that this is due to the cross-linking reaction not due to any evaporation.

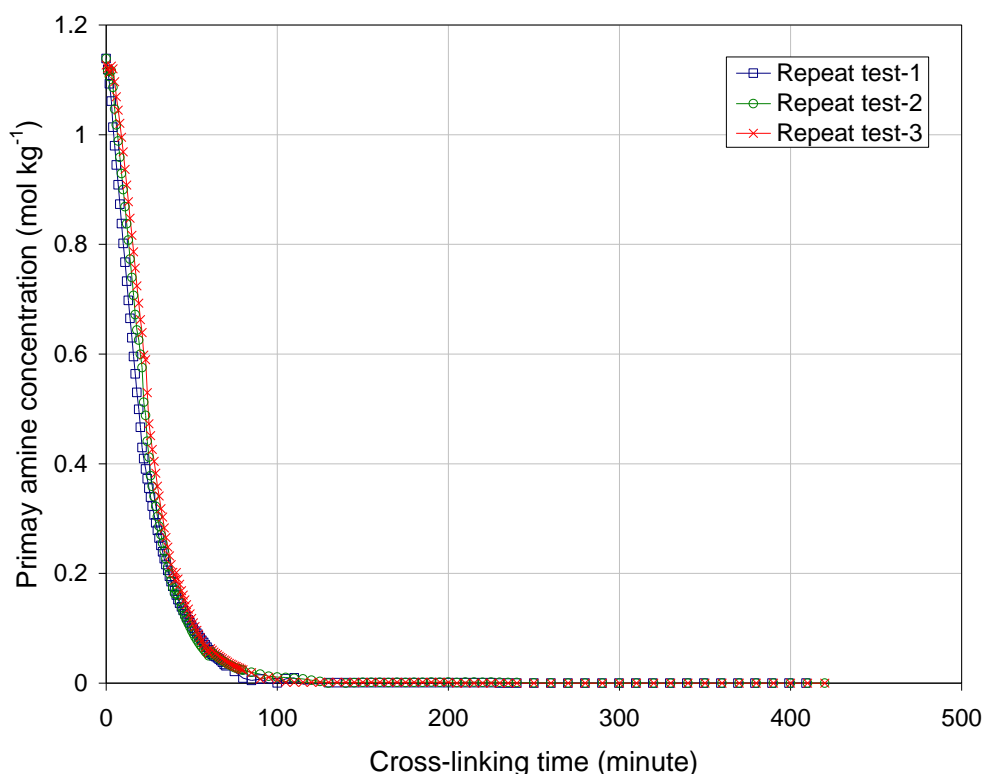


Figure 5.22 Change in the primary amine concentration of the LY3505/XB3403 resin system during cross-linking at 70 °C.

5.3.2.3 Secondary amine group analysis

The change in secondary amine concentration cannot be determined directly in the same way as the concentration of the epoxy and primary amine groups. Well-resolved absorption bands related to secondary amines do not appear in the wavelength range of 1000 – 2500 nm. The only band appearing around 1530 nm overlaps with the primary amine absorption band at 1532 nm. Various methods have been investigated to determine the secondary amine concentration [53,131,148,149,151,152].

Crosby [149] developed a method of determining the secondary amine concentration using the change in concentration of primary amine during cross-linking based on the mechanistic approach proposed by St John and George [148]. Therefore in the current study, secondary

amine concentration was calculated using the method proposed by St John and co-workers [103,148,151,152]. Figure 5.23 shows the relationship of primary amine concentration and epoxy concentration during cross-linking at 70 °C. To satisfy Equation 2.18, the rate of change in epoxy concentration should be same as that of primary amine. Crosby [149] proposed that according to the stoichiometry of the mixture, if only primary amine groups can react with epoxy groups then when $[PA] = 0$, half of the epoxy concentration should be available in the system [149]. The solid line in Figure 5.23 represents the simulated relationship between epoxy and primary amine concentrations. To satisfy this relation, data from the first 15 minutes of cross-linking reaction were considered. For determining the constants, E_1 and E_2 , Equation 2.16 can be rearranged as follows [148,151]:

$$\frac{\Delta A}{[PA]_t} = E_1 + E_2 \frac{[SA]_t}{[PA]_t} \quad \text{Equation 5.3}$$

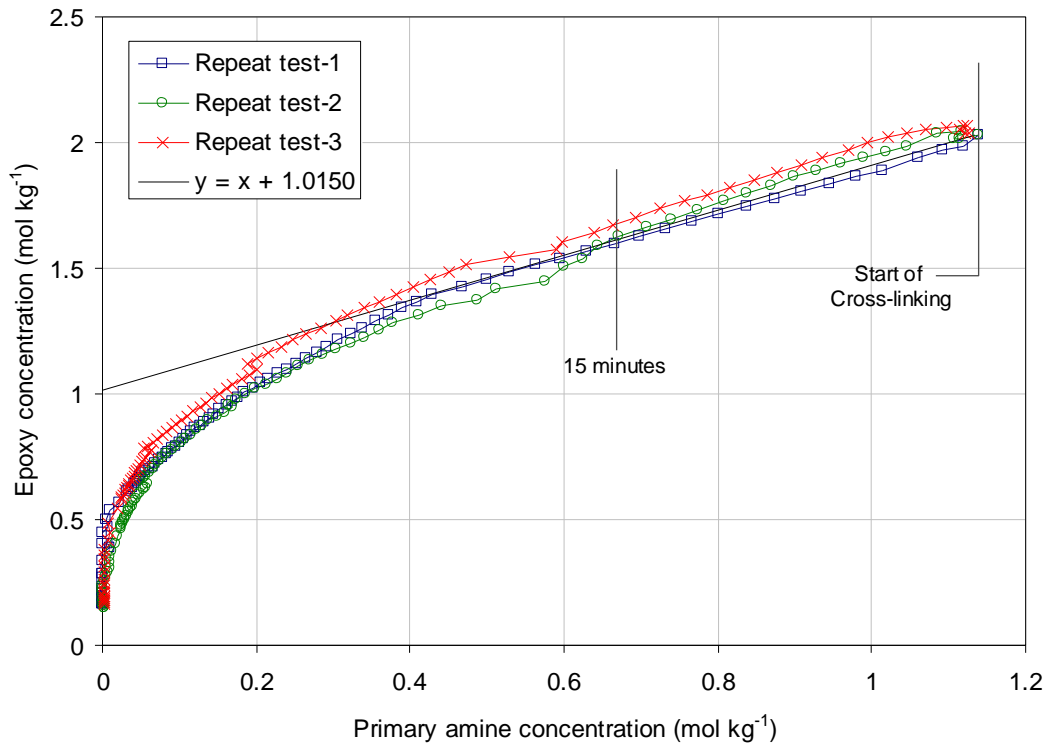


Figure 5.23 Plot of primary amine concentration, $[PA]_t$ and epoxy concentration, $[EP]_t$ of the LY3505/XB3403 resin system during cross-linking at 70 °C.

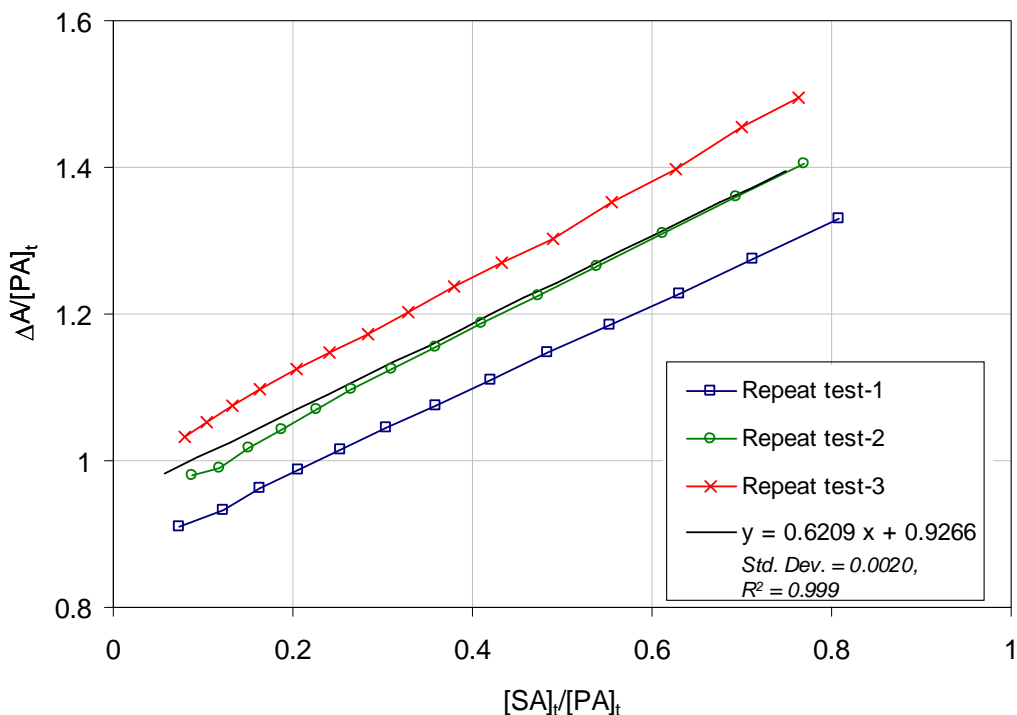


Figure 5.24 Change in $\Delta A/[PA]_t$ as a function of $[SA]_t/[PA]_t$ for the LY3505/XB3403 resin system at 70 °C.

Figure 5.24 represents the relationship between $\Delta A / [PA]_t$ against $[SA]_t / [PA]_t$ for cross-linking reactions at 70°C and E_1 and E_2 can be found from the intercept and gradient of the linear fit. With reference to the linear fit shown in Figure 5.24, E_1 and E_2 were obtained to be 0.9266 and 0.6209, respectively. By substituting these values in Equation 2.16, the contribution of the secondary amine concentration towards the combination band can be determined [148].

Figure 5.25 shows the change in normalised peak area of combination bands from 1507 – 1572 nm as a function of cross-linking time at 70 °C. The aromatic reference peak at 2164 nm was used for normalisation. The combination band decreases towards the end of the cross-linking reaction and reasonable repeatability was observed with the data obtained from three repeat experiments at 70 °C.

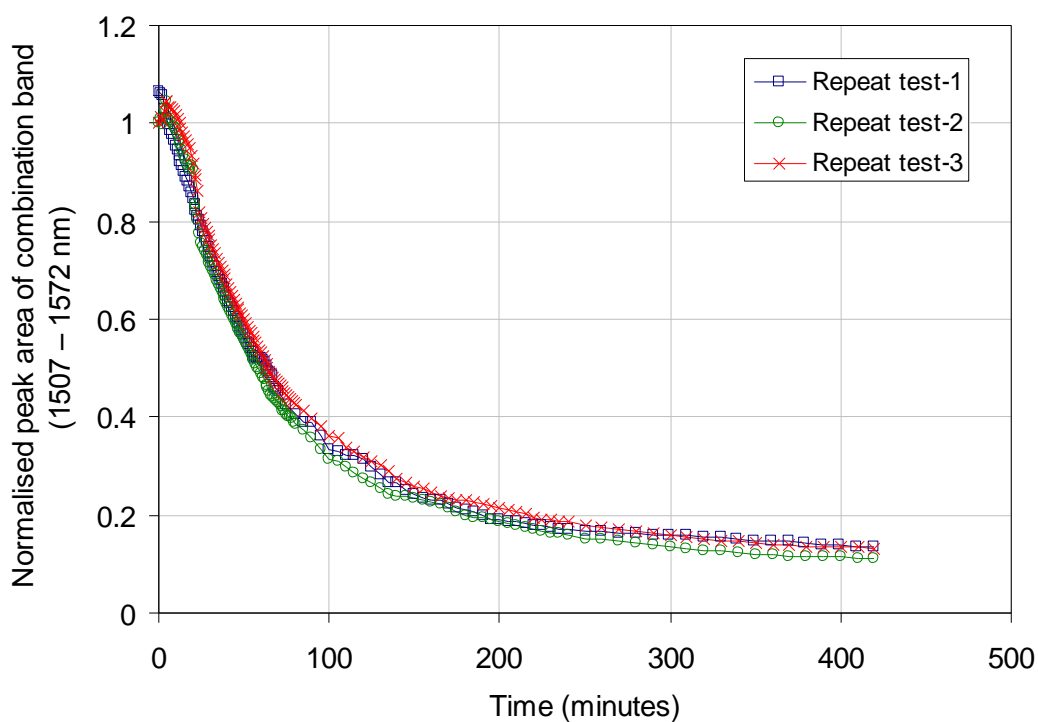


Figure 5.25 Change in normalised combination band of primary and secondary amine during cross-linking of the LY3505/XB3403 resin system at 70 °C.

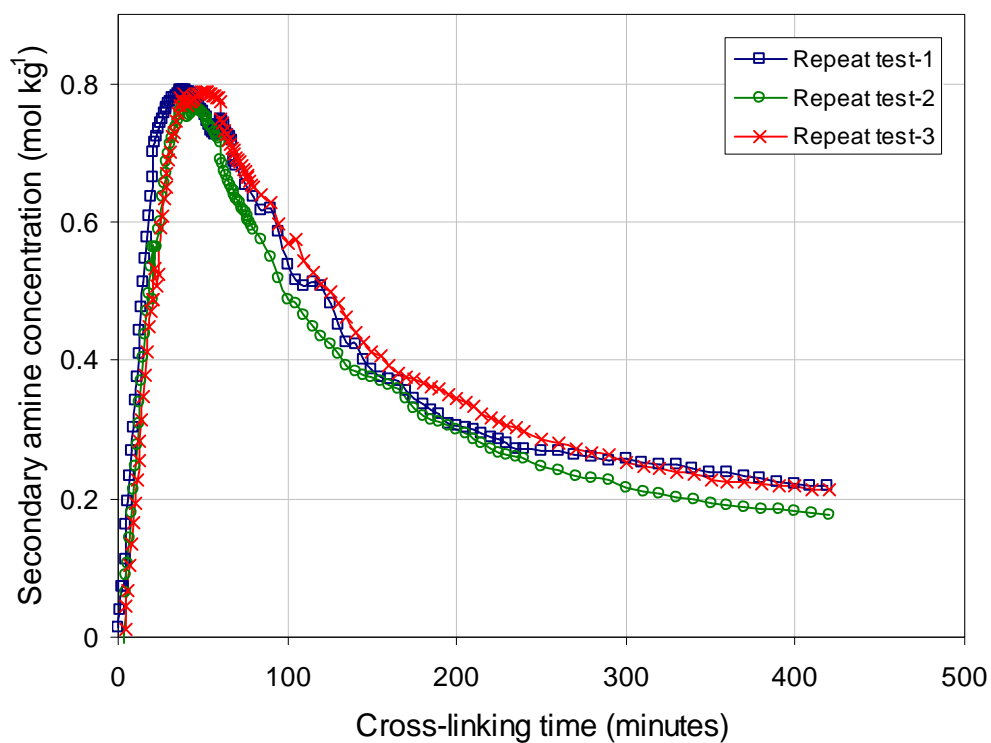


Figure 5.26 Change in secondary amine concentration during cross-linking of the LY3505/XB3403 resin system at 70 °C (see Equation 2.16).

The change in secondary amine concentration was obtained using Equation 2.16 and the results are shown in Figure 5.26. It can be seen that the secondary amine concentration increases for approximately the first 60 minutes at 70 °C before it starts to decrease gradually.

5.3.2.4 Tertiary amine group analysis

Characteristic absorption bands due to tertiary amine groups are not available in the near-IR range. Therefore a relationship between primary amine, secondary amine and tertiary amine was established for a TGDDM/DDS resin system based on mass-balance [148].

$$[TA]_t = [PA]_0 - [PA]_t - [SA]_t \quad \text{Equation 5.4}$$

where $[TA]$ is the concentration of tertiary amine groups. The above equation has been extensively used for determining tertiary amine concentration for different epoxy/amine resin systems [53,80,148,149,151].

The change in tertiary amine concentration obtained using Equation 5.4 against cross-linking time at 70°C can be seen in Figure 5.27. It can be seen that during approximately the first 25 minutes, the concentration of tertiary amine groups remained zero at 70°C. This correlates well with the initial assumption made of zero contribution of secondary amine groups to the cross-linking reaction during this time period.

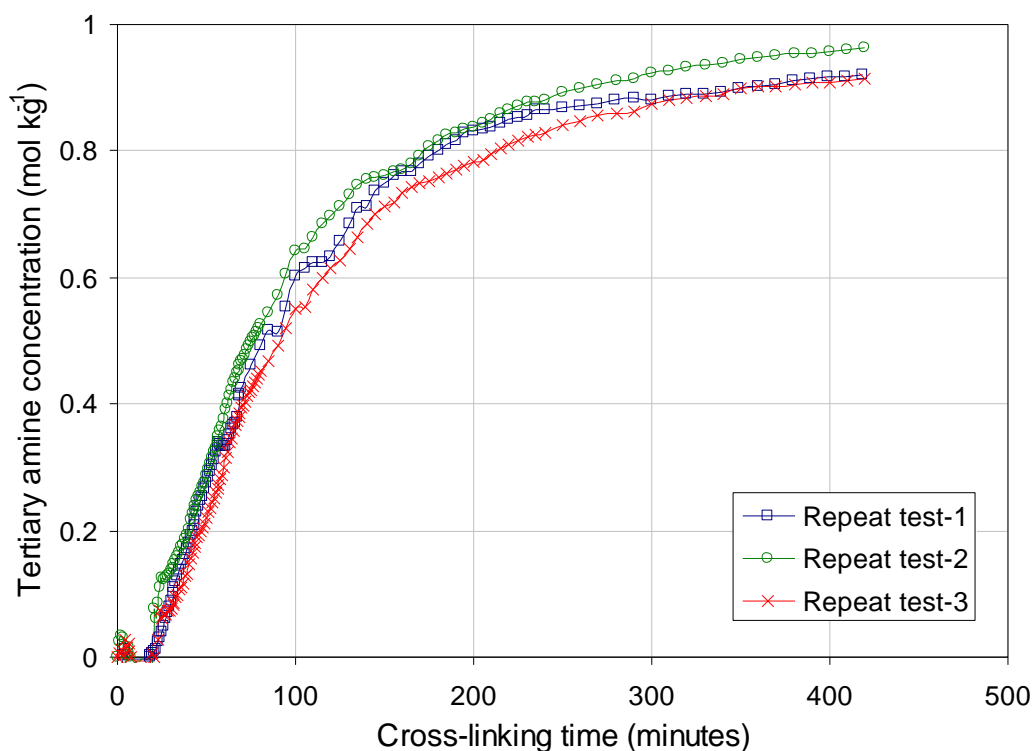


Figure 5.27 Change in tertiary amine concentration during cross-linking of the LY3505/XB3403 resin system at 70 °C (see Equation 5.4).

5.3.2.5 Hydroxyl group analysis

Even though absorption bands due to hydroxyl groups appeared at 1905 nm and 1492 nm, quantitative analysis is difficult due to complex spectral changes associated with the peaks [136,147]. Therefore the following mass balance relationship can be used for determining the change in hydroxyl group concentration [148,151,53]:

$$[OH]_t = [PA]_0 - [PA]_t - [TA]_t \quad \text{Equation 5.5}$$

where $[OH]$ is hydroxyl group concentration. Equation 5.5 was used to determine hydroxyl group concentration by assuming there are no hydroxyl groups present in the epoxy/amine mixture before cross-linking and the reaction between epoxy and amine groups is the only

source for creating hydroxyl groups. With reference to Figure 5.28, the hydroxyl concentration increases as the degree of cross-linking increases.

The same equation was employed by Rigail-Cedeño and Sung [132] for DGEBA/polyoxypropelenediamine (POP) and DGEBA/polyoxyethelenediamine (POE) resin systems. Xu *et al.* [53] studied a PGE/*m*-phenylenediamine system and similar trends in the change in secondary and tertiary amine concentrations were reported. Most of the previous studies on functional group analysis have been focused on using the mass balance approach for determining hydroxyl concentration due to the complex nature of hydroxyl peak evolution during cross-linking.

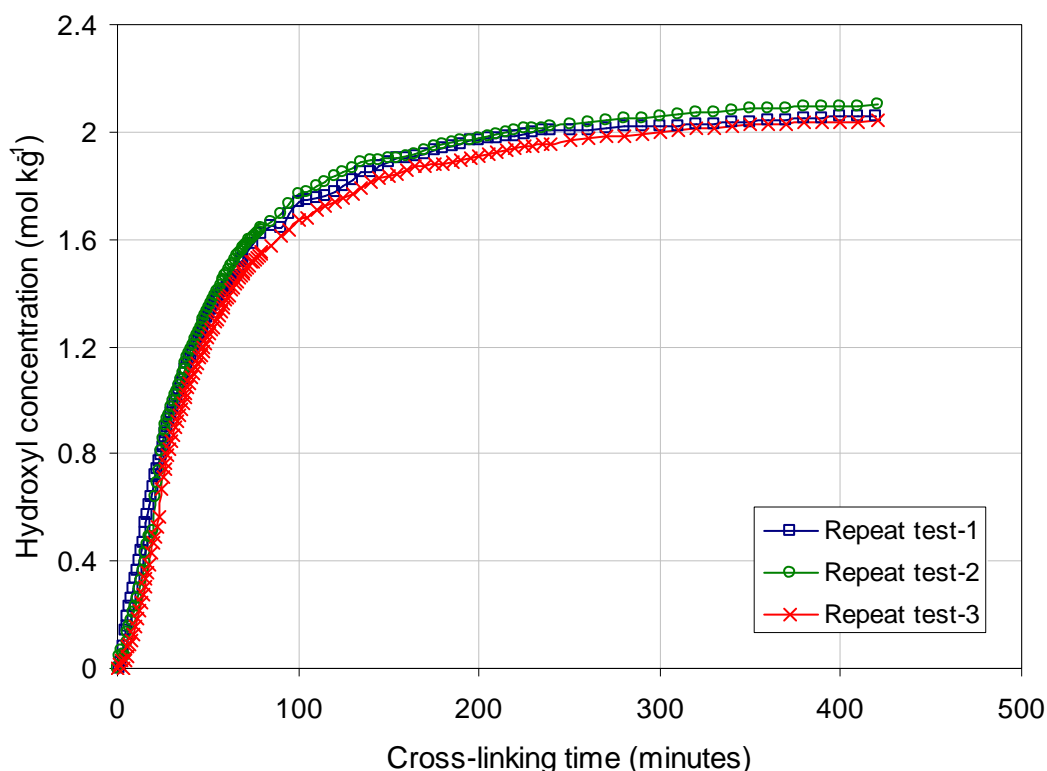


Figure 5.28 Change in hydroxyl concentration during cross-linking of the LY3505/XB3403 resin system at 70 °C (see Equation 5.5).

5.3.2.6 Summary of functional group analysis

A summary of consumption of specified functional groups in the LY3505/XB3403 resin system during cross-linking at 70 °C is shown in Figure 5.29. The results are based on the average of three repeat experiments at the same isothermal temperature. The analysis was also performed for spectral data obtained at 60, 50 and 40 °C using fibre-optic transmission spectroscopy and a similar trend in changing concentration of the functional groups was observed.

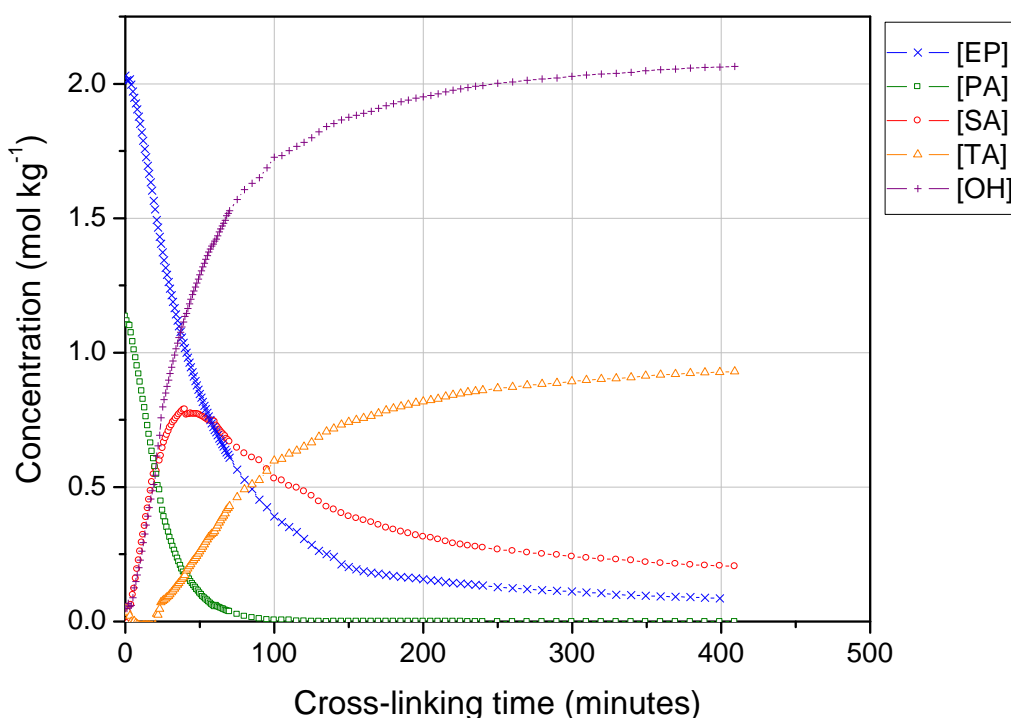


Figure 5.29 A summary of the change in concentration of functional groups during cross-linking at 70°C. [EP], [PA], [SA], [TA] and [OH] are concentrations of epoxy, primary amine, secondary amine, tertiary amine and hydroxyl groups, respectively.

Similar results were reported on changing the concentration of functional groups for DGEBA/POP and DGEBA/POE resin systems [132] and also for PEG/aniline resin systems [53]. Compared with TGDDM/DDS resin systems, a higher percentage of secondary amine

conversion was observed with the resin system that was investigated in this study [103,148,151]. With reference to Figure 5.29 in later stage of reaction, the concentration of tertiary amine groups and hydroxyl groups increases at a comparable rate with the rate of decrease in concentration of epoxy groups. Based on previous research findings, this observation suggested that the contribution of etherification reaction towards the total degree of conversion of the resin system is insignificant at the conditions studied [103,151]. This is also evident from the fact that the concentration of hydroxyl groups approaches the original concentration of epoxy groups at the start of the reaction [53].

Figure 5.30 represents the effect of cross-linking temperature on the consumption of epoxy groups during the reaction. At higher temperatures, the rate of epoxy conversion is higher and also the optimum epoxy conversion is higher. In other words, the free epoxy groups remaining in the system at the end of the reaction decrease as the cross-linking temperature increases. Figure 5.31 shows the change in primary amines during the reaction as a function of cross-linking temperature. An increase in the temperature increases the rate of depletion of the primary amine with respect to reaction time.

The change in secondary amine concentration as a function of cross-linking temperature is presented in Figure 5.32. The rate of production of secondary amine groups during the early stages of the reaction increased with cross-linking temperature. Furthermore, the maximum secondary amine concentration increased with reaction temperature.

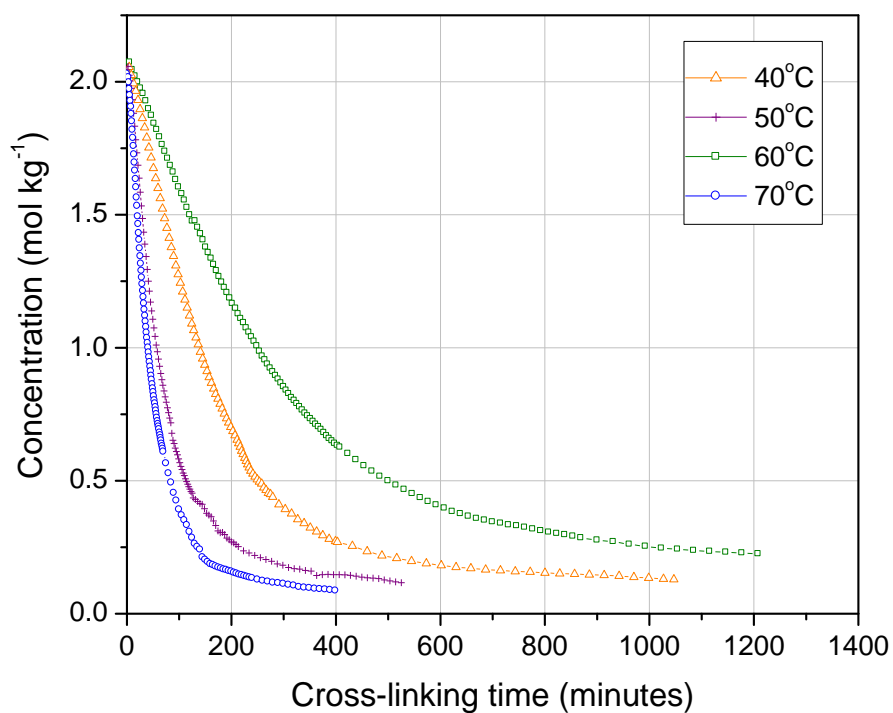


Figure 5.30 Comparison of change in epoxy group concentration during cross-linking of the LY3505/XB3403 resin system at 40, 50, 60 and 70 °C.

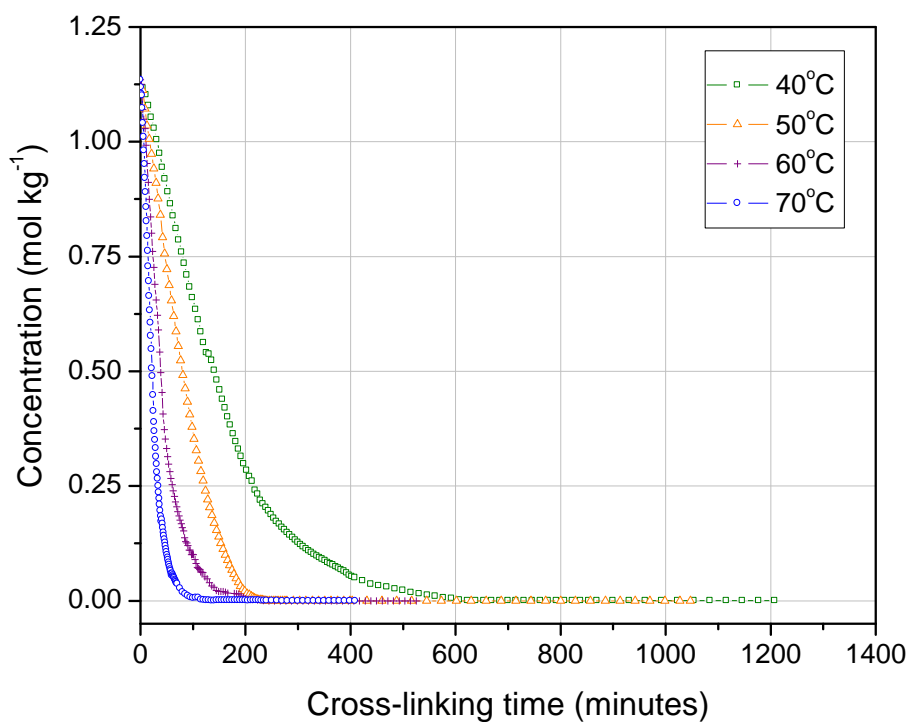


Figure 5.31 Comparison of change in primary amine group concentration during cross-linking of LY3505/XB3403 resin system at 40, 50, 60 and 70 °C.

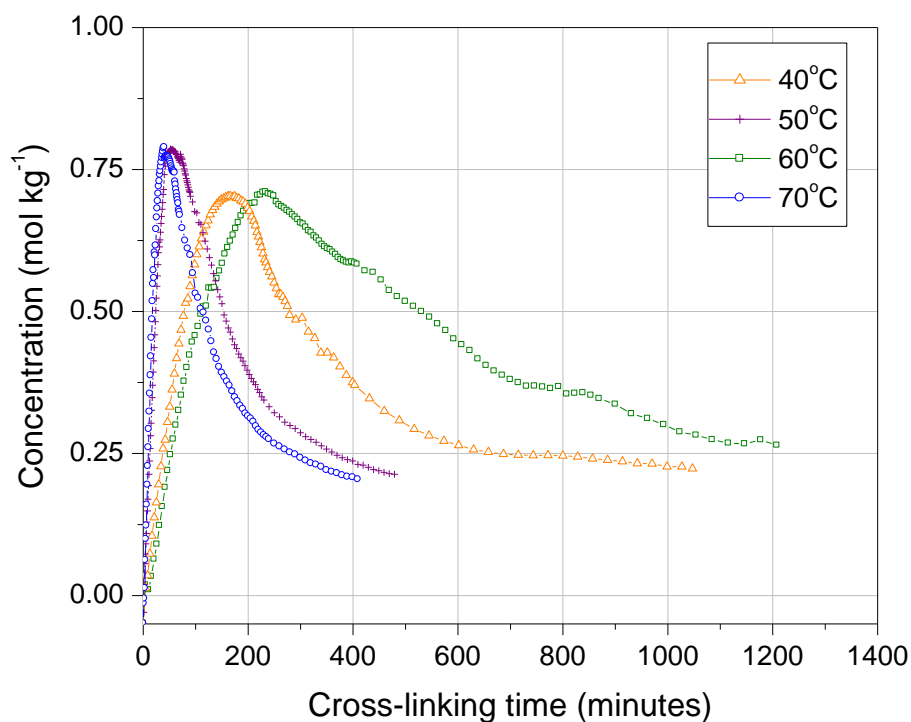


Figure 5.32 Comparison of change in secondary amine group concentration during cross-linking of the LY3505/XB3403 resin system at 40, 50, 60 and 70 °C.

With reference to Figure 5.33, the concentration of tertiary amine groups increased as a function of reaction time following an incubation period at the beginning of the reaction. This may be attributed to the period where only the primary amine groups take part in the cross-linking reaction. The observed increase in highest tertiary amine concentration with increase in cross-linking temperature confirms the increase in secondary amine conversion and hence overall increase in degree of conversion of the resin system.

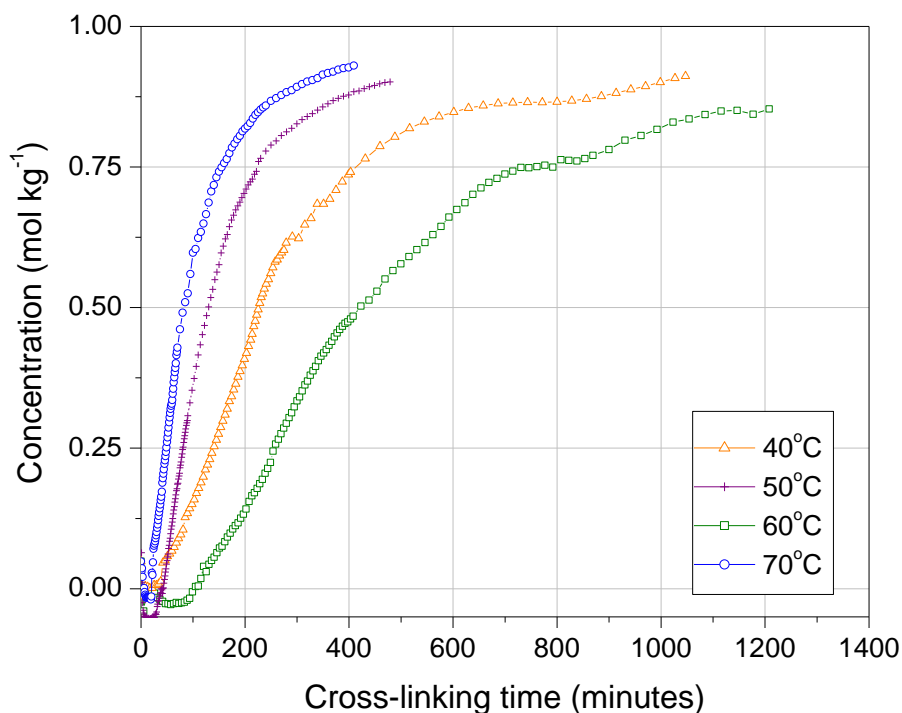


Figure 5.33 Comparison of change in tertiary amine group concentration during cross-linking of LY3505/XB3403 resin system at 40, 50, 60 and 70 °C.

Figure 5.34 shows the change in hydroxyl group concentration as a function of time and reaction temperature. As expected, an increase in hydroxyl concentration throughout the cross-linking reaction can be seen and this is due to the reaction of epoxy with primary and secondary amines and the rate of change of the OH concentration increased with increasing reaction temperature. With respect to Figure 5.30 and Figure 5.34, at all reaction temperatures investigated, the hydroxyl concentration at the end of the reaction approached to a similar value to that of the initial concentration of the epoxy groups in the uncured resin mixture. Since the initial hydroxyl group concentration in the resin mixture was assumed to be negligible, in the epoxy/amine resin system at the reaction conditions used, the etherification reaction may have less influence on the reaction mechanism.

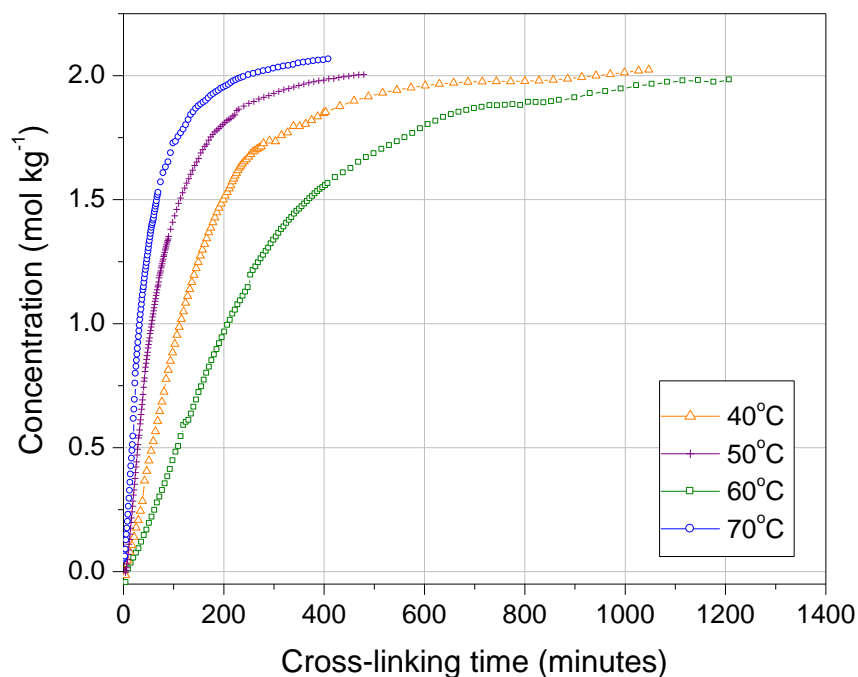


Figure 5.34 Comparison of change in hydroxyl group concentration during cross-linking of LY3505/XB3403 resin system at 40, 50, 60 and 70 °C.

5.3.3 Quantitative analysis of functional groups using fibre-optic reflectance spectroscopy

A typical series of spectra obtained during cross-linking of the LY3505/XB3403 resin system at 40 °C using fibre-optic reflectance spectroscopy is shown in Figure 5.35. The same spectral characteristics discussed in Section 5.2.1 are clearly visible. Cross-linking monitoring of the epoxy/amine resin system was also carried out at 50, 60 and 70 °C using fibre-optic reflectance sensors.

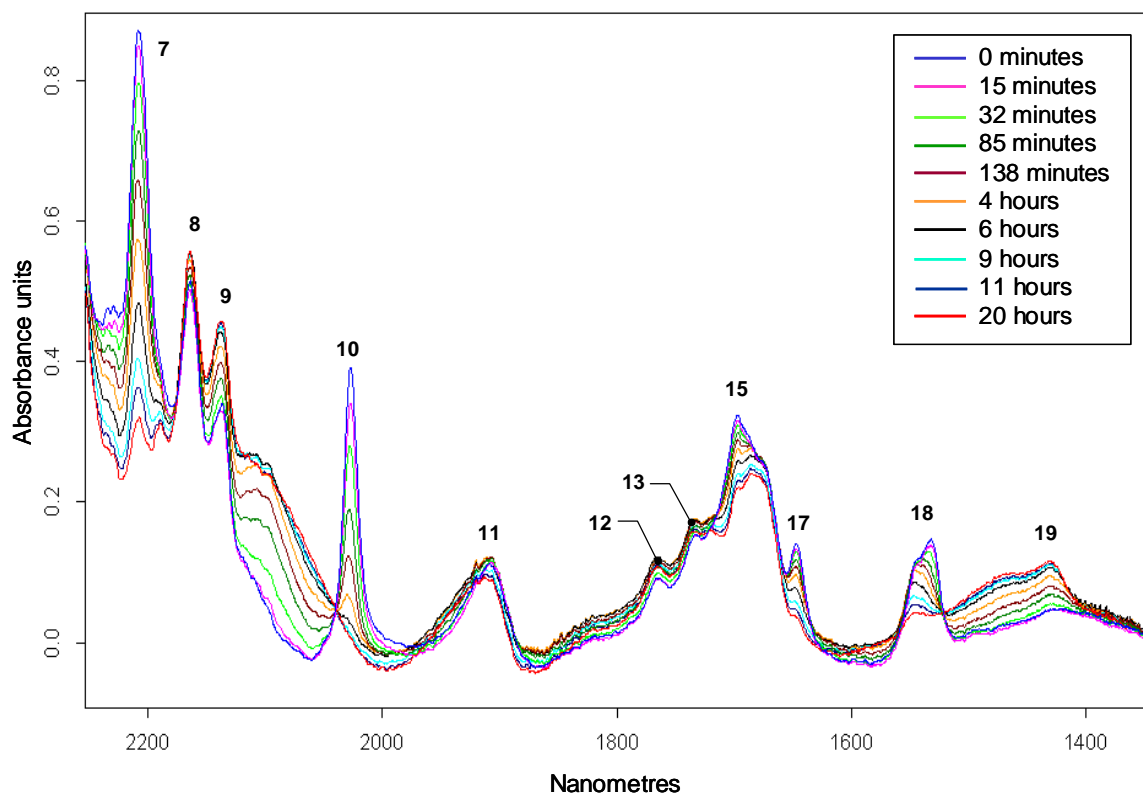


Figure 5.35 Contour spectra recorded during cross-linking of the LY3505/XB3403 resin system at 40 °C using the fibre-optic reflectance spectroscopy.

The same spectral investigation that discussed in Section 5.3.2 was carried out with the spectral data obtained in reflection mode during cross-linking at different reaction temperatures. Figure 5.36 represents the change in concentration of the epoxy, primary amine, secondary amine, tertiary amine and hydroxyl groups at 40 °C. The results are based on the average of three repeat experiments carried out at the same isothermal temperature. The analysis was also performed for spectral data obtained at 50, 60 and 70 °C using fibre-optic reflectance spectroscopy and a similar trend in changing concentration of the functional groups were observed.

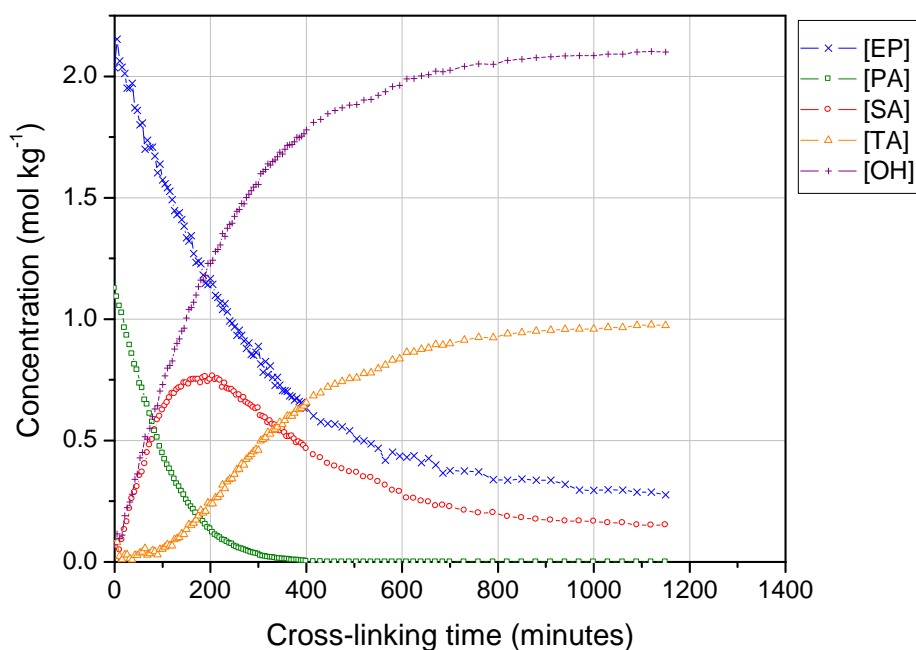


Figure 5.36 Summary of change in the functional group concentrations during cross-linking at 40 °C.

[EP], [PA], [SA], [TA] and [OH] are concentration of epoxy, primary amine, secondary amine, tertiary amine and hydroxyl groups, respectively.

Figure 5.37 shows the change in epoxy group concentration during cross-linking as a function of reaction temperature. The rate of epoxy consumption increased as the cross-linking temperature increases. In addition, free epoxy groups remaining in the system at the end of the reaction decreased as the optimum epoxy conversion increased at higher reaction temperatures. The same trend was observed with the data recorded using the fibre-optic transmission spectroscopy. Figure 5.38 represents the change in primary amine concentration during cross-linking at different reaction temperatures. At higher temperatures, primary amines were consumed at a faster rate compared with that at lower cross-linking temperatures.

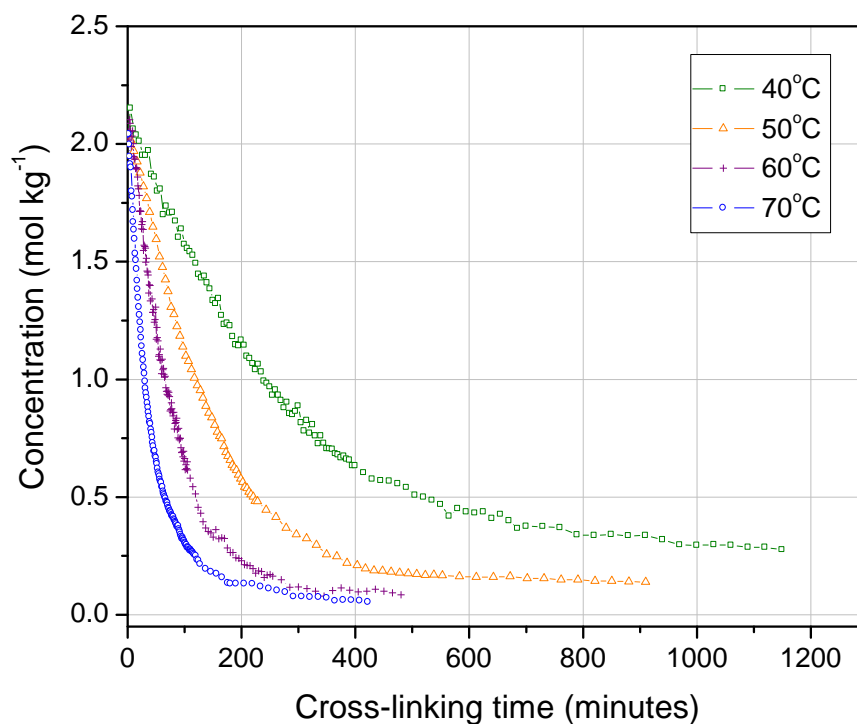


Figure 5.37 Comparison of the change in epoxy group concentration during cross-linking of the LY3505/XB3403 resin system at 40, 50, 60 and 70 °C.

Figure 5.39 shows a plot of the observed changes in the concentration of secondary amine groups during cross-linking as a function of reaction time. It can be seen that the residual secondary amine concentration at the end of the reaction decreased with increase in reaction temperature whereas maximum concentration increased as the reaction temperature increases.

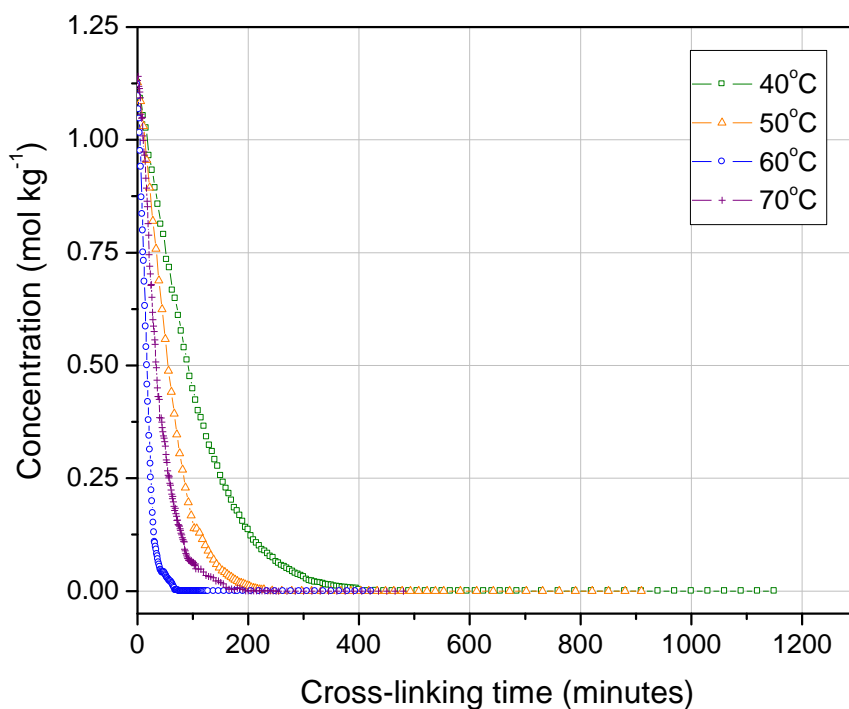


Figure 5.38 Comparison of change in primary amine group concentration during cross-linking of LY3505/XB3403 resin system at 40, 50, 60 and 70 °C.

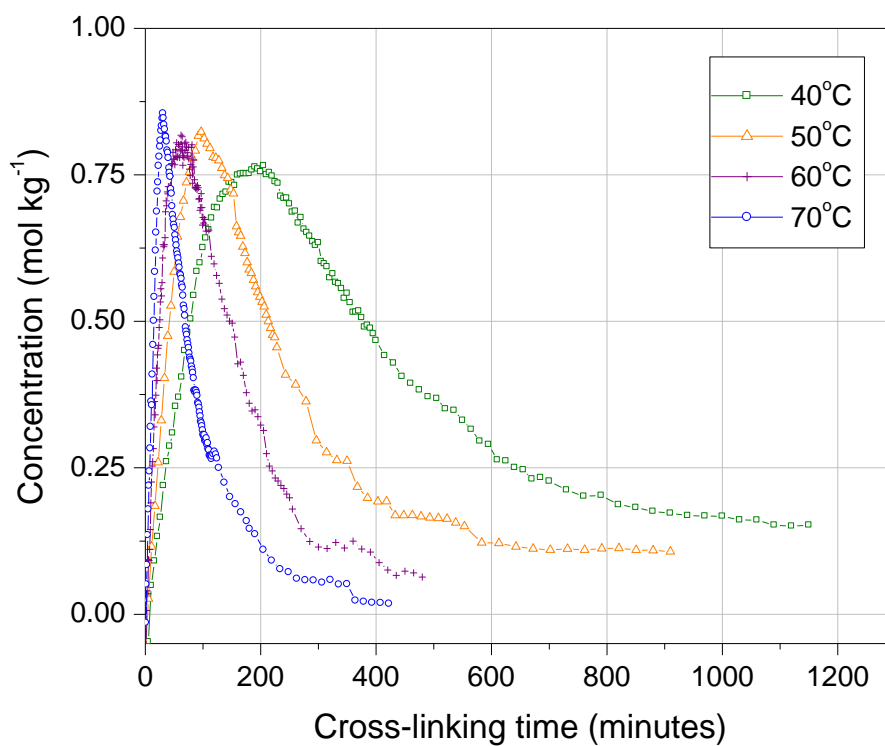


Figure 5.39 Comparison of change in secondary amine group concentration during cross-linking of LY3505/XB3403 resin system at 40, 50, 60 and 70 °C.

Figure 5.40 shows the change in tertiary amine concentration against the reaction time at different cross-linking temperatures. Similarly to the trend obtained using fibre-optic transmission spectroscopy, a dwell time was observed at the start of the reaction followed by an increase in the concentration towards the end of the reaction. The rate of formation of tertiary amine groups as well as the optimum concentration attained increased with increase in reaction temperature.

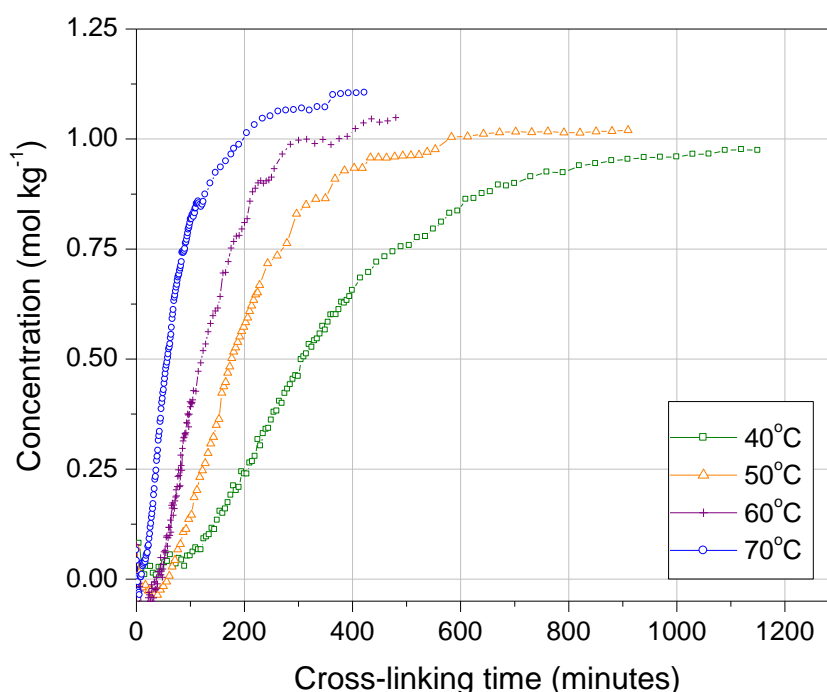


Figure 5.40 Comparison of change in tertiary amine group concentration during cross-linking of the LY3505/XB3403 resin system at 40, 50, 60 and 70 °C.

Figure 5.41 represents the change in hydroxyl concentration as a function of cross-linking time at different reaction temperatures. The rate of hydroxyl formation increased as the cross-linking temperature increases due to the increase in overall epoxy conversion. At higher cross-linking temperatures, the optimum hydroxyl concentration approached the initial

concentration of epoxy groups at the start of the cross-linking confirming that insignificant etherification reactions take place within the resin system.

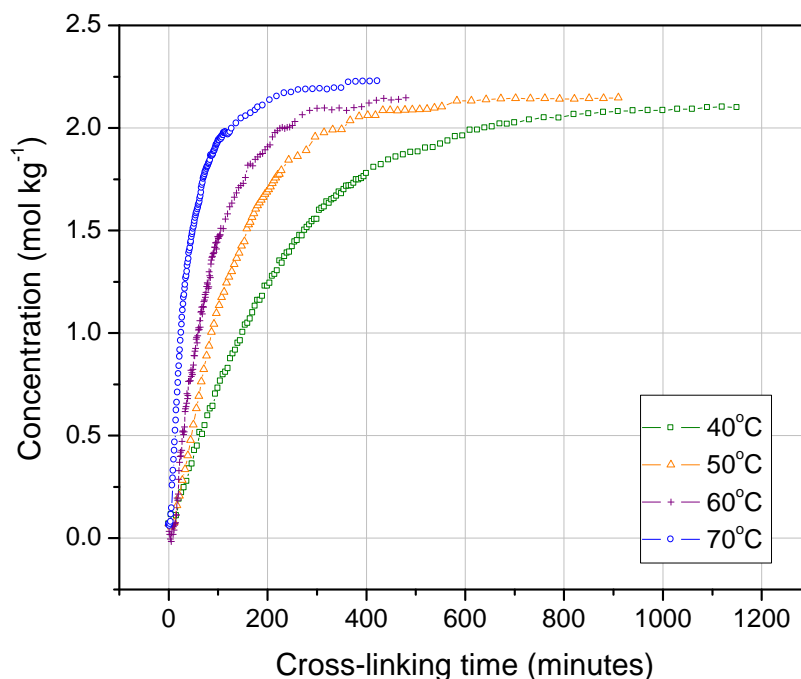


Figure 5.41 Comparison of change in hydroxyl group concentration during cross-linking of the LY3505/XB3403 resin system at 40, 50, 60 and 70 °C.

5.4 Empirical modelling of cross-linking kinetics using fibre-optic spectroscopy

5.4.1 Fibre-optic transmission spectroscopy

The mostly accepted method of obtaining degree of cross-linking is based on change in epoxy group concentration with respect to time and temperature [136,147]. In the current study, the epoxy absorption band at 2207 nm was used for determining the degree of conversion and the

spectral data were normalised against the peak area of aromatic CH at 2164 nm. The degree of conversion at a given cross-linking temperature was calculated as follows:

$$\alpha = 1 - \frac{EP_t}{EP_0} \quad \text{Equation 5.6}$$

where α is the degree of conversion, $[EP]_0$ and $[EP]_t$ are epoxy concentration at $t = 0$ and $t = t$ respectively.

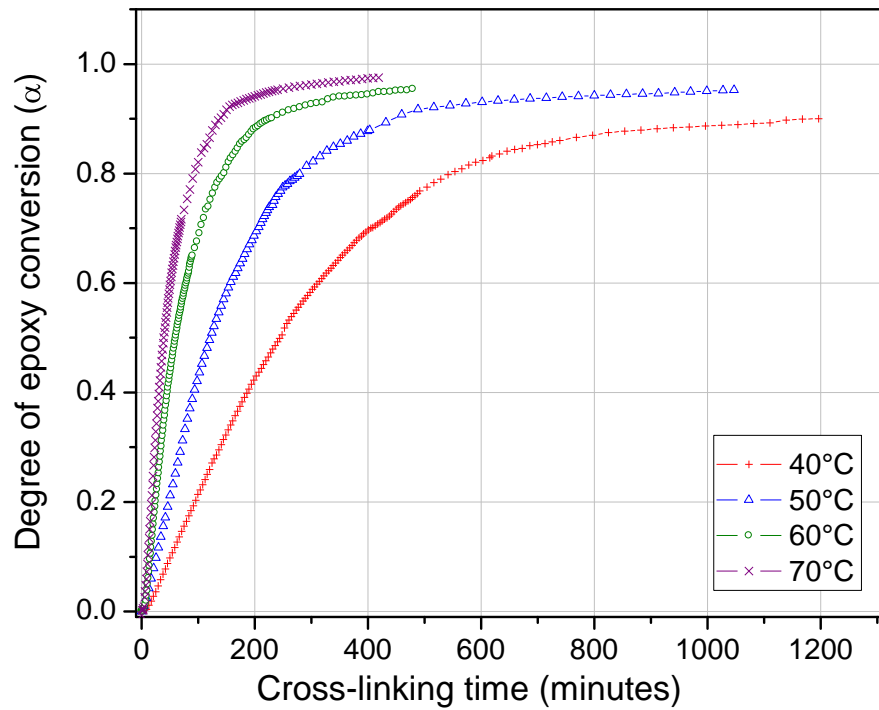


Figure 5.42 Comparison of the degree of epoxy conversion during cross-linking of the LY3505/XB3403 resin system at 40, 50, 60 and 70 °C. Results are based on fibre-optic transmission spectroscopy.

Figure 5.42 shows a comparison of the degree of epoxy conversion as a function of temperature. Both the rate of conversion and the optimum epoxy conversion of the

LY3505/XB3403 resin system increase as cross-linking temperature increases at the conditions used in the study [357,370,375].

The empirical approach for modelling cross-linking kinetics of thermosetting systems is a widely accepted method [66,70,72] and the models commonly employed for epoxy/amine resin systems were highlighted in Section 2.1.2.

In the current study, the model proposed by Kenny and Trivisano [86] was used for determining the cross-linking kinetics of the LY3505/XB3403 resin system. In order to determine the reaction rate as a function of time, the derivative of the plot of degree of conversion versus time, was obtained. For cross-linking reaction at each reaction temperature, Equation 2.10 was fitted to graphs of $d\alpha/dt$ against α using the Origin 7.0 software. A non-linear least-squares curve fitting approach was used in which the best fit is generated by choosing the unknown parameters (i.e. k_1 , k_2 , m and n) so that the sum of the squares of the deviations of the model from the experimental points is minimum for a range of independent variables.

For curve fitting, m and n were assumed to be constants and $n + m = 2$. Reasonable fits were obtained with $m = 0.5$ and $n = 1.5$ and the values seemed to be independent of the reaction temperature. Therefore Equation 2.10 (see Section 2.1.2) can be written for the LY3505/XB3403 resin system as follows:

$$\frac{d\alpha}{dt} = (k_1 + k_2\alpha^{0.5})(\alpha_{\max} - \alpha)^{1.5} \quad \text{Equation 5.7}$$

According to the results obtained, Figure 5.43 illustrates the optimum epoxy conversion (α_{max}) as a function of cross-linking temperature and linear regression can be performed for the range of reaction temperatures studied. According to the best linear fit, the relationship between α_{max} and the reaction temperature can be defined as follows:

$$\alpha_{max} = 0.00244T + 0.811$$

Equation 5.8

where T is the cross-linking temperature. According to the correlation coefficient for the linear fit (R^2), a linear relationship was observed between α_{max} and the reaction temperature in the temperature range of 40 – 70 °C. The standard deviation of the slope of the regression line from the experimental data set was calculated as 0.004. However, there is not enough evidence to extrapolate the linear relationship beyond the temperature range studied. Therefore it may not be valid to use the linear regression to predict the optimum epoxy conversion below and above 40 °C and 70 °C, respectively. The rate constants, k_1 and k_2 were obtained by fitting Equation 2.10 to the experimental data.

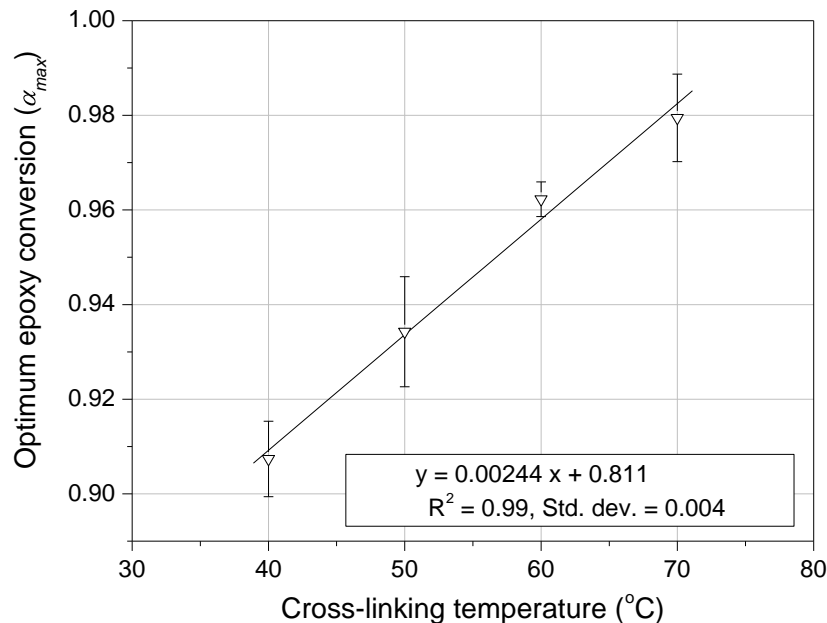


Figure 5.43 Relationship between the optimum epoxy conversion and the cross-linking temperature for the LY3505/XB3403 resin system.

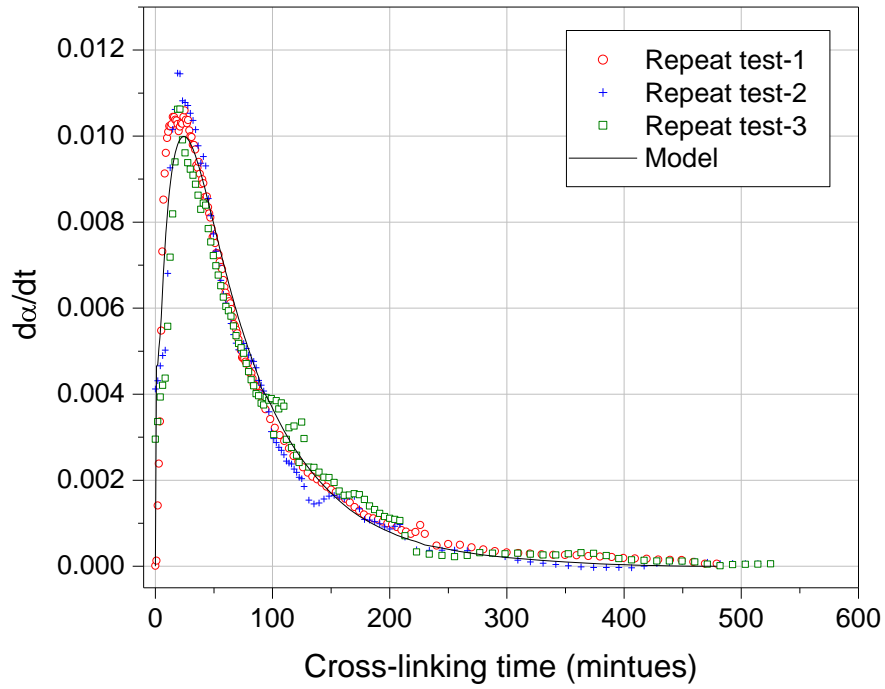


Figure 5.44 Comparison of the experimental data and the kinetic model (see Equation 2.10) for cross-linking monitoring of the LY3505/XB3403 resin system at 60°C.

Figure 5.44 shows a typical plot of $d\alpha/dt$ against cross-linking time for the experiments carried out at 60°C using fibre-optic transmission spectroscopy. Three repeat experiments at the same reaction temperature were cross-plotted with the model. The same procedure was followed for all the cross-linking temperatures and the Arrhenius temperature dependence was observed from the rate constants, k_1 and k_2 as shown in Figure 5.45 and Figure 5.46. Therefore Equations 2.5 and 2.6 can be re-written for k_1 and k_2 related to the LY3505/XB3403 resin system as follows:

$$\ln k_1 = -4094.70 \frac{1}{T} + 6.101 \quad \text{Equation 5.9}$$

$$\ln k_2 = -6382.66 \frac{1}{T} + 15.491 \quad \text{Equation 5.10}$$

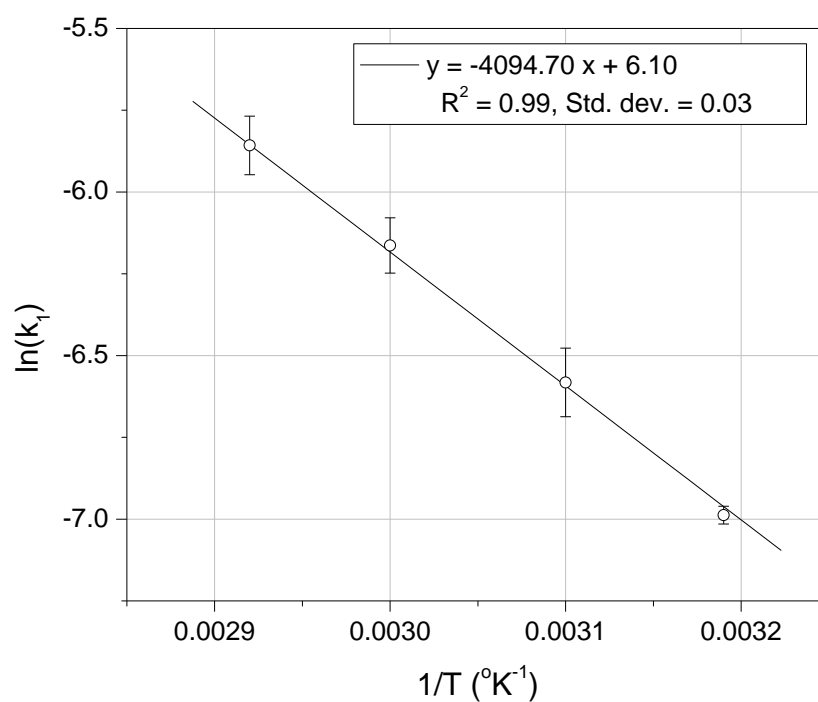


Figure 5.45 Arrhenius temperature dependence of the rate constant, k_1 for the LY3505/XB3403 resin system based on fibre-optic transmission spectroscopy.

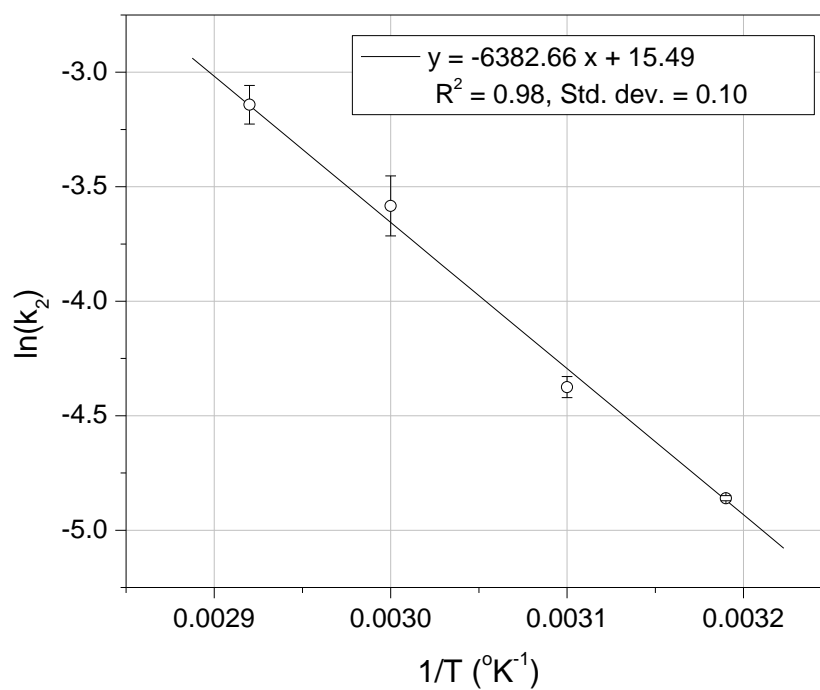


Figure 5.46 Arrhenius temperature dependence of the rate constant, k_2 for the LY3505/XB3403 resin system based on fibre-optic transmission spectroscopy.

The activation energies for cross-linking and the pre-exponential factors relating to k_1 and k_2 can be obtained using Equations 2.5 and 2.6.

5.4.2 Fibre-optic reflectance spectroscopy

Figure 5.47 shows a summary of results obtained for the degree of epoxy conversion at different cross-linking temperatures using fibre-optic reflectance spectroscopy. The conversion is based on the normalised peak area of epoxy absorbance band at 2209 nm against the aromatic reference peak area at 2164 nm.

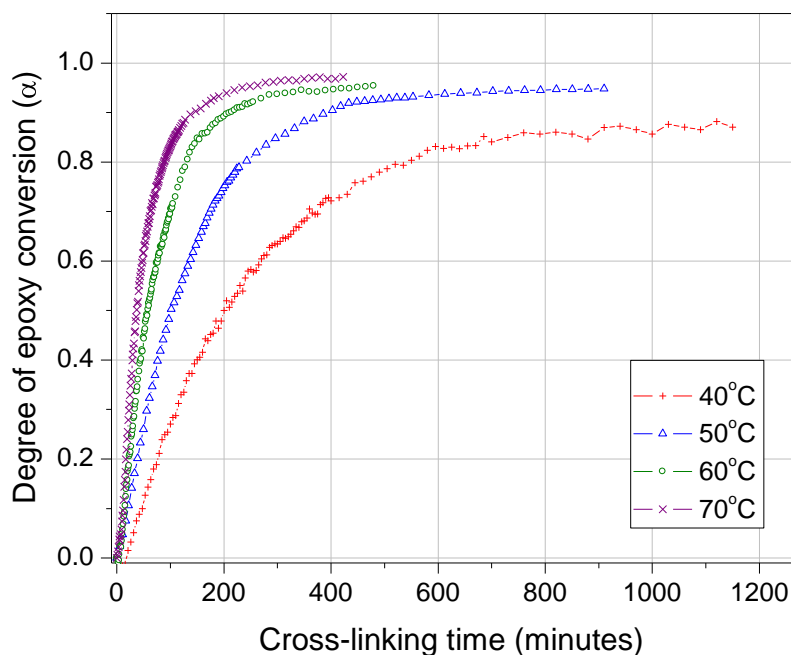


Figure 5.47 Comparison of the degree of epoxy conversion during cross-linking of the LY3505/XB3403 resin system at 40, 50, 60 and 70 °C. Results are based on the fibre-optic reflectance spectroscopy.

The degree of conversion was obtained using Equation 5.6. With reference to Figure 5.47, the degree of epoxy conversion determined using fibre-optic reflectance spectroscopy highlights a characteristic trend of the increase in degree of conversion with increase in reaction temperature.

The same empirical approach was used for the spectral data obtained using fibre-optic reflectance spectroscopy. In order to obtain kinetic parameters, Equation 2.10 was fitted to the experimental data and the Arrhenius relation was observed for k_1 and k_2 as shown in Figure 5.48 and Figure 5.49, respectively. The standard deviation shown in the plots is the deviation of the slope of the linear regression line from the experimental data set. Using linear fits, the Arrhenius temperature dependence of rate constants where obtained based on reflection spectroscopy can be expressed as follows:

$$\ln k_1 = -3818.00 \frac{1}{T} + 4.546 \quad \text{Equation 5.11}$$

$$\ln k_2 = -5857.23 \frac{1}{T} + 13.970 \quad \text{Equation 5.12}$$

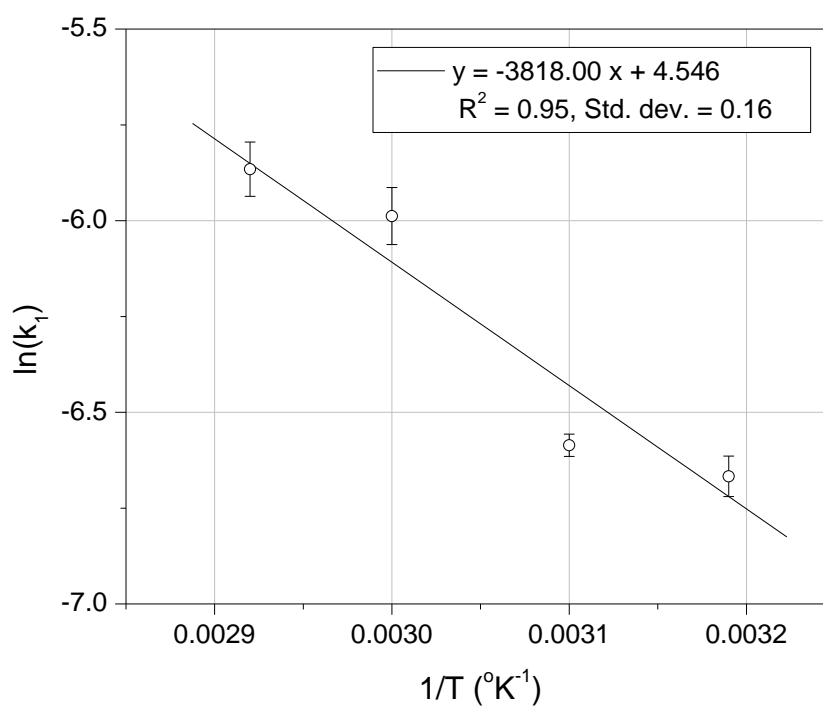


Figure 5.48 Arrhenius temperature dependence of the rate constant, k_1 for the LY3505/XB3403 resin system based on fibre-optic reflectance spectroscopy.

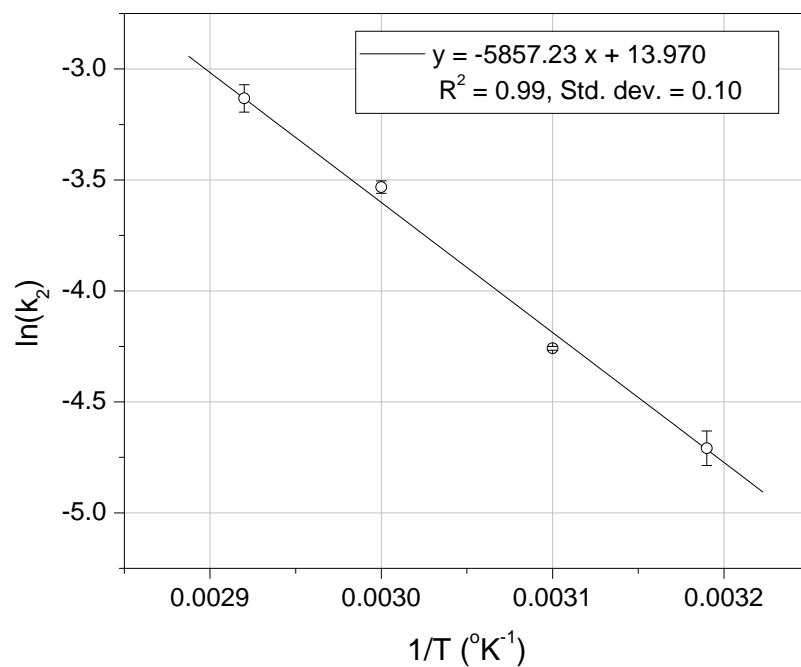


Figure 5.49 Arrhenius temperature dependence of the rate constant, k_2 for the LY3505/XB3403 resin system based on the fibre-optic reflectance spectroscopy.

5.4.3 Comparison of cross-linking kinetics obtained using fibre-optic spectroscopy

The kinetic parameters obtained for cross-linking of LY3505/XB3403 resin system based on fibre-optic transmission and reflectance spectroscopy are summarised in Table 5.3. Values obtained for activation energy for cross-linking using different sensing techniques show a slight variation. However, this difference is well within the scatter of data. The applicability of the model (see Equation 2.10) was investigated for DGEBA/POP [379] and DGEBA/1,6-diaminohexane [149,81] resin systems. The kinetic parameters reported in Table 5.3 are in reasonable agreement with the published data for similar epoxy systems. Values for m and n have been reported as 0.58 and 1.42, respectively for DGEBA/POP based on DSC measurements [379]. In that study, the activation energies corresponding to k_1 and k_2 were quoted as 67.7 and 51.4 kJ mol⁻¹, respectively. Other authors who studied the cross-linking kinetics of DGEBA/POP resin system include Rigail-Cedeño and Sung [132]. However, in their study value for the activation energy was not reported. Results for a DGEBA/1,6-diaminohexane resin system based on near-infrared spectroscopy reported by Crosby [149] and Fernando *et al.* [81] include values for the activation energies between 27 – 70 kJ mol⁻¹. The general Kamal model (Equation 2.4) was also used for kinetic analysis of the resin system used in this study [356,357]. The activation energies reported were in the range of 50 – 52 kJ mol⁻¹. Figure 5.50 shows a comparison of the degree of conversion based on the experimental data obtained using fibre-optic transmission & reflection techniques; the prediction based on the kinetic model developed for the LY3505/XB3404 resin system at 40, 50, 60 and 70 °C are assumed. Equation 5.7 was integrated to obtain the degree of conversion as a function of time

(see Appendix – III). The model shows excellent correlation with the experimental results. The cross-linking reactions follow typical autocatalytic behaviour and can be explained using the modified Kamal model (Equation 5.7).

Table 5.3 Comparison of values obtained for activation energy, E_a and the pre-exponential factor, $\ln A$ related to k_1 and k_2 .

	Fibre-optic transmission spectroscopy		Fibre-optic reflectance spectroscopy	
	Activation energy (E_a) (kJ mol ⁻¹)	Pre-exponential factor ($\ln A$)	Activation energy (E_a) (kJ mol ⁻¹)	Pre-exponential factor ($\ln A$)
k_1	34±1	6.10±0.40	32±6	4.54±0.33
k_2	53±4	15.49±1.54	49±4	13.97±1.40
	$n = 1.5, m = 0.5$			

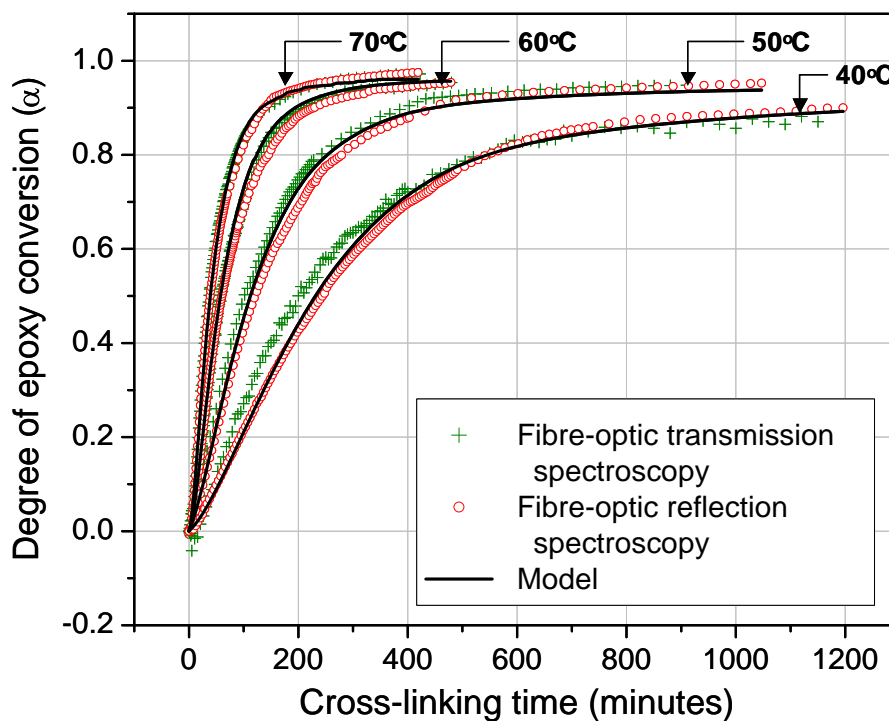


Figure 5.50 Comparison of the kinetic cure model to the experimental data obtained using different fibre-optic techniques for the LY3505/XB3403 resin system at 40, 50, 60 and 70 °C.

5.4.4 Relationship of degree of cross-linking and refractive index

Refractive indices of uncross-linked resin mixture and a cross-linked resin at 60 °C for 8 hours were measured to be 1.5408 and 1.5719, respectively. The measurements were taken at 22.3 °C using the sodium D-line at 589 nm.

Crosby [149] investigated a relationship between concentration and the refractive index of a bisphenol-A/1,6-hexadamine resin system. The author modelled the degree of conversion based on refractive index data and good correlation was observed with that obtained using change in chemical concentration. The validity of the model for the resin system was studied using data obtained at isothermal reaction temperatures ranging from 30 – 60 °C.

An attempt was made to predict the refractive index of the Y3505/XB3403 resin system during cross-linking using the model proposed by Crosby [149]. The model was modified for cross-linking reaction of LY3505/XB3403 epoxy/amine resin system at 60 °C for 8 hours using off-line measurements of refractive index of the resin system before and after cross-linking [149,222,380]. The modified relationship between the refractive index, n_o and degree of conversion, α is given below:

$$n_o = 0.0444\alpha + 1.5275$$

Equation 5.13

5.4.4.1 Ray optics of Fibre-optic transmission spectroscopy

The degree of conversion based on epoxy absorption at 2207 nm was calculated using fibre-optic near-infrared transmission spectroscopy at the same cross-linking temperature and the data set was used for predicting the change in refractive index during the cross-linking

reaction. For *in situ* monitoring of cross-linking reaction, the cavity length of a single-fibre transmission sensor was set to be 500 μm . The predicted refractive index as a function of cross-linking time and also as a function of degree of conversion obtained at 60 °C is plotted in Figure 5.51. As the viscosity of the resin system increases with degree of cross-linking, the density of the resin also increases. Therefore the refractive index of the resin system increases with increasing degree of conversion. As the system approaches the gel point, rate of cross-linking decreases and the rate of increase in refractive index also decreases. Good correlation was observed with the measured and predicted refractive index after cross-linking at 60 °C for 8 hours (see Table 5.4).

Using predicted refractive index of the resin system as a function of cross-linking; it is possible to predict the change in half-angle of cone of acceptance, θ_o with respect to refractive index using Equation 5.13. Figure 5.52 shows the relationship of refractive index and θ_o as a function of cross-linking time. From Figure 5.52 it can be seen that, θ_o decreases as the refractive index of the resin within the sensing cavity, increases. This shows the trend of convergence of cone of acceptance of IR beam emerging at the fibre/resin interface as a function of cross-linking time. Figure 5.53 schematically represents the decrease in θ_o of IR beam towards the end of cross-linking; n_o and θ_o are refractive index of the resin and the half angle of cone of acceptance at input fibre/resin interface. Subscripts “*start*” and “*end*” represent before and after cross-linking, respectively.

Furthermore, the power of IR beam that enters into the output fibre, $P_3(\lambda)$ is a function of refractive index and can be predicted using Equation 4.4. In Equation 4.5, $P_3(\lambda)$ is expressed as a fraction of the power emerging at the input fibre interface, $P_0(\lambda)$.

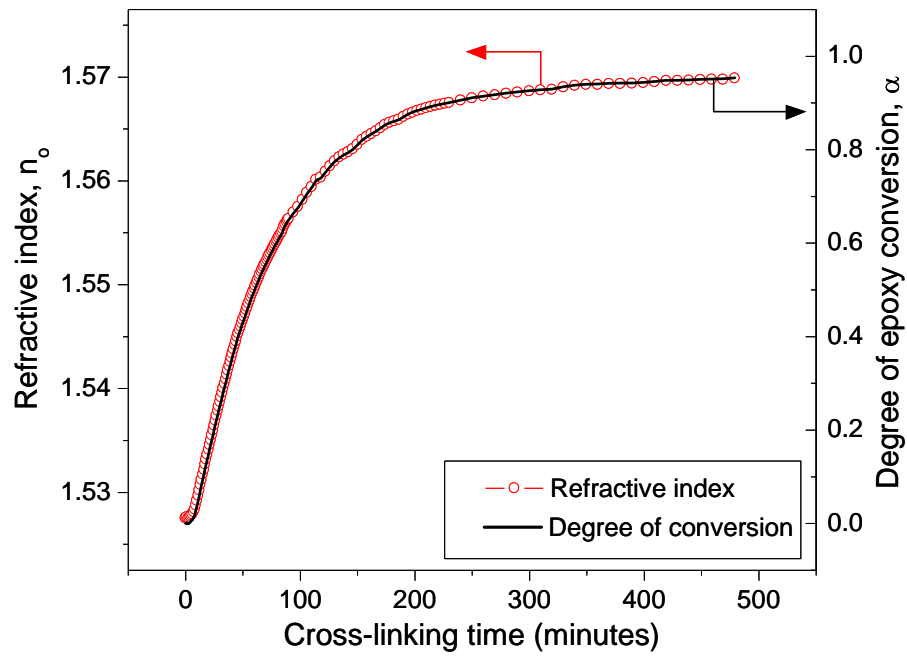


Figure 5.51 Comparison of predicted refractive index (see Equation 4.6) and degree of conversion of LY3505/XB3403 resin system obtained at 60 °C for 8 hours.

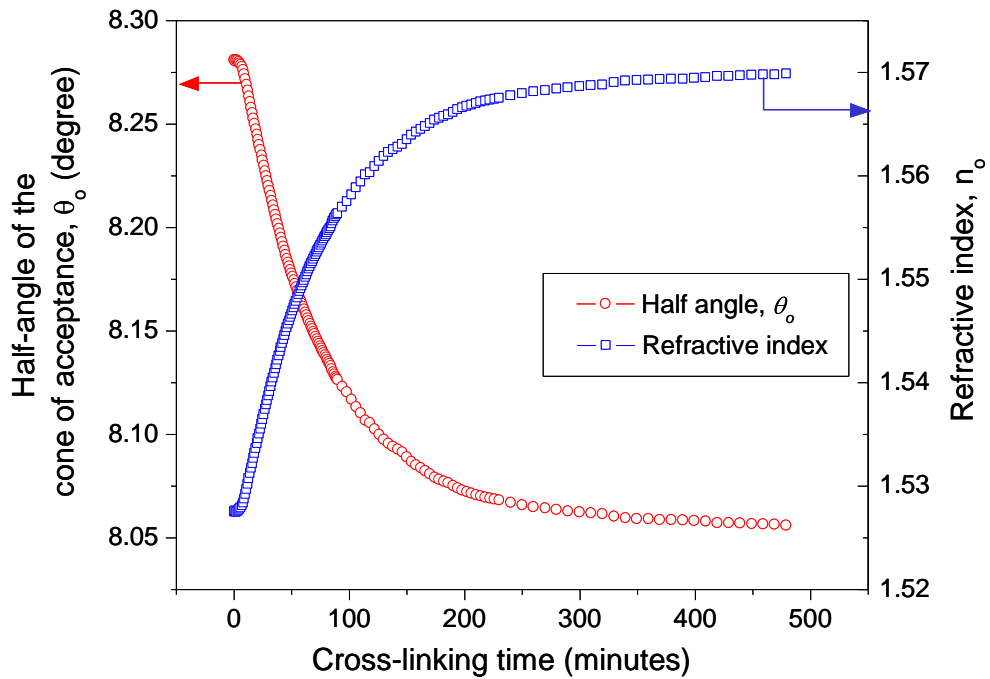


Figure 5.52 Comparison of change in refractive index (see Equation 5.13) of LY3505/XB3403 resin system cross-linked at 60 °C for 8 hours and half-angle of cone of acceptance, θ_o (see Equation 4.3) at the input fibre/resin interface.

Figure 5.54 represents the change in the fractional component, $f(n_o, A, d)$ at 2207 nm as a function of cross-linking time. Absorbance, A was calculated using epoxy absorption band at 2207 nm and $d = 500 \mu\text{m}$ (see Appendix – I). It is obvious that, as θ_o decreases with increase in refractive index of the resin, the fraction of $P_o(\lambda)$ coupling into the output fibre increases.

Table 5.4 Summary of results obtained for ray optics of fibre-optic transmission spectroscopy for the LY3505/XB3403 resin system with in the sensing cavity.

	Before cross-linking	After cross-linking at 60°C for 8 hours
Refractive index (at 60°C)	1.5275	1.5699
Half-angle of cone of acceptance, θ_o (degree)	8.281	8.056
Fraction of input power, $f(n_o, A, d)$	0.042	0.368

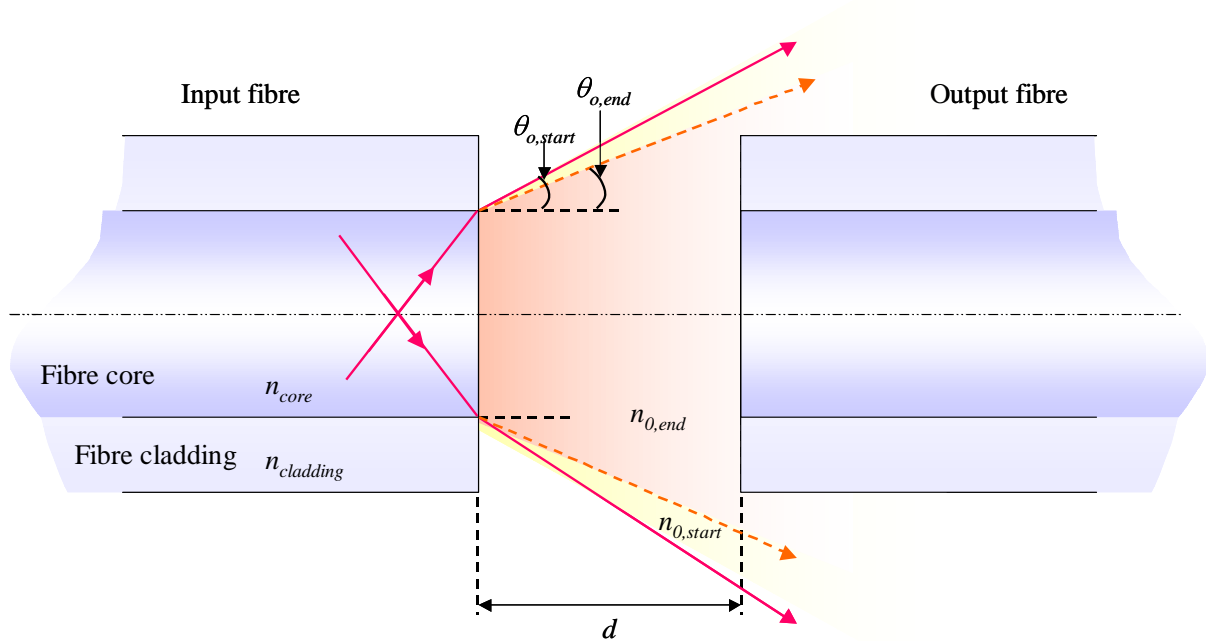


Figure 5.53 Schematic illustration of change in half-angle of cone of acceptance, θ_o at the input fibre/resin interface as a function of change in refractive index of LY3505/XB3403 resin system.

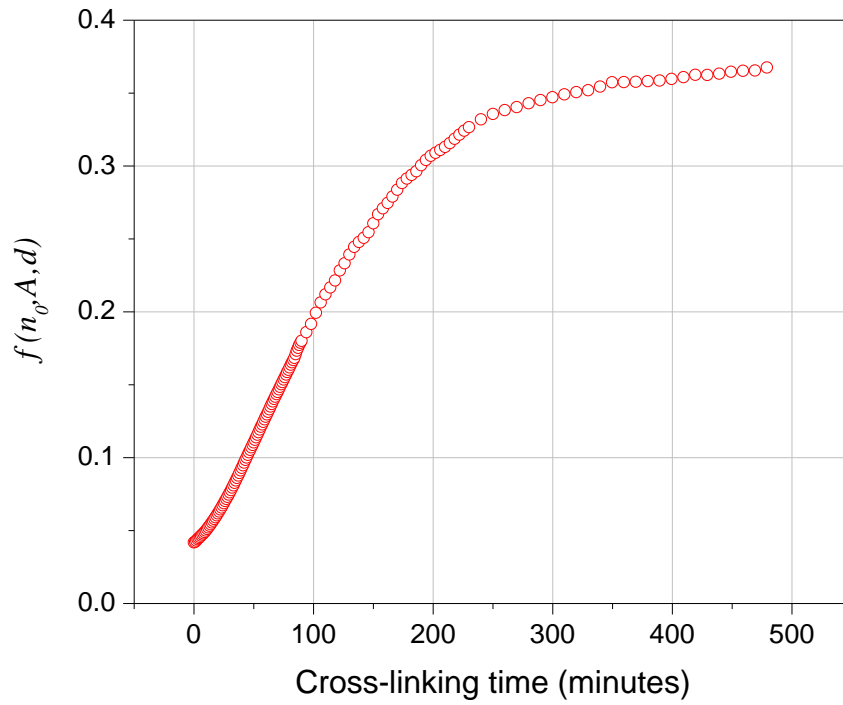


Figure 5.54 Change in $f(n_o, A, d)$ for fibre-optic transmission spectroscopy at 2207 nm and $d = 500 \mu\text{m}$ as a function of cross-linking time.

5.4.4.2 Ray optics of Fibre-optic reflectance spectroscopy

Fibre-optic near-infrared reflectance spectroscopy was also used to predict the refractive index of the epoxy/amine resin during cross-linking using the model proposed by Crosby [149]. Spectral data obtained for monitoring of cross-linking reaction of the LY3505/XB3404 resin system at 60°C using fibre-optic reflectance spectroscopy was used. In Figure 5.55, the predicted refractive index of resin during cross-linking reaction is compared with degree of conversion. The predicted refractive indices of resin, before and after cross-linking show a reasonable fit with the measured values and also with those predicted using fibre-optic near-infrared transmission spectroscopy.

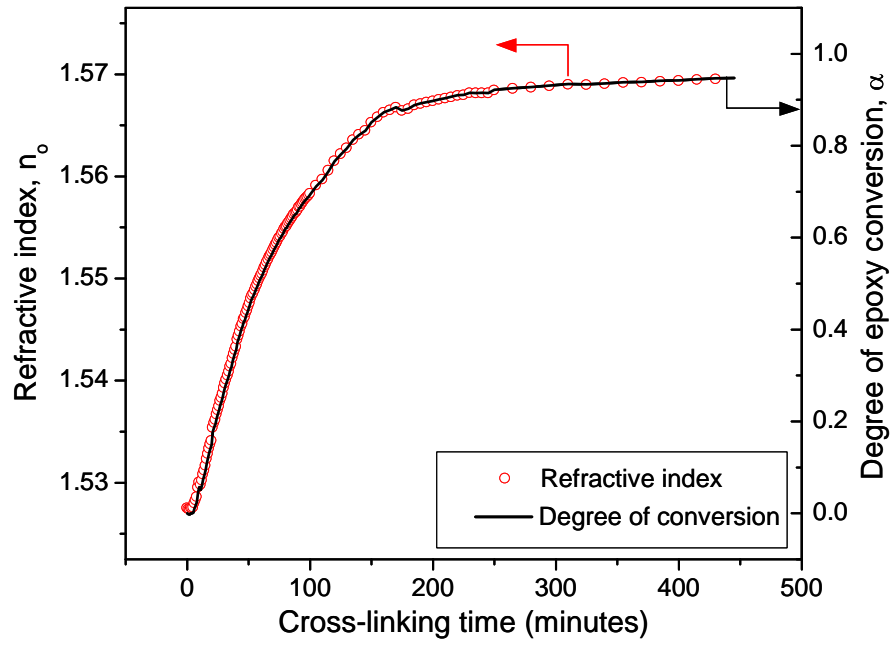


Figure 5.55 Comparison of predicted refractive index (see Equation 5.13) and degree of conversion of LY3505/XB3403 resin system obtained at 60 °C for 8 hours.

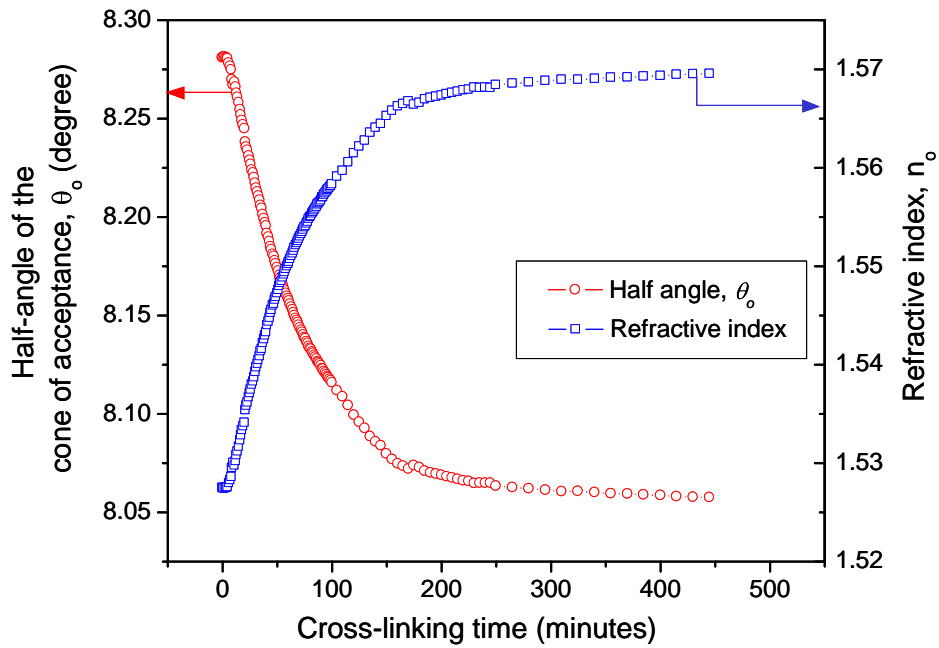


Figure 5.56 Comparison of change in refractive index (see Equation 5.13) of LY3505/XB3403 resin system cross-linked at 60 °C for 8 hours and half-angle of cone of acceptance, θ_o (see Equation 4.3) at the input fibre/resin interface.

Furthermore, the relationship of refractive index of the resin and half-angle of cone of acceptance, θ_o shows a similar trend with that observed with the fibre optic near-infrared transmission spectroscopy (see Figure 5.52 and Figure 5.56). The predicted results of optical parameters before and after cross-linking of LY3505/XB3403 resin system are given in Table 5.5.

The fraction of power of IR radiation that couples back to the sensing fibre as a function of cross-linking time at 60 °C was modelled using Equation 4.7. Spectral data obtained during *in situ* cross-linking using fibre-optic reflectance spectroscopy were used for absorbance calculations. The absorption peak related to the epoxy group at 2209 nm was considered to obtain the change in absorbance during cross-linking. Here, the loss of power due to the reflection of light at the sputter-gold coated reflector was also considered. The reflectance from a thin gold coating in the near-IR region was reported in the range of 95 – 98 % depending on deposition technique used, deposition conditions and the thickness of the sputter-coated gold layer [381,382,383]. Therefore, to stimulate the highest possible loss at the reflector, the reflectance at the sputter-gold coating was considered as 95% of the incident light. As can be seen from the Figure 5.57, the change in fractional component, $f(n_o, A, d)$ that enters back to the fibre increases as refractive index of the resin increases.

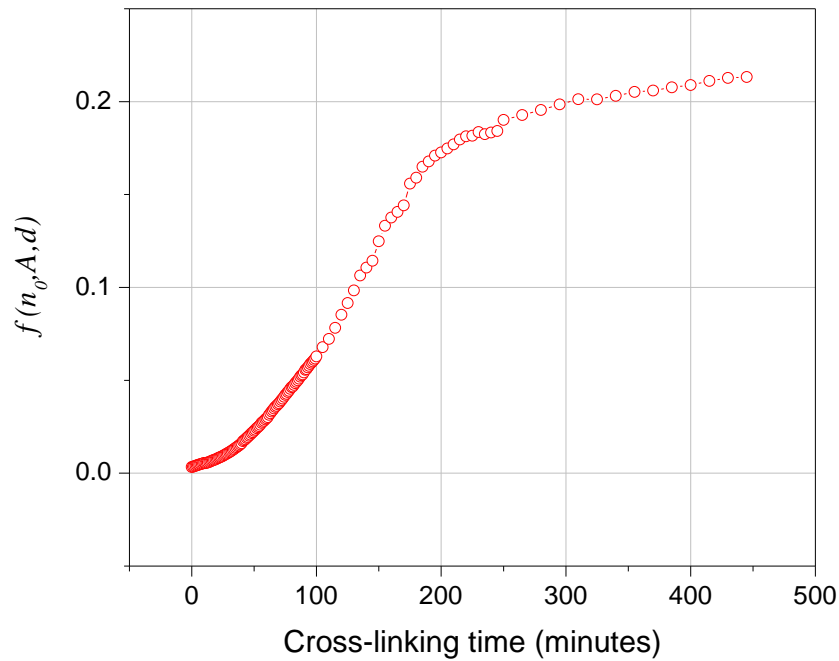


Figure 5.57 Change in $f(n_o, A, d)$ for fibre-optic reflectance spectroscopy at 2209 nm and $d = 500 \mu\text{m}$ as a function of cross-linking time.

Table 5.5 Summary of results obtained for ray optics of fibre-optic reflectance for LY3505/XB3403 resin system with in the sensing cavity.

	Before cross-linking	After cross-linking at 60°C for 8 hours
Refractive index (at 60 °C)	1.5275	1.5702
Half-angle of cone of acceptance, θ_o (degree)	8.281	8.054
Fraction of input power, $f(n_o, A, d)$	0.003	0.211

5.4.4.3 Comparison of ray optics of different fibre-optic techniques

Figure 5.58 compares the change in $f(n_o, A, d)$ during cross-linking of the epoxy resin system under transmission and reflectance modes. It was observed that for same cavity length, d , fibre-optic reflection spectroscopy shows a low coupling ratio of reflected IR radiation back to the detector compared with that observed from fibre-optic transmission spectroscopy (see

Figure 5.58). According to Equation 4.6, this is mainly due to three reasons: the absorption of the IR beam at the reflector, divergence of the IR beam, and the power loss due to the doubling effect of path-length in reflection mode as IR beam travels twice across the sensing cavity (see Figure 4.3).

Nevertheless, in reflectance mode the coupling ratio of reflected IR radiation could be improved by decreasing the cavity length, d (see Equation 4.6). Therefore, the effect of decrease in cavity length on the quality of near-IR spectra obtained via fibre-optic reflectance spectroscopy was investigated and the results will be discussed in Sections 6.3.1.

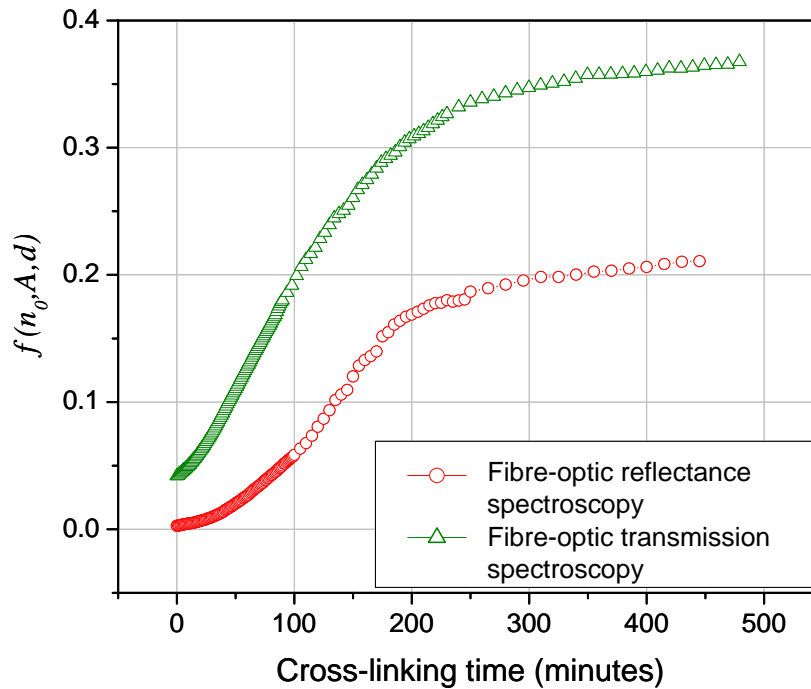


Figure 5.58 Comparison of the change in $f(n_o, A, d)$ at 2207 nm and $d = 500 \mu\text{m}$ as a function of cross-linking time, that predicted using fibre-optic transmission spectroscopy and fibre-optic reflectance spectroscopy.

The increase in light coupling efficiency with increase in refractive index during cross-linking of the resin system also can be evident from near-infrared spectra obtained using fibre-optic

spectroscopy. It was also observed that the baseline of the absorbance spectrum that was acquired using fibre-optic sensors shifts below zero absorbance (see Figure 5.59). The corresponding background spectrum, which was taken in air and the sample spectrum of the LY3505/XB3403 resin system, is shown in Figure 5.60. It can be seen that within 950 – 2160 nm, the signal intensity of the sample spectrum is higher than that of the background spectrum. According to Equation 2.25, absorbance, A_λ become negative because for $I/I_o > 1$, $0 < \log (I/I_o) < 1$.

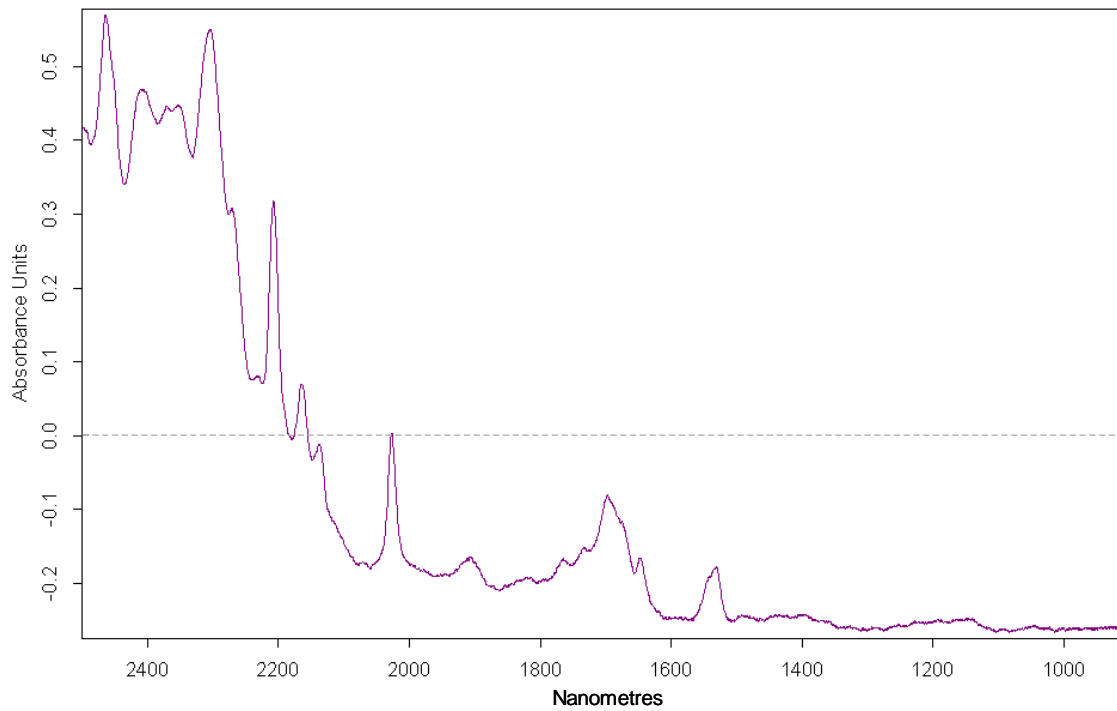


Figure 5.59 Near-infrared spectrum of the LY3505/XB3403 resin system obtained using a single-fibre transmission spectroscopy with 500 μm sensing cavity.

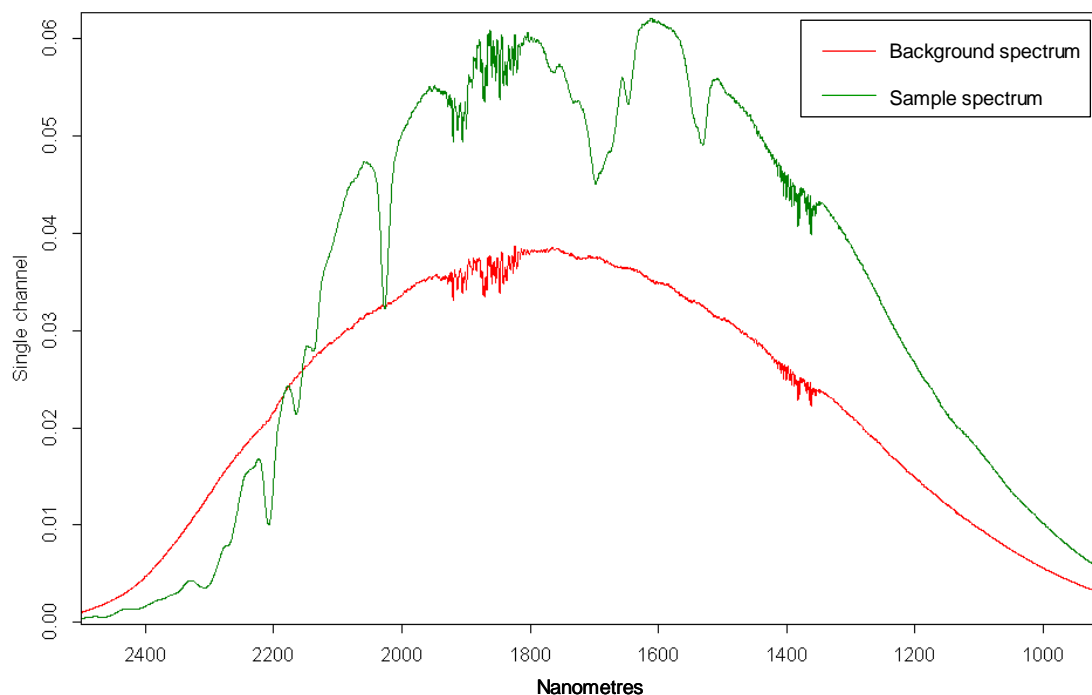


Figure 5.60 Background and sample spectra of the LY3505/XB3403 resin system obtained using a single-fibre transmission spectroscopy with 500 μm sensing cavity length.

The increase in intensity of the sample signal is attributed to the decrease in half-angle of cone of acceptance, θ_o at the input fibre end. During background measurement, the sensing cavity was in air and θ_o was calculated to be 12.709° . This angle converges to 8.281° when the sensing cavity was filled with resin. Therefore, the fraction of the IR beam coupling into the output fibre is higher when the resin was placed in the cavity compared to the case where the background was taken in air.

5.5 Conclusions

Quantitative analysis of the reactive functional groups in the LY3505/XB3404 resin system was carried out using fibre-optic spectroscopy. In order to determine the peak area of the

absorbance band due to epoxy ring at 2207 nm, a method was proposed to deconvolute the overlapped absorbance peak that appeared at 2190 nm.

In situ monitoring of cross-linking reactions in the epoxy/amine resin system was carried out using two fibre-optic sensing techniques: transmission spectroscopy and reflectance spectroscopy. The cross-linking process was evaluated at four reaction temperatures, 40, 50, 60 and 70 °C. The change in concentrations of epoxy, primary amine and secondary amine groups during cross-linking was determined based on the absorption bands at 2207 nm, 2026 nm and 1532 nm, respectively. Absorption bands due to tertiary amine groups are not present in near-infrared region. Although absorption band due to hydroxyl groups was observed at 1430 nm, analysis of this peak is complicated by the presence of hydrogen bonding. Therefore the concentration of tertiary amine and hydroxyl groups were determined using mass-balance equations.

Kinetic modelling of the cross-linking process was carried out based on the results obtained for the degree of epoxy conversion as a function of reaction time and reaction temperature. An autocatalytic model was used to predict the reaction mechanism in the epoxy/amine resin system. Good correlation was observed between the model fits to the experimental data during the cross-linking process.

Spectral data obtained under transmission and reflection modes during cross-linking of the epoxy resin system were used to predict the ray-optic model. The change in light transmission characteristics at the sensing region during cross-linking of the resin system were obtained as a function of absorption of epoxy peak at 2207 nm, refractive index of the resin and the cavity length of the sensor.

Chapter 6

Proof-of-concept of multi-functional sensor design

6.1 Introduction

This chapter presents proof-of-concept of multi-functional sensor design for monitoring the cross-linking reactions of the LY3505/XB3403 resin system. First part of the chapter discusses preliminary results of monitoring strain and temperature sensitivity of the primary EFPI/FBG sensor will be discussed. The second part investigates the feasibility of using a multi-functional sensor design for *in situ* monitoring of multiple parameters during cross-linking of the epoxy/amine resin system was also will be presented.

6.2 Temperature and strain sensitivity of the sensor design

With reference to Figure 3.32, the basic sensor design is based on a conventional extrinsic fibre Fabry-Perot interferometric (EFPI) sensor. Since the gauge length of the EFPI sensor is known (distance between the two fusion joints [D and D'], any changes in the cavity length [C] will enable the strain to be calculated. An array of EFPI and fibre Bragg grating (FBG) sensors (see Figure 3.34) was employed to verify the consistency of EFPI and FBG sensor responses for both temperature and resin shrinkage during cross-linking. Two sensor-interrogation systems were used to cross-correlate the sensitivity of the systems against each other (see Section 3.9.4).

6.2.1 Temperature sensitivity of Fabry-Perot interference sensor and fibre Bragg grating sensor

The sensing principles and relevant equations for strain and temperature measurements using the primary EFPI and FBG sensors are summarised as follows. The primary Fabry-Perot (FP) cavity length, d , can be determined from the interference fringe separation across a spectral width of $\Delta\lambda$ using the following equation:

$$d = \frac{n\lambda_1\lambda_2}{2000\Delta\lambda} \quad \text{Equation 6.1}$$

where λ_1 , λ_2 are optical wavelengths (in nm) that are 2π in the phase separation between adjacent maxima. The cavity length of the EFPI sensor depends on the external strain and thermal effect. Thus the change in FP cavity length, Δd can be represented as [384]:

$$\Delta d = L.\varepsilon + A.\Delta T \quad \text{Equation 6.2}$$

where ε is applied longitudinal strain, L is gauge length, ΔT is change in temperature. A is the change in length of the sensor due to change in temperature and is expressed as $A = L(\alpha_q - \alpha_f)$. Here, α_q and α_f are the linear thermal expansion coefficient (TEC) of the quartz capillary and the optical fibres respectively. According to the experimental data obtained within the temperature range 30 – 80 °C, no clear relationship was found between the cavity length and the temperature (see Figure 6.1). However an attempt was made to calculate the linear TEC of the optical fibre equivalent to the observed variation in cavity length within the test temperature range. The calculated value is of the order of $10^{-7} \text{ }^\circ\text{C}^{-1}$, which is less than the typical TEC of quartz capillary and optical fibre, $0.55 \times 10^{-6} \text{ }^\circ\text{C}^{-1}$ [384]. This is in good agreement with the previous investigations [385,386] and it was suggested that, as the linear TEC of the quartz capillary and the optical fibre are very similar, Equation 6.2 can be rearranged as [384]:

$$\varepsilon = \frac{\Delta d}{L} \quad \text{Equation 6.3}$$

In the case of FBG sensors, the Bragg wavelength shift, $\Delta\lambda_B$, caused by the change in applied strain ($\Delta\varepsilon$) and change of temperature (ΔT) can be expressed as below [387]:

$$\Delta\lambda_B = \alpha.\Delta\varepsilon + \beta.\Delta T \quad \text{Equation 6.4}$$

where $\alpha = \lambda_B(1 - p_e)$ and $\beta = \lambda_B(\alpha_\Lambda - \alpha_n)$, p_e is effective strain-optic constant, α_Λ is the linear TEC for silica, α_n is the thermo-optic coefficient, α and β are the relevant wavelength-strain sensitive factor and wavelength-temperature sensitive factor, respectively.

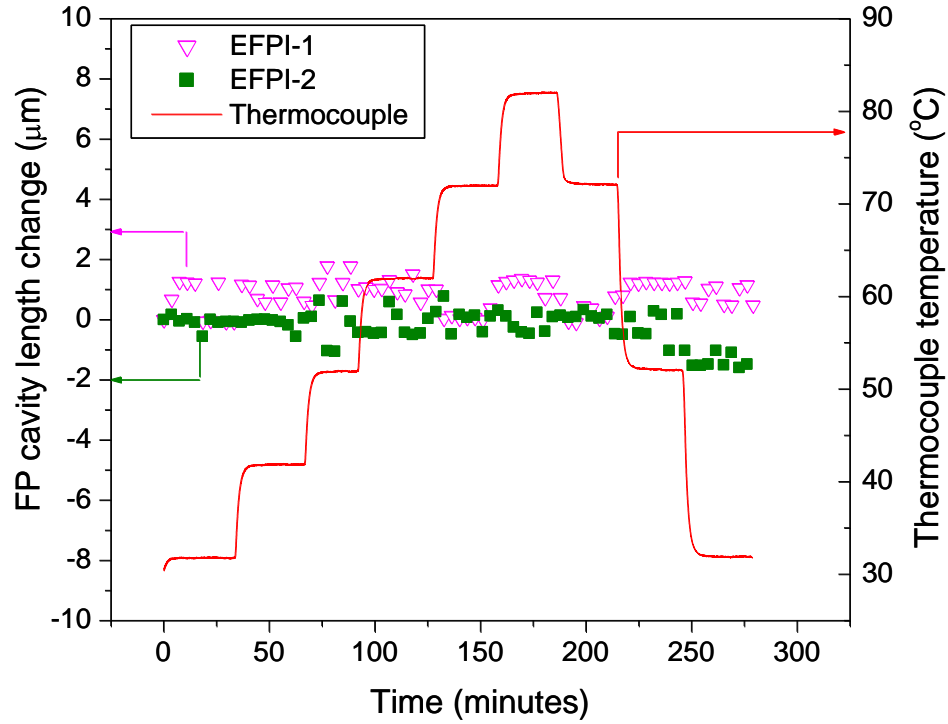


Figure 6.1 EFPI sensor response to temperature when subjected to a series of step/ramp temperature experiments in a temperature-regulated cuvette holder.

Temperature sensitivity of FBG sensors inscribed on Ge-B co-doped single-mode fibre was investigated using sealed gratings. Bragg wavelength shift, $\Delta\lambda_B$ as a function of temperature was measured using sealed FBGs. Here the FBG sensor was sealed in a precision-bore capillary. The experiment was carried out in a temperature-regulated cuvette holder and the temperature of the system was increased from 30 °C to 80 °C in 10 °C steps. The temperature in the vicinity of the sealed FBG sensor was also measured using a K-type thermocouple. The Bragg wavelength shift with temperature was linear over the test temperature range as

shown in Figure 6.2 and the temperature sensitivity factor, β was calculated as $8.91 \text{ pm } ^\circ\text{C}^{-1}$ and $9.86 \text{ pm } ^\circ\text{C}^{-1}$ for FBG-T1 and FBG-T2 interrogated via OSA and FiberPro interrogation unit, respectively. Good correlation was obtained between the results obtained and that published in literature [388]. The difference in β obtained using FiberPro and OSA could be due to specifications of the measurement systems and the sensor packaging.

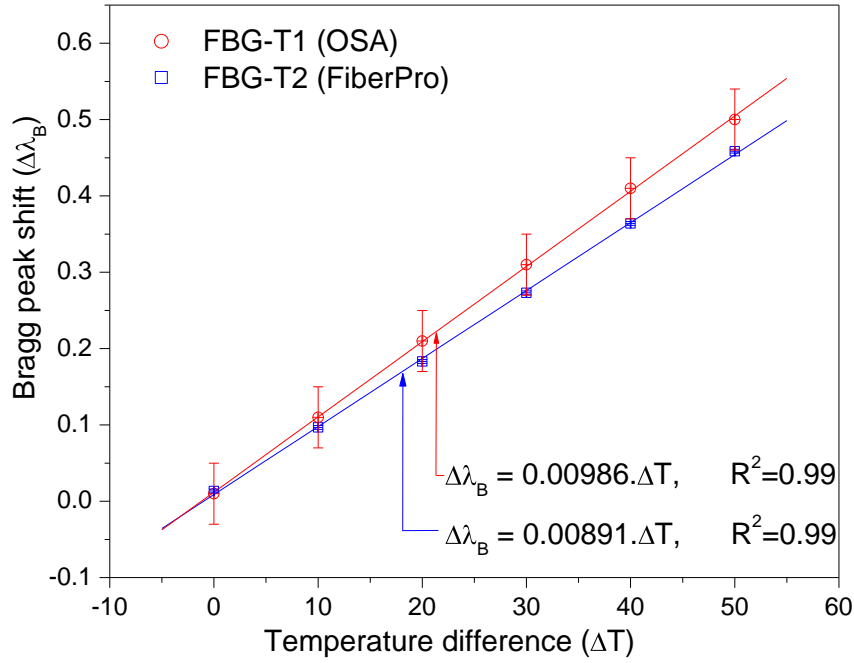


Figure 6.2 Bragg peak shift due to dynamic-step temperature scan that monitored via OSA and FibrePro interrogation unit.

The resolution of the OSA and Fibrepro interrogation units are 0.07 nm [389] and 0.001 nm [390], respectively. Therefore measurements based on the Fiberpro possess higher measurement accuracy in defining the peak wavelength of the FBG. But this only explains the error of the peak maximum determined from the measured data rather than the wavelength accuracy of the data. The OSA wavelength scale has a wavelength accuracy of $\pm 0.05 \text{ nm}$ in the wavelength range of $1530 - 1570 \text{ nm}$ [389]. In contrast, the wavelength accuracy of the Fibrepro system is $\pm 0.005 \text{ nm}$ [390]. Based on these specifications, the measurement error involved in determining change in wavelength as a function of temperature using each system

was plotted as shown in Figure 6.2. It can be clearly seen that the overall error associated with the measurements (FBG-T1) based on OSA is higher compared with that observed based on Fibrepro Interrogation system (FBG-T2).

On the other hand, sensor packaging may have an influence on the sensor response. The same procedure that was used for manufacturing the EFPI in terms of fusing and sealing was used here. It is possible that packaging was different in the two sensors but every effort was taken to keep the dimensions and fabrication procedures similar. The procedure used was as follows.

A precision-bore quartz capillary with 128 μm internal diameter was used for packaging the FBG sensors. Approximately 35 mm long capillary was used and one end was sealed using a fibre-optic splicer. The FBG sensor was then inserted into the capillary using the fibre-optic splicer. The capillary and the fibre were fused together as shown in Figure 6.3 and care was taken to keep the splice well away from the FBG. Approximate distance between the sealed end of the capillary and the end of the sensing fibre was 10 mm.

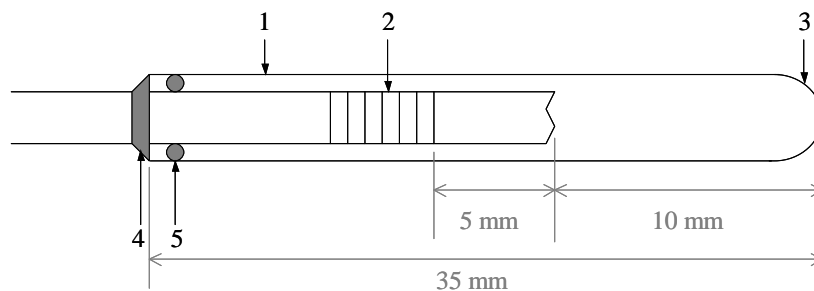


Figure 6.3 Schematic illustration of sealed FBGs [1] fused silica capillary. [2] FBG sensor. [3] fused end of the capillary. [4] high-temperature epoxy adhesive and [5] fusion arc between capillary and the sensing fibre.

Since the same fibre was used to inscribe the gratings, the only possible explanation is that the packaged sensors were different. Possible reasons for this included the following:

- (a) Obstructions/defects in the capillary that preventing ‘free’ thermal expansion of the fibres; and
- (b) Cantilevered sensor where the end of the optical fibre was in contact with the capillary.

Table 6.1 presents a summary of the temperature sensitivity for FBGs inscribed in photo-sensitive fibre. With reference to Table 6.1, it is apparent that the values quoted for the temperature sensitivity of the PS1250/1500 fibre range between $7.37 - 9.37 \text{ pm } ^\circ\text{C}^{-1}$. The values obtained in the current study were 9.86 and $8.91 \text{ pm } ^\circ\text{C}^{-1}$ for the OSA and Fiberpro, respectively. No obvious explanation can be stated for the divergent behaviour of the two data sets in Figure 6.2. This aspect needs a further detailed study.

Table 6.1 Summary of values reported in the literature for the temperature sensitivity of single-mode Germania-Boron (Ge-B) co-doped optical fibre (PS1250/1500, Fibercore Ltd.).

Reference	β (pm °C ⁻¹)	λ_B (nm)	$K_T \times 10^{-6}$ (°C ⁻¹)	Instrument used
Cavaleiro <i>et al.</i> [391]	7.37	1280	5.76*	Optical spectrum analyser.
Pal <i>et al.</i> [392]	8.59	1536	5.59*	HP 86140A (Agilent) optical spectrum analyser. (Based on technical specifications of the model, minimum resolution is reported as ± 0.07 nm.)
Pal <i>et al.</i> [388]	8.99	1534	5.86*	Optical spectrum analyser with a resolution of 0.1 nm.
Yeo <i>et al.</i> [393]	9.3	-	-	si720 swept-laser FBG interrogation unit (Micron Optics). (Based on manufacturer's specifications, typical resolution of the unit is reported as ± 0.001 nm).
Yoon <i>et al.</i> [394]	9.19*	1532	6.00	A tunable laser, a photo detector and a wavelength meter was used at ± 0.1 pm resolution.
De Oliveira <i>et al.</i> [395]	9.37*	1561	6.00	Manufacturer's specifications.
Rysman <i>et al.</i> [396]	8.03	1548	5.19*	AQ6317C optical spectrum analyser and AQ4222 EE LED source. (According to the instrument specifications the resolution is ± 0.1 nm for the range of 600 – 1750 nm).
Harris and Fernando [397]	9.2	1542	5.97*	IS7000 FBG interrogation system with a resolution of ± 0.001 nm.
Park <i>et al.</i> [398]	9.35	1532	6.10*	IS7000 FBG interrogation system with a resolution of ± 0.001 nm.
Current study	9.86	1540	6.40	Optical spectrum analyser with a resolution of ± 0.07 nm
	8.91	1540	5.78	FiberPro 7000 FBG interrogation system at ± 0.001 nm resolution.

*Calculated values using $K_T = \beta / \lambda_B$ on the data reported.

6.2.2 Strain sensitivity of Fabry-Perot interference sensor and fibre Bragg grating sensor

The same sensor configuration was used to determine the resin shrinkage of the epoxy/amine resin system. The experiment started at 30°C in air, mixed resin was injected at 30°C and heated up to 60°C using the thermo-control holder and cross-linking was carried out isothermally at 60°C for 8 hours. After 8 hours, the system was cooled down to 30°C. The resin shrinkage was measured using both embedded EFPI and FBG sensors.

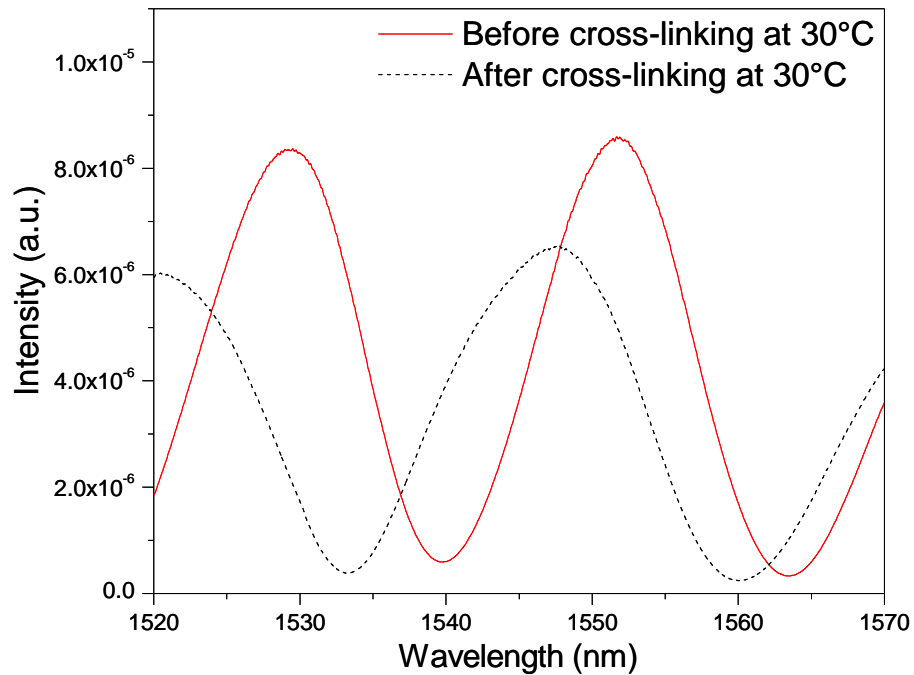


Figure 6.4 Typical EFPI fringes before and after cross-linking of LY3505/XB3403 resin system at 60°C for 8 hours.

The change in FP cavity length due to resin shrinkage is clearly seen from the shift of fringe pattern shown in Figure 6.4. The spectra were obtained using OSA and the longitudinal strain applied on the EFPI sensor was determined using Equation 6.3. Based on EFPI-1 and EFPI-2

sensors, measured compressive strain built up during processing of the epoxy/amine resin system at 60 °C were 178 microstrain and 129 microstrain, respectively.

Figure 6.5 shows the Bragg peak shift of sealed and embedded sensors those located inside the resin and recorded using the FibrePro interrogation unit. It can be clearly seen that the embedded sensor (FBG-S2) shows Bragg peak shift due to both temperature and the stresses built up in the resin during cross-linking reaction. On the other hand, the sealed sensors (FBG-T2 and -T3) were sensitive only for the temperature of the system and the corresponding Bragg peaks reverted back to the initial wavelength upon cooling back down to 30°C. Similar responses were recorded using the OSA. Equation 6.4 was used to obtain strain measured using embedded FBG sensors. Response from the sealed FBG sensors was used to determine the temperature effect on the Bragg peak shift of embedded FBG sensors [169].

Strain build up during cross-linking was monitored via the OSA (FBG-S1) and the FibrePro interrogation unit (FBG-S2) are shown in Figure 6.6. In comparison with the thermocouple reading, it can be clearly seen that the resin shrinkage during cooling has major contribution toward the total residual strain developed within the cross-linked resin. The total resin shrinkage after cooling down to 30°C was determined using FBG-S1 and FBG-S2 and the residual compressive strain was calculated to be 320 microstrain and 309 microstrain, respectively.

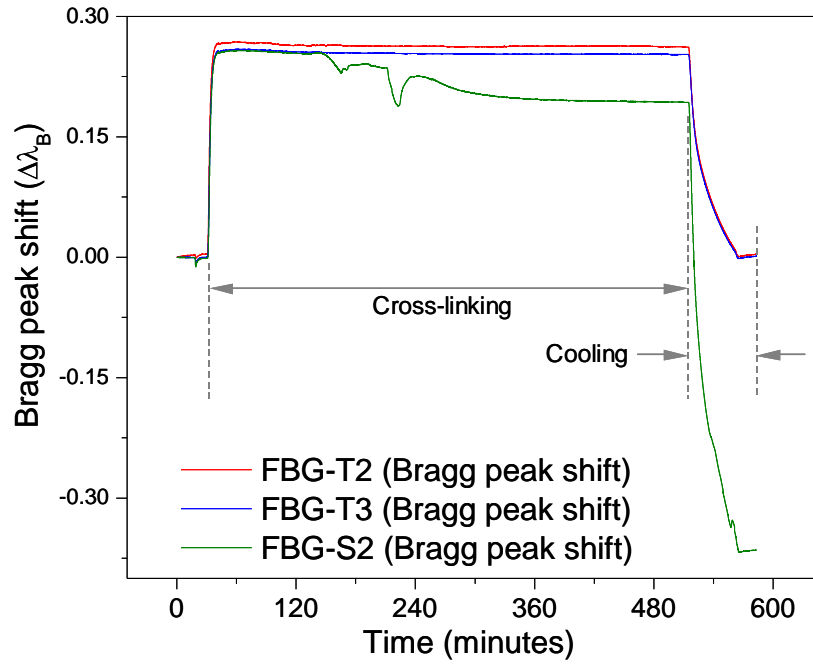


Figure 6.5 Bragg peak shift of sealed and embedded FBGs those monitored via FibrePro interrogation unit. The traces are recorded during cross-linking of LY3505/XB3403 resin system at 60°C for 8 hours and cooling down to 30°C.

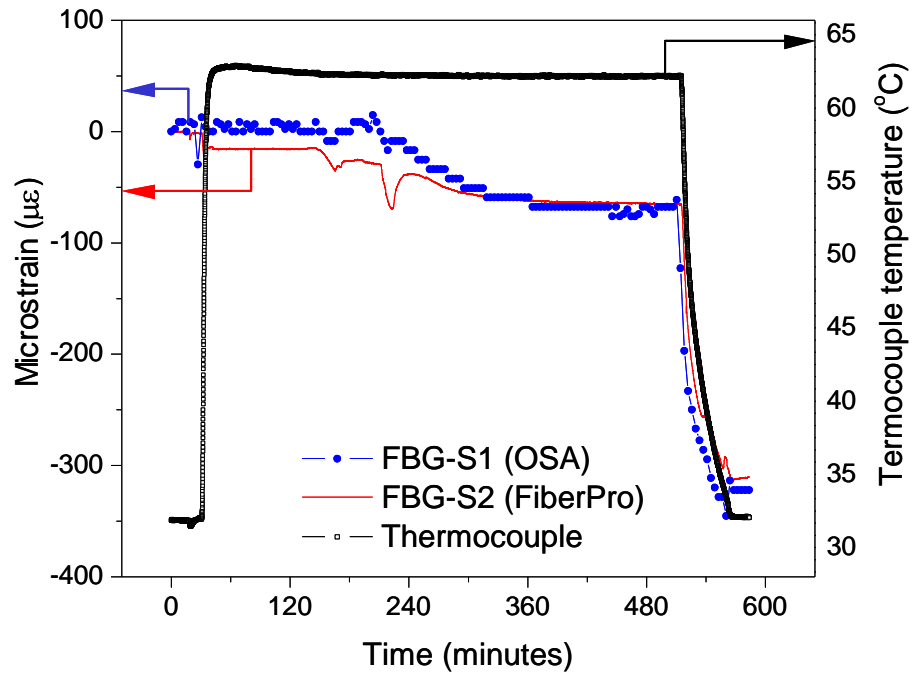


Figure 6.6 Strain due to resin shrinkage in LY3505/XB3403 resin system during cross-linking at 60°C for 8 hours and cooling down to 30°C. Temperature recorded using an independent thermocouple is also presented.

6.3 Monitoring of the cross-linking reactions

In situ monitoring of cross-linking reaction in the LY3505/XB3403 resin system was performed using the multi-functional sensor design. This sensor design is capable of monitoring the relative concentration of specified functional groups using near-infrared spectroscopy, temperature, refractive index and strain during cross-linking of the resin system [375,399,400]. The proof-of-concept for *in situ* monitoring of cross-linking reaction using the fibre-optic multi-functional sensor was carried out at 60 °C for 8 hours.

6.3.1 Quantitative monitoring of the cross-linking reactions

Quantitative analysis of the cross-linking reaction was carried out using fibre-optic reflectance spectroscopy. With reference to Section 3.7.3, one of the secondary fibres that was attached to the multi-functional sensor was used as a fibre-optic reflectance sensor and the cavity length of was 250 μm . The evolution of the near-infrared spectra of the LY3505/XB3403 resin system during cross-linking at 60 °C is shown in Figure 6.7. All the relevant peaks are similar to those described in Section 5.2. For example, the combination band of epoxy at 2207 nm, the combination band of primary amine at 2026 nm and the reference absorption band of aromatic CH at 2164 nm, can be clearly seen. The depletion of the amine and the epoxy functional groups is also readily apparent in Figure 6.7 as the cross-linking reaction proceeds. The degree of conversion based on the concentration of epoxy groups was obtained using Equation 5.11.

However, it is apparent that repetitive fringe pattern is superimposed on the spectra due to the multiple-beam reflections (see Section 5.2). The intensity of the fringes is higher than that was observed from the spectral data presented previously and using fibre-optic reflection spectroscopy with a cavity length of 500 μm (see Figure 5.35). In the multi-functional sensor design, the cavity length was set to be 250 μm ; as the cavity length decreases the intensity of the Fabry-Perot interference increases. Although the light-coupling ratio of the sensor design could be improved with decreasing cavity length, spectral quality decreases due to the interference of the multiple-beam reflection at the sensing cavity. Further work is necessary to optimise the cavity length for the sensor design.

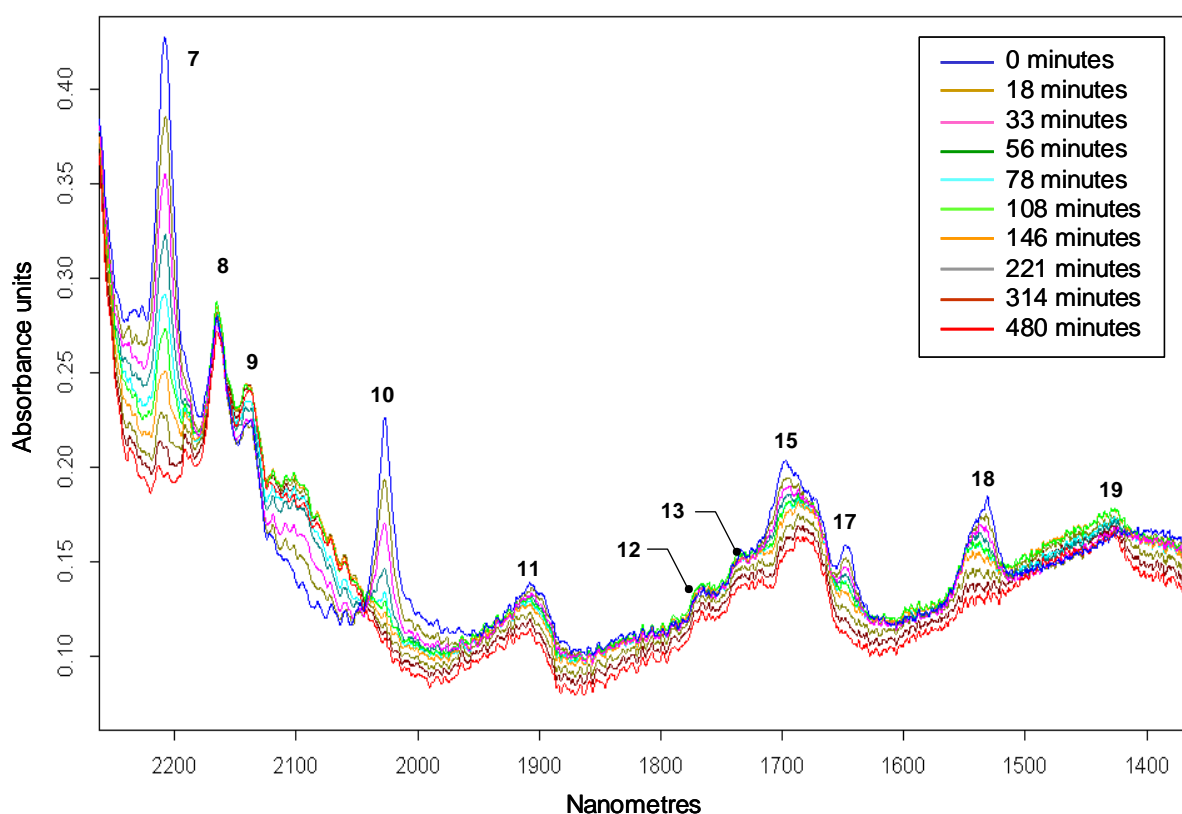


Figure 6.7 Contour spectra recorded during cross-linking of the LY3505/XB3403 resin system at 60 °C using a fibre-optic multi-functional sensor; see Table 5.1 for peak assignments.

Figure 6.8 shows a comparison of the degree of epoxy conversion based on conventional transmission FTIR spectroscopy and that obtained using the multi-functional sensor design (secondary cavities). The data from the multi-functional sensor represents the average of two repeat experiments. Good agreement was observed between the data obtained from the multi-functional sensor and that from the conventional transmission FTIR spectroscopy.

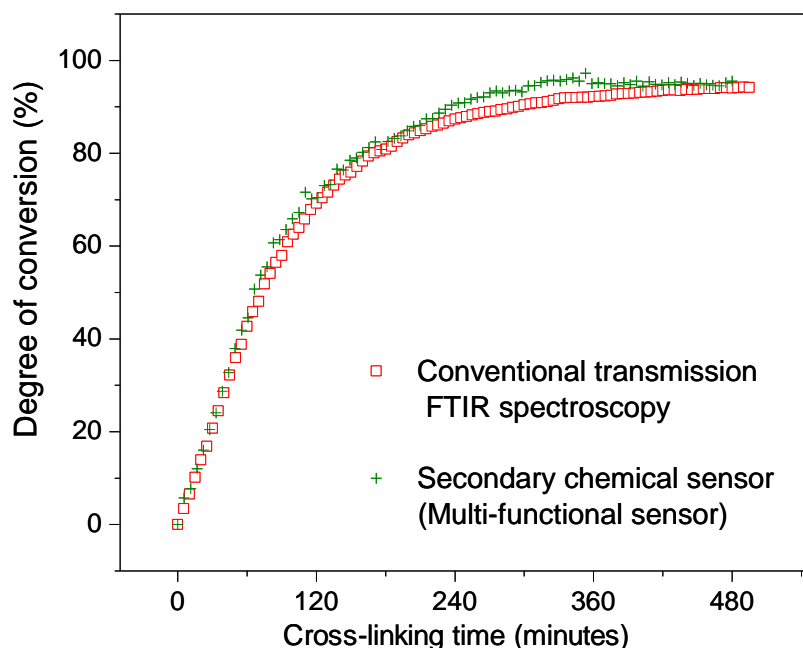


Figure 6.8 a comparison of the degree of conversion of the LY3505/XB3403 resin system at 60 °C based on the multi-functional sensor and the conventional transmission FTIR spectroscopy.

6.3.2 Qualitative monitoring of the cross-linking reactions

With reference to the multi functional sensor, as described in Figure 3.31, the intensity of the reflected light from a pair of cleaved multi-mode optical fibres (distal ends of a 2 x 2 coupler) was used to as a qualitative measure of the changes in the refractive index of the resin during cross-linking. One of the secondary fibres that was mounted on the primary optical fibre of

the multi-functional sensor was used as a Fresnel-based refractive index sensor. The magnitude of the light reflects back due to Fresnel reflection at normal incidence to the cleaved ends of the fibres is a function of the refractive index of the surrounding resin and this can be expressed as:

$$R = \left(\frac{n_{core} - n_{resin}}{n_{core} + n_{resin}} \right)^2 \quad \text{Equation 6.5}$$

where n_{core} and n_{resin} are the refractive indices of the fibre core and the resin, respectively.

With respect to the FTIR-based interrogation of the Fresnel-based reflection sensor, the peak amplitude of the interferogram corresponds to the intensity of the reflected light at the two cleaved fibres immersed in the epoxy resin. The intensity of the reflected light at the fibre/resin interface is a function of the difference between the refractive indices of the fibre core and the resin system. The peak amplitude of the interferogram signal was used as a measure of the intensity of reflected light and this was assumed to be equivalent to the change in the refractive index of the resin during cross-linking.

Qualitative monitoring of the cross-linking reaction using the Fresnel-based reflection sensor is presented in Figure 6.9. The Fresnel-based signal was compared with the degree of conversion obtained using conventional transmission FTIR spectroscopy. The initial decrease of signal amplitude can be attributed to a decrease in the refractive index of the resin mixture when the system was heated from ambient to the required isothermal temperature. Cross-linking of the epoxy/amine resin leads to an increase in the molecular weight, density and the refractive index. The gradual increase followed by stabilization can be attributed to a gradual increase and stabilization of refractive index as the extent of cross-linking approached near-

completion. However, it is important to note that prior calibration is required to determine the degree of conversion. The Fresnel-based sensor can only indicate the reaction rate and the end point of the cross-linking reaction, at a specified temperature. Therefore the sensor can be used to obtain qualitative information on the cross-linking reaction.

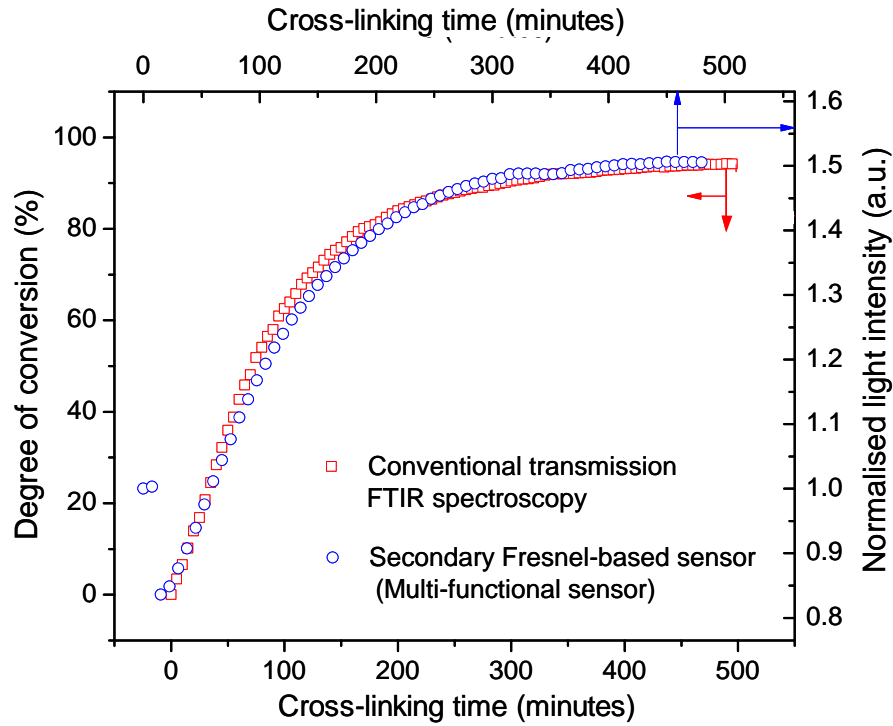


Figure 6.9 comparison of degree of conversion of LY3505/XB3403 resin system at 60 °C obtained using the secondary Fresnel-based sensor and conventional transmission FTIR spectroscopy.

6.3.3 Simultaneous strain and temperature monitoring

One of the main objectives of using the multi-functional sensor design was interrogating the whole sensor assembly using a single interrogation unit. Therefore the attention was also focussed on the light-coupling efficiency of the internal light source of the FTIR spectrometer in the EFPI/FBG sensor. In this set-up, the input fibre was connected to the internal light source of the spectrometer. The response of the combined EFPI/FBG sensor, before and after

cross-linking, at 60 °C is shown in Figure 6.10. It can be clearly seen that the spectral resolution of the fringe pattern is relatively low. It was difficult to define the baseline of the fringes due to spectral noise. This can be attributed to the insufficient light coupling from the internal light source into the single-mode fibres. The optics of the spectrometer is designed for focusing radiation into 600 μm diameter optical fibres. Therefore the percentage of light coupled into a single-mode fibre can be very low. This problem can be solved by using an external light source.

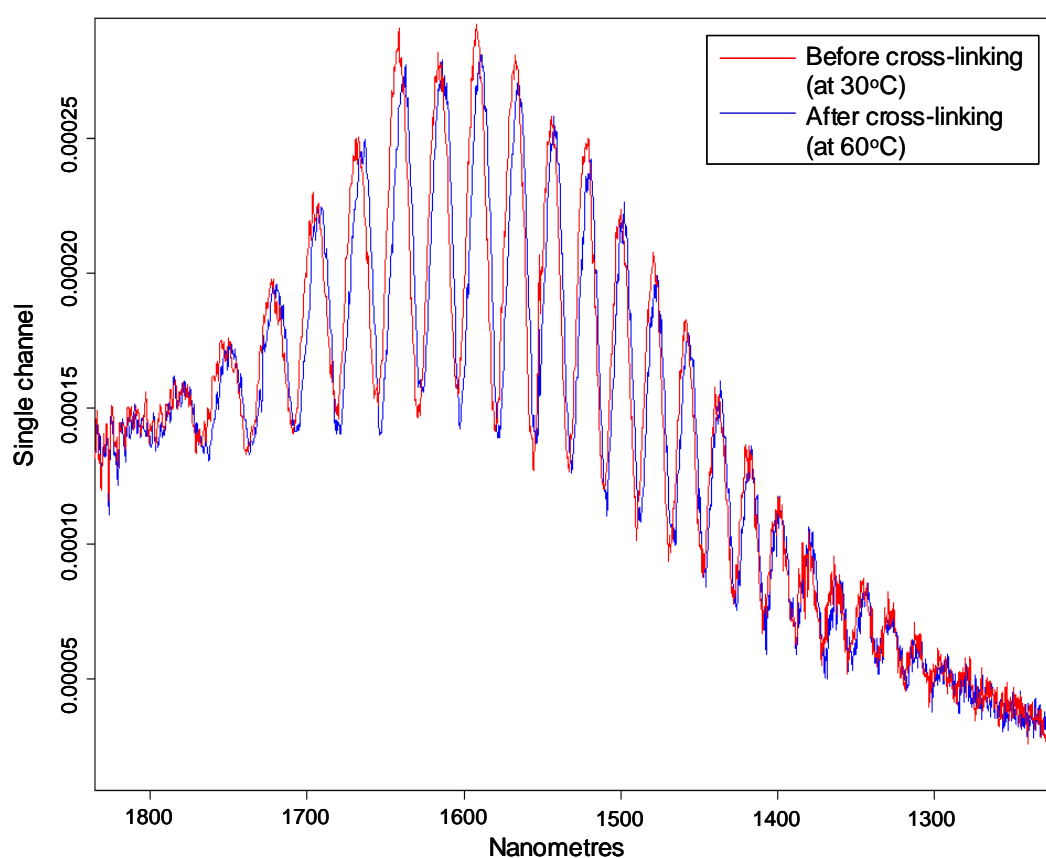


Figure 6.10 Response of a combined EFPI/FBG sensor before and after cross-linking of the LY3505/XB3403 resin system at 60 °C obtained using the internal light source of the FTIR spectrometer.

In an alternative set-up, the combined EFPI/FBG sensor was illuminated using an external ASE light source. Interrogation was carried out using the InGaAs detector on the

spectrometer. The spectral response of the primary FP cavity and the Bragg grating at the start and end of cross-linking reaction at room temperature are shown in Figure 6.11. The inset shows an expanded view where the superimposed FBG peaks are readily visible. It can be seen that the visibility of the fringe pattern is higher compared with that obtained using the internal light source of the spectrometer.

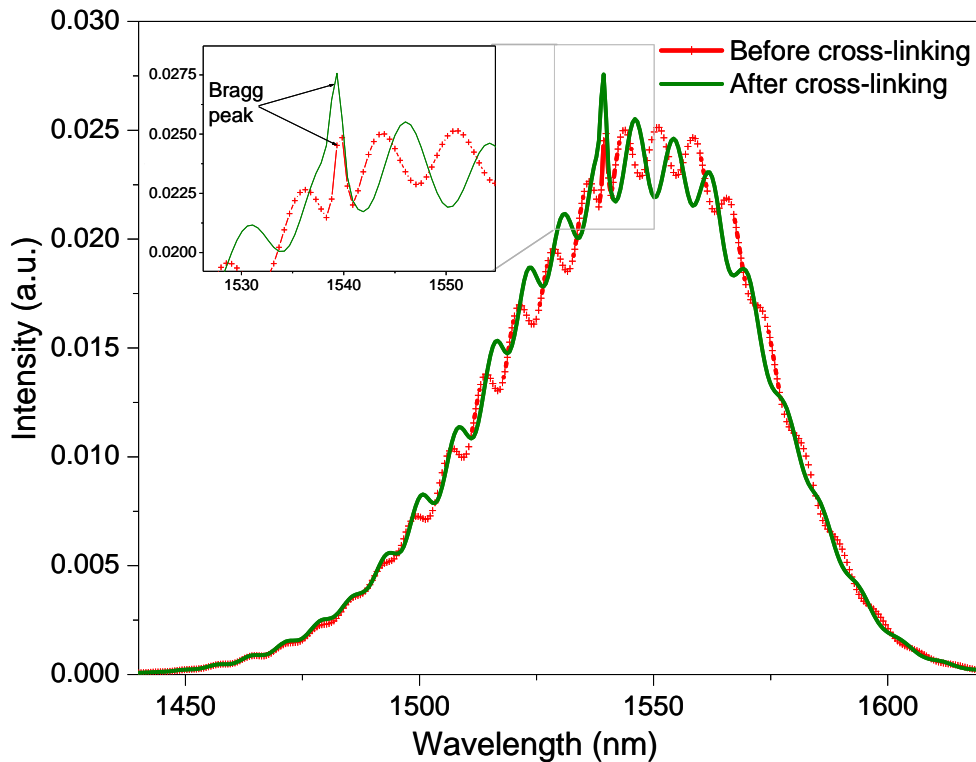


Figure 6.11 Response of a combined EFPI/FBG sensor before and after cross-linking of the LY3505/XB3403 resin system at 60 °C obtained using the external ASE light source.

With reference to the Figure 3.32, the Bragg grating that was inscribed in the primary fibre (located within the cavity) is in a strain-free condition and therefore any shift in the Bragg reflection peak corresponds only to a change in the temperature. This can be clearly seen from Figure 6.11, where no peak shift was observed before and after cross-linking of the resin at room temperature.

A Bragg reflection peak shift of 0.3 nm towards a longer wavelength was observed when the temperature of the resin was raised by 34.6 °C to the isothermal reaction temperature of 60°C. This shift was found to be in good agreement with the Ge-B co-doped Bragg grating temperature sensitivity of 8.59 pm K⁻¹ [388]. The Bragg reflection peak was restored to its initial wavelength when the cross-linked resin was cooled back to room temperature. This demonstrates that the Bragg grating was maintained in a strain-free state during the cross-linking reaction. Figure 6.11 shows the shift of FP interference fringe pattern as a result of the change in the primary FP cavity length due to residual strain and resin shrinkage. The cavity lengths corresponding to before and after cross-linking of the resin system at room temperature were found to be 55.72 mm and 50.15 mm, respectively (see Equation 6.2). The gauge length of the sensors was approximately 36 mm and the compressive residual strain due to process-induced shrinkage of the resin was estimated to be in the range of 150 - 200 microstrain.

6.4 Conclusions

Feasibility of using a new multi-functional sensor design was investigated for monitoring of the cross-linking reactions of thermosetting resins. An attempt was also made to characterise the temperature and strain sensitivity of the EFPI and FBG sensors that were used in the multi-functional sensor design as a combined strain and temperature sensor. The temperature and strain sensitivity during step-temperature ramp in air and also during the cross-linking of the LY3505/XB3403 resin system at 60 °C was investigated. However, in-depth study of the interference of the individual sensor responses on each other is essential in order to generate accurate results using the combined sensor design.

In addition, the multi-functional sensor design was used for monitoring of the cross-linking reactions of the epoxy/amine resin system. Issues related to sensor interrogation of combined FBG/EFPI sensor was also discussed. The degree of conversion obtained based on secondary chemical sensor and secondary Fresnel-based sensor showed good correlation with that obtained using conventional transmission spectroscopy. Residual resin shrinkage developed in the cross-linked resin due to cooling down from reaction temperature to ambient temperature was also determined using the primary EFPI sensor.

Chapter 7

Moisture ingress monitoring using conventional techniques

7.1 Introduction

A wide range of analytical techniques has been used for monitoring the absorption kinetics of epoxy/amine resin systems. In the current study, gravimetry, thermo gravimetric analysis (TGA), differential scanning calorimetry (DSC), dynamic mechanical thermal analysis (DMTA) and conventional transmission Fourier transform near-infrared (FTIR) spectroscopy were used to characterise the absorption of water in the LY3505/XB3403 epoxy/amine resin system. The experiments were carried out at different immersion temperatures and 100% relative humidity (RH). The aims of this study were as follows:

- To determine absorption behaviour and equilibrium moisture content in a cross-linked epoxy/amine resin system using gravimetry as a function of immersion time and temperature.

- To predict the sorption kinetics of the cross-linked epoxy/amine resin system using an appropriate diffusion model.
- To determine the effect of hygrothermal ageing on the thermal, physical, viscoelastic and chemical properties of the cross-linked epoxy/amine resin system.

7.2 Gravimetric method

7.2.1 Kinetics of water absorption

Primary absorption experiments were carried out in order to obtain the overall characteristics of the absorption behaviour of water in the LY3505/XB3403 resin system at different immersion times and temperatures and at 100 % RH. The hygrothermal ageing experiments were carried out in distilled water at 30, 50 and 70 °C. The epoxy resin system was cast between glass plates and cross-linked at 60 °C for 8 hours (see Section 3.8.1.1). Prior to immersion, the as-cast specimens were dried in a dessiccator oven at 50 °C. The drying period was set to approximately eight weeks. The percentage weight loss of the specimens, ΔM was calculated using the following equation:

$$\Delta M = \frac{W_t - W_0}{W_0} \times 100\% \quad \text{Equation 7.1}$$

where W_0 is the initial weight of the specimen and W_t is the weight of the specimen at a given drying time. Typical weight losses observed with five specimens during the drying process are shown in Figure 7.1. The change in weight of cross-linked epoxy at temperatures below T_g could be mainly due to two reasons, evaporation of absorbed moisture and loss of low-

molecular weight components. Due to time constraints, the drying experiments were terminated when the recorded mass-loss was approximately 0.03 % over two consecutive weeks. A similar trend was observed for all the other specimens used in this study. The samples with this preconditioned state were used for all the water uptake experiments.

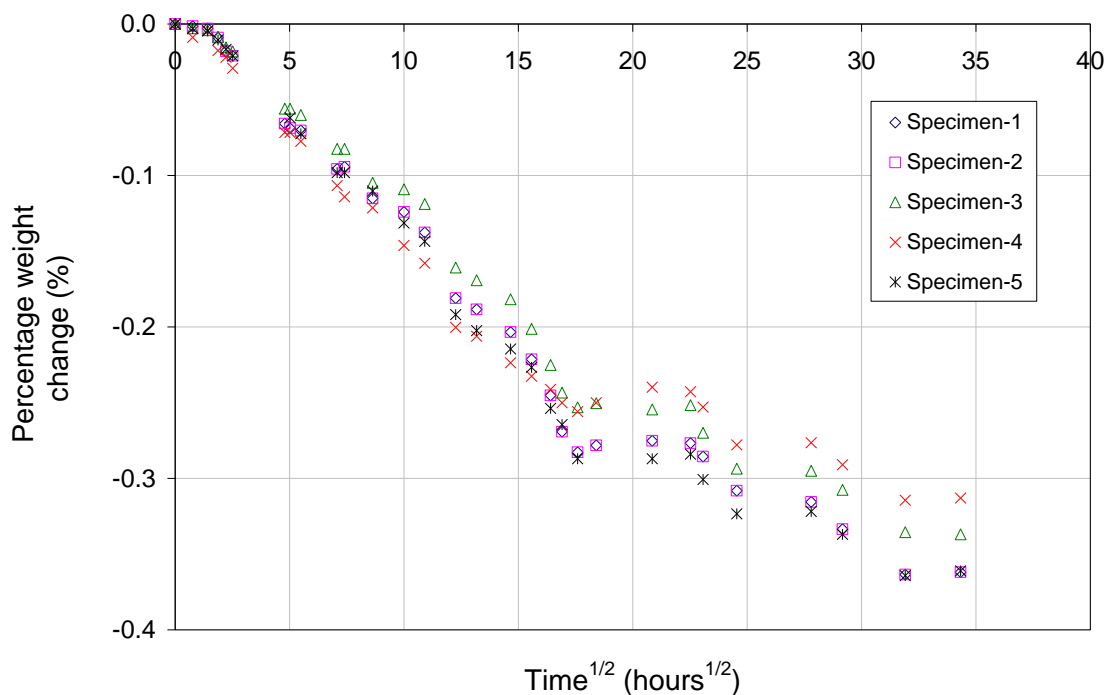


Figure 7.1 Percentage weight change of specimens of the LY3505/XB3403 resin system that conditioned at 50 °C for 8 weeks. The specimens were cross-linked at 60 °C for 8 hours.

The absorption behaviour of the cross-linked epoxy resin after immersion in distilled water at 70 °C is shown in Figure 7.2. The percentage weight gain was plotted against the square root of immersion time (normalised to the thickness, L of the specimen). A negligible weight change was observed during the weighing process of the conditioned specimens; this operation took approximately 5 minutes. An attempt was taken to quantify the weight change whilst the specimens were left at room temperature, in air, for periodic weighing. A sample each was removed from the water-baths that were set at 30, 50 and 70 °C. These samples were transferred to a dessicator for approximately 2 minutes prior recording their individual

masses. The results from these experiments are presented in Figure 7.3. Maximum weight-loss was observed with the specimen that was conditioned at 30 °C and was found to be 0.00015% after 16 minutes of exposure to air at room temperature. Therefore the weight-loss during the weighing process can be neglected.

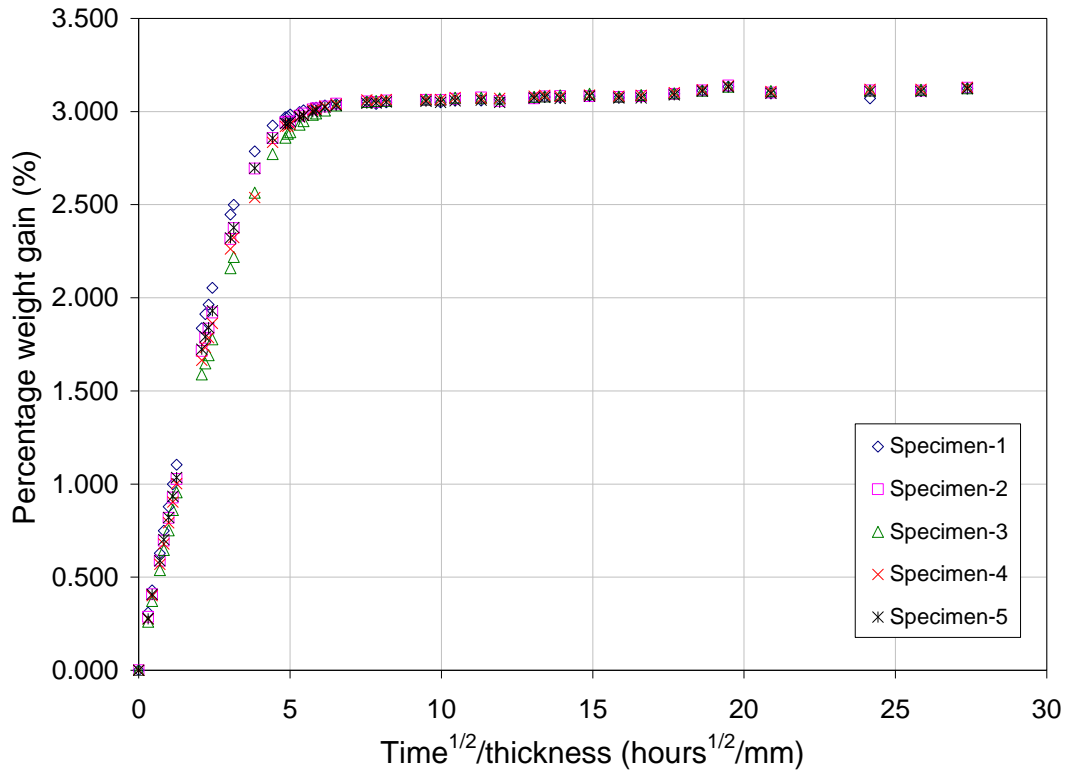


Figure 7.2 Absorption isotherms of water in the LY3505/XB3403 resin system at 70 °C for 20 weeks.

The thickness of the test specimen was made small when compared to the width and length; the dimensions of the specimens were 50 x 50 x 2 mm. The ratio of the edge surface area to the total surface area was only 7%. Therefore, the edge effects can be ignored and simple one-dimensional diffusion can be assumed without incurring significant error [250].

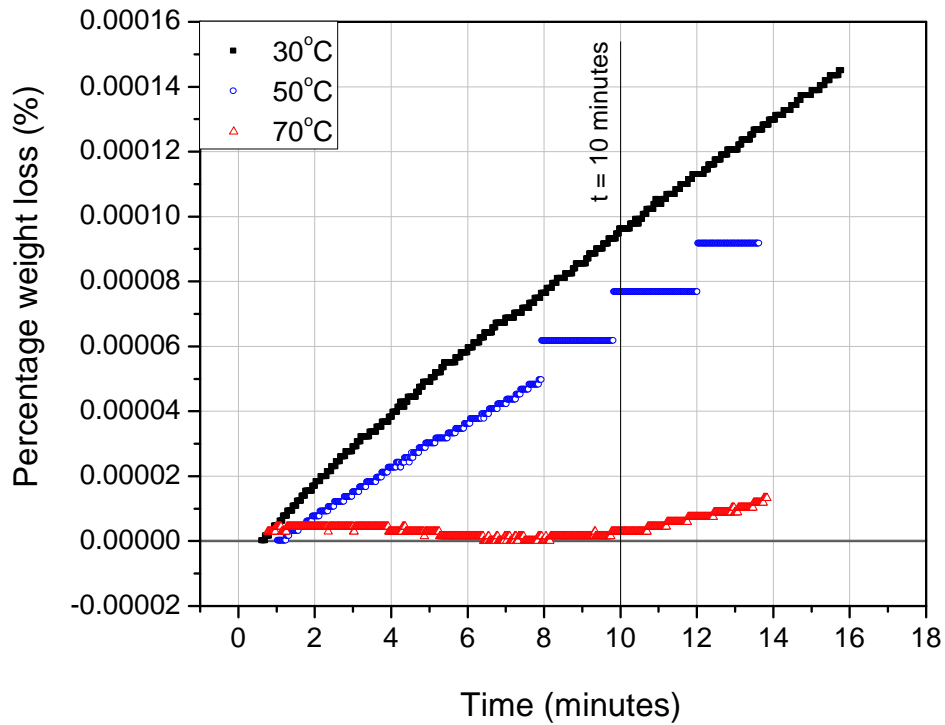


Figure 7.3 Percentage weight-loss of the hygrothermally conditioned specimens during weighing measurements at room temperature.

Figure 7.4 shows the sorption isotherms obtained for the diffusion of water in to the epoxy/amine resin system at different immersion temperatures. Each isotherm represents the average weight gain from five specimens, which were conditioned under identical conditions. The equilibrium moisture contents (M_{∞}) achieved over 2, 9 and 33 weeks, at 70, 50 and 30 °C, respectively were found to be similar irrespective of the immersion temperatures. However, in the case of the samples that were conditioned at 30 °C, the weight gain was seen to increase slowly with immersion time. This may be indicative of the fact that equilibrium moisture content was not achieved at this temperature. However, at longer immersion times at 30 °C, a slow positive deviation from Fickian equilibrium state was observed. At lower temperatures, such continuous slow absorption processes were reported [17] and this could be attributed to either slow relaxation processes of the glassy epoxy network or a more complex, absorption

mechanism which involves an interchange of water ‘cluster’ sizes in the free volume as a function of time and amount of water uptake [401]. The M_{∞} values of the epoxy resin system at each immersion temperature are given in Table 7.1. This absorption behaviour illustrated in Figure 7.4 indicates that the moisture diffusion in the LY3505/XB3403 resin system is Fickian in nature [250,402]. This is in good agreement with the absorption model applied for epoxy/diamine systems [263].

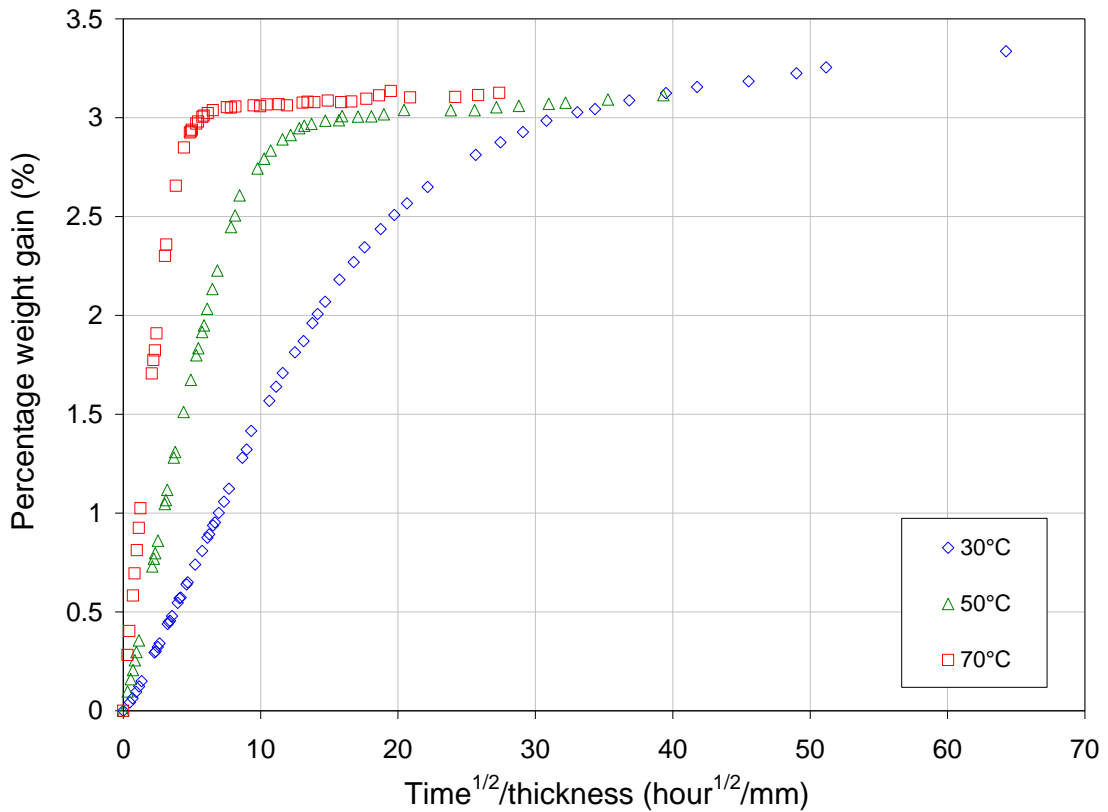


Figure 7.4 Absorption isotherms of water in the LY3505/XB3403 epoxy system at 30, 50 and 70 °C.

Equilibrium moisture content obtained for the epoxy/amine resin system is in good agreement with the values reported by Apicella *et al.* [267], Soles *et al.* [246], Wu *et al.* [279], Maggana and Pissis [403], Abdelkadar and White [277] and DéNève and Shanahan [312] for similar resin systems and for similar hygrothermal conditions. Li *et al.* [249] also observed similar equilibrium moisture content for a DGEBA/DDS system at 40 °C and 100 % RH.

Fick's second law of diffusion has been widely used to model the sorption kinetics of epoxy resin systems. The diffusion coefficients of the epoxy/amine resin system related to each immersion temperature can be calculated using the Fickian diffusion equation. In the case of isotropic thin plates where $L \ll \text{width}$ and $L \ll \text{length}$, the moisture entering the parallelepiped specimen through the edges can be neglected. Using appropriate boundary conditions, a one-dimensional analytical solution proposed by Shen and Springer [255] can be applied to explain the absorption kinetics of the epoxy/amine resin system (see Equation 2.24). For short times, Equation 2.24 can be approximated to Equation 2.25. In Figure 7.5, M_t/M_∞ was plotted against \sqrt{t}/L for the epoxy/amine system at different immersion temperatures. D can then be experimentally obtained from the initial slope of the curves and the values for absorption of water at each immersion temperature are given in Table 7.1. These results are in reasonable agreement with the values reported in the literature [257,249].

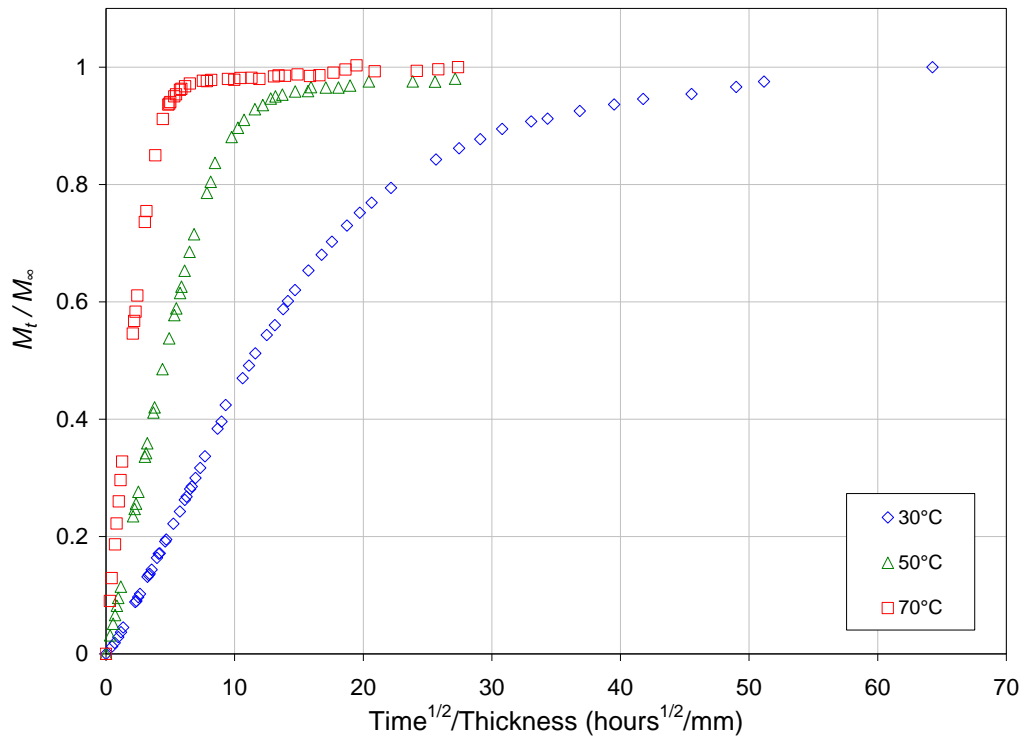


Figure 7.5 Plots of M_t/M_∞ versus \sqrt{t}/L for moisture absorption in the LY3505/XB3403 epoxy system conditioned at 30, 50 and 70 °C.

It can be seen that D varies with temperature, and is expected to follow the classic Arrhenius behaviour:

$$D = D_0 \exp\left(-\frac{Q_d}{RT}\right) \quad \text{Equation 7.2}$$

where D_0 is the temperature-independent pre-exponential factor, Q_d is the activation energy for diffusion, R is the universal gas constant and T is the temperature in K.

Figure 7.6 shows the Arrhenius plot for the diffusion coefficients where a linear relationship was observed. The activation energy for the diffusion of water in to the epoxy/amine resin system was obtained to be 67.89 kJmol⁻¹. These results are in good agreement with the values published in the literature [404,312].

Table 7.1 Summary of sorption kinetics of water in LY3505/XB3403 resin system at different immersion temperatures.

Immersion temperature (°C)	Equilibrium moisture Content (%)	Diffusion constant, $D \times 10^{-6}$ (mm ² sec ⁻¹)
30	3.028±0.030	0.127±0.008
50	3.071±0.022	0.629±0.013
70	3.126±0.055	3.006±0.017

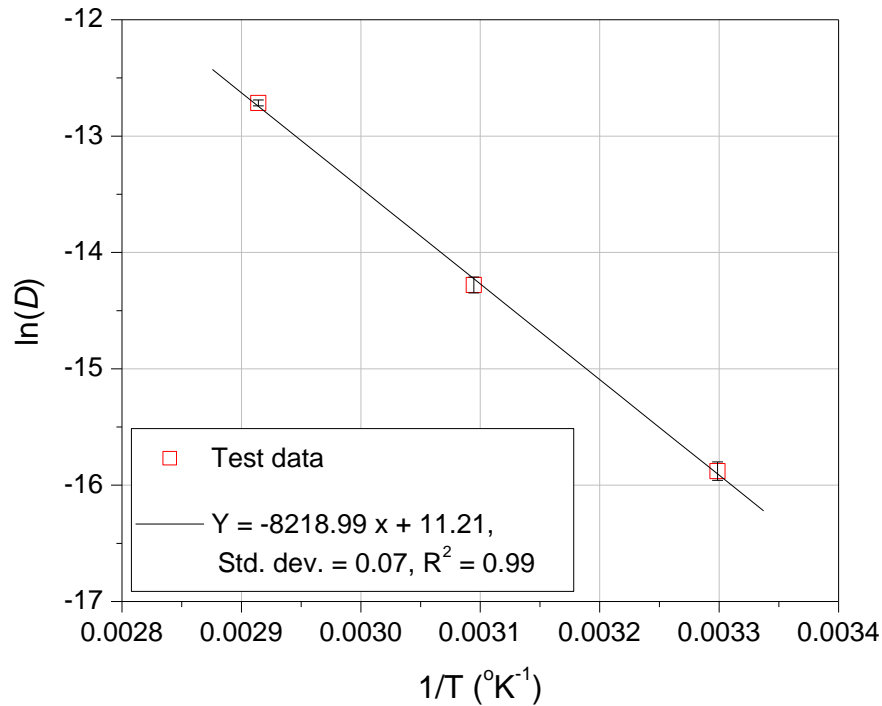


Figure 7.6 Arrhenius dependence of the diffusion coefficients of the LY3505/XB3403 epoxy resin system conditioned at 30, 50 and 70 °C.

7.2.2 Determination of the through-thickness concentration profile of the absorbed moisture

Understanding the distribution of absorbed moisture in polymers as a function of time is important, especially in coating and adhesive applications where design optimisation is paramount to achieve desired physical and mechanical properties [405,406,407,408]. Even though through-thickness moisture diffusion phenomena in polymers have been explored widely, less attention has been paid on modelling the profile of a diffusion front within a material. Mathematical models that have been used for predicting the moisture diffusion profiles in epoxy resins include: integral solutions [409,410,411,292], finite element analysis

[412,413,268] and numerical methods [405,414,415]. Deuterium has also been used to track the concentration profiles in an epoxy-based composite [406].

Crank [260] discussed a wide range of mathematical approaches for predicting the water concentration profiles within a material depending on the sorption kinetics and initial and boundary conditions. In solving mass transfer problems, numerical solutions said to offer many advantages such as accurate modelling of experimental and practical situations [416].

In this study, the Crank-Nicolson implicit method based on a finite-difference solution was used to model the through-thickness concentration profiles within the epoxy/amine resin system. The one-dimensional Fickian diffusion in the resin with constant diffusivity was considered (see Section 2.4.2.1). Equation 2.23 can be generalised by substituting non-dimensional variables and the modified equation is given by:

$$\frac{\partial C}{\partial T} = D \frac{\partial^2 C}{\partial X^2} \quad \text{Equation 7.3}$$

where $C = \frac{c}{c_0}$, $T = \frac{Dt}{L^2}$, $X = \frac{x}{L}$, x is the distance along the thickness of a membrane, D is diffusivity/diffusion coefficient, c is the concentration of diffusing species and t is time and L is the thickness of the epoxy specimen.

Equation 7.2 forms a linear parabolic differential equation and the Crank-Nicolson implicit method gives a more accurate solution with no restrictions on the size of the time step compared with other finite-difference solutions [120,260,416]. As shown in Figure 7.7, the

thickness of the specimen was divided into equal slices of thickness Δx and the co-ordinates (x, t) of the representative mesh point P were considered as:

$$x = iL; \quad t = j \frac{L^2}{D}$$

Hence using the Crank-Nicolson implicit method, the finite-difference approximation for Equation 7.2 is given by:

$$(2 + 2r)C_{i,j+1} - rC_{i-1,j+1} - rC_{i+1,j+1} = rC_{i-1,j} + (2 - 2r)C_{i,j} + rC_{i+1,j} \quad \text{Equation 7.4}$$

where $r = \frac{\delta T}{(\delta X)^2}$

By assuming $X = \frac{1}{10}$ and $\delta T = \frac{1}{100}$, Equation 7.3 can be simplified as below [417]:

$$-C_{i-1,j+1} + 4C_{i,j+1} - C_{i+1,j+1} = C_{i-1,j} + C_{i+1,j} \quad \text{Equation 7.5}$$

where

- (i) $t = 0, C = 1$ for $x = 0$ and $C = 0$ for $x > 0$,
- (ii) $t \geq 0, C = 1$ for $x = 0$ and $x = 1$

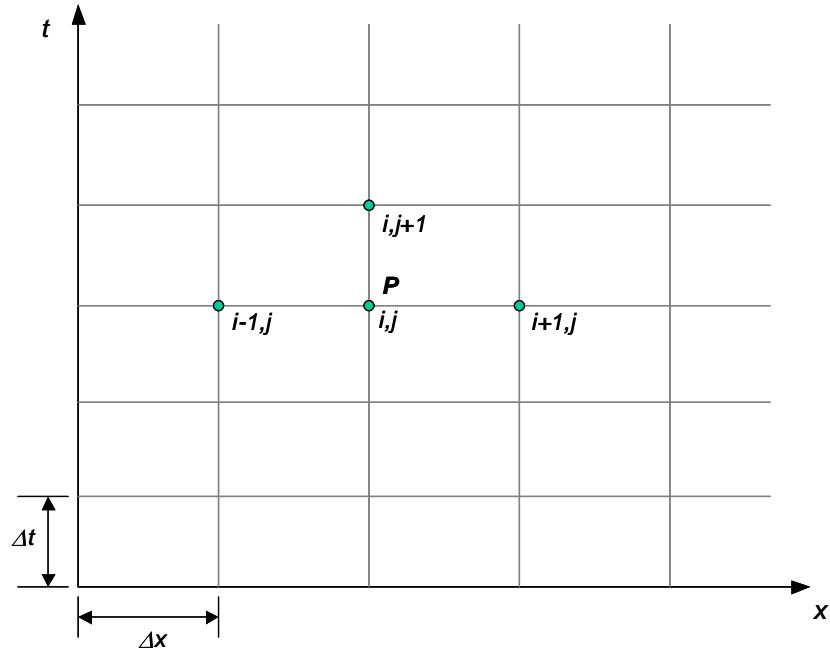


Figure 7.7 A representative mesh along the thickness of the specimen used for the Crank-Nicolson method.

This approach was used to generate the concentration profiles (iso-time lines) for absorption at 30°, 50° and 70°C as shown in Figure 7.8, Figure 7.9 and Figure 7.10, respectively. A steep water concentration gradient was observed next to the surface at the beginning of the ageing process. Table 7.2 presents a summary of the predicted and experimentally derived (based on gravimetric measurements) immersion times for the resin system to attain 90% saturation at 30, 50 and 70 °C. A good correlation was observed between the two techniques for the three temperatures investigated.

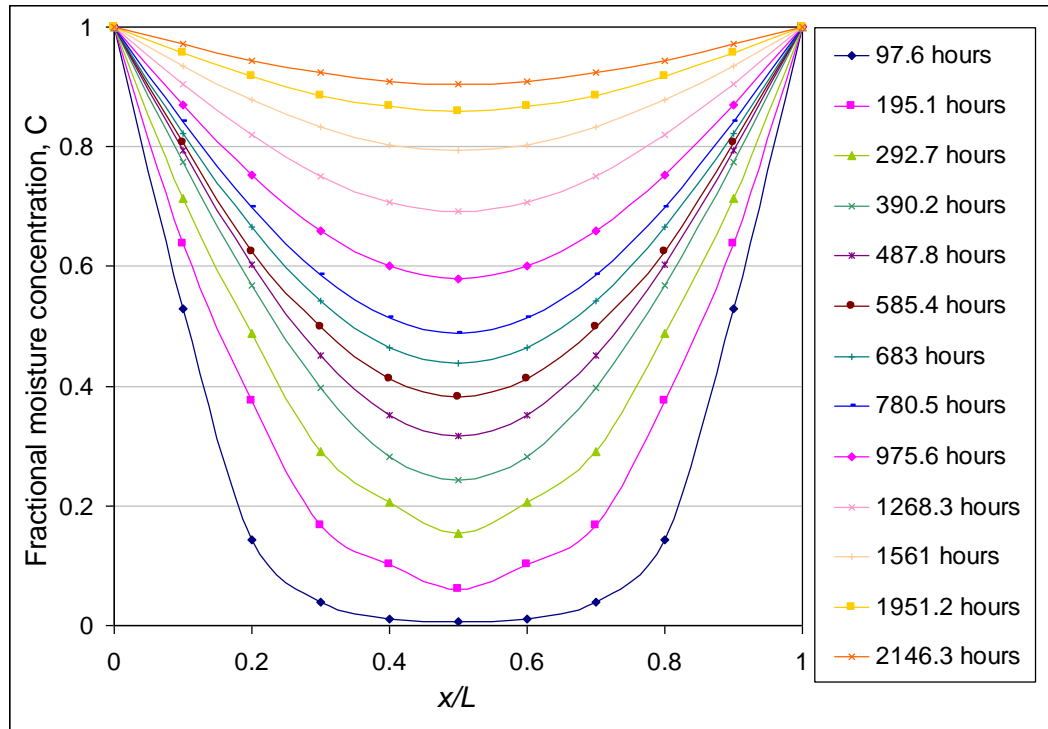


Figure 7.8 The fractional concentration profiles through the thickness of the epoxy/amine resin system at 30 °C.

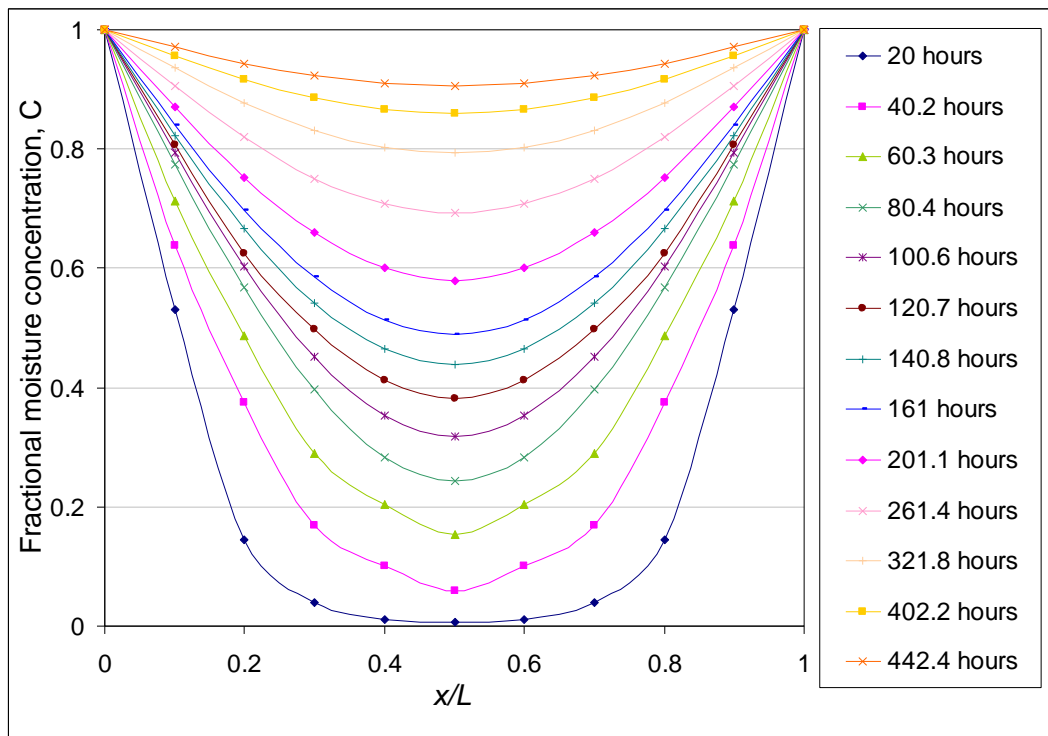


Figure 7.9 The fractional concentration profiles through the thickness of the epoxy/amine resin system at 50 °C.

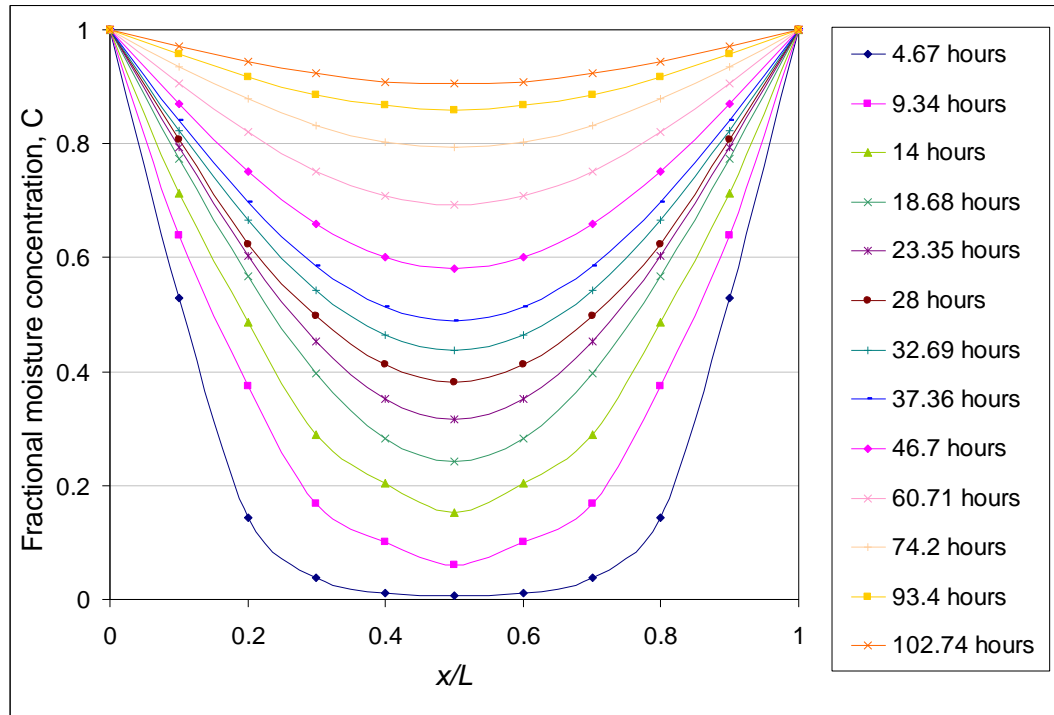


Figure 7.10 The fractional concentration profiles through the thickness of the epoxy/amine resin system at 70 °C.

Table 7.2 Comparison of experimental and predicted immersion times for the LY3505/XB3403 epoxy/amine resin system to attain 90% saturation.

Immersion temperature (°C)	Time taken to reached to 90 % saturation (hours)	
	Experimental data	Predicted data (Equation 7.4)
30	119.0	116.8
50	521.0	502.8
70	2937.0	2439.1

7.3 Effect of hygrothermal conditioning on the properties of the epoxy/amine resin system

Absorption isotherms obtained using preliminary gravimetric measurements at 30, 50 and 70 °C were used as a basis for subsequent measurements based on TGA, DSC, DMTA and FTIR spectroscopy. DMTA specimens of dimension 10 mm x 50 mm x 2 mm were used for all the experiments. With reference to Figure 6.11, the effect of hygrothermal ageing on thermal, chemical and viscoelastic properties was measured at eight points along the absorption isotherms for each immersion temperature. The gravimetric experiments were also carried out for the DMTA specimens and also for a set of reference specimens, which have the same dimensions (50 x 50 x 2 mm) as previous gravimetric specimens, in order to correlate water uptake at the three temperatures directly with the two sets of experiments. Figure 7.11 shows a typical representation of the spread of measurements along the absorption isotherm at 70 °C. Emphasis was given to test more points along the initial linear portion of the absorption curve. It can be clearly seen that the gravimetric measurements of two sets of experiments fit very well. The slight deviation of the percentage weight increase of the DMTA specimens could be attributed to edge effects in the specimens. The data points corresponding to DMTA and reference gravimetric data show the average weight gain of three specimens. The same procedure was followed for choosing measurement points along the sorption isotherms at 30° and 50 °C and the spread of measurement points are shown in Figure 7.12 and Figure 7.13, respectively.

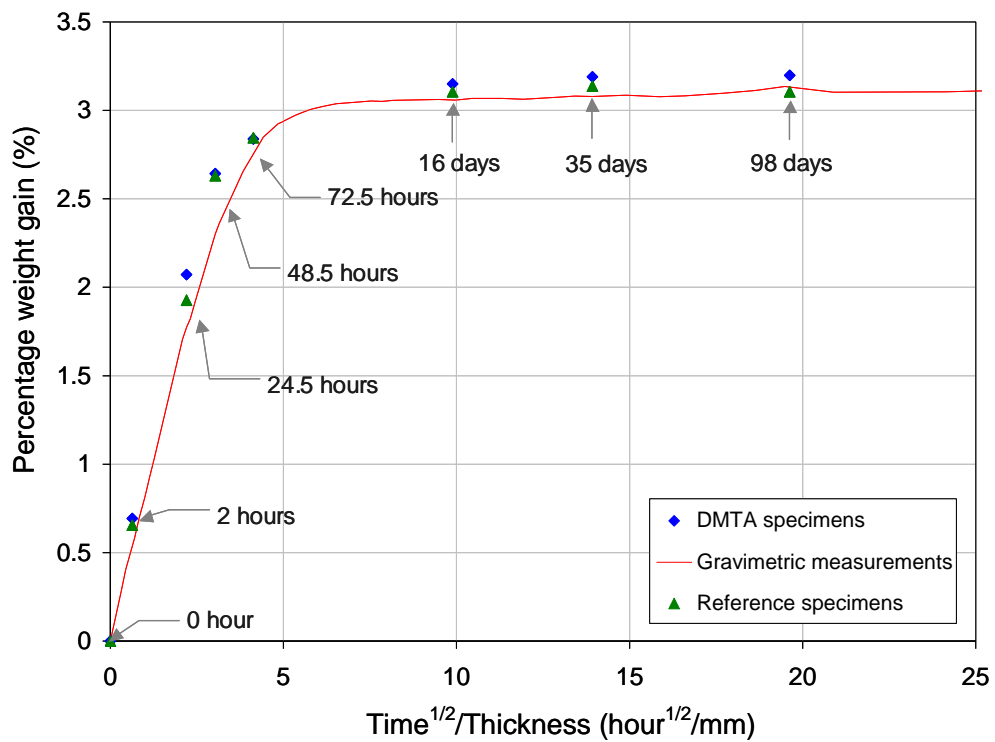


Figure 7.11 Spread of measurements along the sorption isotherm of the LY3505/XB3403 epoxy resin system conditioned at 70 °C.

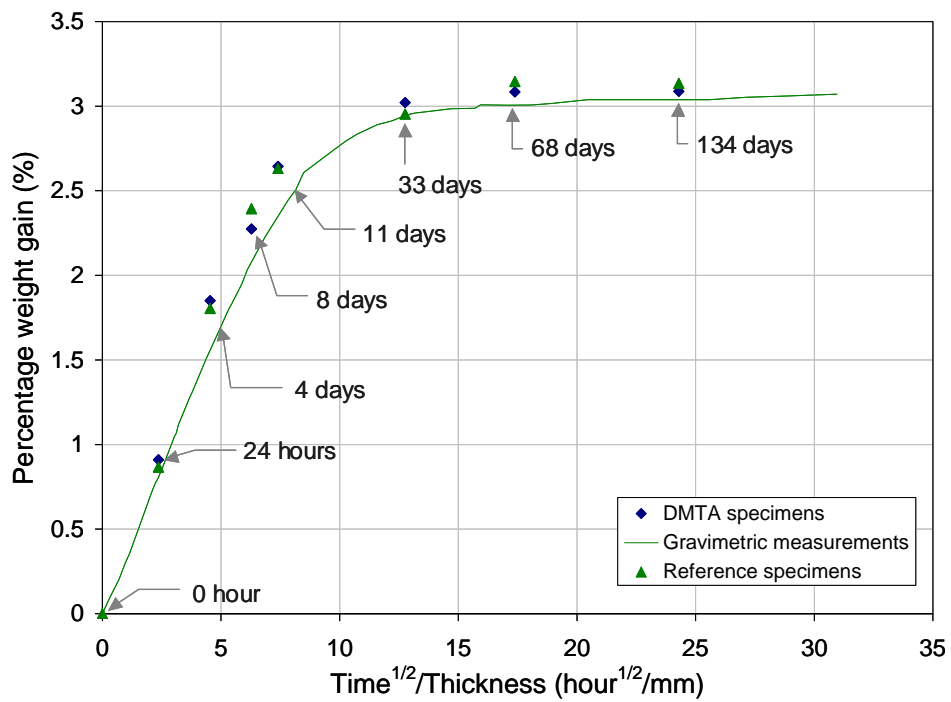


Figure 7.12 Spread of measurements along the sorption isotherm of the LY3505/XB3403 epoxy resin system conditioned at 50 °C.

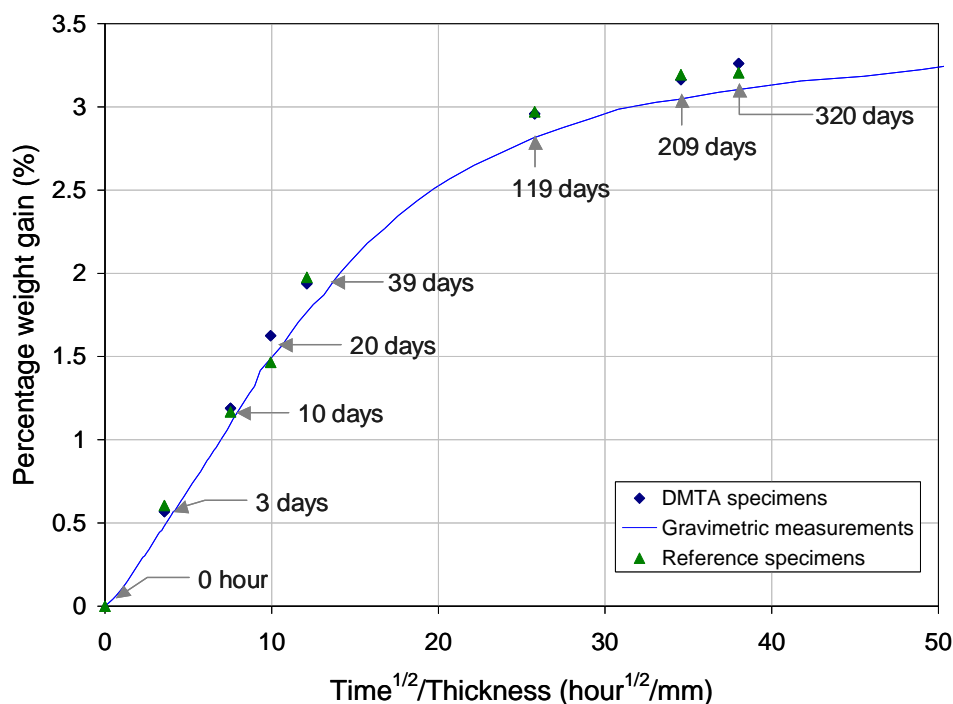


Figure 7.13 Spread of measurements along the sorption isotherm of the LY3505/XB3403 epoxy resin system conditioned at 30 °C.

7.3.1 Thermo gravimetric analysis

TGA of the aged specimens was performed after predetermined immersion times at 30, 50 and 70 °C as explained in the previous section. Since the analysis requires approximately 15 mg of the material, a corner piece of an aged DMTA specimen was cut as shown in Figure 3.23. The TGA experiments were performed to obtain information on desorption behaviour of the epoxy/amine resin after isothermal conditioning at specified temperatures. The sample was heated from 30 to 180 °C at 5 °C/minute in air. Figure 7.14(a) shows the percentage weight-loss obtained from the sample as a function of the immersion time and the temperature. Only one specimen per immersion time at each immersion temperature was tested. A comparison between the amount of absorbed moisture during isothermal immersion

experiments (Figure 7.14(b)) and the corresponding amount of desorbed water at 180 °C during TGA measurements (Figure 7.14(a)) is shown for ease of analysis.

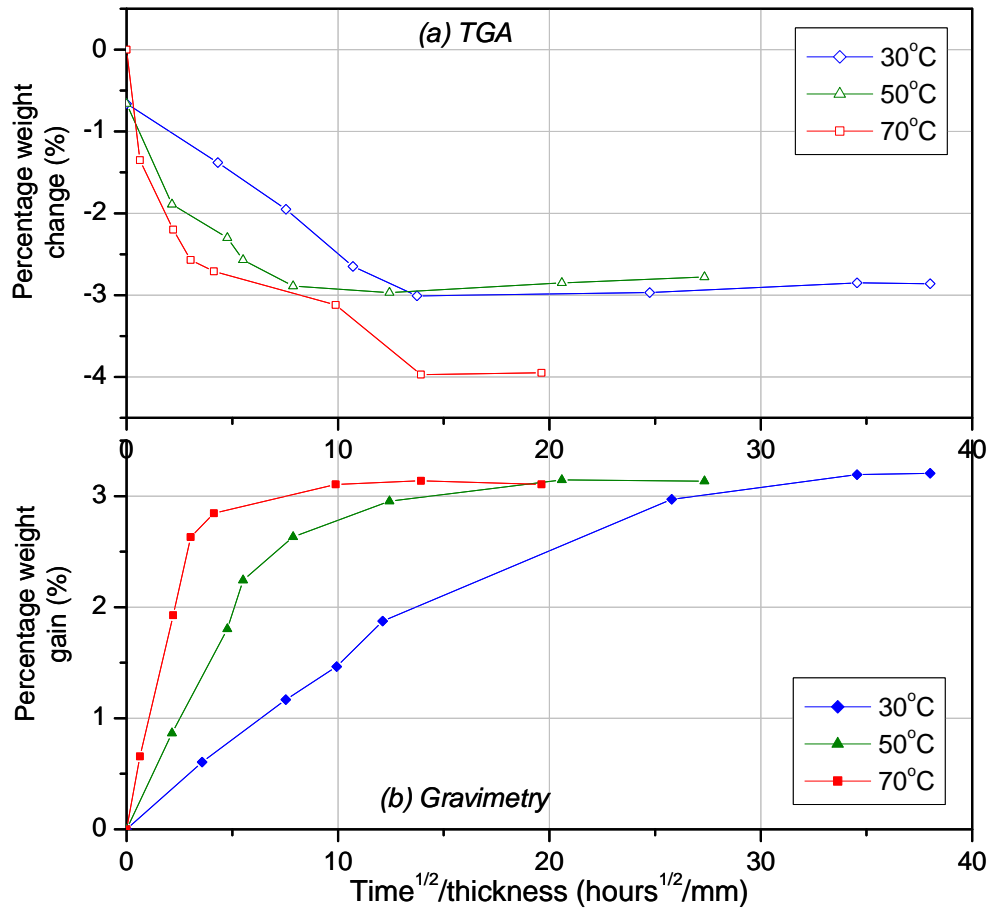


Figure 7.14 (a) Percentage weight loss obtained from TGA traces at 180°C for the LY3505/XB3403 resin system that conditioned at 30°, 50° and 70°C and (b) corresponding gravimetric sorption isotherms; data points were joined to highlight the trend.

With reference to the specimens that were conditioned at 30 and 50 °C, the weight losses from the TGA scans measured at 180 °C were similar to the weight uptake of the epoxy/amine resin system at respective immersion times. However, higher weight losses at 180 °C were observed with the epoxy/amine resin conditioned at 70°C for longer immersion times. This could be due to the thermal degradation of the resin or due to the leaching of low molecular-weight species at elevated temperatures [267,312,164]. Water ingress into a

polymer matrix leads to a range of effects such as plasticisation through interaction of the water molecules with polar groups in the cross-linked network, creation of micro-crazes, leaching of unreacted monomer and in certain cases degradation of the resin [302].

However, it was highlighted that the discrepancies involved in specimen dimensions and sample preparation for TGA may lead to different desorption rates during thermal scanning [314]. In addition, in the current study, evaporation of absorbed moisture during temperature scanning may interfere with the weight losses due to hygrothermal degradation. In particular, due to the small sample size, different specimen dimensions may show a considerable deviation from the real desorption behaviour of the bulk material under the same desorption conditions. Therefore predicting the actual weight losses and/or thermal degradation of the aged epoxy/amine resin under elevated temperatures in terms of the weight losses obtained using TGA, may not be accurate.

7.3.2 Differential scanning calorimetry

DSC is an accepted method for studying changes in the thermal properties of materials due to physical and chemical processes. In this study, DSC analyses were used to investigate the effect of conditioning temperature and immersion time on the glass transition temperature (T_g) of the LY3505/XB3403 epoxy/amine system. The test specimens used in the DSC experiments were similar to that described in Section 7.3.1 (see Figure 3.23) for the TGA experiments. However, each data point presented in the DSC analysis is an average of three independent experiments.

Figure 7.15(a) shows typical DSC traces obtained for the un-aged epoxy/amine resin before immersion. Figure 7.15(b) illustrates typical DSC traces for the specimens that were conditioned at 70 °C for different immersion times. The approximate moisture content in the specimens at specified immersion times can be inferred from Figure 7.11. The data points were taken every 0.4 s. This is equivalent to 16 data points/°C. The temperature range studied was 30 - 140 °C.

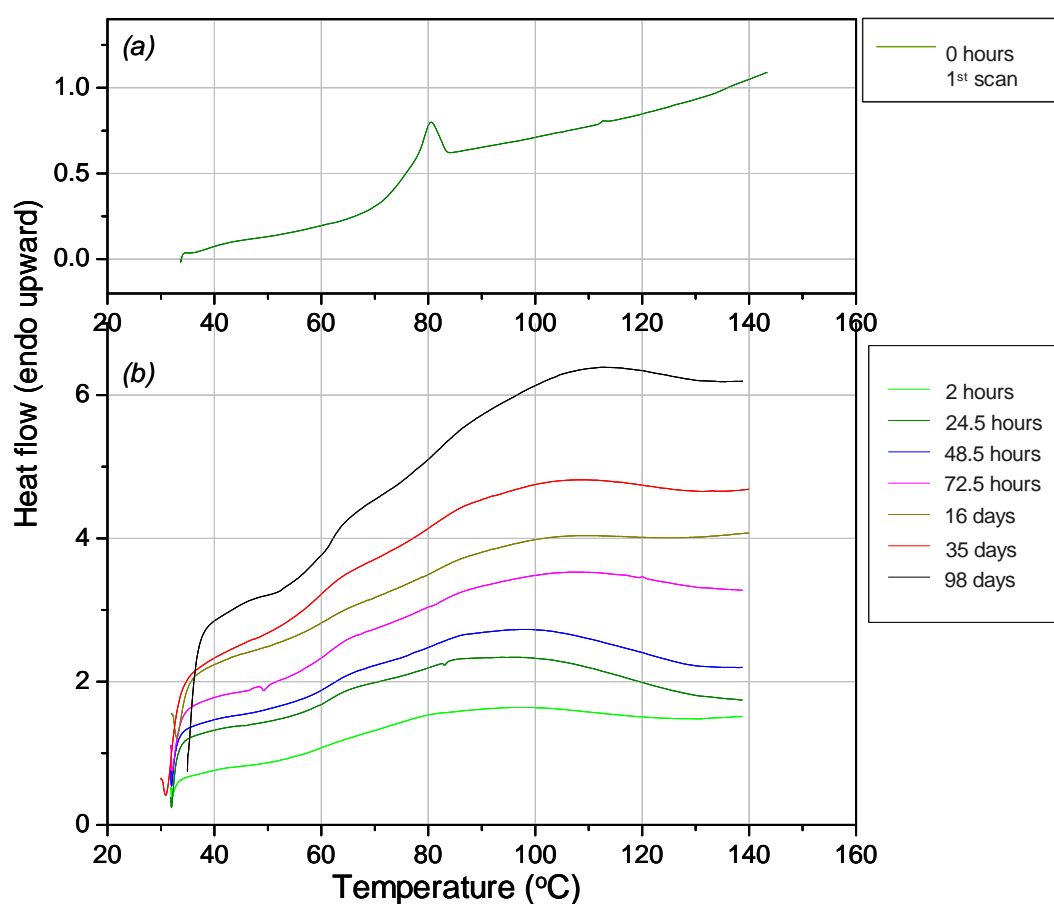


Figure 7.15 Dynamic thermograms from DSC for the LY3505/XB3403 resin system: (a) DSC trace for un-aged epoxy resin and (b) DSC traces for aged epoxy resin that were conditioned at 70 °C for different immersion time.

With reference to Figure 7.15, it is apparent that defining the T_g on the basis of the inflection point of the endothermic-step transition is not possible. The un-aged specimens show an endothermic “physical aging” peak due to network relaxation related to the preconditioning before the hygrothermal ageing experiments. In the case of the environmentally conditioned specimens, the endothermic step transition associated with glass transition of the resin overlapped with the onset of a broad endothermic peak. This peak could be attributed to the evaporation of absorbed moisture in the epoxy/amine resin. The same features have observed with the DSC traces recorded for the epoxy/amine resin conditioned at 30 and 50 °C. Therefore in this study, the onset of the glass transition of DSC traces was defined as the temperature corresponding to un-aged or aged epoxy/amine resin [297].

The analyses indicated that the T_g varies, depending on the hygrothermal ageing conditions, as shown in Figure 7.16. It was seen that the T_g decreases due to absorbed moisture followed by a steady increase at all the conditioning temperatures. The main decrease in T_g can attributed to plasticisation of the matrix. The formation of intermolecular hydrogen bonds between water and polymer molecules, and interruption of intramolecular bonds between polymer chains, can reduce the glass transition temperature [297,298,302,418,419,251]. The initial rate of depression of the T_g is higher at high immersion temperatures. The T_g is seen to reduce from 70.1 °C – 53.2 °C for the samples that were conditioned in water at 70 °C. Similar trends have been reported in the literature [297,14].

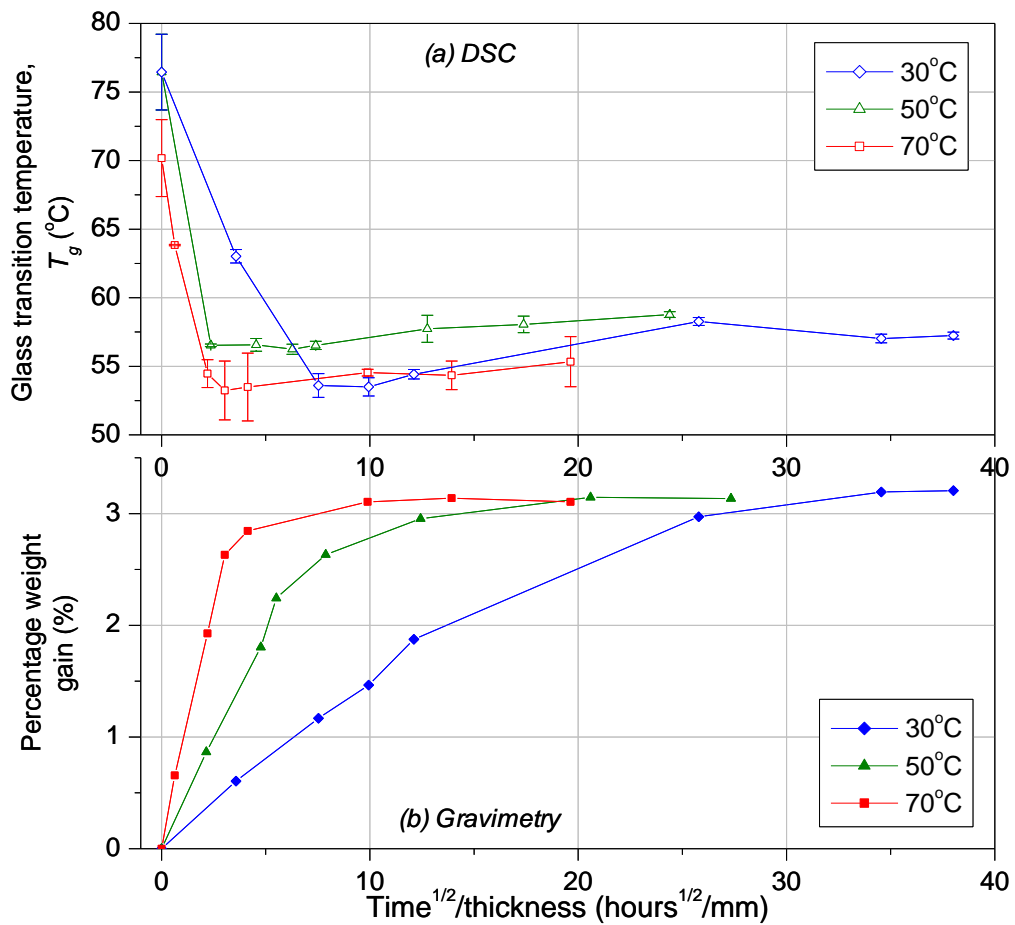


Figure 7.16 (a) Change in T_g of the LY3505/XB3403 resin system that conditioned at 30, 50 and 70 °C as a function of immersion time and (b) Corresponding gravimetric sorption isotherms; data points were joined to highlight the trend.

After the initial rapid lowering on the T_g , a gradual but higher reduction in T_g can be seen at lower immersion temperatures. Figure 7.16(b) illustrates the percentage weight gain for the neat-resin specimens that were immersed in water at 30, 50 and 70 °C, as a function of time. The corresponding lowering of the T_g due to plasticisation of the epoxy resin is shown in Figure 7.16(a).

In Figure 7.16(a), the rate of decrease in the T_g was seen to be explained by the conditioning temperature in water. In other words, the rate of decrease in the T_g was greater at 70 °C

followed by 50 °C and 30 °C conditioning temperatures. However, the T_g for the dry specimen (not conditioned in water) that was subsequently immersed in water at 70 °C was approximately 70 °C. The reason for this was not established but the batches of the neat resin were cross-linked at 60 °C. Therefore it is difficult to explain the lower T_g at $t = 0$ for the conditioned specimens at 70 °C.

The effect of normalising the T_g data for the conditioned specimens in water at specified immersion temperatures is shown in Figure 7.17. Here, the T_g data per batch of specimens was normalised to the T_g at $t = 0$, *i.e.* the T_g of the unconditioned specimens. The normalised data suggested that the initial rate of decrease in the T_g is similar for the specimens conditioned at 50 and 70 °C. T_g of the specimens conditioned at 30 °C showed a slower rate of decrease. However, interestingly the normalised T_g after approximately 48 hours was higher for the specimens conditioned at 70 °C. This trend has followed by the specimens conditioned at 50 and 30 °C. With reference to Figure 7.17, it is surprising to note that the specimens that were conditioned at 70 and 50 °C showed a similar rate of decrease in T_g up to approximately 24 hours of immersion. This may be due to the fact that the T_g recorded over the initial conditioning period was infrequent compared with the specimens that were conditioned at 30 and 70 °C. Other possible features such as inadequate mixing of the resin and the cross-linking agent, deviations from the stoichiometry and error in the processing temperature have been excluded as the experimental procedures were followed methodically.

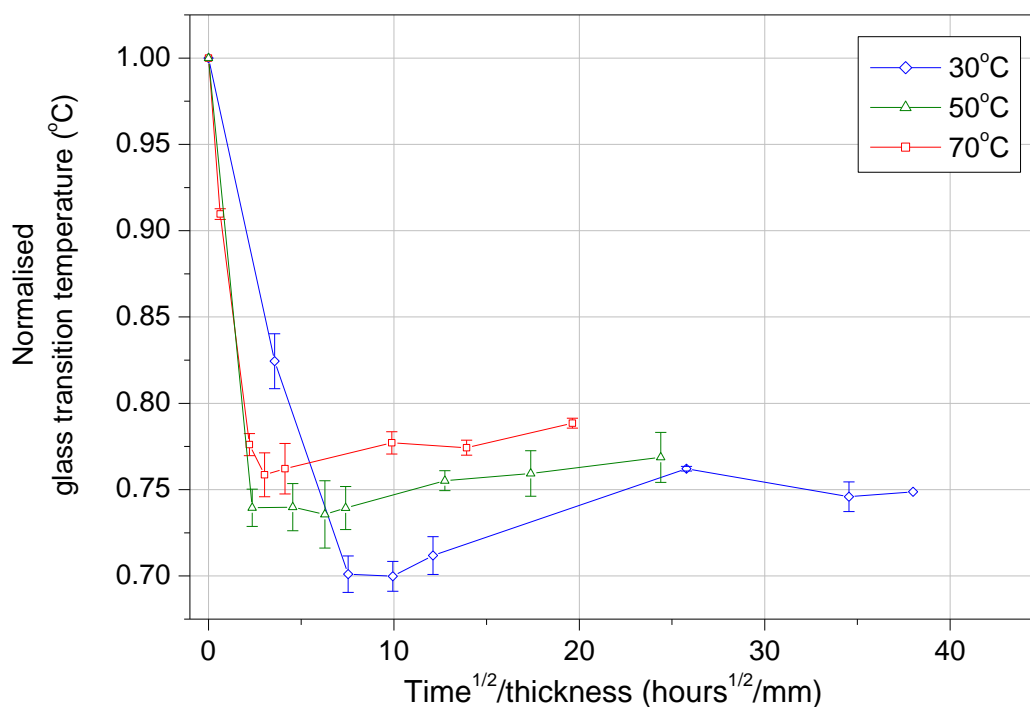


Figure 7.17 Decrease in normalised T_g of the LY3505/XB3403 resin system that conditioned at 30, 50 and 70 °C as a function of immersion time; data points were joined to highlight the trend.

In Figure 7.17, other researchers have observed that the T_g to increase with prolong conditioning time [297]. This has been attributed to increased densification in the resin system and physical aging. The situation with the specimens that were conditioned at 70 °C is more complicated as they were cross-linked at 60 °C. Therefore, conditioning at 70 °C in water will entirely lead to plasticisation followed by possible densification. Regretfully, these findings were not investigated further due to time limitations.

As mentioned in the preceding section, a more accurate comparison between the T_g of the aged epoxy/amine resin as measured by DSC, is not possible. Since analysis of DSC thermogram is based on the assumption that the mass of the specimen remained same during

DSC scan, desorption of absorbed moisture may interfere with the glass transition of the resin. Hence, a definite conclusion on the change in T_g cannot be drawn from these results.

7.3.3 Dynamic mechanical thermal analysis

DMTA is an established technique for characterising the T_g of polymeric materials. DMTA has been identified as a more sensitive technique for measuring change T_g due to hygrothermal aging [279]. Typical traces of $\log E'$, $\log E''$ and $\tan \delta$ related to an un-aged epoxy specimen obtained from dynamic temperature scan at 1 Hz are shown in Figure 7.18.

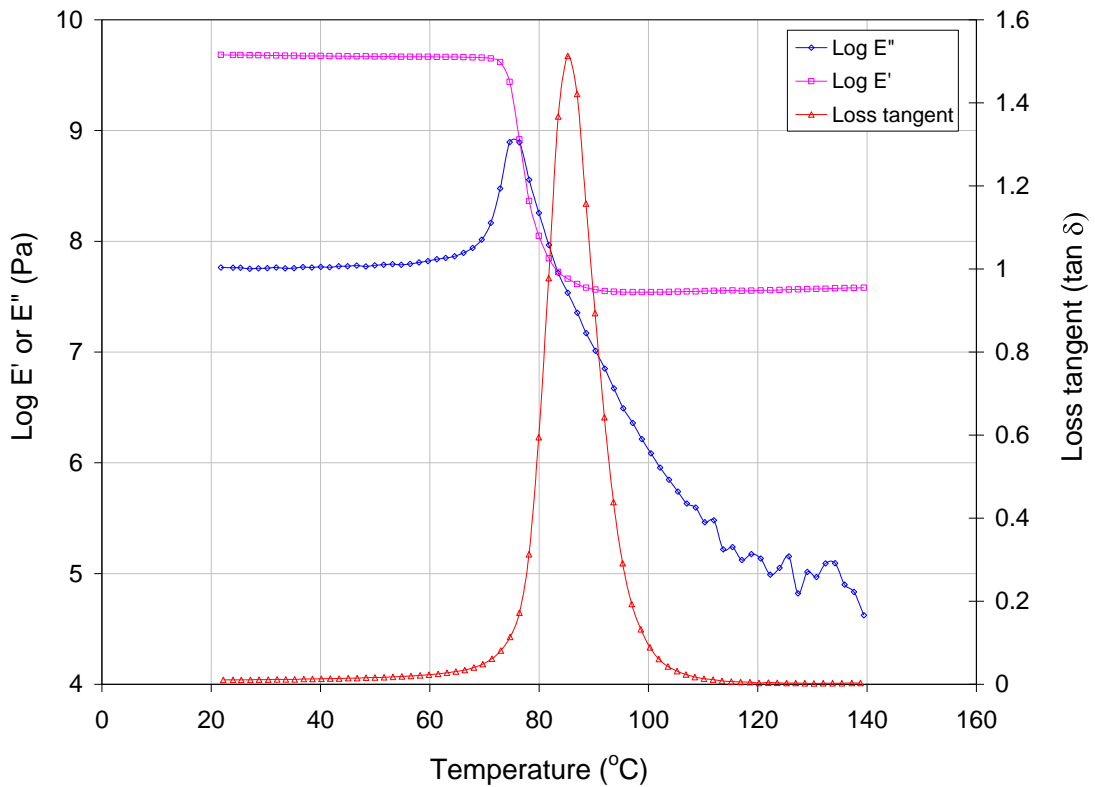


Figure 7.18 Dynamic temperature scan of $\log E''$, $\log E'$ and loss tangent obtained for the un-aged LY3505/XB3403 resin system at 1 Hz.

In the DMTA analysis, the temperature related to the maximum peak height of the $\log E''$ trace has been recommended as a suitable method for defining the T_g of polymers [420]. As can be seen from Figure 7.19, the viscoelastic nature of the cross-linked resin is illustrated by the shift of the $\log E''$ response to higher temperatures by increasing frequencies. This behaviour was also observed from the E' and loss tangent for all the DMTA analyses. Especially at lower frequencies, the thermal and viscoelastic properties obtained from DMTA are said to be specific to the material [420]. Therefore, for comparison of the T_g obtained based on DSC and DMTA techniques, the dynamic moduli and $\tan \delta$ traces that obtained at 1 Hz were considered.

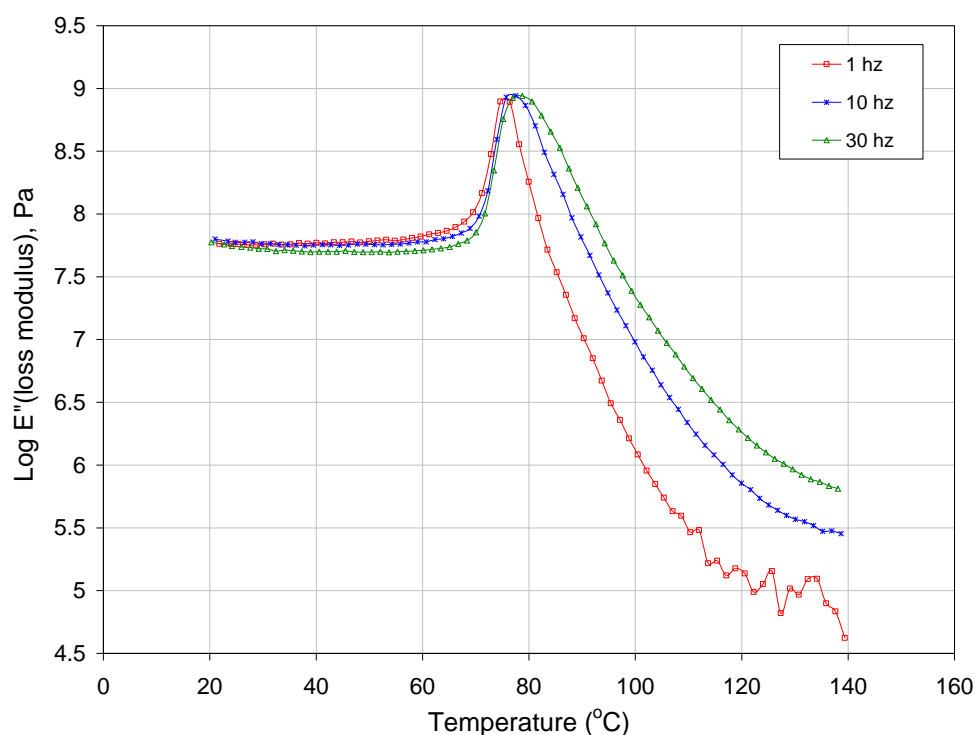


Figure 7.19 Frequency dependence of $\log E''$ traces obtained from DMTA for the un-aged LY3505/XB3403 resin system at 1, 10 and 30 Hz.

The influence of hygrothermal aging on the storage modulus of the epoxy/amine resin conditioned at 70 °C is shown in Figure 7.20. The relative moisture content in the

specimens can be inferred from Figure 7.11. Similar behaviour was observed for the epoxy/amine resin aged at 30° and 50 °C immersion temperatures.

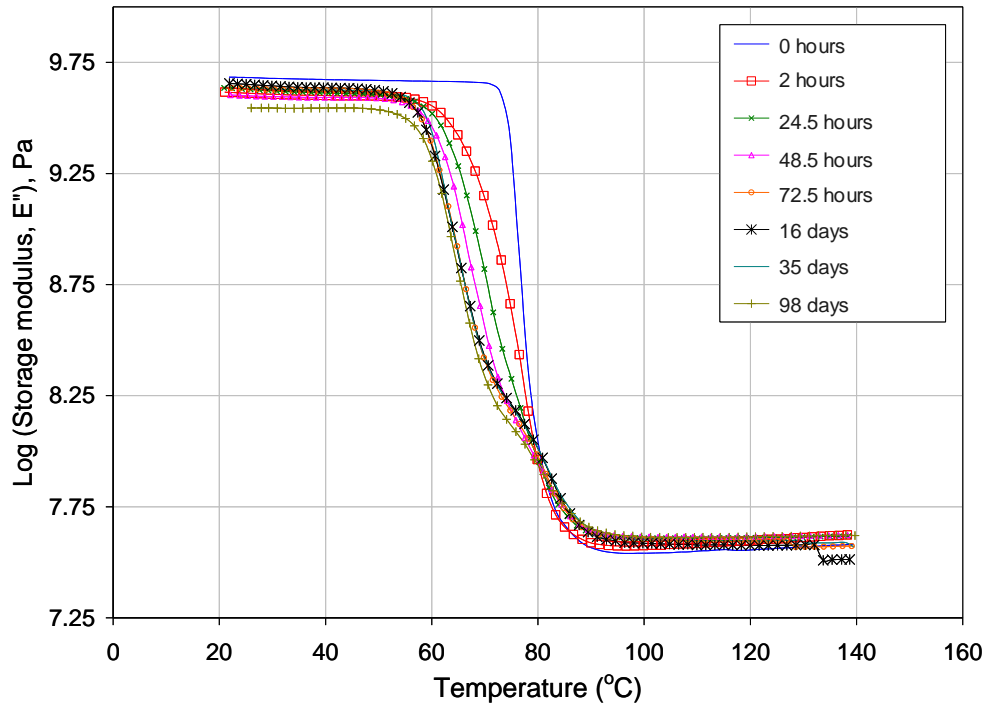


Figure 7.20 Effect of immersion time on the storage modulus (E') of LY3505/XB3403 resin system conditioned at 70 °C.

Typical dynamic traces of loss modulus, E'' of the epoxy/amine system that was conditioned at 70 °C are shown in Figure 7.21. It can be noted that the hygrothermal ageing of the epoxy resulted in a broadening of the α -transition associated with the T_g , and moved towards lower temperatures. As the specimens were dried prior to analysis, these changes cannot be attributed to a physical ageing effect of the epoxy. Instead, this broadening of the $\log E''$ peak could be attributed to the network relaxation associated with plasticisation by absorbed moisture. The water molecules are capable of forming hydrogen bonds with hydroxyl groups by disrupting inter-chain hydrogen bonding [250,251] and hence increase the segmental mobility allowing the network to relax [317].

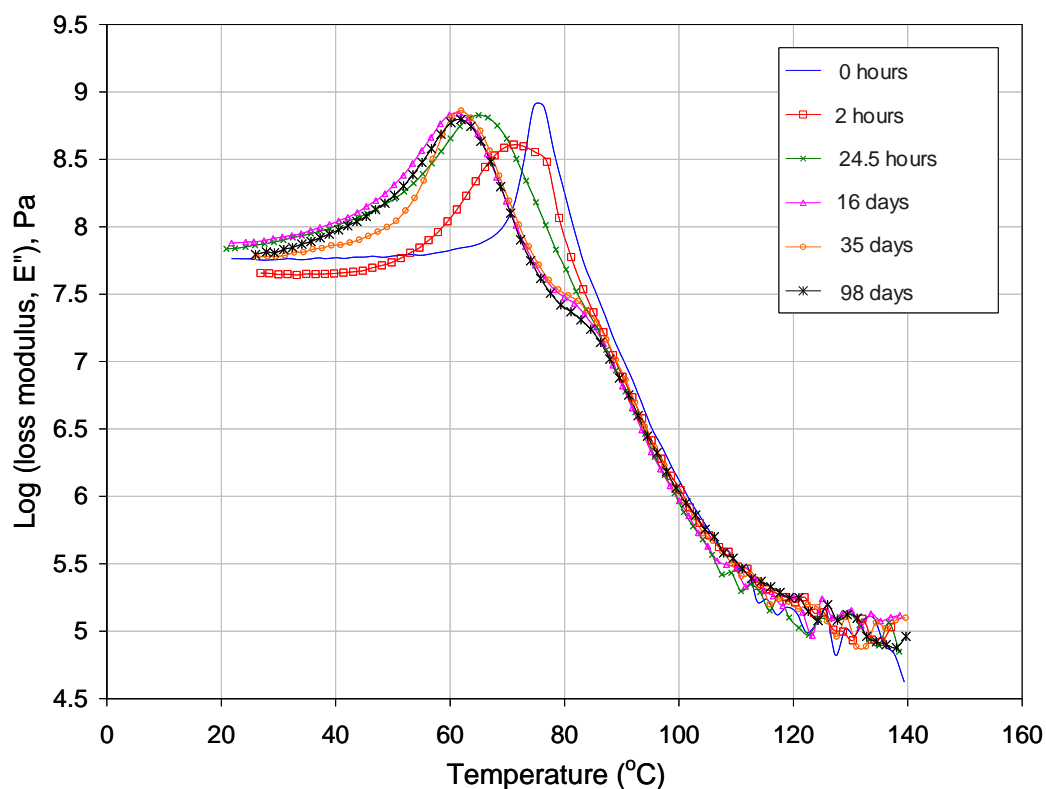


Figure 7.21 Effect of immersion time on the loss modulus (E'') of LY3505/XB3403 resin system conditioned at 70 °C.

However, it must be emphasized that the evolution of the shape of the $\log E''$ peaks is not associated with any decrease in the rubbery storage modulus (see Figure 7.20). Therefore it can be concluded that no significant decrease in the cross-link density of the epoxy resin occurred during ageing [300].

Similar trends were observed for conditioning at 50 °C and 30 °C and the change in the T_g at 1 Hz as a function of immersion time and temperature are plotted in Figure 7.22. The T_g decreases substantially followed by a minor increase over prolonged exposure at all temperatures of immersion. Xian and Karbhari [14] concluded that the increase in T_g after the initial decrease, is attributed to the dissolution loss of low-molecular weight segments takes

place at higher temperatures of immersion over extended periods of time. However, in this study, an increase in T_g after a first depression was observed at all immersion temperatures.

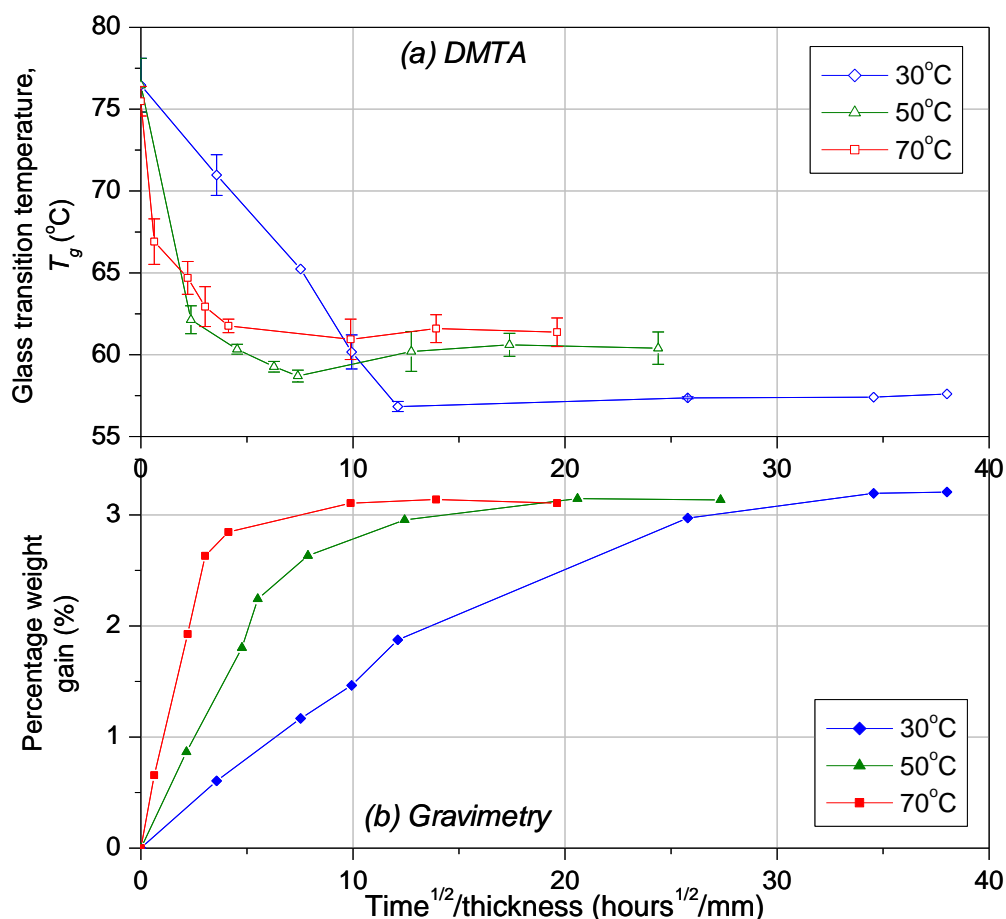


Figure 7.22 (a) Change in T_g based on dynamic loss modulus (E'') traces of the LY3505/XB3403 resin system that conditioned at 30, 50 and 70 °C as a function of immersion time and (b) Corresponding gravimetric absorption isotherms; data points were joined to highlight the trend.

The highest rate of depression of the T_g was noted at the highest temperature of immersion, 70°C. However the lowest T_g was noted from the epoxy conditioned at 30°C confirming the behaviour that was observed with DSC analyses (see Figure 7.16 and Figure 7.17). This behaviour has not been reported extensively. However a similar trend was observed for a 4,4'-isopropylidenephenol-epichlorohydrin/aliphatic amine system but no detailed

explanation was given [14]. According to Zhou and Lucas [250], single hydrogen bonding (*Type-I*) between water and polymer molecules requires lower activation energy whilst multiple interconnecting hydrogen bonding (*Type-II*) possesses high activation energy. The *Type-II* interactions are also known as “secondary cross-linking”. Therefore at higher immersion temperatures these two processes can be competitive, and after a short time of immersion, the secondary cross-linking dominates the ageing mechanism. In case of ageing at low immersion temperature, the plasticisation due to the single hydrogen bonding dominates the water transport until all the hydrophilic sites available in the network are occupied with water molecules followed by secondary cross-linking at prolonged exposure.

In Figure 7.23, the dynamic temperature scans of the loss-tangent obtained for the un-aged and the aged epoxy specimens for different immersion times at 70 °C are presented. As mentioned before, the single $\tan \delta$ peak related to the un-aged epoxy resin that appeared at 78.9 °C is assigned to the α -relaxation of the fully cross-linked epoxy network. Generally, the aged epoxy resin shows lower intensity of the $\tan \delta$ peak that compared with the un-aged epoxy. The intensity of the $\tan \delta$ peak is associated with the energy loss in the transition region, which increases with increase in the local motion of the polymer chains [301]. The single hydrogen bonding between water and polymer molecules allow network relaxation resulting in peak broadening while the multiple interconnecting hydrogen bonding restricts the molecular motions resulting in a decrease in the intensity of $\tan \delta$ in the transition region [14].

With reference to Figure 7.23, after 24 hours of ageing, the onset of peak splitting was observed and after 48 hours of aging, a distinct second peak can be seen. The appearance of the second peak on the loss tangent has been previously reported for different epoxy systems

and different chemical and physical explanations for the behaviour have been proposed [302,314,244,312,313].

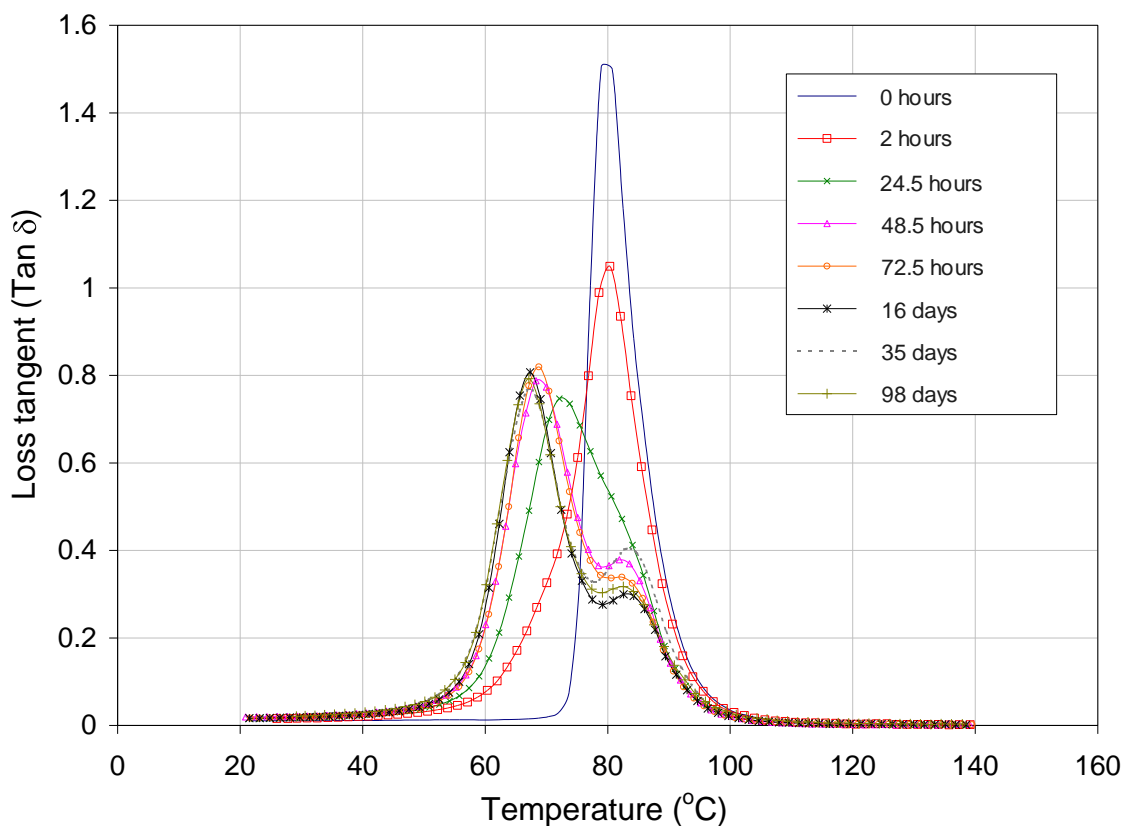


Figure 7.23 A series of loss tangent traces obtained from 1st dynamic scan of the LY3505/XB3403 resin system conditioned for different immersion times at 70 °C.

One of the proposed phenomena to explain the peak splitting of $\tan \delta$ trace is the uneven water sorption within epoxy resins due to the presence of a heterogeneous molecular structure with regions of different cross-linking densities [314]. However, this may not be the case for the epoxy/amine resin system used in this study, since it was suggested that the low-functionality epoxies such as DGEBA resins create more even cross-linking density compared with that created by high-functionality epoxy resins [244]. It has also been argued that an epoxy resin system having correct stoichiometric ratio, is highly unlikely to exhibit a cross-linked structure with low and high cross-linking densities [315,279,421]. An even and fully

cross-linked structure for the epoxy/amine resin used in this study is evident from the narrow and symmetric $\tan \delta$ peak obtained for un-aged specimens (see Figure 7.18).

Chateauminois *et al.* [300] hypothesised that the upper T_g originated from dried region in the samples, which exhibited a T_g close to that of the unexposed material. The same phenomenon was discussed elsewhere [302]. The peak splitting of $\tan \delta$ traces related to the aged samples was assigned to the α -relaxation of the epoxy network that has been plasticised by water [295] and was also assigned to the absorbed water that is not chemically linked to the polymer network [302,314]. Using a series of experiments, Xian and Karbhari [14] confirmed that the peak splitting of the $\tan \delta$ traces is influenced by the dry skin and the wet core of the test specimens. Furthermore, they performed a second DMTA temperature scan on the same test specimens and observed a complete recovery of the peak shape confirming a fully dried resin after two dynamic temperature scans. A shift of the $\tan \delta$ peak of the second scan towards higher temperatures has been attributed to a permanent plasticisation due to hygrothermal aging.

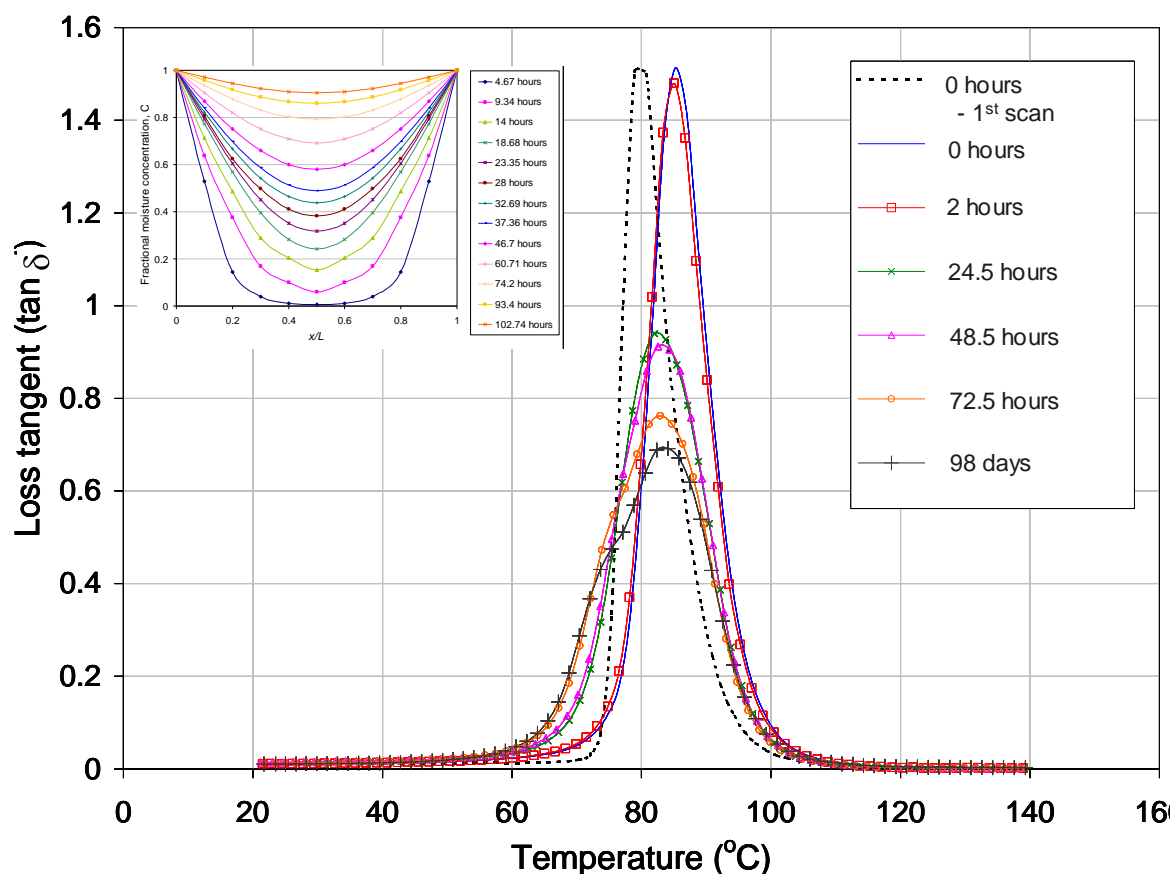


Figure 7.24 A series of loss tangent traces obtained from 2nd dynamic of the LY3505/XB3403 resin system that recorded at different immersion times at 70 °C; inset shows Figure 7.10, which represents predicted fractional concentration profiles through thickness at 70 °C.

Figure 7.24 shows the $\tan \delta$ traces that obtained from the second dynamic temperature scans on the same test specimens that have undergone the first dynamic temperature scan. The $\tan \delta$ trace related to the first scan of the un-aged epoxy resin is also presented for cross-correlation with the shape and the α -relaxation attributed to the second scans. The un-aged specimen and the aged specimen for 2 hours in water at 70 °C showed complete recovery of the peak shape and the intensity however, shifted towards higher temperatures. This higher T_g related to dry, aged epoxy is believed to be due to a complicated process of plasticisation in

the short-term and hydrolysis, leaching of low-molecular weight groups and secondary cross-linking in long-term, especially at high immersion temperatures [278,14].

As can be seen from Figure 7.24, $\tan \delta$ related to the specimens immersed in water at 70 °C for longer than one day showed reduced peak intensity followed by peak broadening for prolonged exposure. This desorption behaviour can be interpreted on the basis of types of water present in the epoxy and types of water-polymer interactions. In the early stage of sorption process, the water molecules attach to the hydrophilic functional groups on the surface of the epoxy [250,422]. This hypothesis also can be explained using the predicted moisture concentration profiles through the thickness of an epoxy specimen at 70 °C (see Section 7.2.2 and inset of Figure 7.24). At early immersion times below 5 hours, the moisture has not reached the middle of the specimen. Therefore complete desorption is possible upon drying. As the exposure time increases, the bound water content increases. Predicted concentration profiles show that after about 23 hours of immersion, the moisture concentration at the middle of the specimen reaches 0.32. As the moisture front moved into the resin, the overall moisture content within the resin increases. It was explained before that the peak broadening with lower intensity is associated with increase in the bound water content (i.e. increase in *Type-I* and *Type-II* water in the resin). Signs of these types of interactions present in the aged and dried specimens can be related to the irreversible plasticisation associated with the *Type-I* bonding and the *Type-II* bonding.

7.3.4 Fourier transform near-infrared spectroscopy

Infrared spectroscopy is a reliable quantitative technique for determining sorption kinetics of water in polymers [374,423]. In this study, conventional transmission FTIR spectroscopy was also carried out to investigate the feasibility and effectiveness of using the method as an on-line technique for monitoring water diffusion in the epoxy/amine system [356,357]. Commercial fibre optic probes were used with a thermo-regulated sample holder for spectral acquisition in the near-infrared range. Near-infrared spectra were obtained on the un-aged epoxy and on the epoxy aged for different immersion times at the three temperatures of 30°, 50° and 70 °C. Since FTIR spectroscopy is a non-destructive technique, the DMTA specimens were used before testing for acquiring the near-infrared spectra. The measurement only takes approximately one minute and the weight loss of the aged specimens during scanning is negligible (see Section 7.1 and Figure 7.3).

Figure 7.25 shows typical FTIR spectra in the range of 1100 – 2300 nm for an epoxy specimen before aging and specimens immersed in water at 70 °C for different exposure times. Considerable increase in absorbance band at 1905 nm, which is due to the combination of asymmetric OH stretching and OH bending vibration, is readily apparent. It was also reported that this band is not due to the alcoholic hydroxyl groups but is a characteristic band for the hydroxyl due to moisture [136]. The increase in the band has been observed at all three immersion temperatures and the peak has widely used for quantitative analysis of moisture absorption in polymer systems [424,21]. The very weak band, which appeared at this wavelength on the spectra of un-aged epoxy resin, could be due to the moisture contaminated with the epoxy and the amine hardener before cross-linking [280].

In addition, a baseline shift of the wide absorption band appearing at 1430 nm was observed and the band has been assigned to the first overtone of the symmetric OH stretching. However the band is wide and overlapped significantly and identified as less usable for quantitative analysis [424] (see Section 5.2). Nevertheless, a minor decrease in peak intensity can be seen as the moisture uptake increases. It was hypothesised that this feature can be used as an indication of the increase in hydrogen bonding with immersion time since the frequency of the OH band decreases for the stretching mode, but it increases for the bending mode, which appears at 1409 nm [319]. Moreover, FTIR analysis confirmed that there was no post-curing taking place in the epoxy specimens.

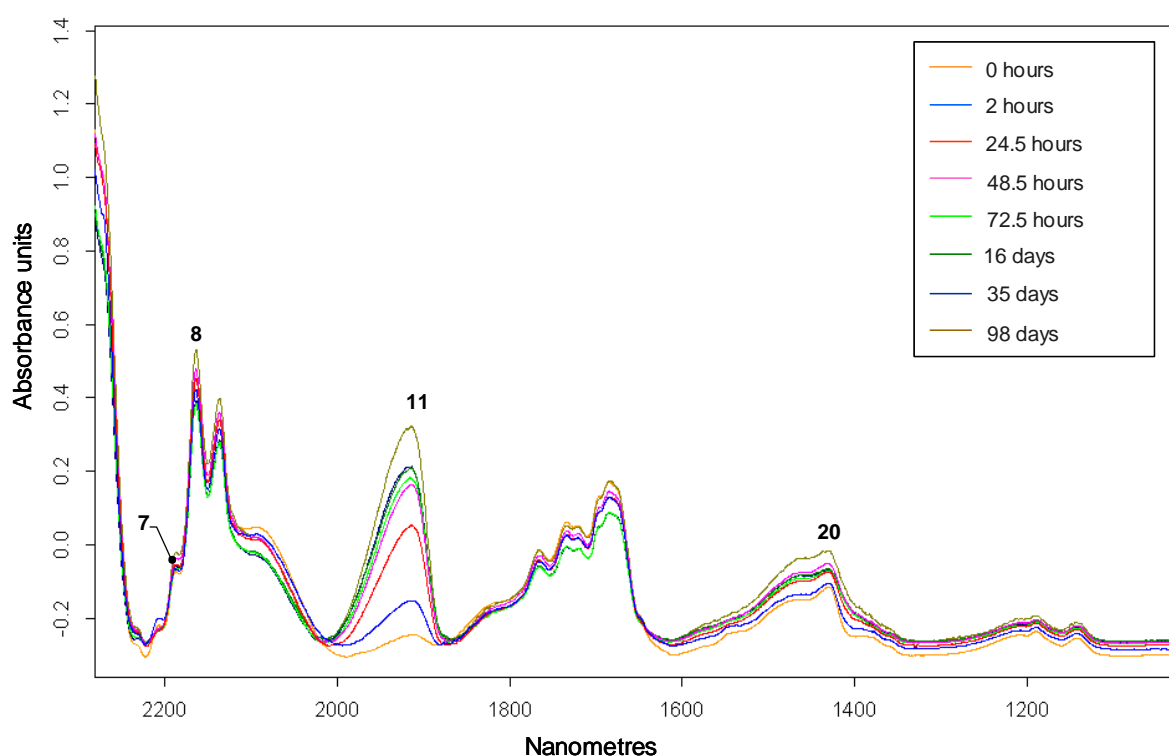


Figure 7.25 Near-infrared spectra obtained under transmission mode for LY3505/XB3403 resin system conditioned at 70 °C; Peak assignments: [1] 2207 nm – epoxy combination band, [2] 2164 nm – aromatic ring combination, [3] 1905 nm – OH band due to absorbed moisture and [4] 1430 nm – OH band due to alcoholic hydroxyl (see Table 5.1).

Conventional FTIR spectroscopy confirmed that there was no detectable post-curing taking place at immersion temperatures. However, no chemical changes were observed due to the leaching of low-molecular weight substances within the spectral range used in this study. This may be due to insufficient spectral information available in the near-infrared region compared with that available in the mid-infrared range [312].

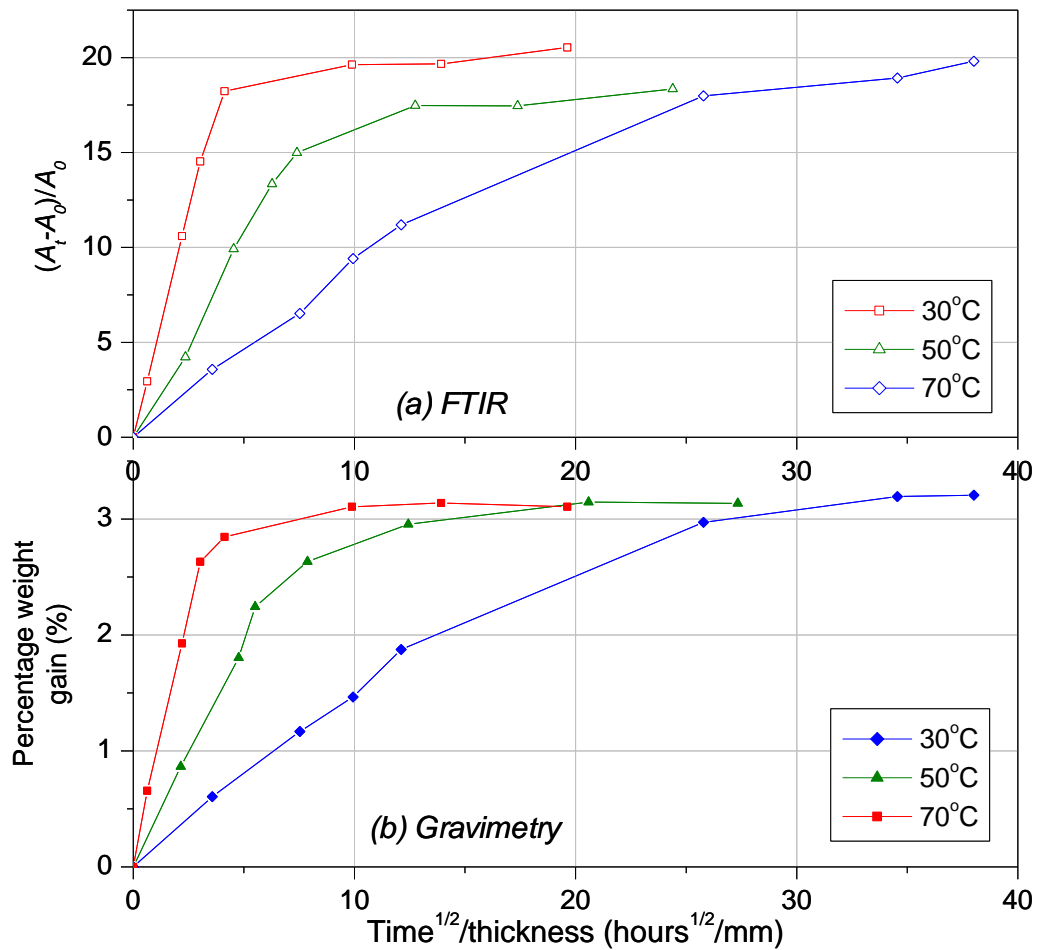


Figure 7.26 (a) Increase in normalised peak area of 1905 nm of the LY3505/XB3403 resin system conditioned at 30, 50 and 70 °C as a function of immersion time and (b) Corresponding gravimetric sorption isotherms; data points were joined to highlight the trend.

Use of FTIR spectroscopy for quantitative analysis of the sorption kinetics of water in epoxy resin systems has been widely explored [374,326,424]. Since the thickness of the samples is

constant, according to the Beer-Lambert law (see Section 2.3.1.1) the concentration or amount of absorbed water can be calculated as follows [374]:

$$\frac{A_t}{A_\infty} = \frac{C_t}{C_\infty} = \frac{M_t}{M_\infty} \quad \text{Equation 7.6}$$

where C is the concentration of water, A is the normalised absorbance at 1409 nm, M is the amount of water absorbed and the subscripts t and ∞ are time at t and at equilibrium, respectively. The peak area of the absorption band at 1409 nm was normalised to a non-reacting reference band at 2164 nm to eliminate the influence of spectral baseline shifts and spectral intensity caused by physical differences among different specimens. Figure 7.26 shows a comparison of the water absorption plots at three immersion temperatures, 30, 50 and 70 °C obtained from the near-infrared spectroscopy (Figure 7.26(a) and the gravimetric data Figure 7.26(b)). A good correlation was observed between the two techniques and it can be concluded that FTIR spectroscopy is an effective method of studying the sorption kinetics of water in the epoxy/amine resin system.

7.4 Conclusions

Based on the gravimetric measurements, moisture absorption in the epoxy/amine resin system satisfies Fickian diffusion behaviour and the equilibrium moisture content and the sorption kinetics obtained are in good agreement with the published results obtained by gravimetric measurements. An attempt was made to predict the moisture diffusion front across the thickness of a specimen as a function of immersion time using a finite-difference solution. A

reasonable correlation was found between the moisture content measured experimentally and that determined using the numerical solution.

Also DSC, TGA, DMTA and FTIR techniques were employed to investigate the absorption mechanism of water in the epoxy/amine resin system that immersed in water at 30, 50 and 70 °C. Possible diffusion phenomena of water in the epoxy resin system were discussed based on the experimental evidence and compared with the published results. Furthermore, the effect of absorbed moisture on the thermal, viscoelastic and chemical properties of the resin system was characterised.

Chapter 8

Monitoring of moisture ingress using fibre-optic transmission spectroscopy

8.1 Introduction

Little attention has been paid to developing fibre-optic sensors for *in situ* monitoring of absorbed moisture and hygrothermal degradation in epoxy-based composites and other related epoxy applications. The use of conventional FTIR spectroscopy to detect the ingress of moisture was discussed in Chapter 7. In this chapter, the fibre-optic transmission sensor discussed in Section 3.4.1.3 was used for monitoring the cross-linking process followed by the detection of moisture ingress.

8.2 Quantitative analysis of changes in functional groups during hygrothermal conditioning

The capillary support sensor design, which was initially used for monitoring the cross-linking reactions, was used for on-line monitoring of moisture ingress [370,356,357]. In other words, the same sensor was used for process monitoring followed by moisture ingress detection. On-line moisture ingress monitoring was studied using three specimen configurations in terms of relative position of the embedded sensors in the through-thickness direction of the cross-linked neat-resin sample (see Section 3.6.2). In order to cross-correlate the data from the sensors with conventional gravimetric measurements, the dimensions of the specimen were the same (50 mm x 50 mm x 2 mm thickness). A set of reference specimens were also used to obtain independent gravimetric measurements using each of the specimen configuration used. The specimens with embedded sensors and the reference specimens were cross-linked at 60 °C for 8 hours.

8.2.1 Specimen configuration – I

Figure 8.1 shows absorption isotherms for the epoxy/amine resin system, that were conditioned at 50 °C & 100% RH based on gravimetric measurements of the reference specimens. The results from these specimens were compared with the gravimetric data obtained previously (see Section 7.1) and good correlation was observed. Therefore, it can be concluded that the specimen thickness and the embedded transmission sensors showed no significant influence on the equilibrium moisture content and the absorption behaviour of the bulk resin.

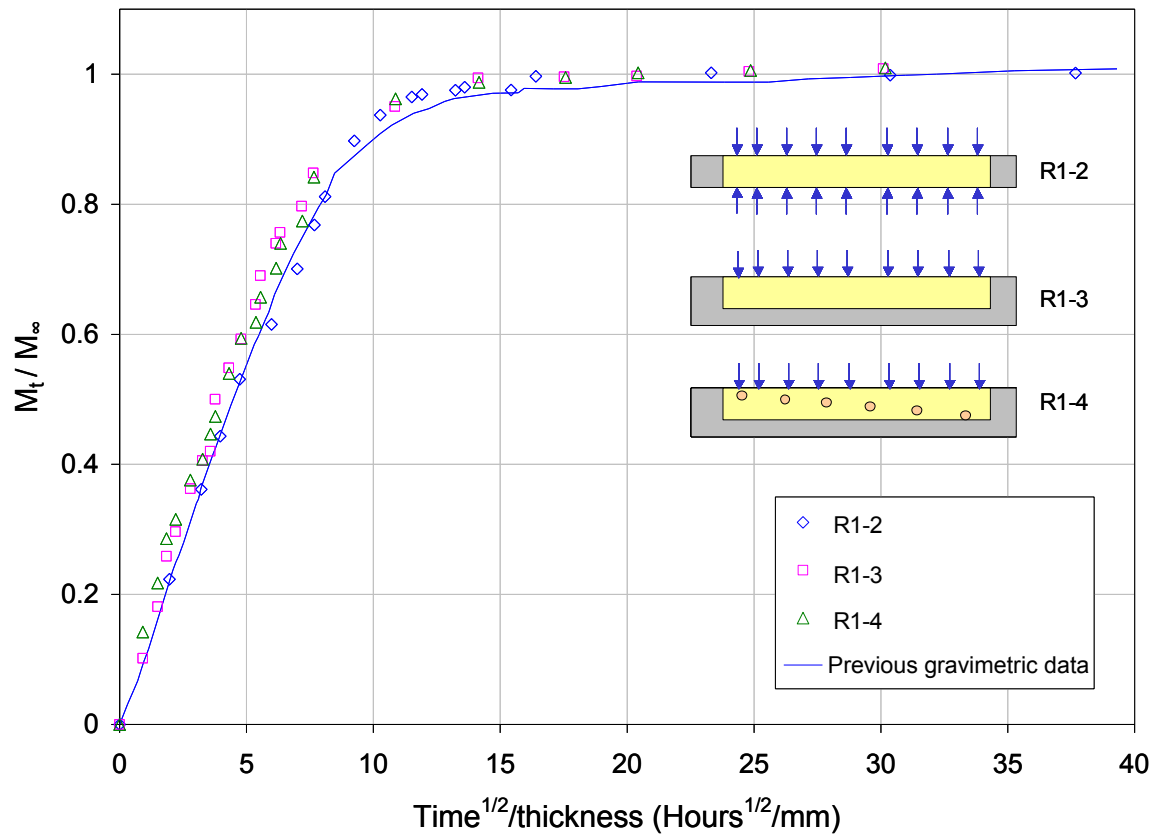


Figure 8.1 Comparison of absorption isotherms of water in the LY3505/XB3403 resin system at 50 °C based on the previous gravimetric data and based on the different reference specimens; inset shows a schematic illustration of the set of reference specimens used for gravimetric analysis.

In this specimen configuration, six sensors were embedded in a neat-cast epoxy/amine specimen (S1-1) at different depths for *in situ* moisture ingress monitoring and only one surface was exposed to water at 50 °C (see Section 3.8.2).

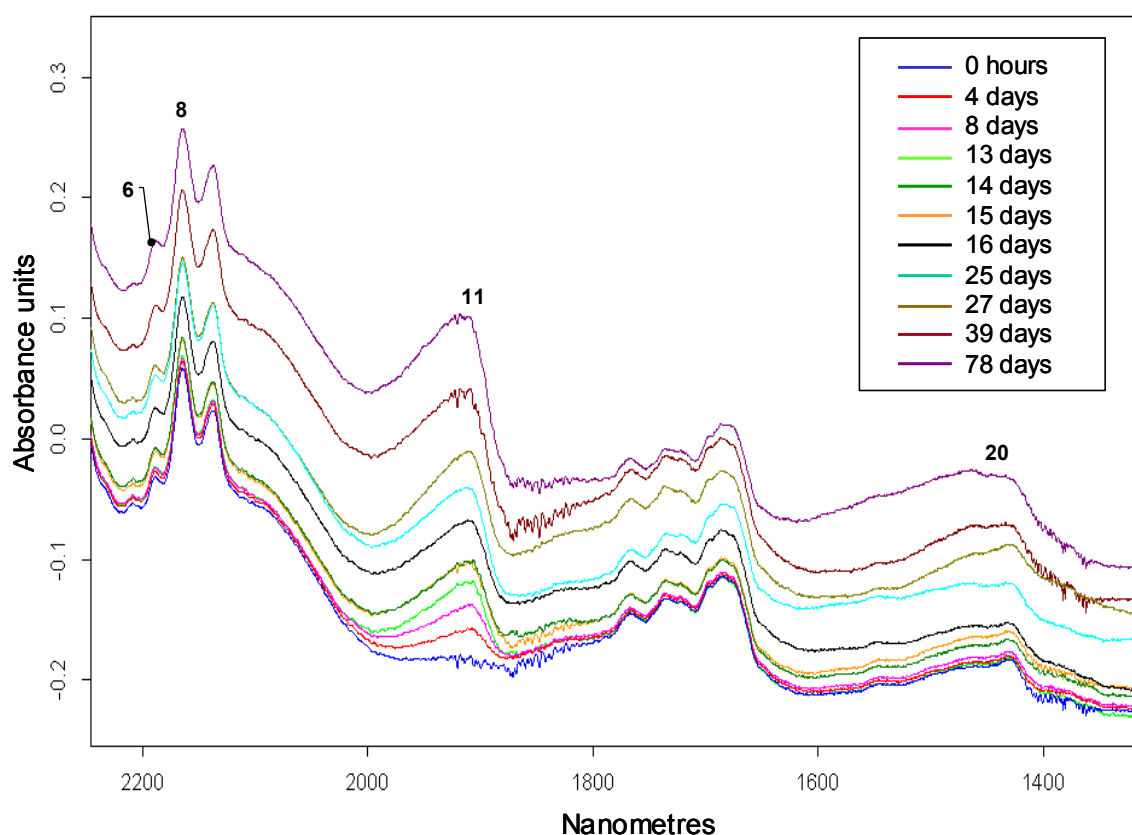


Figure 8.2 Near-infrared spectra of the LY3505/XB3403 resin system conditioned at 50 °C and obtained using the sensor-1; peak assignments: [6] 2207 nm – epoxy combination band, [8] 2164 nm – aromatic ring combination, [11] 1905 nm – OH band due to absorbed moisture and [20] 1430 nm – OH band due to alcoholic hydroxyl (see Table 5.1).

Figure 8.2 shows typical FTIR spectra in the range of 1300 – 2250 nm for the specimen coded as S1-1 before aging and after immersion in water at 50 °C for different exposure times. The major peaks of interest are clearly visible and they correlate well with that obtained using conventional FTIR spectroscopy (see Section 7.3.4). With increasing conditioning time, a gradual increase in absorbance peak at 1905 nm, which is due to the combination of asymmetric OH stretching and bending vibration can be seen. The increase in the absorption band was observed from all the embedded sensors and this peak area was used for quantitative analysis of localised moisture absorption at the sensor locations within the epoxy specimen.

In addition, the wide absorption band at 1430 nm due to the first overtone of the symmetric OH stretching can also be seen. A periodic progressive change in the peak of the absorption band at 1430 nm is visible as a function of immersion time. It was explained in the preceding chapters that this feature could be attributed to the influence of intramolecular and intermolecular hydrogen bonding between hydroxyl groups and the interactions between hydroxyl and the nucleophilic sites of the resin network (see Sections 5.2.1 and 7.3.4). This appeared to be an indication of anomalous diffusion where changes in interactions of free and bound water occur during the water transport process within the cross-linked resin [272]. More detailed discussion on the observed behaviour will be presented later.

The normalised peak area of the combination band at 1905 nm was determined with respect to the peak area of the reference band at 2164 nm. The change in the hydroxyl peak area as a function of conditioning time along with the spatial location of the sensor is shown in Figure 7.26; the conventional gravimetric data have also been cross-plotted to enable comparison. Except for the sensors -1 and -2, the other sensors showed similar rates of increase in the normalised peak area to that of the weight uptake in the bulk resin in the initial linear region. The higher rates of increase in the peak areas observed at sensors -1 and -2, which were embedded near the exposed surface could be attributed to the processing and hygrothermal history of the specimen and the response-time of the sensors will be discussed later.

With reference to Figure 7.26, a delay was observed for the sensors that were embedded away from the exposed surface this delay-time increased with increasing depth of the sensor in the case neat-resin specimen. However, it was difficult to obtain a linear relationship between the sensor location and the delay time observed for each sensor. This could be attributed to the change in the rate of diffusion as the moisture diffusion front moves into the specimen across

the thickness. Leaching of low-molecular weight species from the conditioned specimens also may have influence on the rate of moisture diffusion. On the other hand, this could be attributed to displacement of the sensors across the thickness of the specimen during specimen fabrication. According to the mould set-up illustrated in Figure 3.25, the lead-out optical fibres from the sensors were supported at specified heights outside the mould.

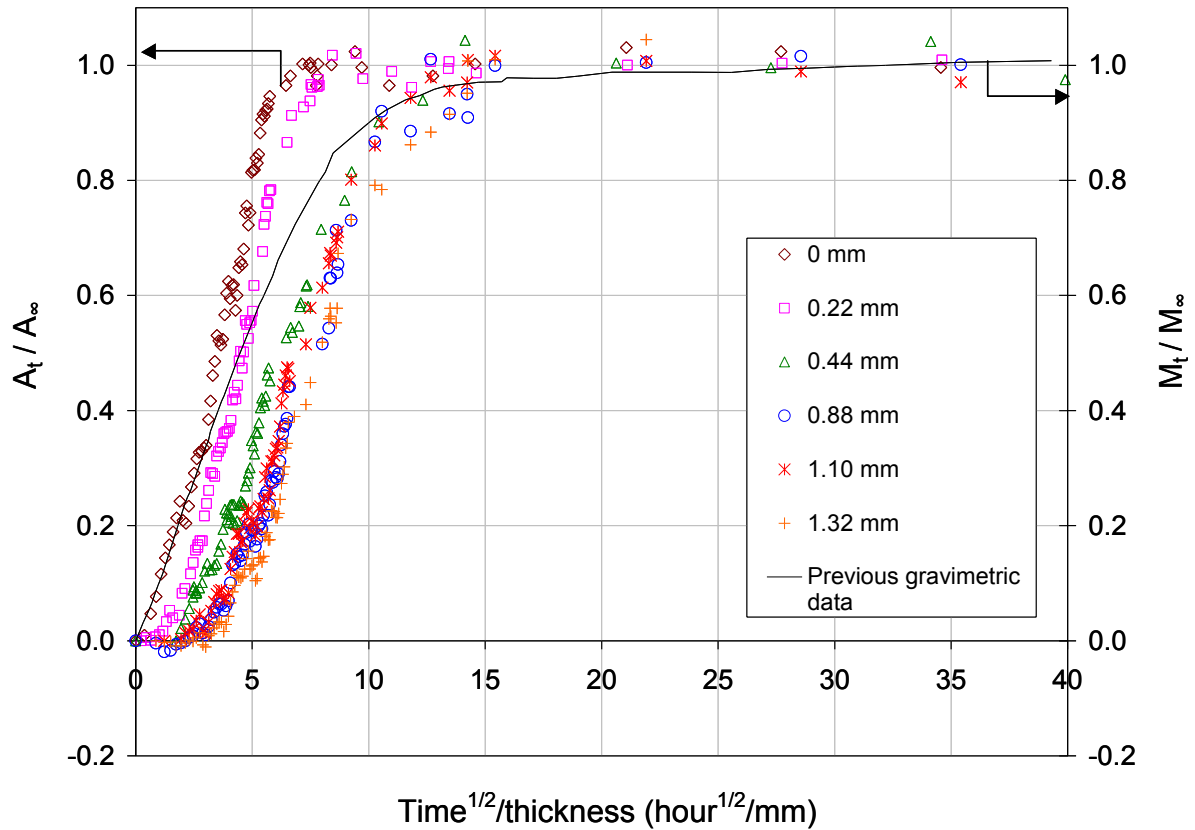


Figure 8.3 Comparison of the sensor responses from the embedded sensors within the specimen configuration – I and the conventional gravimetric results of the LY3505/XB3403 resin system conditioned at 50 °C as a function of immersion time and the sensor location.

With reference to Figure 8.4, due to the flexibility of the optical fibres, the possibility of sensor displacement through the thickness of the specimen is high, especially during mould filling and subsequent cross-linking of the resin. Nevertheless, absorption kinetics of water

in the epoxy/amine resin system was determined based on the spectral data obtained via the sensors -1, -3 and -6.

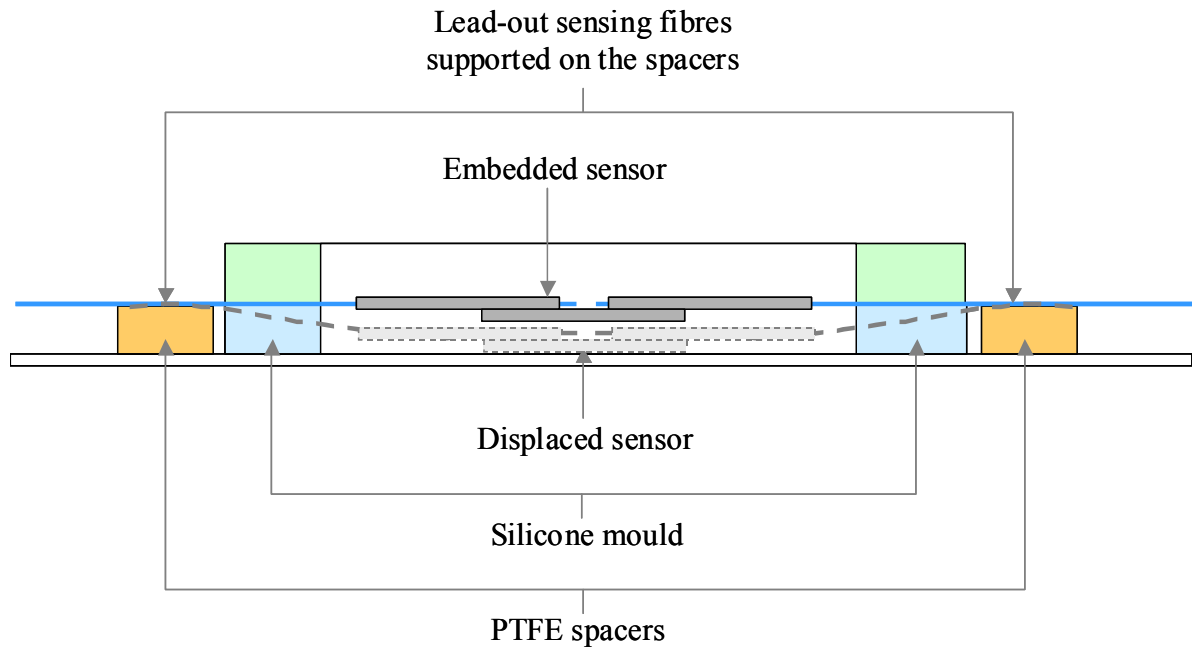


Figure 8.4 Schematic illustration showing the possibility of sensor displacement within the epoxy specimen when the sensors are secured outside the mould cavity.

Figure 8.5 shows localised absorption isotherms within the epoxy specimen based on the sensors -1, -3 and -6 embedded at 0, 0.44 and 1.32 mm, respectively from the surface that was exposed to water. Except for the delayed responses of sensors -3 and -6, the general trend of the absorption isotherms obtained from the three sensors showed similar diffusion behaviour. One-dimensional Fickian diffusion model (see Equations 2.24 and 2.25) was used to predict the localised moisture transport behaviour at three selected sensor locations. The applicability of anomalous diffusion models for predicting the diffusion of water in the epoxy/amine resin system was also investigated. The Carter-Kibler model [272] was used; this model invokes the existence and interactions of bound and mobile water molecules within a material as a

function of immersion time (See Section 2.4.2.2). This model was considered because of the localised step-wise diffusion profile seen in Figure 8.5. Equations 2.32, 2.33 and 2.34 were used to fit the experimental data and a comparison of the Carter-Kibler model and the Fickian model with the experimental data is presented in Figure 8.6(a and b) and Figure 8.7.

Reasonable correlation was observed with the spectral data and the Fickian model. However, a detailed investigation of the spectral response from the individual sensors revealed that the localised water transport, especially the diffusion away from the exposed surface exhibits a minor deviation from Fickian diffusion behaviour. The observed deviation of the localised moisture diffusion from the Fickian behaviour towards a step-increase in diffusion may be due to the following reasons. That may be due to the moisture diffusion through the interface region between the resin and the embedded optical fibres. A similar diffusion mechanism of water (capillary diffusion) has been reported in composite materials, where water enters the system along the interface between matrix and reinforcing fibres [425]. Karalekas *et al.* [426] employed FBG sensors for monitoring process-induced stresses and moisture-induced stresses in an epoxy resin system. They observed interface cracks and fibre/resin debonding after prolonged exposure to hygrothermal environment. Degradation of silicone rubber sealant that was used to protect the fibre exit points, was observed after long immersion times. The authors hypothesised that this may be attributed to combine effect of water penetration from the edges along the fibre/resin interface and the moisture-induced tensile strains developed in the resin. The same capillary diffusion may occur in the interface between the resin and the sensing fibres, which leads to a flow of water through capillary action into the sensing region along the fibres. On the other hand, this may be an over-estimation since the capillary diffusion reported by Karalekas *et al.* [426] was observed at long immersion times and the gravimetric measurements of the reference specimen with embedded “dummy” sensors

showed no significant effect on the weight-uptake compared to that of the neat epoxy specimens (see Figure 8.1).

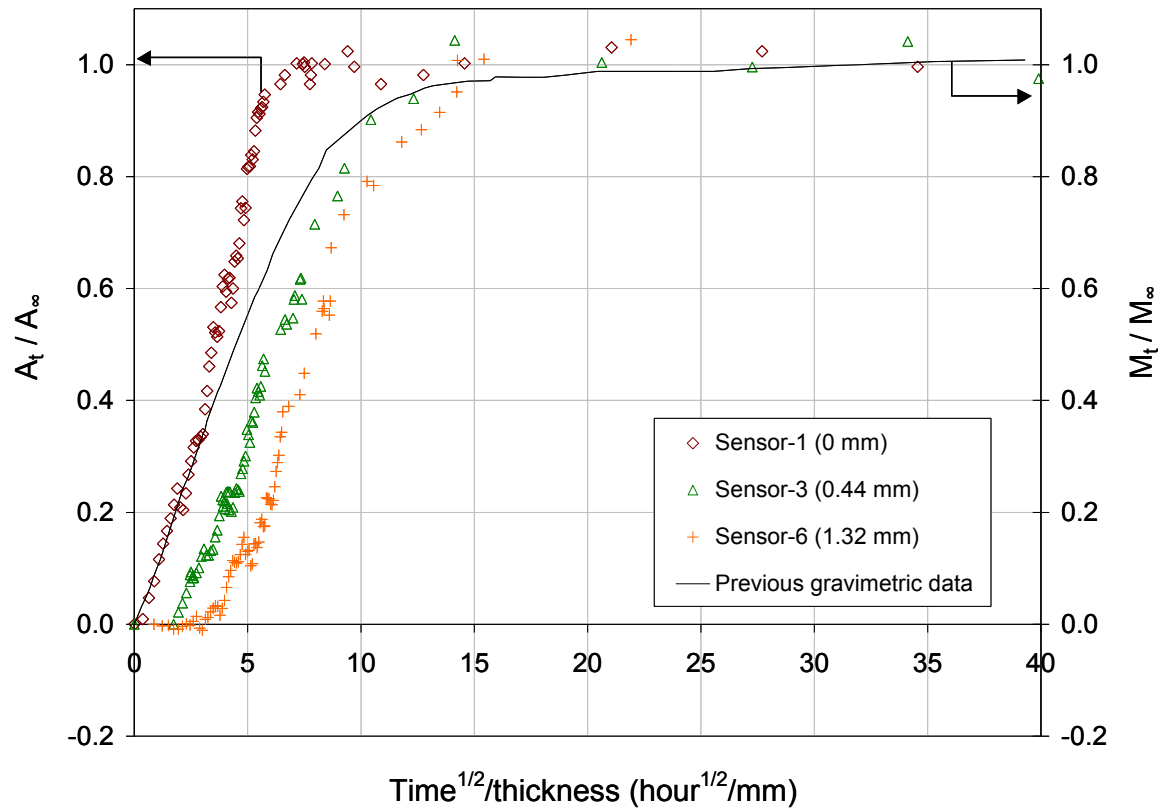


Figure 8.5 Comparison of the responses from the sensors embedded at 0, 0.44 and 1.32 mm from the exposed surface and the conventional gravimetric results of the LY3505/XB3403 resin system conditioned at 50 °C as a function of immersion time.

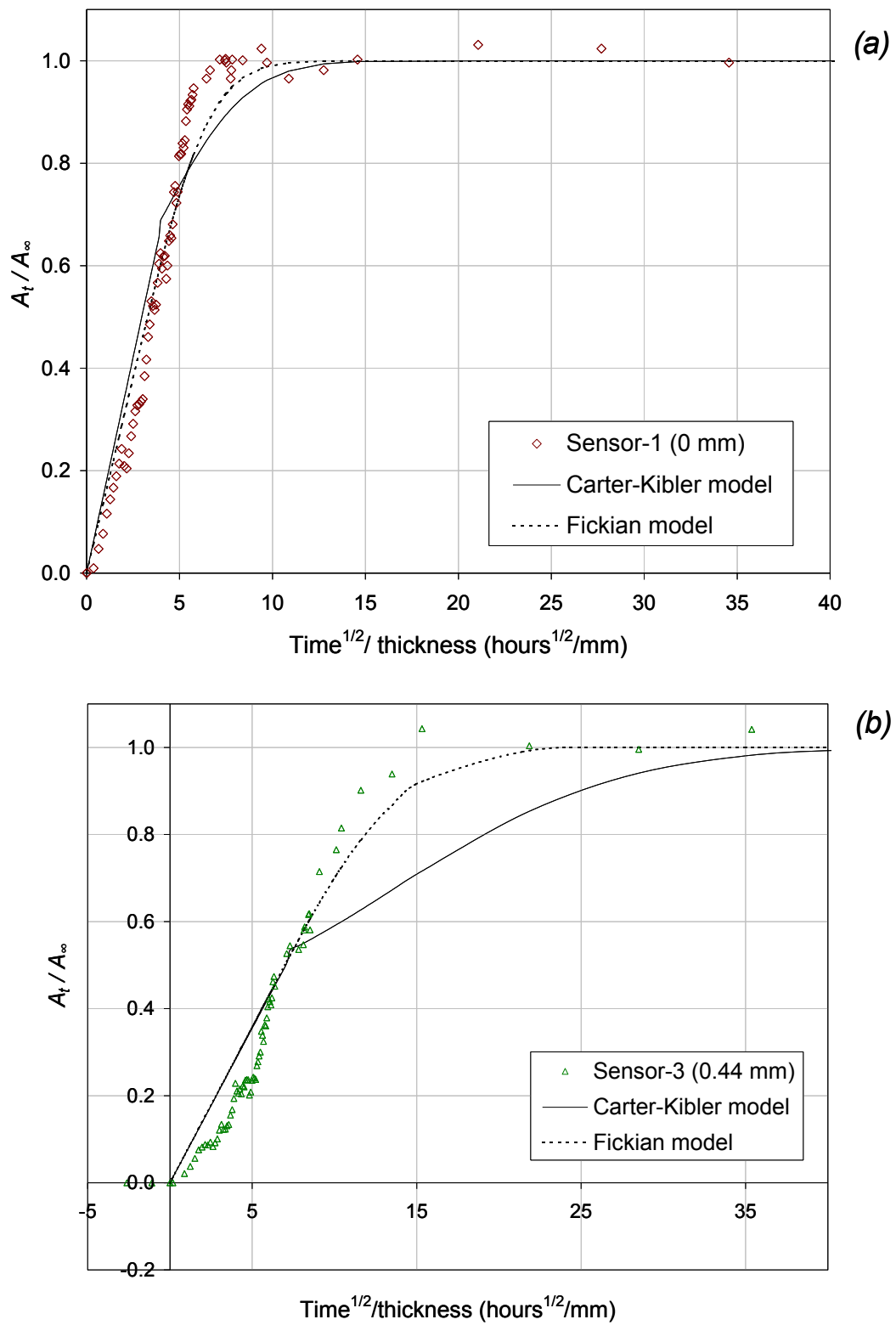


Figure 8.6 Comparison between the sensor response and the diffusion models for hydrothermal conditioning of the LY3505/XB3403 resin system at 50 °C: (a) sensor-1 and (b) sensor-3.

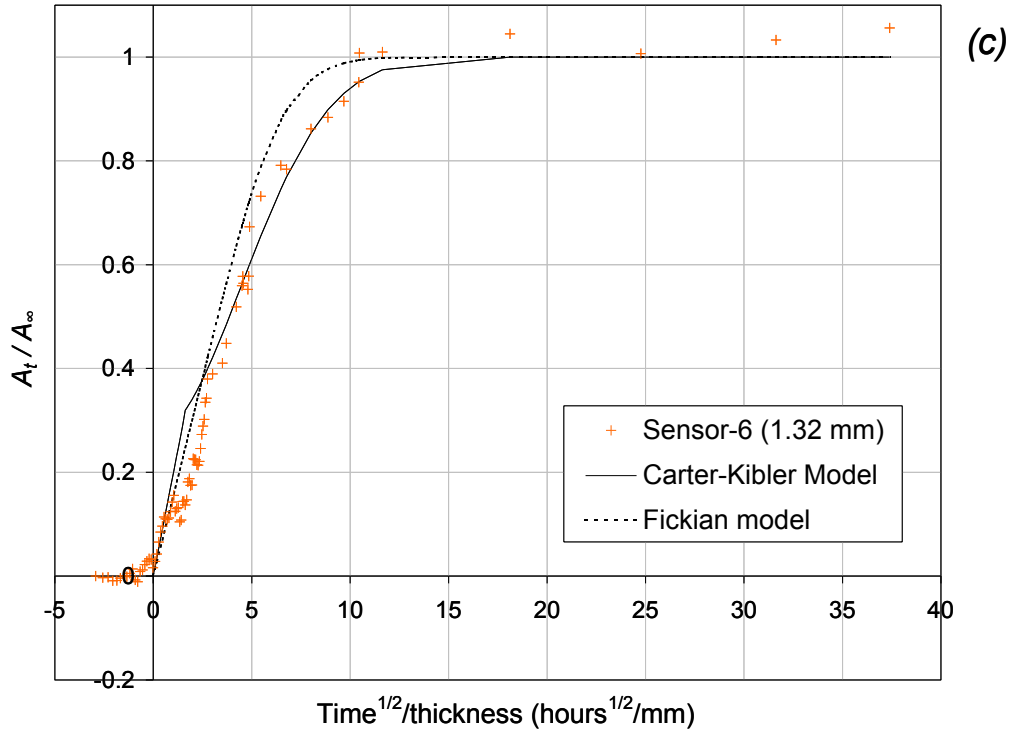


Figure 8.7 Comparison between the sensor response and the diffusion models for hydrothermal conditioning of the LY3505/XB3403 resin system at 50 °C: (c) sensor-6.

Reasonable fits were obtained using Carter-Kibler model for the data recorded from the sensors embedded at the exposed surface (sensor-1) and at 1.32 mm away from the exposed surface (sensor-3). However, with respect to Figure 8.6(b), the models only can be used to explain the initial linear region of the absorption isotherm that was obtained from the sensor embedded at 0.44 mm away from the exposed surface. The kinetic parameters related to the Carter-Kibler and the Fickian models are given in Table 5.5. The initial linear region of the sorption isotherms for $t \leq 0.7/\kappa$ was used to obtain the diffusion coefficient, D_γ . The values corresponding to the best fit to the data obtained from the sensor embedded at 0.44 mm away from the exposed surface do not follow the conditions of $2\gamma, 2\beta \ll \kappa$ to satisfy the Carter-Kibler approximations (Equations 2.33 – 2.34).

Table 8.1 Summary of kinetic parameters corresponding to best fit of the models to the spectral data obtained based on specimen configuration – I for hygrothermal conditioning of the LY3505/XB3403 resin system at 50 °C.

	Sensor Location		
	0 mm	0.44 mm	1.32 mm
D_{γ} (mm ² sec ⁻¹)	4.69×10^{-6}	2.73×10^{-6}	7.69×10^{-6}
κ (sec ⁻¹)	5.66×10^{-6}	3.05×10^{-7}	9.28×10^{-6}
β (sec ⁻¹)	9.10×10^{-7}	9.25×10^{-8}	8.50×10^{-7}
γ (sec ⁻¹)	1.85×10^{-6}	2.15×10^{-7}	2.26×10^{-6}

An attempt was also made to model the observed diffusion behaviour considering time-dependent diffusion coefficient that proposed by Marsh *et al.* [274]. The diffusion coefficient was determined as a function of immersion time using Equation 2.37. One-dimensional Fickian diffusion model (see Equation 2.24) was used to fit the experimental data using the values obtained for diffusion coefficient at different stages. Figure 8.8 shows a comparison of the best fit of the multi-stage model to the experimental data that obtained from the embedded sensors. A good correlation was observed between the spectral data and the model. The step-wise change in diffusion rates observed for data obtained from the sensors could be attributed to the nature of the water-polymer interactions and the transport phenomena associated with bound and mobile water. The effect of the above parameters on the rate of change in diffusion coefficient will be discussed later in this section in more detail.

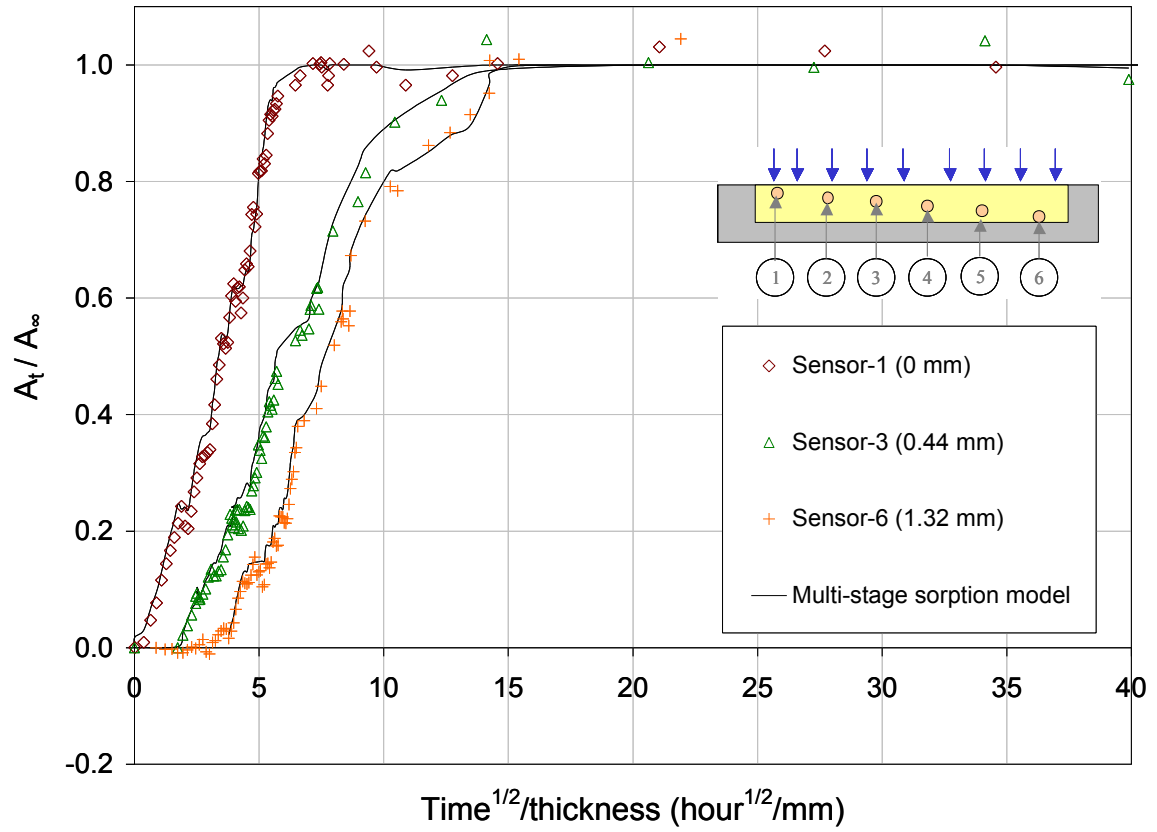


Figure 8.8 Comparison of the sensor responses and the best fits of the multi-stage diffusion model for hydrothermal conditioning of the LY3505/XB3403 resin system at 50 °C.

The multi-stage model was also used to investigate the effect of the concentration of absorbed moisture on the diffusion coefficient and Figure 8.9 shows the change in localised diffusion coefficient at different sensor locations as a function of absorbed moisture content. The diffusion coefficients at the sensor-1 and -3 showed a similar trend in which an overall increase towards the equilibrium moisture content was followed by a decrease towards zero at longer exposure times. A different trend was observed at the sensor-6 where the diffusion coefficient showed a gradual decrease at the very early stage of diffusion and remained at an average of $7.29 \times 10^{-7} \text{ mm}^2 \text{ s}^{-1}$ for $0.1 < A_t/A_\infty < 1.0$.

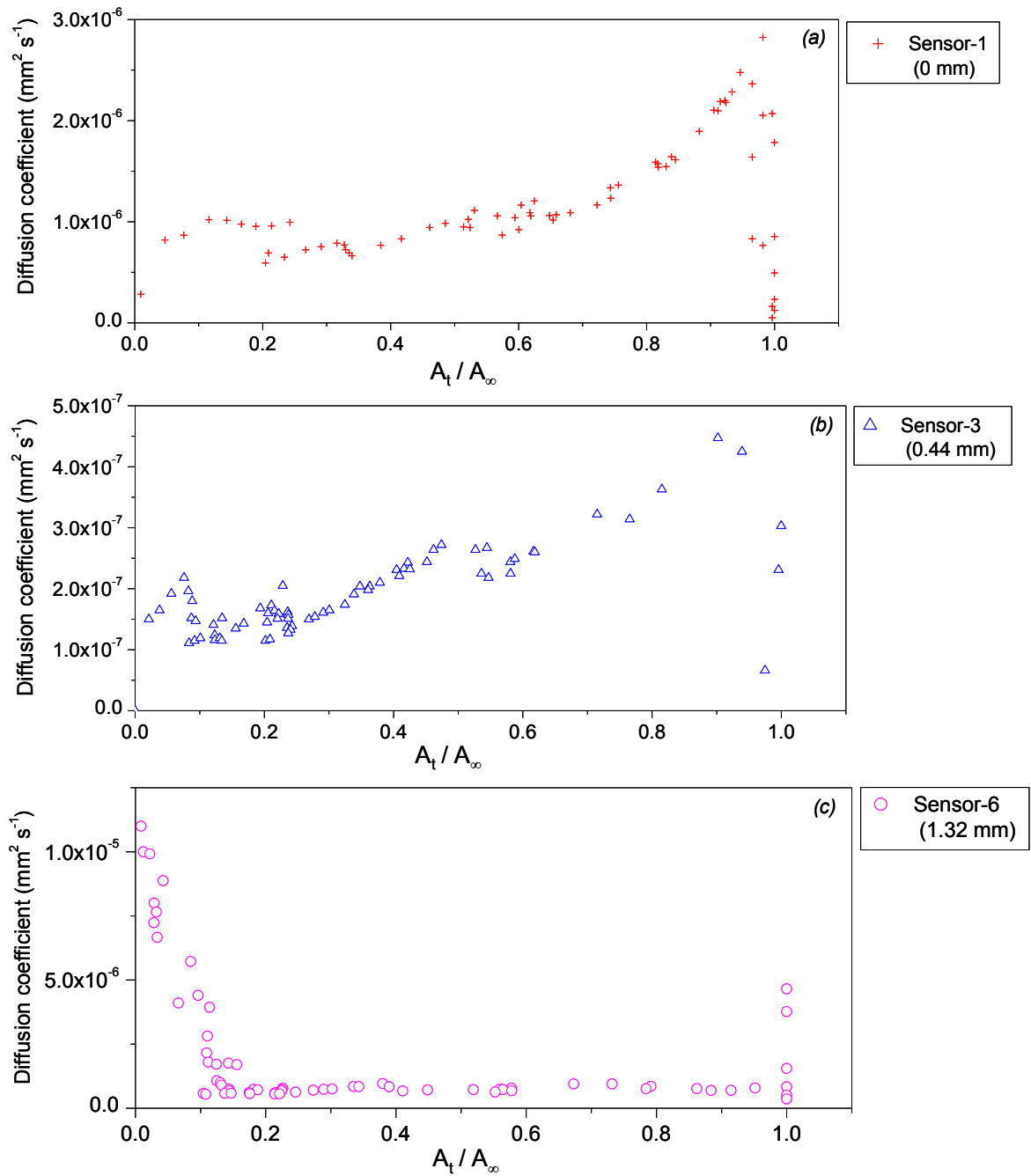


Figure 8.9 Change in localised diffusion coefficient of the LY3505/XB3403 resin system for hydrothermal conditioning at 50 °C based on the sensors embedded in the specimen configuration – I: (a) sensor-1, (b) sensor-3 and (c) sensor-6.

The observed trends of the time-dependent diffusion coefficient at different depths through the thickness of the specimen could be due to several reasons. When a material absorbs water, the local moisture concentration across the thickness varies with time until the

equilibrium moisture content is attained. Therefore swelling due to bound water is not uniform through out the material and residual stresses build up due to localised inhomogeneous swelling. Moisture-induced swelling and hence moisture-induced residual strain in neat epoxy resins has been found to be linearly proportional to the absorbed moisture content [427,428,429].

In addition, residual stresses are also present in the dry material before immersion due to process-induced resin shrinkage (see Section 6.3.3) [8,95,375]. Bogetti and Gillespie [6] studied process-induced stresses develop in thick thermosetting composite laminates during the cross-linking process. They proposed models to predict thermal and chemical strain of the thermosetting resins during cross-linking and modelled stress profiles across the thickness ≤ 2.45 cm. The models were developed for specimens of outer faces in contact and the stress profile across the thickness was found to be parabolic with tensile stresses at the contact surfaces and compressive stresses at the middle of the specimen. They discussed the effect of asymmetric processing parameters such as moulding methods and cross-linking temperature on the gradient of process-induced shrinkage within the material. Also it was reported that higher cooling rates induce higher resin shrinkage for shorter cooling times when a cross-linked material is cooled down to ambient temperature [430]. However, the cooling rate showed a negligible effect on the resin shrinkage strain over longer storage times (*i.e.* $t \geq 2000$ minutes) at room temperature.

Based on *in situ* monitoring of moisture induced strains using FBG sensors, Karalekas *et al.* [426] observed that the process-induced compressive stresses reduce due to absorbed moisture and after prolonged exposure to water, the stresses become tensile due to moisture-induced swelling. Furthermore, they proposed that the capillary diffusion from the edges along the

fibre/resin interface accelerate by the strain mismatch at the interface due to non-hygroscopic nature of the fibre compared with the resin. Therefore the localised diffusivity of moisture is a function of process and hygrothermal history of the material.

As explained in Section 3.8.2, an open mould was used to fabricate the epoxy specimens for hygrothermal conditioning as shown in Figure 3.25. Therefore the process-induced residual stresses may not be symmetric around the mid-plane across the thickness. During cross-linking, the resin at the open side of the mould experiences less restriction towards chemical shrinkage compared to that in contact with the glass moulding plate. Therefore in the cross-linked epoxy specimens used in this study, tensile stresses develop at the surface that was in contact with the glass plate while the free-surface remains at a lower stress level when the specimen was cooled down to room temperature.

In the case of the hygrothermal conditioning experiments, the surface of the specimen that was in contact with the glass moulding plate was exposed to water. Therefore a higher rate of diffusion was observed at the sensor-1 during the initial stage of absorption, which could be attributed to the accelerated water diffusion into free volume present at the surface. The process-induced tensile stresses may restrain network relaxation leaving more the free-volume at the surface region. A gradual deceleration of the diffusion coefficient at the sensor-1 for $0.1 < A_t/A_\infty < 0.2$ could be attributed to the network relaxation due to formation of bound water at nucleophilic sites in the resin. The same transport phenomenon was discussed previously in terms of water-polymer interactions in the polymer network [250,422] and the types of water and their activities [247] at the early stage of sorption process. The formation of bound water has been identified as a reversible exothermic reaction [317] and application

of heat dominates the backward reaction. The periodic change in the diffusion coefficient may lead to multi-stage diffusion of water in the epoxy/amine resin system.

This also can be evident from the near-IR spectra obtained via the embedded sensors (see Figure 8.2). At the early stage of sorption, the absorption band at 1905 nm increased while the overlapped band due to the first overtone of stretching and bending vibrations of OH at 1430 nm remained the same. However, a change in peak shape and a minor decrease in peak intensity can be seen as the moisture uptake increases. This feature was attributed to the formation of bound water within the resin network since the frequency of the OH band decreases for the stretching mode, but it increases for the bending mode due to hydrogen bonding [319]. A periodic change in the above mentioned spectral characteristics of the absorption band at 1430 nm can be associated with the change in probabilities of existence of free and bound water as a function of moisture content and the immersion time. However, clear spectral evidence to support this absorption phenomenon cannot be found in the near-IR spectral region used in this study. The compressive stresses develop due to moisture-induced swelling also may reduce the diffusivity by compensating process-induced tensile stresses at the surface regions.

The absorption isotherm obtained using sensor-3 shows similar multi-stage diffusion behaviour, however the initial diffusion was slower than that observed from the sensor-1. This could be attributed to the localised stress profile at the sensing region away from the exposed surface. With respect to Figure 8.9(a and b) the observed increase in diffusion coefficient at the later stage of diffusion could be due to the loss of protection of the sealant at the exit points of lead-out fibres of sensors -1 and -3 and accelerated capillary diffusion through the fibre/resin interface due to moisture-induced swelling strains [426].

On the other hand, sensor-6 showed a different trend of change in diffusion coefficient against the absorbed moisture content as shown in Figure 8.9(c). The behaviour is more related to Fickian diffusion where the diffusion coefficient decreases with increase in moisture content due to the exothermic nature of the reaction. In addition, as explained earlier, the covered surface of the epoxy specimen for conditioning experiments was not in contact during cross-linking. Therefore, the resin experienced no constraints for shrinkage except surface tension of the resin and can be rearranged to minimise the induced stresses at the surface. This could lead to less influence of the resin shrinkage on the moisture diffusion process at the regions close to the covered surface. The Fickian model shows a good fit to the spectral data obtained from sensor-6 and showed reasonable correlation as shown in Figure 8.8(c). The deviation from the Fickian model towards multi-stage diffusion can be attributed to a combined effect of moisture-induced swelling stresses and the localised water-polymer interactions as discussed before.

8.2.2 Specimen configurations – II and – III

The differences between the specimen configuration – I and the configurations – II and – III were: the method of securing the sensors during specimen fabrication, the number of sensors embedded within the epoxy/amine specimens and the direction of hygrothermal exposure (see Section 3.8.2). Figure 8.10 and Figure 8.11 show a comparison of the absorption isotherms of the epoxy/amine resin system at 50 °C obtained based on the previous gravimetric measurements and that based on the reference specimens corresponding to each specimen configuration. Good correlation was observed between the neat-epoxy specimens (R2-2 and R3-2) and the embedded dummy sensors (R2-3 and R3-3); however, no evidence was found

on anomalous moisture transport due to capillary diffusion from the edges along the fibre/resin interface.

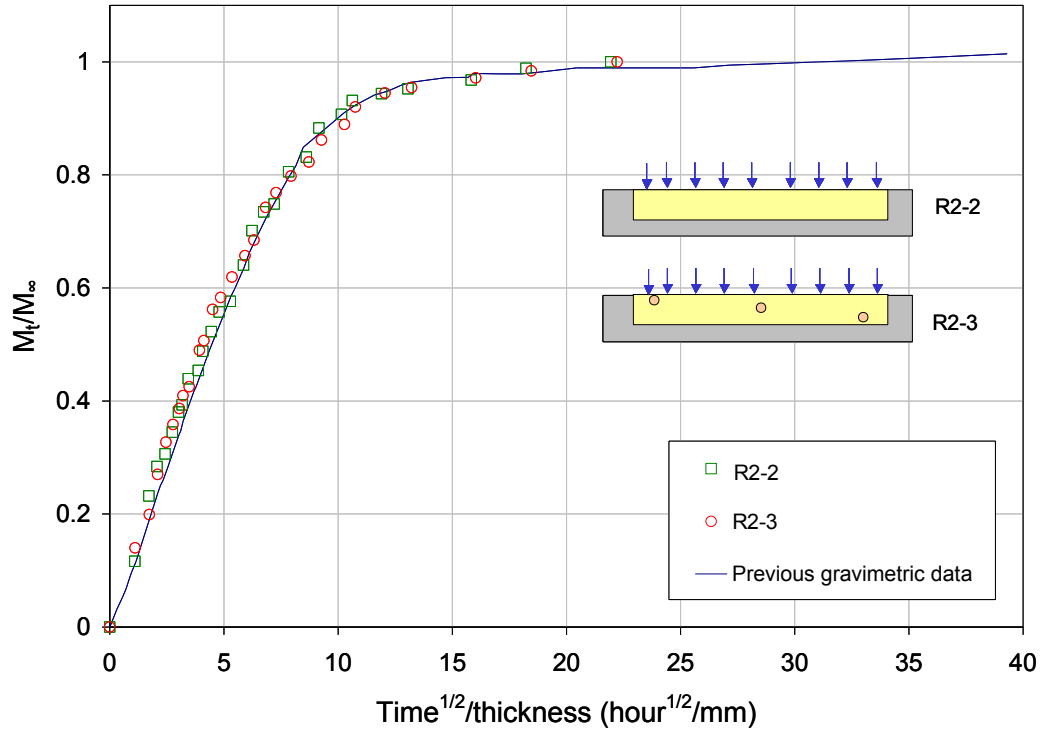


Figure 8.10 Absorption isotherms of water in the LY3505/XB3403 resin system at 50 °C based on the gravimetric measurements of reference epoxy specimens of the specimen configuration – II.

Figure 8.12 shows typical near-IR spectra in the range of 1200 – 2250 nm recorded via the sensor-1 of the specimen configuration – III before aging and after immersion in water at 50°C for different exposure times. The absorption band at 1905 nm due to the asymmetric stretching and bending of O-H showed a rapid response to absorbed moisture. This is due to the sensor location compared with the relative locations of the sensors -2 and -3 from the exposed surface. In addition, the shape of the overlapped band at 1430 nm due to the first overtone of symmetric O-H stretching changed as a function of immersion time.

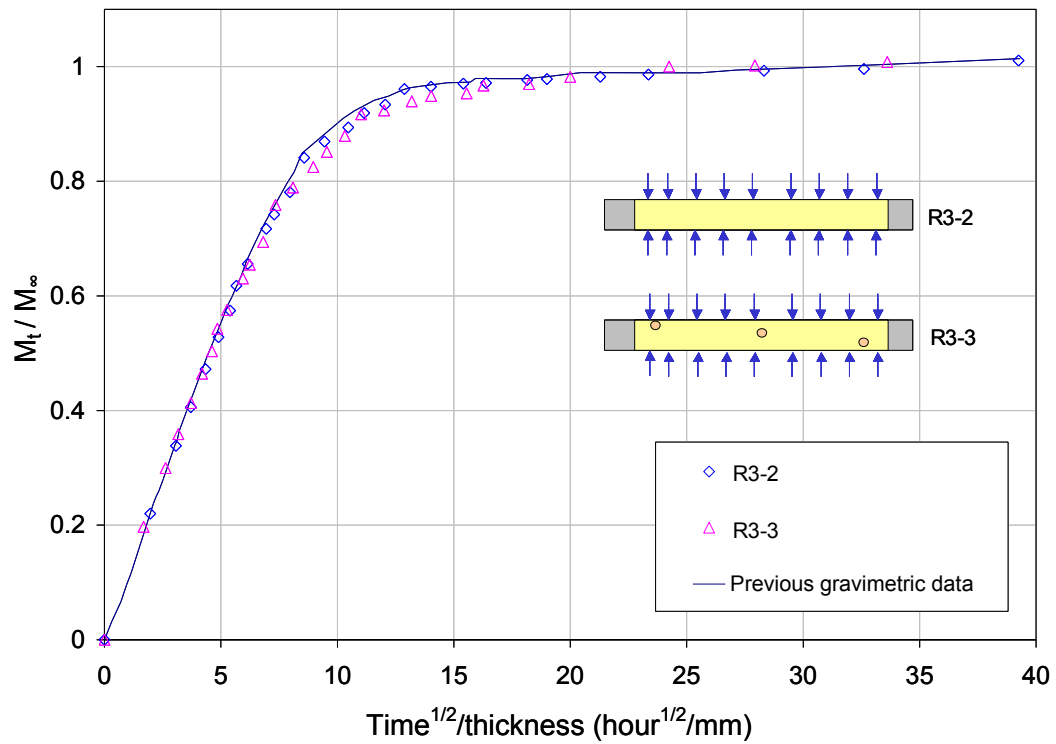


Figure 8.11 Absorption isotherms of water in the LY3505/XB3403 resin system at 50 °C based on the gravimetric measurements of reference epoxy specimens of the specimen configuration – III.

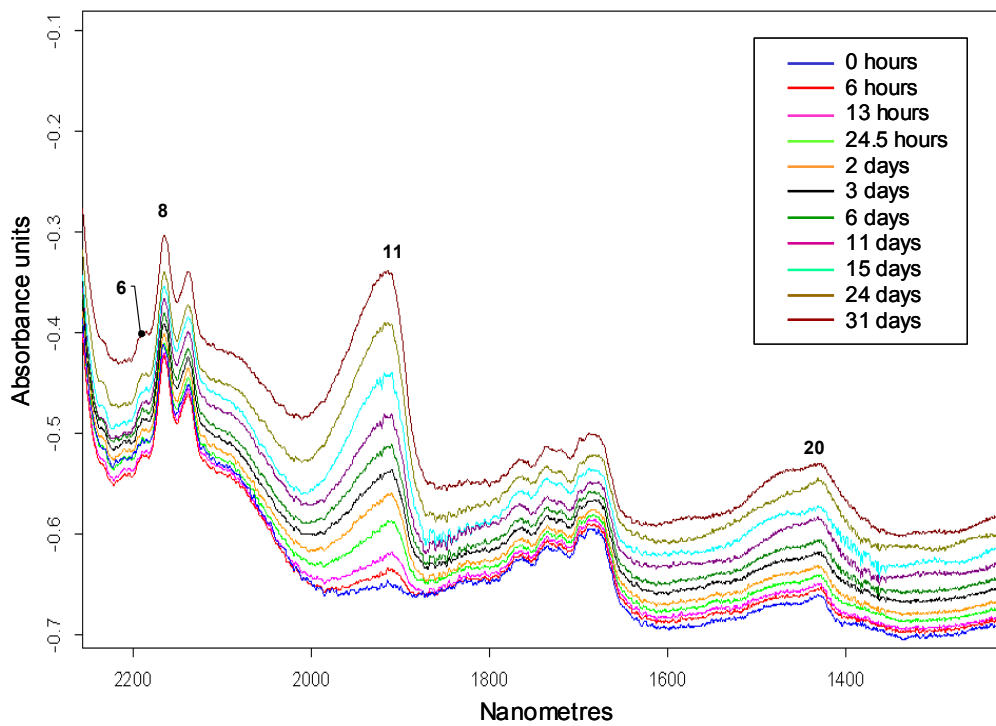


Figure 8.12 Typical near-IR spectra obtained via the sensor-1 embedded in the specimen configuration–III conditioned at 50 °C (see Table 5.1).

8.2.2.1 Absorption kinetics: Specimen configuration – II

For *in situ* monitoring of moisture ingress, only one side of the specimen was exposed to the water and the sensor-1 was embedded at the exposed surface. The locations of the sensors -2 and -3 with respect to the exposed surface are shown in Figure 3.30. Figure 8.13 shows localised absorption isotherms constructed based on the spectral responses from the embedded sensors. During specimen fabrication, the exposed side was in contact with the glass moulding plate and the covered surface was on the open side of the mould.

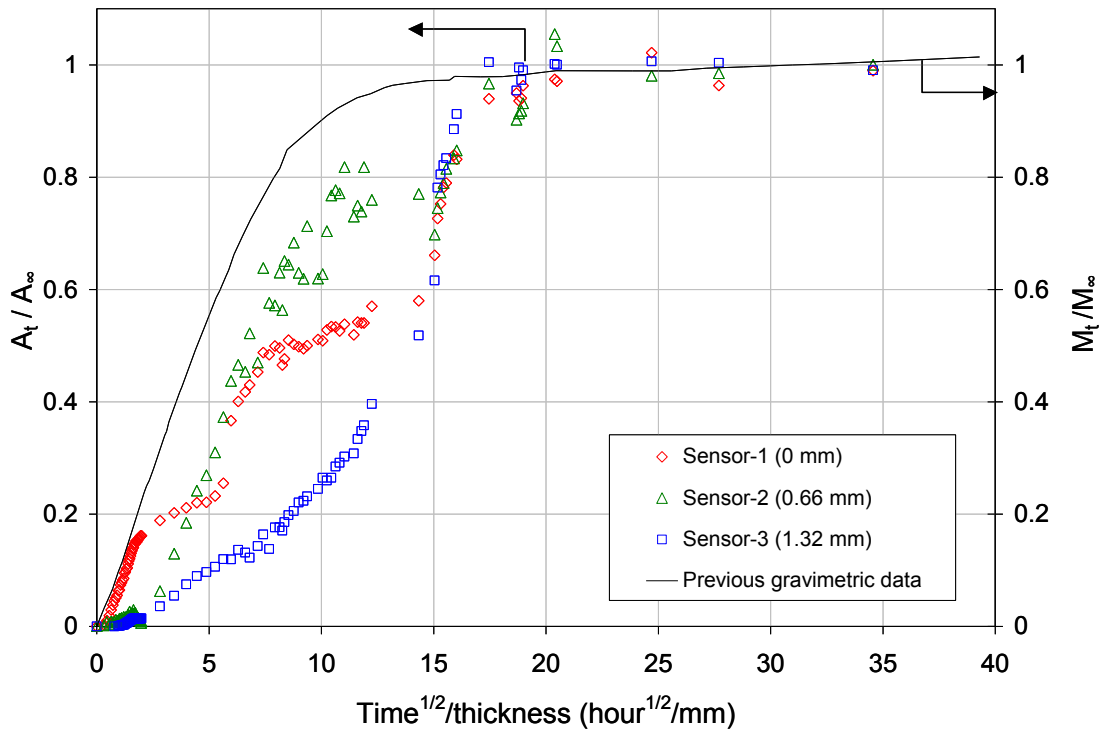


Figure 8.13 Comparison of the sensor responses from the embedded sensors within the specimen configuration – II and the conventional gravimetric results of the LY3505/XB3403 resin system conditioned at 50 °C as a function of immersion time and the sensor location.

The localised diffusion behaviour observed from the embedded sensors were different from that observed from the sensors embedded in the specimen configuration – I. Defining a general trend was difficult since each sensor showed unique diffusion characteristics at the

embedded locations. Moisture reached the sensor-1 at a very early stage of diffusion and followed a similar diffusion rate as that of the bulk epoxy resin for a short time. A step-change in the diffusion rate is clearly apparent at the sensor-1. A delay in response was observed from the sensor-2 compared to the sensor-1 due to the sensor location. As water was permitted to enter the specimen from only one side and the sensor-3 was located 1.32 mm away from the exposed surface, we expected to see a delayed response compared with that was seen from the sensor-2. However both sensors detected moisture approximately at the same time while the rate of increase in the amount of absorbed moisture detected by the sensor-2 was high compared with that detected by the sensor-3. In addition, sensor-3 showed a slower rate of diffusion approximately for first 33 days of immersion followed by an increase in rate up to the equilibrium moisture content. However, after 57 days of exposure, responses from all the sensors overlapped and showed similar absorption behaviour.

The Carter-Kibler model and the multi-stage model were used to predict the localised sorption kinetics of water in the epoxy/amine resin. Figure 8.14(a and b) and Figure 8.15 compare the best fits of the models to the experimental data based on sensor-1, sensor-2 and sensor-3, respectively. The kinetic parameters κ , β and γ were determined by fitting the experimental data to Equations 2.33 – 2.34. It is clearly apparent from the plots that the Carter-Kibler model only can be used to predict the initial stage of diffusion of water for immersion time, $t \leq 0.7/\kappa$ at each sensor location. Table 8.2 shows the summary of fitting parameters obtained for the best fits to the experimental data. It can be clearly seen that for the data obtained from sensors -2 and -3, the probabilities for water to become mobile and bound, β and γ , respectively are greater than κ . Although γ and β obtained for the data from sensor-1 satisfied the condition $2\gamma, 2\beta \ll \kappa$, it should be noted that the model is not capable of describing the

actual sorption behaviour at all the sensor locations for immersion times, $t \gg \frac{1}{\kappa}$. Therefore the Carter-Kibler model seemed not suitable for predicting the complete sorption behaviour through the thickness of the epoxy specimen.

Table 8.2 Summary of kinetic parameters corresponding to best fit of the models to the spectral data obtained from the specimen configuration – II for hygrothermal conditioning of the LY3505/XB3403 resin system at 50 °C.

	Sensor Location		
	0 mm	0.66 mm	1.32 mm
D_γ (mm ² sec ⁻¹)	6.25×10^{-6}	6.25×10^{-4}	1.22×10^{-5}
κ (sec ⁻¹)	1.02×10^{-5}	1.02×10^{-3}	1.99×10^{-5}
β (sec ⁻¹)	1.80×10^{-7}	9.00×10^{-4}	7.00×10^{-4}
γ (sec ⁻¹)	9.90×10^{-7}	1.08×10^{-3}	4.84×10^{-2}

As seen in Figure 8.14(a and b) and Figure 8.15, good correlation was observed between the multi-stage model and the localised transport phenomena of water within the specimen. This suggests that the influence of process and hygrothermal history on the diffusion coefficient of water that was discussed in Section 8.2.1 could be used to describe the anomalous absorption behaviour in the specimen configuration – II.

In particular, sensor-1, which is embedded at the surface showed a fast rate of diffusion followed by an early pseudo-equilibrium level for short immersion times and the feature is not apparent from the sensors -2 and -3. Hahn [427] showed that during the early stage of diffusion, the absorbed water produces relatively little swelling until a critical amount of water is absorbed into the specimen, and then the volume increases proportionally to the additional water content. Li *et al.* [431] explained the behaviour in terms of types of absorbed

water in a polymer. The change in volume of resin due to absorbed moisture was measured using a liquid displacement method. The ASTM D792 standard was used to measure the density of the specimens. The apparent volume of the conditioned specimens was calculated using: $V = M/\rho$. They hypothesised that the mobile water, which occupies existing free volume in the polymer governs the early stage of sorption while the bound water dominates the later stage of sorption process. It was reported that in the early stage of diffusion, the water molecules attach to the hydrophilic functional groups on the surface of the specimen [250].

The transport behaviour can also be affected by the influence of process-induced tensile stresses exist at the exposed surface of the specimen, which was in contact with the glass moulding plate during specimen fabrication. Therefore the first step-change of the diffusion rate could be associated with the fast rate of diffusion of mobile water absorbed through the exposed surface followed by the formation of bound water with the polymer molecules. A gradual increase in compressive stresses due to moisture-induced swelling reduces the diffusion rate by hindering the fabrication stresses. The second pseudo-equilibrium level of moisture uptake was explained in terms of formation of clusters of unbound water within the polymer network [274].

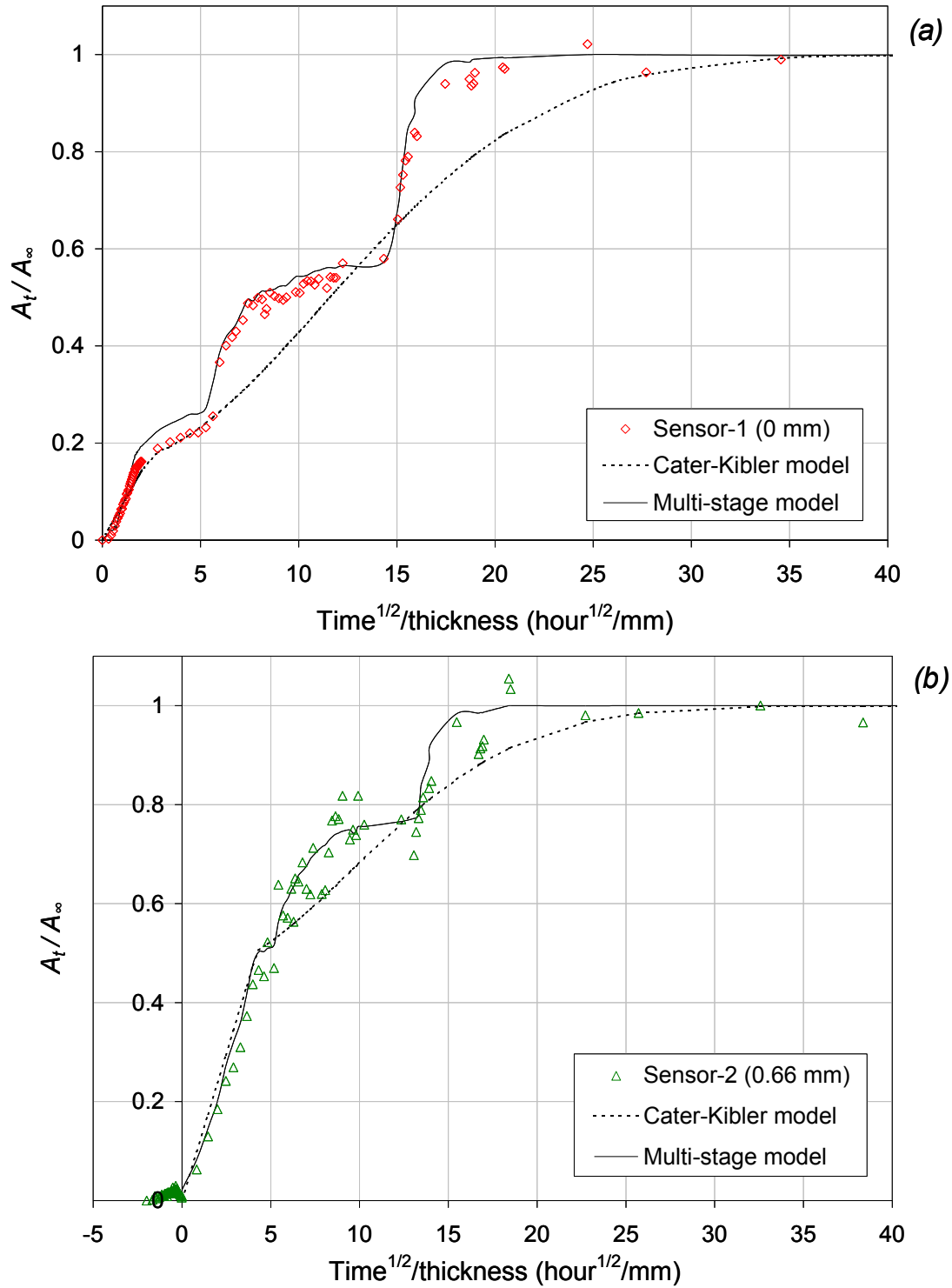


Figure 8.14 Comparison between the sensor response and the diffusion models for hydrothermal conditioning of the LY3505/XB3403 resin system at 50 °C (a) sensor-1 and (b) sensor-2.

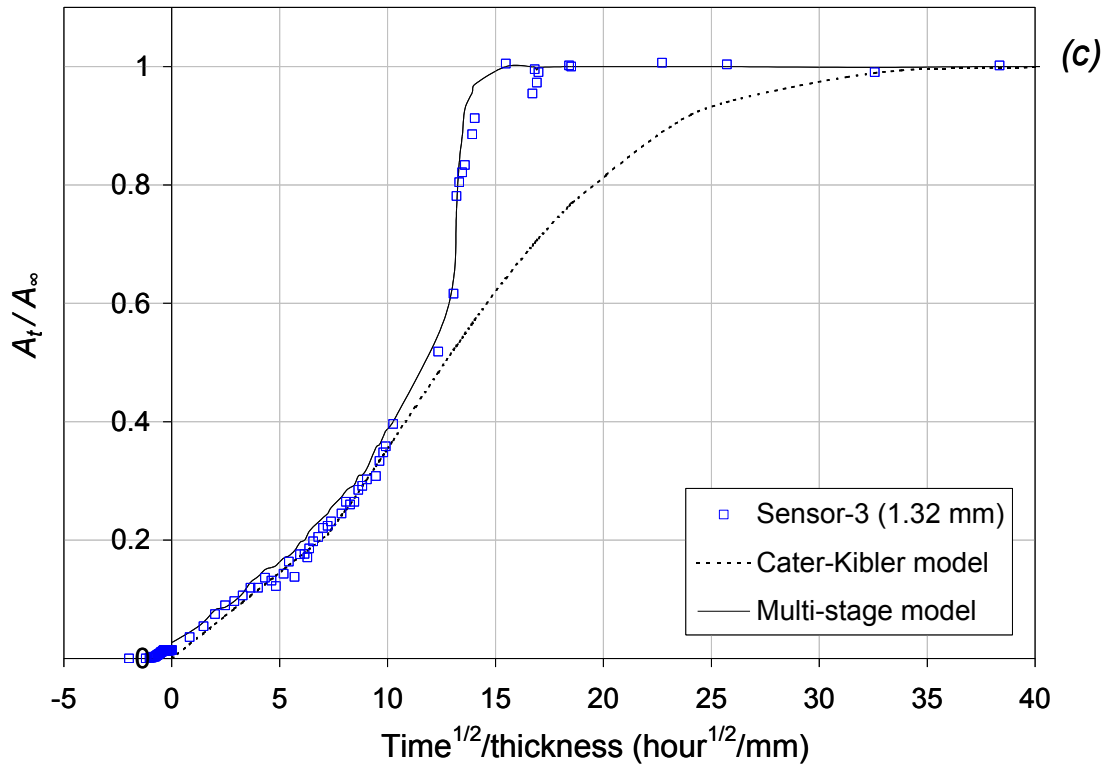


Figure 8.15 Comparison between the sensor response and the diffusion models for hydrothermal conditioning of the LY3505/XB3403 resin system at 50 °C: (c) sensor-3.

As the moisture diffusion front moves into the specimen along the direction of the thickness, different absorption phenomena were observed. As seen in Figure 8.14(b), the pseudo-equilibrium moisture level at the sensor-2 was observed approximately at $A_t/A_\infty \approx 0.75$ while that for sensor-1 appeared at around $A_t/A_\infty \approx 0.55$. However, according to Figure 8.16(b), the first change in the gradient of the diffusion coefficient clearly appeared around 0.5 together with the second deflection at 0.8.

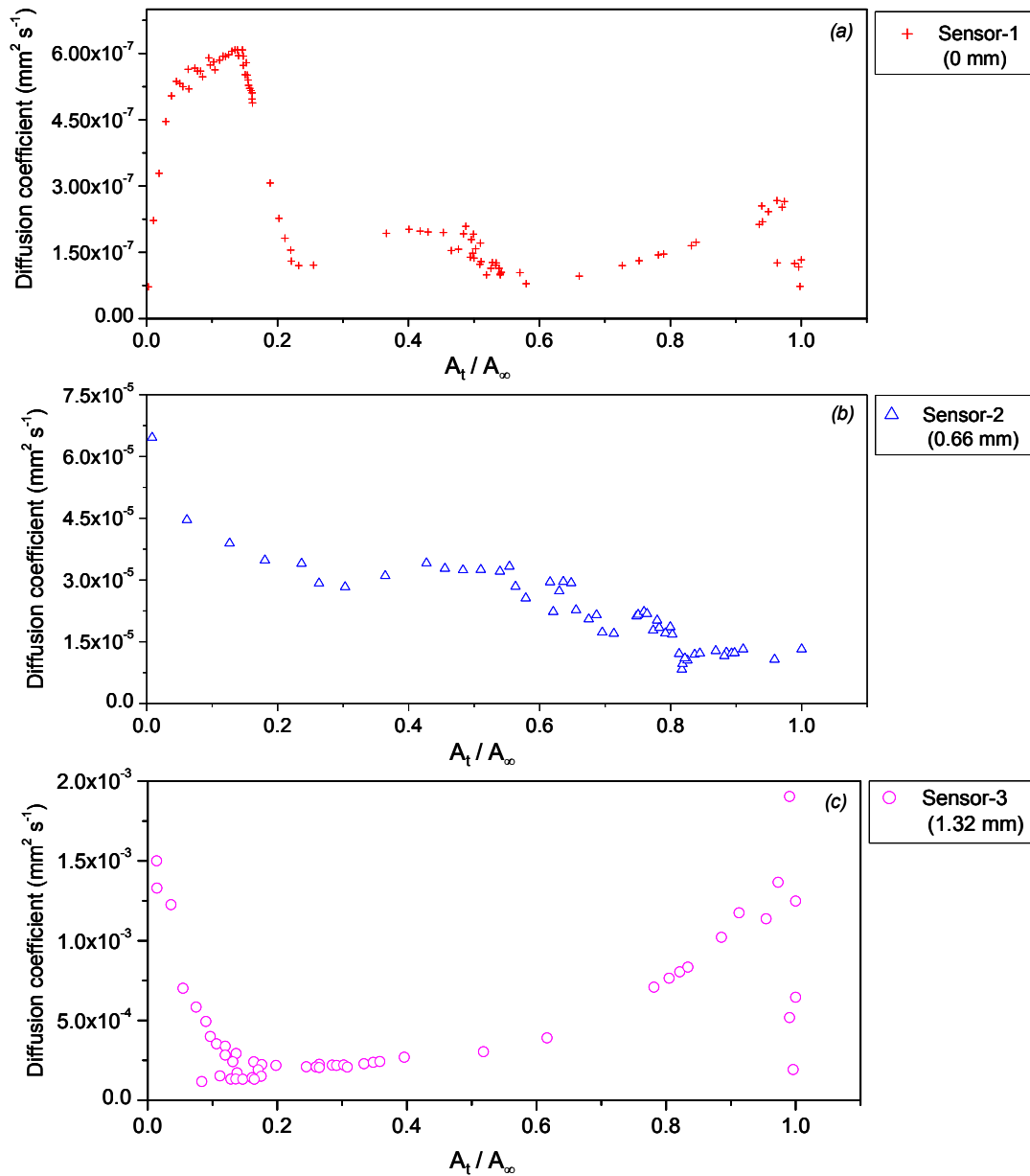


Figure 8.16 Change in localised diffusion coefficient of the LY3505/XB3403 resin system for hydrothermal conditioning at 50 °C based on the sensors embedded in the specimen configuration – II (a) sensor-1; (b) sensor-2 and (c) sensor-3.

At sensor-3, which was embedded 1.32 mm away from the exposed surface, a different transport phenomenon was observed where a decrease in the diffusion coefficient was observed followed by an increase towards the equilibrium moisture content. The trend can be attributed to the combined effect of the localised stresses and the chemical inhomogeneity at

the sensing cavity. It is necessary to emphasize that the sensing region is small compared with the overall specimen dimensions and possible localised material inhomogeneities that could occur during resin mixing show a considerable influence on the moisture diffusion at the sensing region. However, according to the spectra obtained after cross-linking and before immersion of the specimens, it can be verified that there was no excess epoxy resin or amine cross-linking agent left in the cross-linked system at the sensing regions.

On one hand, leaching of low-molecular weight species was observed in epoxy resins at longer immersion times [278]. Therefore an increase in rate of water clustering could be expected due to leaching of low-molecular weight segments by leaving more free volume at prolonged exposure. However the observed absorption behaviour cannot be supported on the basis of leaching due to insufficient spectral evidence. On the other hand, interface debonding due to capillary diffusion along the fibre/resin interface coupled with the influence of increased strain mismatch at the interface may cause an increase in rate of moisture diffusion into the sensing region [426].

8.2.2.2 Absorption kinetics: Specimen configuration – III

In specimen configuration – III, the locations of the embedded sensors through the thickness of the specimens were kept the same as that in the configuration – II (see Figure 3.30). However both sides of the specimens were exposed to water during hygrothermal conditioning at 50 °C. Therefore as can be seen in Figure 3.30, sensor-3 was embedded 1.32 mm away from the surface where sensor-1 was embedded and at the same time the sensor was 0.68 mm away from the opposite side of the specimen, which was also exposed to water in this specimen configuration. Similarly, sensor-2 was 0.66 mm away from sensor-1 and at the same time 1.34 mm away from the opposite surface.

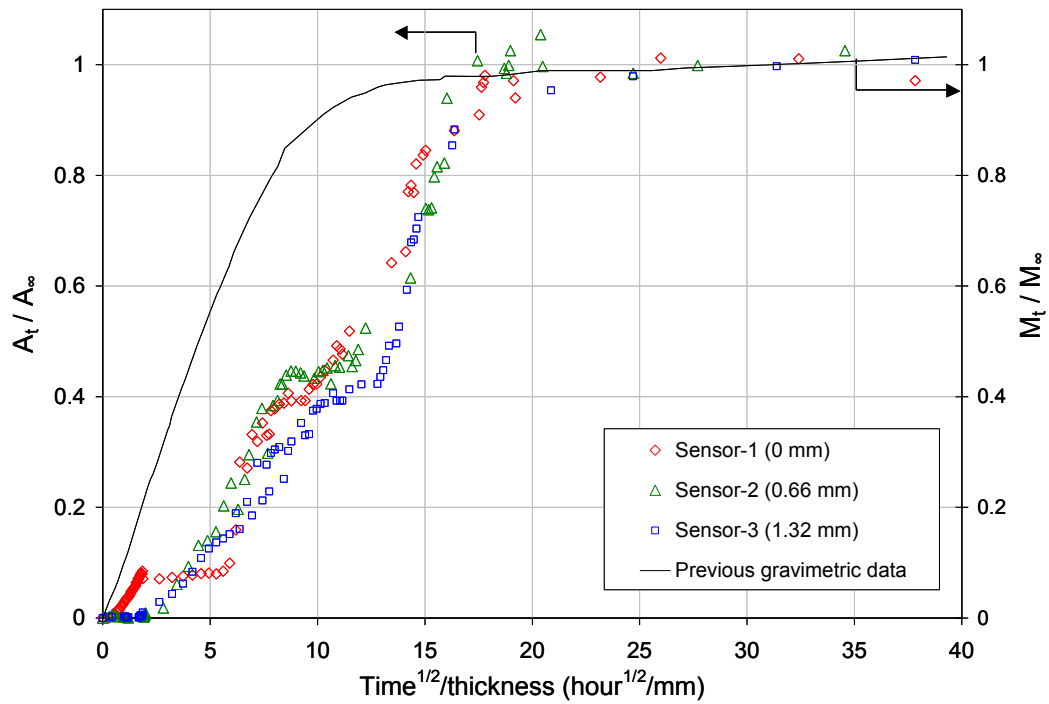


Figure 8.17 Comparison of the sensor responses from the embedded sensors within the specimen configuration – III and the conventional gravimetric results of the LY3505/XB3403 resin system conditioned at 50 °C as a function of immersion time and the sensor location.

The localised absorption isotherms obtained based on the sensor responses are shown in Figure 8.17. According to the observed localised transport phenomena of water, if the early step-change behaviour is attributed to capillary diffusion from the edges as discussed before, it seems unlikely the results are reproducible for the specimen configurations – II and – III. However, the capillary diffusion is possible at prolong exposure to hygrothermal conditions as discussed in Section 8.2.1. Therefore, the observed water transport behaviour could be due to the combined effect of localised stress profile and the types of water-polymer interactions as a function of immersion time.

Although sensor-1 was embedded at the surface, 74 minutes of delay in response to absorbed moisture was observed compared to that seen from the sensor embedded in the specimen

configuration – II. The delay can be attributed to possible deviation of the sensor location along the thickness of the specimen. However, the influence of the magnitude and the mode of process-induced stresses on the initial stage of diffusion are clearly evident from spectral responses from the sensors -1 and -3. Except for the delay in response due to the distance from the exposed surfaces, the initial pseudo-equilibrium level at the early stage of diffusion is not visible at the sensor-3. Therefore it can be hypothesised that transport phenomena of water in the polymer are strongly influenced by the resultant stress profile as a function of immersion time. The resultant stress profile through the thickness of the specimen is a function of process-induced stresses and moisture-induced stresses until equilibrium moisture content is reached.

The effect can be further explained using the initial rates of diffusion observed at sensors -2 and -3. The sensors were approximately equally spaced from the closest surface of exposure to water. Therefore both sensors detected moisture at nearly the same time. However the rate of diffusion is higher at the sensor-2 compared with that apparent at the sensor-3. This can be attributed to the non-uniform stress profile across the thickness of the specimen starting with tensile stresses at the surface that was in contact with the glass moulding plate and decreasing towards the opposite surface, which was on the open side of the mould. During the later stage of diffusion, the first pseudo-equilibrium at the sensors -2 and -3 and the second pseudo-equilibrium at the sensor-1 was attained approximately in the range of 0.4 – 0.5 moisture uptake. After 61 days of exposure, moisture diffusion at all the sensors showed the same transport behaviour. This feature coincides well with the nature of moisture absorption observed from the embedded sensors in the specimen configuration – II for immersion time over 57 days.

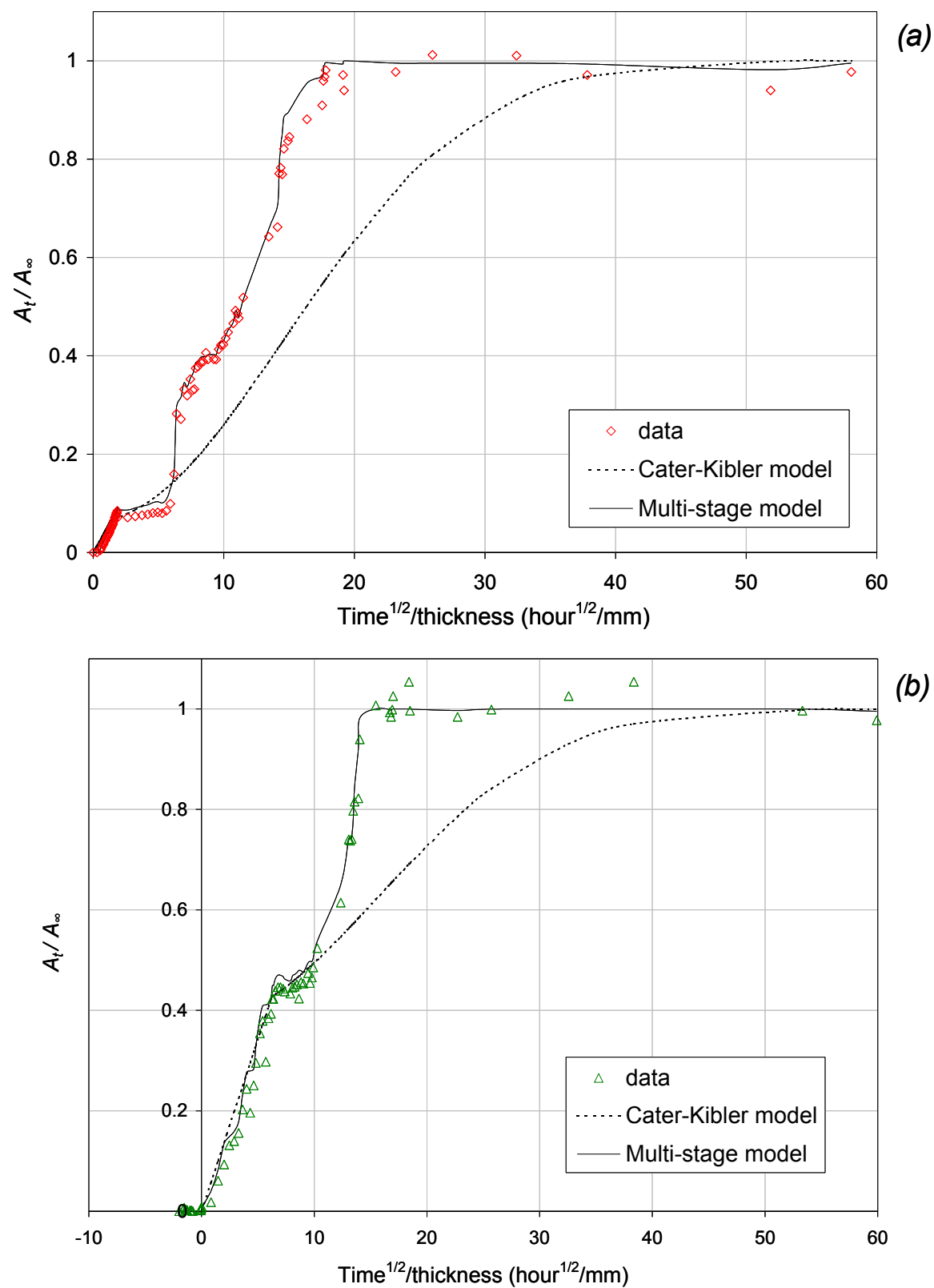


Figure 8.18 Comparison between the sensor response and the diffusion models for hydrothermal conditioning of the LY3505/XB3403 resin system at 50 °C: (a) sensor-1 and (b) sensor-2.

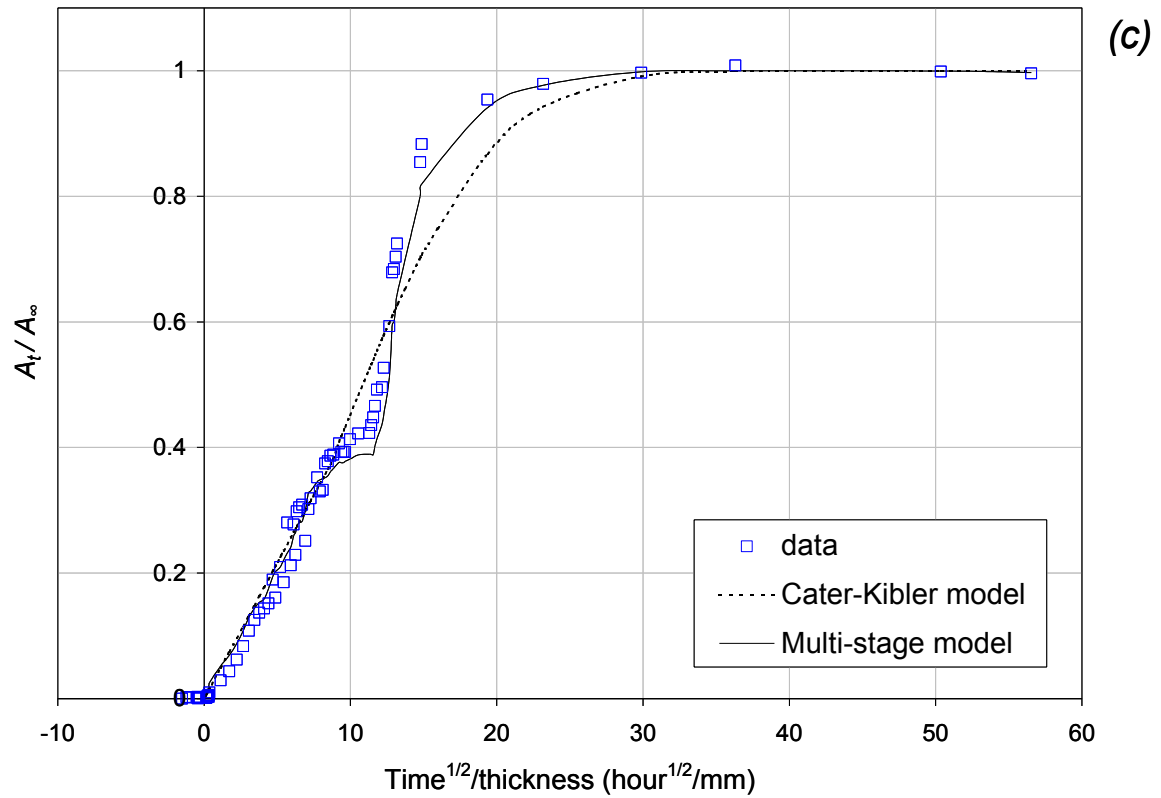


Figure 8.19 Comparison between the sensor response and the diffusion models for hydrothermal conditioning of the LY3505/XB3403 resin system at 50 °C: (c) sensor-3.

Table 8.3 Summary of kinetic parameters corresponding to best fit of the models to the spectral data obtained from the specimen configuration–III for hydrothermal conditioning of the LY3505/XB3403 resin system at 50 °C.

	Sensor Location		
	0 mm	0.44 mm	1.32 mm
D_γ (mm ² sec ⁻¹)	2.22×10^{-5}	2.08×10^{-4}	9.25×10^{-2}
κ (sec ⁻¹)	3.19×10^{-5}	2.98×10^{-4}	3.19×10^{-3}
β (sec ⁻¹)	9.50×10^{-8}	3.00×10^{-4}	3.50×10^{-4}
γ (sec ⁻¹)	1.39×10^{-6}	4.91×10^{-4}	4.01×10^{-3}

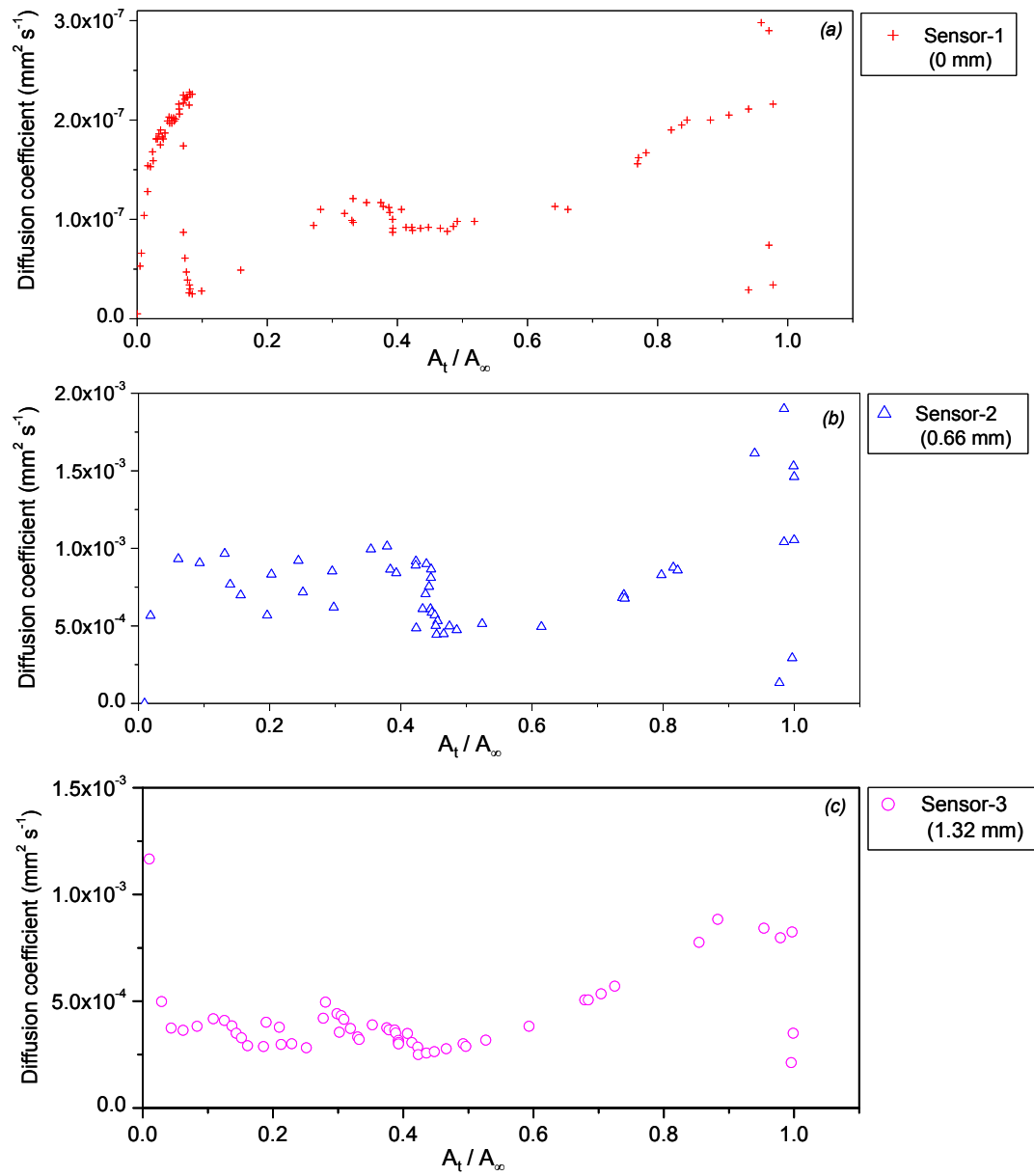


Figure 8.20 Change in localised diffusion coefficient of the LY3505/XB3403 resin system for hydrothermal conditioning at 50 °C based on the sensors embedded in the specimen configuration – III (a) sensor-1; (b) sensor-2 and (c) sensor-3.

The kinetics of moisture diffusion of the specimen configuration – III were analysed using the Carter-Kibler model and the multi-stage model. According to Figure 8.18(a and b), Figure 8.19 and Table 8.3, it can be clearly seen that the Carter-Kibler model is not suitable for

predicting the localised transport phenomena in the epoxy resin while the multi-stage model provides a good approximation to the sensor responses.

Figure 8.20(a-c) shows the change in diffusion coefficient at each sensor location as a function of fractional moisture uptake. It can be clearly seen that the rate of diffusion increases in the range of 0.6 – 1.0 fractional moisture uptake. This could be attributed to either water clustering, capillary diffusion or both as discussed in Section 8.2.1.

8.3 Conclusions

An attempt was made to explain the localized diffusion behaviour observed using embedded fibre optic sensors. A reasonable correlation was observed between sensor response via near-IR transmission spectroscopy and gravimetric results; however, gravimetric analysis found to be less sensitive to localised diffusion characteristics within the resin. Possible issues related to the observed deviation of moisture absorption behaviour in the LY3505/XB3403 resin system from Fickian diffusion model was discussed. The applicability of two other anomalous diffusion models for predicting the moisture transport phenomena in the epoxy resin system was also investigated. It was observed that the residual stresses in the resin system have a considerable influence on the localised moisture diffusion characteristics.

Chapter 9

General conclusions and further recommendations

9.1 Introduction

This chapter contains a brief summary of the results presented in this thesis. The research consisted of four main sections. A brief description is given of the results obtained and conclusions drawn under each section. Some recommendations for future work that could be carried out to further the research also will be discussed.

9.2 Conclusions

Design of low-cost fibre-optic sensors

Three sensor fixtures for obtaining near infrared transmission spectroscopy were designed and evaluated. In the epoxy substrate sensor design, making a sensor with good quality was

observed to be considerably dependent on the experience of the operator. Although the dimensions of the abraded capillary sensor design were smaller compared with other sensor designs, sensor fabrication was found to be more complicated due to practical difficulties experienced during fixture fabrication. In the capillary support sensor design, sensor fabrication was more robust and time-efficient compared to other sensor designs tested. Reasonable dimensional consistency of the sensor was also achieved. Capillary reflector sensor design was evaluated for obtaining near-infrared reflectance spectroscopy and a reasonable reproducibility was achieved in terms of sensor fabrication and the quality of the sensor.

Monitoring of cross-linking reaction using fibre-optic spectroscopy

Capillary support and capillary reflector sensor designs were chosen for *in situ* monitoring of cross-linking reaction of an epoxy resin system under both transmission mode and reflection mode. Cross-linking kinetics of the epoxy/amine resin system was studied at four isothermal reaction temperatures, namely 40, 50, 60 and 70 °C while near infrared spectra were recorded in real-time using the sensor designs.

Detailed peak assignments for the epoxy/amine resin system were given and three different spectral analysis techniques were employed to resolve the overlapped absorption band with the epoxy absorption band in the spectral range of 2180 – 2226 nm. Subtracting the peak area of the hidden absorption band from the total peak area was found to give most accurate results for determining the change in epoxy peak area. The change in epoxy, primary, secondary and hydroxyl groups during cross-linking were monitored. Mass balance equations were used to determine the change in secondary and hydroxyl group concentrations during cross-linking.

Results showed that the contribution of the etherification reaction towards epoxy conversion is negligible at the reaction conditions studied. Good correlation was observed between the data obtained using the transmission sensor (capillary support sensor design) and the reflectance sensor (capillary reflector sensor design).

An empirical model was used to predict the cross-linking kinetics using degree of epoxy conversion and the reaction mechanism of the LY3505/XB3403 resin system showed autocatalytic behaviour. A single equation was developed to describe the cross-linking reaction of the epoxy/amine resin system as a function of reaction temperature. Good agreement was observed between the predicted model and the spectral results obtained using two fibre-optic sensor designs.

Proof-of-concept of multi-functional sensor design

Proof-of-concept of EFPI-based multi-functional sensor design was successfully demonstrated for monitoring of cross-linking reaction. The rationale of the sensor design was to monitor temperature, strain, refractive index and chemical reaction simultaneously using a single interrogation unit, namely a conventional FTIR spectrometer. The feasibility of using the FTIR spectrometer to interrogate the primary Fabry-Perot cavity and the FBG sensor was also demonstrated. Primary EFPI/FBG sensor response to temperature and strain was characterized in detail using separate EFPI and FBG sensors. Temperature sensitivity of the EFPI and FBG sensors were evaluated within the range 30 – 80 °C. With regard to EFPI sensor, no clear relationship was observed between the temperature and the sensor response at the test conditions studied. However, the FBG sensor showed a linear response to the temperature and the temperature sensitivity was in good agreement with the published results.

Strain sensitivity of the sensors was evaluated using embedded EFPI and FBG sensors in the epoxy resin system. The cross-linking reaction was carried out at 60 °C for 8 hours and the residual strain developed in the resin system while cooling down to the ambient temperature was monitored. Reasonable agreement was observed with the strain obtained using EFPI and FBG sensors.

The feasibility of using the multi-functional sensor design for monitoring chemical conversion, strain, temperature, and Fresnel reflection during the cross-linking of the resin system was demonstrated. The conventional FTIR spectrometer was used to interrogate the primary and secondary sensors. Good correlation was observed for degree of conversion obtained from the secondary chemical sensor attached to the multi-functional sensor, and conventional transmission FTIR spectroscopy experiments. Good correlation was also observed between the Fresnel-based secondary sensor results that were monitored via the spectrometer.

Moisture ingress monitoring using conventional analytical techniques

Based on gravimetric measurements, moisture absorption in the LY3505/XB3403 resin system satisfies Fickian diffusion behaviour and the equilibrium moisture content and the absorption kinetics obtained are in good agreement with the published results. The diffusion coefficient appeared to be independent of the thickness. A numerical method based on a finite difference solution was used to predict the moisture diffusion front across the thickness of a specimen as a function of immersion time. Reasonable correlation was observed between experimental measurements and that determined using the numerical solution.

DSC, TGA, DMTA and FTIR techniques were also employed to investigate the absorption mechanism of water in the epoxy/amine resin system that immersed in water at 30°, 50° and 70°C. The results showed that the absorbed water exists in the epoxy/amine resin system as two different types; bound water and free water. The bound water is characterized by strong interactions with hydrophilic groups available in the resin, which govern the absorption kinetics. The bound water molecules are divided into two types. *Type-I* bonding corresponds to the formation of single hydrogen bonding between water molecules and the nucleophilic sites in the network. The water molecules possess lower activation energy and are easy to remove. *Type-II* bonding corresponds to water molecules forming multiple hydrogen bonds in the matrix network. These water molecules possess higher activation energy and are difficult to remove. The overall diffusion within the bulk resin is a combined and competitive process of the two types of water and the overriding mechanism found to be highly dependent on the immersion temperature and exposure time.

A decrease in T_g was observed due to absorbed moisture at all immersion temperatures. The *Type-I* bound water molecules disrupt the intramolecular bonding between epoxy chains and decreases T_g due to plasticisation, whereas *Type-II* bound water contributes to an increase of T_g by forming intermolecular networks. It was also noted that these interactions possess direct influence on the short-term and also on the long-term viscoelastic behaviour of the resin system.

Moisture ingress monitoring fibre-optic spectroscopy

In situ moisture ingress monitoring in the resin system using fibre-optic near-infrared spectroscopy was successfully demonstrated using the capillary support sensor design.

Diffusion kinetics of water in the epoxy/amine resin system at 50 °C was studied in real-time using fibre-optic spectroscopy. Fibre-optic sensors were embedded at different heights relative to the faces of the specimen exposed to water. Three different specimen configurations were used to study the localised diffusion behaviour under different exposure conditions. A set of reference specimens was conditioned at the same environmental conditions to monitor the weight uptake due to absorbed water. With reference to the gravimetric analyses, the presence of fibre-optic sensors does not appear to affect the diffusion kinetics of water in the bulk resin.

The change in normalised peak area of the absorption band at 1905 nm due to a combination of O-H stretching and bending was used to obtain diffusion isotherms corresponding to each sensor location. In addition, the variation in the shape of the absorption band appearing at 1430 nm was used to predict the diffusion behaviour of water as a function of immersion time. The peak was attributed to the first overtone of the symmetric stretching vibration of alcoholic OH. Anomalies associated with localised diffusion behaviour of water observed based on the sensor responses could be attributed to the spectral quality, leaching of low-molecular weight substances and the local stress/strain field due to process- and moisture-induced stresses.

9.3 Further recommendations

The research work presented in this thesis showed the potential benefits of using fibre-optic near-infrared spectroscopy for *in situ* monitoring of cross-linking reaction and moisture ingress in epoxy/amine resin systems. However, the following are suggested to further the

research and to gain in-depth understanding of reaction kinetics of the resin system during processing and diffusion kinetics of water in the cross-linked resin system in a hygrothermal environment.

Analysis of spectral data obtained during cross-linking showed that the absorption band appeared at 1532 nm is an overlapped band of primary and secondary amine peaks. This is the only band appearing in the near infrared region that contains information on the secondary amine group concentration. Due to time constraints, no attempt was made during this study to develop a method to resolve this combination band and to determine the change in secondary amine concentration using spectral data. Instead, a mathematical approach based on the Beer-Lambert law was used to calculate the secondary amine concentration using the concentration of epoxy and primary amine groups. However, to predict the actual reaction mechanism of the epoxy/amine resin system, there is merit in understanding the actual trend of changes in secondary amine group concentration as a function of reaction time and temperature. Therefore, developing a simple and more accurate method would be advantageous.

Chapter 6 presented proof-of-concept of a new multi-functional sensor design for monitoring chemical conversion, strain, temperature and refractive index simultaneously during cross-linking of the epoxy/amine resin system. Although the sensor design showed promising results, further improvements of sensor fabrication, sensor interrogation and data analysis and interpretation are essential to enhance the feasibility of using the sensor design for *in situ* monitoring of cross-linking reactions. The sensor design can be also used for other sensing applications such as monitoring moisture ingress, ingress of other chemicals, H₂ and structural integrity.

The influence of moisture absorption on the chemical properties of the epoxy/amine resin system was investigated using conventional near-infrared spectroscopy. However, the results showed that the spectral evidence available on different types of water/polymer interactions was less compared to that could be available in the mid infrared region. Getting more insight in to the types of water/polymer interactions and the changes in these interactions as a function of immersion temperature and time improves the understanding of diffusion behaviour of water in the resin system. Therefore, extending spectral investigation into both the mid- and near-infrared regions may have a significant impact on predicting diffusion behaviour of water in epoxy/resin systems.

Furthermore, it was suggested that leaching of low-molecular weight species from the aged specimens is possible at long immersion times and at higher temperatures. This may have an impact on the water transport behaviour in cross-linked epoxy resin systems and therefore on the diffusion coefficient. However, no spectral evidence was observed that related to leaching of low-molecular weight species within the near-infrared region. Studies in this area can be further extended by analysing samples of the water that was used for conditioning the epoxy specimens. Analytical techniques such as HPLC or chemical titration could be employed to analyse the water samples as a function of immersion time and temperature. This may also provide evidence for observed trends of the changes in T_g of the resin system due to hygrothermal ageing.

The results presented in Chapter 8 showed that the localised diffusion phenomena observed using embedded fibre-optic sensors significantly deviated from the traditional Fickian diffusion. It was also discussed that the observed behaviour could be due to localised strain developed as a result of process-induced and moisture-induced stresses. The data obtained

via embedded fibre-optic sensors showed promising results for confirming that there could be a significant impact of localised stress/strain fields on the diffusion behaviour of water. However, the sensor designs used in the current study did not provide direct evidence of strain at the sensor locations. Implementation of the experimental set-up to verify these findings would provide a significant understanding of how the localised stress/strain field affects the transport behaviour of water in the epoxy/amine resin as a function of thermal history.

References

- 1 Mouritz, A.P., Gellert, E., Burchill, P. and Challis, K. Review of advanced composite structures for naval ships and submarines: *Comp. Struct.*, **53**, 2001, pp 21-41.
- 2 Ochoa, O. O. and Salama, M. M. Offshore composites: Transition barriers to an enabling technology. *Comp. Sci. Technol.*, **65**, 2005, pp 2588-2596.
- 3 Seica, M. V. and Packer, J. A. FRP materials for the rehabilitation of tubular steel structures for underwater applications. *Comp. Struct.*, **80**, 2007, pp 440-450.
- 4 Liu, L. and Wanger, H. D. Rubbery and glassy epoxy resins reinforced with carbon nanotubes. *Comp. Sci. Technol.*, **65**, 2005, pp 1861-1868.
- 5 Low, I. M., Mai, Y. W. and Bandyopadhyay, S. Effect of temperature and rate on fracture toughness of short-alumina-fibre-reinforced epoxies. *Comp. Sci. Technol.*, **43**, 1992, pp 3-12.
- 6 Bogetti, T. A. and Gillespie, J. W., Jr. Process-induced stress and deformation in thick-section thermoset composite laminates. *J Comp. Mater.*, **26**(5), 1992, pp 626-659.
- 7 Day, D. R. Cure characterization of thick composite parts using dielectric and finite difference analysis. 38th Int. SAMPE Symp. Anaheim, CA., 10 – 13 May 1993.
- 8 Plepys, S. T. and Farris, R. J. Evolution of residual stresses in three-dimensionally constrained epoxy resins. *Polym.*, **31**, 1990, 1932-1936.
- 9 Sala, G. Composite degradation due to fluid absorption. *J. Comp.: Part B*, **31**, 2000, pp. 357-373.
- 10 Karbhari, V. M., Chin, J. W., Hunston, D., Benmokrane, B., Juska, T., Morgan, R., Lesko, J. J., Sorathia, U. and Reynaud, D. Durability gap analysis for fibre-reinforced polymer composites in civil infrastructure. *Journal of Composites for Construction*, 2003, pp 238-247.

- 11 Schutte, C. L. Environmental durability of glass-fibre composites. *Mater. Sci. Eng.*, **R13**, 1994, pp 265-324.
- 12 Wright, W. W. The effect of diffusion of water into epoxy resins and their carbon-fibre reinforced composites, *Composites*, **12**(3), 1981, pp 201-205.
- 13 Vesely, D. Diffusion of liquids in polymers. *Int. Mater. Rev.*, **53**(5), 2008, pp 299-315.
- 14 Xian, G. and Karbhari, V. M. DMTA based investigation of hygrothermal aging of an epoxy system used in rehavilitation. *J. App. Poly. Sci.*, **104**, 2007, pp 1084-1094.
- 15 McEwan, I., Pethrick, R. A. and Shaw, S. J. Water absorption in a rubber-modified epoxy resin; carboxyl terminated butadiene acrylonitrile-amine cured epoxy resin system. *Polym.*, **40**, 1999, pp 4213-4222.
- 16 Merdas, I., ThomINETTE, F., Tcharkhtchi, A. and Verdu, J. Factors governing water absorption by composite matrices. *Comp. Sci. Technol.*, **62**, 2002, pp 487-492.
- 17 Philippe, L., Sammon, C., Lyon, S.B. and Yarwood, J. An FTIR/ATR *in situ* study of sorption and transport in corrosion protective organic coatings Paper 2. The effects of temperature and isotopic dilution. *Progress in Organic Coatings*, **49**, 2004, pp 315-323.
- 18 Lin, Y. C. and Chen, X. Investigation of moisture diffusion in epoxy systems: Experimental and molecular dynamic simulations. *Chem. Phys. Lett.*, **412**, 2005, pp 322-326.
- 19 Arbibili, H., Hillman, C., Natishan, A. E., McCluskey, P. Pecht, M. G. and Peterson, D. A comparison of the theory of moisture diffusion in plastic encapsulated microelectronics with moisture sensor chip and weight-gain measurements. *IEEE Transactions on Components and Packaging Technologies*, **25**(1), 2002, pp 132-139.
- 20 Ganesh, A. B. and Radhakrishnan, T.K. Fibre-optic sensors for the estimation of pH within natural biofilms on metals. *Sensors and Actuators - Part B*, doi:10.1016/j.snb.2006.11.027, (2006).

- 21 Calvert, P., George, G. and Rintoul, L. Monitoring of cure and water uptake in freeformed epoxy resin by an embedded optical fiber. *Chem. Mater.*, **8**, 1996, pp 1298 – 301.
- 22 Bormashenko, E., Sheshnev, A., Pogreb, R., Sutovski, S., Reichlin, Y., Shulzinger, E. and Katzir, A. Study of water diffusion in polyacrylonitrile using IR fibre optic evanescent wave spectroscopy. *Polymers for Advanced Technologies*, **13**, 2002, pp 1039-1045.
- 23 Laralekas, D., Cuganoni, J. and Botsis, J. Monitoring of hygrothermal ageing effects in an epoxy resin using FBG sensor: A methodological study. *Composites Science and Technology*, **69**, 2009, pp 507-514.
- 24 Morgan, R. J. and Neal, J. E. O. A review of the relation between the physical structure and mechanical response of Epoxies. In: Labana, S. S. Ed. *Chemistry and Properties of Crosslinked Polymers*. New York: Academic Press Inc., 1977, pp 289-301.
- 25 Martin, G. C. Tungare, A. V. and Gotro, J. T. Modelling rheological and dielectric properties during thermoset cure. In: Craver C. D. and Provder T. Eds. *Polymer Characterization*. Washington, America Chemical Society, 1990, pp 235-248.
- 26 Jones, F. R. Epoxy resins in: Jones, F.R. Ed. *Handbook of Polymer-Fibre Composites*. UK, Longman Scientific & Technical, 1994, pp 86-96.
- 27 Bar, H., Narkis, M. and Boiteux, G. The electrical behaviour of thermosetting polymer composites containing metal plated ceramic filler. *Polym. Comp.*, 2005, DOI 10.1002/pc.20064.
- 28 Almusallam, A. A., Khan, F. M., Dulaijan, S. U. and Al-Amoudi, O. S. B. Effectiveness of surface coatings in improving concrete durability. *Cement & Concrete Composites*, **25**, 2003, pp 473-481.

- 29 Abdel-Magid, B., Ziaee, S., Gass, K. and Schneider, M. The combined effect of load, moisture and temperature on the properties of E-glass/epoxy composites. *Comp. Struct.*, **71**, 2005, pp 320-326.
- 30 Mika, T. F. and Bauer, R. S. Curing agents and modifiers. In: May, C. A., Ed. *Epoxy resins: chemistry and technology*. 2nd Edition. California, USA, CRC Press, 1988, pp 465-550.
- 31 Jiawu, G., Kui, S. and Mong, G. Z. The cure behaviour of tetraglycidyl diaminodiphenyl methane with diaminodiphenyl sulfone. *Thermochimica Acta*, **352-353**, 2000, pp 153-158.
- 32 Petrie, E. M. *Handbook of Adhesives and Sealants*. 2nd Ed. USA: McGraw-Hill, 2006, pp 378-390.
- 33 Bolger, J. C. Structural Adhesives: Today's State of the Art. In: Schneberger G. L. Ed. *Adhesives in Manufacturing*. New York: Marcel Dekker, Inc. New York, 1983, pp 133-195.
- 34 Soni, H. K., Patel, V. S. and Patel, R. G. Studies on cure kinetics and thermal stability of liquid epoxy resin based on bisphenol-C and epichlorohydrin using different amines as curing agents. *Thermochimica Acta*, **191**, 1991, pp 307-316.
- 35 Pakekh, J. K., Patel, R. G. and Patel, V. S. Studies on the properties of glass-reinforced composites of various difunctional epoxies. in: Bhardwaj I. S. Ed. *Polymer Science: Recent Advances*. Vol. 2. France: Technip, 1994, pp 515-520.
- 36 Teh, P. L., Mariatti, M., Wagiman, A. N. R. and Beh, K. S. Effect of curing agent on the properties of mineral silica filled epoxy composites. *Polym. Comp.*, 2008, DOI 10.1002/pc.20345.

- 37 Luck, R. M. and Sadhir, R. K. Monomers that expand during polymerisation. In: Luck R. M. and Sadhir R. K. Eds. *Expanding Monomers: Synthesis, Characterization and applications*. Florida, CRC Press Inc., Florida, 1992, pp 21-63.
- 38 Rozenberg B. A. Kinetics, thermodynamics and mechanism of reactions of epoxy oligomers with amines. *Advances in Polymer Science*, **75**, 1985, pp 113-165.
- 39 Cole, K. C. A new approach to modelling the cure kinetics of epoxy amine thermosetting resins. 1. Mathematical development. *Macromolecules*, **24**, 1991, pp 3093-3097.
- 40 Smith, I. T. The mechanism of the cross-linking of epoxide resins by amines, *Polym.*, **2**, 1961, pp 95-108.
- 41 Connors, K.A. *Chemical Kinetics: The Study of Reaction Rates in Solution*. John Wiley Publishing, New York, 1990.
- 42 Macan, J. Ivankovic, H. Ivankovic, M. and Mencer, H.J. Study of cure kinetics of epoxy-silica organic-inorganic hybrid materials. *Thermochimica acta*, **414**, 2004, pp 219-225.
- 43 Talbot, J. D. R. The kinetics of the epoxy amine cure reaction from a solvation perspective. *J. Polym. Sci. Part A*, **42**, 2004, pp 3579-3586.
- 44 Girard-Reydet, E., Richardi C. C., Sautereau H., Pascault J. P. Epoxy-Aromatic diamine kinetics. 1. Modelling and influence of the diamine structure. *Macromolecules*, **28**, 1995, pp 7599-7607.
- 45 Bonnet, A., Pascault, J. P., Sautereau, H., Taha, M. and Camberlin, Y. Epoxy-diamine thermoset/thermoplastic blends. 1. Rates of reactions before and after phase separation. *Macromolecules*, **32**, 1999, pp 8517-23.

- 46 Chiao, L. Mechanistic reaction kinetics of 4,4'-Diaminodiphenyl sulfone cured tetraglycidyl-4,4'-diaminodiphenylmethane epoxy resins. *Macromolecules*, **23**, 1990, pp 1286-90.
- 47 Xu, L. and Schlup, J. R. Etherification versus amine addition during epoxy resin/amine cure: An *in situ* study using near-infrared spectroscopy. *J Appl. Polym. Sci.*, **67**, 1998, pp 895-901.
- 48 Gupta, N. and Varma, I. K. Effect of structure of aromatic diamines on curing characteristics, thermal stability and mechanical properties of epoxy resins. *J. Appl. Poly. Sci.*, **68**, 1998, pp 1759-1766.
- 49 Mijovic, J. and Wijaya, J. Reaction kinetics of epoxy/amine model systems. The effect of electrophilicity of amine molecule. *Macromolecules*, **27**, 1994, pp 7589-7600.
- 50 Ašperger, S. *Chemical Kinetics and Inorganic Reaction Mechanisms*. 2nd revised edition. London, Springer, 2003, pp 3-51.
- 51 Frost, A. A. and Pearson, R. G. *Kinetics and Mechanism*. New York: John Wiley & Sons Inc., 1962, pp 8-76.
- 52 Cole, K. C., Hechler, J. J. and Noël, D. A new approach to modelling the cure kinetics of epoxy amine thermosetting resins. 2. Application to a typical system based on Bis[4-(diglycidylamino)phenyl]methane and Bis(4-aminophenyl) sulfone. *Macromolecules*, **24**, 1991, pp 3098-3110.
- 53 Xu, L., Fu, J. H. and Schlup, J. R. In situ near-infrared spectroscopic investigation of the kinetics and mechanisms of reactions between phenyl glycidyl ether (PGE) and multifunctional aromatic amine. *Ind. Eng. Chem. Res.*, **35**, 1996, pp 963-972.
- 54 Shechter, L., Wynstra, J. and Kurkijy, R.P. Glycidyl ether reactions with amines. *Industrial and Engineering Chemistry*, **48**(1), pp 94-97.

- 55 Hong, S. G. and Wu, C. S. DSC and FTIR analyses of the curing behaviour of epoxy/dicy/solvent systems on hermetic specimens. *Journal of Thermal Analysis and Calorimetry*, **59**, 2000, pp 711-719.
- 56 Mijovic, J., Arnon, F. and Wijaya, J. Mechanistic modelling of epoxy-amine kinetics. 1. Model compound study. *Macromolecules*, **25**, 1992, pp 979-985.
- 57 Sautereau, J. P. P. H., Verdu, J. and Williams, R. J. J. *Thermosetting Polymers*. New York: Marcel Dekker, Inc., 2002, pp 6-65.
- 58 St John, N. A., George, G. A., Cole-Clarke, P. A., Mackay, M. E. and Halley, P. J. The effect of impurities on gel times for TGDDM epoxy cured with DDS. *High Perform. Polym.*, **5**, 1993, pp 21-36.
- 59 Swern, D., Billen, G. N. and Knight, H. B. Chemistry of epoxy compounds. VIII. Reaction of allyl alcohol with unsymmetrical oxirane compounds. An electronic interpretation. *J Am. Chem. Soc.*, **71**, 1949, pp 1152-1156.
- 60 Morgan, R. J. and Mones, E. T. The cure reactions, network structure and mechanical response of diaminodiphenyl sulfone-cured tetraglycidyl 4,4' diaminodiphenyl methane epoxies. *J App. Polym. Sci.*, **33**(4), 1987, pp 999-1020.
- 61 Ellis, B. Time-Temperature-Transformation diagrams for thermosets. in: Jones, F. R. Ed. *Handbook of Polymer-Fibre Composites*, UK, Longman Scientific & Technical, 1994, pp 115-121.
- 62 Um, M. K., Daniel, I. M. and Hwang, B. S. A study of cure kinetics by the use of dynamic differential scanning calorimetry. *Comp. Sci. Tech.*, **62**, 2002, pp 29 – 40.
- 63 Blanco, M., Corcuera, M. A., Riccardi, C. C. and Mondragon I. Mechanistic kinetic model of an epoxy resin cured with a mixture of amines of different functionalities. *Polym.*, **46**, 2005, pp 7989-8000.

- 64 Hargis, M., Grady, B. P., Aktas, L., Bomireddy, K. R., Howasman, S., Altan, C., Rose, T. and Rose, H. Calorimetric and rheological measurements of three commercial thermosetting prepreg epoxies. *J. Comp. Mater.*, **40**, 2005, pp 1 – 25.
- 65 Abdelkader, A. F. and White, J. R. Curing characteristics and internal stresses in epoxy coatings: Effect of crosslinking agent. *J. Mater. Sci.*, **40**, 2005, pp 1843-1854.
- 66 Fuller, B., Gotro, J. T. and Martin, G. C. Analysis of the glass transition temperature, conversion and viscosity during epoxy resin curing in: Craver, C. D. and Provder, T. Eds. *Polymer Characterization*, Washington: American Chemical Society, 1990, pp 215-234.
- 67 Acitelli, M. A., Prime, R. B. and Sacher, E. Kinetics of epoxy cure: 1. The system Bisphenol-A dicycidyl ether/m-phenylene diamine. *Polym.*, **12**(5), 1971, pp 335-343.
- 68 Sacher, E. Kinetic of epoxy cure: 3. The systems bisphenol-A epoxides/dicy. *Polym.*, **14**, 1973, pp 91-95.
- 69 Ruiz, E. and Trochu, F. Thermomechanical properties during cure of glass-polyester RTM composites: Elastic and viscoelastic modelling. *J. Comp. Mater.*, **39**(10), 2005, pp 881-916.
- 70 Sourour, S. and Kamal, M. R. Differential scanning calorimetry of epoxy cure: isothermal cure kinetics. *Thermochim Acta*, **14**, 1976, pp 41-59.
- 71 Tai, H. J. and Chou, H. L. chemical shrinkage and diffusion-controlled reaction of an epoxy molding compound. *Euro. Polym. J.*, **36**, 2000, pp 2213 – 2219.
- 72 Kamal, M. R. and Svourour, S. Kinetics and thermal characterization of thermoset cure. *Polym. Eng. Sci.*, **13**(1), 1973, pp 59–64.
- 73 Costa, M. L., Pardine, L. C. and Rezende, M. C. Influence of aromatic amine hardeners in the cure kinetics of an epoxy resin used in advanced composites. *Mater. Res.*, **8**(1), 2005, pp 65-70.

- 74 Deng, Y. and Martin, G. C. Diffusion and diffusion-controlled kinetics during epoxy-amine cure. *Macromolecules*, **27**, 1994, pp 5147-5153.
- 75 Brnardic, I., Ivankovic, M., Ivankovic, H. and Mencer, H.J. "Isothermal and nonisothermal cure kinetics of an epoxy/poly(oxypropylene)diamine/octadecyl ammonium modified montmorillonite system. *J. Appl. Polym. Sci.*, **100**, 2006, pp 1765-1771.
- 76 Lee, J. Y., Shim, M. J. and Kim, S.W. Autocatalytic cure kinetics of natural zeolite filled epoxy composites. *Mater. Chem. Phys.*, **48**, 1997, pp 36-40.
- 77 Ruiz, E. and Billotte, C. Predicting the cure of thermosetting polymers: The isoconversion map. *Polym. Comp.*, 2008, DOI 10.1002/pc.20710.
- 78 Ryan, M. E. and Dutta, A. Kinetics of epoxy cure: a rapid technique for kinetic parameter estimation. *Polym.*, **20**, 1979, pp 203-206.
- 79 Zvetkov, V. L. Comparative DSC kinetics of the reaction of DGEBA with aromatic diamines. 1. Non-isothermal kinetic study of the reaction DGEBA with m-phenylene diamine, *Polym.*, **42**, 2001, pp 6687-6697.
- 80 Musto, P., Martuscelli, E., Ragosta, G., Russo, P. and Villano, P. Tetrafunctional epoxy resins: modelling the curing kinetics based on FTIR spectroscopy data. *J. Appl. Polym. Sci.*, **74**, 1999, pp 532-540.
- 81 Fernando, G. F., Liu, T., Crosby, P., Doyle, C., Martin, A., Brooks, D., Ralph, B. and Badcock, R. A multi-purpose optical fibre sensor design for fibre reinforced composite materials. *Meas. Sci. Technol.*, **8**, 1997, pp 1065-1079.
- 82 Crosby, P. A., Powell, G. R., Fernando, G. F., France, C. M., Spooncer, R. C. and Waters, D. N. *In situ* cure monitoring of epoxy resins using optical fibre sensors. *Smart Mater. Struct.* **5**, 1996, pp 415-428.

- 83 Larranaga, M., Martin, M. D., Gabilondo, N., Kortaberria, G., Corcuera, M. A., Riccardi, C. C. and Mondragon, I. Cure kinetics of epoxy systems modified with block copolymers. *Polym. Int.*, **53**, 2004, pp 1495 – 1502.
- 84 Zhao, H., Gao, J., Li, Y. and Shen, S. Curing kinetics and thermal property characterization of bisphenol-F epoxy resin and MeTHPA system. *J. Therm. Anal. Calori.*, **74**, 2003, pp 227-236.
- 85 Kim, J., Moon, T. J. and Howell, J. R. Cure kinetic model, heat of reaction, and glass transition temperature of AS4/3501-6 graphite-epoxy prepregs. *J. Comp. Mater.*, **36**(21), 2002, pp 2479-2499.
- 86 Kenny, J. M. and Trivisano, A. Isothermal and dynamic reaction kinetics of high performance epoxy matrices. *Polym. Eng. Sci.*, **31**(19), 1991, pp 1426-1433.
- 87 Planting, P. J. An approach for evaluating epoxy adhesives for use in hybrid microelectronic assembly. *IEEE Trans. Parts, Hybrids and Packaging*, **11**(4), 1975, PHP-305-11.
- 88 Stone, G. C., Heeswijk, R. G. V. and Bartnikas, R. Investigation of the effect of repetitive voltage surges on epoxy insulation. *IEEE Trans. Energy Conversion*, **7**(4), 1992, pp 754-760.
- 89 Dodiuk, H. and Kenig, S. Low temperature curing epoxies for structural repairs. *Prog. Polym. Sci.*, **19**, 1994, pp 439-467.
- 90 Ollier-Duréault, V. and Gosse, B. Photo-oxidation and electrical aging of anhydride-cured epoxy resins. *IEEE Trans. Dielectrics and Electrical Insulation*, **5**(6), 1998, pp 935-943.
- 91 Lemma, E. Chen, L. Siores, E. and Wang, J. Study of cutting fibre-reinforced composites by using abrasive water-jet with cutting head oscillation. *Comp. Struct.*, **57**, 2002, pp 297-303.

- 92 Park, J. Shin, D.S., Delucca, J., Theis, C. and Osenbach, J. Critical aspect of curing epoxy adhesive: Fibre pistoning of LC connector. *IEEE Trans. Device and Materials Reliability*, **5**(3), 2005, pp 572-580.
- 93 El-Sonbaty, I., Khashaba, U. A. and Machaly, T. Factors affecting the machinability of GFR/epoxy composites. *Comp. Struct.*, **63**, 2004, pp 329-338.
- 94 Hodges, J., Yates, B., Darby, M. I. and Wostenholm, G. H. Residual stresses and the optimum cure cycle for an epoxy resin. *J. Mater. Sci.*, **24**, 1989, pp 1984-1990.
- 95 White, S. R. and Hahn, H. T. Process modelling of composite materials: Residual stress development during cure. Part I. Model formation. *J. Comp. Sci.*, **26**(16), 1992, pp 2402-2422.
- 96 Adolf, D. and Martin, J. E. Calculation of stresses in crosslinking polymers. *J. Comp. Mater.*, **30**(1), 1996, pp 13-34.
- 97 Wang, S. and Garton, A. Chemical interaction at the interface between a carbon fiber and a boron trifluoride-catalyzed epoxy matrix. *J. App. Polym. Sci.*, **45**, 1992, pp 1743-1752.
- 98 Yu, J. W. and Sung, C. S. P. Interphase cure characterization in epoxy composites by fluorescence technique. *J. Appl. Polym. Sci.*, **63** (13), 1997, pp 1769–1775.
- 99 Guo, Z. S. Effects of storage aging on the cure kinetics of T700/BMI prepreg for advanced composites. *Polym. Comp.*, 2008; DOI 10.1002/pc.20457.
- 100 Frigione, M. and Kenny, J. M. Effects of storage aging on the cure kinetics of bismaleimide prepreps. *Adv. Polym. Technol.*, **24**(4), 2005, pp 253-265.
- 101 Valliappan, M., Roux, J. A. and Vaughan, J. G. Die and post-die temperature and cure in graphite/epoxy composites. *Composites: Part B*, **27B**(1), 1996, pp 1-9.
- 102 Perry, M. J., Lee, L.J. and Lee, C. W. On-line cure monitoring of epoxy/graphite composites using a scaling analysis and a dual heat flux sensor. *J. Comp. Mater.*, **26**(2), 1992, pp 274-292.

- 103 DeBakker, C. J., St John, N. A. and Geroge, G. A. Simultaneous differential scanning calorimetry and near-infra-red analysis of the curing of TGDDM with DDS. *Polym.*, **34**(4), 1993, pp 716-725.
- 104 Costa, M. L., Botelho, E. C., Rezende, M. C. Monitoring of cure kinetic prepreg and cure cycle modelling. *J. Mater. Sci.*, **41**, 2006, pp 4349-4356.
- 105 Adolf, D. and Chambers, R. Verification of the capability for quantitative stress prediction during epoxy cure. *Polym.*, **38**(21), 1997, pp 5481-5490.
- 106 Schoch, K. F. Jr, Panackal, P. A., and Frank, P.P. Real-time measurement of resin shrinkage during cure. *Thermochimica Acta*, **417**, 2004, pp 115-118.
- 107 Mijovic, J., Fishbain, A. and Wijaya, J. Mechanistic modelling of epoxy-amine kinetics. 1. Model compound study. *Macromolecules*, **25**, 1992, pp 9979-9985.
- 108 Zukas, W. X. Torsional braid analysis of the aromatic amine cure of epoxy resins. *J. Appl. Polym. Sci.*, **53**, 1994, pp 429-440.
- 109 Frey, T, Große-Brinkhaus K. -H. and Röckrath, U. Cure monitoring of thermoset coatings, *Progress in Organic Coatings*, **27**, 1996, pp 59-66.
- 110 Yu, D., Chen, H., Shi, Z. and Xu, R. Curing kinetics of benzoxazine resin by torsional braid analysis, *Polym.*, **43**, 2002, pp 3163-3168.
- 111 Hofmann, K. and Glasser, W. G. Cure monitoring of an epoxy-amine system by dynamic mechanical thermal analysis (DMTA), *Thermochimica Acta*, **166**, 1990, pp 169-184.
- 112 Matsuoka, S., Quan, X., Bair, H. E. and Boyle, D.J. A model for the curing reaction of epoxy resins. *Macromolecules*, **22**, 1989, pp 4093-4098.
- 113 Hofmann, K. and Glasser, W. G. Cure monitoring of an epoxy-amine system by dynamic mechanical thermal analysis (DMTA). *Thermochimica Acta*. **166**, 1990, pp 169-184.
- 114 Mopsik, F. I., Chang, S. S. and Hunston, D.L. Dielectric measurements for cure monitoring. *Materials Evaluation*, **47**, 1989, pp 448-453.

- 115 Maistros, G. M., and Partridge, I. K. Dielectric monitoring of cure in a commercial carbon-fibre Composite. *Comp. Sci. Technol.*, **53**, 1995, pp 355-359.
- 116 Núñez-Regueira, L., Gracia-Fernández, C. A. and Gómez-Barreiro, S. Use of rheology, dielectric analysis and differential scanning calorimetry for gel time determination of a thermoset. *Polym.*, **46**, 2005, pp 5979-5985.
- 117 Ishii, Y. and Ryan, A.J. Processing of poly(2,6-dimethyl- 1,4-phenylene ether) with epoxy resin. 2. Gellation mechanism. *Macromolecules*. **33**, 2000, pp 167-176.
- 118 Chen, D. and He, P. Monitoring the cure process of epoxy resin nanocomposites based on organo-montmorillonite – a new application of resin curemeter. *Comp. Sci. Technol.*, **64**, 2004, pp 2501-2507.
- 119 Simpson, J. O. and Bidstrup, S. A. Rheological and dielectric changes during isothermal epoxy-amine cure. *J. Polym. Sci.: Part B.*, **33**, 1995, pp 55-62.
- 120 Smith, B. C. *Fundamentals of Fourier Transform Infrared Spectroscopy*. USA: CRC Press LLC, 1996, pp 7-11.
- 121 Stuart, B. Ed. *Modern Infrared Spectroscopy*. England: DJ. John Wiley & Sons., 1996.
- 122 Mirabella, F. M. Ed. *Modern Techniques in Applied Molecular Spectroscopy*. USA: John Wiley & Sons, Inc., 1998, pp 1-10.
- 123 Leyden, D. E. and Murthy, R. S. S. Diffuse reflectance Fourier transform IR spectroscopy. *Trends in Analytical Chemistry*, **7**(5), 1988, pp 164-169.
- 124 Pate, C. B. and Nofle, R. E. Diffuse reflectance FTIR spectra of conducting polymeric films. *Synthetic Metals*, **38**, 1990, pp 259-261.
- 125 Li, W., Huang, Y. D., Liu, L. and Chen, N.T. Rapid and nondestructive analysis of quality of prepreg cloth by near-infrared spectroscopy. *Comp. Sci. Technol.*, **65**, 2005, pp 1668-1674.

- 126 Arvalo, F., Saavedra, R. and Paulraj, M. Optical characterization of semiconductor materials by FTIR-PAS. *J. Phys.: Conf. Series*, **134**, 2008, doi:10.1088/1742-6596/134/1/012019.
- 127 Occhiello, E., Garbassi, F., Morra, M. and Nicolais, L. Spectroscopic characterization of interfaces in polymer composites. *Comp. Sci. Technol.*, **36**, 1989, pp 133-151.
- 128 Sherman, C-P. *Infrared Spectroscopy in Handbook of Instrumental Techniques for Analytical Chemistry*. Settle F. Ed. New Jersey: Prentice Hall PTR, 1997, pp 247-277.
- 129 Dumitrescu, O. R. Simultaneous differential scanning calorimetry – Fourier transform infrared spectroscopy. Ph.D. Thesis, Cranfield University, England, 2003.
- 130 Degamber, B., Winter, D., Tetlow, J., Teagle, M. and Fernando, G. F. Simultaneous DSC/FTIR/TMA. *Meas. Sci. Technol.*, **15**, 2004, L5-L10.
- 131 Workman, J. and Weyer, L. *Practical guide to interpretative near-infrared spectroscopy*. Florida: CRC Press, 2007.
- 132 Rigail-Cedeno, A. and Sung, C. S. P. Fluorescence and IR characterization of epoxy cured with aliphatic amines. *Polym.*, **46**, 2005, pp 9378 – 9384.
- 133 Varley, R. J., Heath, G. R., Hawthorne, D. G., Hodgkin, J. H. and Simon, G. P. Toughening of a trifunctional epoxy system: 1. Near infra-red spectroscopy study of homopolymer cure. *Polym.*, **36**(7), 1995, pp 1347-1355.
- 134 Maxwell, I. D. and Pethrick, R. A. Low temperature rearrangement of amine cured epoxy resins. *Polymer Degradation and Stability*, **5**, 1983, pp 275-301.
- 135 DeBakker, C. J., George, G. A., St John, N. A. and Fredericks P. M. The kinetics of the cure of an advanced epoxy resin by Fourier transform Raman and near-IR spectroscopy. *Spectrochimica. Acta*, **49A**(5/6), 1993, pp 739-752.
- 136 Mijovic, J., Andjelić, S. and Kenny, J. M. *In situ* real-time monitoring of epoxy/amine kinetics by remote near infrared spectroscopy. *Polym. Adv. Technol.*, **7**, 1995, pp. 1-16.

- 137 Cossins, S. L., Connell, M. E., Cross, W. M., Winter, R. M. and Kellar, J. J. Evanescent wave spectroscopy for *in-situ* cure monitoring. Chemical, Biochemical, and Environmental Fiber Sensors VIII, Lieberman R. A. Ed. *Proc. SPIE*, 2836, 1996, pp 147-156.
- 138 George, G., Hynard, N., Cash, G., Rintoul, L. and O'Shea, M. Spectroscopic probes for real-time monitoring of polymer modification and degradation reactions. *C. R. Chimie*, **9**, 2006, pp 1433-1443.
- 139 Navabpour, P., Nesbitt, A., Degamber, B., Fernando, G., Mann, T. and Day, R. Comparison of the curing kinetics of the RTM6 epoxy resin system using differential scanning calorimetry and a microwave-heated calorimetry. *J. Appl. Polym. Sci.*, **99**, 2006, pp 3658-3668.
- 140 Strehmel, V. and Scherzer, T. Structural investigation of epoxy amine networks by mid- and near-infrared spectroscopy. *Eur. Polym. J.*, 30(3), 1994, pp 361-368.
- 141 Lohman, F. H. and Norteman, W. E. Jr. Determination of primary and secondary aliphatic amines by near-infrared spectrophotometry. *Anal. Chem.*, **35**(6), 1963, pp 707-711.
- 142 Lin, Y. G., Santereau, H. and Pascault, J. P. BDMA-catalyzed DDA-epoxy resin system: temperature and composition effects on curing mechanism. *J. Polym. Sci. Part A*, **24**(9), 1986, pp 2171-2184.
- 143 Prime, R. B. and Sacher, E. Kinetics of epoxy cure: 2. The system bisphenol-A diglycidyl ether/polyamide. *Polym.*, **13**, 1972, pp 455-458.
- 144 Ayambem, A., mecham, S. J., Sun, Y., Glass, T. E. and McGrath, J. E. End group substituent effects on the rate/extent of network formation and adhesion for phenylethynyl-terminated poly(arylene ether Sulfone) oligomers. *Polym.*, **41**, 2000, pp 5109 – 5124.

- 145 Schab-Balcerzak, E., Janeczek, H., Kaczmarczyk, B., Bednarski, H., Sk, D. and Miniewicz, A. Epoxy resin cured with diamine bearing azobenzene group. *Polym.*, **45**, 2004, pp 2483-2493.
- 146 Finzel, M. C., Delong, J. and Hawley, M. C. Effect of stoichiometry and diffusion on an epoxy/amine reaction mechanism. *Polym. Sci.: Part A.*, **33**, 1995, pp 673-689.
- 147 George, G. A., Cole-Clarke, P., St. John, N. A. and Friend, G. Real-time monitoring of the cure reaction of a TGDDM/DDS epoxy resin using fibre optic FTIR. *J. App. Polym. Sci.*, **42**, 1991, pp 643-657.
- 148 St John, N.A. and George, G. A. Cure kinetics and mechanisms of a tetraglycidyl-4,4'-diaminodiphenylmethane/diaminodiphenylsulphone epoxy resin using near i.r. spectroscopy. *Polym.*, **33**(13), 1992, pp 2679-2687.
- 149 Crosby, P. *In-situ* cure monitoring of epoxy resin systems. PhD Thesis. Department of Materials Engineering, Brunel University, England. 1997.
- 150 Liu, T. and Fernando, G. F. Processing of polymer composites: an optical fibre-based sensor system for on-line amine monitoring. *Composites: Part A.*, **32**, 2001, pp 1561-1572.
- 151 St John, N. A. and George, G. A. Diglycidyl amine-epoxy resin networks: Kinetics and mechanisms of cure. *Prog. Polym. Sci.*, **19**, 1994, pp 755-795.
- 152 Kozielski, K. A., George, G. A., St John, N. A. and Billingham, N. C. Kinetic studies by FT-NIR of the curing reactions of two glycidyl ether epoxy resins mixed with stoichiometric quantities of 4,4'-DDS. *High Perform. Polym.*, **6**, 1994, pp 263-286.
- 153 Hoffmann, U., Pfeifer, F., Okretic, S., Volkl, N., Zahedi, M. and Siesler, H. W. Rheo-optical Fourier transform infrared and Raman spectroscopy of polymers. *App. Spect.*, **47**(9), 1993, pp 1531-1539.

- 154 Mijovic, J. and Andjelic, S. Monitoring of reactive processing by remote mid infra-red spectroscopy. *Polym.*, **37**(8), 1996, pp 1295-1303.
- 155 Mijovic, J. and Andjeli, S. In situ real-time monitoring of reactive systems by remote fibre-optic-near-infra-red spectroscopy. *Polym.*, **36**(19), 1995, pp 3783-3786.
- 156 Min, B-G, Stachurski, Z. H. and Hodgkin, J. H. Cure kinetics of elementary reactions of a DGEBA/DDS epoxy resin: 1. Glass transition temperature versus conversion. *Polym.*, **34**(23), 1993, pp. 4908-4912.
- 157 Sichina, W. J. Better characterization of thermosets using stepscan DSC. *Thermal Analysis application note*, ParkinElmer™ Instruments.
- 158 Serrano, B., Cabalelas, J. C., González-Benito, J., Baselga, J. and Bravo, J. Pyrene fluorescence as a probe for the monitoring of polymerisation processes: Simultaneous DSC and fluorescence study. *Journal of Fluorescence.*, **7**(4), 1997, pp 341-345.
- 159 Chern, B-C, Moon, T. J., Howell, J. R. and Tan, W. New experimental data for enthalpy of reaction and temperature and degree-of-cure-dependent specific heat and thermal conductivity of the Hercules 3501-6 epoxy system. *J. Comp. Mater.*, **36**, 2002, pp 2061-2073.
- 160 Sickfeld, J., Mielke, W. Application of thermal analysis for the investigation of epoxy resins. *Progress in Organic Coatings.* **12**, 1984, pp 27-116.
- 161 Richardson, M. J. Curing of thermosets in: *Calorimetry and Thermal Analysis of Polymers*, Mathot, V. B. F. Ed. New York: Hanser Publishers, 1993, pp 189-205.
- 162 Fava, R. A. Differential scanning calorimetry of epoxy resins. *Polym.*, **9**, 1968, pp 137-151.
- 163 Prime, R. B., Kichalski, C. and Neag, C. M. Kinetic analysis of a fast reacting thermoset system. *Thermochimica Acta*, **429**, 2005, pp 213-217.

- 164 Roşu, D., Caşcaval, C. N., Mustaţă, F. and Ciobanu, C. Cure kinetics of epoxy resins studied by non-isothermal DSC data. *Termochimica Acta*, **383**, 2002, pp 119-127.
- 165 Lu, M. G., Shim, M. J. and Kim, S. W. Dynamic DSC characterisation of epoxy resin by means of the Avrami equation. *Journal of Thermal Analysis and Calorimetry*, **58**, 1999, pp 701-709.
- 166 Lee, W. I., Loos, A. C. and Springer, G. S. Heat of reaction, degree of cure, and viscosity of Hercules 3501-6 resin. *J Comp. Mater.*, **16**, 1982, pp 510-520.
- 167 Nunez, L., Fraga, F., Fraga, L., Salgado, T. and Anon, R. Determination of the optimum epoxy/curing agent ratio: A study of different kinetic parameters. *Pure & Appl. Chem.*, **67**(7), pp 1091 – 1094.
- 168 Lelli, G., Terenzi, A., Kenny, J. M. and Torre, L. Modelling of the chemo-rheological behavior of thermosetting polymer nanocomposites. *Polym. Comp.*, 2009, DOI 10.1002/pc.20517.
- 169 Montanini, R., D'Acquisto, L. Simultaneous measurement of temperature and strain in glass fibre/epoxy composites by embedded fibre optic sensors: I. Cure monitoring. *Smart Mater. Struct.*, **16**, 2007, pp 1718-1726.
- 170 Roberts, S. S. J. and Davidson, R. Cure and fabrication monitoring of composite materials with fibre-optic sensors. *Comp. Sci. Technol.*, **49**, 1993, pp 265-276.
- 171 Ungarish, M., Joseph, R., Vittoser, J. and Kenig, S. Cure cycle optimization of composites by dielectric measurements. *Composites*, **21**(6), 1990, pp 481-486.
- 172 Delides, C. G., Hayward, D., Pethrick, R. A. and Vatalis, A. S. Real time dielectric investigations of phase separation and cure in rubber modified epoxy resin systems. *Euro. Polym. J.*, **28**(5), 1992, pp 505-512.

- 173 Mijovic, J., Kenny, J. M., Maffezzoli, A., Trivisano, A., Bellucci, F. and Nicolais L. The principles of dielectric measurements for in situ monitoring of composite processing. *Comp. Sci. Technol.*, **49**, 1993, pp 277-290.
- 174 Shtrauss, V. A study on the information capability of dielectric spectra in monitoring nonisothermal cure processes. *Mechanics of Composite Materials*, **38**(2), 2002, pp 181-186.
- 175 Park, J-M, Lee, S-I and Choi, J-H. Cure monitoring and residual stress sensing of single-carbon fibre reinforced epoxy composites using electrical resistivity measurement. *Comp. Sci. Technol.*, **65**, 2005, pp 571-580.
- 176 Park, J-M, Kong, J-W, Kim, D-S and Lee, J-R. Non-destructive damage sensing and cure monitoring of carbon fibre/epoxyacrylate composites with UV and thermal curing using electro-micromechanical techniques. *Comp. Sci. Technol.*, **64**, 2004 pp 2565-2575.
- 177 Kazilas, M. C. and Partridge, I. K. Exploring equivalence of information from dielectric and calorimetric measurements of thermoset cure-a model for the relationship between curing temperature, degree of cure and electric impedance. *Polym.*, **46**, 2005, pp 5868-5878.
- 178 Kim, J. S. and Lee, D. G. Analysis of dielectric sensors for the cure monitoring of resin matrix composite materials. *Sensors and Actuators B*, **30**, 1996, pp 159-164.
- 179 Saliba, T. E., Hofmann, D. and Smolinski, P. Development of an In situ Hall-effect sensor for on-line monitoring of thickness and compaction during composite curing. *Comp. Sci. Technol.*, **51**, 1994, pp 1-9.
- 180 Urabe, K., Okabe, T. and Tsuda, H. Monitoring of resin flow and cure with an electromagnetic wave transmission line using carbon fibre as conductive elements. *Comp. Sci. Technol.*, **62**, 2002, pp 791-797.

- 181 Zimmermann, B, DiFrancia, C, Murphy, K, Vengsarkar, A. and Claus, R. Optical fibre methods for autoclave and epoxy cure monitoring. in: *Review of Progress in Quantitative Nondestructive Evaluation*. Thompson, D. O. and Chimenti, D. E., Eds. 9, New York: Plenum Press, 1990, pp 2047-2053.
- 182 De Vries, M. J., Nasta, M, Patel, J, Kamdar, K, Lowden, R, Stinton, D, Allison, S, Muhs, J. and Claus R.O. Survivability of optical fiber sensor elements embedded in silicone carbide ceramic matrix composites. Smart Sensing, Processing and Instrumentation. *Proc. of SPIE*. **1918**, 1993, pp 55-59.
- 183 Wolfbeis, O. S. Fiber-optic chemical sensors and biosensors. *Anal. Chem.*, **78**, 2006, pp 3859-3874.
- 184 Fernando, G. F. Fibre optic sensor systems for monitoring composite structures. R P Asia 2005 Conference, Reinforced Plastics, Bangkok, December 2005, pp 41-49.
- 185 Fernando, G. F. and Degamber, B. Process monitoring of fibre reinforced composites using optical fibre sensors. *Inter. Mater. Reviews*, **51**(2), 2006, pp 1-42.
- 186 Jenny, R. *Fundamentals of Fiber Optics – An Introduction for beginners*. New York. Co. Inc., 2000.
- 187 Rao, Y-J, Webb, D J, Jacson, D A., Zhang, L and Bennion, I. In-fiber Bragg-grating temperature sensor system for medical applications”, *J of Lightwave Tech.* **15**(5), 1997, pp 779-785.
- 188 Rolfe, P., Scopesi, F. and Serra, G. Advances in fibre-optic sensing in medicine and biology. *Meas. Sci. Technol.*, **8**, 2007, pp 1683-1688.
- 189 Fan, Y and Kahrizi, D A Characterization of FBG strain gauge array embedded in composite structure. *Sensors And Actuators: Part A*, **121**, 2005, pp 297-305.
- 190 Dersey, A. D., Davis, M. D., Patric, J. H., KeBlanc, M. and Koo, K. P. Fiber grating sensors. *J of Lightwave Tech.*, **15**(8), pp 1442-1463.

- 191 Baulsir, C.F. and Simler, R. J. Design and evaluation of IR sensors for pharmaceutical testing. *Advanced Drug Delivery Reviews*. **21**, 1996, pp 191-203.
- 192 Druy, M. A., Glatkowski, P. J. and Stevenson, W. A. Applications of remote fibre optic spectroscopy using IR fibers and Fourier transform infrared spectrometers. *Infrared Fiber Optics III. Proc. of SPIE*. **1591**, 1991, pp 218-224.
- 193 Tan, W., Shi, Z-Y and Kopelman, R Miniaturized fiber-optic chemical sensors with fluorescent dye-doped polymers. *Sensors and Actuators B*, **28**, 1995, pp 157-163.
- 194 DeGrandpre, M. D. and Baehr, M. M. Calibration-free optical chemical sensors. *Anal. Chem.*, **71**, 1999, pp 1152-1159.
- 195 Rogers, D. G., Marand, E., Hill, D. J. T. and George, G. A. Anomalies between microwave and thermal cure kinetics of epoxy-amine resin systems. *High Perform. Polym.*, **11**, 1999, pp 27-39.
- 196 Powell, G. R., Crosby, P. A., Waters, D.N., France, C. M., Spooncer, R. C. and Fernando, G. F. *In-situ* cure monitoring using optical fibre sensors – a comparative study. *Smart Mater. Struct.*, **7**, 1998, pp 557-567.
- 197 Liu, T. and Fernando, G. F. Processing of polymer composites: an optical fibre-based sensor system for on-line amine monitoring. *Composites: A*, **32**, 2001, 1561-1572.
- 198 Nestitt, A., Navabpour, P., Degamber, B., Nightingale, C., Mann, T., Fernando, G. and Day, R. J. Development of a microwave calorimeter for simultaneous thermal analysis, infrared spectroscopy and dielectric measurements. *Meas. Sci. Technol.*, **15**, 2004 pp 2313-2324.
- 199 Zimmermann, B., Bürck, J. and Ache, H-J. Studies on siloxane polymers for NIR-evanescent wave absorbance sensors. *Sensors and Actuators. B*. **41**, 1997, pp 45-54.
- 200 Brown, J. M., Srinivasan, S., Rau, A., Ward, T. C., McGrath, J. E., Loos, A. C., Hood, D. and Kranbeuhl, D. E. Production of controlled networks and morphologies in toughened

- thermosetting resins using real-time, in situ cure monitoring. *Polym.*, **37**(9), 1996, pp 1691-1696.
- 201 Margalit, E., Katzir, A., Dodiuk, H. and Kosower, E. M. Silver halide infrared fibre-optic evanescent wave spectroscopy for in situ monitoring of the chemical processes in adhesive curing. *Surface and Interface Analysis*. **15**(8), 1990, pp 473-478.
- 202 Chailleux, E., Salvia, M., Jaffrezic-Renault, N., Matejec, V. and Kasik, I. In situ study of the epoxy cure process using a fibre-optic sensor. *Smart Mater. Struct.* **10**, 2001, pp 194-202.
- 203 Johnson, F. J., Cross, W. M., Boyles, D. A. and Keller, J. J. "Complete" system monitoring of polymer matrix composites. *Composites: Part A.*, **31**, 2000, pp 959-968.
- 204 Wang, L., Pandita, S.D., Machavaram, V.R., Malik, S., Harris, D. and Fernando, G. F. Characterization of the cross-linking process in an E-glass fibre/Epoxy composite using evanescent wave spectroscopy. *J. Comp. Sci. Technol.*, **69**(13), 2009, pp 2069-2074.
- 205 Wang, L., Malik, S., Harris, D. and Fernando, G. F. Self-sensing composites: in-situ cure monitoring in: International Conference on Smart Materials and Nanotechnology in Engineering, Du, S., Leng, J. and Asundi, A. K. Eds. *Proc. SPIE*, **6423**, 64231F, July 2007, Harbin, China. 2007.
- 206 Connell, M. E., Cross, W. M., Snyder, T. G., Winter, R. M. and Kellar, J. J. Direct monitoring of silane/epoxy interphase chemistry. *Composites Part A.*, **29A**, 1998, pp 495-502.
- 207 Levy, R. L. and Schwab, S. D. Monitoring the composite curing process with a fluorescence-based fiber-optic sensor. *Polym. Comp.*, **12**(2), 1991, pp 96-101.
- 208 Dang, W., Sung, N-H. In-situ cure monitoring of diamine cured epoxy by fibreoptic fluorimetry using extrinsic ractive fluorophore. *Polym. Eng. Sci.*, **34**(9), 1994, pp 707-715.

- 209 Paik, H-J and Sung, N-H. Fibre-optic intrinsic fluorescence for in-situ cure monitoring of amine cured epoxy and composites. *Polym. Eng. Sci.*, **34**(12), 1994, pp. 1025-1032.
- 210 Jessop, J. L., Scranton, A. B. and Blanchard, G. J. In-situ cure monitoring of a vinyl ester polymer using fiber optic fluorescence sensors. *Polym. Mater. Sci. Eng.*, **72**, 1995, pp 58-59.
- 211 Bur, A. J., Wang, F. W., Thomas, C. L. and Rose, J. L. In-line optical monitoring of polymer injection moulding. *Poly. Eng. Sci.* **34**(8), 1994, pp 671-679.
- 212 Woerdeman, D. L. and Parnas, R. S. Cure monitoring in RTM using fluorescence. *Plastics Engineering*, **L1**(10), 1995, pp 25-27.
- 213 Woerdeman, D. L., Flynn, K. M., Dunkers, J. P. and Parnas, R. S. The use of evanescent wave fluorescence spectroscopy for control of the liquid molding process. *Journal of Reinforced Plastics and Composites*, **15**, 1996, pp 922-943.
- 214 Stewart, G. Fiber optic sensors in environmental monitoring in *Optical Fiber Sensor Technology*. Vol. 4. Grattan KTV, Meggitt BT. Eds. Netherlands: Kluwer Academic Publishers, 1999, pp 87-112.
- 215 Cooney, T. F., Kinner, T. and Angel, S. M. Comparative study of some fibre-optic remote Raman probe designs. Part I: Model for liquids and transparent solids. *Applied Spectroscopy*, **50**(7), 1996, pp 836-48.
- 216 DeBakker, C. J., Federicks, P. M. and George, G. A. Fibre optic FT-Raman spectroscopy for the thermal and microwave cure of advanced composite resins. Preliminary studies. 14th Int. Conf. on Raman Spectroscopy. **524**, 1994, pp 702-703.
- 217 Lyon, R. E., Chike, K. E., and Angel, S. M. In situ cure monitoring of epoxy resins using fibre-optic Raman spectroscopy. *J. App. Polym. Sci.* **53**, 1994, pp 1805-1812.

- 218 Aust, J. F., Booksh, K. S., Stellman, C. M., Parnas, R. S. and Myrick, M. L. Use of in situ fibre-optic Raman spectroscopy to replace calorimetry in the monitoring of polymer and composite curing. *Int. J. Vib. Spect.* **1**, 1997, pp 117-128.
- 219 Aust, J. F., Booksh, K. S. and Myrick, M. L. Novel in situ probe for monitoring polymer curing. *Applied Spectroscopy*. **50**(3), 1996, pp 382-387.
- 220 Zimmermann, B., de Vries, M. and Claus, R. Resin sensors for composite cure monitoring. ADPA/AIAA/ASME/SPIE Conference on Active Materials and Adaptive Structures, 1992, pp 313–316.
- 221 Afromowitz, M. A., Lam, K-Y. The optical properties of curing epoxies and applications to the fiber-optic epoxy cure sensor. *Sensors and Actuators*. **A21-A23**, 1990, pp 1107-1110.
- 222 Lam, K-Y. and Afromowitz, M. A. Fibre-optic epoxy composite cure sensor. I. Dependence of refractive index of an autocatalytic reaction epoxy system at 850 nm on temperature and extent of cure. *Applied Optics*. **34**(25), 1995, pp 5635-5638.
- 223 Lam, K-Y., Afromowitz, M. A. Fiber-optic epoxy composite cure sensor. II. Performance characteristics. *Applied Optics*. **34**(25), 1995, pp 5639-5644.
- 224 Fei, L., Aidong, M., Jianyi, L., Kwangsoo, K. and Dongchang, P. Optical fiber sensing method for the in-situ cure monitoring of composite materials. in *Fiber Optic and Laser Sensors XIV*, Ramon P. DePaula; John W. Berthold; Eds. *Proc. SPIE*. **2839**, 1996, pp 413-419.
- 225 Li, C., Cao, M., Wang, R., Wang, Z., Qiao, Y., Wan, L., Tian, Q., Liu, H., Zhang, D., Liang, T. and Tang, C. Fibre-optic composite cure sensor: monitoring the curing process of composite materials based on intensity modulation. *Comp. Sci. Technol.*, ; **63**(12), 2003, pp 1749-1758.

- 226 Lekakou, C., Cook, S., Deng, Y., Ang, T. W. and Reed, G. T. Optical fibre sensor for monitoring flow and resin curing in composite manufacture. *Composites: Part A*. **37**, 2006, pp 934-938.
- 227 Hecht, E. Optics. Second Edition. California, Sddision-Wesley Co. Inc., 1987.
- 228 Liu, Y. M., Ganesh, C., Stelle, J. P. H. and Jones, J. E. Fiber optic sensor development for real-time in-situ epoxy cure monitoring. *J. Comp. Mater.* **31**(1), 1997, pp 87-102.
- 229 Giordano, M., Nicolais, L., Calabro, A. M., Cantoni, S., Cusano, A., Breglio, G. and Cutolo, A. A fibre optic thermoset cure monitoring sensor. *Polym. Comp.*, **21**(4), 2000, pp 523-530.
- 230 Cusano, A., Cutolo, A., Giordano, M. and Nicolais, L. Optoelectronic refractive index measurements: Application to smart processing. *IEEE Sensors Journal*. **3**(6), 2003, pp 781-787.
- 231 Sanderson, J. M., May, S. G., Murphy, K. A. and Claus, R. O. Multiuse extrinsic sensor for material evaluation. Distributed and Multiplexed Fiber Optic Sensors IV, Alan D. Kersey; John P. Dakin; Eds. *Proc. SPIE*. **2294**, 1994, pp 153-164.
- 232 Michie, W. C., Thursby, G., Johnstone, W. and Culshaw, B. Optical techniques for determination of the state of cure of epoxy resin based systems. Int. Conf. on Fiber Optic Smart Structures and Skins V. *Proc. SPIE*. **1798**, 1992, pp 11-18.
- 233 Cong, J., Zhang, X., Chen, K. and Xu, J. Fibre optic Bragg grating sensor based on hydrogels for measuring sailinity. *Sensors and Actuators B*, **87**, 2002, pp 487-490.
- 234 Falate, R., Kamikawachi, R. C., Muller, M., Kalinowski, H. J. and Fabris, J. L. Fiber optic sensors for hydrocarbon detection. *Sensors and Actuators B*, **105**, 2005, pp 430-436.
- 235 Merzbacher, C. I., Kersey, A. D. and Friebele, E. J. Fiber optic sensors in Concrete structures: a review. *Smart Mater. Struct.*, **5**, 1996, pp 196-208.
- 236 Rao, Y-J. In-fibre Bragg grating sensors. *Meas. Sci. Technol.* **8**, 1997, pp 355-375.

- 237 Buggy, S. J., Chehura, E., James, S. W. and Tatam, R. P. Optical fibre grating refractometers for resin cure monitoring. *Journal of Optics A: Pure and Applied Optics*. **9**(6), 2007; S60.
- 238 Dunphy, J. R., Meltz, G., Lamm, E. P. and Morey, W. W. Multi-function, distributed optical fibre sensor for composite cure and response monitoring. Fiber Optic Smart Structures and Skins III. *Proc. of SPIE*. **1370**, 1990, pp 116-118.
- 239 Murukeshan, V. M., Chan, P. Y., Ong, L. S., Seah, L. K. Cure monitoring of smart composites using fiber Bragg grating based embedded sensors. *Sensors and Actuators*, **79**, 2000, pp 153-161.
- 240 Harsch, M., Karger-Kocsis, J. and Herzog, F. Influence of cure regime on the strain development in an epoxy resin as monitored by a fibre Bragg grating sensor. *Macromol. Mater. Eng.* **292**, 2007, pp 474-483.
- 241 Dunkers, J. P., Lenhart, J. L., Kueh, S. R., Van Aanten, J. H., Advani, S. G. and Parnas R. S. Fiber optic flow and cure sensing for liquid composite moulding. *Optics and Lasers in Engineering*, **35**, 2001, pp 91-104.
- 242 O'Dwyer, M. J., Maistros, G. M., James, S.W., Tatam, R. P. and Partridge, I. K. Relating the state of cure to the real-time internal strain development in a curing composite using in-fibre Bragg gratings and dielectric sensors. *Meas. Sci. Technol.*, **9**, 1998, pp 1153-1158.
- 243 Lou, K-A., Zimmermann, B. and Yaniv, G. Combined sensor system for process and in-service health monitoring of composite structures. Smart Structures and Materials 1994: Smart Sensing, Processing, and Instrumentation, Sirkis JM; Ed. *Proc. SPIE*, **2191**, 1994, pp 32-45.

- 244 Becker, O., Varley, R. J. and Simon, G. P. Thermal stability and water uptake of high performance epoxy layered silicate nanocomposites. *Euro. Polym. J.*, **40**, 2004, pp 187-195.
- 245 Morel, E., Bellenger, V. and Verdu, J. Structure-water absorption relationships of amine-cured epoxy resins. *Polym.*, **26**, 1985, pp 1719-1724.
- 246 Soles, C. L., Chang, F. T., Bolan, B. A., Hristov, H. A., Gidley, D. W. and Yee, A. F. Contributions of the nanovoid structure to the moisture absorption properties of epoxy resins. *J. Polym. Sci. Part B: Polym. Phys.*, **36**, 1998, pp 3035-3048.
- 247 Soles, C. L., Chang, F. T., Gidley, D. W., Yee, A. F. Contributions of the nanovoid structure to the kinetics of moisture transport in epoxy resins. *J. Polym. Sci. Part B: Polym. Phys.*, **38**(5), 2000, pp 776-791.
- 248 Soles, C. L., Yee, A. F. A discussion of the molecular mechanisms of moisture transport in epoxy resins. *J. Polym. Sci. Part B: Polym. Phys.*, **38**(5), 2000, pp 792-802.
- 249 Li, L., Liu, M. and Li, S. Morphology effect on water sorption behaviour in a thermoplastic modified epoxy resin system. *Polym.*, **45**, 2004, pp 2837-2842.
- 250 Zhou, J. and Lucas, J. P. Hygrothermal effects of epoxy resin: Part I: the nature of water in epoxy. *Polym.*, **40**, 1999, pp 5505-5512.
- 251 Apicella, A., Tessieri, R. and Cataldis, C. D. Sorption Modes of Water in Glassy Epoxies. *Journal of Membrane Science*, **18**, 1984, pp 211-225.
- 252 Peppas, N. A., Meadows, D. L. Macromolecular structure and solute diffusion on membranes: An overview of recent theories. *Journal of Membrane Science*, **16**, 1983, pp 361-377.
- 253 Frisch, H. L. Sorption and transport in glassy polymers – A review. *Polym. Eng. Sci.*, **20**(1), 1980, pp 2-13.
- 254 Vieth, W.R. *Diffusion in and through polymers*. Munich: Hanser Publishers, 1991.

- 255 Shen, C-H, Springer, G. S. Moisture absorption and desorption of composite materials. *J.Comp. Mater.*, **10**, 1976, pp 2-20.
- 256 Loos, A. C., Springer, G. S. Moisture absorption of graphite-epoxy composites immersed in liquids and in humid air. *J.Comp. Mater.*, **13**, 1979, pp 131-147.
- 257 Zanni-Deffarges, M. P. and Shanahan, M. E. R. Diffusion of water into an epoxy adhesive: comparison between bulk behaviour and adhesive joints. *Int. J. Adhesion and Adhesives*, **15**, 1995, pp 137-142.
- 258 Laoubi, S. and Vergnaud, J. M. Modelling the process of absorption and desorption of water by coating made of epoxy resin. *Eur. Polym. J.*, **26**(12), 1990, pp 1359-1364.
- 259 Jost, W. *Diffusion in solids, liquids, gases*. New York: Academic Press Inc. Publishers, New York, 1952, pp 2-25.
- 260 Crank, J. *The Mathematics of Diffusion*. 2nd Ed. New York: Oxford University Press, 1975.
- 261 Tang, J. M. and Springer, G. S. Effects of moisture and temperature on the compressive and short beam shear properties of Fiberite T300/976 fabric. *Journal of Reinforced Plastic and Composites*, **7**, 1988, pp 120-135.
- 262 Singh, K. S., Singh, P. N. and Rao, R. M. V. G. K. Hygrothermal effects on chopped fibre/woven fabric reinforced epoxy composites. Part A: Moisture absorption characteristics. *Journal of Reinforced Plastics and Composites*, **10**, 1991, pp 446-456.
- 263 Bonniau, P. and Bunsell, A. R. A comparative study of water absorption theories applied to glass epoxy composites. *J. Comp. Mater.*, **15**, 1981, pp 272-293.
- 264 Loos, A. C., Springer, G. S., Sanders, B.A. and Tung, R. W. Moisture absorption of polyester-E glass composites. *J. Comp. Mater.*, **14**, 1980, pp 142-154.
- 265 Dewimille, B. and Bunsell, A. R. The modelling of hydrothermal aging in glass fibre reinforced epoxy composites. *J. Phys. D: Appl. Phys.*, **15**, 1982, pp 2079-2091.

- 266 Neogi, P. *Transport phenomena in polymer membranes, Diffusion in Polymers*, New York: Marcel Dekker Inc., pp 173-209.
- 267 Apicella, A., Nicolais, L., Astarita, G. and Drioli, E. Effect of thermal history on water sorption, elastic properties and the glass transition of epoxy resins. *Polymer*, **20**, 1979, pp 1143-1148.
- 268 Roy, S., Xu, W. X., Park, S. J. and Liechti, K. M. Anomalous moisture diffusion in viscoelastic polymers: modelling and testing. *Journal of Applied Mechanics*, **67**, 2000, pp 392-396.
- 269 Aditya, P. K. and Sinha, P. K. Effects of fiber shapes on moisture diffusion coefficients. *J. of Reinforced Plastics and Composites*, **12**, 1993.
- 270 Pogany, G. A. Anomalous diffusion of water in glassy polymers. *Polymer*, **17**, 1976.
- 271 Papanicolaou, G. C. and Pappa, A. Water sorption and temperature effects on the dynamic mechanical behaviour of epoxy-matrix particulates. *Journal of Materials Science*, **27**, 1992, pp 3889-3896.
- 272 Carter, H. G. and Kibler, K. G. Langmuir-type model for anomalous moisture diffusion in composite resins. *Journal of Composite Materials*, **12**, 1978, pp 118-131.
- 273 Popineau, S., Rondeau-Mouro, C., Sulpice-Gaillet, C. and Shanahan, M. E. R. Free/bound water absorption in an epoxy adhesive. *Polymer*, **46**, 2005, pp 10733-10740.
- 274 Marsh, L. L., Lasky, R., Seraphim, D. P. and Springer, G. S. Moisture solubility and diffusion in epoxy and epoxy glass composites. *J Res. Develop.*, **28**(6), 1984, pp 655-661.
- 275 William, D. Callister, Jr., *Materials Science and Engineering – An Introduction* (3rd Ed.), John Wiley & Sons Inc., 1994, pp 98-99.
- 276 Li, Y. and Unsworth, J. Effect of physical aging on dielectric, thermal and mechanical properties of cast-epoxy insulators. *IEEE Transactions on Dielectrics and Electrical Insulations*, **1**(1), 1994, pp 9-17.

- 277 Abdelkader, A. F. and White, J. R. Water absorption in epoxy resins: The effects of the cross-linking agent and curing temperature. *J. App. Polym. Sci.*, **98**, 2005, pp 2544-2549.
- 278 Han, S. O. and Drzal, L. T. Water absorption effects on hydrophilic polymer matrix of carboxyl functionalised glucose resin and epoxy resin. *Euro. Polym. J.*, **39**, 2003, pp 1791-1799.
- 279 Wu, L., Hoa, S. V. and Ton-That, M. T. Effects of water on the curing and properties of epoxy adhesive used for bonding FRP composite sheet to concrete. *J. App. Polym. Sci.*, **92**(4), 2004, pp 2261-2268.
- 280 Chen, J., Nakamura, T., Aoki, K., Aoki, Y. and Utsunomiya, T. Curing of epoxy resin contaminated with water. *J. App. Polym. Sci.*, **79**, 2001, pp 214-220.
- 281 Adams, D. F. and Miller, A. K. Hygrothermal microstresses in a unidirectional composite exhibiting inelastic material behaviour. *J. Comp. Mater.*, **11**, 1977, pp 285-299.
- 282 Chen, R. S., Chen, G. S. and Chen, J. R. The effect of environmental humidity after post cure on the optimal temperature path of polymer composites. *Comp. Struct.*, **25**, 1993, pp 101-111.
- 283 Xiao, G. Z. and Shanahan, M. E. R. Water absorption and desorption in an epoxy resin with degradation. *J. Polym. Sc. Part B: Polym. Phys.*, **35**, 1997, pp 2659-2670.
- 284 Xiao, G. Z. and Shanahan, M. E. R. Swelling of DGEBA/DDA epoxy resin during hygrothermal ageing. *Polym.*, **39**(14), 1998, pp 3253-3260.
- 285 Lin, Y. C. and Chen, X. Investigation of moisture diffusion in epoxy systems: Experimental and molecular dynamic simulations. *Chemical Physics Letters*, **412**, 2005, pp 322-326.
- 286 Papanicolaou, G. C., Kosmidou, Th W., Vatalis, A. S. and Delides, C. G. Water absorption mechanism and some anomalous effects on the mechanical and viscoelastic behavior of an epoxy system. *J. App. Poly. Sci.*, **99**, 2006, pp 1328-1339.

- 287 Artemov, D. Y., Samoilenko, A. A. and Iordanskii, A. L. Study of diffusion of water in polyamide-6 using nuclear magnetic resonance intrascopy. *Polymer Science USSR*, **31** (12), 1989, pp 2709-2713.
- 288 VanLandingham, M. R., Eduljee, R. F. and Gillespie, J. W. Jr., Moisture diffusion in epoxy systems. *J. App. Polym. Sci.*, **71**, 1999, pp 787-798.
- 289 Jeffey, K. and Pethrick, R. A. Influence of chemical structure on free volume in epoxy resins: A positron annihilation study. *Euro. Polym. J.*, **30**(2), 1994, pp 153-158.
- 290 Barrie, J. A., Sagoo, P. S. and Johncock, P. The sorption and diffusion of water in halogen-containing epoxy resins. *Polym.*, **26**, 1985, pp 1167-1171.
- 291 Barrie, J. S., Sagoo, P. S. and Johncock, P. The sorption and diffusion of water in epoxy resins. *J. Membrane Sci.*, **18**, 1984, pp 197-210.
- 292 Lin, Y. C. and Chen, X. Moisture sorption-desorption-resorption characteristics and its effect on the mechanical behavior of the epoxy system. *Polym.*, **46**, 2005, pp 11994-12003.
- 293 Kasturiarachchi, K. A. and Pritchard, G. Water absorption of glass/epoxy laminates under bending stresses. *Composites*, **14**(3), 1983, pp 244-250.
- 294 Costa, M. L., De Almeida, S. F. M. and Rezende, M. C. Hygrothermal effect on dynamic mechanical analysis and fracture behaviour of polymeric composites. *Materials Research*, **8**(3), 2005, pp 335-340.
- 295 Arribas, C., Sepúlveda, L., Salom, C., Masegosa, R. M. and Prolongo, M. G. Morphology effect on the hydrothermal ageing of a thermoplastic modified epoxy thermoset. *Polym. Eng. Sci.*, **47**(6), 2007, pp 960-968.
- 296 Apicella, A., Migliaresi, C., Nicodemo, L., Nicolais, L., Iaccarino, L. and Roccotelli, S. Water sorption and mechanical properties of a glass-reinforced polyester resin. *Composites*, 1982, pp 406-410.

- 297 Zhou, J. and Lucas, J. P. Hygrothermal effects of epoxy resin. Part II: variations of glass transition temperature. *Polym.*, **40**(20), 1999, pp 5513-5522.
- 298 Carter, H. G. and Kibler, K. G. Entropy model for glass transition in wet resins and composites. *J. Comp. Mater.*, **11**, 1977, pp 265-275.
- 299 Bellenger, V., Verdu, J., Francillette, J., Hoarau, P. and Morel, E. Infra-red study of hydrogen bonding in amine-crosslinked epoxies. *Polym.*, **28**, 1987, pp 1079-1086.
- 300 Chateauminois, A., Vincent, L., Chabert, B. and Soulier, J. P. Study of the interfacial degradation of a glass-epoxy composite during hygrothermal ageing using water diffusion measurements and dynamic mechanical thermal analysis. *Polym.*, **35**(22), 1994, pp 4766-4774.
- 301 Manfredi, L. B., Fraga, A. N. and Vázquez, A. Influence of the network structure and void content on hygrothermal stability of resol resin modified with epoxy-amine. *J. App. Polym. Sci.*, **102**, 2006, pp 588-597.
- 302 Ivanova, K. I., Pethrick, R. A. and Affrossman, S. Investigation of hydrothermal ageing of a filled rubber toughened epoxy resin using dynamic mechanical thermal analysis and dielectric spectroscopy. *Polym.*, **41**, 2000, pp 6787-6796.
- 303 Apicella, A., Nicolais, L., Astarita, G. and Drioli, E. Hygrothermal history dependance of equilibrium moisture sorption in epoxy resins. *Polym.*, **22**, 1981, pp 1064-1067.
- 304 Pogany, G. A. The α relaxation in epoxy resins. *Euro. Polym.*, **6**, 1970, pp 343-353.
- 305 Jordan, C., Galy, J. and Pascault, J. P. Comparison of microwave and thermal cure of an epoxy/amine matrix. *Polym. Eng. Sci.*, **35**(3), 1995, pp 233-239.
- 306 Pogany, G. A. Gamma relaxation in epoxy resins and related polymers. *Polym.*, **11**, 1970, pp 66-78.

- 307 Li, G., Lee-Sullivan, P. and Thring, R. W. Determination of activation energy for glass transition of an epoxy adhesive using dynamic mechanical analysis. *J. Thermal Analysis and Calorimetry*, **60**, 2000, pp 377 – 390.
- 308 Zarrelli, M., Skordos, A. A. and Partridge, I. K. Thermomechanical analysis of a toughened thermosetting system. *Mechanics of Composite Materials*, **44**(2), 2008, pp 181-190.
- 309 Lee, M. C. and Peppas, N. A. Water transport in graphite/epoxy composites. *J. App. Polym. Sci.*, **47**, 1993, pp 1349-1359.
- 310 Ishisaka, A. and Kawagoe, M. Examination of the time-water content superposition on the dynamic viscoelasticity of moistened polyamide 6 and epoxy. *J. App. Polym. Sci.*, **93**, 2004, pp 560-567.
- 311 Gates, T. S. On the use of accelerated test methods for characterization of advanced composite materials. *NASA report NASA/TP-2003-212407*, Hampton, Virginia, 2003.
- 312 DéNeve, B. and Shanahan, M. E. R. Water absorption by an epoxy resin and its effect on the mechanical properties and infra-red spectra. *Polym.*, **34**(24), 1993, pp 5099-5105.
- 313 Karad, S. K., Attwood, D. and Jones, F. R. Moisture absorption by cyanate ester modified epoxy resin matrices. Part IV: Effect of curing schedules. *Polym. Comp.*, **24**(4), 2003, pp 567-576.
- 314 Akay, M., Kong, A., Mun S., and Stanley, A. Influence of moisture on the thermal and mechanical properties of autoclaved and oven-cured kevla-49/epoxy laminates. *Comp. Sci. Technol.*, **57**, 1997, pp 565-571.
- 315 Dušek, K., Pleštil, J., Lednický, F. and Luňák, S. Are cured epoxy resins inhomogeneous?. *Polym.*, **19**, 1978, pp 393-397.

- 316 Chateauminois, A., Chabert, B., Soulier, J. P. and Vincent, L. Dynamic mechanical analysis of epoxy composites plasticized by water: Artifact and reality. *Polym. Comp.*, **16**(4), 1995, pp 288 – 296.
- 317 Li, Y., Miranda, J. and Sue, H. J. Hygrothermal diffusion behaviour in bismaleimide resin. *Polym.*, **42**, 2001, pp 7791-7799.
- 318 Lin, Y. C., Xu, C., Zhang, H. J. and Wang, Z. P. Effects of hygrothermal aging on epoxy-based anisotropic conductive film. *Materials Letters*, **60**, 2006, pp 2958-2963.
- 319 Lachenal, G. Dispersive and Fourier transform near-infrared spectroscopy of polymeric materials. *Vibrational Spectroscopy*, **9**, 1995, pp 93-100.
- 320 Pereira, M. R. and Yarwood, J. ATR-FTIR spectroscopic studies of the structure and permeability of sulfonated poly(ether sulfone) membranes Part 1. interfacial water-polymer interaction. *Journal of Chemical Society, Faraday Transactions*, **92**(15), 1996, pp 2731-2735.
- 321 Öhman, M., Persson, D. and Leygraf, C. In situ ATR-FTIR studies of the aluminium/polymer interface upon exposure to water and electrolyte. *Progress in Organic Coatings*, **57**, 2006, pp 78-88.
- 322 Wu, P. and Siesler, H. W. Water diffusion into epoxy resin: a 2D correlation ATR-FTIR investigation. *Chemical Physics Letters*, **374**, 2003, pp 74-78.
- 323 Fieldson, G. T. and Barbari, T. A. The use of FTIR-a.t.r spectroscopy to characterize penetrant diffusion in polymers. *Polym.*, **34**(6), 1993, pp 1146-1153.
- 324 Cotugno, S., Larobina, D., Mensitieri, G., Musto, P. and Ragosta, G. A novel spectroscopic approach to investigate transport processes in polymers: the case of water-epoxy system. *Polym.*, **42**, 2001, pp 6431-6438.

- 325 Mensitieri, G., Lavorgna, M., Musto, P. and Ragosta, G. Water transport in densely crosslinked networks: A comparison between epoxy systems having different interactive characters. *Polym.*, **47**, 2006, pp 8326-8336.
- 326 Musto, P., Martuscelli, E., Ragosta, G. and Russo, P. The curing process and moisture transport in a tetrafunctional epoxy resin as investigated by FT-NIR spectroscopy. *High Performance Polymers*, **12**, 2000, pp 155-168.
- 327 Yamazoe, N. and Shimizu, Y. Humidity sensors: Principles and applications. *Sensors and Actuators B*, **10**, 1986, pp 379-398.
- 328 Golnabi, H. and Azimi, P. Design and performance of a plastic optical fibre leakage sensor. *Optics & Laser Tech.*, **39**, 2007, pp 1346-1350.
- 329 Arregui, F. J., Ciaurriz, A., Oneca, M. and Matias, I. R. An experimental study about hydrogels for the fabrication of optical fibre humidity sensors. *Sensors and Actuators B*, **96**, 2003, pp 165-172.
- 330 Ansari, Z. A., Karekar, R. N. and Aiyer, R. C. Humidity sensor using planar optical waveguides with cladding of various oxide materials. *Thin solid Films*, **305**, 1997, pp 330-335.
- 331 Shula, S. K., Parashar, G. K., Mishra, A. P., Misra, P., Yadav, B. C., Shukla, R. K., Bali, L. M. and Dubey, G. C. Nano-like magnesium oxide films and its significance in optical fibre humidity sensor. *Sensors and Actuators B*, **98**, 2004, pp 5-11.
- 332 Slavik, R., Homola, J. and Ctyroky, J. Miniaturization of fibre optic surface plasmon resonance sensor. *Sensors and Actuators B*, **51**, 1998, pp 311-315.
- 333 Dhawan, A. and Muth, J.F. Engineering surface Plasmon based fibre-optic sensors. *Mater. Sci. Eng. B* (2007), doi:10.1016/j.mseb.2007.09.076

- 334 Corres, J. M., Arregui F. J. and Matias, I. R. Sensitivity optimization of tapered optical fibre humidity sensors by means of tuning the thickness of nanostructured sensitive coatings. *Sensors and Actuators B*, **122**, 2007, pp 442-449.
- 335 Russel, A. P. and Fletcher, K. S. Optical sensor for the determination of moisture. *Analytica Chimica Acta*, **170**, 1985, pp 209-216.
- 336 Posch, H. E. and Wolfbeis, O. S. Optical sensors, 13: Fibre-optic humidity sensor based on fluorescence quenching. *Sensors and Actuators B*, **15**, 1988, pp 38-77.
- 337 Choi, M. M. F. and Tse, O. L. Humidity-sensitive optode membrane based on a fluorescent dye immobilized in gelatine film. *Analytica Chimica Acta*, **378**, 1999, pp 127-134.
- 338 Zanjanchi, M. A. and Sohrabnezhad, S. Evaluation of methylene blue incorporated in zeolite for construction of an optical humidity sensor. *Sensors and Actuators B*, **105**, 2005, pp 502-507.
- 339 Potyrailo, R. A., Szumlas, A. W., Danielson, T. L., Johnson, M. and Hieftje, G. M. A dual-parameter optical sensor fabricated by gradient axial doping of an optical fibre. *Meas. Sci. Technol.*, **16**, 2005, pp 235-241.
- 340 Tao, S., Winstead, C. B., Jindal, R. and Singh, J. P. Optical-fiber sensor using tailored porous sol-gel fibre core. *IEEE Sensors J.*, **4**(3), 2004, pp 322-328.
- 341 Gaston, A., Lozano, I., Perez, F., Auza, F. and Sevilla, J. Evanescent wave optical fiber sensing (temperature, relative humidity and pH sensors). *IEEE Sensors*, **3**(6), 2003, pp 806-811.
- 342 Vijayan, A., Fuke, M., Hawaldar, R., Kulkarni, M., Amalnerkar, D. and Aiyer, R. C. Optical fibre based humidity sensor using Co-polyaniline clad. *Sensors and Actuators B*, 2007, doi:10.1016/j.snb.2007.07.113.

- 343 Gupta, B. D. and Rathnanjali, A novel probe for a fiber optic humidity sensor. *Sensors and Actuators B*, **80**, 2001, pp 132-135.
- 344 Khijwania, S. K., Srinivasan, K. L. and Singh, J. P. An evanescent-wave potical fiber relative humidity sensor with enhanced sensitivity. *Sensors and Actuators B*, **104**, 2005, pp 217-222.
- 345 Otsuki, S., Adachi, K. and Taguchi, T. A novel fiber-optic gas-sensing configuration using extremely curved optical fibers and an attempt for optical humidity detection. *Sensors and Actuators B*, **53**, 1998, pp 91-96.
- 346 Lomer, M., Arrue, J., Jauregui, C., Aiestaran, P., Zubia, J. and Lopez-Higuera, J. M. Lateral polishing of bends in plastic optical fibres applied to a multipoint liquid-level measurement sensor. *Sensors and Actuators A*, **137**, 2007, pp 68-73.
- 347 Khijwania, S. K. and Gupta, B. D. Maximum achievable sensitivity of the fibre optic evanescent field absorption sensor based on the U-shaped probe. *Optics Communications*, **175**, 2000, pp 135-137.
- 348 Arregui, F. J., Liu, Y., Matias, I. R. and Claus, R. O. Optical fibre humidity sensor using a nano Fabry-Perot cavity formed by the ionic self-assembly method. *Sensors and Actuators B*, **59**, 1999, pp 54-59.
- 349 Tan, K. M., Tay, C. M., Tjin, S. C., Chan, C. C. and Rahardjo, H. High relative humidity measurements using gelatine coated long-period grating sensors. *Sensors and Actuators B*, **110**, 2005, pp 335-541.
- 350 Liu, Y., Wang, L., Zhang, M., Tu, D., Mao, X. and Liao, Y. Long-period grating relative humidity sensor with hydrogel coating. *IEEE Photonics Tech. Letters*, **19**(12), 2007, pp 880-882.
- 351 Wang, L., Liu, Y., Zhang, M., Tu, D., Mao, X. and Liao, Y. Relative humidity sensor using a hydrogel coated Long-period grating. *Meas. Sci. Tech.*, **18**, 2007, pp 3131-3134.

- 352 Huang, X. F., Sheng, D. R., Cen, K. F. and Zhou, H. Low-cost relative humidity sensor based on thermoplastic polyimide-coated fibre Bragg grating. *Sensors and Actuators B*, **127**, 2007, pp 518-524.
- 353 Yeo, T. L., Sun, T., Grattan, K. T. V., Parry, D, Lade, R and Powell, B. D. Polymer-coated fibre Bragg grating for relative humidity sensing. *IEEE Sensors J.*, **5**(5), 2005, pp 1082-1089.
- 354 Yeo, T. L., Cox, M. A. C., Boswell, L. F., Sun, T. and Grattan, K. T. V. Monitoring ingress of moisture in structural concrete using a novel optical-based sensor approach. *Journal of Physics: Conference Series*, **45**, 2006, pp 186-192.
- 355 Eftimov, T. A. and Bock, W. J. A simple multifunctional fibre optic level/moisuture/vapour sensor using large-core quartz polymer fiber pairs. *IEEE Transactions on Instrumentation and measurement*, **55**(6), 2006, pp 2080-2087.
- 356 Mahendran, R. S., Chen, R., Wang, L., Pandita, S. D., Machavaram, V. R., Kukureka, S. N. and Fernando, G. F. Chemical process monitoring and the detection of moisture ingress in composites. In SPIE/Smart Structures and Materials & Nondestructive Evaluation and Health Monitoring 2008: Smart Sensor Phenomena, Technology, Networks, and Systems, Ecke, W., Peters, K.J. and Meyendorf, N.G., *Proc SPIE*, **6933**, 69330R, March 2008, San Diego, CA, USA, 2008.
- 357 Mahendran, R.S., Wang, L., Machavaram, V.R., Pandita, S.D., Chen, R., Kukureka, S.N., Fernando, G.F. Fibre-optic sensor design for chemical process and environmental monitoring. *Optics and Lasers in Engineering*, **47**, 2009, pp 1069–1076.
- 358 Mahendran R. S., Chen, R, Kukureka, S. N., Fernando, G. F. Monitoring and modelling the diffusion profile in a thermosetting resin in: SPIE/Smart Structures and Materials & Nondestructive Evaluation and Health Monitoring 2009: Smart Sensor Phenomena,

- Technology, Networks, and Systems, Meyendorf, N.G., Peters, K.J. and Ecke, W. *Proc. SPIE*, **7293**, 729319, March 2009, San Diego, CA, USA, 2009.
- 359 Sheshnev, A., Bormashenko, E., Reiclin, J. and Pogreb, R. Mathematical simulation of water and benzene penetration in thin polystyrene films and experimental investigation of the mass transport processes by FEWS-FTIR spectroscopy procedure², *Int. Conf. on Mathematical Modelling and Simulation of Metal Technologies*, MMT-2000, Israel, Nov. 13-15, 2000.
- 360 Texier, S. and Pamukcu, S. Fiber optic sensor for distributed liquid content quantification in subsurface. *6th Int. Symp. On Field Measurements in Geomechanics*, NGI, Oslo, Norway, 2003.
- 361 Lyons, W. B., Ewald, E., Flanagan, C. and Lewis, E. A multi-point optical fibre sensor for condition monitoring in process water systems based on pattern recognition. *Measurement*, **34**, 2003, pp. 301-312.
- 362 Etches, J. A. and Fernando, G. F. Evaluation of embedded optical fibre sensors in composites: EFPI sensor fabrication and quasi-static evaluation. *Polymer Composites*; 2008.
- 363 Druy, M. A. Applications of IR transmitting fibres in *Infrared Fibre Optics*. Sanghera, J. S. and Aggrawal, I. D. Eds. Washington, CRC Press, 1998, pp 305-323.
- 364 Claus, R. O., Bennett, K. D., Vengsarkar, A. M. and Murphy, K. A. Embedded optical fibre sensors for material evaluation. *Journal of Nondestructive Evaluation*, **8**(2), 1989, pp 135-145.
- 365 Archibald, D. D., Lin, L. T. and Honigs, D. E. Remote near-IR spectroscopy over an optical fiber with a modified FT spectrometer. *Applied Spectroscopy*, **42**(3), 1988, pp 468-472.
- 366 Harrington, J. A. *Infrared Fibers and Their Application*. Washington, SPIE Press, 2004.

- 367 Machavaram, V. R., private communication, 2007.
- 368 Griffiths, P. R. and Dahm, D. J. Continuum and discontinuum theories of diffuse reflectance in: *Handbook of near-infrared analysis*. 3rd Edition. Burn, D. A. and Ciurczak, E. W. Eds. Florida, CRC Press, 2008, pp 22-62.
- 369 Griffiths, P. R. and DE Haseth, J. A. *Fourier Transform Infrared Spectrometry*. 2nd Edition., USA, John Wiley & Sons, Inc. pp 349-361.
- 370 Mahendran, R. S., Harris, D., Wang, L., Machavaram, V. R., Chen, R., Kukureka, S. N., and Fernando, G. F. Fibre optic sensor design for chemical process and environmental monitoring. Int. Conf. Smart Materials and Nanotechnology in Engineering, Du, S., Leng, J. and Asundi, A. K. Eds. *Proc. SPIE*, **6423**, 64232S, Nov. 1, 2007.
- 371 Fernando, G. F., Crosby, P. A. and Liu, T. The application of optical fiber sensors in advanced fiber reinforced composites. Part 1. Introduction and issues. In: Grattan, K. T. V. and Meggitt, B. T. Eds. *Optical Fiber Sensor Technology Volume 3*. Kluwer Academic Publishers, Netherlands, 1999, pp 25 – 56.
- 372 Crosby, P. A. and Fernando, G. F. The application of optical fiber sensors in advanced fiber reinforced composites. Part 2. Cure monitoring. In: Grattan, K. T. V. and Meggitt, B. T. Eds. *Optical Fiber Sensor Technology Volume 3*. Kluwer Academic Publishers, Netherlands, 1999, pp 57 – 86.
- 373 Liu, T. and Fernando, G. F. The application of optical fiber sensors in advanced fiber reinforced composites. Part 3. Strain, temperature and health monitoring. In: Grattan, K. T. V. and Meggitt, B. T. Eds. *Optical Fiber Sensor Technology Volume 3*. Kluwer Academic Publishers, Netherlands, 1999, pp 87 – 130.
- 374 Camacho, W., Hedenqvist, M. S. and Karlsson, S. Near infrared (NIR) spectroscopy compared with thermogravimetric analysis as a tool for on-line prediction of water diffusion in polyamide 6,6. *Polym. Int.*, **51**(12), 2002, pp 1366-1370.

- 375 Mahendran, R. S., Machavaram, V. R., Wang, L., Burns, J. M., Harris, D., Kukureka, S. N., Fernando, G. F. A novel multifunctional fibre optic sensor. SPIE/Smart Structures and Materials & Nondestructive Evaluation and Health Monitoring 2009: Smart Sensor Phenomena, Technology, Networks, and Systems, Meyendorf, N.G. Peters, K.J. and Ecke, W. *Proc. SPIE*, **7293**, 72930C, March 2009, San Diego, CA, USA (2009).
- 376 Machavaram, V.R., Mahendran, R. S., Wang, L., Chen, R., Kukureka S.N. and Fernando, G.F. Cure monitoring and water ingress detection using a low-cost fibre-optic sensor. *16th Annual International Conference on Composites/Nanoengineering (ICCE-16)*, Kunming, China, 20 July, 2008.
- 377 Dannenberg, H. Determination of functional groups in epoxy resins by near-infrared spectroscopy. *Polym. Eng. Sci.*, 1963; 3(1): 78 – 88.
- 378 Wang, L., Machavaram, V. R., Mahendran, R., Harris, D., Pandita, S. D., Tomlin, A., Redmore, E., Malik, S. A., Fernando, G. F. A comparison of cure monitoring techniques. Sensors and Smart Structures Technologies for Civil, Mechanical, and Aerospace Systems 2009, Tomizuka, M. *Proc. SPIE*, **7292**, 729213, March 2009, San Diego CA, USA. 2009.
- 379 Macan, J., Brnardić, I., Ivanković, M. and Mencer, H. J. DSC study of cure kinetics of DGEBA-based epoxy resin with poly(oxypropylene)diamine. *Journal of Thermal analysis and Calorimetry*, **81**, 2005, pp 369-373.
- 380 The impact of temperature and phosphor concentration on the refractive index of LED encapsulants. http://www.lrc.rpi.edu/programs/solidstate/cr_impact.asp
- 381 Ltzenkirchen-Hecht, D. and Frahm, R. Structural investigations of sputter deposited thin films: reflection mode EXAFS, specular and non specular X-ray scattering. *Physica B*, **283**, 2000, pp. 108-113.
- 382 <http://www.ealingcatalog.com/pdf/Coatings.pdf>
- 383 http://www.lasergold.com/laser_properties.ssi#reflectivity

- 384 Leng, J. and Asundi, A. Structural health monitoring of smart composite materials by using EFPI and FBG sensors. *Sensors and Actuators. A*, **103**, 2003, pp 330-40.
- 385 Zhao, W., Wang, J., Wang, A. and Claus, R. O. Geometric analysis of optical fibre EFPI sensor performance: *Technical Note. Smart Mater. Struct.*, **7**, 1998, pp 907-910.
- 386 Liu, T., Brooks, D., Martin, A., Badcock, R., Ralph, B., Fernando, G. F. A multi-mode extrinsic Fabry-Perot ineterferometric strain sensor. *Smart Mater. Struct.*, **6**, 1997, pp 464-469.
- 387 Yoon, H-J., Costantini, D. M., Limverger, H. G., Salathe, R. P., Kim, C-G. and Michaud, V. In situ train and temperature monitoring of adaptive composite materials. *J. Intelligent material systems and structures*. **17**, 2006, pp 1059-1067.
- 388 Pal, S., Mandal, J., Sun, T., Grattan, K. T. V., Fokine, M., Carlsson, F., Fonjallaz, P.Y., Wade, S. A. and Collins, S. F. Characteristics of potential fibre Bragg grating sensor-based devices at elevated temperatures. *Meas. Sci. Technol.*, **14**, 2003, pp 1131-1136.
- 389 MS9710B Optical Spectrum Analyser, Operation Manual, Document No.: M-W1283AE-15.0.
- 390 FBG Interrogation System IS7000, Operation Manual.
- 391 Cavaleiro, P. M., Araújo, F. M., Ferreira, L. A., Santos, J. L. and Farahi, F. Simultaneous measurement of strain and temperature using Bragg gratings written in germanosilicate and Boron-codoped Germanosilicate fibres. *IEEE Photonics Technology Letters*, **11**(2), 1999, pp 1635 – 1637.
- 392 Pal, S., Sun, T., Grattan, K. T. V., Wade, S. A., Collins, S. F., Baxter, G. W., Dussardier, B. And Monnom, G. Non-linear temperature dependence of Bragg gratings written in different fibres, optimised for sensor applications over a wide range of temperatures. *Sensors and Actuators A*, **112**, 2004, pp 211 - 219.

- 393 Yeo, T. L., Sun, T., Grattan, K. T. V., Parry, D., Lade, R. And Powell, B. D.
Characterisation of a polymer-coated fibre Bragg grating sensor for relative humidity sensing. *Sensors and Actuators B*, **110**, 2005, pp 148 - 155.
- 394 Yoon, H-J, Costantini, D. M., Limverger, H. G., Salathe, R. P., Kim, C-G and Michaud, V. In situ strain and temperature monitoring of adaptive composite materials. *Journal of Intelligent material systems and structures*, **17**, 2006, pp 1059-1067.
- 395 De Oliveira, R., Lavanchy, S., Chatton, R., Costantini, D., Michaud, V., Salath, R. and Mnson J. –A. E. Experimental investigation of the effect of the mould thermal expansion on the development of internal stresses during carbon fibre composite processing. *Composites: Part A*, **39**, 2008, pp 1083 – 1090.
- 396 Rysman, J-F. And Nikogosyan, D. N. Thermal sensitivity studies of fibre Bragg gratings inscribed by high-intensity femtosecond UV laser pulses. *Optics Comm.*, **282**, 2009, pp 1120-1122.
- 397 Harris, D. and Fernando, G. F. Simultaneous acquisition of data of refractive index, strain, temperature and cross-linking kinetics. Int. conf. on Composite Materials: ICCM-17, July 2009, Edinburgh, United Kingdom, 2009.
- 398 Park, S. O., Jang, B. W., Lee, Y. G., Kim, C. G. and Park, C. Y. Simultaneous measurement of strain and temperature using a reverse index fibre Bragg grating sensor. *Meas. Sci. Technol.*, **21**, 2010, 035703(8pp).
- 399 Mahendran, R. S., Machavaram, V. R., Wang L., Kukureka, S. N., Paget, M., Fernando, G. F. A novel multi-measurand fibre optic sensor. 16th Annual International Conference on Composites/Nanoengineering (ICCE-16), Kunming, China, 20 July 2008.
- 400 Mahendran, R. S., Machavaram, V. R., Wang L., Nair, A. K. R., Burns, J. M., Kukureka, S. N. and Fernando, G. F. A novel multi-functional sensor design for process monitoring. Int. Conf. On Composite Materials: ICCM-17, July 2009, Edinburgh, England, 2009.

- 401 Vieth, W. R. *Diffusion in and through polymers*. Munich, Hanser Publishers, 1991.
- 402 Fujita, H. Organic vapours above the glass transition temperature. In: *Diffusion in Polymers*, Crank, J. and Park, G. S., Eds. London, Academic Press, 1968, pp 75-104.
- 403 Maggana, C. and Pissis, P. Water sorption and diffusion studies in an epoxy resin system. *J. Polym. Sci.: Part B: Polym. Phys.*, **37**, 1999, pp 1165-1182.
- 404 Nakamura, K., Ueda, T., Hosono, S. and Maruno, T. Theoretical analysis of the decay of shear strength of adhesion in metal/epoxy/metal joints in an aqueous environment. *Int. J. Adhesion and Adhesives*, **7**(4), 1987, pp 209-212.
- 405 Shen, C-H. and Springer, G. S. Effects of moisture and temperature on the tensile strength of composite materials. *J. Comp. Mater.*, **11**, 1977, pp 2-16.
- 406 Whiteside, J. B., DeJasi, R. J. and Schulte, R. L. Measurement of preferential moisture ingress in composite wing/spar joints. *Comp. Sci. Technol.*, **24**, 1985, pp 123-145.
- 407 Nakamura, K., Maruno, T., Sasaki, S. Theory for the decay of the wet shear strength of adhesion and its application to metal/epoxy/metal joints. *International Adhesion and Adhesives*, **7**(2), 1987, pp 97-102.
- 408 Laoubi, S., Vergnaud, J. M. Effect of temperature on the transfer between epoxy coatings and water. *Euro. Polym. J.*, **27**(12), 1991, pp 1425-1429.
- 409 Carter, H. G. and Kibler, K. G. Rapid moisture-characterization of composites and possible screening applications. *J. Comp. Mater.*, **10**, 1976, pp 355-370.
- 410 Miller, R. K. Multi-material model moisture analysis for steady-state boundary conditions in: *Environmental Effects on Composite Materials – Volume 2*, Springer, G. S. Ed. Technomic Publishing Inc., 1984, pp 162-169.
- 411 Wapner, K., Grundmeier G. Spatially resolved measurements of the diffusion of water in a model adhesive/silicon lap joint using FTIR-transmission-microscopy. *International Journal of Adhesion & Adhesives*, **24**, 2004, pp 193-200.

- 412 Tay, A. A. O. and Lin, T. Y. Moisture diffusion and heat transfer in plastic IC packages. *IEEE – InterSociety Conference on Thermal Phenomena*, 1996, pp 67-73.
- 413 Duncan, B., Urquhart, J. and Roberts, S. Review of measurement and modelling of permeation and diffusion in polymers. *NPL Report DEPC MPR 012*, Middlesex, England, 2005.
- 414 Newill, J. F., McKnight, S. H., Hoppel, C. P. R., Cooper, G. R. and Berman, M. S. Theoretical evaluation of moisture protection using coatings. *ARL-TR-2016 Report*, Army Research Laboratory, 1999.
- 415 Laoubi, S., Vergnaud, J. M. Modelling the process of absorption and desorption of water by coatings made of epoxy resins. *Euro. Polym. J.*, **26**(12), 1990, pp 1359-1364.
- 416 Özisik, M. N. *Finite difference methods in heat transfer*. Boca Raton: CRC Press, 1994.
- 417 Smith, G. D. *Numerical solution of partial differential equations*. London: Oxford University Press, 1965, pp 9-54.
- 418 Gordon, J. M., Rouse, G. B., Gibbs, J. H. and Risen, W. M. Jr. The composition dependence of glass transition properties. *J. Chem. Phys.*, **66**(11), 1977, pp 4971-4976.
- 419 Couchman, P. R. and Karasz, F. E. A classical thermodynamic discussion of the effect of composition on glass-transition temperatures. *Macromolecules*, **11**(1), 1978, pp 117-119.
- 420 Bower, D. I. *An Introduction to Polymer Physics*. Cambridge: Cambridge University Press, 2002, pp 187-219.
- 421 Feng, J., Gerger, K. R. and Douglas, E. P. Water vapor transport in liquid crystalline and non-liquid crystalline epoxies. *J. Mater. Sci.*, **39**, 2004, pp 3413-3423.
- 422 Ping, Z. H., Nguyen, Q. T., Chen, S. M., Zhou, J. Q. and Ding, Y. D. States of water in different hydrophilic polymers – DSC and FTIR studies. *Polym.*, **42**, 2001, pp 8461-8467.
- 423 Olmos, D., López-Morón, R. and González-Benito, J. The nature of the glass fibre surface and its effect in the water absorption of glass fibre/epoxy composites. The use of

- fluorescence to obtain information at the interface. *Comp. Sci. Technol.*, **66**, 2006, pp 2758-2768.
- 424 Musto, P., Ragosta, G., Scarinzi, G., Mascia, L. Probing the molecular interactions in the diffusion of water through epoxy and epoxy-bismaleimide networks. *J. Polym. Sci. Part B: Polym. Phys.*, **40**(10), 2002, pp 922-938.
- 425 Gopalan, R., Somashekar, B.R. and Dattaguru, B. Environmental effects on fibre-polymer composites. *Polymer Degradation and Stability*, **24**, 1989, pp 361-371.
- 426 Karalekas, D., Cugnoni, J., Botsis, J. Monitoring of hygrothermal ageing effects in an epoxy resin using FBG sensor: A methodological study. *Comp. Sci. Technol.*, **69**, 2009, pp 507-514.
- 427 Hahn, H. T. Residual stresses in polymer matrix composite laminates. *J. Comp. Mater.*, **10**, 1976, pp 266-278.
- 428 Chang, T-W., Tsai, C-L., Yeh, W. and Cheng, J-J. Tracking the moisture expansion of carbon/epoxy composite exposed to varying humidity. *J. Comp. Mater.*, **42**(5), 2008, pp 431-446.
- 429 Tsai, C-L., Hung, I-T. and Chang, T-W. Characterisation of principle diffusivities of composite by suspension method. *Comp. Sci. Technol.*, **66**, 2006, pp 2837-2843.
- 430 Chen, Y., Xia, Z. and Ellyin, F. Evolution of residual stresses induced during curing processing using a viscoelastic micromechanical model. *J. Comp. Mater.*, **35**(6), 2001, pp 522-542.
- 431 Li, Y., Miranda, J. and Sue, H-J. Hygrothermal diffusion behaviour in bismaleimide resin. *Polym.*, **42**, 2001. pp 7791-7799.

Appendix – I

I Ray optic theory of fibre-optic near-infrared transmission spectroscopy

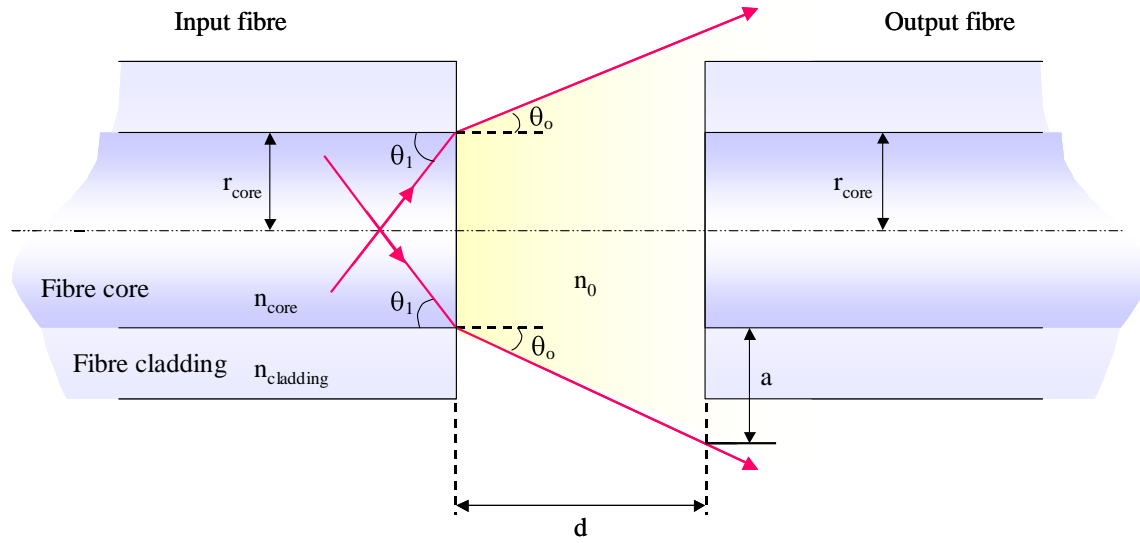


Figure I.1 Schematic illustration of refraction of IR beam at the cleaved fibre interface.

The Figure 4.1 illustrates the ray-optic approach for transmission of IR radiation at a sensing cavity of step-index multimode fibres. Let us consider there is an analyte in the sensing cavity with absorption, A at wavelength, λ and $P_o(\lambda)$ is the power of the IR radiation leaving from the fibre core interface with radius, r_{core} . Then according to the Beer-Lambert law (see Section 4.1.1), the power of the IR radiation at a distance, d along the fibre axis can be expressed as [367]:

$$P_1(\lambda) = \frac{P_o(\lambda)}{10^A}$$

Equation I.1

where $P_1(\lambda)$ is power at a distance, d . If another step-index multimode fibre with radius r_{core} , is brought to the distance, d along the fibre axis, then the power of IR beam, $P_2(\lambda)$ that couples into the second fibre (output fibre) can be expressed by considering the fresnel reflections [82] at the analyte/fibre interface:

$$P_2(\lambda) = P_1(\lambda) \left[1 - \left(\frac{n_0 - n_{core}}{n_0 + n_{core}} \right)^2 \right] \quad \text{Equation I.2}$$

where n_o and n_{core} are refractive indices of the analyte and the fibre core, respectively. However $P_2(\lambda)$ represents the power distributed within the boundary of cone of acceptance at distance, d . The radius of the cone at distance d , $r_{c,d}$ can be expressed as [82]:

$$r_{c,d} = r_{core} + a = r_{core} + d \tan \theta_0 \quad \text{Equation I.3}$$

$$\tan \theta_0 = \tan \left(\sin^{-1} \left(\frac{NA}{n_0} \right) \right)$$

where NA is numerical aperture of the step-index multimode fibre and can be expressed as below:

$$NA = \sqrt{n_{core}^2 - n_{cladding}^2}$$

Therefore, the fraction of the power of IR radiation, $P_3(\lambda)$ that coupling into the output fibre is given by:

$$P_3(\lambda) = \left(\frac{r_{core}}{r_{core} + d \tan \theta_0} \right) P_2(\lambda) \quad \text{Equation I.4}$$

Considering Equation I.1 - I.4, $P_3(\lambda)$ can be written as:

$$P_3(\lambda) = \frac{1}{10^A} \left[1 - \left(\frac{n_0 - n_{core}}{n_0 + n_{core}} \right)^2 \right] \left(\frac{r_{core}}{r_{core} + d \tan \theta_0} \right) P_0(\lambda) \quad \text{Equation I.5}$$

$$P_3(\lambda) = f(n_0, A, d) P_0(\lambda) \quad \text{Equation I.6}$$

where $f(n_0, A, d)$ is a function of refractive index of the analyte, absorbance at λ and distance between input and output fibres at a given time.

Appendix – II

II Ray optic theory of fibre-optic near-infrared reflectance spectroscopy

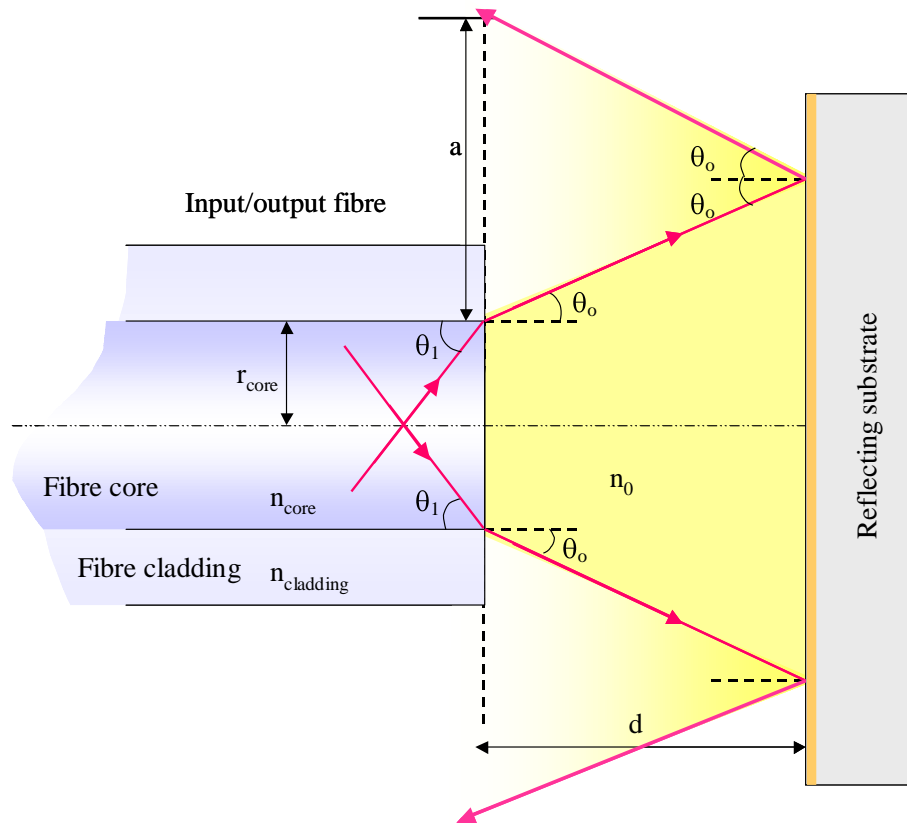


Figure II.1 Schematic illustration of ray-optic approach for specular reflection of IR radiation at the fibre-optic sensing cavity.

The Figure 4.3 illustrates the ray-optic approach for specular reflection of IR radiation at a sensing cavity of step-index multimode fibres. Let us consider there is an analyte in the sensing cavity with absorption, A at wavelength, λ and $P_o(\lambda)$ is the power of the IR radiation emerging from the fibre core interface with radius, r_{core} . It was demonstrated that basis for

transmission spectroscopy can be applied for the ray optic characteristics of the fibre-optic reflectance spectroscopy. Then (see Appendix-I), the power of the IR radiation at a distance, d along the fibre axis can be expressed as:

$$P_1(\lambda) = \frac{P_0(\lambda)}{10^A} \quad \text{Equation II.1}$$

where $P_1(\lambda)$ is power at a distance, d . If a reflective substrate, is brought to the distance, d perpendicular to the fibre axis, the loss of absorbance (A_{refl}) at the reflector can be expressed as [367]:

$$A_{refl} = 10 \log \frac{P_2(\lambda)}{P_1(\lambda)} \quad \text{Equation II.2}$$

where $P_2(\lambda)$ is the power of IR radiation, that reflects at the reflective surface and $P_2(\lambda)$ can be expressed as:

$$P_2(\lambda) = P_1(\lambda) 10^{\frac{A_{refl}}{10}} \quad \text{Equation II.3}$$

Then the fraction of power of reflected IR radiation at distance, d from the reflector, $P_3(\lambda)$ can be written as (see Appendix-I).

$$P_3(\lambda) = \frac{P_2(\lambda)}{10^A} \quad \text{Equation II.4}$$

The power of reflected IR radiation at the analyte/fibre interface, $P_4(\lambda)$ due to the presence of the fibre at distance, d can be expressed as:

$$P_4(\lambda) = P_3(\lambda) \left[1 - \left(\frac{n_0 - n_{core}}{n_0 + n_{core}} \right)^2 \right] \quad \text{Equation II.5}$$

where n_o and n_{core} are refractive indices of the analyte and the fibre core, respectively. However $P_4(\lambda)$ represents the power distributed within a boundary of cone of reflection at distance, d (see Figure 4.3). According to the law of reflection at the reflective surface, the radius of the cone of reflected radiation at distance d , $r_{c,d}$ can be expressed as [227]:

$$r_{c,d} = r_{core} + a = r_{core} + 2d \tan \theta_0 \quad \text{Equation II.6}$$

$$\tan \theta_0 = \tan \left(\sin^{-1} \left(\frac{NA}{n_0} \right) \right)$$

where NA is numerical aperture of the step-index multimode fibre.

Therefore, the fraction of the power of IR radiation, $P_5(\lambda)$ that coupling back to the fibre is given by:

$$P_5(\lambda) = \left(\frac{r_{core}}{r_{core} + 2d \tan \theta_0} \right) P_4(\lambda) \quad \text{Equation II.7}$$

Then considering Equation II.1 - II.7, $P_5(\lambda)$ can be written as:

$$P_5(\lambda) = 10^{\left(\frac{A_{refl}}{10} - 2A \right)} \left[1 - \left(\frac{n_0 - n_{core}}{n_0 + n_{core}} \right)^2 \right] \left(\frac{r_{core}}{r_{core} + 2d \tan \theta_0} \right) P_0(\lambda) \quad \text{Equation II.8}$$

Assuming constant reflectivity within the near-IR wavelength range and at the experimental conditions studied, $P_5(\lambda)$ can be written as:

$$P_5(\lambda) = f(n_0, A, d) P_0(\lambda) \quad \text{Equation II.9}$$

where

$$f(n_0, A, d) = 10^{\left(\frac{A_{refl}}{10} - 2A\right)} \left[1 - \left(\frac{n_0 - n_{core}}{n_0 + n_{core}} \right)^2 \right] \left(\frac{r_{core}}{r_{core} + 2d \tan \theta_0} \right)$$

$f(n_0, A, d)$ is a function of refractive index of the analyte, absorbance at λ and distance between the input/output fibre and the reflector at a given time.

Appendix – III

III Integral solution for kinetic model used for cross-linking kinetics

The modified extended Kamal model that used for obtaining cross-linking kinetics of the LY3505/XB3403 resin system is given as:

$$\frac{d\alpha}{dt} = (k_1 + k_2\alpha^{0.5})(\alpha_{\max} - \alpha)^{1.5} \quad \text{Equation III.1}$$

where $d\alpha/dt$ is the rate of reaction, and k_1 , k_2 , m and n are rate constants and reaction orders, respectively. α_f is optimum conversion and α is conversion at time t . Then the integral of Equation III.1 can be written as:

$$\int_0^{\alpha} \frac{d\alpha}{k_1 + k_2\alpha^{0.5} (\alpha_f - \alpha)^{1.5}} = \int_0^t dt \quad \text{Equation III.2}$$

Considering left-hand side of Equation III.2, I_1 can be defined as:

$$I_1 = \int_0^{\alpha} \frac{d\alpha}{k_1 + k_2\alpha^{0.5} (\alpha_f - \alpha)^{1.5}} \quad \text{Equation III.3}$$

$$\begin{aligned}
&= \left[\frac{d\alpha}{k_1 + k_2 \alpha^{0.5} \alpha_f - \alpha^{1.5}} \right]_0^\alpha - \int_0^\alpha \frac{1}{k_1 + k_2 \alpha^{0.5}} d \alpha_f - \alpha^{1.5} \\
&= \left[\frac{d\alpha}{k_1 + k_2 \alpha^{0.5} \alpha_f - \alpha^{1.5}} \right]_0^\alpha + \frac{1}{2} \int_0^\alpha \frac{d\alpha}{k_1 + k_2 \alpha^{0.5} \alpha_f - \alpha^{0.5}} \\
&= \left[\frac{d\alpha}{k_1 + k_2 \alpha^{0.5} \alpha_f - \alpha^{1.5}} \right]_0^\alpha + \frac{1}{2} I_2
\end{aligned}$$

Equation III.4

I_2 can be defined as below:

$$I_2 = \int_0^\alpha \frac{d\alpha}{k_1 + k_2 \alpha^{0.5} \alpha_f - \alpha^{0.5}}$$

Equation III.5

$$\sqrt{\alpha_f} I_2 = \int_0^c \frac{d\alpha}{k_1 + k_2 \alpha^{0.5} \left(1 - \alpha/\alpha_f\right)^{0.5}}$$

By substituting, $\sqrt{1 - \alpha/\alpha_f} = \cos \theta$, Equation III.5 Can be re-written as bellow:

$$\frac{I_2}{2\sqrt{\alpha_f}} = \int_0^{\pi/2} \frac{\sin \theta}{k_1 + k_2 \sqrt{\alpha_f} \sin \theta} d\theta$$

Then the solution of Equation III.5 is given as:

$$\frac{I_2}{2\sqrt{\alpha_f}} = \frac{\sqrt{1 - \alpha/\alpha_f}}{k_1 + k_2\sqrt{\alpha_f - \alpha}} - \frac{1}{k_2\sqrt{\alpha_f}} \ln |k_1 + k_2\sqrt{\alpha_f - \alpha}| \quad \text{Equation III.6}$$

By substituting solution for the I_1 , the solution for Equation III.2 can be written as:

$$t = \frac{1}{k_1\alpha_f^{1.5}} - \frac{1}{k_1 + k_2\sqrt{\alpha_f}} \frac{1}{\alpha_f - \alpha} + \frac{1}{2} I_2 \quad \text{Equation III.7}$$

Where solution for the integral I_2 , is given below:

$$I_2 = \frac{\sqrt{\alpha_f}}{k_1 + k_2\sqrt{\alpha_f}} - \frac{\sqrt{\alpha_f}}{k_2} \ln |k_1 + k_2\sqrt{\alpha_f}| - \frac{\sqrt{\alpha_f - \alpha}}{k_1 + k_2\sqrt{\alpha_f - \alpha}} + \ln |k_1 + k_2\sqrt{\alpha_f - \alpha}|$$

Appendix - IV

Publications produced during the thesis

Major findings presented in this thesis were published in the following publications [P1-P7].

In addition to the main content of this thesis, five papers were published, which involved developing a broad spectrum of fibre-optic sensors for process monitoring and life assessment of composites. These papers are listed below in [P8-P12] and include studies in the area of self-sensing using reinforcing fibres [P8], strain transfer in fibre Bragg gratings [P9], comparison of fibre sensing techniques [P10], concept of self-healing and self-sensing composites [P11] and low-cost spectroscopic sensors [P12].

First author journal papers

- [P1] Mahendran, R. S., Wang, L., Machavaram, V. R., Chen, R., Kukureka, S. N. and Fernando, G. F., “*Fibre optic sensor design for chemical process and environmental monitoring*”, Optics and Laser Engineering, 47, 1069-1076, (2009).

First author conference papers

- [P2] Mahendran, R. S., Machavaram, V. R., Wang L., Nair, A. K. R., Burns, J. M., Kukureka, S. N. and Fernando, G. F., “*A novel multi-functional sensor design for process monitoring*” Int. Conf. On Composite Materials: ICCM-17, July 2009, Edinburgh, UK (2009).

- [P3] Mahendran, R. S., Chen, R., Kukureka, S. N. and Fernando, G. F., "*Monitoring and modeling the diffusion profile in a thermosetting resin*" in SPIE/Smart Structures and Materials & Nondestructive Evaluation and Health Monitoring 2009: Smart Sensor Phenomena, Technology, Networks, and Systems, edited by Norbert G. Meyendorf, Kara J. Peters, Wolfgang Ecke, Proceedings of SPIE Vol. 7293, 729319, March 2009, San Diego, CA, USA (2009).
- [P4] Mahendran, R. S., Machavaram, V. R., Wang, L., Burns, J. M., Harris, D., Kukureka, S. N. and Fernando, G. F., "*A novel multifunctional fibre optic sensor*" in SPIE/Smart Structures and Materials & Nondestructive Evaluation and Health Monitoring 2009: Smart Sensor Phenomena, Technology, Networks, and Systems, edited by Norbert G. Meyendorf, Kara J. Peters, Wolfgang Ecke, Proceedings of SPIE Vol. 7293, 72930C, March 2009, San Diego, CA, USA (2009).
- [P5] Mahendran, R., Chen, R., Wang, L., Pandita, S. D., Machavaram, V. R., Kukureka, S. N., Fernando, G. F., "Chemical process monitoring and the detection of moisture ingress in composites" in SPIE/Smart Structures and Materials & Nondestructive Evaluation and Health Monitoring 2008: Smart Sensor Phenomena, Technology, Networks, and Systems, edited by Wolfgang Ecke, Kara J. Peters, Norbert G. Meyendorf, Proceedings of SPIE Vol. 6933, 69330R, March 2008, San Diego, CA, USA (2008).
- [P6] Mahendran, R. S., Machavaram, V. R., Wang L., Kukureka, S. N., Paget, M. and Fernando, G. F., "*A novel multi-measurand fibre optic sensor*", 16th Annual

International Conference on Composites/Nanoengineering (ICCE-16), Kunming, China, 20 July (2008).

- [P7] Mahendran, R. S., Harris, D., Wang, L., Machavaram, V. R., Chen, R., Kukureka, S. N. and Fernando, G. F., "*Fibre optic sensor design for chemical process and environmental monitoring*" in International Conference on Smart Materials and Nanotechnology in Engineering, edited by Shanyi Du, Jinsong Leng, Anand K. Asundi, Proceedings of SPIE Vol. 6423, 64232S, July 2007, Harbin, China (2007).

Other conference papers

- [P8] Malik, S. A., Wang, L., Mahendran, R. S., Harris, D., Ojo, S. O., Collins, D., Paget, M., Pandita, S. D., Machavaram, V. R. and Fernando, G. F., "*In-situ damage detection using self-sensing composites*" eds. Tomizuka M., Proceedings of SPIE/Sensors and Smart Structures Technologies for Civil, Mechanical, and Aerospace Systems, Vol. 7292, 729204, March 2009, San Diego CA, USA. (2009).

- [P9] Malik, S. A., Mahendran, R. S., Harris, D., Paget, M., Pandita, S. D., Machavaram, V. R., Collins, D., Burns, J. M., Wang, L. and Fernando, G. F., "*Finite element modelling of fibre Bragg grating sensors and experimental validation*", eds. Tomizuka M., Proceedings of SPIE/Sensors and Smart Structures Technologies for Civil, Mechanical, and Aerospace Systems, Vol. 7292, 72921V, March 2009, San Diego CA, USA. (2009).

- [P10] Wang, L., Machavaram, V. R., Mahendran, R. S., Harris, D., Pandita, S. D., Tomlin, A., Redmore, E., Malik, S. A., Fernando, G. F., "*A comparison of cure monitoring*

techniques" in Sensors and Smart Structures Technologies for Civil, Mechanical, and Aerospace Systems 2009, edited by Masayoshi Tomizuka, Proceedings of SPIE Vol. 7292, 729213, March 2009, San Diego CA, USA. (2009).

[P11] Harris, D., Mahendran, R. S., Brooks, D., Al-Khodairi, F. A., Machavaram, V. R., Reynolds, P., Wang, L., Pandita, S. D., Paget, M., Wedderburn, J., Malik, S. A., Ojo, S. O., Kukureka, S. N., Fernando, G. F., "*Self-sensing, self-healing, and crack-arrestor composites*" in SPIE/Smart Structures and Materials & Nondestructive Evaluation and Health Monitoring 2009: Smart Sensor Phenomena, Technology, Networks, and Systems, edited by Norbert G. Meyendorf, Kara J. Peters, Wolfgang Ecke, Vol. 7293, 72930P, March 2009, San Diego, CA, USA (2009).

[P12] Machavaram, V. R., Mahendran, R. S., Wang, L., Chen, R., Kukureka, S. N. and Fernando, G. F., "*Cure monitoring and water ingress detection using a low-cost fibre-optic sensor*", 16th Annual International Conference on Composites/Nanoengineering (ICCE-16), Kunming, China, 20 July (2008).